2013

Granular mixing visualization and quantification in a double screw mixer

Todd Arnold Kingston
Iowa State University

Granular mixing visualization and quantification in a double screw mixer

by

Todd A. Kingston

A thesis submitted to the graduate faculty

in partial fulfillment of the requirements for the degree of

MASTER OF SCIENCE

Major: Mechanical Engineering

Program of Study Committee:

Theodore J. Heindel, Major Professor

Robert C. Brown

Thomas J. Brumm

Iowa State University

Ames, Iowa

2013

TABLE OF CONTENTS

LIST OF FIGURES

LIST OF TABLES

NOMENCLATURE

Abbreviations

1D	One-dimensional
2D	Two-dimensional
3D	Three-dimensional
AC	Alternating current
ASME	American Society of Mechanical Engineers
ASTM	American Society for Testing and Materials
ANOVA	Analysis of variance
CCD	Charge-coupled device
CFL	Compact fluorescent lamp
CO_2	Carbon dioxide
CoR	Co-rotating
CoV	Coefficient of variation
CT	Computed tomography
CtrR	Counter-rotating
CtrR DP	Counter-rotating down-pumping
CtrR UP	Counter-rotating up-pumping
DC	Direct current
DEM	Distinct element method
DOE	Design of experiments

ECT	Electrical capacitance tomography
EIT	Electrical impedance tomography
ERT	Electrical resistance tomography
FBP	Filtered-back-projection
FEDSM	Fluids Engineering Division Summer Meeting
FPS	Frames per second
GB	Glass beads
GHG	Greenhouse gas
GLCM	Gray-level co-occurrence matrix
GPU	Graphics processing unit
HD	High definition
HVAC	Heating, ventilation, and air-conditioning
ISU	Iowa State University
ISU BRL	Iowa State University Biorenewable Research Laboratory
ISU CNDE	Iowa State University Center for Nondestructive Evaluation
LHT	Left hand thread
MRI	Magnetic resonance imaging
NEMA	National Electrical Manufacturers Association
OOI	Object of interest
PEPT	Positron emission particle tracking
PIV	Particle image velocimetry
PVC	Polyvinyl chloride
RGB	Red, green, blue

RHT	Right hand thread
RO	Red oak chips
RSD	Relative standard deviation
RSS	Root sum of squares
SOP	Standard operating procedure
SO_x	Sulfur oxides
UCT	Ultrasonic computed tomography
XCT	X-ray computed tomography
XFloViz	X-ray flow visualization
XPTV	X-ray particle tracking velocimetry

Roman Symbols

A	Hamaker constant
a	Sieve opening
A_c	Cross-sectional area
A_s	Surface area
b	Particle breadth
D	Diameter
d	Distance
D_h	Hydraulic diameter
F_E	Electrostatic force
F_L	Liquid bridge force
F_V	van der Waals force

H/D	Dimensionless bed height
I	X-ray attenuation
I_0	Emitted X-ray energy
I_s	Intensity of segregation
l	Length
L/D	Dimensionless mixing length
L_c	Characteristic length
M	Mean concentration
m_i	Mass of i^{th} sample
N	Total number of samples
n	Sample number
p	Pressure
p/D	Dimensionless screw pitch
p_C	Capillary pressure
P_w	Wetted perimeter
q	Particle charge
r	Distance between particles
s^2	Composition variance
s_w^2	Weighted composition variance
t	Thickness
U	Fluid velocity
V	Velocity
v	Volume

V_A	Axial velocity
V_p	Particle volume
V_R	Rotational velocity
x	Mixture composition
$\overline{x_w}$	Mass weighted mean mixture composition
z	Particle surface roughness

Greek Symbols

α	Main-effect term associated with factor one
β	Main-effect term associated with factor two
δ	Main-effect term associated with factor three
γ	Two-way, three-way or four-way interaction term
ε	Random deviation from the true treatment mean
	Porosity or void fraction
ε_0	Dielectric constant
ℓ	X-ray path length
μ	Mean response over all levels of factors
	Viscosity
	Linear X-ray absorption coefficient
$\mu \rho^{-1}$	Mass absorption coefficient
Ψ	Sphericity
ρ	True density
ρ_B	Bulk density

ρ_f	Fluid density
ρ_{mix}	True mixture density
τ	Main-effect term associated with factor four
σ	Surface tension
	Standard deviation
σ^2	Variance of sampled data
σ_0^2	Variance of fully segregated state
σ_r^2	Variance of random samples
ω	Screw rotation speed

ACKNOWLEDGEMENTS

I would first like to thank my advisor, Dr. Theodore Heindel, for providing me with this research opportunity in the Experimental Multiphase Flow Laboratory at Iowa State University, and for his advice, guidance, and support throughout this project.

I would also like to thank Dr. Robert Brown and Dr. Thomas Brumm for serving on my program of study committee. Moreover, I would like to thank Dr. Brown's research group and the faculty and staff at Iowa State University's Bioeconomy Institute and Center for Sustainable Environmental Technologies for their collaboration throughout this project.

Thank you to my labmates, especially David Escudero and Timothy Morgan, for their assistance and advice throughout this project, and for their friendship.

Thank you to all the undergraduate research assistants, David Doan, Taylor Geick, Roslyn Melookaran, and Teshia Robinson, for their help in all facets of this project.

I am truly appreciative of all the knowledge, support, and advice I have been given from the faculty and staff at Iowa State University throughout my undergraduate and graduate education. Iowa State University is truly a great university with wonderful people and facilities.

Finally, a special thank you to my wife, Jessica, and my family for their love, support, encouragement, and patience.

This research project is partially based upon work supported by Phillips 66 Company, which is gratefully acknowledged. The X-ray Flow Visualization Facility that

was used in this project was funded by the National Science Foundation under award number CTS-0216367.

ABSTRACT

Granular mixing has a significant influence on the resulting products in a variety of industries, such as pharmaceutical production, food processing, and energy generation. Most commonly, granular mixing processes seek a high degree of homogeneity, and in some particular instances, the purpose is to influence simultaneous processing, such as chemical reactions and heat and/or mass transfer rates. Granular mixing is a complex process because it exhibits multiple rheological differences, many times simultaneously within the same granular bed. A fundamental problem commonly encountered during the mixing of granular materials is the tendency for mixtures to segregate due to differences in particle size, shape, and/or density. While significant effort has been made to improve the granular mixing process, the vast majority of granular mixing research efforts have focused on relatively simple mixer geometries and idealized granular materials compared to what is actually used in industrial practice. For example, the renewable energy industry, or more specifically the biomass thermochemical conversion sector, relies on double screw pyrolyzers to convert cellulosic biomass into bio-oil. Currently, there is a large amount of research that relates the feedstocks being used to the bio-oil yields; however, minimal research efforts have been directed toward studying the granular mixing dynamics inside the double screw pyrolyzer due to the opaque nature of the reactor and the granular flow itself.

The overall goal of this project is to thoroughly understand, characterize, and optimize the granular mixing of low density red oak chips and high density glass beads within a double screw mixer, which geometrically replicates screw pyrolyzers, under

various operating conditions. Moreover, it aims to provide an improved understanding of the biomass and heat carrier media granular mixing dynamics inside the screw pyrolyzer. The increased mixing effectiveness and insight gained through this project will lead to increased heat transfer rates and could enhance product yield and/or quality; thereby improving the economic viability of a screw pyrolyzer.

Throughout this project, a number of different visualization and quantification techniques have been developed and used to evaluate the mixing effectiveness of red oak chips and glass beads inside a screw mixer that was designed and constructed specifically for granular mixing studies. Four parameters were initially investigated: (i) screw rotation speed, (ii) dimensionless screw pitch, (iii) screw rotation orientation, and (iv) material injection configuration. After identifying the influence that these parameters had on the mixing effectiveness, the effect of the dimensionless mixing length was also investigated.

Advanced optical visualization methods were first developed by capturing, and then spatially aligning and temporally syncing four independent projections of the screw mixer. Next, an improved granular sampling procedure which satisfies the two “golden rules of sampling” was developed. Composition analysis of the samples was then coupled to analysis of variance (ANOVA) statistical methods to qualitatively assess the spatial heterogeneity of the granular mixing process. Together, the qualitative optical visualization and quantitative composition and statistical analysis lead to the optimization of the screw mixer’s operating conditions. For the range of parameters that were studied, these conditions were determined to be a screw rotation speed of $\omega = 60$ rpm, a dimensionless screw pitch of $p/D = 1.75$, a counter-rotating down-pumping screw rotation orientation (CtrR DP), and a material injection configuration with the red oak

chips and glass beads injected into port one and two (RO 1, GB 2), respectively. Studies which investigated the mixing effectiveness of the screw mixer as a function of the dimensionless mixing length also indicated that this operating condition lead to the most homogeneous mixture at each of the tested dimensionless mixing lengths.

An improved cone-beam compensated back-projection algorithm enabling X-ray particle tracking velocimetry (XPTV) of the screw mixer was then developed to visualize and quantify the 3D granular flow structures inside the screw mixer under various operating condition using “modified” red oak chip tracer particles. It was shown that these improved XPTV methods provided a significant reduction in error associated with the tracer particle’s position. The influence of the aforementioned four factors on the granular flow structures inside the screw mixer were investigated using XPTV, and similar results in terms of the desired operating conditions to those from the previous studies were noted. Moreover, the counter-rotating down-pumping screw rotation orientation, which was found to be the most influential factor using the composition and statistical analysis methods, was also shown to increase the material residence time, resulting in a longer mixing time.

A number of different methods were developed and used to characterize the granular mixing process inside the screw mixer. While each of the methods provided a different view on mixing behavior, the studies converged on a single double screw mixer operating condition, leading to a conclusive mixing effectiveness optimization.

CHAPTER 1: INTRODUCTION

1.1 Motivation

Granular mixing processes are found in a wide range of industrial processes including pharmaceutical production, food processing, and energy generation. Most commonly, granular mixing processes seek a high degree of homogeneity, and in some particular instances, the purpose is to influence simultaneous processing, such as chemical reactions and heat and/or mass transfer rates (Bridgwater, 2012). However, a fundamental problem commonly encountered during the mixing of granular materials is the tendency for mixtures to segregate due to differences in particle size, shape, and/or density (Yang, 2006). Inadequate mixing can significantly diminish the resulting products, and can have a significant financial burden.

Achieving adequate mixing leading to the formation of a desired product is a nontrivial exercise, and has been a common goal for many researchers for decades. However, a vast majority of granular mixing research efforts have focused on relatively simple mixer geometries and idealized granular materials compared to that which is actually used in industrial practice. These studies have proven to be beneficial in developing a deeper theoretical understanding of the granular mixing mechanisms, but there is still a mismatch between basic research involving idealized conditions and practical industrial needs (Ottino and Khakhar, 2001). Thus, a need to study the mixing effectiveness of mixing equipment for the exact geometry being used in industrial applications exists. For example, the renewable energy industry, or more specifically the

biomass thermochemical conversion sector, relies on double screw pyrolyzers (in addition to other reactors) to convert cellulosic biomass into bio-oil. Currently, there is a large amount of research that relates the feedstocks being used to the bio-oil yields (Brown, 2003). However, minimal research efforts have been directed toward studying the granular mixing dynamics inside the double screw pyrolyzer. An obvious need is to address this gap in the research field because enhanced granular mixing leads to higher heat transfer rates, which have been shown to enhance bio-oil yields (Mohan et al., 2006). Thus, improving the current level of understanding of the granular mixing inside the screw pyrolyzer, and indicating the parameters which influence the mixing processes is needed.

1.2 Goal and Objectives

The overall goal of this project is to thoroughly understand, characterize, and optimize the granular mixing of low density red oak chips and high density glass beads within a double screw mixer under various operating conditions. This goal is realized through the following specific objectives:

Objective 1: Design and construct a laboratory-scale double screw mixer that is transparent in both the visible and X-ray spectrums, allows the granular flow exit stream to be divided enabling composition analysis to be performed, and geometrically resembles the double screw pyrolyzer being used by the Iowa State University Biorenewable Research Laboratory (ISU BRL) for the thermochemical conversion of biomass into bio-oil.

1a: Design and construct two additional double screw mixers that feature dimensionless mixing lengths of L/D = 2 and 5.

1b: Design and construct three single screw mixers that are optically transparent and allows the granular flow exit stream to be divided enabling composition analysis to be performed, and have dimensionless mixing lengths of L/D = 2, 5, and 10.

Objective 2: Develop a two-part measurement technique consisting of qualitative optical visualization and quantitative composition and statistical analysis to quantify the mixing effectiveness of the screw mixer.

Objective 3: Provide qualitative optical visualization of the dynamic mixing process for both the single and double screw mixer using four independent projections that are spatially aligned and temporally synced, for each operating condition.

Objective 4: Divide the screw mixer's granular flow exit stream into individual channels and perform quantitative composition analysis for each of the desired operating conditions and dimensionless mixing lengths, for both the single and double screw mixer.

4a: Utilize analysis of variance (ANOVA) statistical procedures to indicate the most influential factors (i.e. parameters), identify the effect that each factor's level has on the homogeneity of the granular materials, and optimize each screw mixers' operating conditions for the purpose of maximizing the homogeneity of the granular materials.

Objective 5: Develop a cone-beam compensated back-projection algorithm that utilizes spatially independent but temporally synced X-ray stereography images and allows X-ray particle tracking velocimetry (XPTV) to be performed.

Objective 6: Perform XPTV using the X-ray Flow Visualization (XFloViz) Facility and the developed cone-beam compensated back-projection algorithm to investigate the effect that different screw mixer operating conditions have on the 3D granular flow structures.

6a: Characterize the 3D granular flow structures inside the screw mixer at various operating conditions, provide confirmation to previous qualitative optical visualization observations, determine tracer particle residence times, and relate the resulting flow structures to the mixing effectiveness found using the previous quantitative composition and statistical analysis.

1.3 Practical Applications

This project aims to provide an improved understanding of the biomass and heat carrier media granular mixing dynamics inside a screw pyrolyzer by performing granular mixing studies in a double screw mixer. The results of these studies will provide recommendations as how to best modify the operating conditions and/or geometrical configuration of the existing screw pyrolyzer to allow for improved mixing of the biomass and heat carrier media. The parameters being investigated require only slight modifications to screw pyrolyzer designs currently being used, but offer significant

increases in terms of mixing effectiveness. The increased mixing effectiveness and insight gained through this project will lead to increased heat transfer rates and could enhance product yield and/or quality; thereby improving the economic viability of a screw pyrolyzer.

1.4 Outline

This thesis is separated into several chapters which address the objectives listed above. Chapter 2 provides a literature review of four major topics: (i) granular mixing, (ii) digital image analysis techniques, (iii) X-ray visualization techniques, and (iv) biomass thermochemical conversion, followed by a brief summary of the review. Chapter 3 describes the experimental equipment, materials, and methods of this project. Chapter 4 reprints the journal paper that was submitted to *Powder Technology* entitled “Optical Visualization and Composition Analysis to Quantify Mixing in a Double Screw Mixer.” Chapters 5 and 6 reprints part one and two of the two-part journal paper that is in preparation for submission to *Powder Technology* entitled “Granular Mixing Visualization and Quantification in a Double Screw Mixer: Part I – Qualitative Optical Visualization” and “Granular Mixing Visualization and Quantification in a Double Screw Mixer: Part II – Quantitative Composition and Statistical Analysis”, respectively. Chapter 7 reprints the conference paper that is in preparation for submission to the American Society of Mechanical Engineers (ASME) 2014 Fluids Engineering Division Summer Meeting (FEDSM) entitled “Characterizing Granular Mixing Homogeneity at Various Dimensionless Mixing Lengths in a Double Screw Mixer.” Chapter 8 presents the results of the single screw mixer studies. Chapter 9 reprints the journal paper that is in

preparation for submission to *Flow Measurement and Instrumentation* entitled “An Improved Cone-beam Compensated Back-projection Algorithm to Enable X-ray Particle Tracking Velocimetry.” Chapter 10 reprints the journal paper that is in preparation for submission to *Powder Technology* entitled “Characterizing 3D Granular Flow Structures in a Double Screw Mixer using X-ray Particle Tracking Velocimetry.” Chapter 11 summarizes the project conclusions, encountered problems, and recommendations for future work. A thorough and comprehensive Appendix is attached which, in part, includes engineering drawings, experimental data, and snapshots of the dynamics mixing process for different operating conditions.

CHAPTER 2: LITERATURE REVIEW

This chapter is composed of five major sections, and provides general background to shape the context of this project. The first section reviews the fundamentals of granular mixing. The second and third sections focus on noninvasive measurement of granular mixing processes using digital image analysis and X-ray visualization techniques, respectively. The fourth section provides a brief introduction into the fundamentals of the thermochemical conversion of biomass into bio-oil with an emphasis on fast pyrolysis. The fifth section summarizes the main findings from the literature review.

2.1 Granular Mixing

Mixing is defined as the reduction in heterogeneity or gradients in material properties in order to achieve a desired process result (Paul et al., 2004; Weinekötter and Gericke, 2006). Material properties of interest can include, but are not limited to, composition, concentration, phase, and temperature. Mixing is a common process in a number of industrial applications, and can involve either single phase or multiphase flows.

2.1.1 Single Phase and Multiphase Flows

Single phase flows consist of one of the three phases, solid, liquid, or gas, while multiphase flows feature at least two or up to three of the phases (i.e., solid-liquid, solid-gas, liquid-gas, or solid-liquid-gas). Single and multiphase flows can be also subcategorized into single component and multicomponent flows, where a component is

a chemical species such as nitrogen, oxygen, or water. Table 1.1 provides examples of these classifications.

Table 2.1 Examples of single phase and multiphase, and single component and multicomponent flows (adapted from Crowe et al. (2011)).

	Single component	**Multicomponent**
Single phase	Water flow Nitrogen flow	Air flow
Multiphase	Steam-water flow Freon-Freon vapor flow	Air-water flow Slurry flow

In the most technical sense, granular mixing processes are multiphase, multicomponent flows because it includes solid particles and an interstitial gas (e.g., air). However, because the interstitial gas is often of low velocity, some texts in the literature refer to granular flows as a single phase flow, which are then further classified as either single component or multicomponent depending on the number of granular particle types. In granular flows, the solids volume fraction is typically quite large, and particle-particle and particle-wall interactions are much more dominant than the interaction between the particles and the interstitial gas (Crowe et al., 2011). The terms dilute and dense are commonly used to refer to the volume fraction in gas-solid flows. In dilute flows, which consist of low solids volume fractions and often feature high gas velocities, the particle motion is controlled by the interaction between the fluid and the particles (i.e., lift and drag) (Crowe et al., 2011). An example of a dilute flow would be a gas-solid flow in a cyclone separator. In contrast, dense flows feature relatively large solids volume fractions, and the particle motion is controlled by particle-particle or particle-wall collisions or continuous particle-particle contact (Crowe et al., 2011). Dense flow can be subcategorized as either collision-dominated or contact-dominated flows. An example of

a collision-dominated flow is a fluidized bed. An example of a contact-dominated flow is the granular flow in a hopper. Figure 2.1 graphically illustrates these classifications. Currently, a definitive parameter that distinguishes these two categories does not exist (Crowe et al., 2011). All of the granular flows inside the double screw mixer used in this project are assumed to be dense, contact-dominated flows because of its very high solids volume fractions.

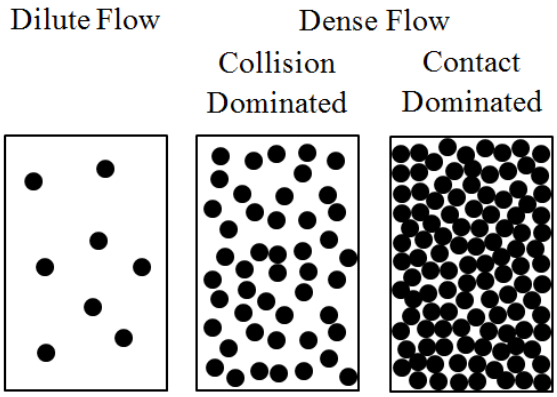

Figure 2.1: Graphical representation for the classification between dilute flows, collision-dominated dense flows, and contact-dominated dense flows (adapted from Crowe et al. (2011)).

2.1.2 Terminology

A number of terms are used to describe granular materials in the literature and in industry, with specific terms being preferred in specific industries. Throughout this paper, the term “granular” is most commonly used, and by definition means composed of individual granules. However, other terms such as particulate, particle, powder, solids, to name a few, are commonly used interchangeable.

A particle is defined as a single entity comprising part of a solid or liquid discontinuous phase (Seville et al., 1997). However, throughout this paper, the discussion

is restricted to solely solid particles (also known as granules), and the introduction of fluid particles and fluid systems are only used for comparison purposes, and will be explicitly stated if used.

2.1.3 History of Granular Mixing

Granular mixing is a complex phenomenon and has attracted many research efforts in recent years, and compared to liquid mixing, the knowledge base of granular mixing is underdeveloped (Jain et al., 2005). The science of fluid dynamics dates back to Archimedes (285-212 B.C.) and has significant contributions from da Vinci, Galileo, Newton, Bernoulli, Euler, Lagrange, with more recent pioneers being Froude, Rayleigh, Reynolds, Navier, Stokes, and Prandtl. However, the science of granular dynamics has only received significant attention beginning in the 1950s (Bridgwater, 2010). Moreover, many granular processes are designed on an empirical basis, and lack fundamental understanding (Seville et al., 1997), making it a relatively new research area which faces many new challenges.

Bridgwater (2010) terms the period prior to 1950 as the “age of intuition and mechanical design” in terms of granular mixing because it relied heavily on observation, physical intuition, and sample analysis. Bridgwater (2010) goes on to declare the period from 1950 to 1990 as the “age of process design science” specifically for chemical engineering because great strides were made in fluid flow, heat and mass transfer, reactor design, and automatic control. But despite the introduction of intuitive designs in these fields, the physics of granular mixing remained poorly understood during this time period. Finally, Bridgwater (2010) termed the period between 1990 and 2010 (the year of publication) as the “start of the age of measurement and IT.” This period marked, and

continues to mark, a significant increase in the number of experimental techniques and more advanced simulation capabilities aided by growing computational power.

2.1.4 Importance

Granular mixing processes are important because they have a significant influence on the resulting products in a large number of industries including chemical, ceramics, pharmaceutical, biotechnology, polymer processing, plastics, consumer products, food processing, pulp and paper, mineral processing, and energy, to name a few. Specific examples of common mixing processes found in these industries are: (i) mixing of particles for homogenization or reduction of heterogeneity (e.g., blending of plastic pellets); (ii) mixing an active ingredient into a carrier material (e.g., formulation of insecticides); (iii) mixing of multicomponent mixtures (e.g., cereal, powders); (iv) mixing of biomass and heat carrier media (e.g., thermochemical conversion of biomass into bio-oil); and (v) coating of a cohesive component onto a carrier particle (e.g., pharmaceutical tablet coating) (Paul et al., 2004).

However, achieving adequate mixing leading to the formation of a desired product is a nontrivial exercise. If a desired mixing state cannot be achieved, and the required product fails to produce acceptable product yield, quality, and/or physical properties, significant efforts may be put forth to improve the granular mixing process resulting in a significant increase in manufacturing costs. Worse yet, the product or process may be discarded because of the cost or time required to achieve acceptable mixing quality.

In 1989 alone, the chemical industry estimated that the cost of poor mixing was between $1 billion to $10 billion in the United States, and that yield losses of 5% were

typical (Paul et al., 2004). Moreover, annual production of granular processes accounts for over a trillion kilograms of granular products, most of which must be uniformly mixed to meet quality criteria (Paul et al., 2004).

2.1.5 Granular Rheology

The behavior of granular material is extremely complex because of its ability to resemble all three phases, and thus exhibits multiple rheological differences, many times simultaneously within the same granular bed. For example, like solids, granular material is able to withstand some deformation. Like liquids, it can be made to flow, and like gases, it can be compressed. However, classifying granular material according to these rheological differences is not entirely correct either. For example, unlike common fluids, granules in a static state are interlocked and must dilate in order to flow, as shown in Figure 2.2a. When interlocked, the granules are said to be behaving very solid-like. The term “solid-like” is used instead of “solid” because the granules do not exactly behave as a solid. When the granules have dilated and are flowing, as shown in Figure 2.2b, they behave very fluid-like, and can even resemble a gas-like material when being applied to high shear rates, as shown in Figure 2.2c. However, when demonstrating fluid-like behavior, the granules transmit shear discontinuously in both space and time, and as a whole, they do not obey the Navier-Stokes equations. Moreover, when demonstrating gas-like behavior, the granular material is not characterized by Maxwell-Boltzmann statistics (Paul et al., 2004). As a result, it is extremely difficult to characterize granular material.

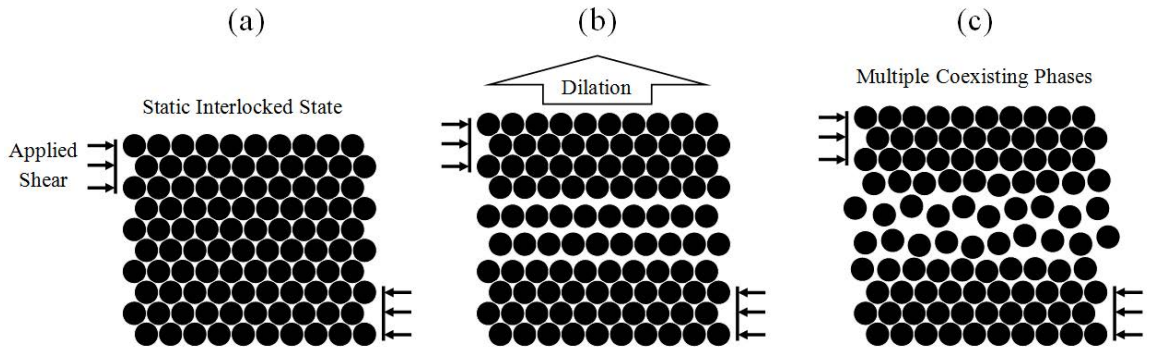

Figure 2.2: Graphical representation of the dilation process that granular materials must undergo to induce flow (adapted from Paul et al. (2004)).

2.1.6 Mixing Classification

When granular materials are being mixed, there is traditionally three different classifications into which the granular mixtures can be separated: (i) perfect, (ii) random, and (iii) segregating mixtures (Rhodes, 2008). These classifications differ slightly from source to source in the literature, but most commonly are referred to as such. Examples of the three different classifications are shown in Figure 2.3.

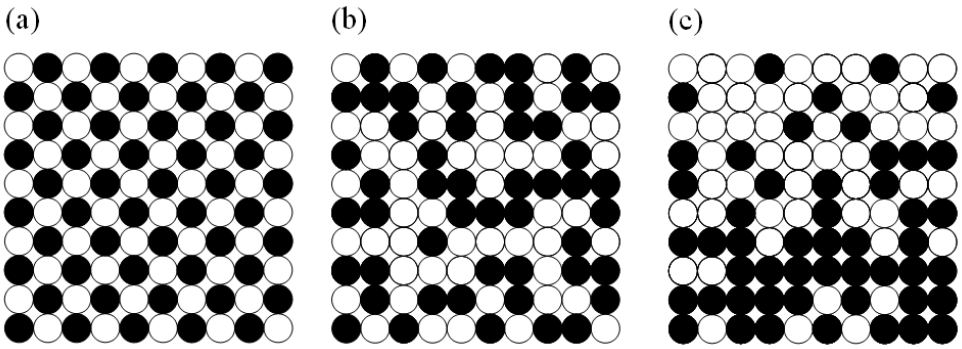

Figure 2.3: Example of a (a) perfect, (b) random, and (c) segregating mixture (adapted from Rhodes (2008)).

By definition, a perfect mixture exists when a group of particles taken from any position in the mixture contain the exact same proportions of each particle as the proportions present in the mixture (Rhodes, 2008), and are orientated along a lattice in a

homogeneous fashion (Paul et al., 2004), as shown in Figure 2.3a. In practice, this mixture cannot be achieved, and a random mixture is often the goal.

A random mixture is most commonly referred to as the best achievable state, and is defined as a mixture whose probability of finding a particle of any component is the same at all locations and equal to the proportion of that component in the mixture as a whole (Rhodes, 2008), and a particle belonging to a certain component is statistically independent of the nature of its neighbors (Paul et al., 2004). In general, this is the best quality that a practical mixture can achieve, with one minor exception, which will be discussed later.

However, granular mixing processes featuring granules that differ in material properties show at least some degree of heterogeneity, which is usually attributed to incomplete mixing, agglomeration, and/or segregation. In this case, particles of one component have a greater probability of being found in one part of the mixture than in another, and are referred to as a segregating mixture (Rhodes, 2008), as shown in Figure 2.3c.

As previously mentioned, it is theoretically possible to achieve better mixing than the random case by taking advantage of the cohesive forces between particles. This prompts additional classification which separates mixtures into ordered and unordered mixtures, as shown in Figure 2.4. During the mixing of cohesive materials, particles apply forces to one another and the formation of agglomerations is observed. When the exact same number of identical “guest” particles (represented by the black particles in Figure 2.4) are attached to identical “host” particles (represented by white particles in Figure 2.4), the mixture is considered ordered, as shown in Figure 2.4a. However, in

reality, a distribution in the number of guest particles attached to host particles is observed, as shown in Figure 2.4b, leading to a more heterogeneous mixture.

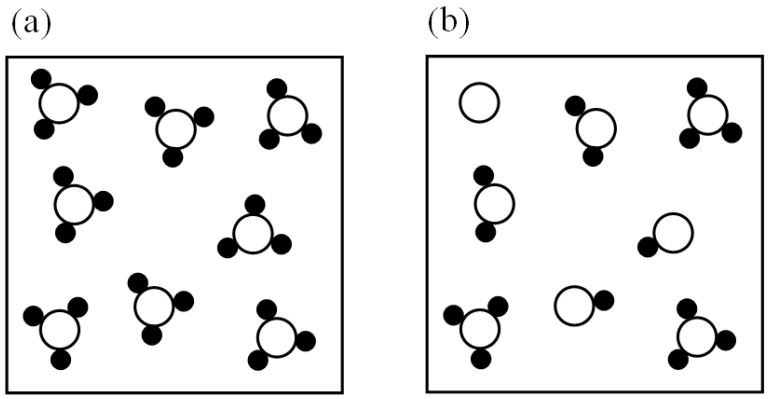

Figure 2.4: Examples of (a) ordered and (b) unordered mixtures, caused by the agglormation of particles resulting from cohesive forces (adapted from Paul et al. (2004)).

2.1.7 Mixing and Segregation

Granular mixing is the process of combining two or more granular material types in an attempt to make one homogeneous mixture. It is also referred to as blending. The general purpose of a granular mixing process is that it produces a mixture with an internal structure of acceptable quality (Bridgwater, 2012). Most commonly, granular mixing processes seek a high degree of homogeneity, and in some instances, the purpose is to influence simultaneous processing, such as chemical reactions and heat and/or mass transfer (Bridgwater, 2012). While the mixing of granular material appears fairly straightforward at first glance, fully understanding and characterizing granular mixing and segregation is an ambitious task that has been a common goal for many researchers.

A fundamental problem commonly encountered during the mixing of granular materials is the tendency for mixtures to segregate due to differences in particle size, shape, and/or density (Yang, 2006). Further complications arise because a considerably

large number of parameters (e.g., operating conditions of the mixing equipment) can either exploit or minimize the differences in material properties, resulting in either enhanced or reduced segregation.

The last two decades has marked a significant advance in the fundamental understanding of granular mixing due to advances in measurement techniques and computational simulations. These studies have analyzed the granular mixing and segregation process in a wide range of systems including rotating cylinders (Aissa et al., 2010a, b; Huang and Kuo, 2012), fluidized beds (Escudero and Heindel, 2011; Gao et al., 2009; Keller et al., 2013), single screw mixers (Tsai and Lin, 1994; Uchida and Okamoto, 2006, 2008), and horizontal impeller mixers (Portillo et al., 2010; Vanarase and Muzzio, 2011), to name a few. More specifically, extensive research has been conducted on the influence of operating conditions and/or material properties for a wide range of mixing processes using simulations (Cleary and Sinnott, 2008; Sarkar and Wassgren, 2009, 2010) and experimental methods (Hilton and Cleary, 2011; Jain et al., 2005; Metzger et al., 2011; Remy et al., 2010). For example, Portillo et al. (2009) demonstrated the effects that rotation rate, mixing angle, and cohesion had on the blend uniformity of powders. Keller (2012) used visual observations to study the mixing characteristics in fluidized beds, and demonstrated the system's mixing effectiveness was heavily influenced by the chosen operating conditions (e.g., superficial gas velocity) and particle properties (e.g. particle size and density). A number of reviews regarding the mixing of granular material are available in the literature (Bridgwater, 2012; Campbell, 2006; Ottino and Khakhar, 2000; Pernenkil and Cooney, 2006). More specifically, some of the challenges associated with the mixing and segregation of granular material was addressed by Ottino and

Khakhar (2001). Despite these advances, many attempts to characterize the mixing effectiveness of granular applications rely solely on sampling the material after exiting the mixer and often involve challenging sampling procedures, which will be discussed in more detail in the following sections (Bridgwater, 2012; Brown, 2009; Gao et al., 2011; Portillo et al., 2009; Tsai and Lin, 1994; Vanarase and Muzzio, 2011).

While significant effort has been made, the vast majority of granular mixing research efforts have focused on relatively simple mixer geometries and idealized granular materials compared to what is actually used in industrial practice. For example, rotating cylinders have been extensively studied by a large number of researchers, both experimentally (Aissa et al., 2010a, b; Huang and Kuo, 2012; Jain et al., 2005) and computationally (Chand et al., 2012; Gui et al., 2010; Gui et al., 2013; Yang et al., 2008) because of its simple mixer geometry. These studies have proven to be beneficial in developing a deeper theoretical understanding of the mixing and segregation mechanisms, which will be discussed in the following sections, but results of these studies are not able to be extended to other mixing configurations.

Additionally, many experimental studies investigating the mixing of granular materials have considered only a small number of factors relating to the operating conditions of the mixing equipment. For example, Uchida and Okamoto (2006) used an X-ray system coupled with a 2D imaging device to track small amounts of tungsten tracer powder in powder flows and investigated the effect of a single factor, dimensionless screw pitch, in a single screw feeder.

In contrast to investigating only one factor, multiple factors can and should be studied simultaneously. This allows for a more thorough understanding of the effects the

operating conditions have on the mixing effectiveness. Furthermore, it allows for the interaction of factors to be analyzed. For instance, Vanarase and Muzzio (2011) researched the effect of impeller rotation rate, flow rate, and blade configuration in a continuous horizontally orientated impeller powder mixer. The rotation rate was determined to be the most influential factor and intermediate rotation rates optimized the overall mixing effectiveness. Ideally, numerous factors that significantly affect the mixing effectiveness of the system would be incorporated in the study, as was done by Vanarase and Muzzio (2011). However, incorporating too many factors can also be problematic because of the resulting size of the design of experiments, time required to collect and analyze the data, and the ability to interpret the results.

2.1.7.1 Mixing mechanisms

Mixing and segregation go hand-in-hand, but the mechanisms which govern their behavior are vastly different. The mixing of granular material features three basic mixing mechanisms: (i) diffusion, (ii) shear, and (iii) convection (Lacey, 1954). These mechanisms are governed by the material properties, geometry of the mixing equipment, and the operating conditions, along with many other factors.

2.1.7.1.1 Diffusive Mixing

Diffusive mixing is caused by the random motion of granules, and is essential for microscopic homogenization (Masuda et al., 2010). While diffusive mixing is critical to microscopic mixing, its influence is relatively small compared to shear and convective mixing in macroscopic mixing applications.

2.1.7.1.2 Shear Mixing

Shear mixing is caused by the momentum exchange between granules of different velocities (Masuda et al., 2010). A velocity distribution develops around the physical mixing device (e.g., screw, impeller, etc.) and the vessel walls, due to compression and dilation of the granular material. The amount of shear mixing is directly proportional to the contact surface area between the mixing equipment and the granular material. Shear mixing is beneficial to both batch and continuous mixing operations.

2.1.7.1.3 Convective Mixing

The rotational motion of a mixer's vessel or mixing device, such as a ribbon, paddle, or screw, causes a circulating granular flow, and induces the transfer of groups of adjacent particles from one location to another. This behavior is known as convective mixing (Lacey, 1954). Convective mixing contributes mostly to macroscopic mixing, and the rate of mixing by convection mixing is large relative to diffusion and shear mixing.

2.1.7.2 Rate of Mixing

The three aforementioned mixing mechanisms occur simultaneously in mixing processes. However, convective mixing is generally dominant in the initial mixing stage, followed by a period of both convective and shear mixing in the intermediate stage, and finally, diffusive mixing is present in the final mixing stage. This behavior is illustrated in Figure 2.5, where the log of the standard deviation of the composition, σ, which represents the heterogeneity of the granular mixture is plotted on the y-axis, and the mixing time, t, is plotted on the x-axis. As shown in Figure 2.5, the initial mixing period (represented by region I) is mainly dominated by convective mixing. Region II then

displays a period of time in which the mixture is undergoing both convective and shear mixing. Finally, region III consists of diffusive mixing.

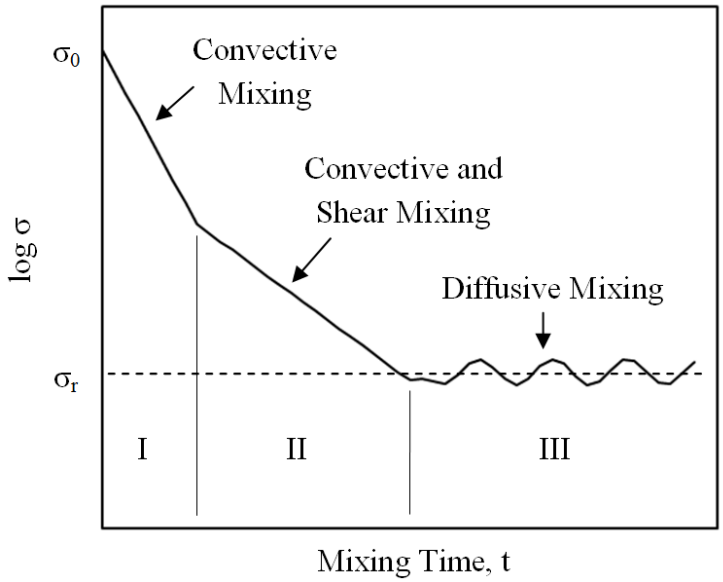

Figure 2.5: Typical rate of granular mixing, and the different stages that the mixture goes through (adapted from Masuda et al. (2010)).

While diffusive and shear mixing give rise to a reduction in the heterogeneity of the granular materials, they can also give rise to segregation in the case of free-flowing mixtures. Thus, convective mixing is the major mixing mechanism used to promote mixing in free-flowing mixtures. This phenomenon is an obvious display of the correlation between granular mixing and segregation.

2.1.7.3 Particle Property Effects on Segregation

Small differences in particle size, shape, and/or density lead to flow-induced segregation in granular systems, and the rate of segregation can be reduced or magnified by changing the operating conditions of the mixing equipment. Combinations of these differences can be combined to produce an even more challenging mixing behavior. Differences in particle size and density cause percolation and buoyancy forces,

respectively, and may either compete or complement each other (Jain et al., 2005). For example, mixing can be achieved, instead of segregation, if the correct combination of materials are selected where denser, larger particles are mixed with less dense, smaller particles such that the percolation and buoyancy forces offset each other (Jain et al., 2005). Despite this knowledge, mixer performance still remains quantitatively puzzling because insufficient efforts have been directed toward investigating the effect that particle size, shape, and density have on mixing effectiveness (Bridgwater, 2010).

Mixture segregation arises when a characteristic of one or more particle species causes that component to separate into specific regions within the mixture. Free-flowing mixtures tend to exhibit enhanced segregation, in contrast to cohesive mixtures, which exhibit minimal segregation because particles have more difficulty moving independently of the granular bed (Paul et al., 2004). Figure 2.6 illustrates two types of segregated mixtures: (a) free-flow and (b) cohesive.

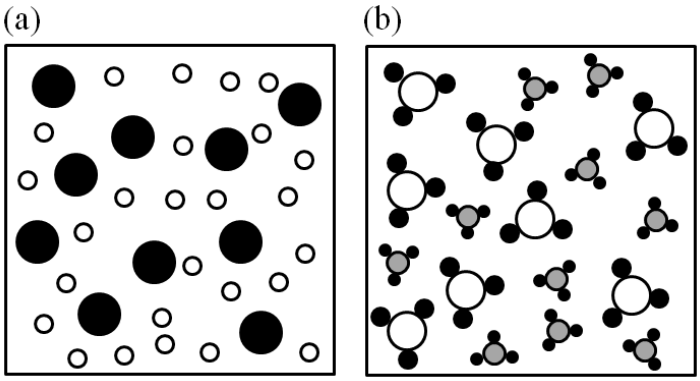

Figure 2.6: Distribution of particles differing in size for (a) free-flowing and (b) cohesive granular materials (adapted from Paul et al. (2004)).

Particle properties play a significant role in the granular processes because of their influence on mixing and segregation, power requirements of equipment, and heat and/or mass transfer rates. One type of classification that has been extensively used in the

particulate processes, particularly those pertaining to particle fluidization, is the Geldart classification. Geldart (1973) classified the fluidization of powders at ambient conditions into four clearly recognizable groups, as shown in Figure 2.7, which are characterized by density difference between the particle and fluid, $\rho_p - \rho_f$, and mean particle size, D. In terms of distinguishing the different groups, Geldart (1973) found groups A and B were the most easily recognizable. Group A materials exhibit fluidization in the absence of bubbling at the minimum fluidization velocity, followed by bubbling fluidization as the fluidizing velocity increases. Group B materials were characterized by bubbling at the minimum fluidization velocity. Group C materials are difficult to fluidize at any operating conditions, and group D materials form stable spouted beds. Geldart (1973) noted that group A particles are ideal for fluidization and exhibit the highest level of solids mixing, followed by group B, D, and C respectively.

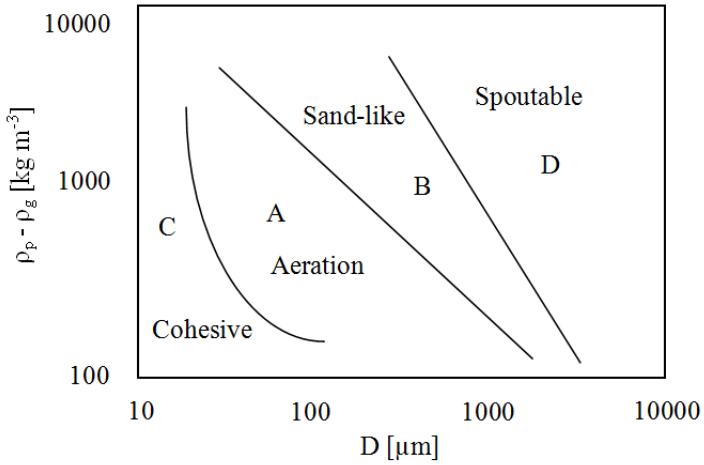

Figure 2.7: Particle fluidization classification known as the Geldart classificaion (Geldart, 1973).

In addition to the Geldart classification, specific particle properties can also be examined. In this paper, only particle size, shape, density, and cohesion are discussed,

because these are the most important characteristics of a particle (Seville et al., 1997). Additional particle properties include, but are not discussed here, are hardness, abrasiveness, toughness, fibrous nature, melting point, and thermal conductivity, to name a few.

2.1.7.3.1 Particle Size

Describing the size distribution of granules is a key component to characterizing the granular material. Particle size is an important, but difficult, parameter to define, particularly when dealing with nonspherical particles. A large number of methods are used to define particle size (Masuda et al., 2010), including: (i) first measuring the breadth, b, length, l, and thickness, t, and then computing one of the different characteristic particles sizes using Eqn. 2.1; (ii) the martin diameter, which is the length of chord dividing the particle's projected area into two equal areas in some fixed direction; and (iii) the sieve diameter, as expressed by Eqn. 2.2, where a_1 and a_2 are sieve openings.

$$L_c = \frac{b+l}{2} \;;\; \frac{b+l+t}{3} \;;\; \left(\frac{b}{t}\right)^{1/3} \;;\; 3\left(\frac{1}{l}+\frac{1}{b}\right)^{-1} \tag{2.1}$$

$$L_c = \frac{1}{2}\left(a_1 + a_2\right) \;;\; \sqrt{a_1 a_2} \tag{2.2}$$

However, it is usually impractical to describe granular material using a single particle dimension. Thus, it is typical to describe the granules using a number distribution, usually presented in form of a frequency histogram. This is typically used because in practice it is quite difficult to obtain a monodispersed bed of material, where monodispersed refers to a collection of granules that have the exact same particle size. Polydispersed beds, which feature a range of particles sizes, are much more common.

Differences in particle size cause a variety of segregation mechanisms to arise, and results in segregation. Rhodes (1990) describes three mechanisms of segregation due solely to size differences: (i) trajectory segregation, (ii) segregation by percolation and (iii) elutriation segregation, as shown in Figure 2.8.

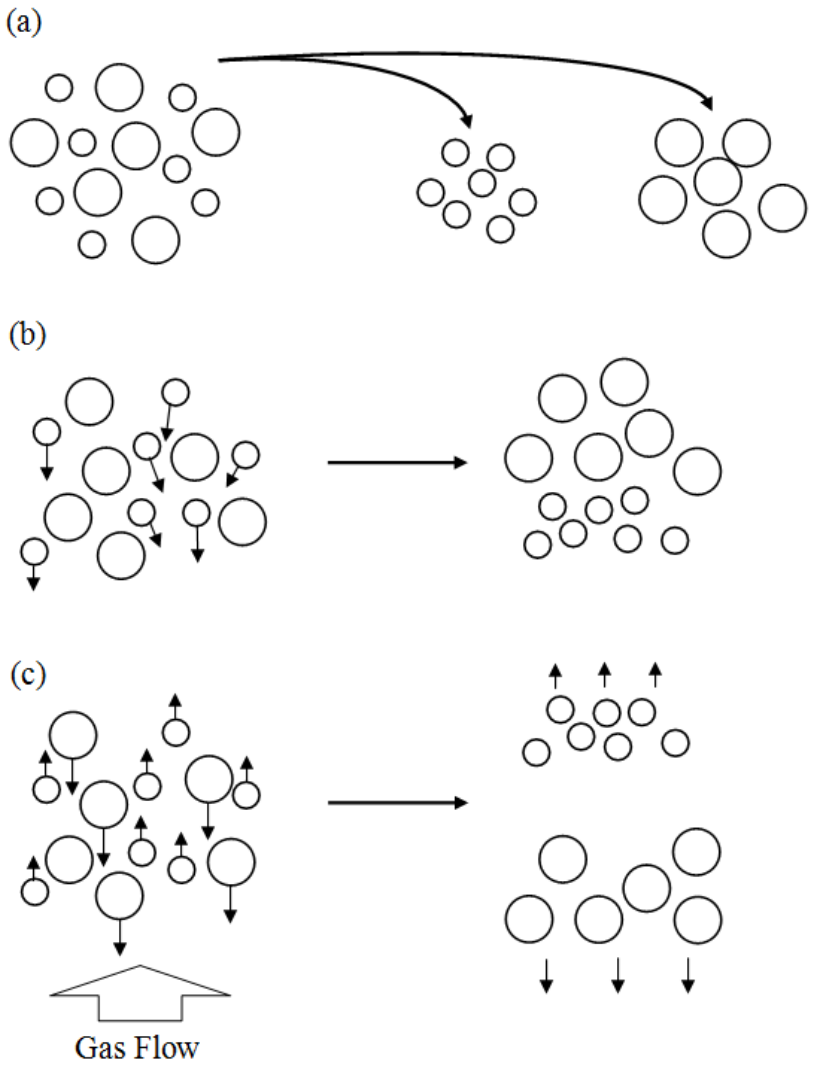

Figure 2.8: The three mechanisms of segregation due solely to size differences: (a) trajectory segregation, (b) segregation by percolation, and (c) segregation by elutriation (adapted from Rhodes (2008)).

2.1.7.3.1.1 Trajectory segregation

Trajectory segregation is based on the principle that if two particles consisting of diameter D and 2D are projected horizontally with velocity U into a fluid of viscosity μ and density ρ_f, the limiting distance that each particle can travel horizontally is:

$$d = \frac{U\rho_f D^2}{18\mu} \tag{2.3}$$

Thus the particle of diameter 2D would travel four times as far before coming to rest, as shown in Figure 2.8a.

2.1.7.3.1.2 Segregation by Percolation

Percolation forces also give rise to segregation. Rhodes (1990) divides granular segregation by percolation into two different causes: (i) percolation of fine particles and (ii) the rise of coarse particles by vibration.

When voidage and flowability increase in a polydispersed granular bed, the smaller granules may easily percolate through the interstices between the larger particles, resulting in the percolation of fine particles; Figure 2.8b illustrates this phenomenon. This flow-induced segregation happens under shear strain or while in flow, and occurs for particle size ratios as small as 1.53 (Masuda et al., 2010). Disruption of the bed can be caused by stirring, shaking, vibration, or pouring of the particles. A traditional example that demonstrates the percolation of fine particles and the rise of coarse particles upon vibration within a granular bed, is a large steel ball placed at the bottom of a beaker full of glass beads. If the beaker is then vertically shaken, the larger, denser steel ball will rise to the top surface of the glass beads. In this case, the percolation forces causing the

upward motion of the steel ball are greater than the buoyance forces which are acting to push the steel ball downwards. This phenomenon is demonstrated in Figure 2.9.

If a polydispersed granular bed is vibrated, the larger particles move upward, as was mentioned in the steel ball and sand example. This phenomenon is known as the rise of coarse particles by vibration, but is commonly referred to as the “Brazil-nut effect”, which has received much attention over recent years (Metzger et al., 2011; Morgan and Heindel, 2010). The rise of the larger, denser “intruder” particle has been explained by the filling of voids beneath the intruder particle and the creation of convection cells within the granular bed. This segregation is similar to the percolation of fine particles, but the two are distinguished because of the force giving rise to the segregation.

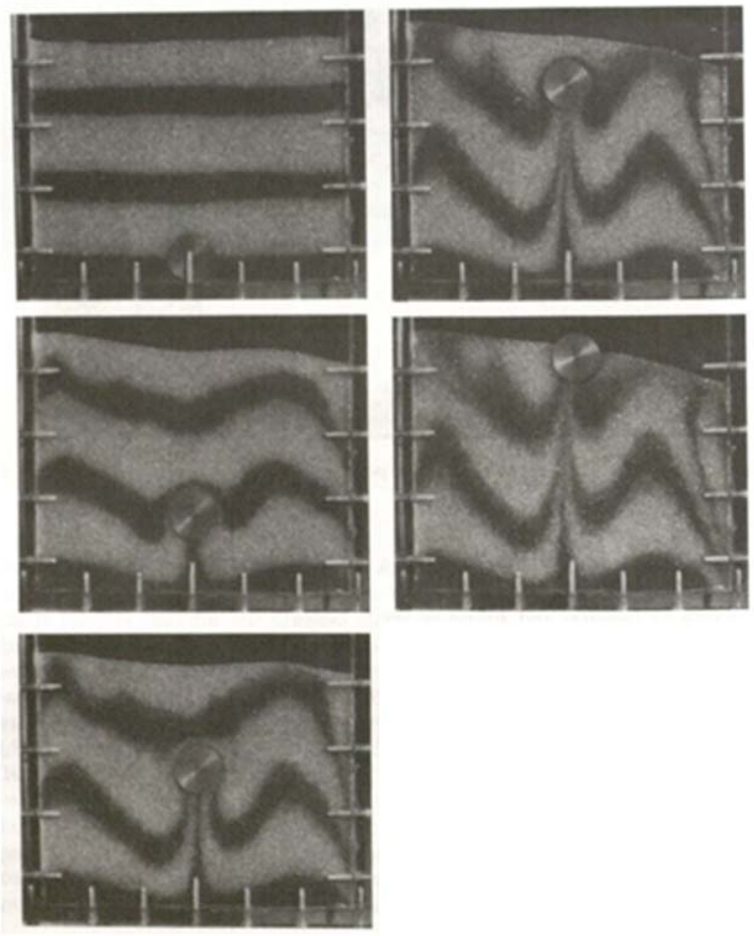

Figure 2.9: A series of photographs that demenstrates the rise of a steel disc through a bed of 2 mm glass spheres (Rhodes, 2008).

2.1.7.3.1.3 Elutriation Segregation

Elutriation of particles occurs when an interstitial gas (e.g., air) is passed through a granular bed, and the upward velocity of the gas exceeds the terminal free-fall velocity of the particles. This generally occurs for relatively small particles, < 50μm, but can occur with larger particles if the gas flow rate is sufficient. This segregation mechanism is shown in Figure 2.8c.

2.1.7.3.2 Particle Shape

Granular particles have various shapes depending on their material, manufacturing method, and mechanical properties. In general, it is very difficult to

explicitly describe their shapes; therefore they have typically been described and classified by the use of various terms, both qualitatively and quantitatively. Qualitative descriptions include terms such as spherical, granular, blocky, flaky, platy, rod-like, fibrous, irregular, etc. (Masuda et al., 2010). This type of classification is based on visual judgment and is thus subjective. Therefore, quantitative descriptions are often necessary. Quantitative descriptions are further classified into three categories based on the scale of the inspection: (i) macroscopic, (ii) mesoscopic, and (iii) microscopic. Because the scale of the particles in this project was evaluated only on a macroscopic basis, this will be the only scale discussed here.

A macroscopic description of the particles characterizes the overall shape of the particle, and refers to the proportion or elongation of the particle. It is calculated from macroscopic geometrical features such as representative diameter, axis length, thickness, etc. More specifically, the elongation and flatness are defined as:

$$\text{elongation} = \frac{l}{b} \tag{2.4}$$

$$\text{flatness} = \frac{b}{t} \tag{2.5}$$

where l is the particle length, b is the particle breadth, and t is the particle thickness. Various other factors relating to the particle shape, such as sphericity can be computed:

$$\psi = \frac{\pi^{\frac{1}{3}}\left(6V_p\right)^{\frac{2}{3}}}{A_s} \tag{2.6}$$

where V_p is the volume of the particle and A_s is the surface area of the particle; note that $\psi \leq 1$ (Wadell, 1933).

The effect of particle shape has been shown to have significant influences on the behavior of granular flows. Hilton and Cleary (2011) performed computational studies involving the pneumatic conveying of granular particles, and found that the flow regimes depend heavily on the particle shape. Spherical, or near spherical, particles displayed a slug flow behavior at high gas flow rates, whereas nonspherical particles displayed dilute flow behavior.

2.1.7.3.3 Particle Density

The density of granular material is a physical property that is very important in granular mixing and handling processes because of its influence on segregation and power consumption of the mixing and handling equipment. Moreover, density differences between different granular material types lead to flow-induced segregation because of the resulting buoyant forces. Although density is typically defined as a ratio of mass to volume, determining the density of granular particles is more complicated because of its various methods of determining particle volume. The density of granular materials can be defined in two ways: (i) true density and (ii) bulk density. True density, ρ, is defined as the ratio of the mass of the particle to its actual particle volume. Bulk density, ρ_B, is defined as the ratio of the mass of the granular bed to the bulk volume of the granular bed, which includes the voids between the particles themselves. The bulk density of granular materials is typically less than the true density.

2.1.7.3.4 Cohesive Forces

Cohesive forces, also known as surface forces or inter-particle forces, between particles or between particles and solid surfaces can have significant influences on the behavior of the granules in mixing and handling processes. These forces arise because of

the summation of intermolecular interaction forces between the molecules in the particles acting across the interstitial medium (Rhodes, 2008). The dominant forces that arise in granular mixing and handling applications are electrostatic forces, van der Waals forces, and liquid-bridge forces. (Masuda et al., 2010).

2.1.7.3.4.1 Electrostatic Forces

Particles in a gas are usually charged, resulting in electrostatic forces acting on the particles (Crowe et al., 2011). The magnitude of the electrostatic force is directly proportional to the product of the charges between the two particles and inversely proportional to the square of the distance between the particles, as shown by the Coulomb formula:

$$F_E = \frac{1}{4\pi\varepsilon_0}\frac{q_1 q_2}{r^2} \tag{2.7}$$

Where q_1 and q_2 are the charges of the particle one and two, respectively, r is the distance between particles' centers, and ε_0 is a dielectric constant of the medium. When the signs of q_1 and q_2 are different, an attractive force acts on the two particles. In contrast, if the signs are the same, a repulsive force arises.

2.1.7.3.4.2 Van der Waals Forces

Van der Waals forces are short-range electromagnetic forces interacting between two molecules, but also interacts between macroscopic bodies such as particle-particle and particle-wall (Masuda et al., 2010). These forces arise from molecular interaction between solid surfaces, and become more apparent when dealing with relatively smooth particles (Crowe et al., 2011). Hamaker (1937) originally proposed a model for the van der Waals force between two spheres, in addition to other geometries, that depended solely on the distance between the two spheres, and what is referred to as the Hamaker

constant. However, Czarnecki and Dabros (1980) later suggested that the effect of roughness of the spherical surfaces modified the van der Waals force, and proposed the new model:

$$F_V = \frac{Ad}{12(r+z)^2} \tag{2.8}$$

where A is the Hamaker constant, r is the separation distance between the two particles, z is the average roughness height of the two particles, and

$$d = \frac{D_1 D_2}{D_1 + D_2} \tag{2.9}$$

where D_1 and D_2 are the diameters of particle one and two, respectively.

2.1.7.3.4.3 Liquid Bridge Forces

Liquid bridge forces are strongly related to the particle shape, surface wettability, and environmental conditions such as humidity and temperature (Uchida and Okamoto, 2006). Liquid bridge forces are formed on the contact point between two particles when the relative humidity of the atmosphere is relatively high (> 65%). The cohesive force caused by the liquid bridge can be determined by the sum of the capillary force and the surface tension force:

$$F_L = \pi r_1^2 p_C + 2\pi\sigma r \tag{2.10}$$

where r is the radius of the liquid bridge, as shown in Figure 2.10, σ is the surface tension of the liquid, and p_c is the capillary pressure inside the liquid bridge (Masuda et al., 2010).

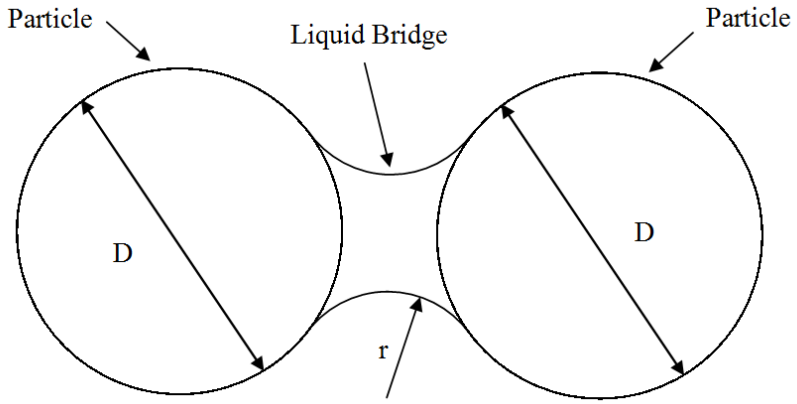

Figure 2.10: Liquid bridge formed between two spherical particles (adapted from Masuda et al. (2010)).

When performing granular mixing studies, careful consideration must be given to the different types of cohesive forces; particularly which forces are most dominant. Figure 2.11 illustrates the magnitude of the three types of cohesive forces as a function of particle diameter for a particle in air and a particle density of 1000 kg m^{-3}. The remaining particle properties (e.g., surface charge density, surface tension, etc.) are typical parameters for granular materials of this size and can be found in the literature (Masuda et al., 2010). When the liquid bridge force is present, it is the dominating force, for the range of particle diameters shown. In the absence of the liquid bridge, van der Waals forces are dominant when the particle diameter is less than 100 µm, above which the electrostatic forces are dominant. Note that the magnitude of these forces is strongly dependent on the material properties and the environmental conditions. Changing these factors will most certainly cause these forces to be more or less dominant relative to each other.

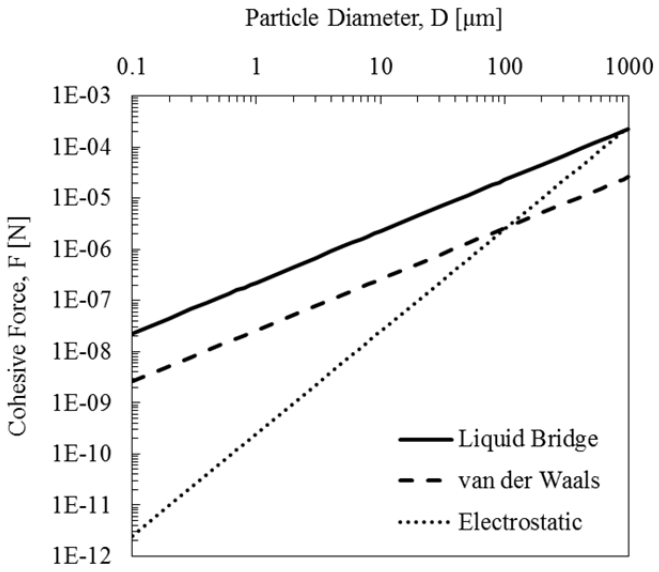

Figure 2.11: Magnitude of the three types of cohesive forces as a function of the particle diamete (adapted from Masuda et al. (2010)).

While the aforementioned cohesive forces represent the induced forces on a particle-particle basis, the two bulk parameters that characterize the frictional behavior of the entire granular bed are: (i) coefficient of internal friction, which is a summation of the aforementioned cohesive forces which determines the stress distribution within the granular bed, and (ii) coefficient of wall friction, which determines the stresses between the granular material and the walls of the vessel (Seville et al., 1997). Because of the influence that these cohesive forces have on the granular mixing dynamics, research efforts have been directed to investigating these parameters.

Uchida and Okamoto (2006) theoretically and experimentally investigated the effect that electrostatic, van der Waals, liquid bridge, and gravity forces had on the following efficiency of tracer particles in a single screw mixer powder flow. After examination, the following was concluded: (i) electrostatic forces were minimal and could be ignored; (ii) the shape difference between the powder and the tracer particles

was not significantly different, as determined by a scanning electron microscope (SEM), and thus the van der Waals forces were minimal; (iii) the screw mixer's screw rotation speed was small and the centrifugal force was negligible relative to the gravity force; and after further investigation which included performing experiments with various particle size and density ratios between the powder and the tracer particles, it was concluded that (iv) the following efficiency was reasonable and fairly independent of the induced gravity forces. However, these findings are only valid for the tests conditions which were being used by Uchida and Okamoto (2006) , and cannot be applied to other granular mixing applications.

Other researchers have investigated the effort of surface roughness on the granular mixing dynamics (Babout et al., 2013). Various empirical methods are used to determine the internal and wall coefficients of granular materials, and are described in great detail in the literature (Carr and Walker, 1968; Fayed and Otten, 1984).

2.1.7.4 Granular Packing

Granular packing is an important parameter in granular mixing and handling processes because the material properties are dependent on the granules geometrical arrangement. If the true density and bulk density are measured, the porosity or void fraction, ε, can be determined:

$$\varepsilon = 1 - \left(\frac{\rho_B}{\rho} \right) \tag{2.11}$$

where ρ is the true density of the granules and ρ_B is the bulk density of granular bed. Furthermore, the packing volume fraction or packing fraction is defined as:

$$\phi = 1 - \varepsilon \tag{2.12}$$

The packing of equal spheres and polydispersed particles has been extensively researched, and a thorough overview of these research efforts can be found in the literature (Masuda et al., 2010).

2.1.7.5 Mixing Quantification

The ability to characterize the mixing of granular materials has advanced quite rapidly over recent decades due to advances in measurement techniques such as digital image analysis (Aissa et al., 2010a, b; Busciglio et al., 2009; Chen and Yu, 2004; Daumann et al., 2009; Daumann and Nirschl, 2008), particle image velocimetry (PIV) (de Jong et al., 2012; Dhenge et al., 2013), magnetic resonance imaging (MRI) (Hardy et al., 2007), positron emission particle tracking (PEPT) (Leadbeater et al., 2012; Portillo et al., 2010), X-ray visualization (Uchida and Okamoto, 2006, 2008), and near-infrared spectroscopy (Koller et al., 2011). While each of these techniques has their advantages, the expense associated with many can be extremely large. Furthermore, many of these techniques can only be applied to mixing processes which feature relatively simple mixer geometry (e.g., rotating cylinders) due to specific constraints. For example, complex mixing geometries can cause image artifacts in the case of X-ray imaging and lead to undesirable results.

Qualitative mixing characterization provides a critical indication of the mixing effectiveness for a number of different mixing processes. In many instances, particularly when developing new mixing equipment, it is typical to perform an initial mixing assessment based on qualitative optical visualization. For example, during the development of a screw pyrolyzer for the thermochemical conversion of biomass into bio-oil, Brown and Brown (2012a) performed preliminary cold-flow mixing trails to

assess the mixing of granular materials, identify problematic operating conditions, and select the operating conditions of the screw pyrolyzer with the goal of maximizing the degree of mixing. Additionally, Hajra et al. (2010) visualized the mixing of glass beads and cellulose acetate particles having differences in both size and density in a rotating cylinder. By using a transparent cylinder, they were able to investigate the degree of radial segregation and identify the preferred mixing conditions. Finally, Kingston and Heindel (2013b) used advance optical visualization techniques to qualitatively characterize the granular mixing process between red oak chips and glass beads in a double screw mixer. In doing so, they were able to identify preferred mixing conditions, and determine which parameters increased the mixing effectiveness of the screw mixer. However, when qualitative assessment is not sufficient, quantitative analysis must be used. But, defining a mixing efficiency of granular mixing processes is a nontrivial exercise, and the methods used to determine granular mixing effectiveness are limited (Siiria and Yliruusi, 2009). Thus, determining an effective mixing assessment has been a common goal for many researchers for a number of decades, as will be discussed in more detail in the following sections.

Statistics are commonly used to define the degree of mixedness for granular mixing processes, and can either be expressed as a degree of homogeneity or a degree of heterogeneity. The most commonly used approach to evaluating granular mixing process, is the use of the composition variance, s^2:

$$s^2 = \frac{\sum_{i=1}^{N}\left(x_i - \bar{x}\right)^2}{N - 1} \tag{2.13}$$

where N is the number of collected samples, x_i is the composition of the i^{th} sample, and $\overline{x_w}$ is the mean composition of all the samples. More recent efforts have utilized a weighted composition variance, which more accurately characterizes the granular mixing:

$$s_w^2 = \frac{\sum_{i=1}^{i=n} m_i \left(x_i - \overline{x_w}\right)^2}{\left(\frac{N-1}{N}\right)\sum_{i=1}^{i=n} m_i} \tag{2.14}$$

where n is the number of the i^{th} sample, m_i is the mass of the i^{th} sample, x_i is the composition of the i^{th} sample, $\overline{x_w}$ is the mass weighted mean composition of the samples, and N is the total number of samples being analyzed (Kingston and Heindel, 2013d). However, the weighted composition variance can only be utilized when sampling the entire cross-section of the exit stream of a continuous mixing process. The use of these techniques is summarized in Chapter 4.

The use of the composition variance to assess granular mixing processes is common, but there are a number of other mixing indices that can be used. Currently, there are more than 40 defined mixing indexes (Aissa et al., 2010a). Many of these indices measure the intensity of segregation, I_s, which is a normalized variance of concentration:

$$I_s = \frac{\sigma^2 - \sigma_r^2}{\sigma_0^2 - \sigma_r^2} \tag{2.15}$$

where σ^2 is the variance of sampled data, σ_r^2 is the variance of the same number of randomly chosen concentration data, and σ_0^2 is the variance of an initial, typically fully segregated state, which again consists of the same number of data points (Paul et al., 2004). This definition of segregation intensity ranges from zero to one, which

corresponds to completely random and completely segregated mixtures, respectively. In practice, values below 0.7 are rare. In contrast to measuring the degree of heterogeneity, various measures for the degree of homogeneity have been used, such as the Lacey mixing index (Lacey, 1954).

$$\text{Lacey mixing index} = \frac{\sigma_0^2 - \sigma^2}{\sigma_0^2 - \sigma_r^2} \tag{2.16}$$

This is essentially a ratio of mixing achieved to mixing potential. A Lacey mixing index of zero represents a completely segregated mixture while a value of one represents a complexly random mixture. However, in practical applications, the values lie between 0.75 and 1, and thus do not provide sufficient discrimination between mixtures.

The relative standard deviation, RSD, also known as the coefficient of variation (CoV), is another typical measure of granular mixing:

$$\text{RSD} = \text{CoV} = \frac{\sigma}{M} \tag{2.17}$$

where σ is the standard deviation and M is the mean concentration over all the collected samples. When attempting to quantify the mixing of granular materials using any of the aforementioned methods, invasive granular sampling techniques must be employed.

2.1.7.6 Granular Sampling

The sampling of granular materials has been a problematic procedure for many decades, and has received significant attention by the United States Food and Drug Administration (FDA), industry, and researchers. One of the best known examples of problematic granular sampling was a court case between the United States and Barr Laboratories in 1993, which lead to a published court ruling (US vs. Barr Laboratories 812, F. Supp 458, D.N.J. 1993), which commonly referred to as the “Barr Decision”. The

ruling ultimately lead to significant attention being directed towards understanding, predicting, monitoring, and controlling granular mixing processes. In conclusion, several specific recommendations were made, including: (i) sampling should resemble all portions of the granular mixture, (ii) small samples no larger than three unit dosages should be sampled to assess blending uniformity, (iii) and granular mixing processes should not generate “hot spots.” Despite the recommendations, the methods to perform these tasks were not discussed. Moreover, little to no attention was given to sampling errors, which can introduce large errors in sample concentration, or segregation.

Granular sampling has also been problematic in academia. Brown (2009) attempted to perform preliminary cold-flow mixing studies by removing the top plate from a screw pyrolyzer designed specifically for chemically reacting flows. The inability to collect samples at locations other than the top layer of material was noted, resulting in the sample composition not accurately reflecting the composition of the entire mixture due to material segregation. Additionally, variations in the material volumetric fill level inside the system resulting from particular operating conditions prohibited collecting samples at all the desired locations.

Due to these complications, more accurate sampling techniques have been a common problem for many researchers wanting to characterize granular flows because of their current limitations (Allen, 1996; Muzzio et al., 2003; Muzzio et al., 1997). In an attempt to improve these sampling procedures, advanced sampling probes are being developed and are commonly used to collect granular samples (Paul et al., 2004). These probes are inserted into the bed and extract a granular sample. When performing sampling, it is critical to collect samples from all regions of the bed. If only sampled at a

few locations, regions of poor mixing could be missed and/or underrepresented. However, the introduction of the probes into the granular bed causes disruption of the material, resulting in undesired results. Two types of errors are often introduced by probes: (i) the mixture is extensively disturbed when the probe is inserted into the granular bed and (ii) particles of different sizes often flow unevenly into the probe cavities. Figure 2.12 shows the disturbances caused by a side-sampling probe, where the granular materials enter the probe from the side; an end-sampling slug probe, where the granular materials enter the probe through the slug on the end of the probe; and an end-sampling probe, where the granular materials enter the probe through the end of the probe, respectively.

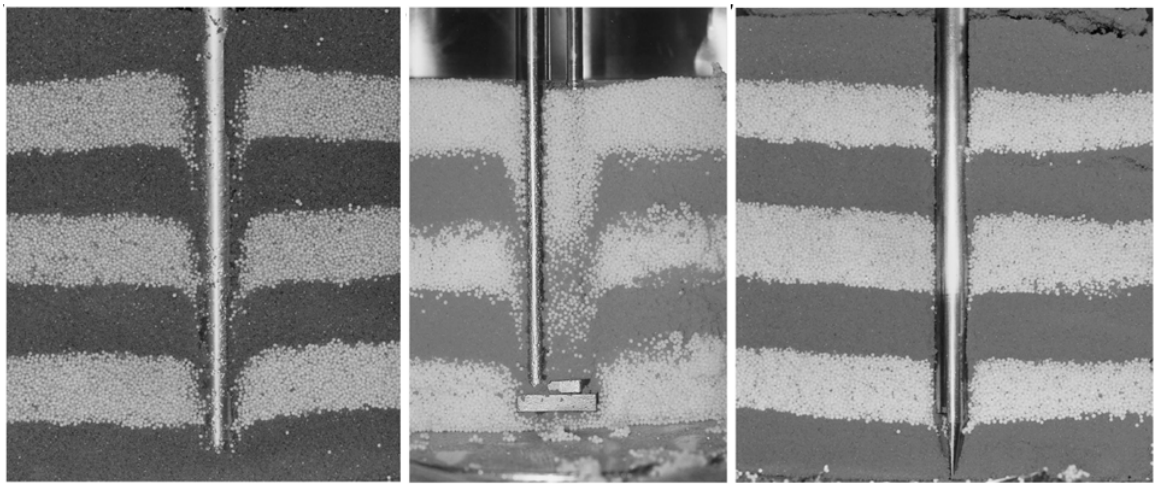

Figure 2.12: Disturbances caused by insertion of a (a) side-sampling probe, (b) end-sampling slug probe, and (c) end-sampling probe (Muzzio et al., 1997).

The disruption of the granular bed through the introduction of the probes causes the composition of the sample to not truly represent the mixture because the particles near the probe are dragged along the path of the insertation causing undesired results. Thus, Muzzio et al. (1997) state that the rationale proposed in the Barr Decision for taking small samples, in an effort to avoid sample averaging, is meaningless. Muzzio et al.

(1997) concludeed that accurate characterization of the structure of a granular mixture using an invasive probe is not feasible with current methods, and thus considerable improvement is needed if reliable prediction and control of the product quality is to be achieved.

According to Allen (1996), the two “golden rules of sampling” are: (i) a granular mixture should be sampled only when it is in motion and (ii) the whole granular stream should be uniformly collected for many short increments. Observance of these rules leads to the best sampling procedures. In order to fulfill the golden rules of sampling proposed by Allen (1996), significant efforts must be made to steer away from snap or slide spoon samplers (also known as sampling probes), which sample small amounts of granular material from several positions, to be directed toward developing full-stream samples methods.

However, to thoroughly understand a granular mixing process, sampling the end products alone does not provide a full assessment. Thus, a two-part measurement technique must be developed which couples qualitative observations of the entire mixing process with quantitative data related to the end products. Recently, Kingston and Heindel (2013d) developed a two-part measurement technique that coupled qualitative optical visualization and quantitative composition and statistical analysis together, and provided a thorough method for characterizing granular mixing processes.

2.1.8 Granular Mixing and Handling Equipment

In contrast to fluid systems, granular mixing processes are subjected to various interactive forces and are not self-diffusive (Masuda et al., 2010). Thus, they cannot be set into motion without an external force, and require specifically designed equipment to

perform these processes. Despite the solids-handling industry being quite mature, process and equipment design and the selection of appropriate operating conditions remain open to speculation because it lacks quantitative justification; it is based primarily on trial-and-error and experience, rather than quantitative science (Bridgwater, 2012). Moreover, the current level of industrial granular mixers operate with no effective control of mixture quality and lack scientific design (Bridgwater, 2010). The design of these mixers are often evaluated through segregation avoidance, which is obtained through serendipity and/or exhaustive trial-and-error procedures (Hajra et al., 2010). Cleary and Sinnott (2008) state that due to the lack of understanding of the interaction between mixer geometry and the granular material, limited progress has been made in optimizing mixer design. Moreover, specific mixing studies and resulting solutions associated with simple mixer geometries are rarely extensive and cannot be applied to more complex mixer geometries. Therefore, complex granular mixing processes must be studied using the specific mixer geometry and materials of interest.

Figure 2.13 illustrates several different types of granular mixers used in industry, including (a) horizontal cylinder, (b) v-type, (c) double cone, (d) ribbon, (e) screw-in-cone, (f) high speed, (g) rotating disk, (h) fluidized bed, (i) motionless (i.e. gravity), and (j) vibrational and mechanical agitation.

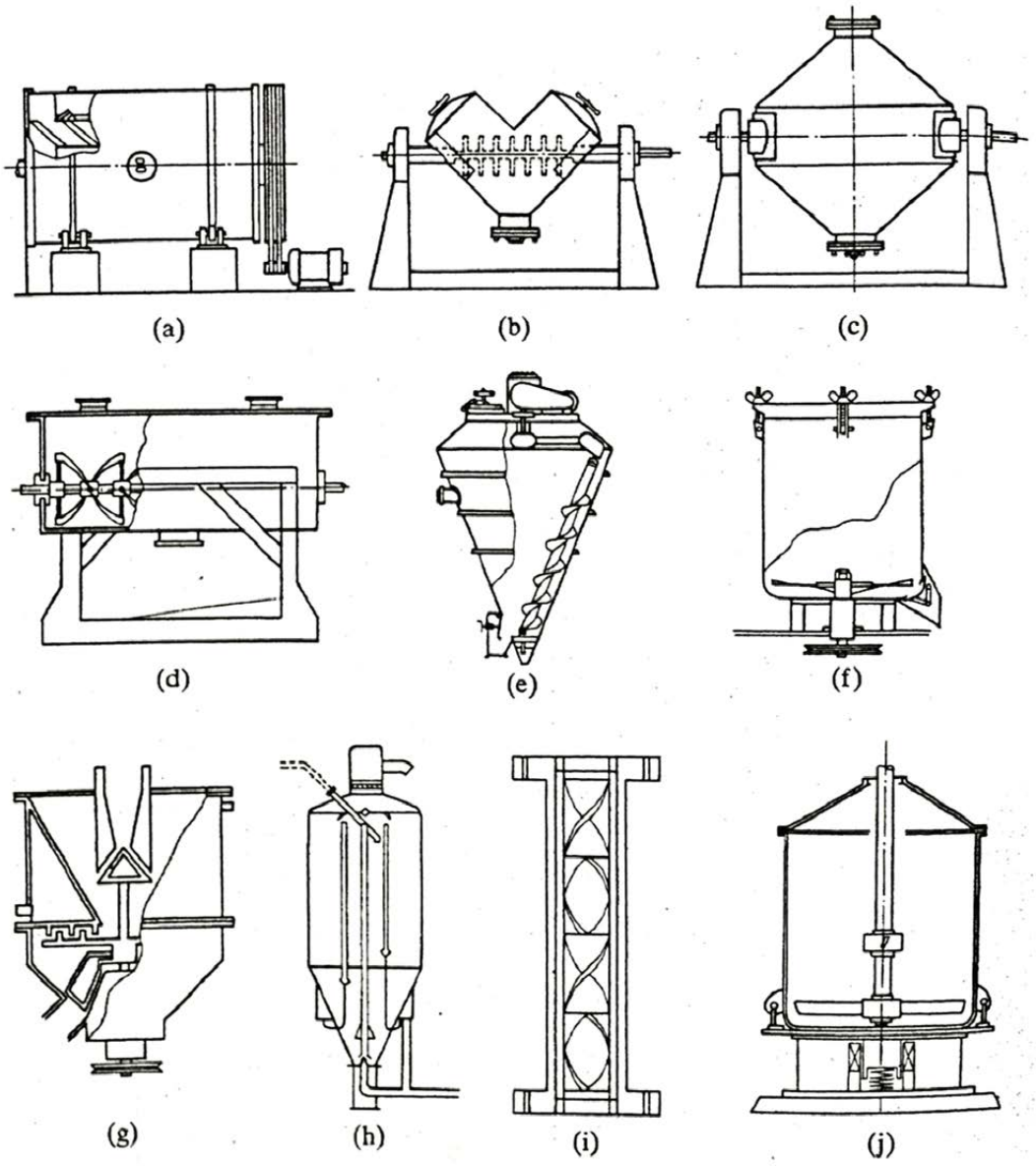

Figure 2.13: Examples of common granular mixers found in industry (Masuda et al., 2010).

Even with the development of a large number of mixers, there is still a mismatch between basic research involving idealized conditions and practical industrial needs (Ottino and Khakhar, 2001). Two primary misconnects are occurring: (i) mixers that are being used in industry have not been studied in laboratory settings because of their complex geometry, and (ii) scale effects from laboratory-scale to industrial-scale mixers

have not been properly addressed. For example, several industrial processes rely on equipment which features similar geometry to that of double screw mixers, such as double screw extruders and double screw pyrolyzers in the thermoplastic and energy conversion industries, respectively. However, minimal research has focused on characterizing the granular mixing dynamics in a double screw mixer despite its advantages over single screw mixers. The limited research which has been conducted on double screw mixers state that they enhance the mixing process and experience reduced power consumption, relative to single screw mixers (Camp, 1990). Thus, an improved understanding of the granular mixing process inside double screw mixers is needed in order to increase process efficiency and improve the quality of the resulting products.

This project addresses this issue by thoroughly understanding, characterizing, and optimizing the granular mixing of low density red oak chips and high density glass beads within a double screw mixer under various operating conditions. For this reason, additional consideration will be given to equipment which involves the use of screws (i.e., augers), to achieve their primary function. In general, this equipment may be separated into three different categories: (i) screw conveyors, (ii) screw feeders, and (iii) screw mixers.

2.1.8.1 Screw Conveyors

Screw conveyors are well-established transporting devices, capable of handling loose solids, liquids, or a combination of both, and provide a compact method of moving material from one location to another for relatively free-flowing materials (Colijn, 1985). Flowability is defined in the Conveyor Equipment Manufacturers Association (CEMA) materials classification standard, and denotes the degree of freedom of individual

material particles to move past each other (Colijn, 1985). This characteristic is important since, most commonly, a screw is mounted inside a stationary pipe or trough, and is rotated to push the material in the axial direction. This motion induces shear forces upon the material which causes it to tumble upon itself. Screw conveyors are used in a variety of industrial applications including the agricultural, milling, mining, pharmaceutical, plastic, and food processing industries, to name a few. However, screw conveyors can also be used to transport materials other than just granular matter. For example, Archimedean screws, attributed to Archimedes, were used to transport water from low lying bodies of water to fields for irrigation purposes in Ancient Egypt (Colijn, 1985). Additionally, multiphase flows can also be transported, such as mining or sewage slurries consisting of solid and liquid material. The application of a screw conveyor is largely dependent on the characteristics of the material being conveyed and must be considered carefully. Overall, screw conveyors are solely used to transport materials from one location to another, with its purpose not being to accurately control the material flow rate or mix the material in which it is transporting.

2.1.8.2 Screw Feeders

Unlike screw conveyors, screw feeders are used to accurately control the volumetric flow rate of the material which is being discharged. Screw feeders consist of a screw, a U-shaped trough or cylindrical casing, a hopper, and a drive motor. As the screw rotates, particles are forced to move from the hopper to the outlet of the feeder. The granular feed rate is proportional to the rotational speed of the screw. However, the instantaneous granular feed rate fluctuates periodically as the screw rotates due to the screw geometry.

Screw feeders are widely used to control the volumetric flow of materials from the bottoms of bins, hoppers, storage piles, etc. Screw feeders commonly incorporate the use of a variable pitch screw flights, as shown in Figure 2.14a, in the region where the material is being withdrawn from (i.e., the hopper). This allows the granular material to be withdrawn from across the entire length of the screw and helps improve the flow rate of the materials. Constant pitch screw flights, as shown in Figure 2.14b, only draw material from one region of the granular bed.

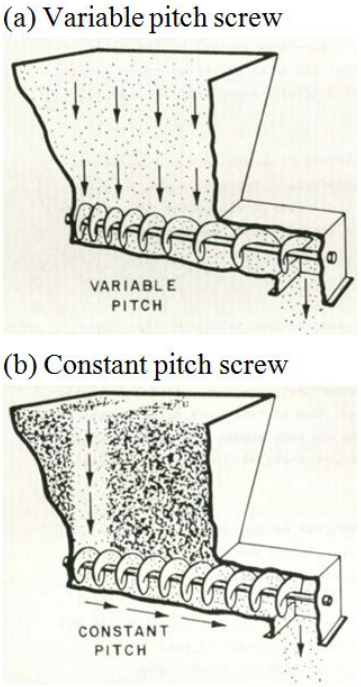

Figure 2.14: Screw feeders featuring a (a) variable pitch screw, and a (b) constant pitch screw (Colijn, 1985).

2.1.8.3 Screw Mixers

In contrast to screw conveyors and screw feeders, a screw mixer's primary function is to mix granular materials. Batch process screw mixers, such as the cone-screw mixer shown in Figure 2.13e, are typically orientated in the vertical direction. In the case of continuous screw mixers, such as the screw mixer used in this project, the screw mixer

also needs to provide the ability to convey the granular materials while performing its mixing operation. Continuous screw mixers are typically orientated in the horizontal direction. Single and double screw mixer configurations can be used. While single screw mixers are commonly used because of their simplicity, double screw mixers are becoming more popular in mixing applications because of their increased mixing effectiveness. However, double screw mixers bring several other important parameters into consideration, including the possibility of either nonintermeshing or intermeshing screw configurations, and the inability to incorporate complex screw geometry.

Martelli (1983) noted that nonintermeshing double screw configurations operate very similarly to single screw configurations, and thus have limited mixing potential. Moreover, Camp (1990) performed studies investigating the pyrolysis of coal, and noted that nonintermeshing screw configurations do not wipe each other because they are separated and produce operational problems such as material clogging. However, a consequence of a double screw configuration is the limited usefulness of mixing paddles, because of the physical interference that could result. Overall, double screw mixers provide significant increases in mixing relative to single screw mixers.

2.1.8.4 Screw Flighting Geometry

A major component which varies dramatically between screw conveyors, feeders, and mixers is the screw flight geometry. The first characteristic in describing a screw is the direction of the screws flights. The flights may be either right hand thread (RHT) or left hand thread (LHT). The direction of the screw flights can be clearly distinguished by looking at the axial end of the screw. A screw flighting that is wrapped around the shaft in a counter-clockwise direction is arbitrarily termed a LHT screw. Meanwhile, a

flighting that is wrapped around the shaft in a clockwise direction is termed a RHT screw. Note that viewing the screw from either end will result in the same configuration.

In addition to the direction of the flighting, the flighting geometry may also differ from application to application. In addition to simple helical flights, screws could include: (i) cut flights, which supplement the conveying action with moderate mixing; (ii) cut and folded flights, which act as lifting vanes to produce a cascading effect and results in agitation and aeration; (iii) flights with paddles, which are spaced at intervals and are typically set to partially oppose the forward flow of material resulting moderate mixing; (iv) cut flights with paddles, which combine the partially opposing paddles with the cut flights to considerably increase mixing, and (v) short pitch flights, which is typically used in devices inclined by more than 20° or even in vertical screw conveyors. Figure 2.15 illustrates the aforementioned designs.

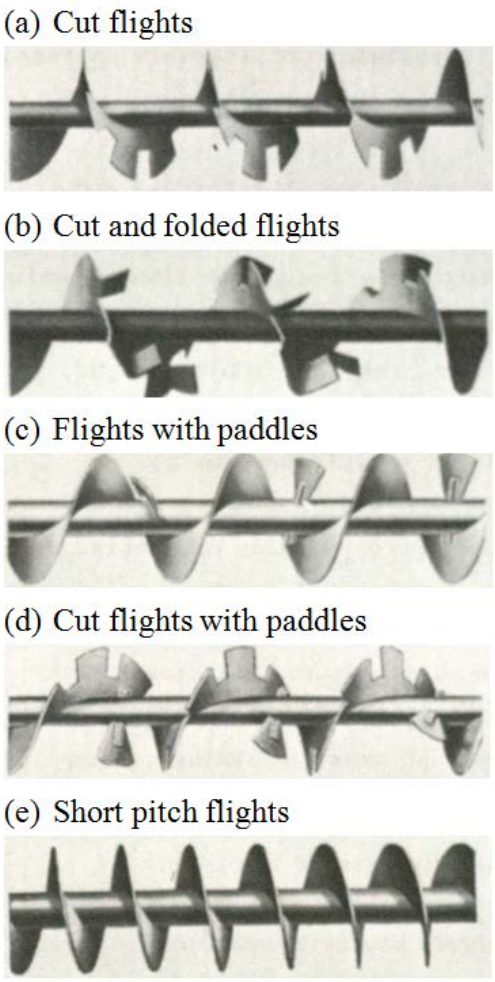

Figure 2.15: Different screw flighting geometries (Colijn, 1985).

In addition to variable pitch flights, other flighting configurations are available, as shown in Figure 2.16, and include: (i) tapered flights, which gradually increase the screw diameter and are commonly used in screw feeders to draw the material uniformly from the entire length of the feed opening; (ii) stepped diameter flights, which are frequently in screw feeding applications to change between tough sizes, pitch flights, (iii) stepped pitch flights, which also are used in screw feeders for the aforementioned reasons; (iv) long pitch flights, which are used as agitators and have been shown in increase the mixing of granular materials; (v) double flights of regular pitch, which promote a smooth flow and

discharge of materials; and (vi) double short pitch flight, which ensure more regulation of material flow.

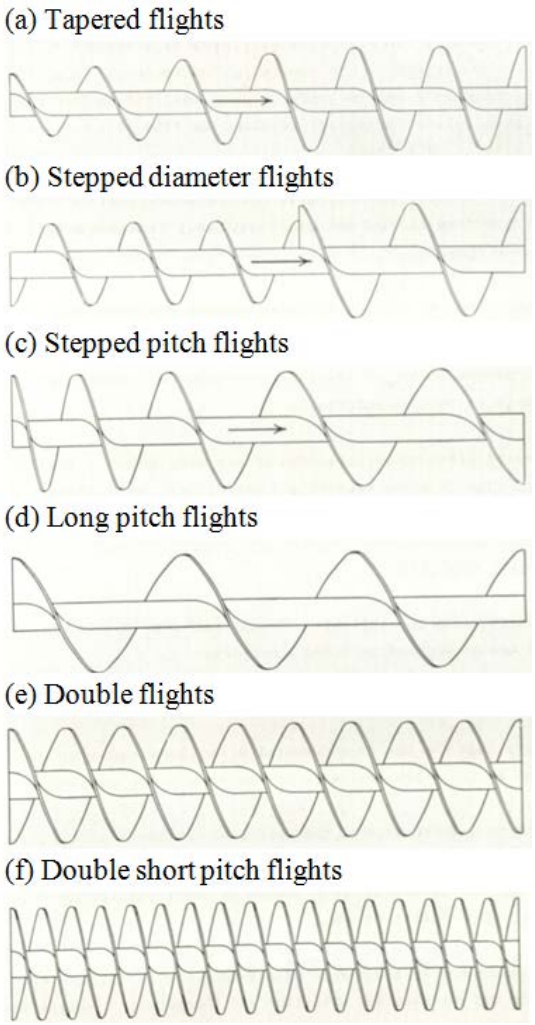

Figure 2.16: Various pitch and flight diameter combinations (Colijn, 1985).

2.1.9 Future of Granular Mixing

Despite a recent surge in the fundamental understanding of granular mixing and mixing equipment, there still remain many areas that need significant improvement. First, the fundamental understanding of granular mixing dynamics needs to be further developed. This includes, but is not limited to, the effects that differences in material properties have in mixing and segregation, and the effect that operating conditions have

in exploiting or minimizing these differences. Theoretical characterization of material properties for a few simple mixer types have been reported, but these fall short of what is needed for practical purposes (Bridgwater, 2010).

Second, scale-up laws allowing the results obtained during laboratory-scale testing to be applied to industrial-scale mixing equipment needs to developed. Current research efforts have primarily focused on laboratory-scale mixing equipment but little work has been done to develop scaling laws. Thus, a link to industrial-scale equipment is not available for granular applications.

Third, there is a need to increase the computational capabilities that currently restrict the number of granular particles that can be used in distinct element method (DEM) modeling (Bridgwater, 2010). Developing more accurate computational models will reduce the need to costly and time-consuming empirical testing. Furthermore, it will help to address the need of developing a more thorough understanding of the fundamental granular mixing dynamics.

Finally, a short coming in the field of granular mixing has been in the lack of quantitative characterization of mixture quality, and research falls short of what is needed for on-line characterization of mixture quality (Bridgwater, 2010). Bridgwater (2010) states that on-line concentration assessment at all length scales is needed, including the scale of individual particles, since it decides the effectiveness of the resulting products. Thus, there is a need to evaluate the particle microstructure. Various measurement methods, such as PEPT and various light reflectance methods give a great deal of information but do not measure composition. However, recent advances in digital image

analysis capabilities have made its use an attractive option for on-line granular mixing characterization.

2.2 Digital Image Analysis Techniques

Recently, a substantial amount of research has been focused on developing measurement techniques capable of continuously measuring mixing processes, quality, efficiency, etc. Advances in digital technology coupled with relatively low-cost equipment has allowed researchers to begin developing digital image processing and analysis techniques capable of determining mixing quality. This analysis technique relies on the ability to extract useful information from digital images, and image processing is often required to achieve desirable results. For example, Aissa et al. (2010a) used a thresholding method to transform a gray-scale digital image comprised of a mixture of white and black particles into a binary image with each pixel representing either a white or black particle. This procedure consisted of carefully calibrating a white and black image, separately, and then determining a gray-scale threshold value using the image intensity. Anything above the threshold value was classified a white particle while anything below the threshold value would be classified a black particle. From which, Aissa et al. (2010a) was able to characterize the mixing effectiveness of the system using a gray-level co-occurrence matrix (GLCM) and a mixing index.

While the prescribed image processing technique involving thresholding works quite well for a binary system with vastly different colored particles, it does not work well with multiple component systems involving particles of many colors. When plotting the intensity on a one-dimensional (1D) gray scale axis, many colors can overlap, and a

significant error is introduced. Thus, Aissa et al. (2010b) proposed to use a red, green, and blue (RGB) color analysis technique to track the mixing dynamics of a quaternary color blend of polymer powders. This technique involved using the RGB intensities to map 2D regions of pixels which exhibit similar color properties. The regions were then used to distinguish the different particle colors and analyze the mixing efficiency. However, one drawback of this method is the reduction from the 3D RGB data to a 2D plane. This limits the ability to distinguish more than about four vastly different colored particle types, or even less if the colors are somewhat similar.

Chen and Yu (2004) also used digital analysis techniques to measure the mixing effectiveness of a binary system of Ti/SiO_2 and C/SiO_2 in a batch mixing process. In contrast to measuring some sort of composition homogeneity (or lack thereof) as is traditionally done in many granular mixing systems, Chen and Yu (2004) measured the number of matched pairs of the two different powders using a four-way, pixel by pixel matching technique. Although the mixing analysis technique was different, a similar gray-scale thresholding technique to that of Aissa et al. (2010a) was implemented, where a gray-scale image was converted to a binary image based on a specifically selected threshold value. A custom computer program was then used to count the number of unmatched pairs (i.e., particles that did not share a common side with that of the other powder type), from which the mixing efficiency was determined. This mixing assessment was chosen because direct contact between different particle types is critical for solid-solid reactions.

The aforementioned digital image analysis methods were all developed to perform mixing assessment on batch granular processes. Significantly less research has been put

forth on developing digital image analysis techniques for continuous granular mixing process. Moreover, a technique which utilizes the full 3D RGB color spectrum to distinguish a large number of colored particles does not exist. Thus, the use of a full 3D RGB digital image analysis technique which evaluates continuous granular mixing processes is needed.

However, the use of digital image analysis methods for the characterization of granular mixing processes only has the ability to analyze the surface of the flow due to the opaque nature of the granular material. Other noninvasive methods, such as X-ray visualization and quantification, are currently being developed to overcome these issues.

2.3 X-ray Visualization Techniques

The ability to visualization and quantify various granular and multiphase flows is highly dependent on the nature of the flow and the limitation of the system itself. Visualizing and quantifying single phase flows is fairly straightforward when the vessel and fluid are optically transparent. However, in many multiphase flows of industrial interest, it is difficult to measure and/or visualize the flow through visual observation due to the opaque nature of the vessel (e.g., tanks, reactors, etc.) or the flow itself (e.g., oil). For example gas-liquid bubble column flows are often impossible to measure visually because the difference in refractive index between air and water distorts measurements at moderate (5%) or higher gas fractions (Seeger et al., 2003). In the case of granular mixing, the granules themselves are usually opaque, making any visual measurements below the surface of the flow impossible. One way to overcome this limitation is the use of invasive probes; however, such probes only provide a single, point-measurement and

their very presence has the potential to disrupt the flow itself (Boyer et al., 2002). Therefore, noninvasive techniques, such as X-ray flow visualization, are then preferred due to their ability to accurately measure the system without causing any disruptions to the flow, and thus significant effort has gone into developing noninvasive methods of measuring flows (Chaouki et al., 1997; Heindel, 2011).

Since X-ray flow visualization was used for this project, it will be further discussed while details regarding the other noninvasive techniques, such as electrical capacitance tomography (ECT) (van Ommen and Mudde, 2008), gamma-ray tomography (Bruvik et al., 2010), magnetic resonance imaging (MRI) (Ehrichs et al., 1995), and ultrasonic tomography (Rahiman et al., 2006), can be found in the literature. First, a review of X-ray fundamentals will be presented. Then, a summary of various X-ray imaging techniques will be discussed which can be further separated into three sub techniques: X-ray radiography, stereography, and computed tomography.

2.3.1 X-ray Fundamentals

X-rays were discovered in 1895 by Wilhelm Conrad Roentgen, a professor at Wurzburg University in Germany. Roentgen first used the X-rays to radiograph a set of weights in an opaque box to show his colleagues, but then later used this same technique to film his wife’s hand. From this point on, X-rays were used for both industrial and medical applications.

X-rays are a form of electromagnetic radiation and has wavelengths between 0.01 and 10 nanometers, and can range in energy from 0.1 keV to 100 MeV (Heindel, 2011). Moreover, X-rays can be split into two categories: (i) hard X-rays, which contain the short wavelength X-ray component and traverse relatively thick or dense objects, and are

widely used in medical and security applications, and (ii) soft X-rays, which contain the longer wavelength X-rays which can enhance image contrast (Heindel, 2011). Most X-ray sources are polychromatic, meaning that they produce X-rays across a spectrum of energies and are composed of both hard and soft X-rays. However, monochromatic X-ray sources are available, but are rare and very costly.

Polychromatic X-ray sources produce both hard and soft X-rays, and the softer, lower energy X-rays are attenuated more readily than hard, higher energy X-rays. This produces a phenomenon called beam hardening, and can cause X-ray artifacts to occur. Various techniques can be applied to reduce the effect of beam hardening, but will not be covered in this paper.

X-rays are produced both naturally and artificially, by sources such as the sun and by ionizing a target source such as tungsten with an electron beam, respectively. In the artificial case, the electrons are emitted from a cathode and accelerated toward an anode by a high voltage potential between the cathode and the anode. After the electrons hit the anode, they are decelerated and the emission of electromagnetic radiation occurs.

The theoretical attenuation of X-ray energy for a single phase medium is predicted by the Beer-Lambert law:

$$I = I_0 \exp\left[-\left(\frac{\mu}{\rho} \right) \rho l \right] \tag{2.18}$$

where I is the X-ray energy recorded by a detector, I_0 is the X-ray energy emitted by a monochromatic X-ray source, μ/ρ is the mass absorption coefficient for the medium, ρ is the medium density, and ℓ is the X-ray path length through the medium (Heindel, 2011). The mass absorption coefficient is a function of the X-ray energy and the atomic

number of the absorbing medium. For two-phase systems consisting, Eqn. 2.18 can be rewritten as:

$$I = I_0 \exp\left[-\left((1-\varepsilon)\mu_1 + \varepsilon\mu_2\right)\ell\right] \tag{2.19}$$

where μ_1 and μ_2 are the linear absorption coefficients of phases 1 and 2, respectively, ε is the volume fraction of phase 2, and ℓ is the path length of the X-ray beam through the two-phase system (Heindel, 2011).

Important X-ray flow visualization parameters include spatial, temporal, and density resolution. Spatial resolution corresponds to the minimum distance that two high-contrast points can be separated. Temporal resolution is related to the frequency that the system is able to resolve successive images for a dynamic system. Density resolution is defined as the smallest difference in mass attenuation coefficients that the system can distinguish. Dudukovic (2000) states that the ideal noninvasive experimental system should have high spatial and temporal volume fraction velocity vector field resolution, and be capable of providing snapshots of the flow and the time history of it over a range of scales. However, a single experimental system that satisfies all these needs does not currently exist (Heindel, 2011); although various X-ray systems do accomplish these tasks individually. For example, X-ray radiography provides high temporal resolution, which is suitable for dynamic flow processes. X-ray computed tomography provides excellent spatial resolution and reasonable density resolution, which is best for time-averaged phase distributions.

2.3.2 Radiography

Radiography is performed by obtaining a shadow image of an object using penetrating radiation, such as X-rays. An X-ray radiography imaging device, as shown in

Figure 2.17, records the 2D projection of the 3D object when the object is positioned between the X-ray source and the 2D detector. The image captured by the detector is a 2D projection map of the X-ray attenuation of the object.

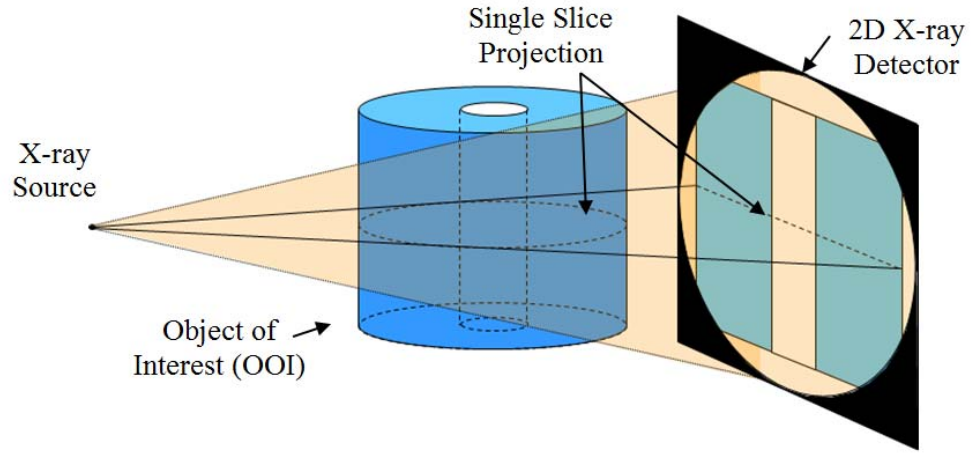

Figure 2.17: X-ray radiography schematic (adapted from Heindel (2011)).

X-rays can be converted to a useable format through a variety of means. Prior to digital photography, X-ray images were processed using traditional photographic film techniques; however digital detectors are now much more common. Digital detection is accomplished through one of two means: (i) direct and (ii) indirect detection. Direct detection utilizes an X-ray photoconductor to directly convert X-ray photons to an electrical charge (Heindel, 2011). Indirect detection utilizes a two-step processes which first converts incident X-rays to visible light using a scintillator, and then the visible light is converted to an electrical signal through a photodetector (Heindel, 2011). Regardless of the method used to convert the X-rays to visible light, an electronic readout mechanism is used to convert the analog signal to a digital signal enabling a digital images to be produced (Heindel, 2011). Digital radiography improves the speed at which the images are acquired and enhances manipulation and storing capabilities.

X-ray radiography has been used in a number of fields including medical imaging (Niki et al., 1993; Shepp and Kruskal, 1978), nondestructive evaluation (Feldkamp et al., 1984; Zolfaghari et al., 2002), and fluid flow visualization. Grohse (1955) was one of the first researchers to use X-rays to visualize and assess gas-solid fluidized beds. His research was focused on qualitatively characterizing density variations in silicon powder fluidized beds as a function of gas flow rate. More recently, X-ray radiography has been used by a number of researchers, (Heindel et al., 2008; Jenneson and Gundogdu, 2006; Roels and Carmeliet, 2006; Uchida and Okamoto, 2006, 2008) to provide characterization of opaque systems.

2.3.2.1 Tracer Particles

Tracer particles can also be used to characterize single phase (Lee and Kim, 2003), multiphase (Drake et al., 2008; Drake et al., 2009b), and granular processes (Morgan and Heindel, 2010). Tracer particles range from radioactive emitting tracer particles to X-ray absorbing tracer particles to neutron absorbing particles (Heindel, 2011), depending on the application being used.

The following efficiency of the tracer particles to critical to successful visualization and characterization, and often depends on the selection and construction of tracer particles themselves. Drake et al. (2009a) outlined the development of small, neutrally buoyant tracer particles allowing successful X-ray imaging of fluidized beds to be performed. Although, neutrally buoyant, these tracer particles featured different X-ray attenuation properties than the fluidized bed materials, allowing them to be detected. Uchida and Okamoto (2006) performed theoretical and experimental studies using X-ray

radiographic imaging to study the following efficiency of different tracer particle types in powder flows with particle sizes between 10^{-6} and 10^{-5} m.

2.3.3 Stereography

X-ray stereographic measurement techniques utilize information from two 2D projections to calculate the 3D location of particular features within the object of interest (OOI). The two independent 2D projections can be separated by a rotational or translational offset. Moreover, if identical source and detector equipment is used for both projections, these projections can be acquired simultaneously. Figure 2.18 shows a schematic representation of the X-ray stereography process where one source and detector pair provides a radiographic projection of the x-z coordinate as a function of time, and the other source and detector pair provides the y-z coordinate as a function of time (Heindel, 2011). From these two independent projections, the 3D coordinate of the OOI can be obtained as a function of time.

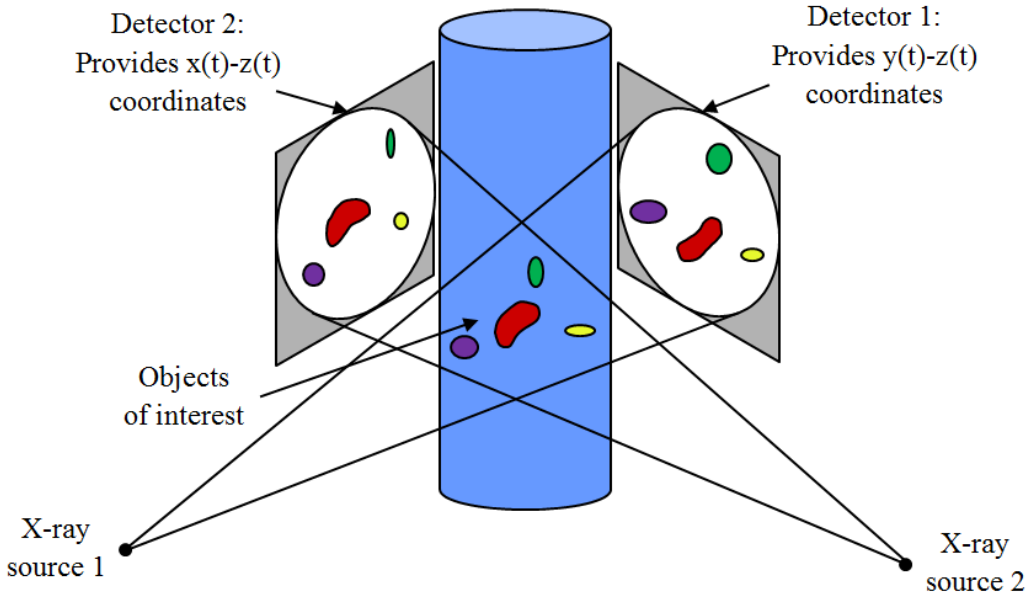

Figure 2.18: X-ray stereography schematic (adapted from Heindel (2011)).

Stereography techniques provide unique visualization capabilities including 3D flow structures, and the ability to determine flow characteristics such as bubble rise and particle settling velocities, and breakup and coalescence rates. The use of tracer particles enables X-ray particle tracking velocimetry (XPTV) to be performed. Seeger et al. (2003) outlined several advantages that XPTV offers over other velocimetry techniques, such as particle image velocimetry (PIV), including: (i) the ability to track velocities in opaque flows, (ii) determination of 3D position and velocity components, and (iii) being noninvasive. XPTV has been shown to provide a balance between spatial and temporal resolution (Drake et al., 2009b; Seeger et al., 2003). This technique has been shown to obtain temporal resolutions of up to 1000 FPS for 2D studies (Morgan et al., 2013), and 25 FPS for 3D studies (Seeger et al., 2003). A thorough review of noninvasive velocimetry techniques with applications in multiphase flows is available in the literature (Chaouki et al., 1997).

One drawback of some previous XPTV work is its failure to account for the conical beam geometry of the X-ray source (Drake et al., 2008; Drake et al., 2009a; Drake et al., 2009b; Lee et al., 2009; Morgan et al., 2013; Morgan and Heindel, 2010; Shimada et al., 2007; Xiao et al., 2005). When the cone-beam is assumed to be parallel, the tracer particle's position and resulting velocities will be incorrect; particularly near the edges of the system. Another drawback of some previous XPTV measurements is the time difference between the acquisition of the left frame and the right frame (Seeger et al., 2003). While small, this difference can make it difficult to match a particle between frames, and poses a challenge for the determination of the particle velocity. Recently, Kingston et al. (2013) performed XPTV studies using temporally synchronized X-ray

imaging equipment and also utilized a cone-beam compensated back-projection algorithm to account for the cone-beam X-ray source. In doing so, they demonstrated its usefulness over parallel-beam back-projection algorithms.

Disadvantages associated with XPTV are low image frequency and the challenging selection of tracer particles with the desired flow characteristics while still offering differences in X-ray attenuation, as previously mentioned. These challenges were also addressed by Kingston et al. (2013), and will be presented in Chapter 10.

2.3.4 Computed Tomography

Tomography refers to the cross-sectional imaging of a system from either transmission or reflection data collected by illuminating the system from many different angles (Heindel, 2011; Kak and Slaney, 2001). Quantitative noninvasive techniques include electrical impedance tomography (EIT), electrical resistance tomography (ERT), electrical capacitance tomography (ECT), ultrasonic computed tomography (UCT), and X-ray computed tomography (XCT), to name a few (Heindel et al., 2008).

Tomography systems are often classified into soft field or hard field measurement techniques. In soft field techniques, such as ECT, a change in the measured property (e.g., capacitance) in one location changes the recorded field through the entire domain (Heindel, 2011). In hard field techniques, such as X-ray computed tomography, the field lines of the measured property (e.g., X-ray attenuation) remain straight and are not influenced by property changes out of the line-of-sight (Heindel, 2011). Due to the nature of the systems, soft field techniques require more complicated reconstruction process and can produce multiple solutions, relative to hard field techniques.

X-ray computed tomography was first developed by Godfrey N. Hounsfield in 1972. Hounsfield would later share the 1979 Nobel Prize in Medicine for his development of the mathematical reconstruction process of multiple projections, which was originally proposed by Radon in 1917 (Kak and Slaney, 2001). X-ray CT imaging consists of the collection of several hundred individual radiographic projections, which are then reconstructed using various algorithms, such as a filtered back-projection (Heindel, 2011). Unlike X-ray radiography and stereography techniques, X-ray computed tomography must take many images of the same object. This process takes a long time to acquire the needed imaging data relative to X-ray radiographic techniques, and is on the order of minutes, but can take up to several hours. Consequently, it is not possible to capture dynamic processes in real time. Thus, X-ray CTs produce a time-averaged representation of a dynamic system. Figure 2.19 illustrates the X-ray CT process.

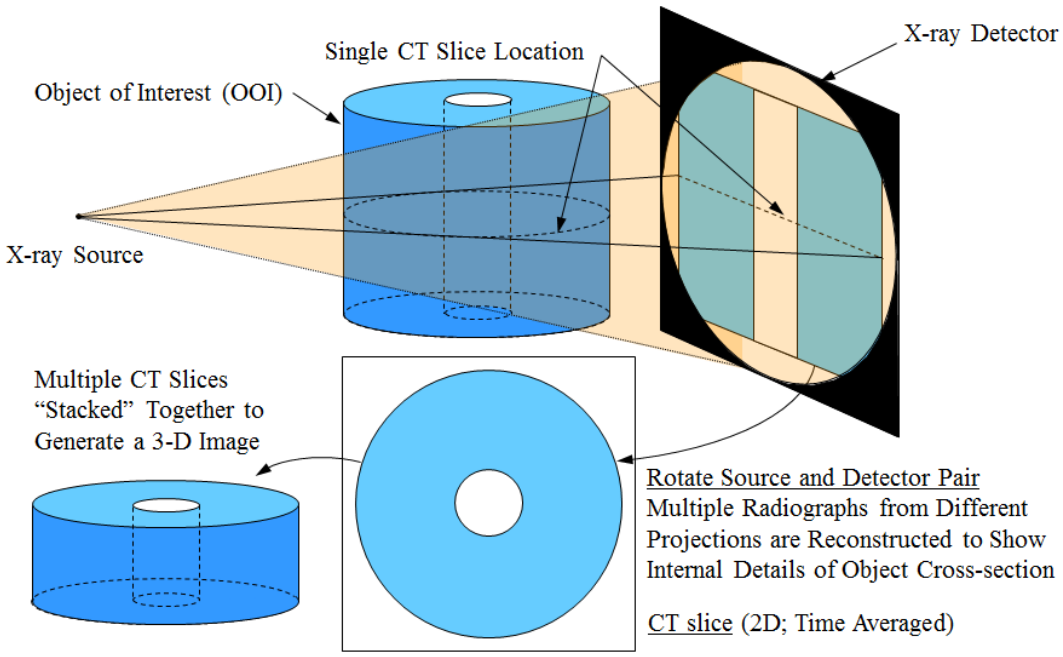

Figure 2.19: X-ray Computed Tomography (CT) process (adapted from Heindel (2011)).

After the collection of several 2D radiographic images from different angles, a number of reconstruction methods are available to process the data. In general, three different types of back-projections and three different algorithm methods are used. The three different types of back-projections are parallel-beam, fan-beam, and cone-beam. Ideally, the selected back-projection type would match the type of X-ray source being used. However, this is not always the case. Parallel-beam back-projection reconstructions are computational less intensive than fan-beam, and even less intensive than cone-beam back-projection reconstructions, and are therefore most commonly used. However, most X-ray sources are cone-beam sources. Using a back-projection type which does not match the type of X-ray source introduces error into the reconstruction, similar to what was mentioned in the XPTV back-projections.

The three different types of algorithms are filtered-back-projection (FBP), iterative back-projection, and algebraic back-projection. The FBP algorithm is the standard algorithm of tomography (Defrise et al., 2005), and utilizes a filter to reduce image noise. Moreover, FBP projections are less computational intensive and render much faster. Additional details regarding iterative and algebraic back-projections can be found in the literature (Defrise et al., 2005).

2.4 Biomass Thermochemical Conversion

This section provides a brief introduction into the thermochemical conversion of biomass into bio-oil and is merely presented to provide context to the motivation behind this project. It is in no way exhaustive and it is not meant to provide the reader with a significant background as to why bio-oils should or should not be produced.

2.4.1 Motivation

In 2011, 82% of the United States' energy consumption was attributed to nonrenewable energy resources (Energy Information Administration, 2012). Moreover, despite improved product efficiency, greenhouse gas (GHG) emissions have increased by 17.5% from 1990 to 2010 (Davis, 2012). In contrast to fossil fuels, bio-oil derived from cellulosic biomass provides significant environmental and sociological advantages such as being carbon dioxide (CO_2)/GHG neutral, releasing zero sulfur oxide (SO_x) emissions, and providing a dependable and domestic energy source (Mohan et al., 2006). Furthermore, bio-oil can also substitute for fuel oil or diesel in many static applications including boilers, furnaces, engines, and turbines for electricity generation in addition to being upgraded to serve as transportation fuels (Bridgwater, 2003). The thermochemical conversion of biomass into bio-fuels through pyrolysis, gasification, or combustion is a promising non-nuclear form of future energy (Mohan et al., 2006) and is the best option for reducing the use of petroleum and other fossil fuels (Brown and Brown, 2012b). In addition, energy from other renewable sources such as wind, solar, geothermal heat, and hydro are more costly and less infrastructure compatible than bio-fuels (Brown and Brown, 2012b).

However, current economics do not favor bioenergy and bio-based products (Brown, 2003). Other factors are attracting the use of bioenergy such as environmental quality, national security, excess agricultural production, and rural development (Brown, 2003). While the economics of biorenewable resources is not a topic of discussion in this review, several introductions to the economics are available in the literature (Brown, 2003; Brown and Stevens, 2011; Yoder et al., 2011).

2.4.2 Biomass

Biomass, also known as biorenewable resources, is organic material of recent biological origin (Brown, 2003). Cellulose biomass, the fibrous, woody, and generally inedible portions of plants that make up 75% or more of all plant materials, is the most abundant form of biomass on the planet (Brown and Stevens, 2011). Particular industries, such as the logging industry, generate a considerable amount of waste that is simply not used, and thus could be used to produce bio-oil. This review focuses solely on the thermochemical conversion of cellulosic biomass for the production of bio-oil.

2.4.3 Thermochemical Conversion

Thermochemical conversion of biomass uses heat and catalysts to convert plant polymers into fuels, chemicals, or electric power (Brown and Stevens, 2011). Thermochemical conversion occurs at temperatures that are at a minimum several hundred degrees Celsius and up to 1000°C above ambient temperatures (Bridgwater and Peacocke, 2000; Brown and Stevens, 2011; Mohan et al., 2006); causing these processes to occur very rapidly. A number of different thermochemical pathways are available for the conversion of cellulose biomass, including combustion, gasification, fast pyrolysis, hydrothermal processing, and hydrolysis to sugars, as shown in Figure 2.20 (Brown and Stevens, 2011). This section will primary focus on the fast pyrolysis path because of its use in screw pyrolyzers and relevance to double screw mixers, but reviews of other pathways are available in the literature (Bridgwater, 2003; Brown and Stevens, 2011).

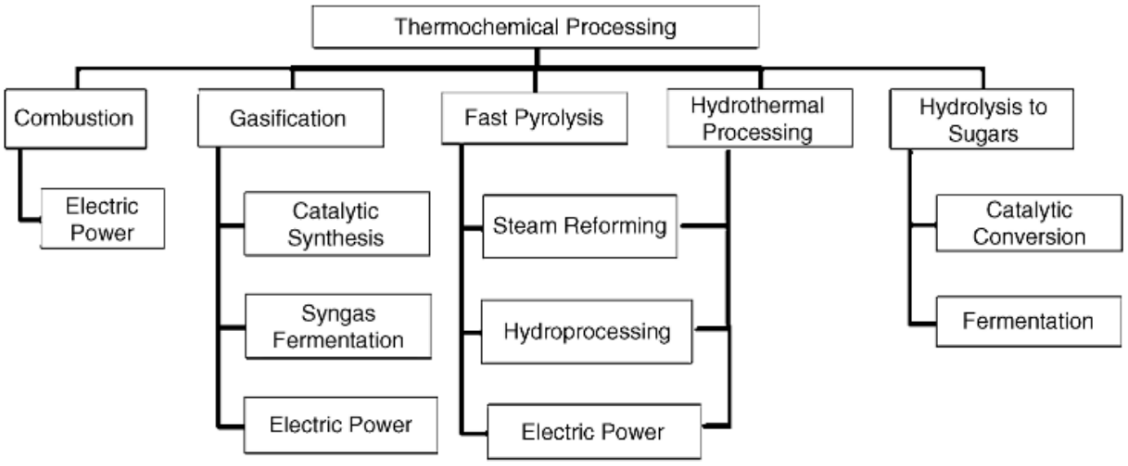

Figure 2.20: Thermochemical pathways for the production of fuels, chemical, and power (Brown and Stevens, 2011).

2.4.3.1 Pyrolysis

Pyrolysis is the thermal decomposition of organic material in the absence of oxygen (Mohan et al., 2006). Pyrolysis processes were first used by ancient Egyptians for creating tar for caulking boats (Mohan et al., 2006), but being more recently used for the thermochemical conversion of biomass into bio-oil. Pyrolysis processes may be separated into two types, depending on the operating conditions: (i) slow pyrolysis and (ii) fast pyrolysis. The terms slow and fast refer to the heat transfer rates into the biomass particles, and despite being vastly different, they are somewhat arbitrary and lack absolute classification. A brief review of both slow and fast pyrolysis will be presented with emphasis given to the fast pyrolysis.

2.4.3.1.1 Slow pyrolysis

Slow pyrolysis has been applied for thousands of years and has been mainly used for the production of charcoal (Mohan et al., 2006). Lower heat transfer rates combined with longer vapor residence times, which can range from 5 to 30 minutes, causes the vapor phase to continually react with each other as the solid char and any liquid are being

formed (Mohan et al., 2006). In the 1980s, researchers found that the pyrolysis liquid yields could be increased using fast pyrolysis, where a biomass feedstock is heated at a rapid rate and the vapors produced are also condensed rapidly (Mohan et al., 2006).

2.4.3.1.2 Fast pyrolysis

Advances in fast pyrolysis processes have been relatively recent because it is in a relatively early stage of development (Bridgwater, 2002), and is currently the least understood thermal degradation process (Mohan et al., 2006). Fast pyrolysis is the rapid thermal decomposition of organic compounds at moderate temperatures in the absence of oxygen to produce mostly condensable gases and aerosols that are condensed to form an energy-rich liquid known as bio-oil, but can also yield noncondensable gases and solid biochar (Brown, 2003; Mohan et al., 2006). Fast pyrolysis relies on four essential features: (i) very high heat transfer rates, (ii) carefully controlled reactor operating conditions (typically between 425-500 °C), (iii) short vapor residence times (typically less than 2 seconds), and (iv) rapid cooling of pyrolysis vapors and aerosols (Mohan et al., 2006).

Fast pyrolysis is an attractive option for the thermochemical conversion of biomass, and is the leading method for producing bio-oil for several reasons: (i) virtually any form of biomass can be used, (ii) low production costs, (iii) high thermal efficiency, (iv) CO_2 neutral, and (v) high bio-oil yields (Mohan et al., 2006). Despite being the least understood thermal degradation process, the high heat transfer rates of fast pyrolysis significantly increase bio-oil yields compared to liquefaction, gasification, combustion, and traditional slow pyrolysis (Bridgwater, 2003; Mohan et al., 2006).

2.4.3.1.2.1 Heat Transfer Requirements

Various methods are available to transfer heat to biomass particles using pyrolysis, including: (i) hot preheated gases, (ii) hot preheated gases and heated reactor walls; (iii) heated reactor walls, (iv) hot heat carrier media, (v) and preheated gases and hot heat carrier media (Bridgwater and Boocock, 1997). Various reactors including fluidized beds, screw pyrolyzers, and other mechanical mixing devices are used to accomplish the high heat transfer rates.

Brown and Brown (2012a) reported that an indirectly heated screw pyrolyzers (i.e., screw pyrolyzers that don't use a heat carrier media) have limited usefulness to the development of advanced biofuels because the use of a heat carrier will be mandatory for a commercial-scale screw pyrolyzer to provide the high heat transfer rates required for fast pyrolysis. The high-temperature heat carrier transfers its heat to the biomass with the aid of the mechanical mixing of the double screws. As a result, the heat transfer rates and resulting bio-oil yields are significantly influenced by the screw pyrolyzer's operating conditions and its ability to mechanically mix high density heat carrier media (e.g., stainless steel shot, refractory sand, etc.) with low density biomass particles (e.g., red oak chips, ground corncobs, switchgrass, etc.). However, minimal research efforts have been directed towards understanding the granular mixing dynamics. High heating rates which ultimately result from quick, efficient, and adequate mixing are needed. This is the fundamental motivation behind this project.

An approach to maximizing bio-oil yields is to subject the biomass to extremely high conduction and convection heat transfer rates, which are the dominant modes of heat transfer for fast pyrolysis, while still maintaining moderate temperatures. Heat transfer

rates as high as 1000 or 10000°C/s has been claimed for temperatures under 650°C; these high heating rates minimize biochar formation (Mohan et al., 2006). However, in order to achieve high heat transfer rates, biomass particles must be relatively small in size (heat penetration depth of less than 2 mm) (Brown, 2003; Brown and Stevens, 2011; Mohan et al., 2006).

2.4.3.1.2.2 Fast Pyrolysis Products

Fast pyrolysis processes which feature relatively short residence times (0.5-2 s), moderate temperatures (400-600°C), and rapid condensation at the end of the process produce 60-75% by weight liquid bio-oil, 15-25% by weight solid biochar, and 10-20% by weight noncondensable gases, depending on the feedstock used (Bridgwater, 2002; Mohan et al., 2006). The resulting liquids are highly oxygenated and can contain up to 15-20% water, but shows no appreciable phase separation (Brown, 2003). No waste is generated from fast pyrolysis because the bio-oil and solid biochar can be used as a fuel, and the gas can be recycled back into the process (Mohan et al., 2006).

The resulting products from fast pyrolysis have been shown to be extremely dependent on the selected operating conditions. Brown and Brown (2012a) performed 30 experiments involving the fast pyrolysis of White Spruce and Poplar wood in a laboratory-scale double screw pyrolyzer. The heat carrier inlet temperature, total nitrogen sweep gas volumetric flow rate, screw rotation speed, and heat carrier mass flow rate were the four experimental variables. From their experiments, the bio-oil and biochar yields ranged from 42.4 to 73.6% by weight and 11.0 to 38.7% by weight, respectively, while the non-condensable gases ranged from 9.1 to 22.1% by weight. Response surface methodology was used in this study to optimize the pyrolysis process for maximum bio-

oil production, and the heat carrier inlet temperature was determined to be the most influential.

2.4.3.1.3 Chemical Reactors

A number of different chemical reactors are used to convert biomass to bio-oil via pyrolysis, including: (i) entrained flow reactors, (ii) ablative pyrolysis reactors (iii) bubbling fluidized beds, (iv) circulating fluidized beds, (v) rotating-cone pyrolyzers, (vi) vacuum pyrolysis reactors, and (vii) screw pyrolyzers. In this review, emphasis will only be given to screw pyrolyzers because of their relevance on this project. However, reviews on different reactor types are available in the literature (Bahng et al., 2009; Bridgwater, 2002; Bridgwater, 2003; Bridgwater et al., 1999; Donahue and Brandt, 2009; Meier and Faix, 1999; Mohan et al., 2006; Scott et al., 1999). Tradeoffs between different reactor types exist, and Scott et al. (1999) claim that none of the reactor concepts in their present state satisfy all the requirements needed for the production of bio-oil with trouble-free operation, proven scale-up technology, and economically competitive performance. For example, entrained flow, vacuum, and ablative pyrolysis reactors exhibit poor heat transfer rates, low bio-oil yields, and reaction rates limited by heat transfer to the reactor instead of the biomass, respectively (Bridgwater, 2003). One relatively new reactor type that is currently being developed is the screw pyrolyzer.

2.4.3.1.3.1 Screw Pyrolyzers

Screw pyrolyzers are being developed for the thermochemical conversion of biomass into bio-oil, and are a relatively new chemical reactor design compared to more traditional fluidized beds, rotating cones, and ablative reactors. Screw pyrolyzers, more specifically double screw pyrolyzers, feature two intermeshing and offset screws

(typically twin screws) encased in a reactor which mechanically conveys and mixes biomass and heat carrier media. The reactor is typically purged with nitrogen such that it is an oxygen deficient environment. The heat carrier media is externally heated and provides the heat required to decompose the biomass and promote pyrolysis. Screw pyrolyzers offer several advantages over other reactor types including: (i) compact size, (ii) does not require a fluidizing gas, (iii) operates at lower process temperatures, (iv) operates continuously, (v) lower energy requirements, (vi) allows for adjustment of vapor residence time. However, one disadvantage of screw pyrolyzers is that they are mechanical complexity.

The screw pyrolyzer's high heat transfer rates and resulting bio-oil yields are significantly influenced by its operating conditions and its ability to mechanically mix high density inert heat carrier media (e.g., stainless steel shot, refractory sand, etc.) with low density biomass particles (e.g., red oak chips, switchgrass, etc.). Previous research efforts featuring screw pyrolyzers have primarily focused on the quality of the products and how they relate to the feedstocks used (Ingram et al., 2008) or the reactor operating conditions (Brown and Brown, 2012a). However, no research efforts have focused on relating the granular mixing inside a double screw pyrolyzer to its operating conditions. Thus, a thorough understanding of the granular mixing dynamics is needed for more efficient operation and higher bio-oil yields.

The screw mixer's improved mixing effectiveness will have far reaching effects, particularly in the case of screw pyrolyzers because the increased mixing will lead to higher heat transfer rates, which have been shown to increase bio-oil yields (Mohan et al.,

2006). Through these research efforts, the economic feasibility of the screw pyrolyzer for the production of bio-oil will be improved by reaching higher bio-oil yields.

2.4.4 Bio-oil

The thermochemical conversion of biomass into bio-oil offers several advantages such as: (i) lower transport costs, (ii) smaller storage requirements, and (iii) ease of conveyance into the reactor (Brown and Stevens, 2011). Bio-oils are dark red-brown to almost black, free flowing organic liquids that are comprised of highly oxygenated compounds (Mohan et al., 2006), as shown in Figure 2.21. It is this presence of oxygen that gives rise to the difference in properties and behavior between hydrocarbon fuels and biofuels. Bio-oil can be made from a variety of forest and agricultural biomass wastes and yields depend highly on the operating conditions and feedstock composition. Bio-oil's may also be commonly referred to as pyrolysis oils, pyrolysis liquids, wood oils, liquid smoke, wood distillates, and liquid wood, to name a few (Bridgwater, 2003; Mohan et al., 2006). For simplicity, the term bio-oil will only be used in an attempt to avoid confusion.

Figure 2.21: Bio-oil (Dynamotive Energy Systems (2010)).

2.4.4.1 Applications for Bio-oil

Technoeconomic analysis states that bio-oil could be upgraded to synthetic gasoline and diesel for $2-3 per gallon gasoline equivalent (Wright et al., 2010). Thus, fast pyrolysis for the production and upgrading of bio-oil has generated recent interest.

Bio-oil can be used in a number of different ways, including (i) burning it as a source of fuel through direct combustion, thermal gasification, or anaerobic digestion, and converting the heat into work; (ii) converting or upgrading it to transportation fuels such as ethanol, methanol, and biodiesel; and (iii) extracting chemicals for a wide range of purposes (Bridgwater, 2002; Brown, 2003). Typical chemicals include wood flavorings, liquid smoke, resins, agri-chemicals, fertilizers, preservatives, adhesives, and emissions control agents (Bridgwater, 2003). Additional details regarding the chemicals from bio-oils can be found in the literature (Bridgwater, 2002; Brown, 2003; Brown and Stevens, 2011).

2.5 Summary

A review of the literature indicates that granular mixing processes are found in a large number of industries. For example, screw pyrolyzers rely on the granular mixing of biomass and heat carrier media to produce bio-oil. However, like many other granular mixing processes, the fundamental understanding of the granular mixing process is still underdeveloped, partly due to complex rheology, poorly understood mixing dynamics, challenging sampling procedures, subjective mixing quantification methods, limited noninvasive measurement techniques, and underdeveloped computational models. This project aims to address part of this problem by developing and utilizing various

visualization and quantification techniques, both invasive and non-invasive, to understand, characterize, and optimize the granular mixing process inside a double screw mixer. These research efforts will ultimately result in a better understanding between the operating conditions of the screw mixer and its mixing effectiveness and an improved mixing process, resulting in more efficient screw pyrolyzer operation and higher bio-oil yields.

CHAPTER 3 EQUIPMENT, MATERIALS, AND METHODS

This chapter thoroughly describes the design of each of the screw mixer's components, the equipment needed to perform the various mixing studies, and the different granular materials used throughout this project. It also provides some supplemental information relating to the experimental methods used in the project that may or may not be covered in following chapters. Detailed engineering drawings and the equipment's calibration data are shown in Appendix A and B, respectively, and will be referred to throughout this chapter.

3.1 Screw Mixer Design

The screw mixer that was designed for this project was centered primarily on the screw pyrolyzer currently being used by the Iowa State University Biorenewables Research Laboratory (ISU BRL). A brief overview of the screw pyrolyzer is described below to shape the context of the screw mixer that was designed and constructed in this project. The description of the screw pyrolyzer is in no way exhaustive and is presented only to provide background information and insight into the design process used for this project.

3.1.1 Screw Pyrolyzer

A screw pyrolyzer is a chemical reactor used for the thermochemical conversion of biomass into bio-oil via fast pyrolysis. Figure 3.1 illustrates the screw pyrolyzer

experimental set-up being used by the ISU BRL; a detailed description of the screw pyrolyzer is available in the literature (Brown, 2009).

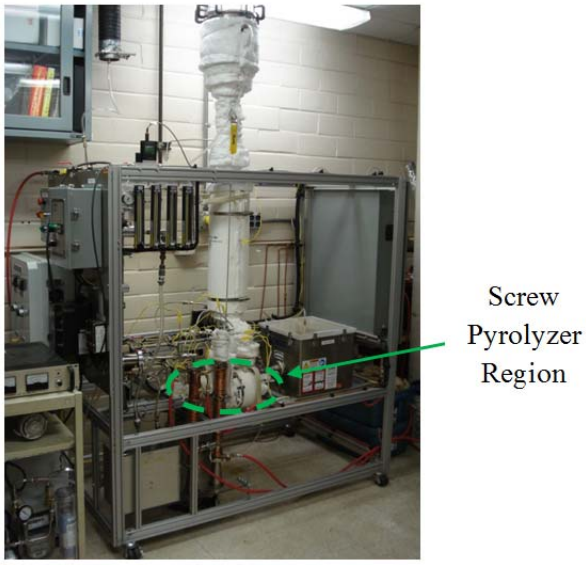

Figure 3.1: Iowa State University Biorenewable Research Laboratory (ISU BRL) screw pyrolyzer.

The screw pyrolyzer features two parallel and horizontally mounted intermeshing noncontact #16 auger screws [2.54 cm (1 in) flighting outside diameter, 0.356 cm (0.14 in) flighting thickness, 3.175 cm (1.25 in) screw pitch, and 0.794 cm (0.3125 in) shaft diameter] co-rotating inside a stationary housing. The auger size number represents the number of 1/16 inch increments in the flighting outside diameter. For example, in the case of a #4 and #16 auger screw, the flighting outside diameter is 4/16 in (1/4 in) and 16/16 in (1 in), respectively. The screw shafts' center to center horizontal offset is 2.16 cm (0.85 in). Because the offset it less than the screw flighting outside diameter, the screws are intermeshing and must be correctly phased to avoid contact. The bottom side of the housing features an omega-shaped (ω) profile thus eliminating any potential "dead space" between the screw flights. A flat top plate is bolted to the top of the housing

giving the top half of the housing a square-shaped profile. The inside diameter of the housing's bottom contour is 2.86 cm (1.125 in); providing a 0.159 cm (0.0625 in) clearance gap between the screw flights and the housing. The effective mixing length, measured from the centerline of the downstream injection port (port two) to the beginning of the outlet port in the bottom of the housing, is 25.4 cm (10 in), providing a dimensionless mixing length of L/D = 10. Most of this geometry was replicated when designing the double screw mixer for this project for the purpose of applying the mixing visualization and quantification results to the ISU BRL screw pyrolyzer.

3.1.2 Screw Mixer

The laboratory-scale double screw mixer shown in Figure 3.2 was designed and constructed specifically for granular mixing studies. The geometry nearly replicates the previously mentioned screw pyrolyzer. An additive manufacturing process (i.e., 3D printing) was used to fabricate all of the screw mixer's parts. The screw mixer's housing was manufactured using a plastic material that is transparent in both the optical and X-ray spectrums, thus allowing optical access to the mixing region's periphery (360°) and X-ray imaging to be performed. All remaining components were fabricated using an optically opaque plastic material, but is still transparent in the X-ray spectrum. The screw mixer features two parallel and horizontally mounted intermeshing noncontact screws. The screw outside diameter, D = 2.54 cm (1 in), was chosen as the characteristic length of the system. A variable-speed motor drives the screws through a set of specifically designed spur gears. Two material injection ports are axially positioned two characteristic lengths apart from one another and are laterally positioned on the mid-plane between the two screws. Four uniquely designed outlet ports in the bottom of the screw mixer's

housing, that span in the horizontal direction, divide the entire granular flow exit stream into four separate channels. The granular materials exit through the outlet ports through the bottom of the screw mixer and free-fall to individual collection basins. The effective mixing length is measured from the centerline of the downstream injection port (port two) to the beginning of the outlet ports, thus providing a dimensionless mixing length of L/D = 10.

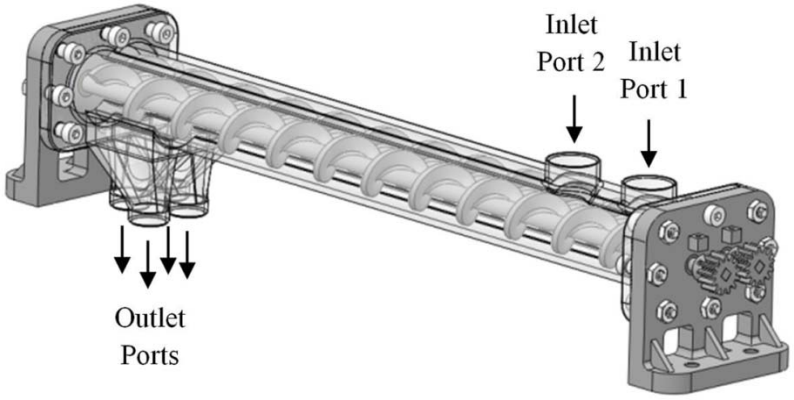

Figure 3.2: Screw mixer assembly that was designed and constructed specifically for granular mixing studies.

The following sections thoroughly describe the design constraints and the design of the individual components that make up the screw mixer. The complete specifications of all the screw mixer's parts that were designed for this project are shown in Appendix A.

3.1.2.1 Design Constraints

3.1.2.1.1 Screw Mixer Material

Typically, fast pyrolysis is performed in a carefully controlled 425-500 °C operating range (Mohan et al., 2006). Thus, the mechanical components of typical chemical reactors (e.g., housing, screws, injection piping, etc.) are often made of stainless

steel because of its high melting temperature, and resistance to corrosion and chemically reacting flows. However, stainless steel presents challenges when attempting to visualize the granular mixing dynamics inside a screw pyrolyzer using optical or X-ray imaging techniques. For example, in order to perform cold-flow granular mixing studies, Brown (2009) had to remove the stainless steel top plate from a screw pyrolyzer that was designed for performing chemical reactions, and replace it with a clear Plexiglas plate. Noteworthy problems included the inability to collect samples at locations other than the top layer of the material and only having optical access to the top surface were consequences of this set-up. In order to effectively visualize the dynamic granular mixing of the red oak chips and glass beads in the screw mixer, two major requirements needed to be met: (i) 360° optical access to the mixing region's periphery would need to be provided and (ii) a low density and low X-ray absorbing material needed to be chosen in order to perform X-ray imaging. In other words, the chosen material would need to be transparent in both the visible and X-ray spectrums. For example, a glass screw pyrolyzer housing would satisfy requirement one but not requirement two due to its high density and X-ray absorption. In contrast, an opaque and lightweight plastic would satisfy requirement two, but would not allow optical access. An optically transparent and lightweight plastic material was thus the only material choice. However, consideration had to be given to design of the housing such that seams, flanges, and an unequal material wall thickness needed to be eliminated in order to minimize X-ray imaging artifacts. Therefore, a logical and cost effective choice was to use a rapid prototype machining processes (i.e., 3D printer) to manufacture the experimental apparatus.

Objet Ltd. is an industry leading provider of inkjet based rapid prototype machining systems and offers a vast selection of devices and materials. Objet's VeroClear and VeroGray materials were chosen for the screw mixer's housing and the remaining screw mixer parts due to its optically transparent appearance and relatively high rigidity, respectively. Examples objects made from Objet's VeroClear and VeroGray materials are shown in Figure 3.3. In addition to meeting the material requirements, Objet's devices offer the ability to manufacture complex geometries that would normally being considered next to impossible using traditional machining techniques. Paradigm Development Group, Inc. in Elk Grove Village, Illinois was chosen as the manufacturer of the screw mixer's parts.

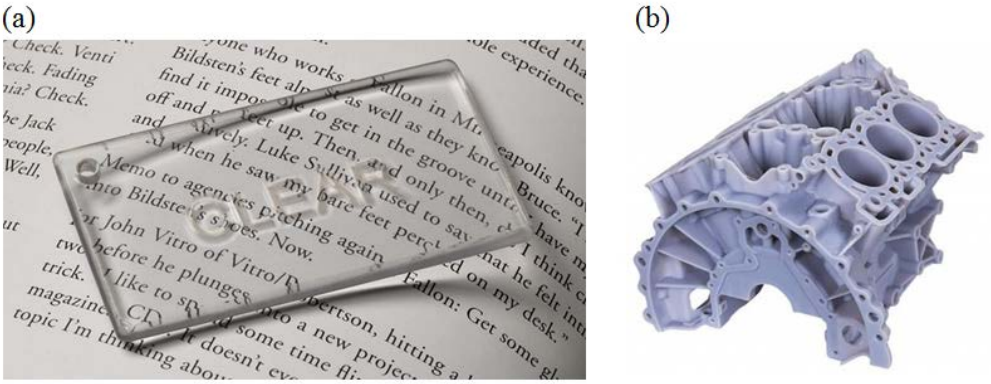

Figure 3.3: Example objects made from Objet's (a) VeroClear and (b) VeroGray materials, respectively.

3.1.2.2 Component Design

The design of each individual component comprising the assembly shown in Figure 3.2 will be described in this section.

3.1.2.2.1 Screws

The initial screw geometry was selected from the already existing #16 left hand thread (LHT) screws already being used by the ISU BRL. The screws feature a

dimensionless screw pitch of p/D = 1.25, where p is the screw pitch and D is screw diameter. This dimensionless screw pitch was selected as the “nominal” level for the dimensionless screw pitch. Increasing the dimensionless screw pitch has been shown to enhance the diffusion coefficient in single screw mixers (Uchida and Okamoto, 2008), but has yet to be investigated for a double screw mixer. Therefore, the dimensionless screw pitch was an obvious parameter of interest in terms of enhancing the mixing effectiveness. An optimal dimensionless screw pitch was thought to exist for a double screw mixer due to two primary reasons: (i) as the dimensionless screw pitch decreases, minimal clearance between the intermeshing screw flights exist, thus limiting the material particle size being used and (ii) as the screw pitch increases, the rotational velocity of the granular materials significantly increases relative to the axial velocity, and the granular material essentially “spins” inside the screw mixer, and is not conveyed axially. Due to the intermeshing screw design of the double screw mixer, a dimensionless screw pitch lower limit exits. As it becomes too small, the screw flighting clearance gap is reduced and the potential for material clogging exists. After careful consideration a dimensionless screw pitches of p/D = 0.75 was chosen, and offers a large enough reduction in the dimensionless screw pitch relative to the nominal condition of p/D = 1.25 (i.e., 40% reduction), while still providing a large enough clearance gap for the granular materials. A dimensionless screw pitch of p/D = 1.75 was then chosen as the other level, and represents a 40% in the dimensionless screw pitch relative to the nominal condition.

In addition to dimensionless screw pitch, screw rotation orientation was also a parameter of interest. Thus, RHT screws were also designed and constructed. Figure 3.4 illustrates the six combinations of dimensionless screw pitch and screw threads that were

used for this project. With the exception of the dimensionless screw pitch, the ISU BRL screw geometry (e.g., flighting and shaft diameter, flighting thickness, etc.) was replicated.

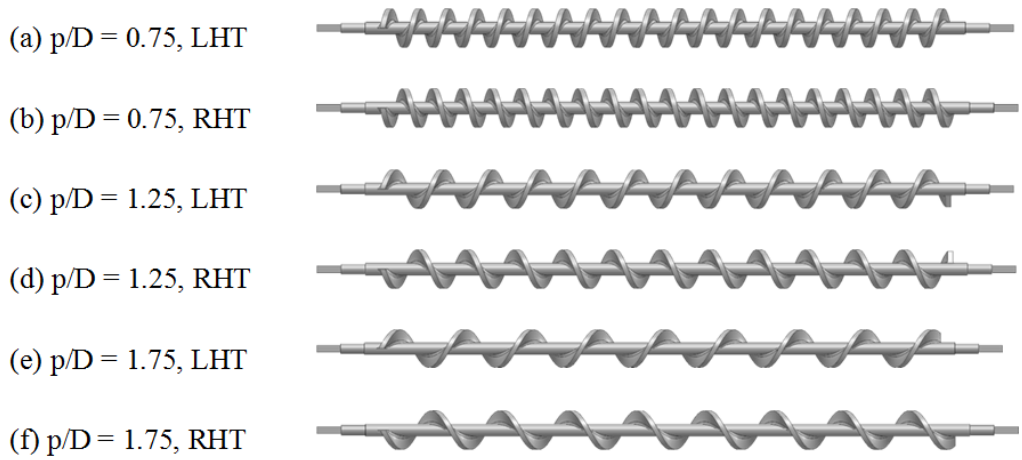

Figure 3.4: The six combinations of dimensionless screw pitch and screw flighting thread directions used in this project.

A study was conducted which investigated the use of mixing paddles. Thus, an additional LHT, p/D = 1.25 screw which incorporates the use of mixing paddles was designed and constructed, as shown in Figure 3.5. The paddles are positioned 3.76 cm (1.48 in) from one another in the axial direction. The thickness of the paddles replicates the screw flighting thickness [0.36 cm (0.14 in)]. The paddles extend out 0.71 cm (0.28 in) from the outside surface of the screw shaft, and are rotated 45° such that they partially oppose the forward flow of motion. According to the literature, partially opposing the forward flow of the granular material helps enhance mixing (Colijn, 1985).

Figure 3.5: Mixing paddle screw.

3.1.2.2.2 Housings

The screw mixer housing geometry in the mixing region geometrically replicates the ISU BRL screw pyrolyzer design, with only one minor modification. The omega-shaped (ω) contoured profile was used on both the top and bottom surfaces, in contrast to only the bottom surface that is used in the ISU BRL screw pyrolyzer, thus eliminating potential dead space where problematic mixing conditions could arise. The clearance gap between the screw flighting and the housing identically replicates the ISU BRL screw pyrolyzer design. However, the screw mixer housing cross-section was designed to yield a constant wall thickness in all directions in an effort to minimize the potential for X-ray imaging artifacts and increase optical transparency, as shown in Figure 3.6.

The red oak chips and glass beads are injected vertically downward through two circular material injection ports in the top of the housing. The material injection ports are axially positioned two characteristic lengths (L_c = D = 2.54 cm) apart from one another and are laterally positioned on the mid-plane between the two screws. This geometry very closely replicates the ISU BRL screw pyrolyzer material injection geometry.

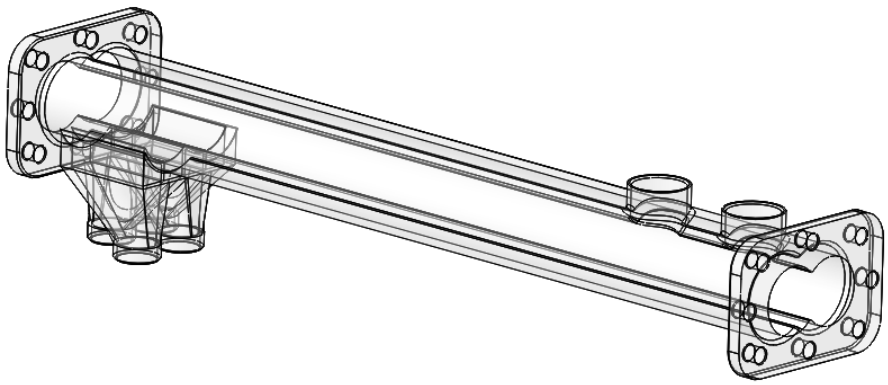

Figure 3.6: Screw pyrolyzer housing made from Objet's VeroClear material.

In the ISU BRL screw pyrolyzer, solid and liquid products resulting from the thermochemical conversion process exit the screw pyrolyzer through a single rectangular hole in the bottom of the housing. For this project, various designs were considered in an attempt to divide the granular flow, enabling composition analysis to be completed. In the first-generation screw mixer design, the vertical plane at the end of the mixing region was divided into eight channels which separated the material in both the vertical and horizontal direction in an effort to quantify both vertical and horizontal segregation. However, this dividing methodology caused too much restriction when the material was being pushed horizontally through small channels without a mechanical conveying mechanism present. This caused an accumulation of material at the end of the screw mixer and undesirable back-mixing. The current design, which more closely resembles the ISU BRL screw pyrolyzer, features four equally sized rectangular sections in the bottom of the screw mixer that span in the horizontal direction, and divide the granular flow. This geometry is shown in Figure 3.7. The thin dividers between exit ports one and two and exit ports three and four are directly beneath screw's one and two shafts, respectively. The divider between ports two and three is on the mid-plane between the screws. These rectangular sections then gradually transition downward into 1.59 cm (0.625 in) inside diameter circles where polyethylene tubing is attached and used to capture the granular mixtures. This dividing methodology allows composition analysis to be performed. The effective mixing length is measured from the centerline of the downstream injection port (port two) to the beginning of the outlet ports thus providing a dimensionless mixing length of L/D = 10; identical to the ISU BRL screw pyrolyzer.

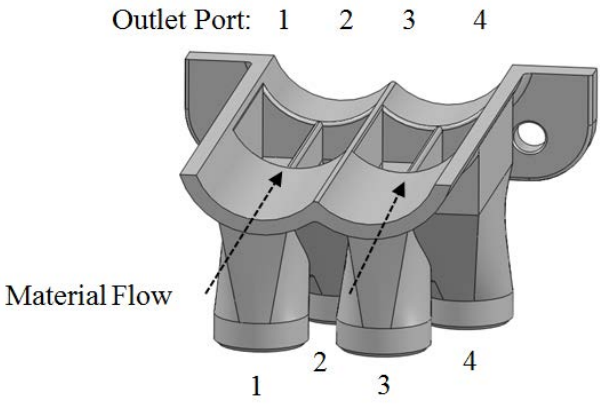

Figure 3.7: Cross-sectional view of the screw mixer housing's outlet ports allowing composition analysis to be performed (opaque material is shown for clarity).

One objective of this project was to determine the mixing effectiveness of the screw mixer as shorter mixing lengths. To accomplish this objective, two more screw mixer housings were designed and constructed which feature dimensionless mixing lengths of L/D = 2 and 5. This was accomplished by moving the outlet ports closer to the injection ports without changing the overall length of the screw mixer; resulting to the back end of the screw mixer to not be used. This was chosen over shortening the entire screw mixer because the already constructed screws could be used for any mixing length and was ultimately cheaper. Figure 3.8 shows the three different housing.

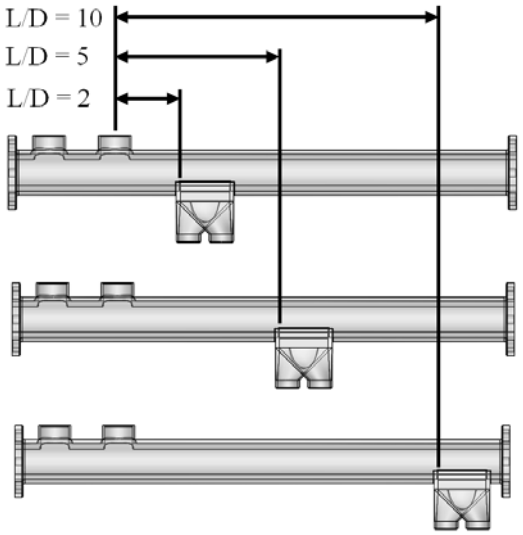

Figure 3.8: Screw mixer housings featuring dimensionless mixing lengths of L/D = 2, 5, and 10, respectively.

A single screw mixer was also designed and constructed. For clarity, the term "single screw mixer" will be used though this paper when referring to the single screw mixer. The term "screw mixer" implies that the double screw mixer is being referenced. Identical geometry in terms of the housing inside and outside diameter, length, material injection ports, etc. to that of the double screw mixer was used. However, the two intermeshing countered sections were replaced with one cylindrical section to house the single screw, as shown in Figure 3.9. Outlet ports were used to divide the granular material exit stream and allow for composition analysis, similar to the double screw mixer. However, due to the large red oak particle size and small screw mixer size, the number of outlet ports had to be reduced from four to two.

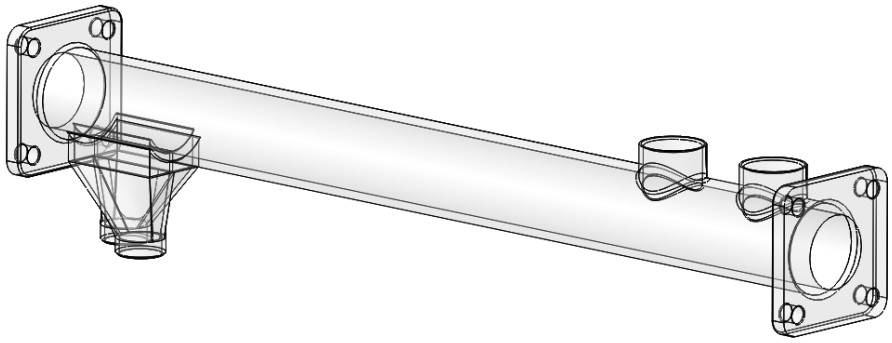

Figure 3.9: Single screw mixer housing.

3.1.2.2.3 Supports and Bushings

The screw mixer's supports, shown in Figure 3.10, were specifically designed to serve multiple purposes: (i) elevate the screw mixer allowing optical and X-ray imaging access to the entire mixing periphery; (ii) hold the housing and screws in their appropriate positions; (iii) support the screws' radial and thrust loads; (iv) lock the screws in place for static X-ray computed tomography imaging; and (v) house the bushings, which allow for smooth operation. Complete details of the supports can be found in Appendix A.

Rulon J flanged sleeve bushings [0.635 cm (0.25 in) shaft diameter, 0.953 cm (0.375 in) outside diameter, 1.27 cm (0.5 in) flange outside diameter] were selected and feature a very low coefficient of friction and prevent wear of the screw shafts. The bushing flanges are positioned opposite from one another thereby supporting thrust loads in either direction. The bushings are protected by u-cup shaft seals [0.635 cm (0.25 in) height, 0.635 cm (0.25 in) inside diameter, 1.905 cm (0.75 in) outside diameter] mounted on the screw shafts. This minimizes contact between the bushings and the granular materials thus reducing wear and ensuring smooth operation. Each support is attached to the housing flange using eight nylon shoulder bolts [0.635 cm (0.25 in) shoulder diameter, 0.953 cm (0.375 in) length shoulder, 10-24 thread] and nylon nuts (10-24

thread). The bushings, u-cup shaft seals, shoulder bolts, and nut were purchased from McMaster-Carr.

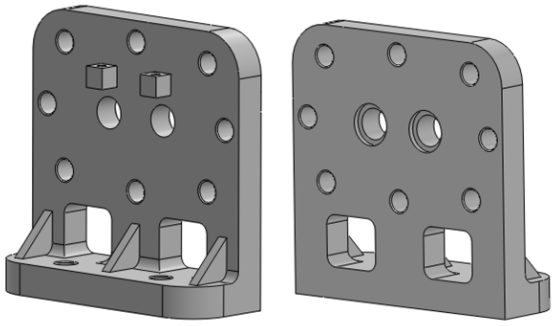

Figure 3.10: Screw mixer supports.

Single screw mixer supports were also designed and constructed, as shown in Figure 3.11. Similar geometry and design considerations to that of the double screw mixer were for the single screw mixer supports. However, the number of bushing slots and shoulder bolt holes were reduced from two to one and from eight to four, respectively, to account for the single screw and reduced housing flange surface area.

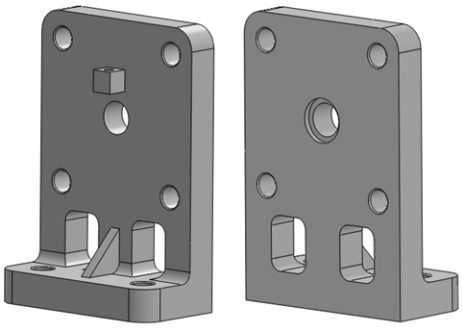

Figure 3.11: Single screw mixer supports.

3.1.2.2.4 Gears

The spur gears shown in Figure 3.12 transfer the torque from the motor to the screws, and were specifically designed for the screw mixer. Screw rotation speeds

ranging from 20-60 rpm were desired based on typical ISU BRL screw pyrolyzer operating conditions. A 35 rpm (maximum) gearmotor was used to drive the screws; therefore a 2:1 motor to screw gear ratio was needed. Co-rotating (CoR) and counter-rotating (CtrR) screw rotation orientations were of interest so different gearing systems were needed for each screw rotation configuration. For the co-rotating screw rotation orientation, the screw gears were designed to have a 1.905 cm (0.75 in) outside diameter, thus ensuring independent rotation since they are smaller than the 2.159 cm (0.85 in) shaft offset. A single co-rotating screw rotation orientation gearmotor gear drives the screw gears. In contrast, the counter-rotating screw rotation orientations screw gears were designed with a 2.159 cm (0.85 in) outside diameter, exactly matching the horizontal screw shaft offset and allowing the gears to mesh together and rotate in opposite directions relative to each other. A square hole was designed through the center of the screws gears to fit over the end of the square tip on the screws to help transfer the torque to the screws. Furthermore, four 6-32 threaded holes are placed perpendicular to each other on the gears' hub allowing set screws to securely tighten to the screw shaft and axially lock them in place. The larger gearmotor gears feature a similar design, but have 1.27 cm (0.5 in) circular holes in the center. Together these gear sets provide the necessary 2:1 gear ratio needed to achieve the desired screw rotation speeds.

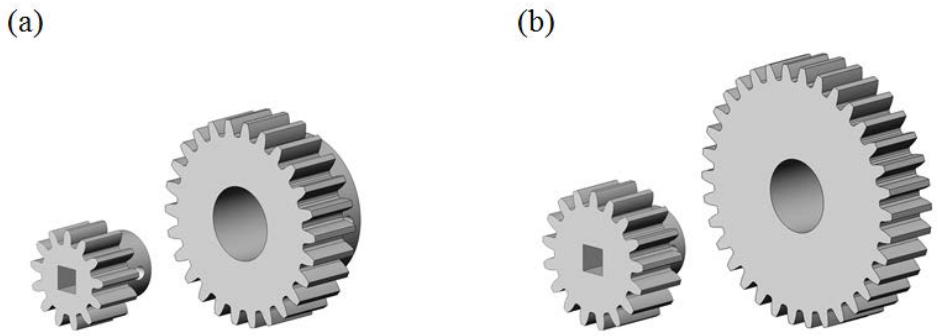

Figure 3.12: Screw and gearmotor gear sets for (a) co-rotating and (b) counter-rotating screw rotation orientations, respectively.

To accommodate the stepper motor which was used to perform X-ray imaging, which is discussed in more detail in following sections, different gears had to be designed and constructed. The stepper motor gears replace and geometrically replicated the previously mentioned gearmotor gears with one minor change. The hole in the center of the shaft was reduced from 1.27 cm (0.5 in) to 0.64 cm (0.25 in) and a flat was added on one side; allowing for secure placement on the stepper motor's shaft. Figure 3.13 illustrates the co-rotating and counter-rotating screw rotation orientation stepper motor gears.

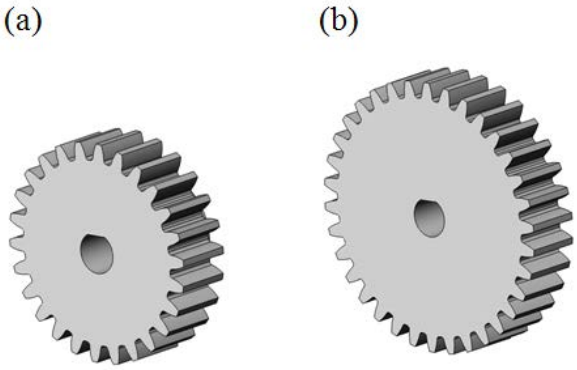

Figure 3.13: Stepper motor gears for a (a) co-rotating and (b) counter-rotating screw rotation orientation, respectively.

3.1.2.3 Characteristic Length

Defining the characteristic length of a system is a critical parameter that defines the scale of the system, and can have a significance impact when trying to nondimensionalize the system. However, the characteristic length can be dependent on the geometry and operating conditions, making its selection a challenge. Traditionally, it is mathematically defined using one of three definitions:

$$L_c = L\ ;\ \frac{A}{L}\ ;\ \frac{V}{A} \tag{3.1}$$

where L is a specified length, A is a specified area, and V is a specified volume. For example, the characteristic length of a circular heating, ventilation, and air-conditioning (HVAC) duct is simply the duct's inside diameter. However, for a rectangular channel transporting water, the characteristic length is dependent on two factors: (i) geometry (e.g., cross-sectional length and width) and (ii) operating conditions (e.g., amount of water being transported). For this situation, the characteristic length of the channel is defined using a hydraulic diameter:

$$L_c = D_h = \frac{4A_c}{P_w} \tag{3.2}$$

where L_c is the characteristic length, D_h is the hydraulic diameter, A_c is the cross-sectional area, and P_w is the wetted perimeter (i.e., the perimeter in contact with the water).

After careful consideration, the screw flighting outside diameter, D = 2.54 cm (1 in) was chosen as the characteristic length of the screw mixer. This approach produced a straight forward definition which is only dependent on geometry, and not the screw mixer's operating conditions. If the hydraulic diameter was selected for the characteristic

length, different operating conditions (e.g., screw rotation orientations) resulting in vastly different mixing dynamics, would cause the wetted perimeter to change. Moreover, accurately measuring the wetted perimeter would be difficult, and this approached to defining the characteristic length was not used.

3.2 Equipment

3.2.1 Volumetric Auger Feeders

The red oak chips (RO) and glass beads (GB) were independently metered into the screw mixer by two stainless steel Tecweigh CR5 volumetric auger feeders. A similar volumetric feeder to the two used in this study is shown in Figure 3.14. The most obvious difference between the volumetric feeder shown in Figure 3.14 and the volumetric feeders being used in this project is the outlet tube in Figure 3.14 is much larger than was actually used.

Figure 3.14: Similar Tecweigh CR5 volumetric auger feeder to the one being used in this project, which is used to meter the granular materials into the screw mixer are specified flow rates.

Each volumetric feeder features a 0.0142 m^3 (0.5 ft^3) hopper and a 15.24 cm (6.0 in) long, 2.54 cm (1.0 in) outside diameter feed tube. Open flight 1.27 cm (0.5 in) and 1.91 cm (0.75 in) outside diameter augers meter and convey the red oak chips and

glass beads, respectively. A smaller auger diameter was chosen for the red oak chips due its larger particle size. The augers were activated using an illuminated mushroom on/off switch on the control box. The auger rotation speed was adjusted using a potentiometer which controlled a variable-speed 1/8 horsepower, 167 rpm maximum gearmotor. The material inside the hopper was agitated by alternating massage paddles connected to the drive system which flex the hopper's walls, helping maintain a relatively consistent volumetric flow rate by minimizing air pockets from forming inside the material bed. A clear polycarbonate lid was placed on top of the hopper to ensure the granular material was not contaminated. The ends of the feed tubes were positioned approximately 38 cm (15 in) vertically above the material injection ports on the screw mixer's housing. Each volumetric feeder conveyed their respective material horizontally out the feeder. A polyvinyl chloride (PVC) 90° elbow was placed on the end of the feeder tube and a semi-clear polyethylene tube connected the housing inlet ports to the PVC elbow. Each feeder was mounted on an adjustable track system enabling them to slide back and forth; allowing the material injection ports to be swapped. A Tecweigh 14A-20M sprocket kit was swapped with the standard 16A-16M sprocket kit to upgrade the drive system on the red oak chips volumetric feeder, and was used to increase the red oak chips volumetric output. The 14A-20M sprocket kit features 14 teeth on the auger sprocket (i.e., 14A) and 20 teeth on the motor sprocket (i.e., 20M). The gearmotor to auger gear ratio was increased by using a larger motor sprocket and a smaller auger sprocket.

3.2.1.1 Volumetric Feeder Calibration

The volumetric flow rate of the volumetric feeders depends on the material being used; resulting in the need for calibration for each material. The mass flow rate of each

feeder was calibrated for their respective materials in 100 unit potentiometer increments ranging from 100 to 900 and also at 999 (maximum setting). The feeders were allowed to reach steady state before collecting the granular material being discharged during a fixed time period. The red oak chips and glass beads volumetric feeders were operated for three and two minutes for each potentiometer setting, respectively. The longer duration for the red oak chips was chosen because the mass of material being discharged was much less than that of the glass beads. The three minute red oak chip duration yielded more accurate results, relative to a two minute red oak chip duration, because the influence of minor fluctuations in the material flow rate were lessened. After the material was collected, the mass was measured and the mass flow rate at each setting was determined. This procedure was repeated five times at each potentiometer setting for each feeder. The red oak chips and glass beads mass flow rates were then averaged and are shown in Figure 3.15. The vertical error bars overlaid on the data points represent plus and minus one standard deviation that was calculated from the five trials. The empirical correlation shown by the regression model equation was used to determine the mass flow rates used during experimental testing. Full calibration data are shown in Appendix B.

As illustrated in Figure 3.15 and shown by the coefficient of determination, R^2, the volumetric feeders discharge the granular materials at a very linear flow rate relative to the potentiometer setting. The slightly larger variation in the red oak chips was attributed to the material properties of the red oak; particularly the particle geometry and cohesion between particles.

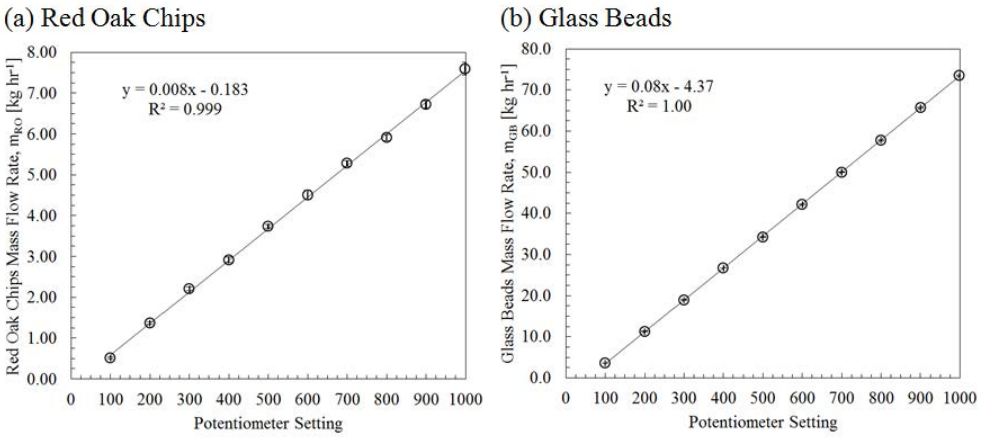

Figure 3.15: Volumetric feeder calibration results for the (a) red oak chips and (b) glass beads.

3.2.2 Gearmotor

The screw mixer's screws were driven using a Leeson 985-627H gearmotor, which requires a 90 V direct current (DC) to achieve a 35 rpm rotation speed and 44 W (1/17 hp). The gearmotor has a 1.27 cm (0.5 in) output shaft with a flat and keyway. As previously mentioned, the spur gears were specifically designed for this motor. The motor was mounted on a one-axis adjustable track; allowing the x-position to be adjusted to accommodate for the co-rotating and counter-rotating screw rotation orientations. The track was positioned on a flat metal plate with slots; allowing the y-position to be adjusted. The flat metal plate was mounted on a set of four 1/2 in-13 threaded rods; allowing the z-position to be adjusted. Combining these features resulted in the gearmotor being effectively positioned on a three axis support system, allowing complete control over its position. The gearmotor was powered by a Mastech HY10010EX digital DC power supply.

An emergency shut-off switch was used to simultaneously deactivate both volumetric feeders and the gearmotor. An alternating current (AC) control relay was used

to break the circuit between the power supply and the gearmotor; allowing the power supply to remain energized while the motor was not. Doing so allowed the power source's internal capacitors to remain charged; eliminating the time delay in startup and shut down.

3.2.2.1 Gearmotor Calibration

To calibrate the screw mixer's screw rotation speed to the voltage being supplied by the power supply, the voltage was varied in 10 V increments from 20 to 90 V. The time required for the screws to rotate 25 revolutions was measured at each 10 V increment. This process was repeated five times for each voltage setting and the average screw rotation speed as a function of supply voltage was calculated, as shown in Figure 3.16. As expected, the screw rotation speed exhibited a very linear behavior. Note that the maximum screw rotation speed was twice that of the maximum motor rotation speed because of the 2:1 gear ratio. The developed empirical correlation shown by the regression model equation was used to adjust the desired screw rotation speed during experimental testing. The calibration data are shown in Appendix B.

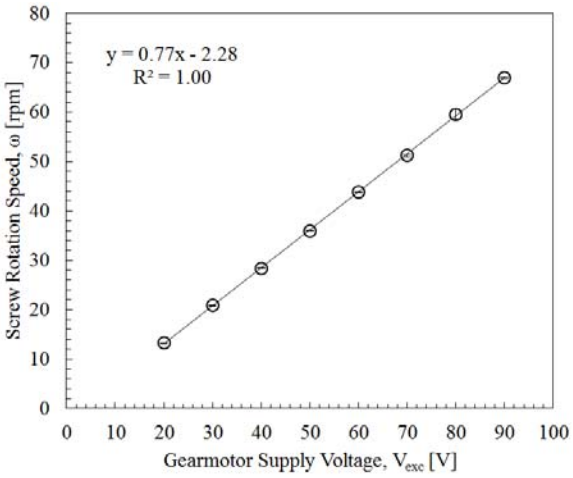

Figure 3.16: The screw mixer's screw rotation speed as a function of the gearmotor supply voltage.

3.2.3 Stepper Motor

To enable successful computed tomography imaging, the rotational position of the screws within the screw mixer needed to be the same both before and after the test and between different tests themselves. The gearmotor does not have the ability to accommodate these needs. Thus, a stepper motor was needed to ensure accurate rotational position while still maintaining a variable screw rotation speed. Stepper motors are brushless DC electric motors that divide the stepper motor's full rotation into a number of equally sized steps. Steppers motors are unique in that its position, velocity, acceleration, rotation direction, and run and hold torque can be accurately controlled by the user. Furthermore, open-looped and closed-loop systems are available, and closed-loop systems offer further accuracy and precision.

In order to select the size of the stepper motor needed to operate the screw mixer, the torque needed to drive both of the screw mixer's screw and convey the granular materials needed to be determined. However, trying to determine the necessary torque for a wide range of operating conditions and granular materials is not an easy task. The methods outlined by Colijn (1985) for determining the power requirements for single screw conveyors was used to estimate the necessary torque needed to size the stepper motor, with only one major modification. Because the screw mixer has two screws, the power required using Colijn's (1985) methods for single screw conveyors was doubled, thus providing the power consumption for a single screw mixer that is essentially twice as long. This approximation is thought to be a slight overestimate of the actual power needed for the double screw mixer because its surface area is less than a single conveyor that is twice as long, thus having less friction. Furthermore, the screws inside the double

screw mixer are intermeshing thus the cross-sectional area is less than two single screw conveyors side-by-side. From the range of operating conditions considered in this study, the worst-case-scenario was used in the power analysis. For example, the maximum screw speed and highest material flow rates were used. The full details of the power analysis can be found in Appendix C. Overall, the required power and resulting torque was determined to be 11.2 W (0.015 HP) and 1.78 N-m (1.314 ft-lbs), respectively.

From the prescribed analysis, a Lin Engineering integrated motor-driver-controller-encoder Silverpak 23CE model CE-5718L-01P stepper motor was selected. This motor features a National Electrical Manufacturers Association (NEMA) size 23 frame and a 1.8° bipolar closed-loop step motor with step resolutions ranging from full step to 1/256. Selecting a full step resolution causes the stepper motor to rotate 1.8° when commanded to move one step, whereas selecting the 1/256 resolution causes the motor to rotate 0.007° (1.8°/256) when commanded to move one step. This resolution option allows for precision control of the motor. Furthermore, the stepper motor has a maximum holding torque of 2.08 N-m (1.531 ft-lbs), which is 17% larger than the torque requirement from the prescribed analysis.

The stepper motor was powered using a Pyramid PS3KX 12 V power supply, and controlled using a workstation's serial connection in addition to Lin Engineering's RS485 to RS232 converter card. Two different modes of Lin Engineering's software interface was used to perform X-ray imaging: (i) the basic mode with predefined functions was used for X-ray stereography imaging and (ii) the advanced mode which features the ability to write custom programs was used for X-ray computed tomography imaging. Custom programs were written to accurately control the beginning and ending position,

number of revolutions, and rotational velocity of the screw mixer's screws, and trigger off the volumetric screw feeders, ensuring accurate X-ray CT imaging. The details of these programs are shown in Appendix D.

3.2.4 Pycnometer

A Pentapyc 5200e gas pycnometer from Quantachrome Instruments was used to perform the composition analysis, as shown in Figure 3.17. The pycnometer features five (hence penta) sample chambers that were used to compute the true density by measuring the true volume for a given sample mass.

Figure 3.17: Quantachrome Instruments Pentapyc 5200e Gas Pycnometer.

The measurement process is completely autonomous once the samples have been loaded and the appropriate commands selected. The analysis process is based Archimedes' principle of fluid displacement and gas expansion and is governed by the ideal gas equation:

$$pv = nRT \tag{3.3}$$

where p is the pressure, v is the volume, n is the number of moles of gas, T is the temperature, and R is the molar gas constant. Helium was used as the displacing fluid in the pycnometer since it penetrates the finest pores, approaching one Angstrom (10^{-10} m), due to its small atomic dimensions. Its behavior as an ideal gas is also favorable and it

doesn't absorb to surfaces like nitrogen can. The helium is added to the 135 cm^3 stainless steel cell, called the volume cell (v_c) which has a known volume, until a target pressure (typically 10 psi) is reached. The sample chamber is then sealed and the equilibrium pressure is measured (p_A). The sample chamber is then opened to another chamber of known volume, called the volume added (v_A), and the new stable equilibrium pressure is measured (p_B). The change in pressure is related to the change in overall volume, from which the volume of the sample (v_s) can be calculated:

$$p_A (v_C - v_S) = p_B (v_C - v_S + v_A) \tag{3.4}$$

For the 135 cm^3 cell, the accuracy and repeatability of the pycnometer is $< \pm 0.02\%$ and $< \pm 0.01\%$, respectively.

True density is different from bulk density in that particle density does not include the sample's void space between the individual particles as part of the sample volume. For the same sample, the measured bulk volume will be much larger than the true volume thereby resulting in the bulk density much less than the particle density. However, bulk density measurements do not require special equipment needed to obtain the samples true volume. The testing conditions of the bulk density measurements due play a large role in the accuracy of the results. For example, various levels of compaction can cause the volume to be significantly reduced for a constant mass sample.

3.2.5 Material Separator

After mixing the red oak chips and glass beads, a separation process was used, allowing the granular materials to be reused for future mixing studies. The first step was to manually sieve the combined red oak chips and glass beds using an America Society

for Testing and Materials (ASTM) #35 Sieve [500 µm, (0.020 in)]. This sieve size was selected because the red oak chips had a minimum theoretical particle size of 500 µm (0.020 in) from preprocessing. Furthermore, more than 99.99% of the glass beads were smaller than 500 µm (0.020 in). The red oak chips that were retained in the sieve were collected and used again. However, there were some small red oak particles and fine dust that passed through the sieve and were mixed in with the glass beads. Figure 3.18 illustrates the mixture of red oak chips and glass beads before and after using the ASTM #35 Sieve, respectively. Ironically, the large density and size difference between the red oak and glass beads leading to segregation within the screw mixer was exploited during the material separation process.

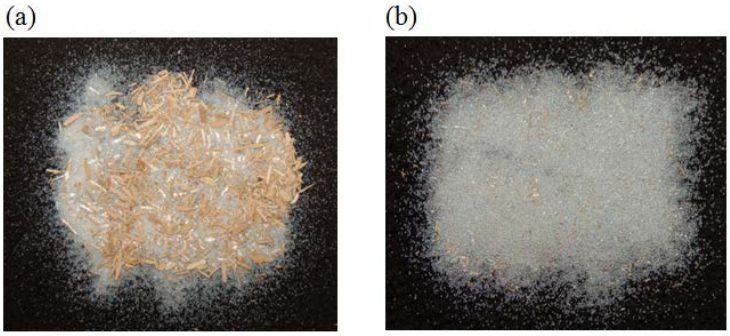

Figure 3.18: Mixture of red oak and glass beads (a) before and (b) after using the ASTM #35 Sieve to separate the materials, respectively.

The mixture of fine red oak particles and glass beads (approximately 99% glass beads by mass) was placed inside a 15.24 cm (6 in) inside diameter cold-flow fluidized bed until it was approximately two bed diameters high [H/D = 30.48 cm (12 in)], as shown in Figure 3.19. The fluidized bed was positioned on two closely located small cylinders enabling it to pivot back and forth. The two cylinders were positioned on both sides of the air injection port and prevented the fluidized bed from leaning in one

direction. The side of the fluidized bed was attached to a vibratory shaker through a mechanical linkage system.

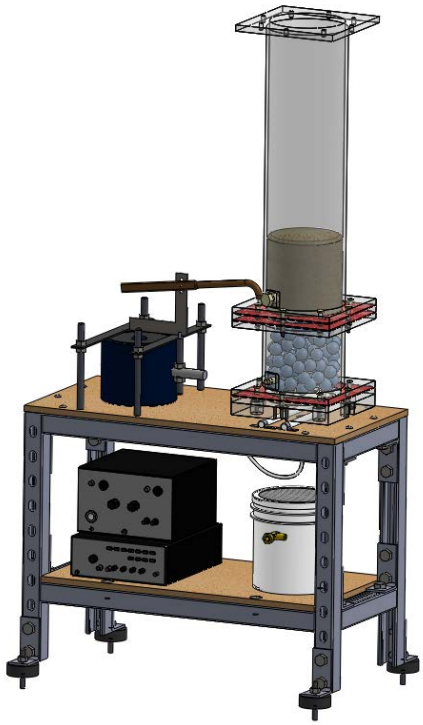

Figure 3.19: The material separator device used to separate the fine red oak chips from the glass beads.

Air from the building's air supply was injected into the bottom of the fluidized bed. The air was first distributed by a collection of marbles in the plenum. The air then passed through a distributor plate with small circular holes which were covered by a fine wire mesh, distributing the air more evenly. The air flow rate was set just above the minimum fluidization velocity needed to fluidize the granular material. The combination of mechanical vibration and relatively low air flow through the particles causes the material to segregate instead of mix. This segregation phenomenon further demonstrates the significance that operating conditions have on mixing and segregation processes in granular systems. For each batch of material, the material separator was run for

approximately 10-15 minutes, causing a large amount of small red oak chips to accumulate on the top layer of the material. A custom-made Venturi vacuum was used to skim off and discard the thin red oak chip layer. The fluidized bed was then violently mixed by increasing the air flow rate far above the minimum fluidization velocity causing any static red oak chip agglomerations within the granular bed to be redistributed. The air flow rate is then decreased to just above the minimum fluidized velocity and the vibratory shaker was turned on for another 5-10 minutes, and the process was repeated 3-4 times. After doing so, the glass beads were very pure (> 99.99%) and ready for reuse.

3.2.6 Optical Visualization Equipment

The experimental setup used to capture qualitative optical visualization of the screw mixer's dynamic mixing process inside the screw mixer is shown in Figure 3.20. To accomplish this task, special equipment was needed.

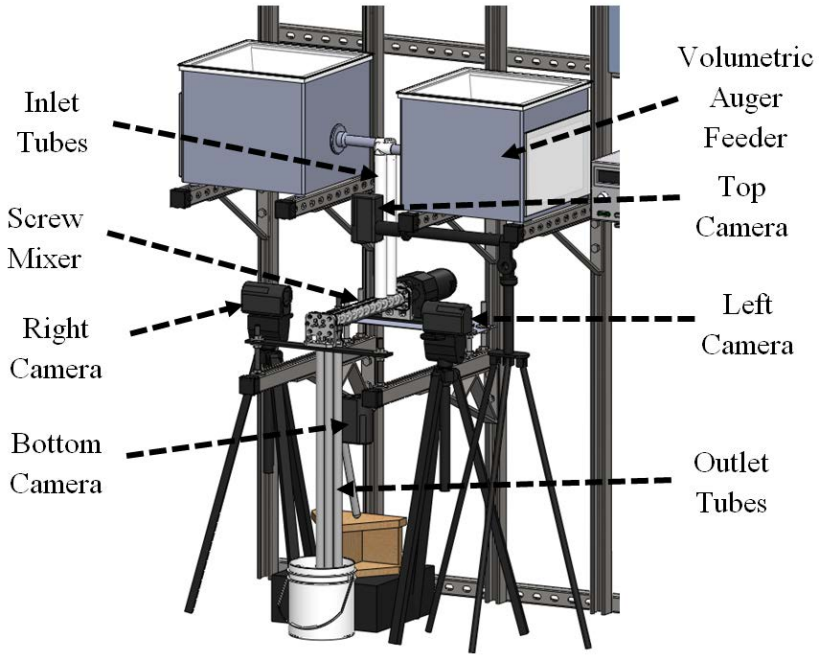

Figure 3.20: Optical visualization experiemental setup.

Four Panasonic HC-V700M high definition (HD) cameras were used to capture the dynamic mixing process from four independent projections simultaneously. The cameras capture images at 60 FPS with 1920 x 1080 resolution. The cameras were positioned using various tripods. The left and right projection cameras each use a Sony VCT-50AV three-way pan head tripod. Meanwhile, the top projection camera uses a Promaster UT25 Tripod System. This tripod was specifically selected because it featured a cantilever arm that was suspended outward, holding the camera directly above the screw mixer. The bottom projection camera utilized a Sunpak Platinum Plus Mini-D tripod. This camera was positioned under the screw mixer and was pointed vertically upward.

Providing the necessary amount of lighting needed to capture high quality videos while eliminating glare was specifically difficult due to the housings contoured outer profile. The four projections perpendicular to the housing's curved outer surfaces and parallel to the camera directions were surrounded by black fleece fabric; thus eliminating any light from having direct contact with the housing surface. Each axial end of the screw mixer was then covered by a reflecting umbrella. Six Satco 85 W (350 W incandescent equivalent) commercial spiral compact fluorescent lamps (CFL), three on each end, were placed between the reflecting umbrellas and the axial ends of the mixer. Each bulb had a 4100 Kelvin color temperature profile and produced 5700 lumens, providing a bright and natural lighting environment. The reflecting umbrellas redirected the light approximately parallel to the mixer's axial direction and helped enhance the lighting environment. Furthermore, all metallic equipment surfaces (e.g., volumetric auger feeders) were covered in black fabric to eliminate any reflecting surfaces.

3.2.6.1 Video Editing Software and Hardware

Capturing the screw mixer's dynamic mixing process from four different projections provides very useful information in characterizing the mixing effectiveness of the screw mixer. Combining all that information into a manageable and intuitive presentation method was a one objective of this project, and was accomplished with the use of Adobe Premiere Pro CS6 video editing software. Premiere is a top-of-the-line video editing software package giving users extreme flexibility and numerous options to manipulate videos in any way they see fit. Adobe has partnered with NVidia to create the Adobe Mercury Playback Engine, which enhances the speed at which the videos can be rendered. To enable this feature, an MSI N680GTX Twin Frozr 4GD5/OC graphics processing unit (GPU) was purchased and installed in the computer workstation where the video editing was done. Most importantly, this GPU features NVidia chips which allow CUDA technology to be used, a requirement of the Adobe Mercury Playback Engine. The purchased GPU features four gigabytes of memory allowing ultra-high performance and high-definition videos to be easily edited.

3.2.7 X-ray Flow Visualization Facility

This project was completed with the use of the X-ray Flow Visualization (XFloViz) Facility at Iowa State University. A brief overview of the facility with an emphasis on the equipment and imaging capabilities will be presented here. A more detailed review can be found in the literature (Heindel et al., 2008).

3.2.7.1 X-ray Equipment

The XFloViz Facility used in this project is illustrated in Figure 3.21 with a 32.1 cm bubble column located in the imaging region. The facility includes a 3.7 m × 4.2 m

lead-lined room that is 3.7 m off the laboratory floor and on top of a lead-lined vertical lift structure. The facility consists of two X-ray source and detector pairs, offset by 90° from one another about the vertical axis. All the equipment is mounted on a slew ring with a 1.0 m inside diameter, and allows for complete rotation around the OOI.

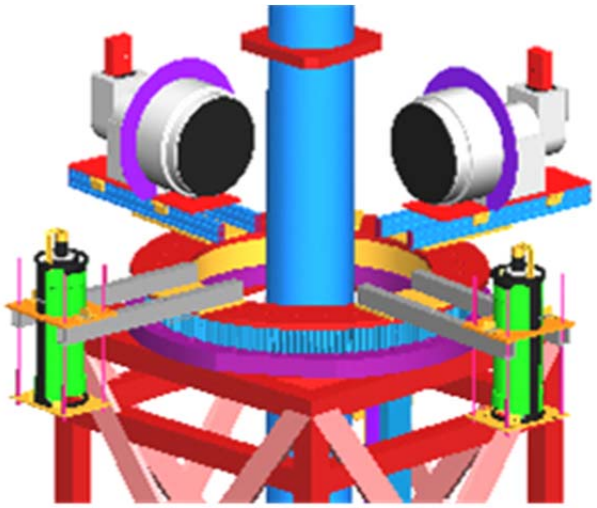

Figure 3.21: X-ray Flow Visualization (XFloViz) Facility at Iowa State University.

The X-ray system features two liquid-cooled LORAD LPX200 portable X-ray sources with beryllium windows in the source head that emits an approximately 60° horizontal and 40° vertical conical beam. Each source is encased by cylindrical lead shield with a rectangular window near the source head. The X-ray source's voltage and current are adjusted from 10 to 200 keV and 0.1 to 10.0 mA, respectively, with a maximum power output of 900 W. To minimize low energy X-ray being passed through the OOI, a combination of metallic filters (e.g., copper, aluminum, etc.) can be used. All of these factors are adjusted to yield the highest image resolution for a given OOI.

Two different detector systems are used to perform X-ray imaging in the XFloViz Facility. The first system is used for X-ray radiography and stereography imaging, which uses Precise Optics PS164X image intensifiers with a 40.6 cm input phosphor and 3.5 cm

diameter output phosphor. The input phosphor is backed by a vacuum chamber causing the X-ray photons to be re-emitted as electrons in the vacuum chamber. These electrons are accelerated and focused onto the output phosphor using high voltage electric fields. This causes a significantly brighter visible light image on the output phosphor than could be obtained using a direct X-ray to visible light scintillator. Coupled to the image intensifiers are two identical DVC-1412 12-bit, monochrome, charge-coupled device (CCD) cameras which read the image remotely using an adjustable zoom lens. Each camera has a resolution of 1388 × 1024 with each pixel size measuring 6.45 μm × 6.45 μm. To improve light sensitivity and increase imaging speed, a 2 × 2 binning configuration, where the signal from adjacent pixels is added together, is used. This yielded an effective resolution of 640 × 512 and an effective pixel size of 12.9 μm × 12.9 μm. Using this binning configuration, the cameras captured images in 55 ms increments thus having an effective frame rate of 18.18 FPS. For X-ray radiography, a single X-ray source and intensifier are used. Meanwhile, for X-ray stereography, each of the two X-ray sources is paired to an image intensifier.

The second detector system utilizes a single 44 × 44 cm cesium-iodide (CsI) phosphor screen scintillator coupled to a thermoelectric cooled Apogee Alta U9 cooled CCD camera via a 50 mm f1.2 lens. This camera features a 3072 × 2048 resolution with a pixel size of 9 μm × 9 μm. A 4 × 4 binning configuration is used, yielding an effective resolution of 768 × 512 and an effective pixel size of 36 μm × 36 μm. This camera provides high resolution CT images, but has an increased expose time relative to the X-ray radiography and stereography cameras. Thus, computed tomography imaging provides only time-averaged data.

The X-ray sources and detectors are mounted on a slew ring which provides 360° rotation around the OOI. The slew ring is driven by a stepper motor that is controlled by an in-house software program. For X-ray CT imaging, the stepper motor's step size was 1°.

A 910 kg (2000 lb) vertical lift system is positioned in the center of the slew ring an houses the OOI. A custom leveling platform designed specifically for the screw mixer was constructed and placed on top of the lift.

Image acquisition is performed by custom software developed by the Iowa State University Center for Nondestructive Evaluation (ISU CNDE). A 64-node LINUX cluster from ISU CNDE is used to perform CT reconstruction using a multislice filtered-back-projection fan-beam reconstruction algorithm.

3.2.7.2 X-ray Image Processing

To compensate for imperfections in the imaging hardware, three different corrections can be applied to produce more desirable results: (i) image unwarping, (ii) pixel normalization, and (iii) beam hardening. Image unwarping in applied to X-ray radiography and stereography imaging. Pixel normalization can be applied to X-ray radiography, stereography, and computed tomography, but it typically only applied to radiography and stereography. Beam hardening is only applied to X-ray CT images. For a more thorough review of these image processing corrections, refer to Heindel et al. (2008).

Due to the nature of the intensifier's design, the images experience a pincushion distortion whereby the edges of the image are magnified more than the center. This phenomenon is known as warping, and without proper correction, the images are

distorted and yield undesired results. Furthermore, there is a magnetic field within the XFloViz Facility that causes nonuniform warping at each angular location. Therefore, in the case of X-ray radiography and stereography, the unwarping parameters must be obtained for the exact experimental setup. However, in the case of the X-ray scintillator (the CsI phposphor screen), image unwarping is not needed because the imaging information is carried by visible light, not electrons.

Due to the nature of the equipment used in this study, a more complicated procedure was employed to determine the unwarping parameters. This procedure was necessitated by the presence of the stepper motor used to drive the screws, which caused an additional magnetic field to be added to the naturally occurring magnetic field inside the X-ray intensifier. Moreover, the physical presence of the leveling plate and the stepper motor caused parts of the image to be obscured due to their high X-ray attenuation. Thus, a modified warping correction procedure was used. Moreover, the different rotational speeds of the motor produced different magnetic fields. Thus, a calibration image had to be acquired for each of the three screw rotation speed (i.e., 20, 40, and 60 rpm).

To correct the warping phenomenon, an unwarping algorithm is used. To obtain the parameters for this correction, a grid consisting of a 1.59 mm thick stainless steel plate with 2 mm holes drilled in a rectangular grid at 12.7 mm increments is place on the front of the image intensifier. This provides an image with a series of bright dots, which should be in a rectilinear grid, but are not due to the warping phenomenon. From this calibration image, the unwarping parameters are calculated by using a threshold to find the location of the dots corresponding to the holes in the unwarping calibration grid. The

difference between the holes' apparent locations and the known locations on the grid is then fit to a polynomial curve. This curve is then used to calculate the unwarped position of each pixel, with a bilinear interpolation used to fill any gaps in the resulting images. The parameters of the unwarping correction were obtained using the aforementioned X-ray power setting. Additional details regarding the unwarping process can be found in the literature (Doering, 1992; Heindel et al., 2008).

The parameters of the unwarping correction were obtained using the aforementioned X-ray power setting. To enable a more accurate unwarping correction, the holes in the grid below the leveling plate and near the stepper motor were filled in by placing a 2 mm lead shot particle in the hole. This allowed for a continuous row of bright dots to be present without interruption in the desired region, a requirement of the unwarping algorithm. Therefore, the calibration algorithm is only the rectangular region above the leveling plate and to the left of the stepper motor. Figure 3.22 displays the original calibration plate image taken (a) without and (b) with the leveling plate and stepper motor in the imaging region, and (c) with the screw mixer added in, respectively, prior to the unwarping procedures being applied. As shown, the images have a significant amount of distortion.

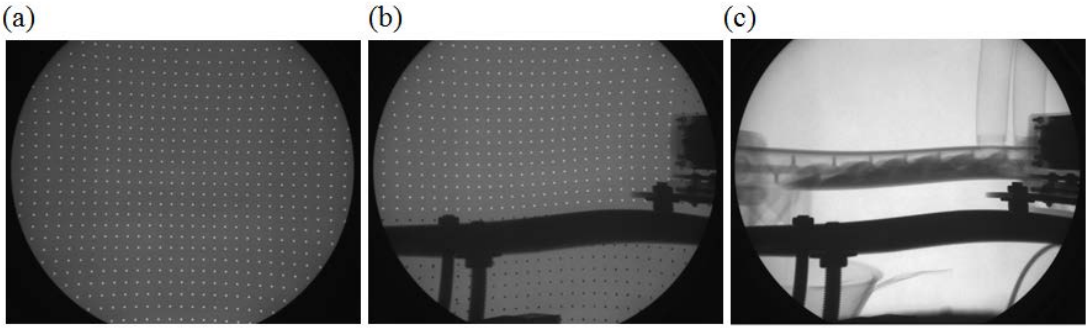

Figure 3.22: X-ray images of the (a) original calibration plate, (b) modified calibration plate, and (c) screw mixer, taken before image unwarping corrections were applied.

After the unwarping procedure has been applied, the images produce much more desirable results. Figure 3.23 displays the original calibration plate image taken (a) without and (b) with the leveling plate and stepper motor in the imaging region, and (c) with the screw mixer added in, respectively, after the unwarping procedures have been applied.

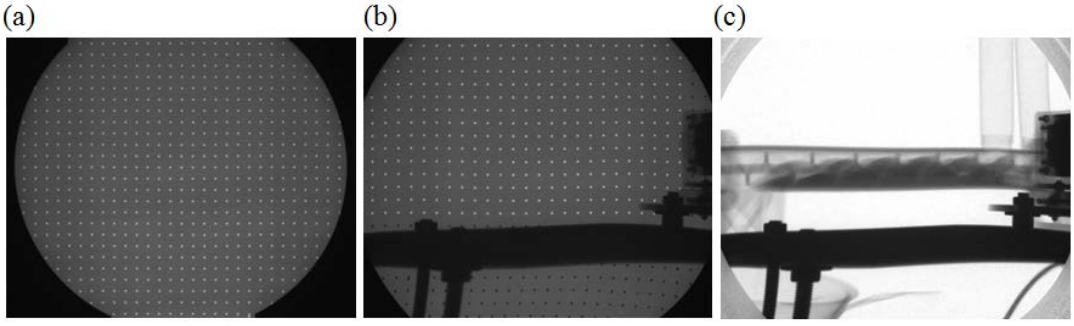

Figure 3.23: X-ray images of the (a) original calibration plate, (b) modified calibration plate, and (c) screw mixer, after the image corrections were applied.

Even after the unwarping procedure has been applied, the leveling plate and the supporting threaded rods on which it is attached do not appear to be straight, as shown in either Figure 3.23b or 3.23c. This observed bending behavior is a result of the modified unwarping procedure that was used in which only the rectangular region above the

leveling plate and to the left of the stepper motor was unwarped. In other words, the screw mixer is unwarped, as shown by the straight lines on the outside surface of the screw mixer, but the other objects in the images are not.

When performing X-ray CT reconstruction, the nonuniformaity in the pixel response must be accounted for via pixel normalization. Ideally, when the CsI phosphor screen is subjected to X-rays, each pixel will react identically, given the X-ray intensity; however, this is not the case. Due to the scintillator's characteristics, pixel-to-pixel variations are present. To minimize the pixel-to-pixel variations, a software correction is applied by applying a "dark" and "flat" image, as shown in Figure 3.24. The dark image consists of an image taken without the X-rays being applied. The flat image consists of an image taken with the X-ray source power slightly below the power required for pixel saturation (i.e., maximum pixel intensity). The dark image is then subtracted from the flat image, and an average pixel response is then obtained. The pixel normalization factor is then obtained by comparing each pixel's intensity to the average pixel intensity, and each image is corrected by this factor. This pixel normalization technique was used when performing X-ray CTs in this project.

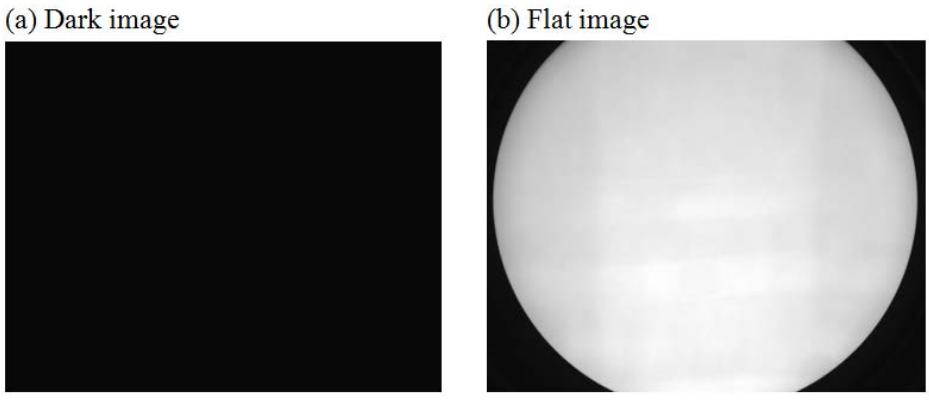

Figure 3.24: Normalization images consisting of a (a) dark and (b) flat image, which were captured with the X-rays off and on, respectively.

Beam hardening is a well-known phenomenon, and is the most commonly encountered artifact in X-ray CT reconstruction (Heindel et al., 2008). This phenomenon is caused by lower energy X-rays being more readily attenuated than the higher energy X-rays. If not accounted for properly, the center (thicker) region of the OOI will be artificially darker than the edges of the OOI. The effect of beam hardening can be reduced by passing the X-ray beam through a metallic filter (typically copper, brass, and/or aluminum). Doing so minimizes the amount of low energy X-rays that are passed through the OOI, and improves the imaging results. Throughout this project, a single 0.61 mm copper filter was used for each X-ray source.

Beam-hardening corrections can also be applied, and was done in the case of X-ray CT imaging in this project. These corrections account for the nonlinear X-ray attenuation at different material thickness, and then apply a correction to account for the nonlinear behavior. The influence that beam-hardening has on the imaging quality depends heavily on the material being considered. For low density materials (e.g., red oak chips, ground walnut shells), beam-hardening is minimal, whereas for high density materials (e.g., glass beads) beam-hardening can cause significant artifacts. Additional details regarding beam-hardening corrections can be found in the literature (Heindel, 2011; Heindel et al., 2008; Keller, 2012).

3.3 Granular Materials

The type of biomass material used for thermochemical conversion can differ quite significantly depending on the availability, cost, geographical location, desired bio-oil products, etc. Likewise, various types of heat carrier media can be used in chemical

reactors, ranging from refractory sand to stainless steel shot. The granular mixing dynamics these reactors depend heavily on the particle size, shape and/or density. However, it would be nearly impossible to characterize the mixing inside each type of reactor for every combination of biomass and heat carrier media. The granular materials used in this project were held constant, and will be discussed in the following sections.

3.3.1 Red Oak Chips

Red oak chips were chosen as the biomass material in this project. The red oak chips were preprocessed multiple times by being run through a hammer mill with a screen opening of 0.635 cm (0.25 in) to reduce the size of the particles. A 500 µm (0.020 in) sieve is then repeatedly used to remove any small particles and dust. The resulting theoretical red oak chip particle size range is 500-6350 µm. However, the red oak chips are needle-shaped and depending on the orientation of the particle, any particle with a diameter slightly smaller than 0.635 cm (0.25 in) could pass through the hammer mill screen regardless of length, if orientated correctly. Figure 3.25a shows an image of the red oak chips captured using an Olympus Infinity microscope with a 4x magnification lens. Figure 3.25b shows a larger scale image of many red oak chips taken with Nikon D50 camera.

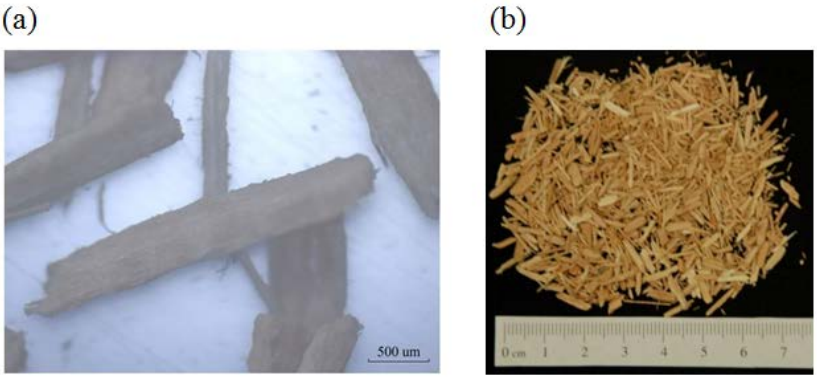

Figure 3.25: Red oak chips taken using a (a) Olympus Infinity microscope with a 4x magnified lens and a (b) Nikon D50 camera.

In order to eliminate excessively large particles from being injected into the screw mixer, a manual screening process was used. Before the red oak chips were added to the volumetric feeder, they were spread out in a thin layer and checked for abnormally large particles. Any abnormally large particles, some approaching 5.08 cm (2 in) in length, or those resembling a knot in the wood were discarded, as shown in Figure 3.26. The number of discarded particles was approximately on the order of one part per thousand. The average red oak chip true density was also analyzed using a pycnometer, resulting in 1350 kg m^{-3}. The details of the analysis are shown in Appendix G.

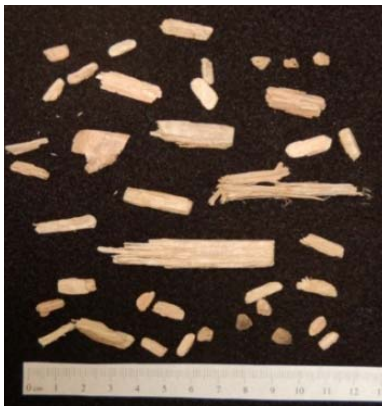

Figure 3.26: Abnormally large red oak chips that were discarded during the manual screening process.

3.3.2 Heat Carrier Media

Sand is commonly used as a heat carrier media in the thermochemical conversion industry. One type that is used is Quikrete commercial grade (fine No: 1961) sand, which works well in a screw pyrolyzer made from stainless steel; however it would quickly cause damage to the plastic screw mixer used in this project. The sand granules are not spherical and have rough edges which make them very abrasive, as shown in Figure 3.27a. A suitable replacement was selected in order to closely resemble the sand and provide similar mixing results while not causing damage to the screw mixer. Despite Quickrete's advertised sand particle range of 200-600 µm (0.0079-0.0263 in), a distribution analysis was needed to either confirm or reject this claim and provide a more detailed analysis of the distribution. A 1.5 kg (3.31 lb) sample of sand was run through a mechanical material shaker using sieves ranging from ASTM Sieve Size #120 (125 µm) to #20 (800 µm). The retained mass in each sieve was recorded and yielded the particle size distribution shown in Figure 3.28. The glass beads particle size distribution is also shown in Figure 3.28 for comparison. The majority of the sand granules, 24%, were between 425 and 500 µm. Furthermore, 95% of the sand granules were between 212 and 710 µm. The sand's average true density was determined using the pycnometer, which was 2680 kg m^{-3}.

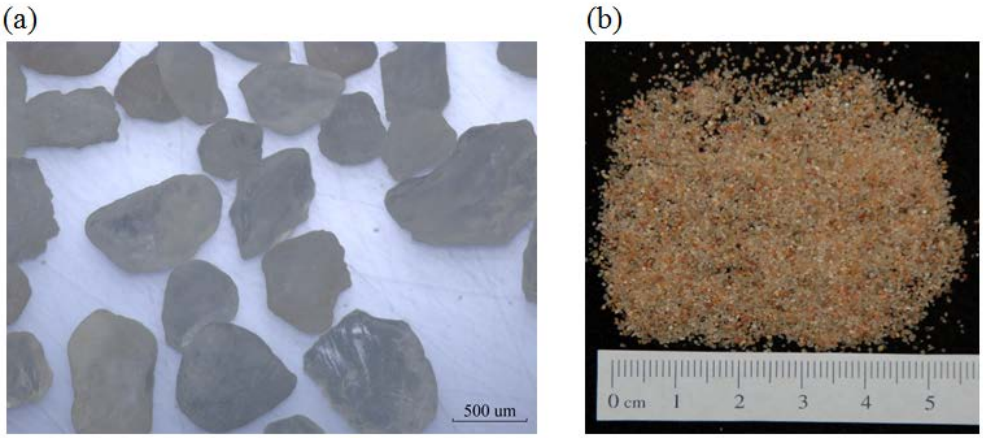

Figure 3.27: Quikrete sand taken using a (a) Olympus Infinity microscope with a 4x magnified lens and a (b) Nikon D50 camera.

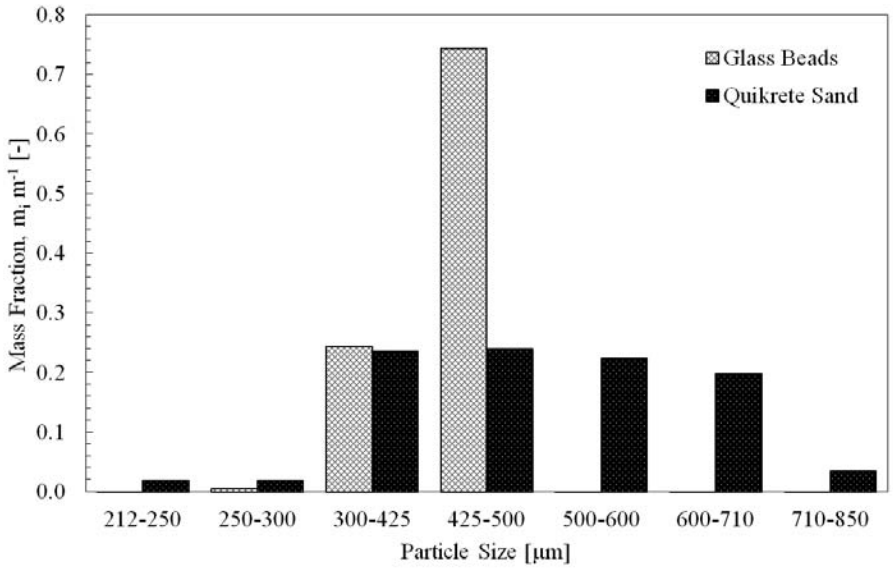

Figure 3.28: Glass beads and Quikrete sand particle size distribution.

3.3.3 Glass Beads

In order to accurately model the behavior of the sand, a replacement heat carrier media with a similar size distribution, true density, and X-ray absorption properties was needed. Glass beads were intuitively selected because of their various particle size availability, spherical shape, and similar density and X-ray absorbing properties. The spherical shape of the granules is well characterized and minimizes abrasive damage to

the screw mixer. Potters Industries' glass beads, shown in Figure 3.29, were selected because of their similar size distribution and density to that of the Quikrete sand. As shown, 75% of the glass beads lie in the 425-500 µm range, which matches the peak range of the sand. Furthermore, 99% of the glass beads lay between 300-500 µm. Despite the glass beads having a more concentrated particle size range that the sand, the size of the two materials resembles each other quite well.

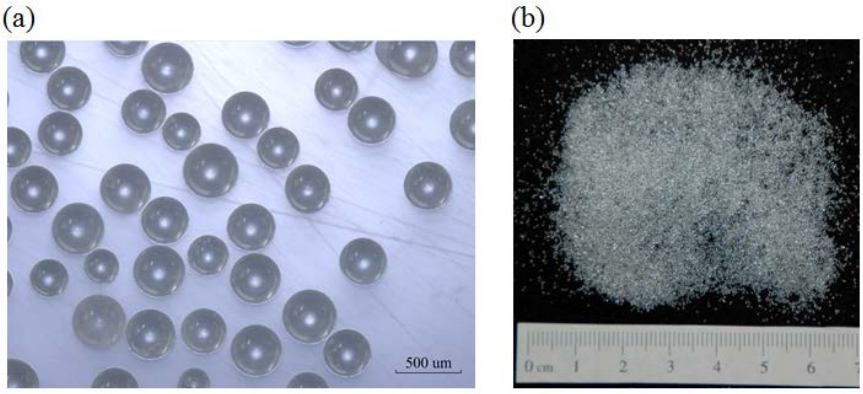

Figure 3.29: Glass beads taken using a (a) Olympus Infinity microscope with a 4X magnified lens and a (b) Nikon D50 camera.

The glass beads true density was determined to be 2510 kg m^{-3}, just 6.3% less than the 2680 kg m^{-3} sand. Because the glass beads were slightly less dense than the sand, the buoyance forces resulting from the density difference between the red oak and glass beads would be slightly less. However, the glass beads were also slightly smaller, on average, than the sand. Thus, the percolation forces resulting from the difference in particle size between the red oak and glass beads would be slightly more. These two changes would, to some extent, offset each. Overall, the glass beads are thought to resemble the sand quite well in terms of mixing because of their near identical material properties.

3.3.4 Biomass Tracer Particles

To accurately characterize the dynamic granular mixing processes inside the screw mixer, the tracer particles needed to satisfy two main criteria: (i) they needed to resemble the granular materials being used in the screw mixer in terms of particle size, shape, and density, and (ii) they needed to provide a large enough X-ray attenuation contrast to be easily identifiable.

After many attempted trails which involved the use of individual lead shot particles and the use of a steel shot tracer "crowd", it was determined that these tracer particle(s) did not resemble the actual granular mixing process because they featured much smaller and denser particles than either of the red oak chips or glass beads. After many preliminary tests, the best representation for the actual granular mixing process which leads to successful tracer particles was the use of "modified" red oak chips.

Individual red oak chips were selected at random and first allowed to soak in a 58%, by weight, solution of potassium iodide and water for 24 hours before being allowed to dry for 48 hours. Five coats of silver paint (more specifically, pure silver particles in an acrylic lacquer based carrier) were then applied to the outside surface of the red oak chips. Finally, a single coat of fingernail polish was applied to increase the visual contrast between the tracer particles and the other red oak chips, allowing for extraction and reuse. The tracer particles had an average true density of 1570 kg m^{-3}, thus representing a true density which is between that of the red oak chips and glass beads.

The tracer particles were injected into the vertical tube that connects the outlet tube of the red oak volumetric auger feeder and the screw mixer's material injection port

one. Doing so allowed the tracer particles to be injected into the screw mixer in the same fashion as the other red oak chips.

3.4 Parameter Selection and Design of Experiments

3.4.1 Selection of Parameters

The mixing effectiveness of the screw mixer can be affected by a large number of parameters (i.e., factors). Possible parameters could include, but are not limited to: (i) screw rotation speed, (ii) dimensionless screw pitch, (iii) screw flighting geometry, (iv) screw rotation orientation, (v) material injection configuration, (vi) material injection geometry, (vii) dimensionless mixing length, (viii) volumetric fill ratio, (ix) glass beads to red oak chips mass flow rate ratio, and (x) granular material properties (e.g., particle size, shape, and density).

The aforementioned list was considered and several of these parameters were held constant. The screw mixer's volumetric fill ratio was set to 65% based on recommendations from years of previous work in the industry and research regarding screw conveyors (Colijn, 1985). In screw conveying and mixing applications, volumetric fill ratios above 65% tend to cause binding and should be avoided. The glass beads to red oak chips mass flow rate ratio was set at 10:1, which is based on the thermodynamic and heat transfer requirements needed to pyrolyze the red oak chips. This ratio is dependent on the heat carrier media injection temperature, biomass and heat carrier media particle size, desired screw pyrolyzer operating temperature, etc. The heat carrier media and biomass material used in this study were also fixed parameters.

In addition to the requested fixed parameters, a number of additional parameters were also fixed in order to relate the results of the project to the ISU BRL screw pyrolyzer. For example, the material injection geometry and screw geometry being used in the ISU BRL screw pyrolyzer were replicated. The screw geometry changed for one specific study which was conducted in the single screw mixer which featured the use of mixing paddles, but was otherwise held constant. Furthermore, after determining the optimal operating conditions, studies were conducted which explored the effect that dimensionless mixing length has on the mixing effectiveness of the screw mixer.

The remaining factors consist of: (i) screw rotation speed, (ii) dimensionless screw pitch, (iii) screw rotation orientation, and (iv) material injection configuration. After selecting the desired factors, the levels of each had to be determined. The ISU BRL screw pyrolyzer is currently set up to operate under the following conditions: screw rotation speed of $\omega = 40$ rpm, dimensionless screw pitch of $p/D = 1.25$ where p is the screw pitch and D is the screw diameter, a co-rotating screw rotation orientation, and a material injection configuration with the biomass and heat carrier media being injected into port one and two, respectively. For convenience and for the purpose of comparison, this operating condition was defined as the “nominal” operating condition.

3.4.1.1 Selection of Parameter Levels

Vanarase and Muzzio (2011) researched the effect of operating conditions and design parameters in a continuous powder mixer. A 10.2 cm (4 in) diameter, 30.5 cm (12 in) long, horizontally orientated impeller was used to mechanically mix the powder and measure the mixing effectiveness. Rotation rates between 39 and 254 rpm were tested and it was determined that higher rotation rates gave rise to better rotational

mixing; however this also decreased the time available for mixing by having a shorter residence time. This tradeoff was optimized and the overall mixing effectiveness was highest at intermediate rotation rates, between 100 and 162 rpm. A similar tradeoff was thought to exist with a screw mixer; thus, two levels in addition to the screw rotation speed of ω = 40 rpm were selected: ω = 20 and 60 rpm.

The effect of dimensionless screw pitch has been shown to be a critical factor in the powder industry. Uchida and Okamoto (2006) used an X-ray system coupled with a 2D imaging device to track powder flows in a single screw feeder. Small amounts of tungsten tracer powder were injected and tracked as they moved downstream. Uchida and Okamoto (2008) later used this imaging system to measure the diffusion coefficient (a measure of mixing effectiveness) of four screw designs each having a 25 mm diameter. Three screws featured a single flighting design with dimensionless screw pitches of p/D = 1, 1.5, and 2.3. The diffusion coefficient was determined to be the largest for the screw with a dimensionless screw pitch of p/D = 2.3 and decreased as the pitch decreased. Uchida and Okamoto (2008) concluded that increasing the screw pitch reduced the transmitted powder velocity, increased the diffusion coefficient, and increased the frequency of the path line sine curve.

The two additional dimensionless screw pitch levels were selected in this study: p/D = 0.75 and 1.75. Geometrical considerations used to determine the acceptable lower limit (i.e., p/D = 0.75) of the dimensionless screw pitch because as it becomes too small, minimal clearance exists between screw flights and can potentially result in screw binding due to material being jammed. The 40% reduction from the nominal

dimensionless screw pitch to the lower limit case was also replicated for the contrary; resulting in a 40% increase (i.e., p/D = 1.75).

The effects of co-rotating (CoR) and counter-rotating (CtrR) screws have been investigated in the plastic extrusion industry and literature suggests that co-rotating screws are favored for several reasons (Martelli, 1983): (i) material pushed out of a channel of one screw by the flighting of the other moves into the channel of the second screw, (ii) the transfer of material from one screw to another creates movement around both screws, (iii) radial pressure is similar between the two screws, therefore squeezing of the material does not exist, and (iv) no radial forces exist between the screws, keeping the screws centered. Despite the previous knowledge, screw rotation orientation has not been investigated in a double screw mixer, and was thought to have a significant impact on the mixing effectiveness. A counter-rotating screw orientation was chosen in addition to the nominal co-rotating set-up. However, when considering counter-rotating screws, there are two different rotation directions: counter-rotating up-pumping (CtrR UP) and counter-rotating down-pumping (CtrR DP), as shown in Figure 3.32. Up-pumping and down-pumping refers to the direction of movement between the two screws. In contrast, the rotation direction of co-rotating screws only depends on your reference frame and does not change the mixing dynamics of the screw mixer.

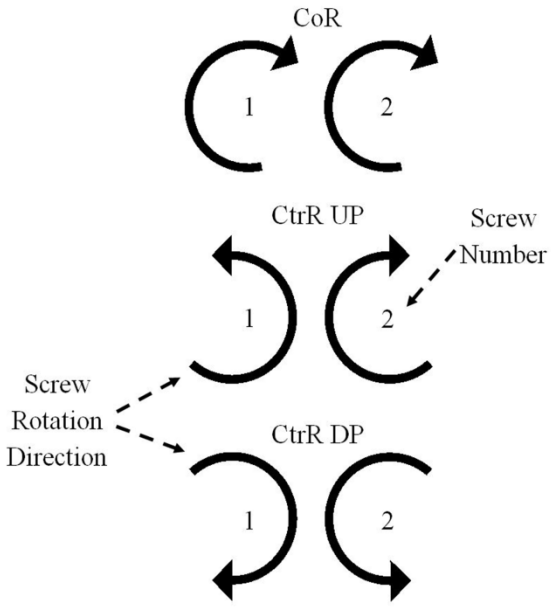

Figure 3.30: Co-rotating (CoR), counter-rotating up-pumping (CtrR UP), and counter-rotating down-pumping (CtrR DP) screw rotation orientations, respectively.

As previously noted, the material injection geometry was replicated in this project for the purpose of applying the results to the ISU BRL screw pyrolyzer. However, the effect of the material injection configuration was investigated. The ISU BRL is currently injecting the biomass and heat carrier media into port one and two, respectively. This injection configuration was chosen for a couple different reasons. First, the lighter, larger biomass particles were thought to be conveyed along the bottom of the pyrolyzer until encountering the heat carrier media, which would be dropped from above. Because the biomass is less dense and features larger particles relative to the heat carrier media, the biomass was thought to segregate upward while the heat carrier media would work its way downward. This change in vertical position was thought to encourage mixing. Furthermore, in a reacting screw pyrolyzer, the heat carrier media is heated to a desired temperature prior to being injected into the screw pyrolyzer. If injected first, some of its

heat would be lost before encountering the biomass. The aforementioned material injection configuration was selected when constructing the ISU BRL screw pyrolyzer; however there has been no testing to confirm the selection of this parameter. Thus, this was made an experimental parameter in an effort to confirm or deny this choice.

3.4.1.2 Design of Experiments

3.4.1.2.1 Screw Mixer

3.4.1.2.1.1 Full Study

The four experimental factors mentioned above were chosen for preliminary testing in an attempt to determine which combination of factors produced the highest mixing effectiveness of the red oak chips and glass beads. A full-factorial design of experiments (DOE) was chosen thereby taking on all the possible combinations of levels across all the experimental factors. Doing so allows studying the effect of each factor on the mixing performance as well as the effects of interactions between factors. As mentioned, the number of levels for the factors was set to three, three, three, and two for the screw rotation speed, dimensionless screw pitch, screw rotation orientation, and material injection configuration, respectively; resulting in 54 ($3 \times 3 \times 3 \times 2 = 54$) different operating conditions (i.e., treatments). The term treatments and operating conditions will be used interchangeably because treatment is the preferred terminology in the statistical analysis literature, and will be used to model the mixing process. A list of each of the 54 treatments and their respective factors and levels are shown in Table 3.1. The accompanying operating condition numbering convention will be used throughout the project.

Furthermore, repeatability was incorporated into the DOE by performing three tests (i.e., observations) at each operating condition, totaling 162 individual tests that were performed. As previously mentioned, four samples were collected across the exit stream for each test totaling 648 samples that were collected and analyzed. The breadth and depth resulting from the number of different operating conditions and collected samples is far beyond previous granular mixing studies reported in the literature. A fractional-factorial design in which only a subset of the full factorial design could have been employed, but this would have reduced the statistical power of the analysis, compromising the ability to recognize significant factors, and resulting in undesired results.

Table 3.1: A complete list of all 54 operating conditions and their respective levels for the screw mixer.

Operating Condition	Screw Rotation Speed ω [rpm]	Dimensionless Screw Pitch p/D [-]	Screw Rotation Orientation [-]	Material Injection Configuration RO, GB [-]
1	20	0.75	CoR	1, 2
2				2, 1
3			CtrR UP	1, 2
4				2, 1
5			CtrR DP	1, 2
6				2, 1
7		1.25	CoR	1, 2
8				2, 1
9			CtrR UP	1, 2
10				2, 1
11			CtrR DP	1, 2
12				2, 1
13		1.75	CoR	1, 2
14				2, 1
15			CtrR UP	1, 2
16				2, 1
17			CtrR DP	1, 2
18				2, 1
19	40	0.75	CoR	1, 2
20				2, 1
21			CtrR UP	1, 2
22				2, 1
23			CtrR DP	1, 2
24				2, 1
25		1.25	CoR	1, 2
26				2, 1
27			CtrR UP	1, 2
28				2, 1
29			CtrR DP	1, 2
30				2, 1
31		1.75	CoR	1, 2
32				2, 1
33			CtrR UP	1, 2
34				2, 1
35			CtrR DP	1, 2
36				2, 1

Table 3.1: Continued

Operating Condition	Screw Rotation Speed ω [rpm]	Dimensionless Screw Pitch p/D [-]	Screw Rotation Orientation [-]	Material Injection Configuration RO, GB [-]
37	60	0.75	CoR	1, 2
38				2, 1
39			CtrR UP	1, 2
40				2, 1
41			CtrR DP	1, 2
42				2, 1
43		1.25	CoR	1, 2
44				2, 1
45			CtrR UP	1, 2
46				2, 1
47			CtrR DP	1, 2
48				2, 1
49		1.75	CoR	1, 2
50				2, 1
51			CtrR UP	1, 2
52				2, 1
53			CtrR DP	1, 2
54				2, 1

3.4.1.2.1.2 Shorter Mixing Length Study

One key topic of interest in granular mixing systems is either the time required to achieve adequate mixing in batch processes, or the length of the mixer and/or resulting mixing time in continuous mixing processes. In this project, the mixing effectiveness of the screw mixer was evaluated as a function of the dimensionless mixing length, L/D, where L is the effective mixing length measured from the centerline of injection port two (downstream injection port) to the beginning of the outlet ports, and D is the screw diameter. The already existing ISU BRL screw pyrolyzer features a dimensionless mixing length of L/D = 10. Additional levels of L/D = 2 and 5 were chosen in an effort to characterize the mixing effectiveness at shorter mixing lengths. Longer dimensionless

mixing lengths were not used because of the limitations and costs associated with the screw mixer's additive manufacturing processes. Furthermore, fast pyrolysis typically occurs within the first few seconds, and undesired products can be produced with biomass materials are subjected to relatively long residence time, as previous mentioned in Chapter 2.

After the optimized condition (operating condition 53) was determined, which will be discussed in Chapters 5 and 6, only a selected number of parameters were investigated in addition to the dimensionless mixing length. The screw rotation speed was incorporated into the design of experiments because of its influence on the material residence time. Moreover, the effect of dimensionless screw pitch was also investigated. Solely for comparison purposes, the nominal operating condition was also investigated at various dimensionless mixing lengths. The corresponding levels of the other factors, screw rotation orientation and material injection configuration, were held constant at their respectively optimized levels. These optimized levels were selected from the previous studies and are outlined is Chapters 5 and 6. The optimized level of the screw rotation orientation is counter-rotating down-pumping, while the material injection configuration was having the red oak chips and glass beads injected into ports one and two, respectively.

From the selection of these three factors (screw rotation speed, dimensionless screw pitch, and dimensionless mixing length) and their respectively levels, 27 different operating conditions are possible ($3 \times 3 \times 3 = 27$). As previously done in the full study, a full-factorial design of experiments was used in this study. The nominal condition was also performed at all three dimensionless mixing lengths, but this condition represents

several parameter changes not being address in this study (e.g., screw rotation orientation and material injection configuration), and was thus not incorporated into the DOE. These trials were performed independent of the others, but did raise the total number of operating conditions up from 27 to 30. As previously done, repeatability was incorporated into the design of experiments by performing three tests (i.e., observations) at each operating condition, totaling 90 individual tests that were performed for this study. A complete list of operating conditions, including the nominal conditions (i.e., operating condition 25) is listed in Table 3.2. Note that the previously defined operating condition numbering convention was held constant, and the addition of the dimensionless mixing length was added to it. For example, operating condition 5 was changed to 5(2), 5(5), and 5(10) for dimensionless mixing lengths of L/D = 2, 5, and 10, respectively.

Table 3.2: A list of all 30 operating conditions that were used and their respective levels for the screw mixer's shorter mixing length study.

Operating Condition	Screw Rotation Speed ω [rpm]	Dimensionless Screw Pitch p/D [-]	Dimensionless Mixing Length L/D [-]
5(2)	20	0.75	2
5(5)			5
5(10)			10
11(2)		1.25	2
11(5)			5
11(10)			10
17(2)		1.75	2
17(5)			5
17(10)			10
23(2)	40	0.75	2
23(5)			5
23(10)			10
25(2)		1.25	2
25(5)			5
25(10)			10
29(2)			2
29(5)			5
29(10)			10
35(2)		1.75	2
35(5)			5
35(10)			10
41(2)	60	0.75	2
41(5)			5
41(10)			10
47(2)		1.25	2
47(5)			5
47(10)			10
53(2)		1.75	2
53(5)			5
53(10)			10

3.4.1.2.2 Single Screw Mixer

Single screw conveyors have been used to mechanically transport granular materials for decades. They have also been used to mechanically mix granular materials, but are thought to be less advantageous in terms of mixing than double screw applications. A study was conducted which investigated the mixing effectiveness of a single screw mixer. In terms of the parameters, the same factors and their corresponding levels as the full double screw mixer study were used, with the exception of the screw rotation orientation. The screw rotation orientation was obviously omitted because only one screw is present thus defining a co-rotating or counter-rotating screw rotation orientation is not possible. As mentioned with the co-rotating screw rotation orientation in the double screw mixer, the rotation direction also depends on the rate of reference and does not change the mixing dynamics. The same is true for the single screw mixer.

The factors under investigation included the screw rotation speed, dimensionless screw pitch, and the material injection configuration, from which 18 different operating conditions are possible ($3 \times 3 \times 2 = 18$). As previously done in the full study, a full-factorial design of experiments was used in this study. As previously done, repeatability was incorporated into the design of experiments by performing three tests (i.e., observations) at each operating condition, totaling 54 individual tests that were performed for this study (not to be confused with the 54 different operating conditions used in the double screw mixer's full study). A complete list of operating conditions is listed in Table 3.3. The addition of the "s" behind the operating condition number symbolizes the single screw mixer, and is used to avoid confusion between the 54 operating conditions in the double screw mixer.

Table 3.3: A list of all 18 operating conditions that were used and their respective levels for the single screw mixer.

Operating Condition	Screw Rotation Speed ω [rpm]	Dimensionless Screw Pitch p/D [-]	Material Injection Configuration RO, GB [-]
1s	20	0.75	1, 2
2s			2, 1
3s		1.25	1, 2
4s			2, 1
5s		1.75	1, 2
6s			2, 1
7s	40	0.75	1, 2
8s			2, 1
9s		1.25	1, 2
10s			2, 1
11s		1.75	1, 2
12s			2, 1
13s	60	0.75	1, 2
14s			2, 1
15s		1.25	1, 2
16s			2, 1
17s		1.75	1, 2
18s			2, 1

3.4.1.2.2.1 Mixing Paddles

As previously mentioned in Chapter 2, the use of mixing paddles and complex impeller geometry has sometimes been used to enhance granular mixing. In this study, the use of mixing paddles in the single screw mixer was tested. Mixing paddle design, like many other granular mixing processes, was based on intuition and not fundamental science or previous research. The design of the mixing paddle screw is shown in Chapter 2. This study was performed as a side project and was not incorporated in the previously mentioned single screw mixer design of experiments.

3.4.2 Red Oak Chips and Glass Beads Mass Flow Rates

A 65% volumetric fill ratio is recommended in screw conveyor applications involving granular materials (Colijn, 1985), and was maintained for all experimental tests by selecting the appropriate red oak chips and glass beads injection mass flow rates for each combination of screw rotation speed and dimensionless screw pitch. The selected mass flow rates for the double and single screw mixer as shown in Table 3.4 and 3.5, respectively. A 10:1 glass beads to red oak chips mass flow rate ratio was maintained for all tests.

Table 3.4: Red oak chips and glass bead mass flow rates required to maintain a 65% volumetric fill ratio for the double screw mixer.

Double Screw Mixer			
Screw Rotation Speed ω [rpm]	Dimensionless Screw Pitch p/D [-]	Red Oak Chips Mass Flow Rate $\dot{m}_{RO}$ [kg hr^{-1}]	Glass Beads Mass Flow Rate $\dot{m}_{GB}$ [kg hr^{-1}]
20	0.75	1.13	11.3
	1.25	1.75	17.5
	1.75	2.00	20.0
40	0.75	2.00	20.0
	1.25	3.50	35.0
	1.75	4.00	40.0
60	0.75	3.25	32.5
	1.25	5.00	50.0
	1.75	5.75	57.5

Table 3.5: Red oak chips and glass bead mass flow rates required to maintain a 65% volumetric fill ratio for the single screw mixer.

Single Screw Mixer			
Screw Rotation Speed ω [rpm]	Dimensionless Screw Pitch p/D [-]	Red Oak Chips Mass Flow Rate $\dot{m}_{RO}$ [kg hr^{-1}]	Glass Beads Mass Flow Rate $\dot{m}_{GB}$ [kg hr^{-1}]
20	0.75	0.56	5.6
	1.25	1.00	10.0
	1.75	1.13	11.3
40	0.75	1.13	11.3
	1.25	2.00	20.0
	1.75	2.13	21.3
60	0.75	1.63	16.3
	1.25	3.00	30.0
	1.75	3.13	31.3

CHAPTER 4: OPTICAL VISUALIZATION AND COMPOSITION ANALYSIS TO QUANTIFY MIXING IN A DOUBLE SCREW MIXER[1]

Todd A. Kingston[2] and Theodore J. Heindel

Department of Mechanical Engineering, Iowa State University, Ames, Iowa, 50011, USA

kingston.todd@gmail.com and theindel@iastate.edu

Abstract

The mixing of granular materials has a significant influence on the yield and/or quality of the desired products in numerous industrial processes including energy generation, food processing, and pharmaceutical production. However, characterizing the mixing effectiveness of systems or processes in granular applications is difficult due to challenging sampling procedures and measurement techniques. In this study, a two-part measurement technique consisting of optical visualization and composition analysis is developed to provide qualitative and quantitative mixing characteristics of granular mixing in a double screw mixer, respectively. Mixing studies are performed using a binary mixture of 500-6350 μm red oak chips and 300-500 μm glass beads. The effect of

[1] Kingston, T.A., Heindel, T.J. (2014). Optical visualization and composition analysis to quantify mixing in a double screw mixer. *Powder Technology* (in review).

[2] Corresponding author: Todd A. Kingston (kingston.todd@gmail.com)

screw rotation speed and dimensionless screw pitch on the mixing effectiveness is investigated for ω = 20, 40, and 60 rpm and p/D = 0.75, 1.25, and 1.75, respectively. Optical visualization is captured across the entire mixing region's periphery, providing extensive qualitative observations. Quantitative composition analysis is performed on samples collected across the screw mixer and a two-way analysis of variance (ANOVA) statistical model is applied. Overall, the mixing effectiveness is maximized at an intermediate screw rotation speed of ω = 40 rpm and a dimensionless screw pitch of p/D = 1.75. The developed measurement techniques and resulting trends are compared to previous granular mixing studies featuring similar mixing equipment found in the literature.

Keywords: Composition analysis, granular mixing, optical visualization, screw mixer.

4.1 Introduction

Granular mixing processes can have a significant influence on the resulting products in many industrial processes including energy generation, food processing, and pharmaceutical production. For example, screw pyrolyzers are being developed for the thermochemical conversion of biomass into bio-oil. Screw pyrolyzers are a relatively new chemical reactor design compared to traditional fluidized beds, rotating cones, and ablative reactors. Detailed descriptions of various reactor types used for thermochemical conversion have been previously described in the literature (Bahng et al., 2009; Bridgwater, 2003; Mohan et al., 2006). The screw pyrolyzer's high heat transfer rates and resulting bio-oil yields are significantly influenced by its operating conditions and its ability to mechanically mix high density inert heat carrier media (e.g., stainless steel shot,

refractory sand, etc.) with low density biomass particles (e.g., red oak chips, switchgrass, etc.). Previous research efforts featuring screw pyrolyzers have primarily focused on the quality of the products and how they relate to the feedstocks used (Ingram et al., 2008) or the reactor operating conditions (Brown and Brown, 2012a). However, no research efforts have focused on relating the granular mixing inside a double screw pyrolyzer to its operating conditions. Thus, a thorough understanding of the granular mixing dynamics is needed for more efficient operation and higher bio-oil yields.

The general purpose of a granular mixing process is that it produces a mixture with an internal structure of acceptable quality (Bridgwater, 2012). Most commonly, granular mixing processes seek a high degree of homogeneity, and in some particular instances, the purpose is to influence simultaneous processing, such as chemical reactions and heat and/or mass transfer (Bridgwater, 2012). A fundamental problem commonly encountered during the mixing of granular materials is the tendency for mixtures to segregate due to differences in particle size, shape, and/or density (Yang, 2006). Further complications arise because a considerably large number of factors can influence this mixing process.

Despite the solids-handling industry being quite mature, process and equipment design and the selection of operating conditions remains open to speculation because it lacks quantitative justification; it is based primarily on trial-and-error and experience, rather than quantitative science (Bridgwater, 2012). Moreover, the methods used to determine granular mixing effectiveness are limited (Siiria and Yliruusi, 2009). Many experimental studies investigating the mixing of granular materials have considered only a small number of factors relating to the operating conditions of the mixing equipment.

For example, Uchida and Okamoto (2006) used an X-ray system coupled with a 2D imaging device to track small amounts of tungsten tracer powder in powder flows and investigated the effect of a single factor, dimensionless screw pitch, in a single screw feeder.

In contrast to investigating only one factor, multiple factors can and should be studied simultaneously. This allows for a more thorough understanding of the effects the operating conditions have on the mixing effectiveness. Furthermore, it allows for the interaction of factors to be analyzed. For instance, Vanarase and Muzzio (2011) researched the effect of impeller rotation rate, flow rate, and blade configuration in a continuous horizontally orientated impeller powder mixer. The rotation rate was determined to be the most influential factor and intermediate rotation rates optimized the overall mixing effectiveness. Ideally, numerous factors that significantly affect the mixing effectiveness of the system would be incorporated in the study, as was done by Vanarase and Muzzio (2011). However, incorporating too many factors can also be problematic because of the resulting size of the design of experiments, time required to collect and analyze the data, and the ability to interpret the results.

Many attempts to characterize the mixing effectiveness of granular applications rely solely on sampling the material after exiting the mixer and often involve challenging sampling procedures (Bridgwater, 2012; Brown, 2009; Gao et al., 2011; Portillo et al., 2009; Tsai and Lin, 1994; Vanarase and Muzzio, 2011). While sampling the granular material after exiting the mixer is very useful, it alone does not provide insight into the mixing dynamics of the mixer during the mixing process. To thoroughly understand the mixing mechanisms, a two-part measurement technique must be developed which

couples qualitative observations of the entire mixing process with quantitative data related to the end products.

Accurate sampling techniques have been a common problem for many researchers wanting to characterize granular flows. For example, Brown (2009) attempted to perform preliminary cold-flow mixing studies by removing the top plate from a screw pyrolyzer designed specifically for chemically reacting flows. The inability to collect samples at locations other than the top layer of material was noted, resulting in the sample composition not accurately reflecting the composition of the entire mixture due to material segregation. Additionally, variations in the material volumetric fill level inside the system resulting from particular operating conditions prohibited collecting samples at all the desired locations. An improved sampling procedure is needed to provide a solution to this commonly encountered problem.

The purpose of this study is to develop a measurement technique capable of determining the mixing effectiveness of a laboratory-scale double screw mixer under various operating conditions. The unique screw mixer designed specifically for this mixing study and the granular materials used will first be described. The developed measurement technique, discussed below in great detail, overcomes the previously noted problems by: (i) capturing optical visualization of the entire mixing region, thus providing a complete picture of the mixing process and qualitative assessment; (ii) utilizing recent advances in rapid prototyping machining processes to enable a more thorough sampling procedure; and (iii) applying a two-way analysis of variance (ANOVA) statistical model to quantitatively indicate the most influential factors, determine the mixing effectiveness, and optimize the mixing effectiveness for the factors

under consideration. The effect of screw rotation speed and dimensionless screw pitch on mixing effectiveness is investigated to demonstrate the developed measurement technique. The results of the study are then presented and feature both qualitative observations and quantitative justification. Finally, the experimental procedures are validated by comparing the results of this study to previous mixing studies found in the literature that feature similar mixer geometry.

4.2 Experimental Setup

A laboratory-scale double screw mixer was designed and constructed specifically for granular mixing studies, as shown in Figure 4.1. A rapid prototyping machining process (i.e., 3D printer) was used to fabricate all of the screw mixer's parts. The screw mixer's housing was manufactured using a transparent plastic material allowing optical access to the mixing region's periphery (360°). All remaining components were fabricated using an opaque plastic material.

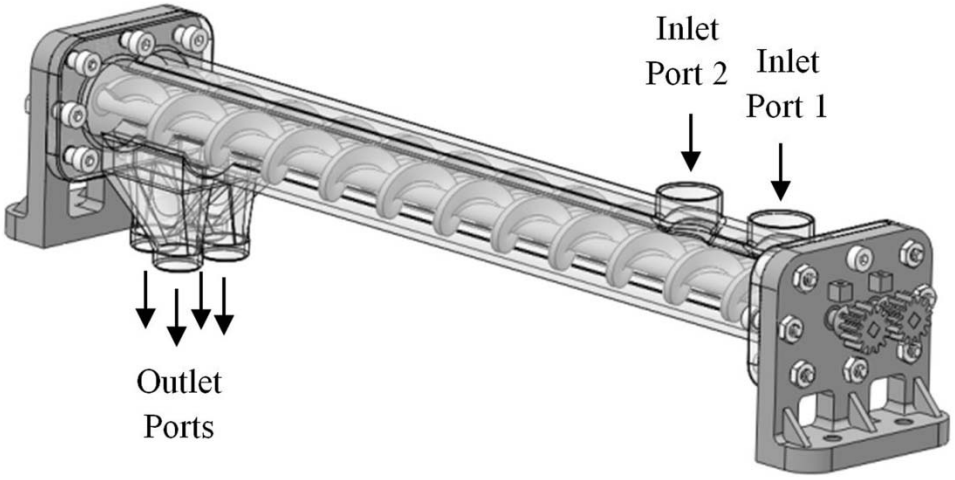

Figure 4.1: Screw mixer designed and constructed for optical visualization and composition analysis mixing studies.

The screw mixer features two parallel and horizontally mounted intermeshing noncontact left hand threaded screws. The screw diameter, D = 2.54 cm, was chosen as the characteristic length of the system. A variable speed gearmotor drives the screws through a set of specifically designed spur gears. A co-rotating screw rotation orientation was maintained for all mixing studies. Two injection ports are axially positioned two characteristic lengths apart from one another and are laterally positioned halfway between the two screws. Four uniquely designed outlet ports in the bottom of the screw mixer's housing horizontally divides the entire granular flow exit stream into four separate channels. The granular materials exit through the outlet ports in the bottom of the screw mixer and free-fall to individual collection basins. The effective mixing length is measured from the centerline of the downstream injection port (port two) to the beginning of the outlet ports thus providing a dimensionless mixing length of L/D = 10.

Qualitative optical visualization of the dynamic granular mixing inside the screw mixer was captured from four independent projections simultaneously (i.e., left, top, right, and bottom). Figure 4.2 illustrates the experimental setup used to perform the optical visualization, and demonstrates the positioning of four Panasonic HC-V700M HD cameras, two volumetric screw feeders used to independently meter in the granular materials, the polyethylene inlet and outlet tubes, and the screw mixer. The cameras capture images at 60 frames per second with 1920 × 1080 resolution. Six 85 W compact fluorescent lamps (CFL) are used to provide adequate lighting to the mixing region. Direct lighting on the outside surfaces of the screw mixer's housing produced significant reflection and other undesired lighting conditions. To minimize these effects, the lights were carefully positioned to provide only indirect lighting and the entire experimental

setup was surrounded in black fleece fabric to block any outside light sources. Furthermore, all metallic equipment surfaces (e.g., volumetric screw feeders) were covered in black fabric to eliminate any reflecting surfaces.

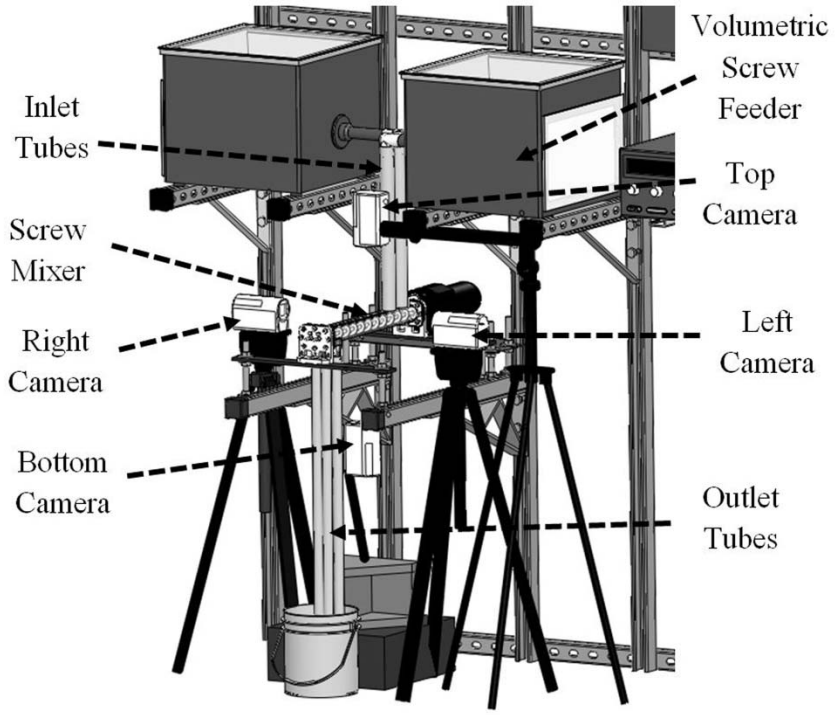

Figure 4.2: Optical visualization experimental setup.

The screw mixer mechanically mixes a binary mixture of biomass and heat carrier media. The biomass and heat carrier media used in this study were red oak chips and glass beads, respectively. Figure 4.3 shows images of the two granular material types that were taken with an Olympus Infinity microscope using a 4x magnification lens. The red oak chips had a particle size range and true density of 500-6350 µm and 1350 kg m^{-3}, respectively. The glass beads had a particle size range and true density of 300-500 µm and 2510 kg m^{-3}, respectively. Glass beads were chosen to model traditional heat carrier media such as refractory sand because the glass beads are well characterized and less abrasive. Furthermore, the glass beads and refractory sand feature similar material

properties because the composition of the two materials is very similar. The red oak chips and glass beads were independently metered into port one and two, respectively, by two variable speed volumetric screw feeders. A polyvinyl chloride 90° elbow and a vertical polyethylene tube connected the volumetric screw feeders' outlet tubes to the screw mixer housing's inlet ports, injecting the granular materials vertically downward into the screw mixer.

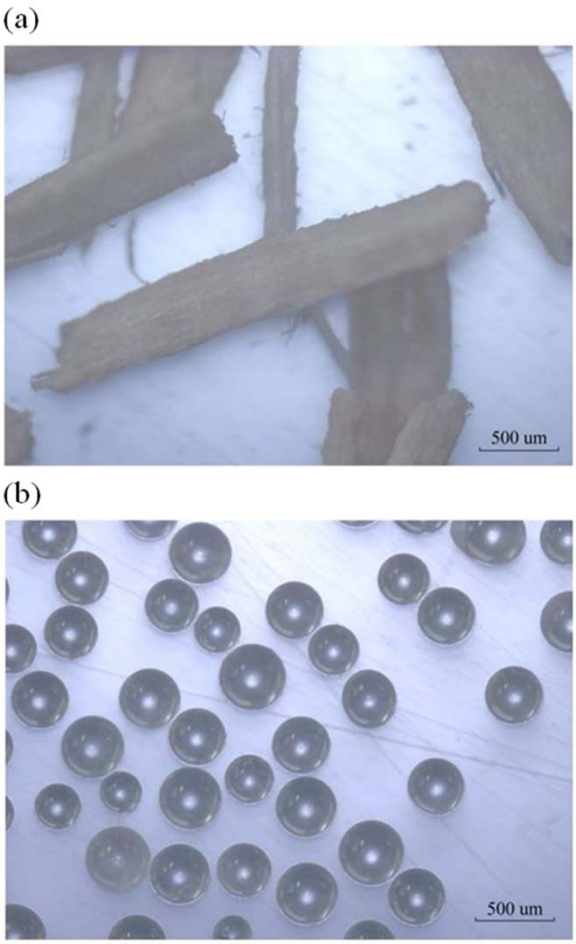

Figure 4.3: Magnified images of (a) 500-6350 μm red oak chips and (b) 300-500 μm glass beads, respectively.

The current study investigates the effect of two factors on the mixing effectiveness, screw rotation speed, ω, and dimensionless screw pitch, p/D. Screw

rotation speeds of ω = 20, 40, and 60 rpm and dimensionless screw pitches of p/D = 0.75, 1.25, and 1.75 were chosen as the levels for each of the two factors. A 65% volumetric material fill level is recommended in screw conveyor applications involving granular materials (Colijn, 1985), and was maintained for all experimental tests by selecting the appropriate red oak chips and glass beads injection mass flow rates for each combination of screw rotation speed and dimensionless screw pitch, as shown in Table 4.1. A 10:1 glass beads to red oak chips mass flow rate ratio was maintained for all tests.

Table 4.1: Red oak chips and glass beads mass flow rates required to maintain a 65% volumetric material fill level.

Screw Rotation Speed ω [rpm]	Dimensionless Screw Pitch p/D [-]	Red Oak Chips Mass Flow Rate $\dot{m}_{RO}$ [kg hr^{-1}]	Glass Beads Mass Flow Rate $\dot{m}_{GB}$ [kg hr^{-1}]
20	0.75	1.13	11.3
	1.25	1.75	17.5
	1.75	2.00	20.0
40	0.75	2.00	20.0
	1.25	3.50	35.0
	1.75	4.00	40.0
60	0.75	3.25	32.5
	1.25	5.00	50.0
	1.75	5.75	57.5

4.3 Experimental Methods

Two general techniques are available for characterizing the mixing of granular materials: (i) noninvasive methods enabling observations to be made without requiring sampling and (ii) invasive methods requiring materials to be sampled and analyzed. Each technique offers advantages that are needed to fully understand the mixing dynamics and

results of this study. Both techniques are used in the developed measurement technique and, coupled together, provide a thorough method to quantify mixing in a screw mixer.

4.3.1 Optical Visualization

Temporal and spatial syncing of the mixing visualization was accomplished using Adobe Premiere Pro CS6. Figure 4.4 illustrates the four projections from which optical visualization was captured and the cropped projections with a typical path line of a particle being injected into port two, respectively. A specific event (e.g., audio spike) in each of the four independent videos was temporally synced, coupling the four projections into one combined video. The top and right projections were captured in the orientation shown in Figure 4.4a but the left and bottom projections were spatially synced by inverting them about their vertical and horizontal axis, respectively. This enables the granular material to flow from left to right in all projections and for screw one and two to be aligned in the top and bottom projections. The four projections were combined into a simple and compact visualization interface by cropping everything outside the mixing region and labeling each projection, as shown in Figure 4.4b. This interface allows observations of the entire mixing region to be made and provides critical information needed to understand the granular mixing dynamics. Figure 4.4b also illustrates a typical particle pathline for a particle injected into inlet port two.

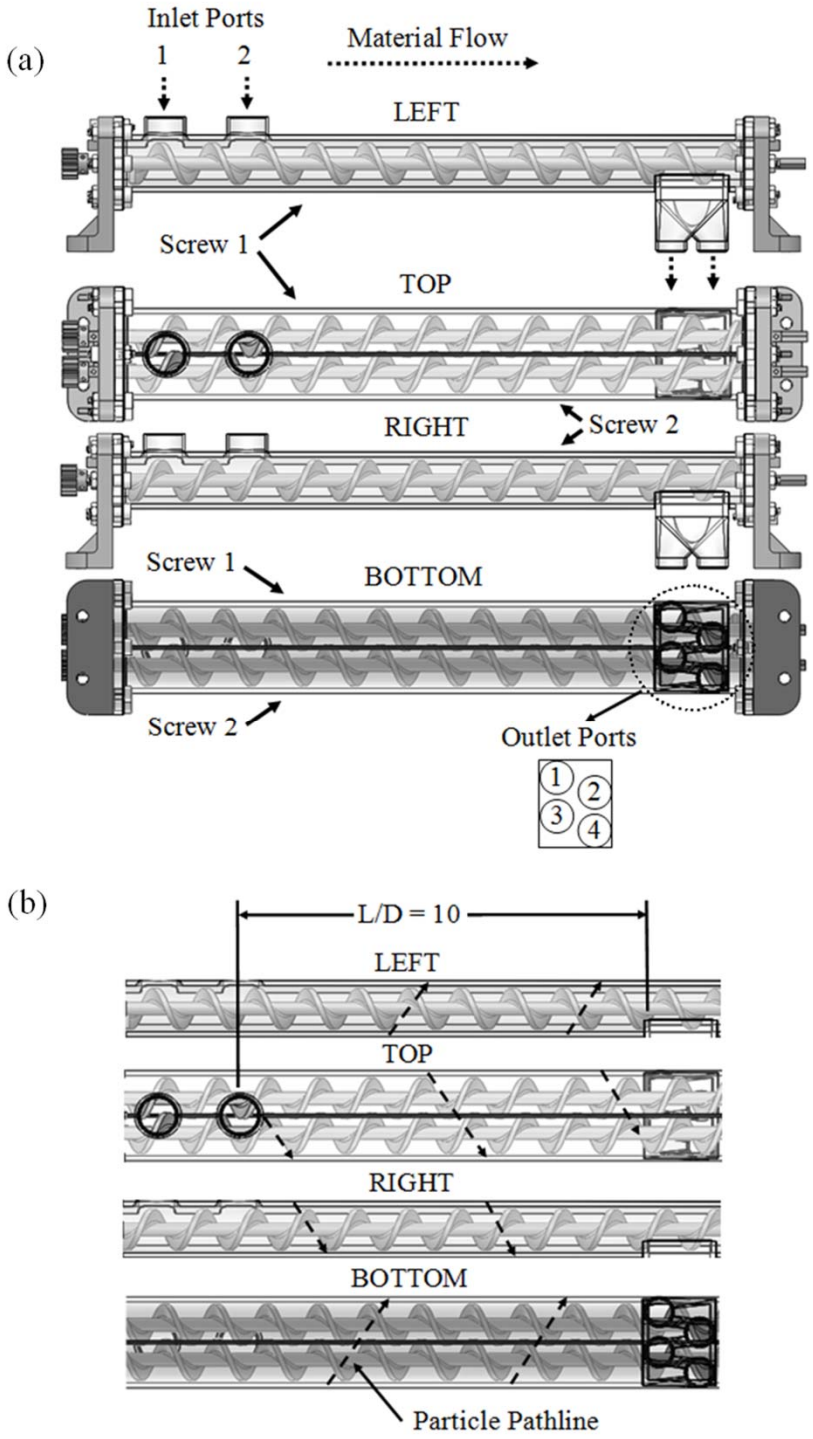

Figure 4.4: (a) Four projections of the screw mixer from which optical visualization was captured. (b) Cropped projections with a typical particle pathline.

4.3.2 Sampling Procedure

Accurate sampling techniques have been a common challenge for researchers wanting to characterize powder and granular flows (Brown, 2009). Many current methods involve the use of invasive probes to extract granular samples. However, the presence of these probes disrupts the granular bed and yields undesired results. Allen (1996) states that the two "golden rules of sampling" are: (i) a granular mixture should be sampled only when it is in motion and (ii) the whole granular stream should be uniformly collected for many short increments. In this study, the unique design of the screw mixer's exit region dividing mechanism allowed the entire cross-sectional exit stream of the granular flow to be sampled by dividing it into the four separate outlet ports. This technique eliminates the assumption that the collected sample exhibits similar composition to that of the population because the four samples being collected comprise the entire population. Moreover, multiple samples were collected from each of the four outlet ports. These methods eliminate traditional problematic sampling techniques and fulfill Allen's (1996) "golden rules of sampling."

The screw mixer was set up with the first of the randomly ordered trials' operating conditions and was allowed to reach steady state by running the granular materials through the system for a sufficiently long time period. A quick shut-off switch was triggered, simultaneously stopping the screws and volumetric feeders. Collection bags were then placed at the end of outlet tubes before reactivating the screws and volumetric feeders. The system was run for approximately 5-10 seconds until the sample collection bags reached a desired fill level. The screw mixer was then stopped and the collection bags were removed and sealed. The sampling process was then repeated for the

remaining operating conditions. The sample size collected from the outlet ports was specifically determined such that the entire sample would fit in the measuring device used to determine the mixture's true volume (a pycnometer, which will be described in more detail in the following section). It was critical that the entire collected sample be analyzed using the pycnometer because if only a portion were analyzed, the prescribed assumption that the analyzed sample represents the sample population would need to be made and would introduce a large amount of error.

4.3.3 Composition Analysis

The degree of heterogeneity of the four samples collected from the outlet ports provided an indication of the screw mixer's mixing effectiveness. Ideally, a homogenous mixture of red oak chips and glass beads would be present everywhere within the screw mixer. However, segregation resulting from particular operating conditions and differences in particle size, shape, and/or density may occur.

The mixing effectiveness of granular processes is commonly determined by measuring the mixture composition. However, much difficultly lies in measuring granular composition. Quantitative characterization has most commonly relied on determining the spread of the composition, symbolized by the composition variance, s^2 (Bridgwater, 2012).

In this study, the mixture composition is defined as the glass beads mass fraction and ranges from zero to one. The mixture composition was determined by developing an empirical correlation between the mixture density and the mixture composition by artificially creating eleven mixtures of red oak chips and glass beads in 10% increments by mass, ranging from 0% glass beads (100% red oak chips) to 100% glass beads (0%

red oak chips) and measuring the effective mixture density. The empirical correlation is illustrated in Figure 4.5 by the solid line and is shown in Eqn. 4.1, where ρ_{mix} is the mixture density and x is the mixture composition.

$$\rho_{mix} = 623.4\, x^2 + 526.8\, x + 1358 \tag{4.1}$$

The empirical correlation was used to determine each collected samples' mixture composition by measuring the effective mixture density. The uncertainty in the mixture density was measured using Taylor's series expansion propagation of error procedure (Ku, 1966). The error in the mixture mass and volume was combined using a root sum of squares (RSS). The uncertainty in the mixture density was less than 1%, and is illustrated by the vertical error bars overlaid on the data points; the error bars fall within the circular symbols. The correlation's least squares regression equation had a coefficient of determination, R^2, greater than 0.999. The correlation exhibits an interesting phenomenon; the mixture density is nonlinear with respect to the mixture composition. More specifically, the correlation corresponds to a harmonic mean, in contrast to an arithmetic mean. The theoretical harmonic mean equation consisting of a binary mixture of red oak chips and glass beads is:

$$\rho_{mix} = \left(\frac{x}{\rho_{GB}} + \frac{1 - x}{\rho_{RO}} \right)^{-1} \tag{4.2}$$

where ρ_{mix} is the mixture density, x is mixture composition, and ρ_{GB} and ρ_{RO} are the individual densities of glass beads and red oak chips, respectively. The theoretical harmonic mean equation is illustrated in Figure 4.5 by the dashed line. Less than 2% relative error exists between the experimental data and the harmonic mean equation over the entire composition range.

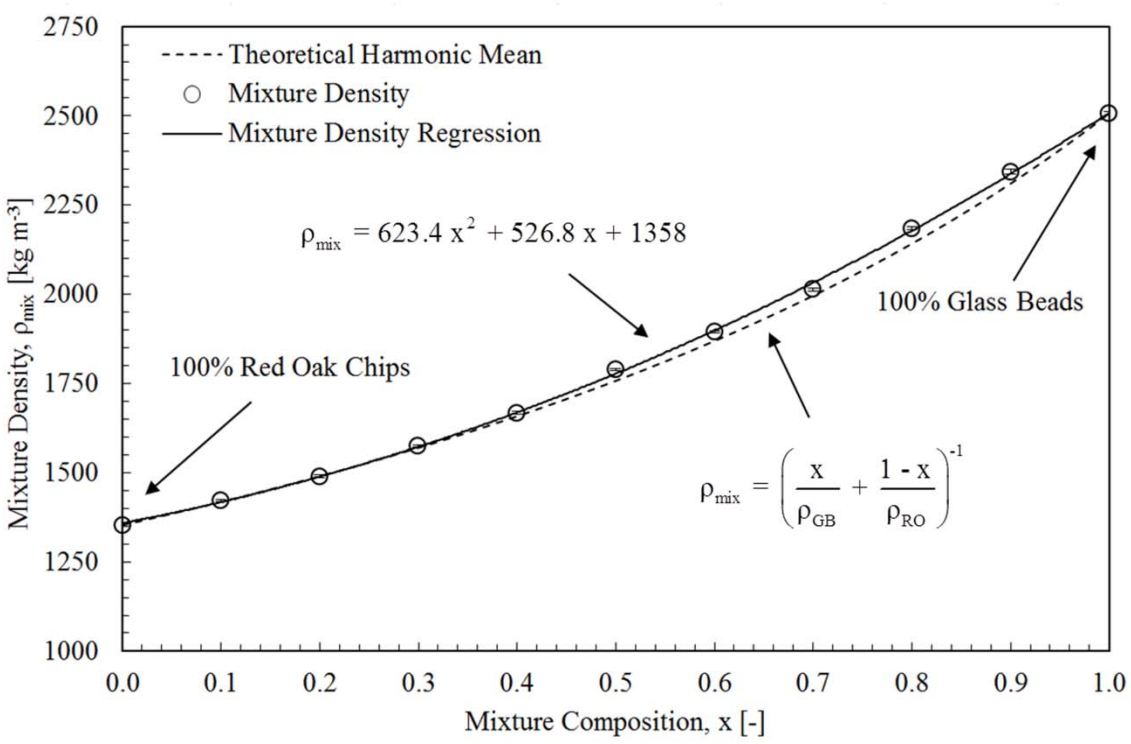

Figure 4.5: Empirical correlation between the mixture composition and the mixture density.

After collecting the actual samples from the outlet ports during the experimental testing, the mixture mass was measured using a Cole-Parmer Symmetry PA-Analytical Balance, and the true volume of the mixtures was analyzed using a Quantachrome Instruments Pentapyn 5200e Gas Pycnometer. After determining the effective mixture density, the mixture composition was determined using the prescribed empirical correlation.

4.3.4 Statistical Analysis

The screw rotation orientation can have a significant influence on the volumetric distribution of the granular materials inside the screw mixer. The co-rotating screw orientation used in this study produces a nonuniform mass flow rate through the four outlet ports. Figure 4.6 shows the average mass flow rate ratio through each of the four

outlet ports from all 27 tests that were performed. The error bars shown in Figure 4.6 represent plus and minus one standard deviation of the mass flow rate ratio. Port one has the largest mass flow rate ratio, 0.35, while port four only has a flow rate ratio of 0.09. This volumetric distribution is a result of the co-rotating, clockwise screw rotation orientation. A co-rotating, counterclockwise screw rotation orientation would simply flip the volumetric distribution of the granular materials about the vertical axial plane (i.e., plane between ports two and three) of the screw mixer.

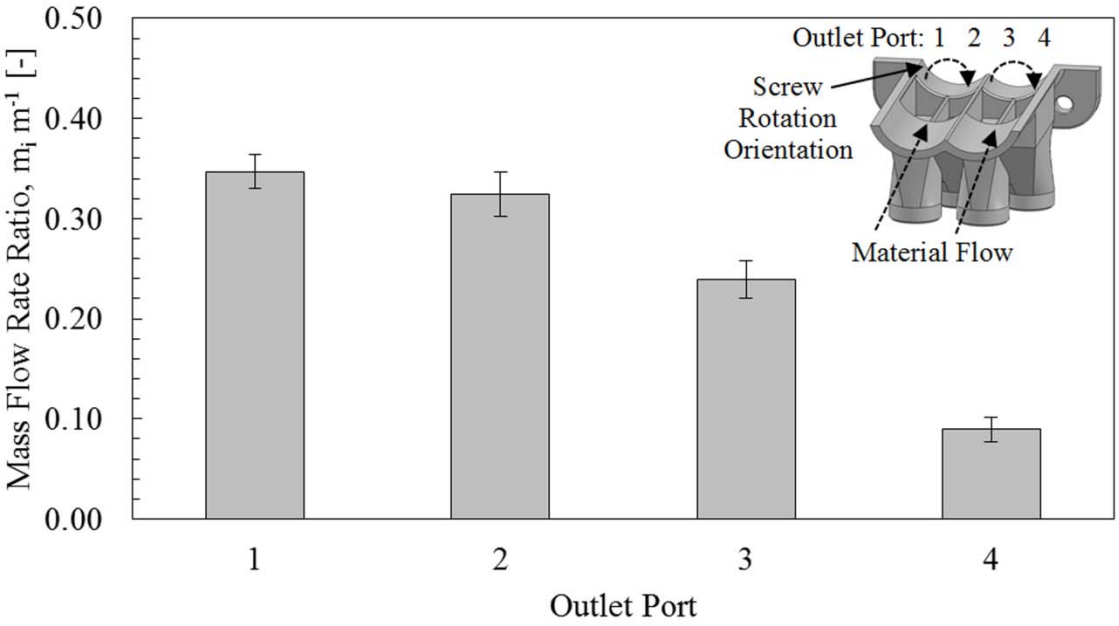

Figure 4.6: Average mass flow rate ratio through each of the four outlet ports.

The response variable used for the statistical analysis is the weighted composition variance between the four samples collected from each outlet port:

$$s^2 = \frac{\sum_{i=1}^{i=n} m_i \left(x_i - \overline{x_w}\right)^2}{\left(\frac{N-1}{N}\right)\sum_{i=1}^{i=n} m_i} \tag{4.3}$$

where s^2 is the weighted composition variance, n is the number of the i^{th} sample, m_i is the mass of the i^{th} sample, x_i is the composition of the i^{th} sample, $\overline{x_w}$ is the weighted mean composition of the samples, and N is the total number of samples (four in this study which correspond to the four outlet ports). If simply the composition variance was used instead of the weighted composition variance, the composition of port one would be equally weighted to the composition in port four and would introduce a significant error because the mass flow rate ratio through the outlet ports is vastly different as shown in Figure 4.6. However, the weighted composition variance can only be used when collecting and analyzing the entire granular material exit stream, as was done in this study. For simplicity, the weighted composition variance will be referred to as the composition variance. The composition variance is a dimensionless quantity because composition is dimensionless. Ideally, the composition of the four outlet ports would be identical, resulting in a composition variance of zero and a homogeneous mixture (best degree of mixing). However, as segregation occurs and the degree of mixing worsens, the composition variance increases.

A full-factorial design of experiments with repeatability was used in this study. Nine different operating conditions (i.e., treatments) resulting from all the possible combinations of the three screw rotation speeds and three dimensionless screw pitches were tested, and three observations were collected from each operating condition, totaling 27 tests. A two-way analysis of variance (ANOVA) statistical model (DeVore, 2008) was applied using JMP Pro 10 to compare the composition variance to the operating conditions. The model equation is:

$$y_{ijk} = \mu + \alpha_i + \beta_j + \gamma_{ij} + \varepsilon_{ijk} \tag{4.4}$$

where: y_{ijk} is the measured response variable (i.e., composition variance) made for factor one at level i, factor two at level j, and observation k; μ is the mean response averaged over all levels of both factors; α_i is the effect of factor one at level i; β_j is the effect of factor two at level j; γ_{ij} is the interaction of the factor one at level i and factor two at level j; and ε_{ijk} is the random deviation from the true treatment mean (DeVore, 2008).

To determine if the two main effect terms and the interaction term have a significant influence on the composition variance, a statistical procedure involving three sets of hypotheses were tested:

$$\begin{array}{llllll} H_{o,1}: & \alpha_1 = \ldots = \alpha_I = 0 & \text{versus} & H_{a,1}: & \text{at least one } \alpha_i \neq 0 & \\ H_{o,2}: & \beta_1 = \ldots = \beta_J = 0 & \text{versus} & H_{a,2}: & \text{at least one } \beta_j \neq 0 & (4.5) \\ H_{o,12}: & \gamma_{ij} = 0 \text{ for all i, j} & \text{versus} & H_{a,12}: & \text{at least one } \gamma_{ij} \neq 0 & \end{array}$$

where I is the number of levels of factor one and J is the number of levels of factor two; in this study I and J = 3. Hence, the null hypotheses suggest that the main effect and interactions terms do not have a significant influence on the composition variance, while the alternative hypotheses suggests that at least one of the terms do have an effect on the composition variance. The F-test statistic and its corresponding p-value was used to determine if the null hypotheses fails to be rejected or was rejected in favor of the alternative hypotheses at an alpha level of 0.05.

4.4 Results and Discussion

4.4.1 Optical Visualization

Static images taken from the dynamic mixing process were captured using the prescribed optical visualization techniques are shown in Figure 4.7. Nine images are

presented and correspond to all possible combinations of screw rotation speed and dimensionless screw pitch considered in this study. The images are rotated counterclockwise 90° to increase the size of the images. The red oak chips appear brown and were injected into port one. Meanwhile, the glass beads appear gray and were injected into port two through the dark polyethylene tube shown in the top projection. The granular materials are mechanically mixed and conveyed from left to right and exit through the four outlet ports shown on the right edge of the bottom projection.

The influence that the screw rotation speed has on the mixing process is difficult to demonstrate when looking only at static images because the mixing mechanics are vastly similar. However, it's worth noting that increasing the screw rotation speed increased the velocity of the granular materials, both in the axial and rotational direction, and reduced the material residence time. The effect the dimensionless screw pitch had on the mixing mechanics was very noticeable. As the dimensionless screw pitch increased, several important observations were noted: (i) the rotational velocity of the granular materials increased relative to the axially velocity; (ii) less adhesion between the screw flights and granular materials was noted due to the decreased screw flighting surface area; (iii) a larger clearance gap between the intermeshing screws existed; (iv) the material residence time decreased; (v) variations in volumetric material fill level between the individual screw flights became more apparent; (vi) the volumetric material fill level in the two screws regions became more uniform; and (vii) the mixing effectiveness appeared to increase.

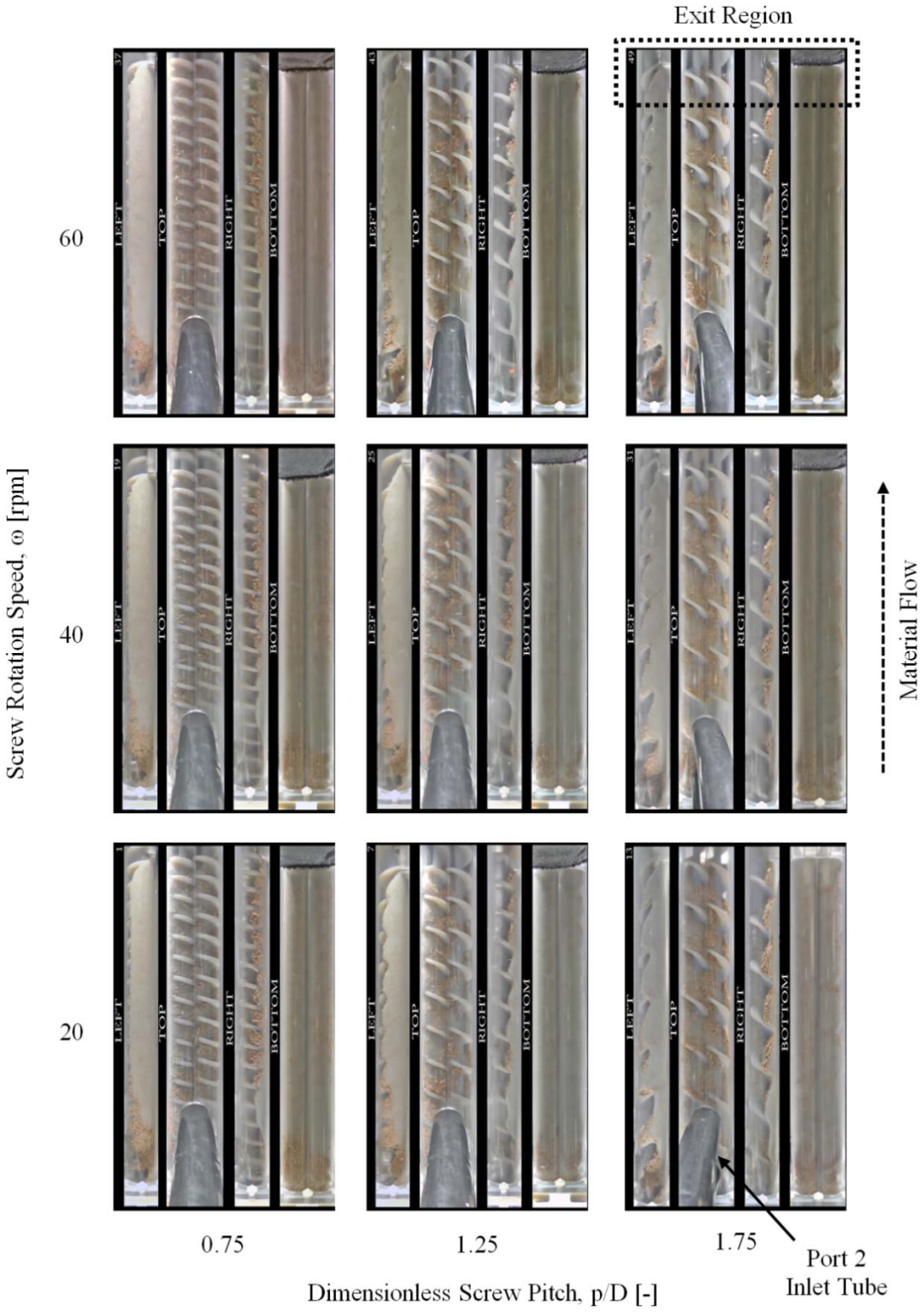

Figure 4.7: Static images taken from mixing videos of the dynamic mixing process captured using optical visualization techniques.

4.4.2 Composition Analysis

In addition to the qualitative observations made using the optical visualization methods, the effect of screw rotation speed and dimensionless screw pitch on the composition variance was quantified using the prescribed two-way ANOVA statistical model (DeVore, 2008). The key parameters of the analysis are summarized in the ANOVA table shown in Table 4.2 where the degrees of freedom is symbolized by df, the sum of squares by SS, the mean square by MS, the F-test statistic by F. For the main effect and interaction terms to be declared statistically significant, their corresponding p-values must be less than the alpha level of 0.05. Thus, the screw rotation speed and dimensionless screw pitch are statistically significant because they have p-values of 0.003 and less than 0.001, respectively. In addition to the two main effect terms, the two-way interaction term is also significant because it has a p-value of 0.002.

Table 4.2: ANOVA table highlighting key parameters of the statistical analysis.

ANOVA Table					
Source	**df**	**SS**	**MS**	**F**	**p-value**
Screw Rotation Speed	2	$7.841E^{-7}$	$3.921E^{-7}$	8.247	0.003
Dimensionless Screw Pitch	2	$5.974E^{-6}$	$2.987E^{-6}$	62.824	< 0.001
Screw Rotation Speed × Dimensionless Screw Pitch	4	$1.261E^{-6}$	$3.154E^{-7}$	6.633	0.002
Error	18	$8.558E^{-7}$	$4.754E^{-8}$		
Total	26	$8.875E^{-6}$			

To fully understand the relationship between the different levels of each factor and their interactions, the highest order significant interaction must be investigated. Figure 4.8 illustrates the results of the composition analysis and the effect that the interaction between the screw rotation speed and the dimensionless screw pitch had on the composition variance. Three data points corresponding to the three observations that were performed at each operating condition are shown for each of the nine combinations

of screw rotation speed and dimensionless screw pitch. Furthermore, the average of the three data points at each operating condition was computed and is illustrated using the averaging line for each level of dimensionless screw pitch. An uncertainty analysis was performed using Taylor's series expansion propagation of error procedure (Ku, 1966). The uncertainty in the measurements was combined with the uncertainty in the empirical correlation using the root sum squares (RSS) procedure. Overall, the uncertainty in the composition variance, U_{s^2}, ranged from 1.1 to 3.2% and is illustrated graphically in Figure 4.8 by vertical error bars overlaid on the data points.

Recall that the composition variance and the mixing effectiveness are inversely proportional (i.e., a small composition variance corresponds to a high mixing effectiveness). Furthermore, a homogeneous mixture, representing an ideal state of mixing, would have a composition variance of zero.

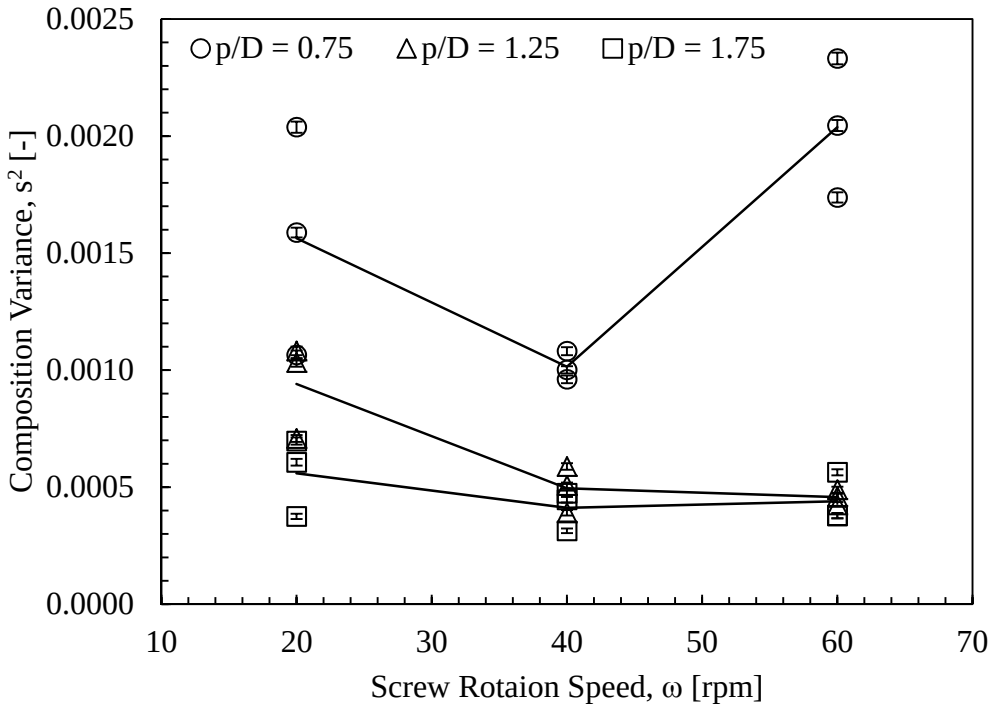

Figure 4.8: Composition variance as a function of screw rotation speed and dimensionless screw pitch.

First consider the effect that the screw rotation speed had on the composition variance at a dimensionless screw pitch of p/D = 0.75. The composition variance was minimized at the intermediate screw rotation speed of ω = 40 rpm. As the screw rotation speed increased or decreased from 40 rpm, the composition variance increased and the mixing effectiveness worsened. Meanwhile, for a dimensionless screw pitch of p/D = 1.25 and 1.75, the composition variance reduced as the screw rotation speed increased from 20 to 40 rpm. However, as the screw rotation speed further increased from 40 to 60 rpm, minimal effects on the composition variance were found, as illustrated by the relatively constant slope of the averaged line.

Secondly, it is important to consider the relationship between the within-treatment variance (i.e., variance within the three data points at each combination of screw rotation

speed and dimensionless screw pitch) and the between-treatment variance (i.e., variance between the nine different combinations of screw rotation speed and dimensionless screw pitch). For example, consider the three data points at each level of dimensionless screw pitch for the screw rotation speed of $\omega = 60$ rpm. The variance within the three data points (within-treatment) is very small for the dimensionless screw pitches of $p/D = 1.25$ and 1.75, and reasonably small for the dimensionless screw pitch of $p/D = 0.75$, which illustrates a high degree of experimental repeatability. The slightly larger within-treatment variance associated with the dimensionless screw pitch of $p/D = 0.75$ is attributed to small periodic fluctuations in the mass flow rates of the biomass and heat carrier media being injected into the screw mixer by the two volumetric screw feeders, which creates a pulsing phenomenon that is magnified for these conditions. In contrast, any small fluctuations in the feed rates are dampened for the other operating conditions, producing extremely consistent results. Comparing the within-treatment variance to the between-treatment variance for the dimensionless screw pitches of $p/D = 1.25$ and 1.75, these two variances are fairly similar, and it cannot be concluded that the dimensionless screw pitches of $p/D = 1.25$ and 1.75 are different from one another. However, when comparing the within-treatment variance to the between-treatment variance of the dimensionless screw pitch of $p/D = 0.75$ to that of either $p/D = 1.25$ or 1.75, the variances are vastly different because the between-treatment variance is much larger than the within-treatment variance.

Overall, the composition variance was minimized at a screw rotation speed of $\omega = 40$ rpm and a dimensionless screw pitch of $p/D = 1.75$. The intermediate screw rotation rate is a result of the trade-off between the velocity of the granular material and

the material residence time. As the screw rotation rate increases the materials mix faster and more violently, but also have a reduced material mixing time. Increasing the dimensionless screw pitch increases the rotational velocity of the granular materials relative to the axial velocity and results in a reduced composition variance because the material is being rotated more frequently, rather than simply being conveyed in the axial direction. It is worth noting that the composition variance was lower for a dimensionless screw pitch of p/D = 1.75 than that of p/D = 0.75 or 1.25, independent of screw rotation speed. This finding is important because it allows the system to be operated at a large range of flow rates by simply changing the screw rotation speed, allowing external factors such as product demand to be met.

The magnitude of the composition variance, which is analogous to the degree of segregation, can be significantly influenced by changing the granular materials being used. If the material density ratio (i.e., heat carrier media to biomass density ratio) was further increased, it is likely that the magnitude of the composition variance would increase due to enhanced segregation. In contrast, if the density ratio were to approach unity for similarly sized particles, a reduction in the composition variance would most likely occur, and segregation of the materials would only arise from the chosen operating conditions and the differences in particle size and/or shape. Similar effects are expected if the particle sizes or shapes were to change. Increasing the difference in particle size or shape between the biomass and heat carrier media would likely cause an increased composition variance and worsen the mixing effectiveness.

The results of this study are consist to that of Uchida and Okamoto (2008), who also concluded that the mixing effectiveness was enhanced by increasing the

dimensionless screw pitch. Additionally, the observed increase in rotational velocity relative to the axial velocity due to the increased dimensionless screw pitch in this study, is analogous to the increase in the frequency of the path line sine curve observed by Uchida and Okamoto (2008). The effect of screw rotation speed on the mixing effectiveness found in this study is also consistent with that of Vanarase and Muzzio (2011), who found that intermediate rotation rates optimized the overall mixing effectiveness. These similar findings confirm that mixing visualization and quantification techniques developed in this study are valid as it is consistent with previous literature results.

4.5 Conclusions

Characterizing the mixing effectiveness of systems or processes in granular applications is difficult due to challenging sampling procedures and quantifiable measurement techniques. In this study, a two-part measurement technique consisting of optical visualization and composition analysis was developed to provide qualitative and quantitative mixing characteristics of granular mixing in a screw mixer, respectively. Both methods are needed to get a complete picture of the mixing process in the double screw mixer. The optical visualization provides qualitative mixing assessment of the entire mixing region and helps explain the composition analysis results. Meanwhile, the composition analysis is needed to quantify the mixing process and provide quantitative justification to the qualitative observations acquired from the optical visualization. These techniques overcome many traditional quantification issues found in other measurement techniques. The optical visualization produced several noteworthy qualitative

observations, which indicated that increasing the dimensionless screw pitch led to an increase in the mixing effectiveness. However, the effect of screw rotation speed was more difficult to visualize using solely the optical visualization methods, particularly when only looking at the still images captured from the dynamic mixing process that are presented in this paper. Composition analysis provided a quantitative mixing assessment by measuring the composition variance from the four outlet ports, and confirmed that increasing the dimensionless screw pitch resulted in an increase in the mixing effectiveness, independent of the screw rotation speed. Meanwhile, the screw rotation speed's effect on the mixing effectiveness was largely dependent on the dimensionless screw pitch, as illustrated in Figure 4.8, resulting in a statistically significant two-way interaction term in the ANOVA model. Overall, the composition variance was minimized (i.e., high mixing effectiveness) at a screw rotation speed of $\omega = 40$ rpm and a dimensionless screw pitch of $p/D = 1.75$. The results of this study were consistent with previous granular mixing measurement techniques featuring similar experimental set-ups found in the literature.

While the methods developed in this study have been shown to be effective in determining the screw mixer mixing effectiveness and are consistent with previous studies, they still have some limitations. For example, the ability to distinguish between the different granular materials using the optical visualization methods is largely dependent on the visual contrast (i.e., color) between the two materials. Increasing the contrast between the different granular material types will most certainly increase the ability to recognize the qualitative mixing dynamics. Another limitation of this method is that the number of collected data points heavily influences the statistical power of the

composition analysis procedure. A more rigorous analysis procedure using more data points could possibly result in an enhanced ability to distinguish differences between the levels of factors under consideration. However, a trade-off between the time required to perform the experimental testing and the statistical power of the analysis needs to be addressed, particularly when considering a larger number of factors. A thorough investigation of design of experiments methodologies will be useful in addressing this issue.

The two-part measurement technique developed in this study provides a through method to evaluate the mixing effectiveness of many mixing processes, which can be applied to both continuous and batch processes. The relatively low cost equipment used to perform the optical visualization could be used to characterize the mixing of a variety of applications, including fluidized beds, rotating cylinders, etc. Furthermore, the quantitative composition analysis technique can be coupled to the optical visualization methods and used to evaluate any continuous mixing process such as horizontal impeller mixers. Future studies will utilize this measurement technique to investigate an increased number of critical factors that could affect the screw mixer's mixing effectiveness.

Acknowledgements

Support for portions of this work by Phillips 66 Company is gratefully acknowledged.

CHAPTER 5: GRANULAR MIXING VISUALIZATION AND QUANTIFICATION IN A DOUBLE SCREW MIXER: PART I – QUALITATIVE OPTICAL VISUALIZATION[1]

Todd A. Kingston[2] and Theodore J. Heindel

Department of Mechanical Engineering, Iowa State University, Ames, Iowa, 50011, USA

kingston.todd@gmail.com and theindel@iastate.edu

Abstract

The selection of mixing equipment and its operating conditions can have a significant influence on the homogeneity of granular material. However, determining the mixing effectiveness of the mixing equipment and identifying problematic operating conditions can be difficult. Optical visualization provides a relatively inexpensive, and quite effective, technique for characterizing granular mixing compared to other imaging techniques such as particle image velocimetry (PIV) and magnetic resonance imaging (MRI). In this study, qualitative optical visualization from four spatially aligned and

[1] Kingston, T.A., Heindel, T.J. (2013). Granular mixing visualization and quantification in a double screw mixer: Part I – Qualitative optical visualization. *Powder Technology* (in review).

[2] Corresponding author: Todd A. Kingston (kingston.todd@gmail.com)

temporally synced projections is used to characterize the dynamic mixing of red oak chips and glass beads in a double screw mixer. The effects of four factors were investigated and, for the parameters considered in this study, it was determined that increasing the screw rotation speed and dimensionless screw pitch resulted in favorable mixing characteristics. Moreover, a counter-rotating down-pumping screw rotation orientation and a material injection configuration with the red oak chips and glass beads injected into port one and two, respectively, improved the screw mixer effectiveness. These conditions provided the best mixing for the parameters considered in this study.

Keywords: Granular mixing, optical visualization, particulate, screw mixer, segregation.

5.1 Introduction

The mixing of granular material is a critical process to a wide range of applications in many industries including tablet coating and biomass thermochemical conversion in the pharmaceutical and energy industries, respectively. While the mixing of granular material appears fairly straightforward at first glance, fully understanding and characterizing particle-particle mixing and segregation is an ambitious task that has been a common goal for many researchers. A number of reviews regarding the mixing of granular material are available in the literature (Bridgwater, 2012; Campbell, 2006; Pernenkil and Cooney, 2006). More specifically, some of the challenges associated with the mixing and segregation of granular material was addressed by Ottino and Khakhar (2001). Segregation is primarily driven by differences in particle size, shape, and/or density, but can be reduced or magnified by changing the operating conditions of the

mixing equipment. Extensive research has been conducted on the influence of operating conditions and/or material properties for a wide range of mixing processes using simulations (Cleary and Sinnott, 2008; Sarkar and Wassgren, 2009, 2010) and experiments (Hilton and Cleary, 2011; Jain et al., 2005; Metzger et al., 2011; Remy et al., 2010). For example, Portillo et al. (2009) demonstrated the effects that rotation rate, mixing angle, and cohesion had on the blend uniformity of powders. Moreover, Keller (2012) used visual observations to study the mixing characteristics in fluidized beds, and demonstrated that the system's mixing effectiveness was heavily influenced by its chosen operating conditions (e.g., superficial gas velocity) and granular material properties (e.g. particle size and density).

Granular mixing and segregation has been widely studied in a number of systems including rotating cylinders (Aissa et al., 2010a, b; Huang and Kuo, 2012), fluidized beds (Escudero and Heindel, 2011; Gao et al., 2009; Keller et al., 2013), and single screw mixers (Tsai and Lin, 1994; Uchida and Okamoto, 2006, 2008). However, minimal research has focused on characterizing the granular mixing dynamics in a double screw mixer despite its advantages over single screw mixers, such as improved mixing and reduced power consumption (Camp, 1990). Moreover, several industrial processes rely on equipment which features similar geometry to that of double screw mixers, such as double screw extruders and double screw pyrolyzers in the thermoplastic and energy conversion industries, respectively. Thus, an improved understanding of the granular mixing process in double screw mixers is needed to increase process efficiency and improve the quality of the resulting products.

The ability to characterize the mixing of granular material has advanced quite rapidly over recent years due to advances in measurement techniques such as digital image analysis (Aissa et al., 2010a, b; Busciglio et al., 2009; Chen and Yu, 2004; Daumann et al., 2009; Daumann and Nirschl, 2008), particle image velocimetry (PIV) (de Jong et al., 2012; Dhenge et al., 2013), magnetic resonance imaging (MRI) (Hardy et al., 2007), positron emission particle tracking (PEPT) (Leadbeater et al., 2012; Portillo et al., 2010), X-ray visualization (Uchida and Okamoto, 2006, 2008), and near-infrared spectroscopy (Koller et al., 2011). While each of these techniques has their advantages, the expense associated with many of them can be extremely large. Furthermore, many of these techniques can only be applied to mixing processes which feature relatively simple mixer geometries (e.g., rotating cylinders) due to various constraints. For example, complex mixing geometries can cause image artifacts in the case of X-ray imaging and lead to undesirable results.

Qualitative mixing characterization provides a critical indication of the mixing effectiveness for a number of different mixing processes. In many instances, particularly when developing new mixing equipment, it is typical to perform an initial mixing assessment using qualitative optical visualization. For example, during the development of an auger pyrolyzer for the thermochemical conversion of biomass into bio-oil, Brown and Brown (2012a) performed preliminary cold-flow mixing trails to assess the mixing of granular material, identify problematic operating conditions, and select the operating conditions of the device with the goal of maximizing the degree of mixing. Additionally, Hajra et al. (2010) visualized the mixing of glass beads and cellulose acetate particles having differences in both size and density in a rotating cylinder. By using a transparent

cylinder, they were able to investigate the degree of radial segregation and identify the preferred mixing conditions.

The goal of part one of this two-part study is to qualitatively characterize the dynamic granular mixing of low density red oak chips and high density glass beads in a double screw mixer. A brief overview of the optical visualization experimental setup will first be presented, followed by a detailed description of the granular materials used. Next, the spatial alignment and temporal syncing techniques enabling optical visualization to be performed will be presented. The effect of four factors will be investigated: (i) screw rotation speed, (ii) dimensionless screw pitch, (iii) screw rotation orientation, and (iv) material injection configuration. Snapshots of the dynamic mixing process will be shown, and qualitative mixing characteristics will be discussed. Finally, the conclusions of the study will be summarized and suggestions for future work will be made. Part two of this two-part study (Kingston and Heindel, 2013c) will provide quantitative justification of the mixing characteristics using composition and statistical analysis, and coupled with part one's qualitative optical visualization, will provide a thorough assessment of the mixing dynamics inside the screw mixer.

5.2 Experimental Setup

A laboratory-scale double screw mixer was used to mechanically mix the granular materials. The screw mixer features two parallel and horizontally mounted intermeshing noncontact screws. The screw diameter, D = 2.54 cm, was chosen as the characteristic length of the system. The ability to optically visualize the granular mixing process relies heavily on the material chosen to fabricate the screw mixer. A three-dimensional (3D)

printer was used to fabricate all of the screw mixer's components, as shown in Figure 5.1. The housing was manufactured using a transparent plastic material allowing optical access to the mixing region's periphery (i.e., 360°). All remaining components were fabricated using an opaque plastic material. Two independent Tecweigh CR5 volumetric auger feeders were used to meter in the granular materials at the chosen flow rates through two injection ports in the top of the housing that are axially positioned two characteristic lengths apart from one another and are laterally positioned on the mid-plane between the two screws. The granular material exits the screw mixer under the force of gravity through outlet ports in the bottom of the housing. The effective mixing length is measured from the centerline of the downstream injection port (port two) to the beginning of the outlet ports thus providing a dimensionless mixing length of L/D = 10.

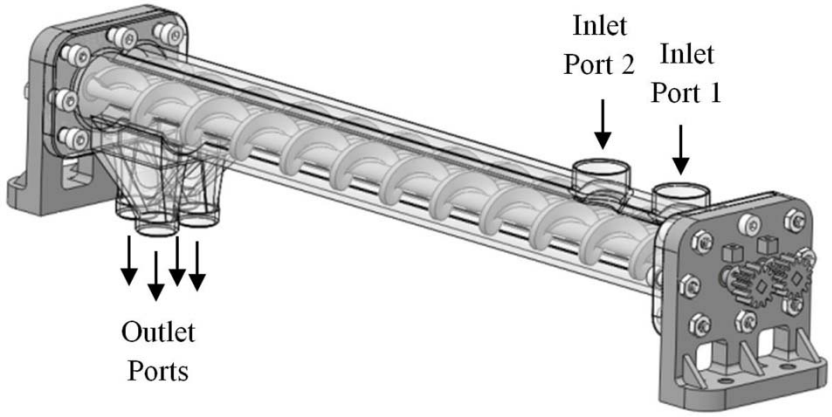

Figure 5.1: Double screw mixer featuring a transparent housing used to perform optical visualization mixing studies.

Qualitative optical visualization of the dynamic granular mixing process inside the screw mixer was captured from four independent projections simultaneously (i.e., left, top, right, and bottom) using the techniques outlined by Kingston and Heindel (2013d). Figure 5.2 illustrates the experimental setup used to perform the optical

visualization, and demonstrates the positioning of four Panasonic HC-V700M HD cameras, two volumetric auger feeders used to independently meter in the granular materials, the polyethylene inlet and outlet tubes, and the screw mixer. The cameras capture images at 60 frames per second (FPS) with 1920 × 1080 resolution. Six 85 W compact fluorescent lamps (not shown) are used to provide adequate lighting to the mixing region. All components, except for the mixing region of the screw mixer, are covered in black fabric to minimize reflection, and the entire test facility is enclosed in black fabric curtains to enhance image quality.

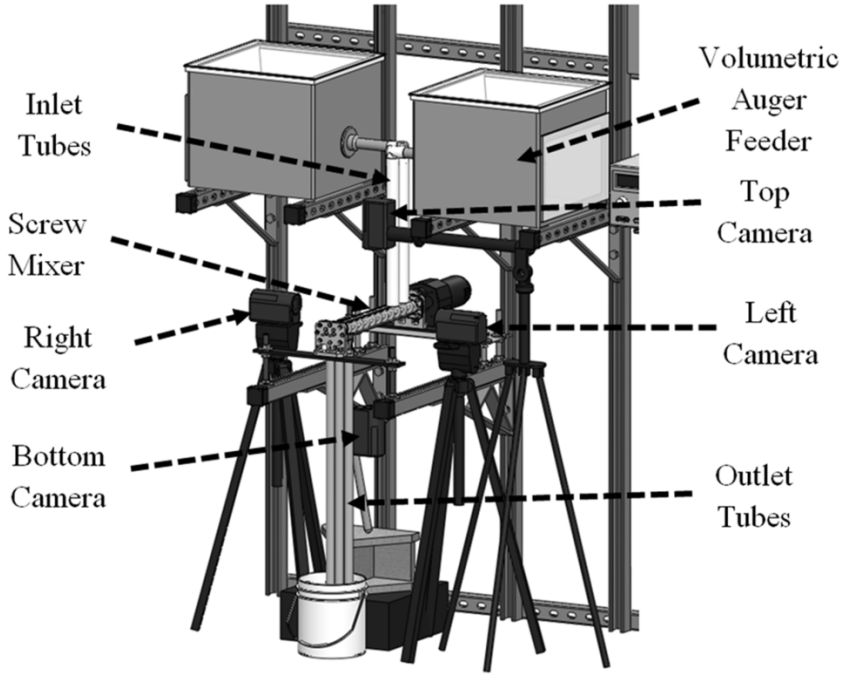

Figure 5.2: Optical visualization experimental setup.

5.2.1 Materials

Granular materials segregate. The cause of segregation can be attributed to a large number of factors including mixer geometry and chosen operating conditions, but it fundamentally arises due to differences in particle size, shape, and/or density. In this

study, experiments were performed using a binary mixture of red oak chips and glass beads because of their relevance to industrial mixing processes involving biomass and heat carrier media. The red oak chips are considerably less dense than the glass beads; having true densities, measured with a pycnometer, of 1350 and 2510 kg m^{-3}, respectively. Glass beads were chosen to model traditional heat carrier media such as refractory sand because the glass beads are better characterized and less abrasive. The size and shape of the two granular material types used in this study are also vastly different, as shown in Figure 5.3. The red oak chips resemble a needle-like shape and were sieved multiple times to achieve a particle size range of 500-6350 μm, whereas the glass beads are quite spherical and have a particle size range of 300-500 μm.

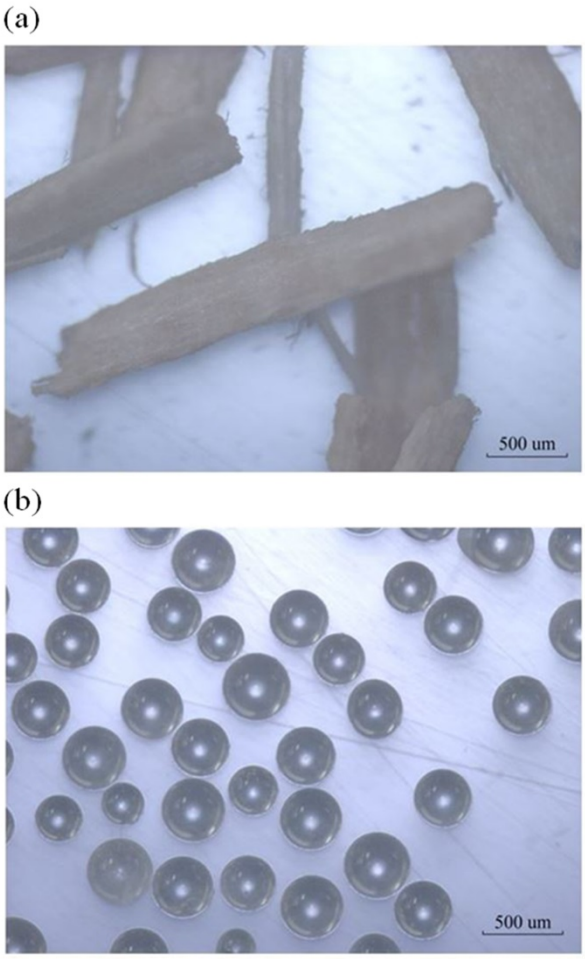

Figure 5.3: Magnified images of (a) 500-6350 μm red oak chips and (b) 300-500 μm glass beads.

More desirable granular materials, in terms of their material properties, could have been chosen such that the rate of segregation would have been reduced. However, the purpose of this study was to relate the mixing effectiveness of the screw mixer to its operating conditions while holding the granular material types constant. Many research efforts have investigated the effect of the initial particle concentration ratios (Aissa et al., 2010a, b; Gosselin et al., 2008), or mass flow rate ratios (Brown and Brown, 2012a). However, many times the selection of these ratios is dependent on either thermodynamic or chemical reaction considerations. Thus, it would be exhaustive to attempt to

characterize the mixing effectiveness of the screw mixer for various combinations of granular materials and/or mass flow rate ratios in addition to the factors already being investigated in this study. Therefore, the granular materials were fixed and the glass beads to red oak chips mass flow rate ratio was constant at 10:1 (glass beads:red oak chips). This ratio is typical of industrial processes involving the thermochemical conversion of biomass into bio-oil. In addition to initial particle concentration ratio, the effect of the volumetric fill ratio has been thoroughly investigated in the literature, particularly for batch operations (Ingram et al., 2005; Nielsen et al., 2011; Remy et al., 2010; Sarkar and Wassgren, 2009). However, in continuous mixing processes, particularly in screw conveying applications, design recommendations have been made through years of industrial experience, and a 65% volumetric fill ratio is recommended to avoid problematic operating conditions (Colijn, 1985). Thus, the magnitude of the red oak chips and glass beads mass flow rates was required for each combination of screw rotation speed and dimensionless screw pitch in order to maintain a 65% volumetric fill ratio; these mass flow rates are summarized in Table 5.1.

Table 5.1: Red oak chips and glass beads mass flow rates required to maintain a 65% volumetric fill ratio for all operating conditions.

Screw Rotation Speed ω [rpm]	Dimensionless Screw Pitch p/D [-]	Red Oak Chips Mass Flow Rate $\dot{m}_{RO}$ [kg hr^{-1}]	Glass Beads Mass Flow Rate $\dot{m}_{GB}$ [kg hr^{-1}]
20	0.75	1.13	11.3
	1.25	1.75	17.5
	1.75	2.00	20.0
40	0.75	2.00	20.0
	1.25	3.50	35.0
	1.75	4.00	40.0
60	0.75	3.25	32.5
	1.25	5.00	50.0
	1.75	5.75	57.5

5.3 Experimental Methods

In this study, the effect of four factors on the mixing effectiveness of the screw mixer was investigated. The levels of each of the factors were selected based on traditional operating conditions found in the literature (Brown and Brown, 2012a; Dai and Grace, 2011; Ingram et al., 2008; Mohan et al., 2006; Uchida and Okamoto, 2008) and common practice in industry. The four factors and their respective levels that were tested are: (i) screw rotation speeds of ω = 20, 40, and 60 rpm; (ii) dimensionless screw pitches of p/D = 0.75, 1.25, and 1.75, where p is the screw pitch and D is the screw diameter; (iii) screw rotation orientations of co-rotating (CoR), counter-rotating up-pumping (CtrR UP), and counter-rotating down-pumping (CrtR DP), where up-pumping and down-pumping refer to the direction of material flow between the two screws, as shown in Figure 5.4; and (iv) material injection configurations of the red oak chips and

glass beads injected into port one and two (RO 1, GB 2) and into port two and one (RO 2, GB 1), respectively, as shown in Figure 5.1.

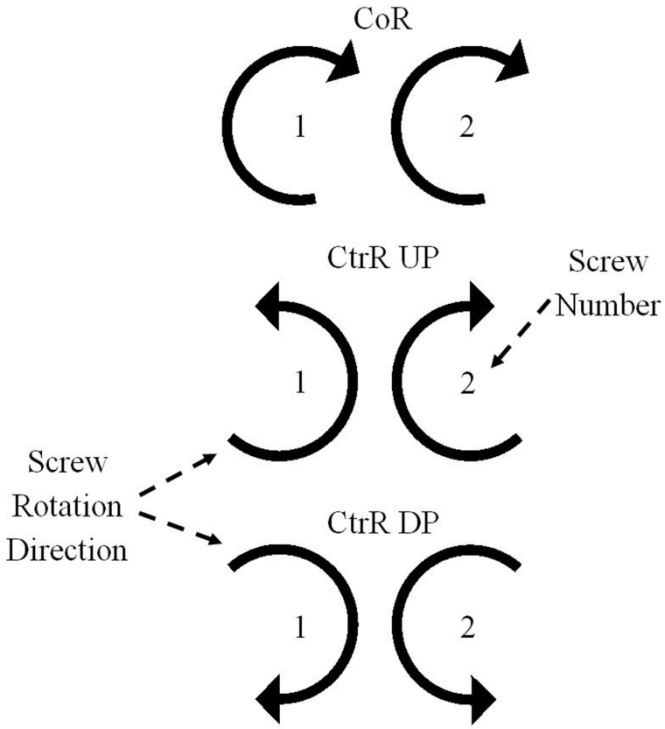

Figure 5.4: Co-rotating (CoR), counter-rotating up-pumping (CtrR UP), and counter-rotating down-pumping (CtrR DP) screw rotation orientations, respectively.

Part one of this two-part study focuses on the qualitative optical visualization of the granular mixing process inside the screw mixer. Spatial alignment and temporal syncing of the mixing videos was accomplished using Adobe Premiere Pro CS6. Figure 5.5 illustrates the four projections from which optical visualization was captured, and the cropped projections with a typical pathline of a particle being injected into port two, respectively. A specific event (e.g., audio spike) in each of the four independent videos was temporally synced, coupling the four projections into one combined video. The top and right projections were captured in the orientation shown in Figure 5.5a, but the left

and bottom projections were spatially aligned by inverting them about their vertical and horizontal axis, respectively. This enables the granular material to flow from left to right in all four projections and for screw one and two to be aligned in the top and bottom projections. The four projections were combined into a simple and compact visualization interface by cropping everything outside the mixing region and labeling each projection, as shown in Figure 5.5b. This interface allows observations of the entire mixing region to be made and provides critical information needed to understand the granular mixing dynamics.

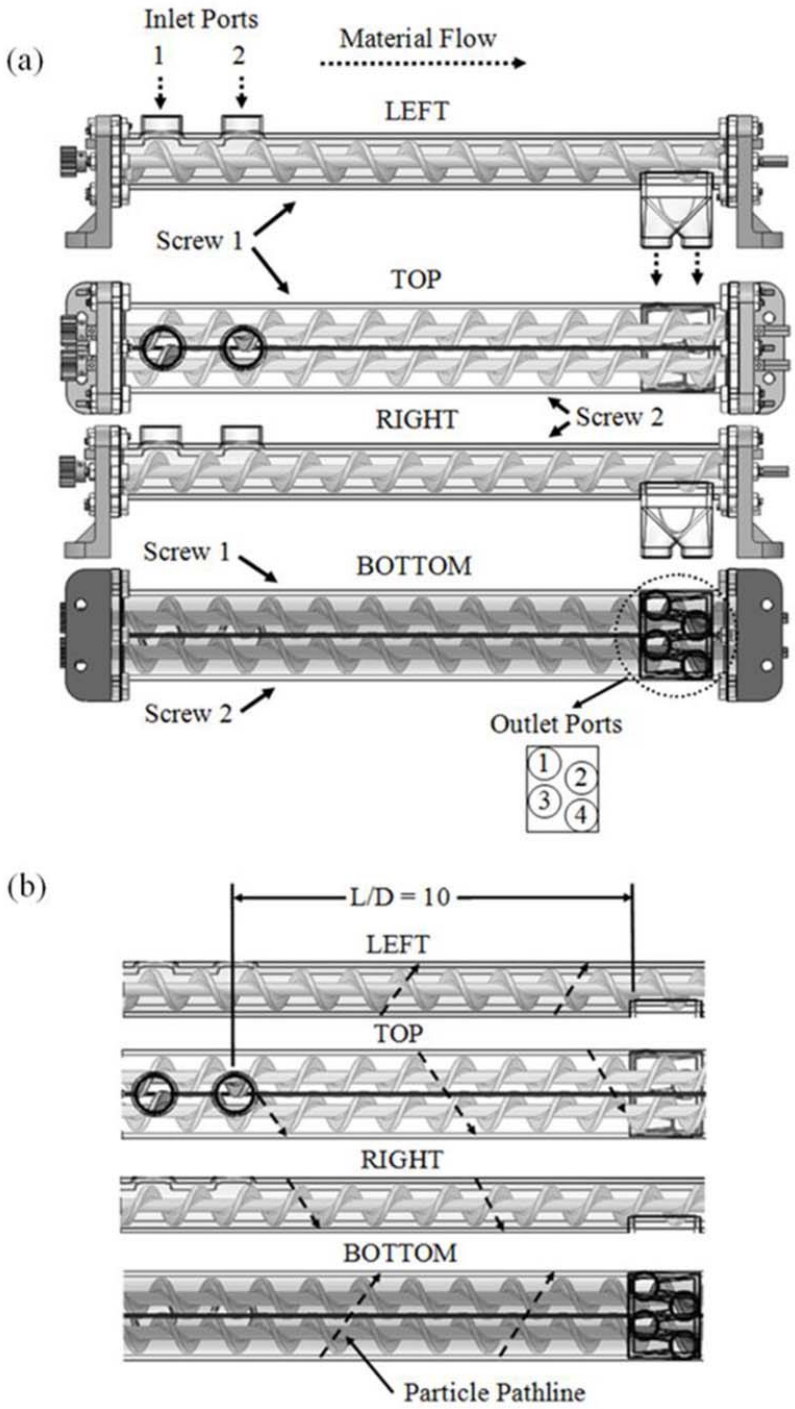

Figure 5.5: (a) Four projections of the screw mixer from which optical visualization was captured and (b) cropped projections with a typical particle pathline.

5.4 Results and Discussion

To visualize the effect that each of the factors has on the mixing effectiveness of the screw mixer, a reference condition was selected in order to make comparisons. For simplicity, the intermediate levels of the screw rotation speed, $\omega = 40$ rpm, and dimensionless screw pitch, $p/D = 1.25$, were selected as the reference levels for these two factors. Numerous studies have been conducted on mixing processes which feature a single convective mixing mechanism (i.e., screw, impeller, etc.) (Conway et al., 2005; Portillo et al., 2009; Remy et al., 2010; Sarkar and Wassgren, 2009; Uchida and Okamoto, 2006, 2008). However, few research efforts have focused on the mixing of granular materials inside a mixer which features more than one convective mixing mechanism. There are a few examples in the literature which feature a double (more specifically a twin) screw design (Dhenge et al., 2013; Martelli, 1983; White and Kim, 2010). For example, twin screw extruders, which traditionally feature a co-rotating screw rotation orientation, are used in the plastic processing industry. Furthermore, Iowa State University currently houses a screw pyrolyzer which features a co-rotating screw rotation orientation (Brown and Brown, 2012a). For these reasons, a co-rotating screw rotation orientation was chosen as the reference level. Finally, a material injection configuration in which the red oak chips and glass beads are injected into port one and two, respectively, was chosen as the reference level for this factor because of theoretical granular mixing considerations which will be discussed in following sections.

The reference condition was selected for the sole purpose of comparing static images taken from the dynamic mixing process, which were captured using the prescribed optical visualization techniques. A complete collection of all the mixing

videos can be found at http://www.youtube.com/channel/UCbSytey_jHsjZJ6ZSMFEpsw. Alternatively, the videos can be found by searching YouTube for “ISU Multiphase Flow Lab.” The following sections outline the effect that each of the factors have on the mixing effectiveness of the screw mixer. The reference condition is shown in each section for the convenience of comparison, while the other image(s) represent a change in the level of the factor under consideration. The interaction between the different levels of factors is not considered in this part of the study, but is addressed and statistically quantified in part two of this study (Kingston and Heindel, 2013c).

In each image, the granular materials enter the screw mixer through their respective inlet tubes shown on the left side of the image. The red oak chips appear brown and the glass beads appear gray. The granular materials are mechanically mixed and conveyed from left to right in the image and exit the screw mixer through the outlet ports in the bottom of the housing, shown on the right side of the image.

5.4.1 Screw Rotation Speed

The influence of screw rotation speed on the mixing effectiveness of the screw mixer is easily recognizable when visualizing the dynamic mixing videos that were produced using the prescribed optical visualization methods (i.e., see the videos on YouTube). However, illustrating these characteristics in static images is more difficult, but an attempt to describe the behavior of the granular materials is made.

Illustrated in Figure 5.6 are snapshots of the dynamic mixing process at steady state conditions for screw rotation speeds of ω = 20, 40, and 60 rpm. All four projections (i.e., left, top, right, and bottom) are shown from top to bottom in the images. All three screw rotation speeds show similar mixing dynamics. The left projections show that the

glass beads cover the outside surface of the screw mixer's left side, and the glass beads climb up the wall to make it appear almost 100% full. In contrast, the right projections show red oak chips are transported on top of the glass beads, and screw two appears to be less than half full. Both screws are clearly observed in the top projections, with regions of red oak chips intermingling with regions of glass beads. Finally, the bottom projections show that the bottom surfaces of the screw mixer are primarily covered with glass beads.

The dynamic mixing videos revealed that increasing the screw rotation speed increased the velocity of the granular materials inside the screw mixer. Moreover, the increased screw rotation speed seemed to produce a more chaotic mixing process, primarily from an increase in the shear rate being imparted on the granules from the screws. However, the pathlines of the materials remained relatively unchanged because the direction of the forces transmitted on the materials from the fixed screw pitch did not change. As one would expect, increasing the screw rotation speed decreased the material residence time (amount of time the material is present inside the screw mixer); thus a tradeoff exits between the rate of mixing and the mixing time. From this tradeoff, and previous studies by Vanarase and Muzzio (2011) who also noted a tradeoff between the rotation rate and the mixing time in a horizontal impeller mixer, it is hypothesized that an intermediate screw rotation rate will maximize the mixing effectiveness of the screw mixer. This hypothesis will be quantified in part two of this study (Kingston and Heindel, 2013c).

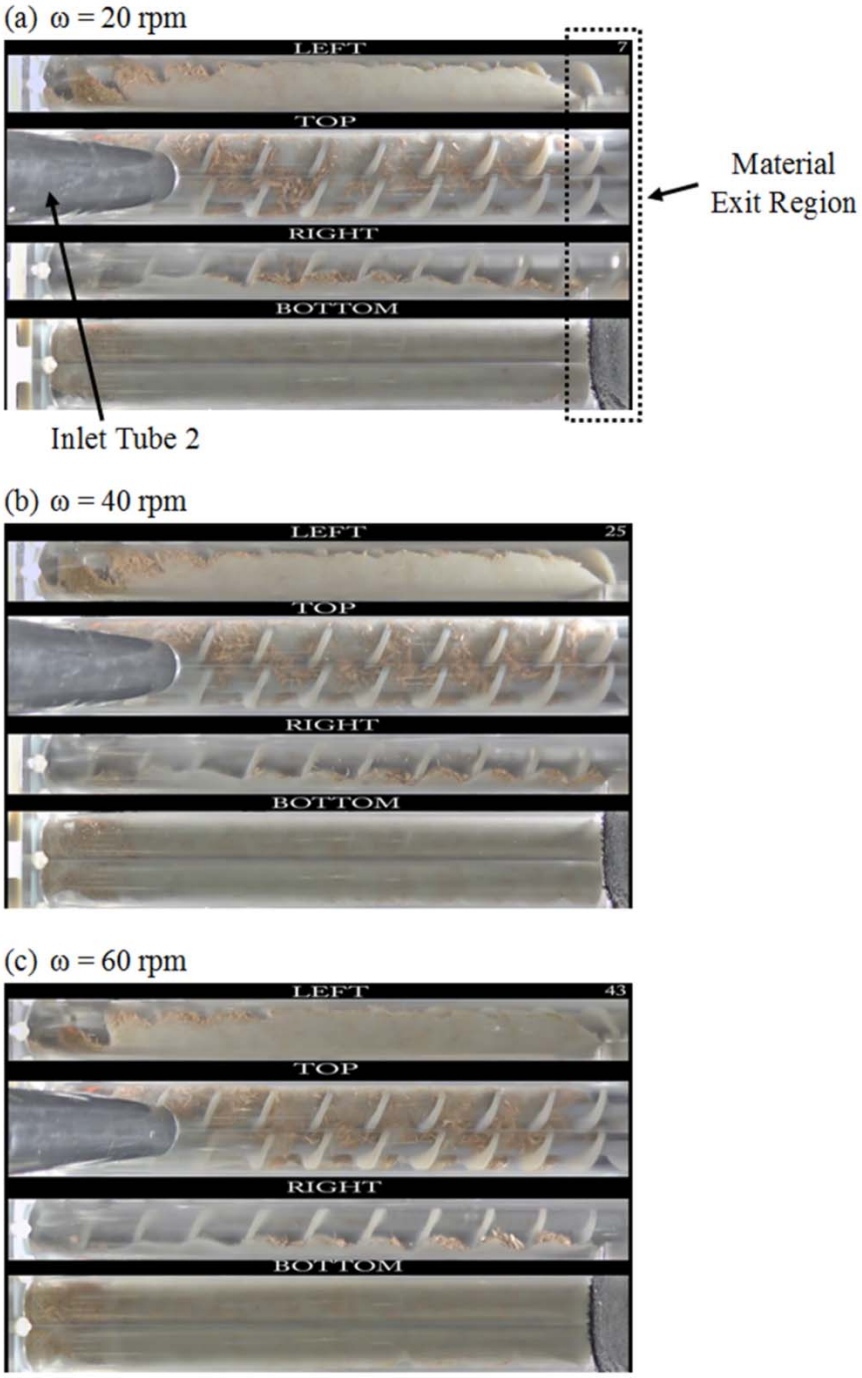

Figure 5.6: Snapshots of the dynamic mixing process captured at steady state conditions for screw rotation speeds of ω = 20, 40, and 60 rpm, with a dimensionless screw pitch of p/D = 1.25, a co-rotating screw rotation orientation, and the red oak chips and glass beads injected into port one and two, respectively.

5.4.2 Dimensionless Screw Pitch

The dimensionless screw pitch had a significant influence on the behavior of the granular material inside the screw mixer. Illustrated in Figure 5.7 are snapshots of the dynamic mixing process for dimensionless screw pitches of p/D = 0.75, 1.25, and 1.75. As the dimensionless screw pitch increased, several important observations were noted from the mixing videos: (i) the rotational velocity (V_R) of the granular materials increased relative to the axially velocity (V_A) due to the changing angle at which the screws impart forces on the granules, causing more rotation as opposed to simply axially conveying the particles (schematically illustrated in Figure 5.7); (ii) less cohesion between the screw flights and granular material is observed due to the decreased screw flighting surface area; (iii) a larger clearance gap between the intermeshing screws existed, which could be increasingly important when attempting to mix larger particles; (iv) the velocity of individual granules (V) increased resulting in a reduced material residence time, even at a fixed screw rotation speed (schematically illustrated in Figure 5.7); (v) variations in the volumetric material fill ratio between the individual screw flights became more noticeable, as shown in the left projections of Figure 5.7; (vi) the volumetric fill ratio of the two screws became more uniform; and (vii) the mixing effectiveness of the screw mixer appeared to increase, at least qualitatively.

The effect of dimensionless screw pitch has been researched in other screw conveying applications. Uchida and Okamoto (2008) researched the effect that dimensionless screw pitch had on the diffusion coefficient in powder flows by injecting a small amount of tungsten tracer powder into a single screw feeder, and tracking the movement of the tungsten powder as it moved downstream. It was noted that increasing

the dimensionless screw pitch increased the frequency of the tungsten particle's sine-like pathline, which is analogous to the increase in the rotational velocity relative to the axial velocity found in this study. Moreover, Uchida and Okamoto (2008) concluded that increasing the dimensionless screw pitch increased the diffusion coefficient of the single screw mixer, which is consistent to the qualitative increase in the mixing effectiveness of the double screw mixer found in this study.

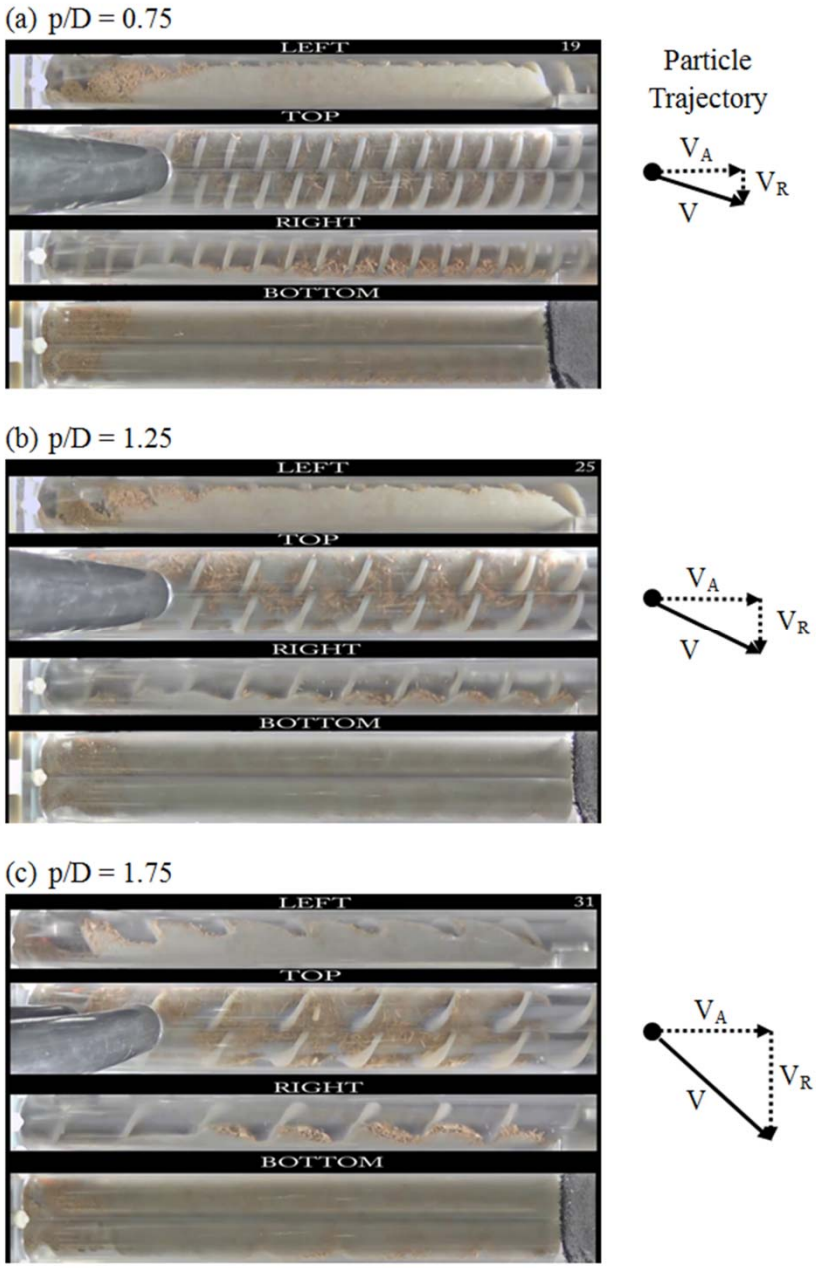

Figure 5.7: Snapshots of the dynamic mixing process captured at dimensionless screw pitches of p/D = 0.75, 1.25, and 1.75, with a screw rotation speed of ω = 40 rpm, a co-rotating screw rotation orientation, and the red oak chips and glass beads injected into port one and two, respectively.

5.4.3 Screw Rotation Orientation

The selection of the screw rotation orientation had the most significant influence on the granular mixing process. Vastly different mixing dynamics were found,

particularly with regards to the volumetric distribution of the materials within the screw mixer, as the screw rotation orientation was changed from a co-rotating orientation to either a counter-rotating up-pumping or down-pumping orientation. Illustrated in Figure 5.8 are snapshots of the dynamic mixing process for the co-rotating (CoR), counter-rotating up-pumping (CtrR UP), and counter-rotating down-pumping (CtrR DP) screw rotation orientations.

Operating the screw mixer in a co-rotating screw rotation orientation causes the mixing of the red oak chips and glass beads to exhibit desired and undesired characteristics. One desirable characteristic was the red oak chips did not appear to significantly accumulate on the walls facing the left and right projections. However, some undesired characteristics were that few red oak chips were observed in the bottom projection, indicating enhanced segregation which causes the red oak chips to rise to the top surface of the granular mixture. Another negative effect of the co-rotating screw rotation orientation is that the left screw has a much larger volumetric fill ratio (~90%) than that of the right screw (~40%) and minimal granular material was observed between the right screw and the housing's outside surface, as shown in the right projection of Figure 5.8a; thus, minimal mixing is present in this region of the screw mixer. Moreover, the low volumetric fill ratio in this region of the screw mixer causes the relatively few red oak chips that are actually present in the right projection to be simply conveyed on top of the glass beads, and exhibit minimal mixing.

Operating the screw mixer in a counter-rotating up-pumping screw rotation orientation produced mostly negative effects on the granular mixing process. Most notably, significantly large agglomerations of red oak chips are pushed towards the

outside surfaces of the screw mixer, as illustrated in the left and right projections of Figure 5.8b. The counter-rotating up-pumping screw rotation orientation lifts the larger, lighter red oak chips to the top surface of the granular mixture and results in large agglomerations of red oak chips, which are undesired because they exhibit minimal mixing. In the case of the thermochemical conversion of biomass into bio-oil, these agglomerations would significantly reduce the heat transfer rates from the heat carrier media to the biomass, and would result in lower bio-oil yields.

Finally, the counter-rotating down-pumping screw rotation orientation, shown in Figure 5.8c, produced the most favorable results in terms of improving the mixing effectiveness of the screw mixer. First, minimal red oak chip agglomerations were found at any location or projection. Second, increased concentrations of red oak chips are observed in the bottom projection, suggesting that the counter-rotating down-pumping screw rotation orientation pushes the red oak chips from the top surface down through the granular mixture. Finally, the screw mixer appeared to reach a respectable mixing effectiveness at relatively short mixing lengths, compared to the other screw rotation orientations. From these observations, a counter-rotating down-pumping screw rotation orientation is expected to exhibit better mixing; this will be confirmed in part two of this study (Kingston and Heindel, 2013c).

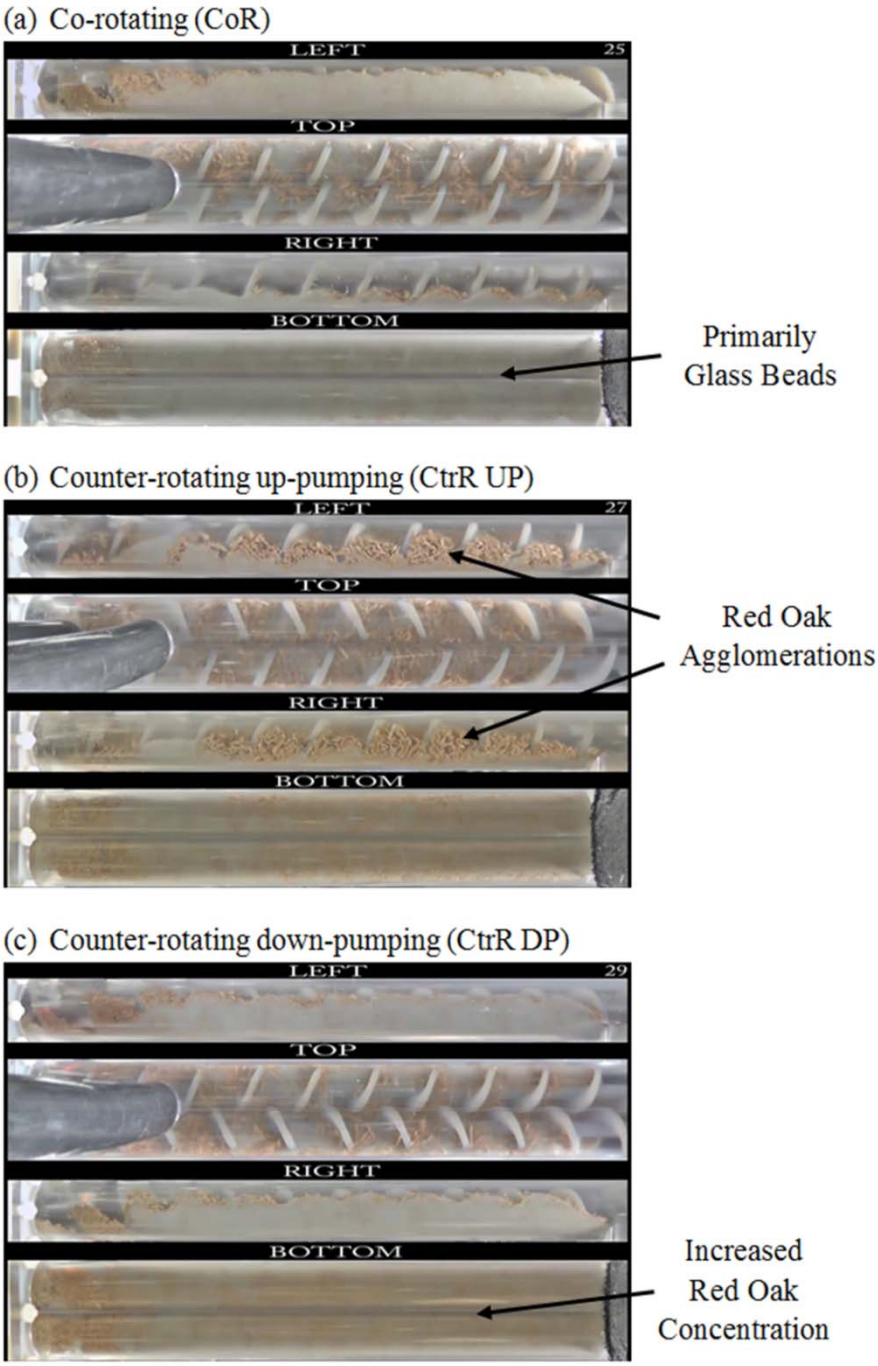

Figure 5.8: Snapshots of the dynamic mixing process captured at screw rotation orientations of (a) co-rotating (CoR), (b) counter-rotating up-pumping (CtrR UP), and (c) counter-rotating down-pumping (CtrR DP), with a screw rotation speed of $\omega = 40$ rpm, a dimensionless screw pitch of $p/D = 1.25$, and the red oak chips and glass beads injected into port one and two, respectively.

5.4.4 Material Injection Configuration

Unlike the screw rotation speed, dimensionless screw pitch, and screw rotation orientation, the material injection configuration's impact on the granular mixing process dissipates as the dimensionless mixing length increases. Illustrated in Figure 5.9 are two snapshots of the dynamic mixing process. Figure 5.9a illustrates the reference condition which features the red oak chips and glass beads injected into port one and two (RO 1, GB 2), respectively, while Figure 5.9b features an interchanged material injection configuration, with the red oak chips and glass beads injected into port two and one (RO 2, GB 1), respectively. As shown, changing the material injection configuration from the reference configuration (RO 1, GB 2) to the other configuration (RO 2, GB 1) causes several noteworthy changes to the mixing process including: (i) large red oak chip agglomerations are more apparent, particularly in the right projection, because the red oak chips are pushed towards screw two immediately after being injected; (ii) minimal amounts of red oak chips are present in the left projection; (iii) a larger opportunity for granular material jamming exits immediately after the red oak chips are injected into port two because the larger, less dense red oak chips are unable to penetrate the glass beads and cause the volumetric fill ratio to be temporarily higher than the recommended 65%; and (iv) the mixing effectiveness is reduced, at least qualitatively.

In addition to these observations, further investigation into the material properties provides evidence to support these claims. Because the red oak chips used in this study were much larger in size and less dense than the glass beads, the red oak chips will naturally segregate to the top of the mixture due to percolation and buoyancy forces. Thus, the glass beads will tend to sink while the red oak chips will tend to rise as they are

conveyed in the screw mixer. The material injection configuration used in the reference condition (RO 1, GB 2) allows the red oak chips to be positioned on the bottom of the screw mixer prior to the glass beads being dropped on top. Initially, the glass beads will penetrate downward through the red oak chips while the red oak chips will rise upward. This will induce a natural mixing process, at least temporarily. In contrast, changing the material injection configuration to RO 2, GB 1 will cause the glass beads to be positioned on the bottom of the screw mixer, prior to the red oak chips being dropped on top. The granular materials will then tend to stay in this configuration due to the percolation and buoyancy forces, and minimal mixing exists. The selection of the material injection configuration is critically important, particularly in the case of biomass thermochemical conversion where high heat transfer rates are desired in the first few seconds of the biomass being injected into the screw pyrolyzer. In summary, it is recommended that the material injection configuration be chosen such that the red oak chips and glass beads are injected into port one and two, respectively.

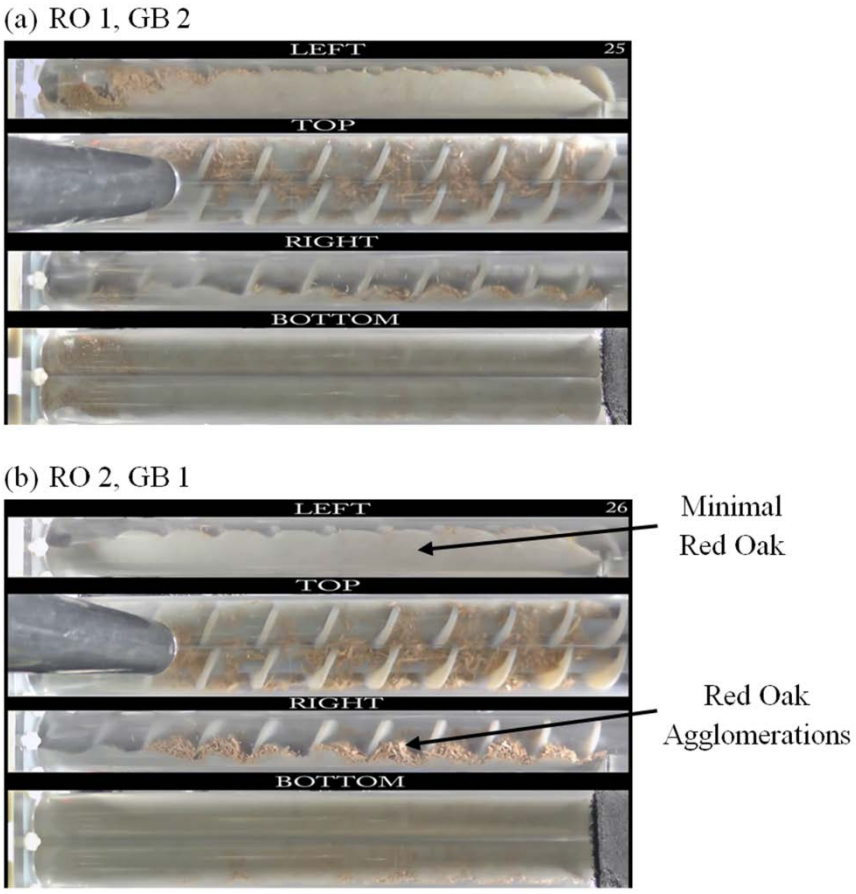

Figure 5.9: Snapshots of the dynamic mixing process captured at material injection configurations of (a) red oak chips and glass beads being injected into port one and two (RO 1, GB 2), and (b) two and one (RO 2, GB 1), with a screw rotation speed of ω = 40 rpm, a dimensionless screw pitch of p/D = 1.25, and a co-rotating screw rotation orientation.

5.5 Conclusions

Part one of this two-part study featured a qualitative mixing assessment of two granular material types which exhibited vastly different particle sizes, shapes, and densities. The materials were mechanically mixed using a double screw mixer under various operating conditions. Advanced optical visualization imaging techniques were used to capture critical qualitative mixing characteristics across the screw mixer's entire periphery. It was determined, at least qualitatively, that a tradeoff exists between the

screw rotation speed and mixing time, and a general recommendation could not be made based solely on the qualitative mixing assessment. However, it was determined that increasing the dimensionless screw pitch resulted in an increase in the screw mixer's mixing effectiveness. Furthermore, a counter-rotating down-pumping screw rotation orientation and a material injection configuration with the red oak chips and glass beads injected into port one and two, respectively, resulted in improved mixing dynamics compared to other operating conditions. The qualitative observations that were found across the entire mixing region are absolutely critical to fully understanding the mixing dynamics of the screw mixer, and provide reasoning and confirmation into why certain operating conditions are more favorable than others.

Despite being quite useful, there are a couple limitations to a qualitative optical visualization methods used to characterize the mixing of granular materials in a screw mixer. First, it alone does not provide quantitative data to justify the noted observations; part two of this two-part study (Kingston and Heindel, 2013c) accomplishes that task by providing quantitative data and justification for the selection of the screw mixer's operating conditions. Second, the ability to distinguish the different granular material types relies heavily on the visual contrast between the two materials. Finally, this technique provides only surface visualization, and does not give insight into the internal structure of the granular mixture. This would be particularly concerning when using a mixer of much larger size because the volume to surface area ratio would dramatically increase. However, for laboratory-scale experiments, there is much to gain from simple surface visualization and the relatively inexpensive equipment needed to perform this type of mixing assessment makes this an attractive option.

Acknowledgements

Support for portions of this work by Phillips 66 Company is gratefully acknowledged.

CHAPTER 6: GRANULAR MIXING VISUALIZATION AND QUANTIFICATION IN A DOUBLE SCREW MIXER: PART II – QUANTITATIVE COMPOSITION AND STATISTICAL ANALYSIS[1]

Todd A. Kingston[2] and Theodore J. Heindel

Department of Mechanical Engineering, Iowa State University, Ames, Iowa, 50011, USA

kingston.todd@gmail.com and theindel@iastate.edu

Abstract

Granular mixing processes often seek a high degree of homogeneity, and in some instances, can influence simultaneous processing, such as chemical reactions and heat and/or mass transfer. However, differences in particle size, shape, and/or density lead to segregation and reduce the mixing effectiveness of these processes. In this study, red oak chips and glass beads are mechanically mixed and the mixing effectiveness of a laboratory-scale double screw mixer is evaluated under various operating conditions.

---

[1] Kingston, T.A., Heindel, T.J. (2013). Granular mixing visualization and quantification in a double screw mixer: Part II – Quantitative composition and statistical analysis. *Powder Technology* (in review).

[2] Corresponding author: Todd A. Kingston (kingston.todd@gmail.com

Quantitative composition analysis is coupled to analysis of variance (ANOVA) statistical procedures to determine the optimal operating conditions. For the parameters addressed in this study, the best mixing performance occurs when the screw rotation speed is $\omega = 60$ rpm, the dimensionless screw pitch is $p/D = 1.75$, the screw rotation orientation is counter-rotating down-pumping, and the material injection configuration features the red oak chips and glass beads injected into port one and two, respectively.

Keywords: Analysis of variance, composition analysis, granular mixing, homogeneity, screw mixer, quantification.

6.1 Introduction

Granular mixing processes are unquestionably important because they arise in numerous industrial applications including energy generation, pharmaceutical production, and food processing. Most commonly, granular mixing processes seek a high degree of homogeneity, and in some instances, can influence simultaneous processing, such as chemical reactions and heat and/or mass transfer (Mohan et al., 2006). However, granular materials segregate. Small differences in particle size, shape, and/or density lead to flow-induced segregation. Furthermore, combinations of these differences can be combined to produce an even more challenging mixing behavior. Differences in particle size and density cause percolation and buoyancy, respectively, and may either compete or complement each other (Jain et al., 2005). For example, mixing can be achieved, instead of segregation, if the correct combinations of materials are selected where larger, denser particles are mixed with smaller, less dense particles such that the percolation and buoyancy forces offset each other (Jain et al., 2005).

Granular mixing is a complex phenomenon and has attracted many research efforts in recent years, and when compared to liquid mixing, the knowledge base on granular mixing is underdeveloped (Jain et al., 2005). A vast majority of granular mixing research efforts have focused on relatively simple mixer geometries and idealized materials compared to what is actually used in industrial practice. For example, rotating cylinders have been extensively studied by a large number of researchers, both experimentally (Aissa et al., 2010a, b; Huang and Kuo, 2012; Jain et al., 2005) and computationally (Chand et al., 2012; Gui et al., 2010; Gui et al., 2013; Yang et al., 2008) because of its simple mixer geometry. These studies have proven to be beneficial in developing a deeper theoretical understanding of the mixing mechanisms, but there is still a mismatch between basic research involving idealized conditions and practical industrial needs (Ottino and Khakhar, 2001). Mixer design is evaluated through segregation avoidance, which is often obtained through serendipity and/or exhaustive trial-and-error procedures (Hajra et al., 2010). Cleary and Sinnott (2008) state that due to the lack of understanding of the interaction between mixer geometry and the granular material, limited progress has been made in optimizing mixer design. Moreover, specific mixing studies and resulting solutions associated with simple mixer geometries are rarely extensive and cannot be applied to more complex mixer geometries. Therefore, complex granular mixing processes must be studied using the specific mixer geometry and materials of interest.

Screw pyrolyzers are a relatively new chemical reactor design compared to other traditional reactors such as fluidized beds, and are being developed for the thermochemical conversion of biomass into bio-oil (Kingston and Heindel, 2013d). The

screw pyrolyzer's high heat transfer rates and resulting bio-oil yields are significantly influenced by its operating conditions and its ability to mechanically mix low density biomass particles (e.g., red oak chips, switchgrass, etc.) with high density inert heat carrier media (e.g., stainless steel shot, refractory sand, etc.) (Kingston and Heindel, 2013d). Previous research efforts featuring screw pyrolyzers have primarily focused on the quality of the products and how they relate to the feedstocks used (Ingram et al., 2008) or the reactor operating conditions (Bahng et al., 2009; Brown and Brown, 2012a). However, no research efforts have focused on relating the granular mixing inside a double screw pyrolyzer to its operating conditions. Thus, a thorough understanding of the granular mixing dynamics is needed for more efficient operation and higher bio-oil yields (Mohan et al., 2006). Hence, through these research efforts, the economic feasibility of the screw pyrolyzer for the production of bio-oil will be improved by reaching higher bio-oil yields.

In this study, the mixing effectiveness of a laboratory-scale double screw mixer, which almost identically replicates the geometry of typical double screw pyrolyzers (Brown and Brown, 2012a), is evaluated. Red oak chips and glass beads are mechanically mixed under various operating conditions in an attempt to optimize the mixing process. This paper is a companion to Kingston and Heindel (2013b), where qualitative observations using a unique optical visualization set-up was presented. In the current study, the screw mixer's exit stream was sectioned into four equally sized regions and samples were collected across the exit stream to determine the mixture's composition variance, which indicates the spatial heterogeneity of the granular mixture. The effect of four factors (i.e., parameters) on the composition variance was investigated: (i) screw

rotation speed, (ii) dimensionless screw pitch, (iii) screw rotation orientation, and (iv) material injection configuration. Statistical analysis techniques were then used to determine the most influential factors contributing to the mixing performance, and the operating conditions were then optimized by investigating each factor's effect on the composition variance.

This paper will begin by briefly describing the screw mixer's experimental setup and the granular materials used. Next, the experimental methods, including the design of experiments and composition and statistical analysis procedures, will be presented. The results of the study will then be thoroughly presented followed by a comprehensive discussion. Finally, the conclusions of this research will be summarized.

6.2 Experimental Procedures

In this study, experimental tests were performed in a laboratory-scale double screw mixer. Recent advances in rapid prototype machining processes allowed for all the parts to be manufactured using a three-dimensional (3D) printer. The 3D printer allowed for complex geometry to be easily constructed without the constraints typically placed on traditional machining processes. A unique dividing mechanism was designed for the purpose of spatially dividing the granular flow into four separate channels, allowing composition uniformity to be assessed across the entire material exit stream. The four outlet ports divided the granular material flow into four channels that span in the horizontal direction, as shown in Figure 6.1, allowing port-to-port variances to be evaluated. However, this dividing methodology does not have the ability to evaluate the segregation within each of the individual ports, reiterating the need for a two-part

measurement technique which combines qualitative visualization and quantitative justification, as was done in this study. The advantage of analyzing the entire material exit stream is that the assumption that the collected sample's composition resembles that of the entire population does not have to be made, which can introduce a significant amount of error due to the segregation of the granular materials. Moreover, it satisifies Allen's (1996) two "golden rules of sampling": (i) a granular mixture should be sampled only when it is in motion and (ii) the whole granular stream should be uniformly collected for many short increments.

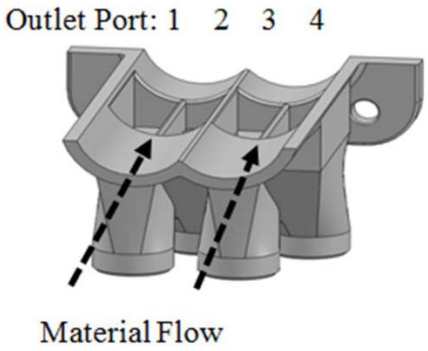

Figure 6.1: The screw mixer's dividing mechanism used to section the granular flow's exit stream.

6.2.1 Design of Experiments

To fully understand the influence that the operating conditions of the screw mixer have on the mixing effectiveness, a relatively large number of factors were considered when compared to what is typically done in other granular mixing studies (Dhenge et al., 2013; Hajra et al., 2010; Sarkar and Wassgren, 2009; Uchida and Okamoto, 2006). As previously mentioned, the effect of four factors on the mixing effectiveness of the screw mixer was investigated. The levels of each of the factors were selected based on traditional operating conditions found in the literature (Brown and Brown, 2012a; Dai

and Grace, 2011; Ingram et al., 2008; Mohan et al., 2006; Uchida and Okamoto, 2008) and common practice in industry. The four factors and their respective levels that were tested are: (i) screw rotation speeds of ω = 20, 40, and 60 rpm; (ii) dimensionless screw pitches of p/D = 0.75, 1.25, and 1.75, where p is the screw pitch and D is the screw diameter (D = 2.54 cm); (iii) screw rotation orientations of co-rotating (CoR), counter-rotating up-pumping (CtrR UP), and counter-rotating down-pumping (CrtR DP), where up-pumping and down-pumping refer to the direction of material flow between the two screws; and (iv) material injection configurations of the red oak chips and glass beads being injected into port one and two (RO 1, GB 2) and port two and one (RO 2, GB 1), respectively.

As a result, 54 different operating conditions are possible ($3 \times 3 \times 3 \times 2 = 54$). A randomized full-factorial design of experiments methodology was utilized in order to provide a comprehensive understanding of the granular mixing dynamics in the screw mixer. Furthermore, repeatability was incorporated into the design of experiments by performing three tests (i.e., observations) at each operating condition, totaling 162 individual tests that were performed. As previously mentioned, four samples were collected across the exit stream for each test totaling 648 samples that were collected and analyzed. The breadth and depth resulting from the number of different operating conditions and collected samples is far beyond previous granular mixing studies reported in the literature. A fractional-factorial design of experiments in which only a subset of the full-factorial design could have been employed, but this would have reduced the statistical power of the analysis, compromising the ability to recognize significant factors and resulting in undesired results.

6.2.2 Composition Analysis

The mixing effectiveness of the screw mixer was evaluated by determining the degree of heterogeneity from the four spatially divided exit samples that were collected for each observation. The composition of each collected sample was determined using the methods outlined by Kingston and Heindel (2013d). A brief review of the methods is presented here for convenience.

The collected sample's mass and true volume were analyzed using a Cole-Parmer Symmetry PA-Analytical Balance and Quantachrome Instruments' Pentapyn 5200e Gas Pycnometer, respectively. This allowed for the determination of the sample's true mixture density. The empirical correlation proposed by Kingston and Heindel (2013d), shown in Figure 6.2, was developed by artificially creating granular mixture samples with known mixture compositions and then analyzing the mixture densities. An empirical correlation was used to convert the measured mixture density to its composition:

$$\rho_{mix} = 623.4\, x^2 + 526.8\, x + 1358 \qquad (6.1)$$

where ρ_{mix} is the mixture density and x is the mixture composition in terms of glass bead mass fraction ranging from zero to one.

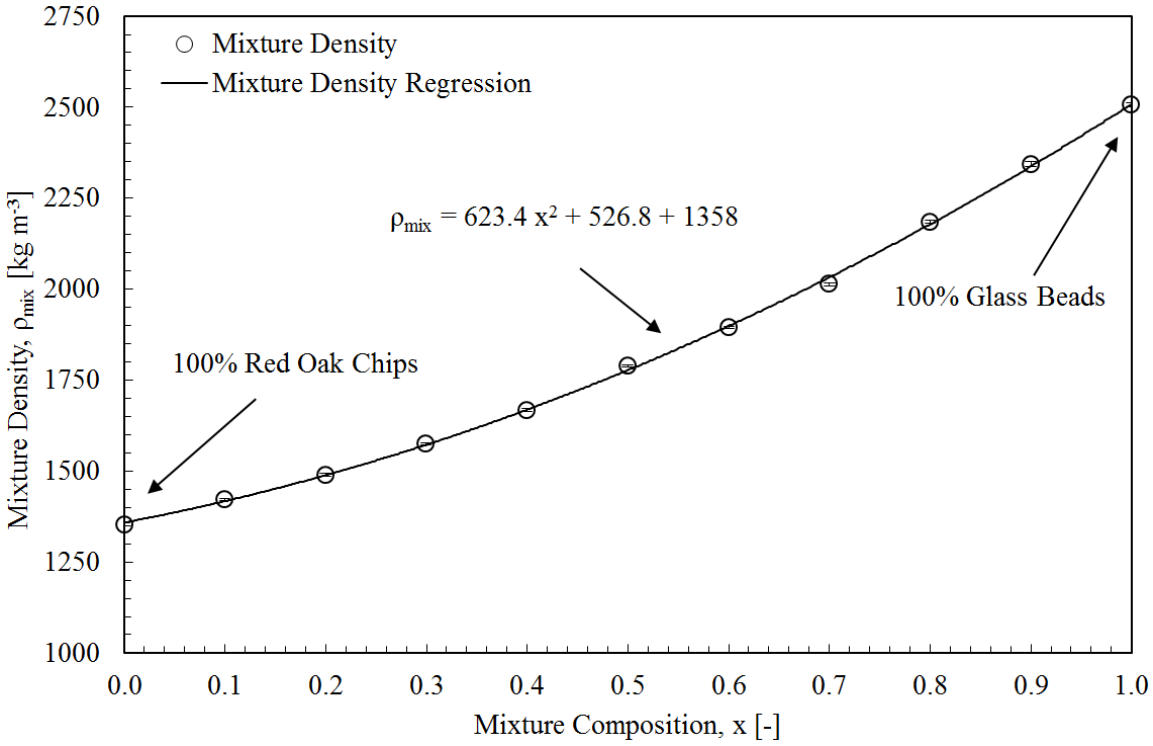

Figure 6.2: Emprical correlation used to relate the mixture density to the mixture composition (Kingston and Heindel, 2013d).

The heterogeneity of the granular samples was then determined by computing the weighted composition variance, s^2:

$$s^2 = \frac{\sum_{i=1}^{i=n} m_i \left(x_i - \overline{x_w} \right)^2}{\left(\frac{N-1}{N} \right) \sum_{i=1}^{i=n} m_i} \tag{6.2}$$

where n is the number of the i^{th} sample, m_i is the mass of the i^{th} sample, x_i is the composition of the i^{th} sample, $\overline{x_w}$ is the mass weighted mean composition of the samples, and N is the total number of samples. In this study, the number of samples used to compute the composition variance is four, corresponding to the four samples that were collected from the outlet ports. Granular mixing processes typically seek a high degree of homogeneity. Thus, a composition variance of zero is the best case scenario and

corresponds to a homogeneous mixture. As the composition variance increases, segregation becomes more dominant and the mixing effectiveness of the screw mixer is effectively worsening.

6.2.3 Statistical Analysis

The determination of significant factors affecting the mixing effectiveness of the screw mixer can be subjective without the use of statistical analysis techniques. Thus, a four-way full-factorial analysis of variance (ANOVA) statistical model was applied using JMP Pro 10 to indicate the most influential factors in terms of their effect on the composition variance. The resulting model equation is:

$$\begin{aligned} y_{ijklm} = \mu + \alpha_i + \beta_j + \delta_k + \tau_l + \gamma_{ij}^{12} + \gamma_{ik}^{13} + \gamma_{il}^{14} + \gamma_{jk}^{23} + \gamma_{jl}^{24} + \gamma_{kl}^{34} \\ + \gamma_{ijk}^{123} + \gamma_{ijl}^{124} + \gamma_{ikl}^{134} + \gamma_{jkl}^{234} + \gamma_{ijkl}^{1234} + \varepsilon_{ijklm} \end{aligned} \tag{6.3}$$

where y_{ijklm} is the measured response variable (i.e., composition variance); μ is the mean response averaged over all levels of all factors; α_i , β_j, δ_k , and τ_l are the effects of the main-effect factors; γ_{ij}^{12}, γ_{ik}^{13}, γ_{il}^{14}, γ_{jk}^{23}, γ_{jl}^{24}, and γ_{kl}^{34} are the two-way interaction effects; γ_{ijk}^{123}, γ_{ijl}^{124} , γ_{ikl}^{134} , and γ_{jkl}^{234} are the three-way interaction effects; γ_{ijkl}^{1234} is the four-way interaction effect; and ε_{ijklm} is the random deviation from the true treatment mean (DeVore, 2008). Three observations were performed at each operating conditions thus m ranges from 1 to M, where M = 3.

To determine the significance of the 15 terms in the model equation, 15 hypotheses were tested, one for each of the terms listed above. Due to the large number of hypotheses, only the first two and the last hypotheses are shown here:

$$H_{o,1}: \quad \alpha_1 = \ldots = \alpha_I = 0 \quad \text{versus} \quad H_{a,1}: \quad \text{at least one } \alpha_i \neq 0$$

$$H_{o,2}: \quad \beta_1 = \ldots = \beta_J = 0 \quad \text{versus} \quad H_{a,2}: \quad \text{at least one } \beta_j \neq 0 \qquad (6.4)$$

...

$$H_{o,1234}: \quad \gamma_{ijkl}^{1234} = 0 \text{ for all i, j, k, l} \quad \text{versus} \quad H_{a,1234}: \quad \text{at least one } \gamma_{ijkl}^{1234} \neq 0$$

where I, J, K, and L are the number of levels of factor one through four, respectively. In other words, the null hypotheses suggest that each term in the model equation does not have a significant influence on the composition variance, while the alternative hypotheses suggests that at least one of the levels from each term does have an effect on the composition variance. Therefore, these statistical tests require evidence to prove that the factors are significant. In this study, I, J, and K are all equal to three because factors one, two, and three (i.e., screw rotation speed, dimensionless screw pitch, and screw rotation orientation) were all tested at three different levels (e.g., ω = 20, 40, and 60 rpm). Meanwhile, L = 2, and corresponds to the two different material injection configurations. The F-test statistic and its corresponding p-value were used to determine if the null hypotheses failed to be rejected or were rejected in favor of the alternative hypotheses at an alpha level of 0.05.

6.3 Results and Discussion

6.3.1 ANOVA

The influence that the main-effect and interaction terms, shown in the statistical model in Equation 3, had on the composition variance was quantified using the four-way ANOVA procedure. The key parameters of the analysis are summarized in the ANOVA table shown in Table 6.1, where the degrees of freedom are symbolized by df, the sum of

squares by SS, the mean square by MS, and the F-test statistic by F. For the terms to be declared statistically significant, their corresponding p-value must be less than the alpha level of 0.05. As shown, eight of the 15 terms are statistically significant. The model equation had a coefficient of determination of $R^2 = 0.878$.

Table 6.1: ANOVA table illustrating the key statistical parameters in the model equation [Eqn. (6.3)].

ANOVA Table						
Source	**df**	**SS**	**MS**	**F**	**p-value**	**Significant**
Screw Rotation Speed	2	$4.30E^{-7}$	$2.15E^{-7}$	5.30	0.006	Y
Dimensionless Screw Pitch	2	$1.96E^{-6}$	$9.80E^{-7}$	24.11	< 0.001	Y
Screw Rotation Orientation	2	$1.05E^{-6}$	$5.23E^{-6}$	128.79	< 0.001	Y
Material Injection Configuration	1	$1.00E^{-8}$	$8.33E^{-9}$	0.21	0.652	N
Screw Rotation Speed × Dimensionless Screw Pitch	4	$1.20E^{-6}$	$3.01E^{-7}$	7.41	< 0.001	Y
Screw Rotation Speed × Screw Rotation Orientation	4	$6.40E^{-7}$	$1.59E^{-7}$	3.91	0.005	Y
Screw Rotation Speed × Material Injection Configuration	2	$2.00E^{-8}$	$9.59E^{-9}$	0.24	0.790	N
Dimensionless Screw Pitch × Screw Rotation Orientation	4	$1.26E^{-5}$	$3.15E^{-6}$	77.40	< 0.001	Y
Dimensionless Screw Pitch × Material Injection Configuration	2	$1.10E^{-7}$	$5.55E^{-8}$	1.37	0.260	N
Screw Rotation Orientation × Material Injection Configuration	2	$4.00E^{-8}$	$1.97E^{-8}$	0.49	0.617	N
Screw Rotation Speed × Dimensionless Screw Pitch × Screw Rotation Orientation	8	$2.21E^{-6}$	$2.76E^{-7}$	6.80	< 0.001	Y
Screw Rotation Speed × Dimensionless Screw Pitch × Material Injection Configuration	4	$3.60E^{-7}$	$8.92E^{-8}$	2.19	0.074	N
Screw Rotation Speed × Screw Rotation Orientation × Material Injection Configuration	4	$9.90E^{-7}$	$2.46E^{-7}$	6.07	< 0.001	Y
Dimensionless Screw Pitch × Screw Rotation Orientation × Material Injection Configuration	4	$1.80E^{-7}$	$4.51E^{-8}$	1.11	0.356	N
Screw Rotation Speed × Dimensionless Screw Pitch × Screw Rotation Orientation × Material Injection Configuration	8	$5.30E^{-7}$	$6.60E^{-8}$	1.63	0.126	N
Error	108	$4.39E^{-6}$	$4.06E^{-8}$			
Total	161	$3.61E^{-5}$				

To reduce the complexity of the result, a reduced model equation which includes only the eight statistically significant terms, was applied:

$$y_{ijklm} = \mu + \alpha_i + \beta_j + \delta_k + \gamma_{ij}^{12} + \gamma_{ik}^{13} + \gamma_{jk}^{23} + \gamma_{ijk}^{123} + \gamma_{ikl}^{134} + \varepsilon_{ijklm} \quad (6.5)$$

The reduced model equation had a coefficient of determination of $R^2 = 0.844$. As the number of terms in the model equation was reduced by 46% (i.e., from 15 to eight),

the coefficient of determination was only reduced by 3.9%, reiterating the nonsignificance of the seven eliminated terms. The resulting ANOVA table for the reduced model equation is shown in Table 6.2. The p-value for all eight terms was less than 0.05, emphasizing the importance of all remaining terms.

Table 6.2: ANOVA table illustrating the key statistical parameters in the reduced model equation [Eqn. (6.5)].

ANOVA Table					
Source	**df**	**SS**	**MS**	**F**	**p-value**
Screw Rotation Speed	2	$4.30E^{-7}$	$2.15E^{-7}$	5.01	0.008
Dimensionless Screw Pitch	2	$1.96E^{-6}$	$9.80E^{-7}$	22.79	< 0.001
Screw Rotation Orientation	2	$1.05E^{-5}$	$5.23E^{-6}$	121.74	< 0.001
Screw Rotation Speed × Dimensionless Screw Pitch	4	$1.20E^{-6}$	$3.01E^{-7}$	7.00	< 0.001
Screw Rotation Speed × Screw Rotation Orientation	4	$6.40E^{-7}$	$1.59E^{-7}$	3.70	0.007
Dimensionless Screw Pitch × Screw Rotation Orientation	4	$1.26E^{-5}$	$3.15E^{-6}$	73.16	< 0.001
Screw Rotation Speed × Dimensionless Screw Pitch × Screw Rotation Orientation	8	$2.21E^{-6}$	$2.76E^{-7}$	6.42	< 0.001
Screw Rotation Speed × Screw Rotation Orientation × Material Injection Configuration	4	$9.90E^{-7}$	$2.46E^{-7}$	5.73	< 0.001
Error	131	$5.63E^{-6}$	$4.30E^{-8}$		
Total	161	$3.61E^{-5}$			

6.3.2 Interpretation of Factor Interaction

Critical information pertaining to the granular mixing process in the screw mixer was gathered by further investigation of the eight significant terms shown in Table 6.2, which lead to several noteworthy findings. In ANOVA procedures, it is typical to begin by looking at the highest order interaction terms and progress to the main-effect terms, which will be done here. First, the four-way interaction term between the four factors under consideration was not significant, as shown in Table 6.1, and was thus not included in the reduced model equation. This is a fortunate result because the ability to visually

illustrate higher order interactions becomes exponentially more difficult. Second, there are two statistically significant three-way interaction terms: (i) screw rotation speed, dimensionless screw pitch, and screw rotation orientation and (ii) screw rotation speed, screw rotation orientation, and material injection configuration. The three-way interactions are the highest order statistically significant terms and thus must be used for interpretation purposes in order to develop a clear understanding of the interaction between the factors and their respective levels. The two three-way interaction terms are approximately equal in terms of their influence on the mixing effectiveness of the screw mixer because they both have similar F-test statistic values and p-values of less than 0.001.

Finally, the three two-way interactions and three main-effect terms that are statistically significant are comprised of the same three factors, that being the screw rotation speed, dimensionless screw pitch, and screw rotation orientation. The material injection configuration does not appear in these terms, but does appear in one of the three-way interaction terms. As far as the two-way interaction terms, the interaction between the dimensionless screw pitch and screw rotation orientation is the most influential, having a F-test statistic of 73.16, compared to that of 3.76 and 7.00 for the interaction between the screw rotation speed and screw rotation orientation and the screw rotation speed and dimensionless screw pitch, respectively.

Investigation of the main-effect terms shows that the screw rotation orientation is clearly the most significant main-effect term because of its large F-test statistic (121.74), compared to that of the dimensionless screw pitch and the screw rotation speed. The key parameters summarized in Table 6.2 provide a clear indication into the most influential

factors. However, no information is provided on the influence of the individual levels of each factor. The two three-way interaction effects are plotted in Figures 6.3 and 6.4 to provide vital information relating to the interaction between the different levels of the factors. For convenience, an averaging line was added to the plots to help identify trends. The three-way interaction between the screw rotation speed, dimensionless screw pitch, and screw rotation orientation are shown in Figure 6.3. Plotted on the left vertical axis is the composition variance, s^2. The top and bottom horizontal axes display the screw rotation orientation and dimensionless screw pitch, respectively, while the screw rotation speed is plotted on the right vertical axis. Note that the effect of the material injection configuration is not illustrated in Figure 6.3, as it is averaged across both levels thus giving six data points (2 levels × 3 observations = 6) at each set of conditions. Recall that a composition variance of zero corresponds to a homogeneous mixture and is the desired state.

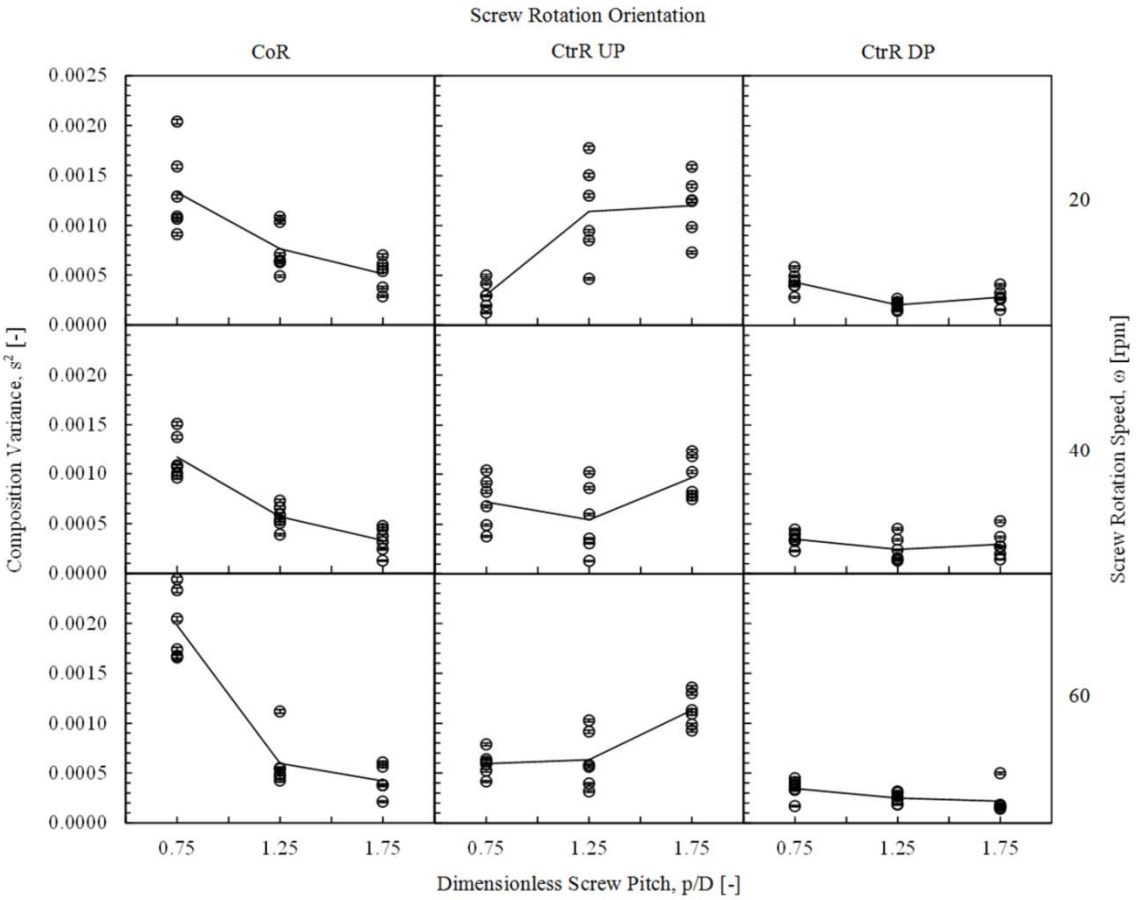

Figure 6.3: Composition variance as a function of the three-way interaction between the screw rotation speed, dimensionless screw pitch, and screw rotation orientation.

The three-way interaction between the screw rotation speed, screw rotation orientation, and material injection configuration is shown in Figure 6.4. Plotted on the left vertical axis is the composition variance, s^2. The top and bottom horizontal axes display the screw rotation speed and screw rotation orientation, respectively. Finally, the material injection configuration is plotted on the right vertical axis. Note that the effect of the dimensionless screw pitch is not shown in Figure 6.4, as it is averaged across all its levels thus giving nine data points (3 levels × 3 observations = 9) at each set of conditions. It is also worth noting that Figures 6.3 and 6.4 each illustrate the 162 data points that were taken during this study.

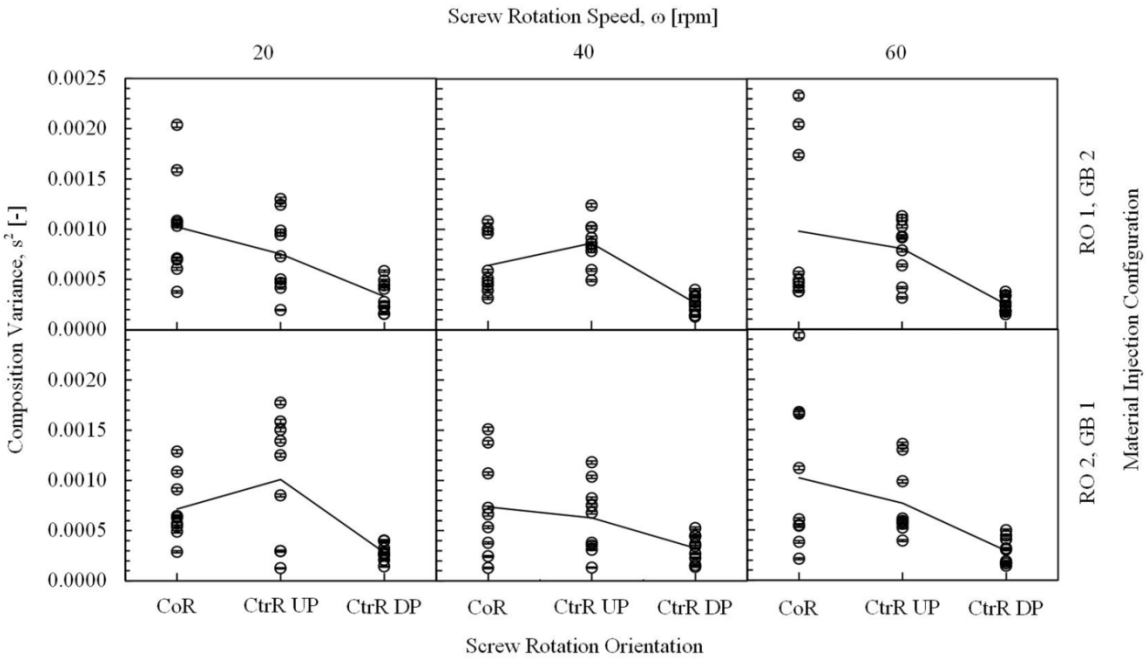

Figure 6.4: Composition variance as a function of the three-way interaction between the screw rotation speed, screw rotation orientation, and material injection configuration.

An uncertainty analysis was performed to quantify the amount of error associated with computing the composition variance from the four granular samples using Taylor's series expansion propagation of error procedure (Ku, 1966). The uncertainty in the measurements was combined with the uncertainty in the empirical correlation using the root sum squares (RSS) procedure. Overall, the uncertainty in the composition variance, U_{s^2}, ranged from 1 to 5% of the composition variance, s^2, and is illustrated graphically in Figures 6.3 and 6.4 by vertical error bars overlaid on the data points. As shown, all error bars fall within the circular symbols. This error is only associated with the determination of the composition variance, and is not associated with the variance (not to be confused with the composition variance) within or between the factors itself, which was quantified using the prescribed ANOVA analysis.

As previously mentioned, the interaction plots shown in Figures 6.3 and 6.4 show the interaction between the three corresponding factors that make up each of the three-way interactions, and average across all the levels of the forth factor and the three observations that were performed at each operating condition. This visualization method, which is commonly used in multi-factor ANOVA, does show large variation within the data because it displays every single collected data point, but it is the preferred visualization method to fully understand the higher-order interactions between factors. These variances are magnified when periodic fluctuations occur within the mixing process, which is common in screw mixing applications, and when changing mixing dynamics occur from the factor not being considered in each particular interaction plot. This effect is very noticeable at co-rotating and counter-rotating up-pumping screw rotation orientations, for reasons which will be discussed in the following sections.

6.3.3 Screw Rotation Speed

The effect of screw rotation speed is shown in Figures 6.3 and 6.4 and is described here by beginning with Figure 6.3. It is worth noting that the increased screw rotation speed imparts a higher shear stress on the granular materials and introduces a more chaotic mixing process. This effect is analogous to the influence of turbulence in fluid applications. While the screw rotation speed was determined to be statistically significant, it must be interpreted within the context of the other factors. For example, Figure 6.3 shows that increasing the screw rotation speed from $\omega = 40$ to 60 rpm for a dimensionless screw pitch of $p/D = 0.75$ and a co-rotating screw rotation orientation causes the composition variance to increase. Meanwhile, increasing the screw rotation speed for a dimensionless screw pitch of $p/D = 1.75$ and a counter-rotating down-

pumping screw rotation orientation reduces the composition variance. Moreover, Figure 6.4 shows that intermediate screw rotation speeds (i.e., ω = 40 rpm) maximized the composition variance for a counter-rotating up-pumping screw rotation orientation and material injection configuration of the red oak chips and glass beads injected into port one and two, respectively. The selection of the screw rotation speed must be carefully considered because of its influence on the material residence time, especially when heat and/or mass transfer is occurring, as is the case for chemically reacting screw pyrolyzers. A general recommendation cannot be made for the selection of the screw rotation speed, as it must be considered and selected within the context of the other factors.

6.3.4 Dimensionless Screw Pitch

The dimensionless screw pitch has a profound influence on the composition variance, particularly for the co-rotating and counter-rotating up-pumping screw rotation orientations. In contrast, minimal effects are noticed for the counter-rotating down-pumping screw rotation orientation. For a co-rotating screw rotation orientation, increasing the dimensionless screw pitch significantly reduces the composition variance, as shown in Figure 6.3. At screw rotation speeds of ω = 20 and 40 rpm, the composition variance is reduced by approximately 60% by increasing the dimensionless screw pitch from p/D = 0.75 to 1.75. Furthermore, for the ω = 60 rpm case, the composition variance is reduced by about 80%. However, a diminishing reduction in the composition variance is shown as the dimensionless screw pitch increases, as illustrated by the asymptotic reduction of the averaging line. Further increasing the dimensionless screw pitch beyond p/D = 1.75 would likely have minimal effects on the mixing effectiveness, at least for the range of screw rotation speeds considered in this study.

In contrast to the co-rotating screw rotation orientation, the counter-rotating up-pumping screw rotation orientation has the opposite effect on the composition variance. In general, increasing the dimensionless screw pitch increases the composition variance and therefore worsens the mixing effectiveness. Increasing the dimensionless screw pitch for the counter-rotating up-pumping screw rotation orientation causes the lighter red oak particles to be lifted up through the mixture and causes enhanced segregation due to the increased rotational movement that was noted in part one of this study (Kingston and Heindel, 2013b).

Finally, for a counter-rotating down-pumping screw rotation orientation, the dimensionless screw pitch seems to have a minimal effect on the composition variance, as illustrated by the relatively constant averaging line shown in Figure 6.3. However, at the 60 rpm screw rotation speed, there is a slight reduction in the composition variance at a dimensionless screw pitch of p/D = 1.75, compared to that of p/D = 0.75 and 1.25. Overall, increasing the dimensionless screw pitch has a beneficial influence on the composition variance for the co-rotating screw rotation orientation, but must be considered in parallel with the screw rotation speed for the counter-rotating up-pumping and down-pumping screw rotation orientations.

The effect of dimensionless screw pitch in particulate mixing process has also been investigated by other researchers. Uchida and Okamoto (2006) used an X-ray system coupled with a two-dimensional imaging device to measure the diffusion coefficient (a measure of the mixing effectiveness) of a single screw feeder by injecting and tracking small amounts of tungsten tracer powder. Uchida and Okamoto (2008) performed experiments using screws featuring dimensionless screw pitches of p/D = 1.0,

1.5, and 2.3, and found that increasing the dimensionless screw pitch increased the diffusion coefficient.

6.3.5 Screw Rotation Orientation

The screw rotation orientation was determined to be the most influential factor, as previously mentioned, and offers the largest opportunity for improvement in terms of maximizing the mixing effectiveness of the screw mixer compared to the other factors under consideration. The screw rotation orientation's effect is illustrated in Figures 6.3 and 6.4. First, Figure 6.3 will be considered. Most importantly, the magnitude of the composition variance is dramatically reduced for the counter-rotating down-pumping screw rotation orientation, independent of screw rotation speed and dimensionless screw pitch. This phenomenon arises because this screw rotation orientation causes the larger needle-like red oak chips that tend to segregate on top of the mixture to be pushed down through the mixture; this causes the glass beads, which tend to segregate on the bottom of the screw mixer, to be swept up from the bottom surface and be remixed with the flow. Visual observations of this phenomenon can be found in the optical visualization (Kingston and Heindel, 2013b); see also www.youtube.com/channel/UCbSytey_jHsjZJ6ZSMFEpsw. Furthermore, the variance, or spread in the individual data points (not to be confused with the composition variance), for this screw rotation orientation is significantly less, and represents a much more consistent mixing process. This low variance is attributed to the relatively small red oak chip agglomerations that occur within the screw mixer at the counter-rotating down-pumping screw rotation orientation, compared to the co-rotating and counter-rotating up-pumping screw rotation orientations. Because the red oak agglomerations are minimal,

the granular material experiences a more uniform distribution throughout the screw mixer, and minimizes periodic fluctuations in the mixing process. This is an important result because it demonstrates that the mixing effectiveness will be more accurately known if choosing the counter-rotating down-pumping screw rotation orientation, compared to the uncertainty in other screw rotation orientations.

The effect of the screw rotation orientation is also shown in Figure 6.4 and resembles similar trends. Most notably, the composition variance is reduced for the counter-rotating down-pumping screw rotation orientation relative to the other orientation, and, in addition to the screw rotation speed, is independent of the material injection configuration. After investigating the response of the composition variance as a function of the screw rotation orientation, it is recommended that the screw mixer be operated in a counter-rotating down-pumping screw rotation orientation in order to reduce the segregation of the granular materials and increase the mixing effectiveness. This result quantitatively confirms the same recommendation made in part one of this study (Kingston and Heindel, 2013b).

6.3.6 Material Injection Configuration

The influence of the material injection configuration on the mixing effectiveness of the screw mixer was shown to be quite significant in part one of this study (Kingston and Heindel, 2013b). However, in part two of this study, only the end products of screw mixer are being considered, and the influence of the material injection configuration only has some minor repercussions, as illustrated in Figure 6.4. It is also worth noting that the material injection configuration is quite different from that of the other three factors being investigated. Its influence on the granular mixing process is magnified at the

location of where this change occurs (i.e., at the beginning of the screw mixer) and is effectively damped as the granular materials are mechanically conveyed away. In contrast, the screw rotation speed, dimensionless screw pitch, and screw rotation orientation influences the granular materials throughout the entire mixing region. Also, the sampling method used in this study evaluates the composition variance between the four outlet ports, which only spans in the horizontal direction. Vertical segregation within the screw mixer was visually observed in part one of this study (Kingston and Heindel, 2013b). This result reiterates the importance of needing both qualitative visualization and quantitation justification to thoroughly characterize the mixing effectiveness of the screw mixer.

Recall that the main-effect term associated with the material injection configuration was not determined to be a statically significant term, as shown in Table 6.1. However, the material injection configuration was determined to be a significant parameter in the three-way interaction between the screw rotation speed, screw rotation orientation, and material injection configuration. For example, consider the change in the shape of the averaging line shown in Figure 6.4 for a screw rotation speed of $\omega = 20$ rpm when the material injection configuration is changed from the red oak chips and glass beads being injected into port one and two (RO 1, GB 2), and port two and one (RO 2, GB 1), respectively. As shown, the composition variance is maximized for a co-rotating screw rotation orientation for material injection configuration one (RO 1, GB 2), and decreases as the screw rotation orientation is changed to counter-rotating up-pumping, and then to counter-rotating down-pumping. Meanwhile, for material injection configuration two (RO 2, GB 1), the composition variance is maximized for a counter-

rotating up-pumping screw rotation orientation and is reduced as the orientation is changed to co-rotating and further reduced when changed to counter-rotating down-pumping. In contrast, for a screw rotation speed of ω = 40 rpm, the opposite trend exists. The composition variance is higher for a counter-rotating up-pumping screw rotation orientation for material injection configuration one (RO 1, GB 2), and then lower when changed to material injection configuration two (RO 2, GB 1). Finally, for the screw rotation speed of ω = 60 rpm, the material injection configuration has a minimal influence on the composition variance because the trends remain relatively unchanged. This change in behavior at different levels of multiple factors is a clear indication of the significance of the higher-order interactions.

Because the effective mixing length for this study was quite large, L/D = 10, it is possible that the majority of the effects of the material injection configuration were not able to propagate all the way to the end of the screw mixer. If the effective mixing length was reduced to L/D = 5 or less, it is likely that the material injection configuration would be more influential and perhaps the main-effect term would be statistically significant.

6.3.7 Screw Mixer Optimization

Overall, the smallest composition variance (i.e., highest mixing effectiveness) was observed at a screw rotation speed of ω = 60 rpm, a dimensionless screw pitch of p/D = 1.75, a screw rotation orientation of counter-rotating down-pumping, and a material injection configuration of the red oak chips and glass beads into port one and two, respectively. This condition represents the optimized condition for the screw mixer used in this study, for the given granular materials and chosen operating conditions. This operating condition produced the highest degree of homogeneity and will ultimately

result in improved mixing performance which could translate to higher heat and/or mass transfer rates in thermochemical conversion processes or improved blend uniformity in food processing applications.

The most influential factors were determined to be the screw rotation orientation and the dimensionless screw pitch, respectively, which are both geometrical factors (i.e., requires geometrical changes to the screw mixer to adjust the levels of these factors). Meanwhile, for the optimized operating condition, the influence of the screw rotation speed on the mixing effectiveness of the screw mixer was minimal. Therefore, for a counter-rotating down-pumping screw rotation orientation, the screw rotation speed could be easily adjusted because it is a continuous variable, allowing user flexibility in terms of material residence time and product output.

6.4 Conclusions

The selection of operating conditions in granular mixing processes is unquestionably important because of its influence on the particle segregation rate. In this study, composition and statistical analysis techniques were used to evaluate the mixing effectiveness of a laboratory-scale double screw mixer. A total of 648 samples were collected using the screw mixer's unique dividing mechanism, and the spatial heterogeneity of the collected samples was analyzed by computing the composition variance. The effect of four factors on the mixing effectiveness was investigated, and a full-factorial design of experiments was employed. After the analysis, eight of the 15 terms in the model equation were determined to be statistically significant, two of which were three-way interaction terms which were used to graphically visualize the effect each

level of factors had on the composition variance. The screw rotation orientation was determined to be the most influential factor, followed by the dimensionless screw pitch. Overall, the composition variance was minimized (i.e., best degree of mixing) for a screw rotation speed of $\omega = 60$ rpm, dimensionless screw pitch of $p/D = 1.75$, counter-rotating down-pumping screw rotation orientation, and material injection configuration of the red oak chips and glass beads being injected into port one and two, respectively. The optimization of the screw mixer's operating conditions will ultimately lead to increased mixture homogeneity and result in improved mixing processes.

Acknowledgements

Support for portions of this work by Phillips 66 Company is gratefully acknowledged.

CHAPTER 7: CHARACTERIZING GRANULAR MIXING HOMOGENEITY AT VARIOUS DIMENSIONLESS MIXING LENGTHS IN A DOUBLE SCREW MIXER[1]

Todd A. Kingston[2] and Theodore J. Heindel

Department of Mechanical Engineering, Iowa State University, Ames, Iowa, 50011, USA

kingston.todd@gmail.com and theindel@iastate.edu

Abstract

Granular mixing processes are commonly used to increase product homogeneity in many industrial applications involving pharmaceuticals, food processing, and energy conversion. Determining the appropriate granular mixing length is necessary to avoid over/under mixing and unnecessary power consumption. Currently, experimental studies are used to provide this critical characterization because the current level of computation simulations in granular mixing processes often falls short, particularly for complex particle and mixer geometries. The goal of this study is to experimentally characterize the

[1] Kingston, T.A., Heindel, T.J. (2014). Characterizing granular mixing homogeneity at various dimensionless mixing lengths in a double screw mixer. ASME FEDSM, Chicago, Illinois, Aug. 3-7, 2014 Paper No. FEDSM2014-21048 (abstract accepted, paper in preparation for submission).

[2] Corresponding author: Todd A. Kingston (kingston.todd@gmail.com)

granular mixing process and determine, under various operating conditions, the needed mixing length to achieve adequate mixing in a laboratory-scale double screw mixer. Nine different combinations of screw rotation speeds and dimensionless screw pitches are used to investigate the rate of mixing at dimensionless mixing lengths of L/D = 2, 5, and 10. Composition and statistical analysis methods are employed, and it is determined that the dimensionless mixing length is the most influential factor in terms increasing granular homogeneity. For all the conditions tested, the granular mixture approaches an acceptable level of mixing for all testing conditions when the dimensionless mixing length is L/D = 10. However, the segregation rate throughout the screw mixer is vastly different for various combinations of screw rotation speed and dimensionless screw pitch, and is partly attributed to the influence of entrance effects caused by the material injection process.

Keywords: Granular mixing, homogeneity, mixing length, screw mixer.

7.1 Introduction

Granular mixing processes are found in a large number of industries including chemical, pharmaceutical, plastics, food and mineral processing, and renewable energy, to name a few. Most commonly, granular mixing processes seek a high degree of homogeneity and in many cases can influence chemical reactions and heat and/or mass transfer rates (Bridgwater, 2012). However, determining granular mixing homogeneity and the necessary mixing time and mixer length in continuous mixing processes is an ambitious task which is often based on exhaustive trial-and-error procedures (Hajra et al., 2010). Currently, there does not exist an accepted set of governing equations for granular

mixing (McCarthy et al., 1996), making computation efforts an ongoing endeavor. Thus, computation models fall short of accurately predicting granular mixing processes, particularly when particle and mixer geometry are complex (Ottino and Khakhar, 2001), resulting in the need for experimental methods.

Previous research efforts in the biomass thermochemical conversion industry have indicated that the operating conditions and material residence time of biomass particles significantly influenced the trade-off between bio-oil and bio-char production (Brown and Brown, 2012a; Mohan et al., 2006). Therefore, accurate control of material residence time is needed to achieve high product yields. However, inappropriately designing the mixing geometry, more specifically the mixer length, and controlling the material residence time by solely changing the operating conditions of the mixer equipment (e.g., impeller rotation speed) can result in undesired characteristics, such as increased power consumption and mechanical wear. Careful consideration must be given to the mixing equipment's design such that under/over mixing is avoided. Therefore, determining the optimal mixing length needed for adequate mixing in continuous mixing processes while still allowing for variability in material residence time is needed, and will minimize under/over mixing, power consumption, and equipment costs.

The goal of this study is to characterize the granular mixing process and determine the necessary dimensionless mixing length needed to achieve adequate mixing in a double screw mixer under various operating conditions. A two-part hypothesis for this study has been proposed: (i) the heterogeneity of the granular mixture would experience an asymptotic reduction as the dimensionless mixing length increased and (ii) the rate of mixing would depend on the operating conditions of the screw mixer.

This paper will begin by briefly describing the experimental procedures, including the screw mixer, granular materials, and composition and statistical analysis methods used in this study. The results of the study will then be presented followed by a thorough discussion with particular emphasis placed on the prescribed hypothesis. Finally, conclusions from the study and suggestions for future work will be made.

7.2 Experimental Procedures

7.2.1 Screw Mixer

Granular mixing studies were conducted in the laboratory-scale double screw mixer shown in Figure 7.1. The screw mixer features two intermeshing noncontact screws with a screw diameter of D = 2.54 cm. One left hand and one right hand threaded screw was used to produce a screw rotation orientation of counter-rotating down-pumping, which was maintained for all experimental tests. Down-pumping refers to the direction of the material flow between the two screws. Kingston and Heindel (2013c) previously determined that the selection of this parameter was the most influential in terms of maximizing the mixing effectiveness of the screw mixer, and was therefore held constant in this study.

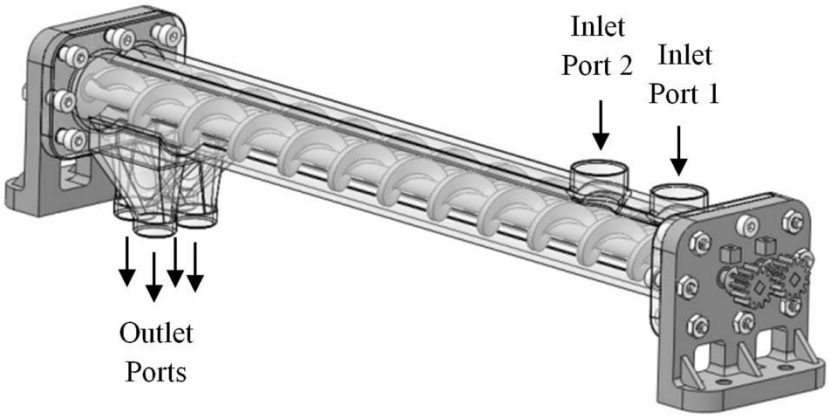

Figure 7.1: Screw mixer used to perform granular mixing studies.

Three different screw mixer housings were designed and constructed, as shown in Figure 7.2, using a rapid prototype machining processes. The housings provided dimensionless mixing lengths of L/D = 2, 5, and 10, respectively, where L is the effective mixing length and D is the screw diameter. The effective mixing length is measured from the centerline of the downstream injection port (port two) to the beginning of the outlets ports in the bottom of the housing. The outlet ports were specifically designed to spatially divide the entire granular flow exit stream into four outlet ports that span in the horizontal direction, allowing the composition variance, s^2, to be computed. Additional details related to the screw mixer design, including the outlet port geometry, can be found in the literature (Kingston and Heindel, 2013d).

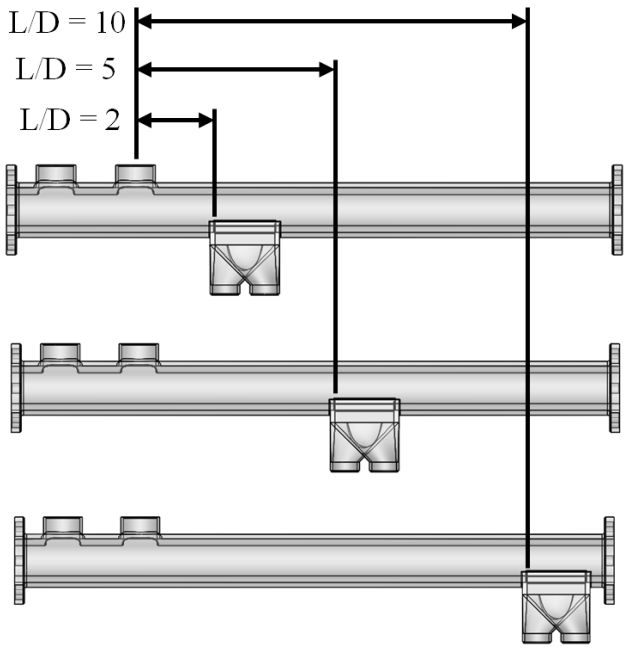

Figure 7.2: Screw mixer housings featuring dimensionless mixing lengths of L/D = 2, 5, and 10.

Nine different operating conditions resulting from the nine combinations of screw rotation speeds at levels of ω = 20, 40, and 60 rpm and dimensionless screw pitch at levels of p/D = 0.75, 1.25, and 1.75, where p is the screw pitch and D is the screw diameter, were tested in this study. By testing the dimensionless mixing lengths influence on the composition variance at different operating conditions, the rate of mixing for these operating conditions could be determined. A randomized full-factorial design of experiments for the 27 different combinations of factors ($3 \times 3 \times 3 = 27$) was used. Three observations were performed at each of the 27 combinations of factors thus totaling 81 observations, and four samples per observation (from the four outlet ports) resulted in 324 samples that were collected and analyzed in this study.

7.2.2 Granular Materials

A binary mixture of red oak chips and glass beads, as shown in Figure 7.3, were mechanically mixed inside the screw mixer. The red oak chips have a particle size ranging from 500 to 6350 μm and an average true density, measured with a pycnometer, of 1350 kg m^{-3}. The glass beads have a particle size ranging from 300 to 500 μm and a true density of 2510 kg m^{-3}. Red oak chips and glass beads were chosen because of their similar material properties to that of biomass and heat carrier media, respectively, which are used in the biomass thermochemical conversion industry. Because the granular materials differ in size, shape, and density, they are subject to percolation and buoyance forces which ultimately lead to segregation. The granular materials are metered into the screw mixer by two independent Tecweigh volumetric auger feeders, and are injected vertically downward into the injection ports. A material injection configuration which featured the red oak chips and glass beads being injected into port one and two, respectively, was maintained for all test conditions per the recommendations made by Kingston and Heindel (2013b). Other parameters which were held constant include a 10:1 glass beads to red oak chips mass flow rate ratio because of its relevance in biomass thermochemical conversion processes, and a 65% total volumetric fill ratio, which is based on decades of experience by researchers in screw conveying applications (Colijn, 1985).

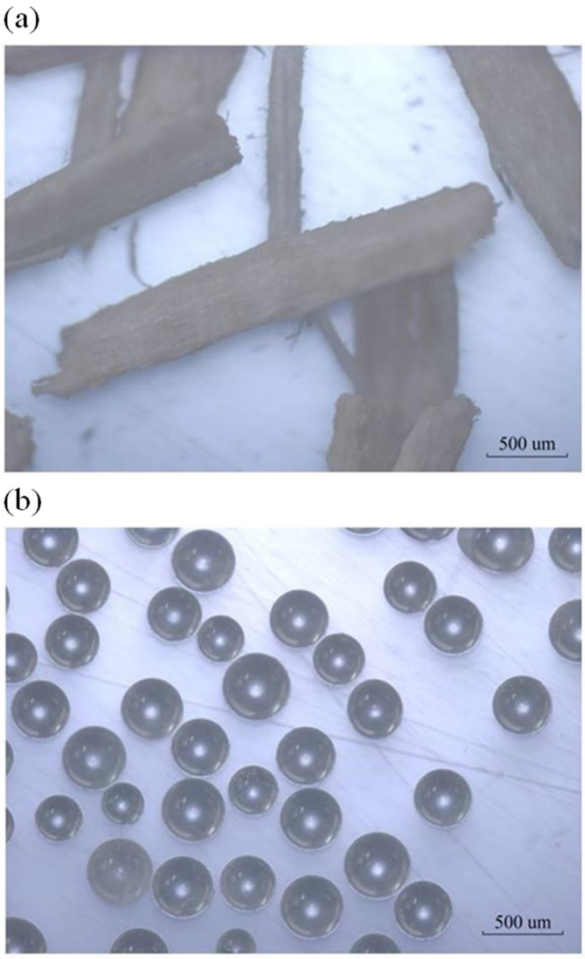

Figure 7.3: Magnified images of (a) 500-6350 μm red oak chips and (b) 300-500 μm glass beads.

7.2.3 Composition Analysis

The evaluation of granular mixing processes often involves the collection and composition analysis of samples. The methods outlined by Kingston and Heindel (2013d) were used to determine the composition of the individually collected samples and compute the composition variance, s^2. These methods evaluate the mixing effectiveness of the screw mixer by measuring the spatial heterogeneity from the four outlet ports, which divide the entire granular flow exit stream into separate channels across the exit. A composition variance equal to zero corresponds to a homogeneous mixture (within the

ability to detect spatial differences using these methods), and represents the best case scenario. As the magnitude of the composition variance increases, the mixing process effectively worsens, and the mixture becomes more segregated. Note that this procedure allows segregation quantification between the screw mixer's outlet ports, but segregation within the individual outlet ports is not quantified.

7.2.4 Statistical Analysis

After performing the composition analysis, statistical analysis methods are used to relate the composition variance to the different dimensionless mixing lengths and operating conditions, allowing the most influential factors to be determined. The model equation which was fitted to the experimental data and corresponds to the design of experiments used in this study is:

$$y_{ijkl} = \mu + \alpha_i + \beta_j + \delta_k + \gamma_{ij}^{12} + \gamma_{ik}^{13} + \gamma_{jk}^{23} + \gamma_{ijk}^{123} + \varepsilon_{ijkl} \qquad (7.1)$$

where y_{ijkl} is the measured response variable (i.e., composition variance); μ is the mean response averaged over all levels of all factors; α_i, β_j, and δ_k are the effects of the main-effect factors (i.e., screw rotation speed, dimensionless screw pitch, and dimensionless mixing length); γ_{ij}^{12}, γ_{ik}^{13}, and γ_{jk}^{23} are the two-way interaction effects; γ_{ijk}^{123} is the three-way interaction effect; and ε_{ijkl} is the random deviation from the true treatment mean (DeVore, 2008). Three observations were performed at each of the 27 combinations of factors; thus "el" ranges from one to L, where L = 3.

To determine the significance of the seven terms in the model equation, seven hypotheses were tested, one for each of the terms listed above. However only the first two and the last hypothesis are shown here:

$$
\begin{array}{llllll}
H_{o,1}: & \alpha_1 = \ldots = \alpha_I = 0 & \text{versus} & H_{a,1}: & \text{at least one } \alpha_i \neq 0 & \\
H_{o,2}: & \beta_1 = \ldots = \beta_J = 0 & \text{versus} & H_{a,2}: & \text{at least one } \beta_j \neq 0 & (7.2) \\
\ldots & & & & & \\
H_{o,123}: & \gamma_{ijk}^{123} = 0 \text{ for all i, j, k} & \text{versus} & H_{a,123}: & \text{at least one } \gamma_{ijk}^{123} \neq 0 &
\end{array}
$$

where I, J, and K are the number of levels of factor one through three, respectively (DeVore, 2008). The F-test statistic and its corresponding p-value are used to determine if the null hypotheses failed to be rejected or were rejected in favor of the alternative hypotheses at an alpha level of 0.05.

7.3 Results and Discussion

Previous studies by Kingston and Heindel (2013b) focused on performing optical visualization of the dynamic granular mixing process inside the screw mixer. Four cameras were used to capture the mixing process from the left, top, right, and bottom projections. A static image taken from the dynamic mixing process is shown in Figure 7.4. The four different projections (i.e., left, top, right, and bottom) are spatially aligned and temporally synced. The red oak chips appear brown and the glass beads appear gray. The granular materials are injected into the material injection ports shown on the left side of the image, and are mechanically mixed and conveyed from left to right before exiting the screw mixer through the four outlet ports in the bottom of the screw mixer. The operating condition of the screw mixer shown in Figure 7.4 are a screw rotation speed of $\omega = 60$ rpm, a dimensionless screw pitch of $p/D = 0.75$, and a dimensionless mixing length of $L/D = 10$. These previous studies by Kingston and Heindel (2013b) only focused on capturing mixing videos for a screw mixer with a dimensionless mixing

length of L/D = 10, therefore shorter dimensionless mixing lengths are not available. However, the approximate location of the outlet ports for dimensionless mixing lengths of L/D = 2 and 5 as shown in Figure 7.4.

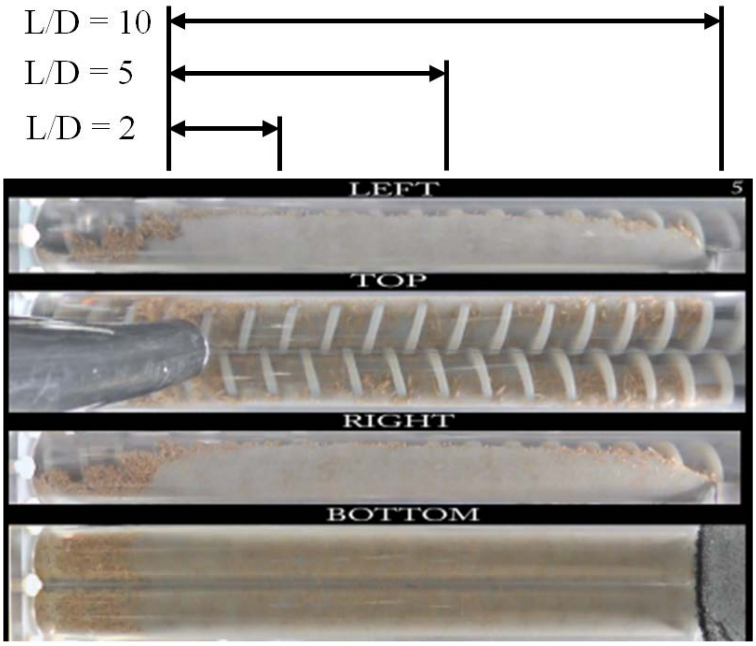

Figure 7.4: Snapshot of the dynamic mixing process inside the screw mixer with a dimensionless screw pitch of p/D = 0.75.

7.3.1 ANOVA

The key parameters of the analysis are summarized in the ANOVA table shown in Table 7.1, where the degrees of freedom are symbolized by df, the sum of squares by SS, the mean square by MS, and the F-test statistic by F. For the terms to be declared statistically significant, their corresponding p-value must be less than the alpha level of 0.05. As shown, six of the seven terms are statistically significant, with only the main-effect term associated with the screw rotation speed being declared nonsignificant. The model equation had a coefficient of determination of $R^2 = 0.948$.

Table 7.1: ANOVA table illustrating the key statistical parameters in the model equation [Eqn. (7.1)].

ANOVA Table						
Source	**df**	**SS**	**MS**	**F**	**p-value**	**Significant**
Screw Rotation Speed	2	$2.10E^{-7}$	$1.07E^{-7}$	2.87	0.065	N
Dimensionless Screw Pitch	2	$5.12E^{-6}$	$2.56E^{-6}$	70.82	< 0.001	Y
Dimensionless Mixing Length	2	$9.41E^{-6}$	$4.71E^{-6}$	130.10	< 0.001	Y
Screw Rotation Speed × Dimensionless Screw Pitch	4	$1.53E^{-6}$	$3.82E^{-7}$	10.55	< 0.001	Y
Screw Rotation Speed × Dimensionless Mixing Length	4	$1.34E^{-6}$	$3.34E^{-7}$	9.25	< 0.001	Y
Dimensionless Screw Pitch × Dimensionless Mixing Length	4	$1.69E^{-5}$	$4.22E^{-6}$	116.56	< 0.001	Y
Screw Rotation Speed × Dimensionless Screw Pitch × Dimensionless Mixing Length	8	$9.20E^{-7}$	$1.14E^{-7}$	3.16	0.005	Y
Error	54	$1.95E^{-6}$	$3.62E^{-8}$			
Total	80	$3.73E^{-5}$				

As indicated by their respective p-values, all of the terms in the model equation were determined to be statistically significant, except for the main-effect term associated with the screw rotation speed. Furthermore, the three-way interaction term was determined to be statistically significant, thus it must be further investigated for an indication into the effect that each of the levels of factors have on the composition variance. From the ANOVA results shown in Table 7.1, it is obvious that the dimensionless mixing length had the most influence on the granular mixing process because of its high F value (130.10) and corresponding low p-value (< 0.001). The dimensionless screw pitch was the second most influential parameter with an F value of 70.82 and a p-value of < 0.001, and when combined with the dimensionless mixing length, these two factors produced the most influential two-way interaction term which yielded an F value of 116.56 and a p-value of < 0.001. However, in order to identify

which levels of factors produce the most desirable operating conditions, the three-way interaction term must be visualized.

7.3.2 Visualizing Factor Interaction

The three-way interaction term is shown graphically in Figure 7.5, and provides critical information relating the various levels of each factor to its influence on the composition variance. For convenience, an averaging line was added to each of the nine plots to help identify trends. The nine plots correspond to the nine different operating conditions resulting from all the possible combinations of screw rotation speed and dimensionless screw pitch. Plotted on the left vertical axis is the composition variance, s^2. Recall that a composition variance of zero corresponds to a homogeneous mixture and is the desired state of mixing. The top and bottom horizontal axes display the dimensionless screw pitch, p/D, and the dimensionless mixing length, L/D, respectively. The screw rotation speed, ω, is plotted on the right vertical axis. The three data points at each dimensionless mixing length for each operating condition correspond to the three observations that were performed. A high degree of repeatability was present, as indicated by the small variance (not to be confused with the composition variance) within the three observations.

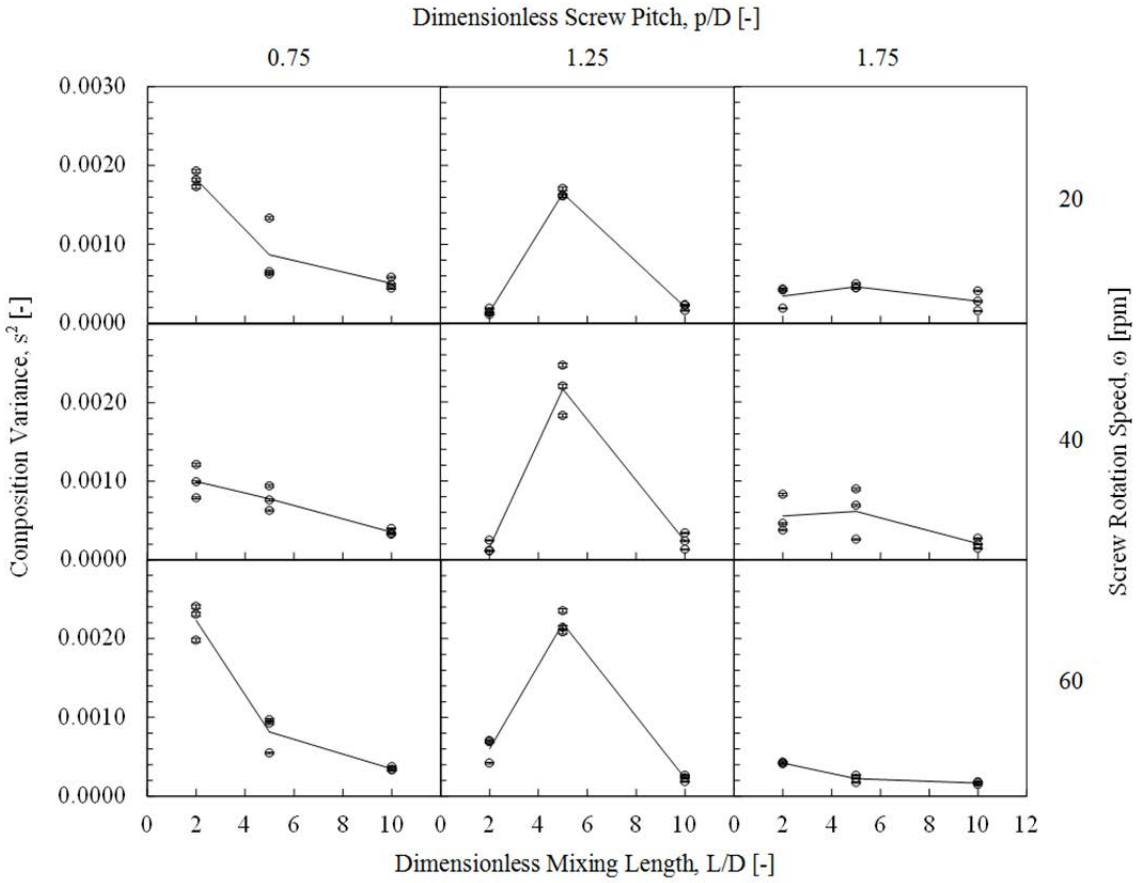

Figure 7.5: Composition variance as a function of the three-way interaction between the screw rotation speed, ω, dimensionless screw pitch, p/D, and dimensionless mixing length, L/D.

7.3.3 Uncertainty Analysis

An uncertainty analysis was performed to quantify the error associated with the composition variance using Taylor's series expansion propagation of error procedure (Ku, 1966). Overall, the uncertainty in the composition variance, U_{s^2}, ranged from 1 to 5% of the composition variance, s^2, and is shown in Figure 7.5 by vertical error bars overlaid on the data points; all error bars fall within the circular symbols. This error is only associated with the determination of the composition variance and is not associated with the variance within the factors themselves, which is shown graphically by the spread of the three observations, and was quantified using the prescribed ANOVA methods.

7.3.4 Interpreting Factor Interaction

Before interpreting the factor interaction, it is important to mention that when the granular materials are injected into the screw mixer, they undergo a very chaotic process because they bounce off the geometrical features of the screw mixer (e.g., screws, housing, etc.) and consequently are fairly well distributed within the screw mixer, as shown on the left side of the image in Figure 7.4. Furthermore, the material injection configuration used in this study featured the larger, less dense red oak particles being injected into port one, and the smaller, denser glass being injected into port two. This configuration was chosen because the granular materials would be positioned in such a way that it would induce a natural mixing process caused by percolation and buoyant forces, as noted by Kingston and Heindel (2013b). Thus, there essentially exists an entrance region “boundary condition” which features a relatively low composition variance at short mixing lengths. This is analogous to internal fluid flow in pipes, which features a region where the flow is still being influenced by the upstream features (i.e., developing flow) before it reaches a state of fully developed flow. This same behavior exists near the inlet and outlet of the screw mixer. The granular material begins to experience changes in its flow structures and mixing process due to the entrance/exit of the material upstream/downstream of the point of interest. Because the material experiences minimal mixing near these boundary conditions, the actual “mixing length” of the screw mixer is effectively shortened. Thus, instead of sampling the mixture at L/D = 10, for example, it is effectively being sampled slightly upstream from this location. This behavior does not appear to have any influence on the mixing

quantification results because the selection of the sampling location, in terms of the dimensionless mixing length, is arbitrary.

These effects were noted in previous studies by Kingston and Heindel (2013b) which featured the visualization of the dynamic mixing process from the entire screw mixer's periphery. As a result, these effects must be taken into consideration when interpreting the results of this study in order to fully understand the granular mixing behavior.

The following three sections separate the three different levels of the dimensionless screw pitch, and consider the effects of the screw rotation speed and dimensionless mixing length within each section. Comparisons between different levels of dimensionless screw pitch are then explicitly compared. This presentation methodology is utilized because of the vastly different results found at each of the dimensionless screw pitches.

7.3.4.1 Dimensionless Screw Pitch of p/D = 0.75

First consider the response of the composition variance versus the dimensionless mixing length at the three levels of the screw rotation speed, while holding the dimensionless screw pitch constant at p/D = 0.75. As shown, there appears to be an asymptotic reduction in the composition variance as the dimensionless mixing length increases and this trend remains fairly consistent for all three screw rotation speeds. For example, for a screw rotation speed of ω = 20 rpm, the composition variance is approximately equal to 0.0018 at L/D = 2, and then reduces by approximately 50% to about 0.0009 at L/D = 5, and then is further reduced by approximately 50% to approximately 0.0005 at L/D = 10. This result confirms part one of the aforementioned

hypothesis, at least for a dimensionless screw pitch of p/D = 0.75, that there is an asymptotic reduction in the composition variance as the dimensionless mixing length increases.

Despite similar trends, the magnitude of the composition variance in the first half of the screw mixer (i.e., before L/D = 5) varies as the screw rotation speed varies, and is significantly lower for ω = 40 rpm (s^2 = 0.0010) than it is for ω = 20 and 60 rpm (s^2 = 0.0018 and 0.0022, respectively). However, the differences in the composition variance at L/D = 2 are minimized as the granular material moves through the screw mixer and approaches L/D = 5 and 10 because all three levels of the screw rotation speed now exhibit nearly identical composition variances of approximately s^2 = 0.0008 and 0.0005, respectively. This difference is a clear indication into why the statistical analysis indicated that the screw rotation speed is one of the three significant factors in three-way interaction term.

The dimensionless screw pitch of p/D = 0.75 features a screw flighting profile which is primarily perpendicular to the axial flow direction, as shown in Figure 7.4. Furthermore, there are a relatively large number of flights in a short distance. The previously noted entrance effects are unable to propagate into the screw mixer very far into the screw mixer because of these two geometric constraints, and may be on the order of one dimensionless mixing length (L/D = 0.5). This allows segregation to take place at relatively short mixing lengths, and is the reason for the large composition variance at L/D = 2.

7.3.4.2 Dimensionless Screw Pitch of p/D = 1.25

Unlike the continuous reduction in composition variance as a function of dimensionless mixing length shown for p/D = 0.75, the dimensionless screw pitch of p/D = 1.25 shows vastly different behavior. As shown in Figure 7.5, the granular material indicates minimal segregation at L/D = 2 and 10, but a large increase in composition variance occurs at L/D = 5, indicating a high degree of segregation. Initially, it was thought to be user error during the sample collection and/or analysis process. Thus, three additional independent observations were conducted at dimensionless mixing lengths of L/D = 2 and 5 for a dimensionless screw pitch of p/D = 1.25; totaling 6 observations (3 original + 3 repeated = 6) at each of these conditions. However, after analyzing and plotting the additional observations, the new data points were essentially overlaid on the old data points and displayed a highly degree of reproducibility; eliminating the likelihood for user error and confirming the trend shown in Figure 7.5.

The shape of the screw flight profile for a screw which features a dimensionless screw pitch of p/D = 1.25 is slightly rotated such that it offer less restriction in the axial direction, and has fewer screw flights in the same axial distance relative to the dimensionless screw pitch of p/D = 0.75. This change in screw geometry is illustrated in Figure 7.6. As a result, when the granular materials enter the screw mixer for a dimensionless screw pitch of p/D = 1.25, they almost instantaneously begin to leave the screw mixer when the outlet ports are positioned at L/D = 2. Therefore, segregation does not have adequate time to take place and the composition variance initially remains fairly low. In other words, by changing the dimensionless screw pitch from p/D = 0.75 to 1.25, the entrance effects are being prolonged a further distance into the screw mixer.

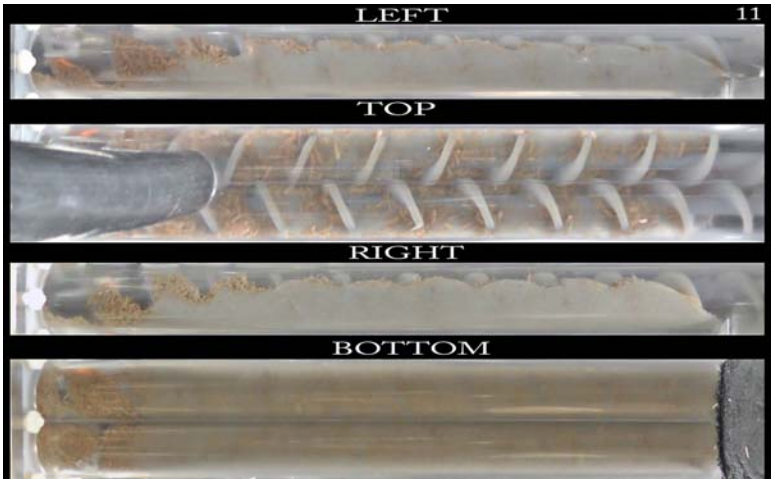

Figure 7.6: Snapshot of the dynamic mixing process inside the screw mixer with a dimensionless screw pitch of p/D = 1.25.

As the dimensionless mixing length increases to L/D = 5, the material residence time increases and the granular mixture simultaneously segregates and mixes, with segregation taking place at a much higher rate causing the large increase in the composition variance. As the screw mixer continues to mix the two granular components together, it begins to break up the red oak agglomerations, causing the mixture to become more homogeneous and resulting in a reduction in the composition variance near L/D = 10, as shown on the right side of Figure 7.6.

The effect of the screw rotation speed does not have a significant influence on the mixing effectiveness at a dimensionless screw pitch of p/D = 1.25. This is shown by the relatively unchanged results shown in Figure 7.5.

7.3.4.3 Dimensionless Screw Pitch of p/D = 1.75

As part two of the study hypothesis stated, the rate of reduction in the heterogeneity of the granular material as a function of dimensionless mixing length is expected to depend on the operating conditions of the screw mixer. Therefore, it is not surprising that the behavior of the composition variance for the dimensionless screw pitch

of p/D = 1.75 is vastly different than it is for either the p/D = 0.75 or 1.25 case. As shown in Figure 7.5, the magnitude of the composition variance at L/D = 2 for p/D = 1.75 is substantially lower than it is for p/D = 0.75, and approximately the same as the p/D = 1.25 case. This is once again a consequence of the entrance regions effects being prolonged in the screw mixer. As the granular materials begin to propagate through the screw mixer and reach L/D = 5, the composition variance is much lower than it is for either the p/D = 0.75 or 1.25 case because the longer dimensionless screw pitch offers an advantageous mixing process and produces a more homogeneous mixture, as shown in Figure 7.7. The mixing of the two granular materials continues and the composition variance reduces as the mixture exits the screw mixer at L/D = 10.

In this study, and previous studies (Kingston and Heindel, 2013b, c, d; Uchida and Okamoto, 2008), it has been shown that increasing the dimensionless screw pitch increased the mixing effectiveness in screw mixing applications.

Similar to the dimensionless screw pitch of p/D = 1.25, the screw rotation speed had a small, but slightly noticeable influence on the mixing effectiveness of the screw mixer for a dimensionless screw pitch of p/D = 1.75. In previous studies, Kingston and Heindel (2013c) noted that higher screw rotation speeds produced a more chaotic mixing process and increased the mixing effectiveness; a result which also shown in Figure 7.5 by the reduction in composition variance as the screw rotation speed increases from ω = 20 rpm to ω = 60 rpm. However, only a slight reduction in the composition variance is observed as the screw rotation speed increases.

This independence from the screw rotation speed coupled with its relatively low composition variance is why this geometrical configuration (p/D = 1.75) offers a mixing

process which will produce more adequate mixing in a much shorter mixing length (and consequently less time), than the other conditions. A favorable result as this will minimize power input and equipment costs.

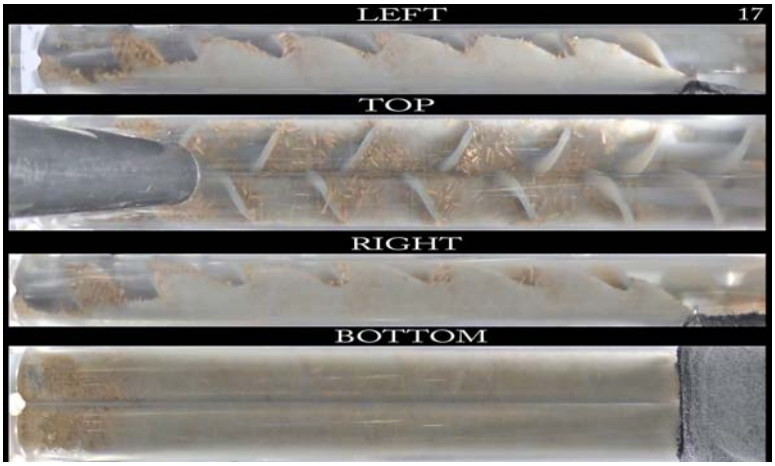

Figure 7.7: Snapshot of the dynamic mixing process inside the screw mixer with a dimensionless screw pitch of p/D = 1.75.

7.4 Conclusions

Overall, the granular mixture approaches an acceptable level of homogeneity as the dimensionless mixing length nears L/D = 10 for all nine operating conditions, as shown in Figure 7.5. The screw rotation speed had a moderate influence on the mixing process at a dimensionless screw pitch of p/D = 0.75, but a minimal influence at p/D = 1.25 and 1.75. However, the dimensionless screw pitch had a dramatic influence on two major items: (i) the distance that the entrance effects were able to propagate into the screw mixer and (ii) the mixing effectiveness of the screw mixer. A screw rotation speed of ω = 60 rpm and a dimensionless screw pitch of p/D = 1.75 reduced the degree of heterogeneity within the granular mixture and was found to be relatively independent of the dimensionless mixing length. This operating condition represents the optimal

operating condition for the factors considered in this study, and allows the user to make design decisions based on material residence time considerations and not based on mixing effectiveness.

To fully confirm the hypothesis that increasing the dimensionless screw pitch allows the entrance effects to penetrate further into the screw mixer, addition tests would need to be conducted. These tests would need to sample the granular material with finer resolution in terms of the dimensionless mixing lengths, perhaps on the order of L/D = 1 across the entire screw mixer length. By only sampling the granular mixture at three axial locations used in this study, the influence of the entrance effects can only by proposed, and cannot be confirmed. However, performing these additional tests would require the construction of a series of mixers or a mixer with a variable sampling location; resulting in additional equipment costs. Obviously this reinforces the need for the development of more accurate granular mixing computation models.

Acknowledgements

Support for portions of this work by Phillips 66 Company is gratefully acknowledged.

CHAPTER 8: ASSESSMENT OF THE MIXING EFFECTIVENESS OF A SINGLE SCREW MIXER

8.1 Introduction

Mixers featuring a single convective mixing component (e.g., impeller, screw, etc.) are found in a wide number of processes. More rarely found are mixers that feature two or more mixing components, partly due to the increased mechanical complexity. However, many times, mixers with more than one convective mixing device do provide beneficial results. For example, Camp (1990) noted that double screw configurations experience a reduced power consumption and exhibit an increased mixing effectiveness relative to single screw configurations.

One objective of this project was to investigate the mixing effectiveness of a single screw mixer, and compare its mixing effectiveness to the double screw mixer. Thus, the goal of this study was to: (i) qualitatively and quantitatively assess the mixing effectiveness of a single screw mixer under various operating conditions, (ii) indicate the most influential factors contributing to mixing performance, and (iii) compare the single and double screw mixers in terms of their mixing effectiveness.

8.2 Methods

The single screw mixer that was described in Chapter 3 was used to perform granular mixing studies. The same red oak chips and glass beads that were used throughout this project were used in this study. However, unlike the double screw mixer,

which featured four outlet ports, the single screw mixer only featured two outlet ports. This design change was a result of the reduced size of the single screw mixer relative to the double screw mixer, and the rather large red oak chips that were used. As a result, a direct quantitative comparison between the single and double screw mixer could not be made using the composition and statistical analysis, resulting in the need for qualitative comparison via optical visualization.

The methods used to accomplish this goal were identical to the methods outlined in Chapter 4, and used in Chapters 5 and 6. In other words, qualitative optical visualization was captured using four spatially aligned and temporally synced video projections and quantitative composition and statistical analysis methods were employed. The optical visualization allowed for a qualitative assessment of the single screw mixers mixing effectiveness, and enabled comparisons between the single and double screw mixer to be made. The composition and statistical analysis enabled the effects of the single screw mixer's operating conditions on the mixing effectiveness to be investigated, but could not be used to compare to the double screw mixer for the aforementioned reasons.

The influences of three factors were investigated: (i) screw rotation speed at levels of ω = 20, 40, and 60 rpm; (ii) dimensionless screw pitch at levels of p/D = 0.75, 1.25, and 1.75; and (iii) material injection configuration at levels of the red oak chips and glass beads being injected into port one and two, and two and one, respectively. These factors and their corresponding levels were identical to those investigated in the double screw mixer studies, with the exception of the screw rotation orientation because this factor does not exist in the case of the single screw mixer. A total of 18 different operating

conditions ($3 \times 3 \times 2 = 18$) are possible from these combinations of factors and levels, and all 18 conditions were tested in this study. The details for all 18 different operating conditions are shown in Table 3.4. A randomized full-factorial design of experiments methodology was used. Moreover, three observations were performed at each operating condition, resulting in 54 different trials. Two samples were collected (corresponding to the two outlet ports in the single screw mixer) for each trial, resulting in 108 samples that were collected and analyzed in this study. The composition variance between the two outlet ports was computed to provide a gross indication into the mixing effectiveness of the single screw mixer. A three-way full-factorial ANOVA model was applied using JMP Pro 10, and the resulting model equation is:

$$y_{ijkl} = \mu + \alpha_i + \beta_j + \delta_k + \gamma_{ij}^{12} + \gamma_{ik}^{13} + \gamma_{jk}^{23} + \gamma_{ijk}^{123} + \varepsilon_{ijkl} \tag{8.1}$$

where y_{ijkl} is the measured response variable (i.e., composition variance); μ is the mean response averaged over all levels of all factors; α_i , β_j, and δ_k are the effects of the main-effect factors; γ_{ij}^{12}, γ_{ik}^{13}, and γ_{jk}^{23} are the two-way interaction effects; γ_{ijk}^{123} is the three-way interaction effect; and ε_{ijklm} is the random deviation from the true treatment mean (DeVore, 2008). The three observations that were performed at each operating condition result in “el” ranging from one to L, where L = 3.

To determine the significance of the seven effect terms in the model equation, seven hypotheses were tested, one for each of the terms listed above. Due to the large number of hypotheses, only the first two and the last hypotheses are shown here:

$$H_{o,1}: \quad \alpha_1 = \ldots = \alpha_I = 0 \quad \text{versus} \quad H_{a,1}: \quad \text{at least one } \alpha_i \neq 0$$

$$H_{o,2}: \quad \beta_1 = \ldots = \beta_J = 0 \quad \text{versus} \quad H_{a,2}: \quad \text{at least one } \beta_j \neq 0 \qquad (8.2)$$

...

$$H_{o,123}: \quad \gamma_{ijk}^{123} = 0 \text{ for all i, j, k} \quad \text{versus} \quad H_{a,123}: \text{ at least one } \gamma_{ijk}^{123} \neq 0$$

where I, J, and K are the number of levels of factor one through three, respectively. In other words, the null hypotheses suggest that each term in the model equation does not have a significant influence on the composition variance, while the alternative hypotheses suggest that at least one of the levels from each term does have an effect on the composition variance. Therefore, these statistical tests require evidence to prove that the factors are significant. In this study, I and J are equal to three because factors one and two (i.e., screw rotation speed and dimensionless screw pitch) were all tested at three different levels (e.g., ω = 20, 40, and 60 rpm). Meanwhile, K = 2, and corresponds to the two different material injection configurations. The F-test statistic and its corresponding p-value were used to determine if the null hypotheses failed to be rejected or were rejected in favor of the alternative hypotheses at an alpha level of 0.05.

8.3 Results and Discussion

8.3.1 Optical Visualization

Optical visualization of the dynamic mixing process was captured for each of the 18 aforementioned operating conditions. However, the results of the composition and statistical analysis indicated that not all of the 18 operating conditions produced statistically different results, as will be shown in the following section. A significant difference was only noticed when the material injection configuration was swapped, for a

dimensionless screw pitch of p/D = 1.25. Figure 8.1 displays snapshots of the dynamic mixing process for operating conditions 9s and 10s. Operating conditions 9s and 10s feature screw rotation speeds of ω = 40 rpm, dimensionless screw pitches of p/D = 1.25, and material injection configurations with the red oak chips and glass beads being injected into port one and two, and two and one, respectively. In Figure 8.1, the red oak chips appear brown and the glass beads appear gray, and were injected through the dark polyethylene tubes shown in the top projection. The granular materials are mechanically mixed and conveyed from left to right and exit the single screw mixer through the two outlet ports shown on the right edge of the bottom projection.

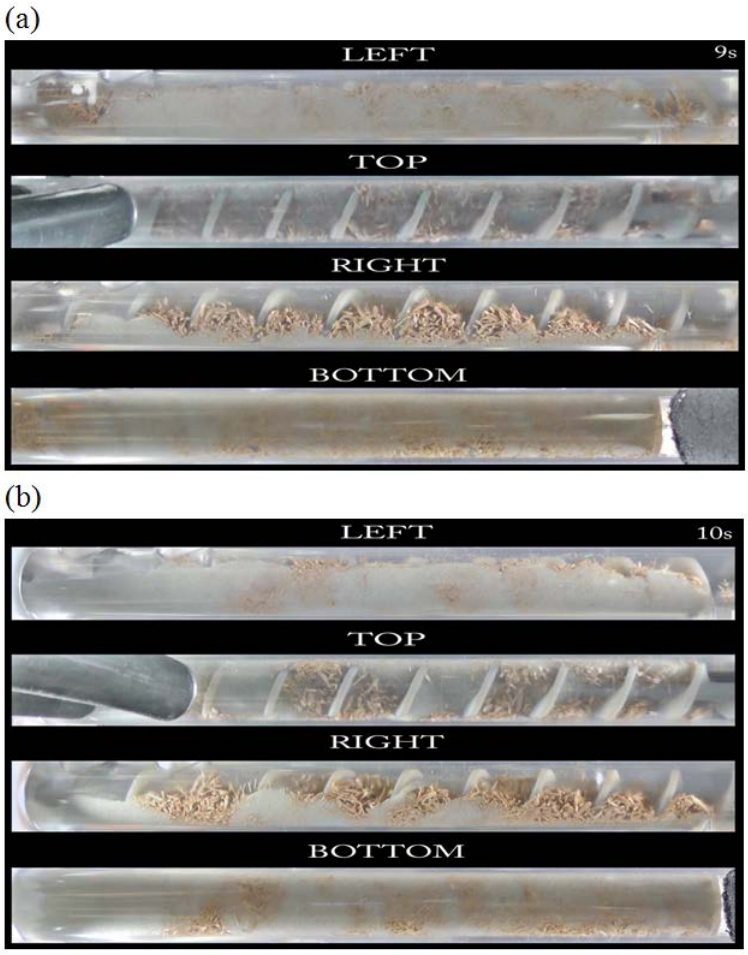

Figure 8.1: Snapshots of the single screw mixer's dynamic mixing processes captured using the optical visualization methods for operating conditions (a) 9s and (b) 10s.

The most noticeable difference between operating conditions 9s and 10s are that when the red oak chips are being injected into port one (i.e., operating condition 9s), the red oak chips are fairly well distributed between each screw flight. Then, a fairly uniform amount of glass beads are dropped on top of the red oak chips in between each screw flight. This behavior produces a granular mixture that exhibits a fairly uniform granular bed as a function of the single screw mixer's axial direction. In contrast, when the red oak chips are being injected into port two (i.e., operating condition 10s), the red oak chips periodically agglomerate, resulting in regions of high and low red oak chip

concentrations. This phenomenon is most easily visualized in the top and right projections of Figure 8.1b. This behavior is undesired because it causes additional segregation between the red oak chips and glass beads, and produces an unpredictable mixing process.

While operating condition 9s resulted in a higher mixing effectiveness relative to operating condition 10s, at least qualitatively, it still showed a considerable large amount of segregation. Moreover, the dynamic mixing process for all the single screw mixer's videos showed a larger amount of segregation relative to the double screw mixer's videos. The single screw mixer appears to convey the granular materials more than mixing them, resulting in a lower mixing effectiveness.

8.3.2 Composition and Statistical Analysis

The influence that the main-effect and interaction terms, shown in Eqn. (8.1), had on the composition variance were quantified using the three-way ANOVA procedure. The key parameters of the analysis are summarized in the ANOVA table shown in Table 8.1, where the degrees of freedom are symbolized by df, the sum of squares by SS, the mean square by MS, and the F-test statistic by F. For the terms to be declared statistically significant, their corresponding p-value must be less than the alpha level of 0.05. As shown, three of the seven terms are statistically significant; two main effect terms and one two-way interaction term. The model equation had a coefficient of determination of $R^2 = 0.643$; thus, the model equation did not fit the experimental data very well, for reasons which will be discussed in the following section.

Table 8.1: ANOVA table illustrating the key statistical parameters in the model equation [Eqn. (8.1)].

ANOVA Table						
Source	**df**	**SS**	**MS**	**F**	**p-value**	**Significant**
Screw Rotation Speed	2	$2.93E^{-6}$	$1.50E^{-6}$	0.724	0.492	N
Dimensionless Screw Pitch	2	$5.82E^{-5}$	$2.91E^{-5}$	14.385	< 0.001	Y
Material Injection Configuration	1	$2.09E^{-5}$	$2.09E^{-5}$	10.311	0.003	Y
Screw Rotation Speed × Dimensionless Screw Pitch	4	$5.51E^{-6}$	$1.40E^{-6}$	0.681	0.610	N
Screw Rotation Speed × Material Injection Configuration	2	$1.51E^{-6}$	$8.00E^{-7}$	0.374	0.691	N
Dimensionless Screw Pitch × Material Injection Configuration	2	$4.05E^{-5}$	$2.03E^{-5}$	10.020	< 0.001	Y
Screw Rotation Speed × Dimensionless Screw Pitch × Material Injection Configuration	4	$1.89E^{-6}$	$5.00E^{-7}$	0.234	0.918	N
Error	36	$7.28E^{-5}$	$7.73E^{-6}$			
Total	53	$2.04E^{-4}$				

As shown in Table 8.1, the main-effect terms associated with the dimensionless screw pitch and the material injection configuration, and the two-way interaction term between the dimensionless screw pitch and the material injection configuration were determined to be statistically significant. The main-effect term associated with the screw rotation speed, and all the higher order interaction terms which included the screw rotation speed, including the three-way interaction between all the factors, were determined to be nonsignificant.

While Table 8.1 indicates which factors are significant, it does not indicate which levels of these factors are significant. Thus, the highest order significant term in the model equation (i.e., the two-way interaction terms associated with the interaction between the dimensionless screw pitch and the material injection configuration) needs to be visualized, which is shown in Figure 8.2. The filled triangular symbols represent data points that were collected for the three levels of the dimensionless screw pitch at a material injection configuration featuring the red oak chips and glass beads injected into

port one and two, respectively. A solid averaging line that connects the average composition variance at each level of the dimensionless screw pitch is shown for this material injection configuration to help identify trends. Moreover, the open square symbols represent data points that were collected for the three levels of the dimensionless screw pitch at a material injection configuration featuring the red oak chips and glass beads injected into port two and one, respectively. Likewise, a dotted averaging line that connects the average composition variance at each level of the dimensionless screw pitch is shown for this material injection configuration. The nine different data points shown for each combination of dimensionless screw pitch and material injection configuration correspond to the three different observations that were performed at the three different levels of the screw rotation speed ($3 \times 3 = 9$). Note that a small composition variance corresponds to a more homogeneous mixture, and is the preferred state of mixing.

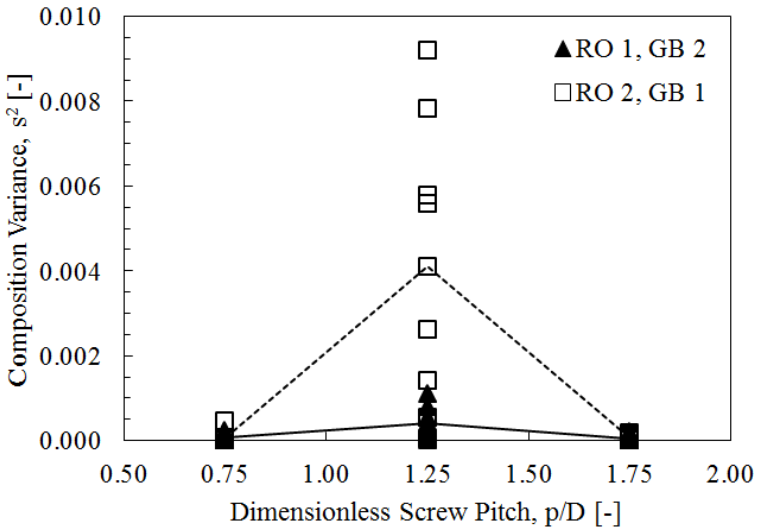

Figure 8.2: Composition variance as a function of the two-way interaction between the dimensionless screw pitch and the material injection configuration.

As shown in Figure 8.2, the level of the dimensionless screw pitch makes a considerable difference in the collected sample's composition variance. At dimensionless

screw pitches of p/D = 0.75 and 1.75, a minimal difference in the composition variance exists for the two different levels of the material injection configuration. Whereas for the dimensionless screw pitch of p/D = 1.25, the level of the material injection configuration results in a large change in the composition variance. When the single screw mixer featured the red oak chips and glass beads being injected into port one and two, respectively, a relatively small composition variance was found for each observation. In contrast, a wide range of composition variances were found when the material injection configuration was changed, resulting in a much higher average composition variance. This change in the composition variance for two different levels of the material injection configuration at only one of the three levels of the dimensionless screw pitch is a clear indication as to why the two-way interaction term between these two factors in the model equation was determined to be statistically significant.

The large variance (not to be confused with the composition variance) found at this condition is thought to be attributed to a phenomenon similar to aliasing. More specifically, the periodic fluctuations in the volumetric feeder's red oak chip flow rate is aligned in such a way with the dimensionless screw pitch of p/D = 1.25 that it causes the large red oak agglomerations to occur in about every other screw flight opening, as was noted in the previous optical visualization results and shown in Figure 8.1. The large composition variances that are shown in some of the data points in Figure 8.2 are obtained when the collected granular samples include these large red oak agglomerations. Meanwhile, the lower composition variance data points occur when the granular samples do not include these agglomerations.

Overall, the low composition variances associated with remaining operating conditions are a result of the reduced number of outlet ports used in the single screw mixer. Dividing the granular flow into only two separate channels, compared to four separate channels as was done in the double screw mixer studies, results in the granular mixture to appear more homogeneous. This behavior is the obvious reason for a two part measurement techniques which couples qualitative optical visualization and quantitative composition and statistical analysis techniques. Moreover, it results in the inability to quantitatively compare the single and double screw mixers.

8.4 Conclusions

The amount of segregation visualized in the mixing videos for the single screw mixer was considerably higher than the double screw mixer. As previously mentioned, the single screw mixer tends to convey the granular material, and exhibit minimal mixing. For this reason, it is recommended that a double screw mixer be used instead of a single screw mixer.

If a single screw mixer is required, a dimensionless screw pitch of either $p/D = 0.75$ or 1.75 is preferred because it results in a more homogeneous mixture, relative to a dimensionless screw pitch of $p/D = 1.25$. Furthermore, if a dimensionless screw pitch of $p/D = 1.25$ must be used, a material injection configuration which features the red oak chips and glass beads being injected into port one and two, respectively, is preferred because it results in a more reproducible mixing process and a smaller composition variance.

CHAPTER 9: AN IMPROVED CONE-BEAM COMPENSATED BACK-PROJECTION ALGORITHM TO ENABLE X-RAY PARTICLE TRACKING VELOCIMETRY[1]

Todd A. Kingston[2,3], Timothy B. Morgan[3], Taylor A. Geick,

Teshia R. Robinson, and Theodore J. Heindel

Department of Mechanical Engineering, Iowa State University, Ames, Iowa, 50011, USA

kingston.todd@gmail.com, tbmorgan@iastate.edu, tgeick@iastate.edu,

teshiar@iastate.edu, and theindel@iastate.edu

Abstract

Characterizing multiphase or granular flows is difficult due to the opaque nature of the system. While invasive measurement techniques provide detailed information of a single point, assessing the entire system is a laborious task due to the large number of samples required. Therefore, significant work has gone into developing noninvasive

[1] Kingston, T.A., Morgan, T.B., Geick, T.A., Robinson, T.R., Heindel, T.J. (2014). An improved cone-beam compensated back-projection algorithm to enable X-ray particle tracking velocimetry. *Flow Measurement and Instrumentation* (in preparation for submission).

[2] Corresponding author: Todd A. Kingston (kingston.todd@gmail.com)

[3] Equal contribution

methods of measuring these flow systems. In this study, an identical pair of X-ray source and detector systems is used to provide two simultaneous but spatially independent X-ray radiographs, which are then coupled together to perform X-ray stereography imaging of the granular flow. An improved cone-beam compensated back-projection algorithm is developed to enable X-ray particle tracking velocimetry (XPTV) to be performed. This improved method accurately corrects for the X-ray source's cone-beam geometry, which is incorrectly ignored in parallel-beam methods. To demonstrate the need for the cone-beam compensation, a direct comparison between the cone-beam and parallel-beam back-projection algorithms is used, and significant differences are presented. These methods are then used to perform XPTV in a double screw mixer, allowing the position and velocity of individual tracer particles to be characterized.

Keywords: Back-projection, cone-beam, granular flow, stereography, X-ray particle tracking velocimetry

9.1 Introduction

In many multiphase flows of industrial interest, it is difficult to measure and/or visualize the flow through visual observation due to the opaque nature of the flow. For example gas-liquid bubble column flows are often impossible to measure visually because the difference in refractive index between air and water distorts measurements at moderate (5%) or higher gas fractions (Seeger et al., 2003). In the case of granular mixing, the granules themselves are usually opaque, making visual measurements below the surface of the flow impossible. One way to overcome this limitation is the use of invasive probes; however, such probes only provide a single point-measurement and their

very presence has the potential to disrupt the flow itself (Boyer et al., 2002). Therefore, significant effort has gone into developing noninvasive methods of flow measurement (Chaouki et al., 1997; Heindel, 2011).

Many of the noninvasive measurement methods have significant trade-offs between temporal and spatial resolution. One of the most common noninvasive measurement methods is electrical capacitance tomography (ECT). ECT operates using electrodes placed around the wall of a flow, which are energized sequentially. When one electrode is energized, the remaining electrodes are used to measure the electrical capacitance in the system. These measurements can then be reconstructed into a two-dimensional (2D) slice of electrical permittivity, which can be correlated to material properties. While ECT systems are capable of measuring at speeds above 1000 frames per second (FPS) for a full tomographic slice, they are limited in spatial resolution (van Ommen and Mudde, 2008). In a typical ECT system, only 5% of the pipe diameter can be resolved (Chaouki et al., 1997).

In addition to ECT, there are several other tomographic techniques that have been applied to multiphase flows. Among these are gamma-ray tomography (Bruvik et al., 2010), X-ray tomography (Ford et al., 2008), magnetic resonance imaging (MRI) (Ehrichs et al., 1995), and ultrasonic tomography (Rahiman et al., 2006). All these techniques provide good spatial resolution and have the capability to take three-dimensional (3D) measurements of flows. However, all the techniques suffer from very poor temporal resolution, and individual scans can take on the order of an hour or more to acquire (Chaouki et al., 1997), and thus are better suited for time-averaged measurements or extremely slow-moving processes.

One noninvasive measurement technique that has been shown to provide a balance between spatial and temporal resolution is X-ray particle tracking velocimetry (XPTV) (Drake et al., 2009b; Seeger et al., 2003). XPTV is an extension of X-ray radiography in which one or more X-ray attenuating tracer particles are placed in the flow (Drake et al., 2008). A time-sequence of radiographs is taken, from which the location of each particle is determined in each frame. By using two temporally synchronized but spatially independent X-ray source and detector pairs, a 3D particle location can be determined (Seeger et al., 2003). XPTV has been shown to obtain temporal resolutions of up to 1000 FPS for 2D studies (Morgan et al., 2013), and 25 FPS for 3D studies (Seeger et al., 2003). However, one drawback of some previous XPTV is its failure to account for the conical beam geometry of the X-ray source (Drake et al., 2008; Drake et al., 2009b; Lee et al., 2009; Morgan et al., 2013; Morgan and Heindel, 2010; Shimada et al., 2007; Xiao et al., 2005). When the cone-beam is assumed to be parallel, the tracer particle's position and resulting velocities will be incorrect. This paper provides a correction for this error and demonstrates a sample application for which it would not be possible to properly image without the correction. Another drawback of some previous XPTV measurements is the time difference between the acquisition of the left frame and right frame (Seeger et al., 2003). While small, this difference can make it difficult to match a particle between frames, and poses a challenge for the determination of the particle velocity. This problem is further exacerbated by high flow velocities. In this study, this challenge is overcome by using temporally synchronized X-ray imaging equipment.

To demonstrate the usefulness of the cone-beam back-projection, XPTV is performed in a double screw mixer allowing the position and velocity of individual tracer

particles to be characterized. Double screw mixers are currently being used in various industrial applications. For example, double screw pyrolyzers are being developed for the thermochemical conversion of biomass into bio-oil. The screw pyrolyzer's high heat transfer rates and resulting bio-oil yields are significantly influenced by its ability to mechanically mix high density inert heat carrier media (e.g., stainless steel shot, refractory sand, etc.) with low density biomass particles (e.g., red oak chips, switchgrass, etc.) (Kingston and Heindel, 2013d). However, characterizing the granular mixing process is difficult due to the opaque nature of the screw pyrolyzer and granular materials. In this study, these two complications are overcome by using an X-ray transparent double screw mixer that geometrically resembles double screw pyrolyzers and by using XPTV to characterize the granular flow.

This paper will first describe the X-ray Flow Visualization (XFloViz) Facility and the screw mixer that were used to perform granular mixing studies. Next, the two granular material types used and the fabrication of tracer particles will be presented. The cone-beam compensated back-projection algorithm that was developed, allowing XPTV to be completed, will be detailed, followed by a unique calibration procedure. Next, comparisons will be made between a parallel-beam and cone-beam back-projection thus demonstrating the significance of the cone-beam compensation. A sample result from one of the screw mixer's operating conditions will be presented and discussed to demonstrate the usefulness of the methods. Finally, conclusions and recommendations for future work will be made.

9.2 Experimental Procedures

9.2.1 Equipment

9.2.1.1 X-ray Flow Visualization Facility

X-ray stereography was performed using the X-ray Flow Visualization (XFloViz) Facility at Iowa State University. Two X-ray source and detector pairs were used to simultaneously capture spatially independent X-ray radiographs, which were then coupled together to provide the X-ray stereography imaging technique. Each X-ray source is a liquid-cooled LORAD LPX200 portable cone-beam source. The cone-beam spans approximately 60° and 40° in the horizontal and vertical directions, respectively. The sources feature a variable power output with voltage and current ranging from 10 to 200 keV and 0.1 to 10.0 mA, respectively, and a maximum power output of 900 W. Despite the X-ray source and detector pairs being identical in terms of the make and model, some inherent variations do exist, causing the necessary power settings to be slightly different. In this study, X-ray sources one and two featured voltage and current configurations of 150 keV and 3.1 mA, and 140 keV and 3.5 mA, respectively. A single 0.61 mm copper filter was place in front of each X-ray source to absorb the low energy X-rays prior to entering the imaging region, minimizing beam-hardening effects.

Both detectors were identical Precise Optics PS164X image intensifiers which feature a 40.6 cm input phosphor and 3.5 cm diameter output phosphor. The input phosphor is backed by a vacuum chamber causing the X-ray photons to be re-emitted as electrons in the vacuum chamber. These electrons are accelerated and focused onto the output phosphor using high voltage electric fields. This causes a significantly brighter visible light image on the output phosphor than could be obtained using a direct X-ray to

visible light scintillator. Coupled to the image intensifiers are two identical DVC-1412 12-bit, monochrome, charge-coupled device (CCD) cameras. Each camera has a resolution of 1388 × 1024 with each pixel size measuring 6.45 μm × 6.45 μm. To improve light sensitivity and increase imaging speed, a 2 × 2 binning configuration, where the signal from adjacent pixels is added together, was used. This yielded an effective resolution of 640 × 512 and an effective pixel size of 12.9 μm × 12.9 μm. Using this binning configuration, the cameras captured images in 55 ms increments thus having an effective frame rate of 18.2 FPS. The image exposure time for both cameras was 5 ms. The X-ray source and detector pairs were mounted at 90° from one another about the central vertical axis in the XFloViz Facility to provide two independent projections of the object of interest (OOI).

The X-ray sources and detectors are mounted on a slew ring which provides 360° rotation around the OOI. A large stepper motor is used to control the angular alignment of the X-ray source and detector pairs relative to the OOI. Located in the center of the XFloViz Facility is a vertical lift system with a custom leveling platform designed to specifically hold the screw mixer in place. For this study, the position of the X-ray source and detector pairs was held constant with respect to the screw mixer. A 45° angle between the mid-line from X-ray source one to detector one and the screw mixer's axial direction was used to provide a more uniform image between the two X-ray source and detector pairs. Furthermore, it conveniently placed additional equipment outside the imaging region, reducing possible interference from highly X-ray attenuating objects (e.g., screw mixer motor), and also enabled the entire OOI to be placed inside the

imaging region. Additional details regarding the XFloViz Facility's equipment and capabilities can be found in the literature (Heindel et al., 2008).

9.2.1.2 Screw Mixer

XPTV was performed on the laboratory-scale double screw mixer shown in Figure 9.1. The screw mixer features two intermeshing noncontact screws with a screw diameter of D = 2.54 cm. An integrated motor-driver-controller-encoder Silverpak 23CE stepper motor, manufactured by Lin Engineering, was used to rotate the screws at the desired screw rotation speed. The screw mixer's housing is transparent in both the optical and X-ray spectrums. The housing features a profile which contours to the screws, and was constructed using an additive manufacturing process (i.e., 3D printing). Two material injection ports are positioned in the top of the housing and allow the different granular materials types and the tracer particles to be injected. A series of outlet ports are positioned in the bottom of the housing at the opposite end of the screw mixer, and allow the granular material to exit under the force of gravity. The effective mixing length is measured from the centerline of the downstream injection port (port two) to the beginning of the outlet ports, and provides a dimensionless mixing length of L/D = 10. Additional details regarding the screw mixer's design can be found in the literature (Kingston and Heindel, 2013d).

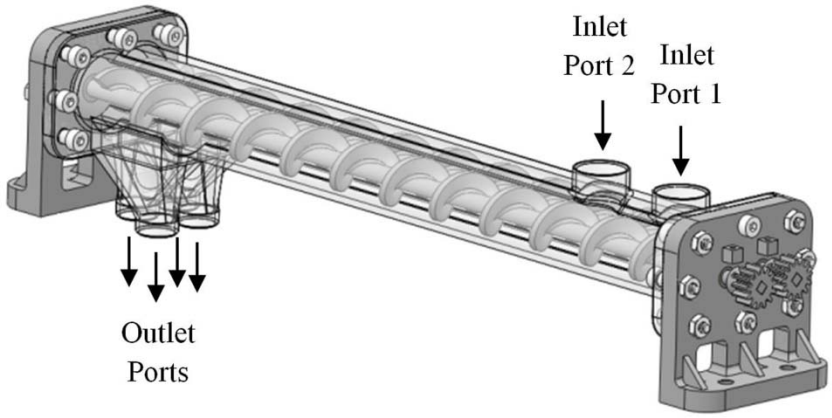

Figure 9.1: X-ray transparent screw mixer used to perform X-ray particle tracking velocimetry (XPTV) studies.

9.2.1.2.1 Granular Materials

A binary mixture of red oak chips and glass beads, as shown in Figure 9.2, were mechanically mixed inside the screw mixer. The red oak chips have a particle size ranging from 500 to 6350 μm and an average true density, measured with a pycnometer, of 1350 kg m^{-3}. The glass beads have a particle size ranging from 300 to 500 μm and a true density of 2510 kg m^{-3}. The granular materials are metered into the screw mixer by two independent Tecweigh CR5 volumetric auger feeders, and are injected vertically downward into the screw mixer's material injection ports.

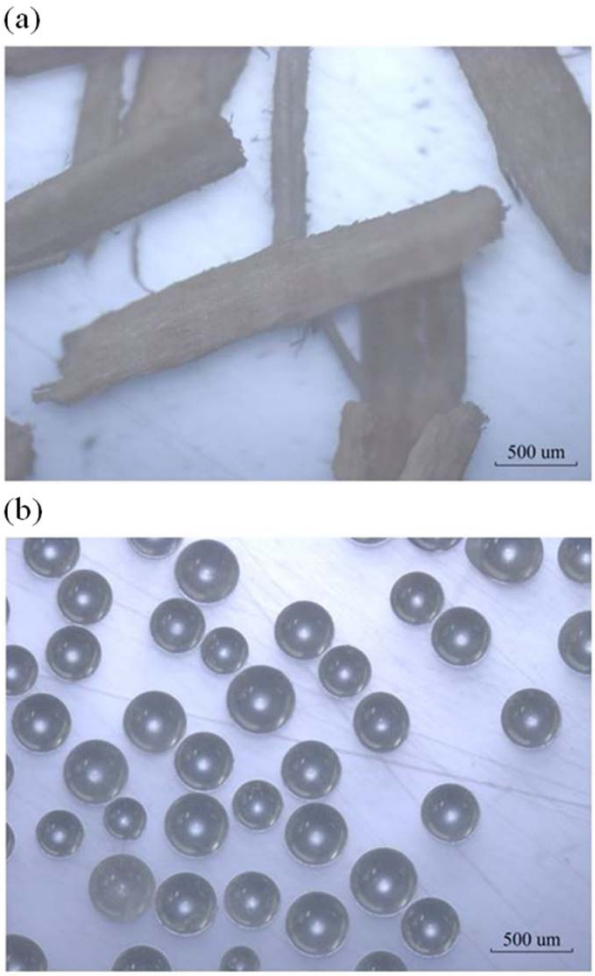

Figure 9.2: Magnified images of (a) 500-6350 μm red oak chips and (b) 300-500 μm glass beads, respectively.

9.2.1.2.1.1 Tracer Particles

To accurately characterize the dynamic granular mixing processes inside the screw mixer, the tracer particles needed to satisfy two main criteria: (i) they needed to resemble the granular materials being used in the screw mixer in terms of particle size, shape, and density, and (ii) they needed to provide a large enough X-ray attenuation contrast to be easily identifiable.

After many attempted trails which involved the use of individual lead shot particles and the use of a steel shot tracer “crowd”, it was determined that these tracer

particles did not resemble the actual granular mixing process because they featured much smaller and denser particles than either the red oak chips or glass beads. After many preliminary tests, the best representation for the actual granular mixing process was the use of “modified” red oak chips.

Individual red oak chips were selected at random and first allowed to soak in a 58% by weight solution of potassium iodide and water for 24 hours before being allowed to air dry for 48 hours. Five coats of silver paint (more specifically, pure silver particles in an acrylic lacquer based carrier) were then applied to the outside surface of the red oak chips. Finally, a single coat of fingernail polish was applied to increase the visual contrast between the tracer particles and the other red oak chips, allowing for extraction and reuse. The combination of potassium iodide and silver paint resulted in higher X-ray absorbing materials, but did slightly increase the average true density to 1570 kg m^{-3}.

A small burst of compressed air was used to propel the tracer particle into the vertical tube that connects the outlet tube of the red oak chips volumetric auger feeder and the screw mixer’s material injection port one. Doing so allowed the tracer particles to be injected into the screw mixer in the same fashion as the other red oak chips. The compressed air was vented to the atmosphere prior to injection to prevent a change in air pressure in the screw mixer.

9.2.1.2.2 Operating Conditions

The operating condition chosen in this study represents the optimized operating condition (operating condition 53) from previous mixing studies performed by Kingston and Heindel (2013c). This condition features a screw rotation speed of $\omega = 60$ rpm, a dimensionless screw pitch of $p/D = 1.75$ where p is the screw pitch and D is the screw

diameter, and counter-rotating down-pumping screw rotation orientation where down-pumping refers to the direction of the material flow between the two screws, and a material injection configuration with the red oak chips and glass beads being injected into port one and two, respectively, as labeled in Figure 9.1. Other parameters which were held constant include a 10:1 glass beads to red oak chips mass flow rate ratio, and a 65% volumetric fill ratio which is based on previous experience by researchers in screw conveying applications (Colijn, 1985). To fulfill the aforementioned operating conditions, the mass flow rates of the red oak chips and glass beads being injected into the screw mixer were 5.75 kg hr^{-1} and 57.5 kg hr^{-1}, respectively.

9.2.2 X-ray Stereography

The X-ray stereographic measurement technique utilizes information from two 2D projections to calculate the 3D location of a tracer particle within the OOI. Figure 9.3 shows a graphical representation of the X-ray stereography process where one X-ray source and detector pair provides a radiographic projection of the x-z coordinate as a function of time, and the other X-ray source and detector pair provides the y-z coordinate as a function of time. From these two temporally synced and spatially independent projections, the 3D coordinate of the tracer particle can be obtained as a function of time.

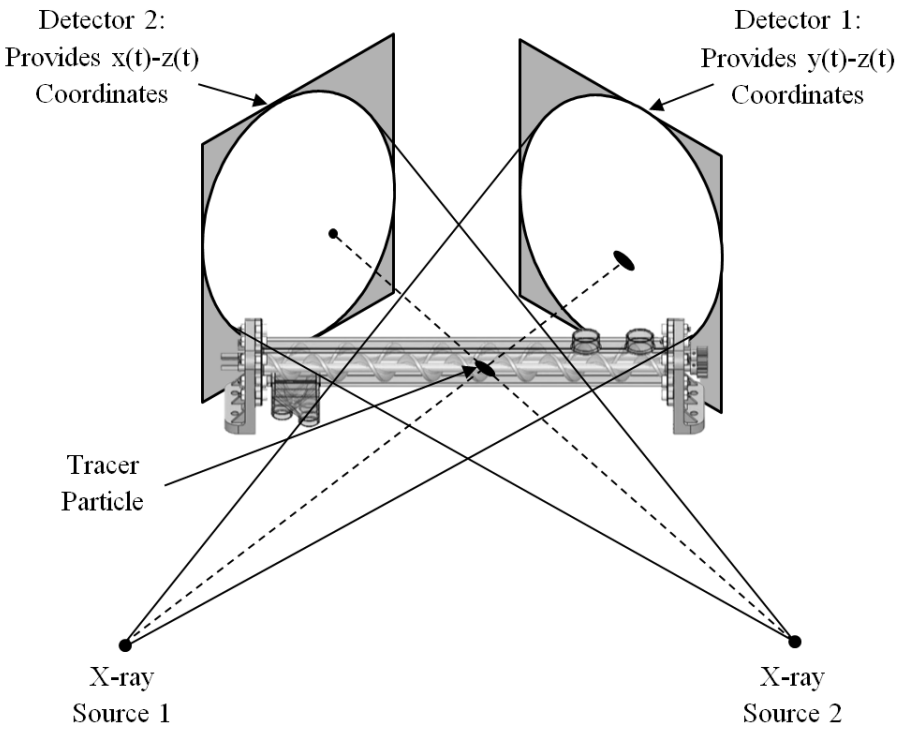

Figure 9.3: X-ray stereography schematic indicating the placement of both X-ray source and detector pairs around the screw mixer.

9.2.2.1 Unwarping

Due to the nature of the intensifier's design, the images experience a pincushion distortion whereby the edges of the image are magnified more than the center. This phenomenon, also referred to as warping, and without proper correction the images are distorted. To correct for this, an unwarping algorithm is used. To obtain the parameters for this correction, a grid consisting of a 1.59 mm thick stainless steel plate with 2 mm holes drilled in a rectangular grid at 12.7 mm on-center increments is placed on the front of the image intensifier. This provides an image with a series of bright dots, which should be in a rectilinear grid, but are not due to the warping phenomenon. From this calibration image, the unwarping parameters are calculated by using an intensity threshold to find the location of the dots corresponding to the holes in the unwarping calibration grid. The

difference between the holes' apparent locations and the known locations on the grid is then fit to a polynomial curve. This curve is then used to calculate the unwarped position of each pixel, with a bilinear interpolation used to fill any gaps in the resulting images. The parameters of the unwarping correction were obtained using the aforementioned X-ray power setting. Additional details regarding the unwarping process can be found in the literature (Doering, 1992; Heindel et al., 2008).

Due to the nature of the equipment used in this study, additional effort was required to determine the unwarping parameters. This procedure was necessitated by the presence of the stepper motor used to drive the screws, which caused an additional magnetic field to be added to the naturally occurring magnetic field inside the X-ray intensifier. Moreover, the physical presence of the leveling plate and the stepper motor caused parts of the image to be obscured due to their high X-ray attenuation. Thus, a modified warping correction procedure was used. Shown in Figure 9.4a is a single frame of the stainless steel plate that was collected using the X-ray imaging system before the unwarping parameters were applied. The presence of the leveling plate and stepper motor cause some of the calibration holes in the plate to be hidden, and thus were unusable in the unwarping procedure. To enable a more accurate unwarping correction, the holes in the grid below the leveling plate and near the stepper motor were filled in by placing a 2 mm lead shot particle in the holes. This allowed for a continuous row of bright dots to be present without interruption in the desired region, a requirement of the unwarping algorithm implementation. Therefore, the unwarping algorithm is only applied to the rectangular region above the leveling plate and to the left of the stepper motor. Figure 9.4b shows the exact same frame of the stainless steel plate that was collected using the

X-ray imaging system that was presented in Figure 9.4a, but with the unwarping parameters applied. As shown, this rectangular region is no longer warped and has been zoomed in slightly to correct for the uneven magnification across the image; yielding the desired results.

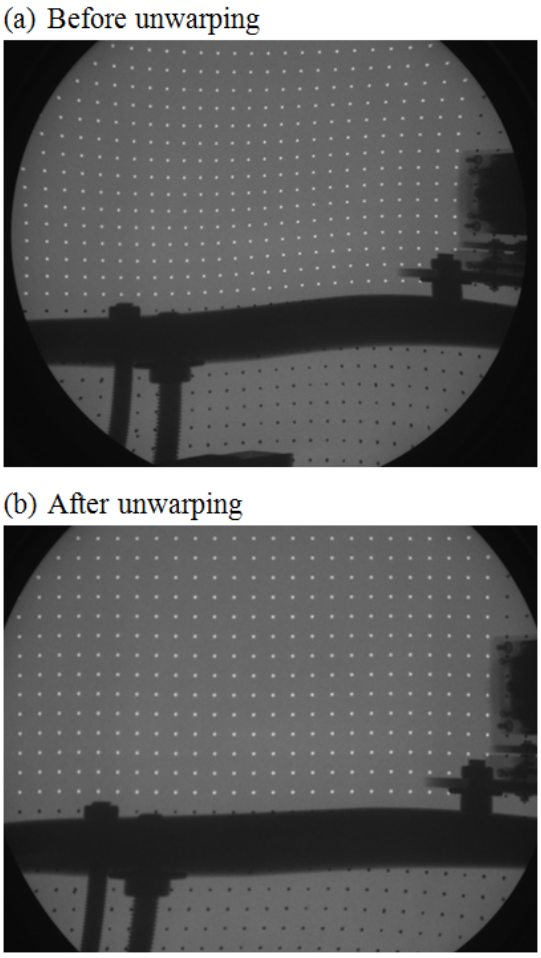

Figure 9.4: X-ray stereography images of the stainless steel unwarping calibration grid (a) before and (b) after the unwarping alogirthm was applied.

9.2.2.2 Sample Image

A single frame from detector one and two that was captured using the prescribed X-ray stereography techniques is shown in Figure 9.5. The tracer particle is shown approximately halfway between material injection port one and two, and is identifiable

because its X-ray attenuation is higher than that of the surrounding materials. In Figure 5a, the left side of the screw mixer appears to be larger than the right side. Likewise, in Figure 9.5b the right side of the screw mixer appears to be larger than the left side. This is a result of the placement of the screw mixer relative to the X-ray sources and detectors; more specifically, the 45° angle between the midline of the X-ray source and detector and the axial direction of the screw mixer. This angular rotation causes one end of the screw mixer to be positioned closer to the X-ray source, and thus experience increased geometrical magnification. If the cone-beam compensated back-projection algorithm that was used in this study was replaced with a traditional parallel-beam back-projection algorithm, the geometrical magnification of the screw mixer would not be accounted for and would result in inaccurate determination of the tracer particle's position. The details of the cone-beam back-projection algorithm and comparisons with a parallel-beam back-projection will be discussed in more detail in the following sections.

The leveling plate and the supporting threaded rods do not appear to be straight in Figure 9.5. This observed bending behavior is a result of the modified unwarping procedure that was used, in which only the rectangular region above the leveling plate and to the left of the stepper motor was unwarped. In other words, the screw mixer is unwarped, as shown by the straight lines on the outside surface of the screw mixer, but the other objects in the images are not.

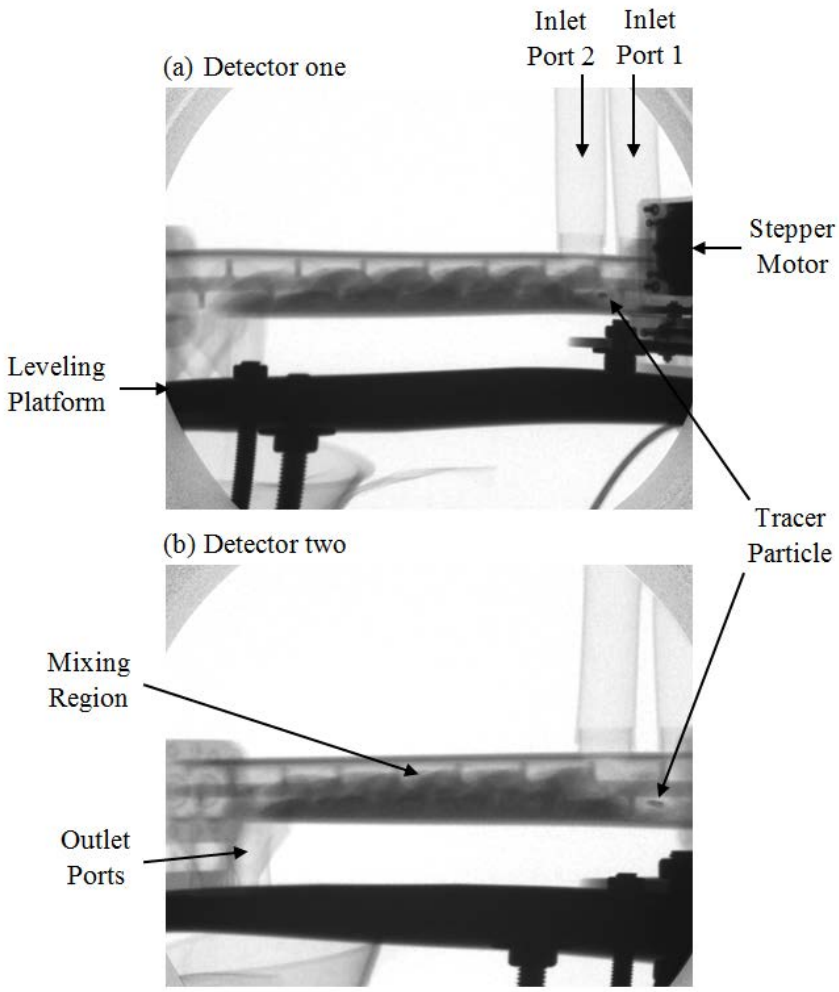

Figure 9.5: A single frame that was captured from X-ray source and detector pair (a) one and (b) two using the X-ray stereography techniques.

9.2.3 Cone-beam Compensated Back-projection Algorithm

9.2.3.1 Particle Detection

Ideally, the determination of the tracer particle location would be done using an automated process, such as the local intensity thresholding methods that have been used in previous studies (Seeger et al., 2003). Unfortunately, due to the relatively low contrast between the particle and the background, and the existence of highly X-ray attenuating objects (e.g., leveling plate, stepper motor, etc.), such a method was not feasible. Another

method that has been used in previous studies is normalized cross-correlation template matching. However, the normalized cross-correlation method is not rotation invariant; therefore, to achieve high detection rates, the particle must either be constrained so it cannot rotate, or be designed to project the same shape irrespective of its angle of rotation (e.g., a sphere). In this particular system, neither of those conditions could be met while still producing tracer particles that were representative of the granular mixing process. Therefore, the tracer particle location on the image for each frame had to be determined manually. Using the manual detection, multiple particles can easily be tracked since a human eye can discern which particles match between the successive frames more easily than an automated process can; yet this would significantly increase the effort needed to determine all of the tracer particles' locations. While it has been found that multiple particles, up to about 10, can be tracked with only moderately more effort, the ability to track more than 10 tracer particles becomes significantly more difficult due to overlapping particle projections on the detectors. For simplicity, only one tracer particle was used in this study.

9.2.3.2 Cone-beam Back-projection

Once the location of the tracer particles on the image is determined, the location of the particle in real space must be determined. Since the X-ray source and detector pairs are located at 90° to each other, the simplest form of this calculation is to assume all X-ray beams are parallel, thus one projection provides the x-z coordinates and the other provides the y-z coordinates. However, the XFloViz Facility features cone-beam X-ray sources, requiring the X-ray beam originating from the approximately point-source X-ray head to the position of the particle on the detector to be accounted for. The 3D position at

which the beams from the two X-ray source and detector pairs intersect is the position of the particle. Shown in Figure 9.6 is a 2D representation of the cone-beam back-projection in the x-y plane.

In order to determine the tracer particle's physical location within the screw mixer, the projection of the tracer particle on the camera coordinate system must be transformed into 3D spatial coordinates. This is done through a series of steps. First, the camera's coordinate system, which is comprised of a 2D pixel location, is converted to a 2D spatial coordinate system for the image. A pixel-to-distance conversion factor was calculated for the resulting image by using a lead-labeled radiographic ruler that was attached to the input phosphor of the intensifier. Next, the image's spatial coordinate system needed to be converted to a coordinate system on the intensifier. While it is known from careful alignment that the center of the X-ray cone-beam is targeted at the center of the input phosphor on the intensifier, the camera is not perfectly centered on the output phosphor of the intensifier. A circle was inscribed over the visible edges of the output phosphor from a sample output image taken with the X-ray system, and the center of that circle was taken as the center of the intensifier. Then a 2D translation was applied to convert the image spatial coordinates to the intensifier coordinates. Finally, the particle's location on the intensifier coordinate system was converted to a 3D spatial coordinate within the screw mixer using a cone-beam back-projection algorithm. The tracer particle's x- and y-position is calculated first by solving a simple system of equations:

$$\frac{x_P}{d_{SO} + y_P} = \frac{x_{Im}}{d_{SD}} \tag{9.1}$$

$$\frac{y_P}{d_{SO} + x_P} = \frac{y_{Im}}{d_{SD}} \tag{9.2}$$

where x_P and y_P are the distances from the tracer particle to the center of the OOI along the x- and y-directions, respectively, x_{Im} and y_{Im} are the distances from the tracer particle's projection on its corresponding detector to the center of detector along the x- and y-directions directions, respectively, d_{SO} is the distance from the X-ray source to the center of the OOI, and d_{SD} is the distance from the X-ray source to the detector (Figure 9.6). In this study, the distance from the X-ray sources to the OOI and to the detector are identical for both source and detectors pairs. However, this is not required.

Once the x- and y-position are calculated, the tracer particle's location is known to be somewhere on a vertical line parallel to the z-axis that passes through the determined x-, y-position. For computational simplicity, the tracer particle's x- and y-position is then projected onto the y-z plane between the X-ray source and detector. The z-position on the y-z plane can be calculated by:

$$\frac{z_P}{d_{SO} + x_P} = \frac{z_{Im}}{d_{SD}} \tag{9.3}$$

where z_P is the distance from the tracer particle to the center of the OOI along the z-direction and z_{Im} is the distance from the tracer particle's projection on its corresponding detector to the center of the detector along the z-direction. This procedure yields the same z-position as if the tracer particle's position had been calculated on the plane of the ray between the X-ray source and tracer particle's projection on the detector. This cone-beam compensation has been well established in the X-ray computed tomography (CT)

literature (Feldkamp et al., 1984), but its application to XPTV has been limited up to this point.

The aforementioned cone-beam compensation is required to account for the cone-shaped beam of the X-ray sources. As shown in Figure 9.5, the X-ray source's conical beam causes a geometric magnification of the object, which increases with decreasing distance from the OOI to the X-ray source. While the geometric magnification is a minimal issue when the OOI is near the mid-line between the X-ray source and the center of the detector, for a relatively large object or one with a large aspect ratio that is askew to the detector plane, such as the screw mixer in this study, failure to compensate for the cone-beam geometry causes significant distortions. These distortions will be quantified in the following sections.

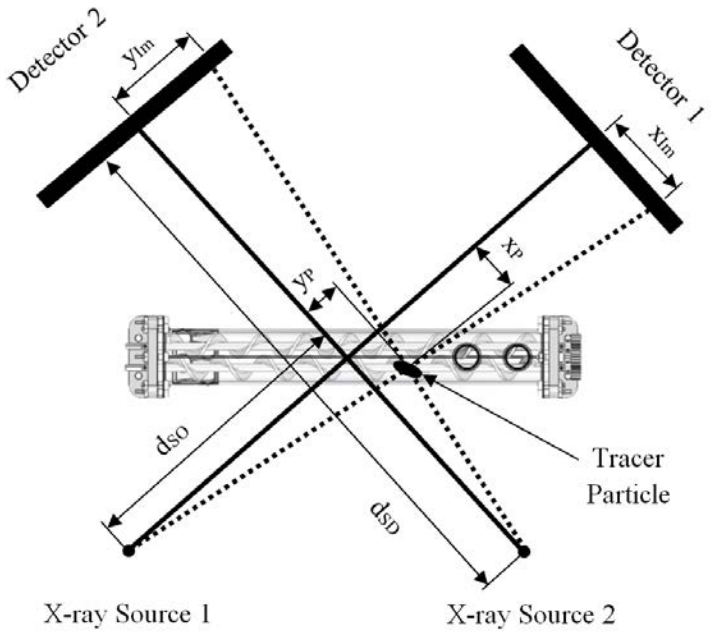

Figure 9.6: Graphical representation of the cone-beam compensated back-projection algorithm in the x-y plane.

9.2.3.3 Axis Rotation and Translation

Once all three coordinates of the particle's position (x, y, and z) are calculated, the system must be transformed from the X-ray coordinate system to a coordinate system with a meaningful relation to the screw mixer. The initial screw mixer origin was determined to be the center of the effective mixing length. In other words, this point represented the mid-plane between the two screws, an axial location of L/D = 5, the mid-plane of the screw shafts. This origin was used to center the screw mixer inside the XFloViz Facility, and allowed for the critical granular mixing region to be analyzed. Furthermore, the configuration in which the X-ray stereographs were captured featured the screw mixer's axial direction positioned 45° relative to the mid-line between X-ray source and detector pair one. However, to more easily visualize the tracer particle's position and velocity, it was determined that the origin should be moved to the beginning of the mixing region (i.e., L/D = 0) but still be located on the mid-plane between the two screws and the mid-plane of the screw shafts. Additionally, the axial direction of the screw mixer should be aligned with the mid-line between the X-ray source and detector pair number two. The original x-y plane, represented by the dashed lines, and the new x-y plane (x'-y'), represented by the solid lines, are shown in Figure 9.7. To perform this transformation, a rotational and translational offset were applied to the tracer particle's position data set. A +45° rotation was applied about the z-axis (i.e., vertical axis) before a -12.7 cm translation (equivalent to L/D = 5) was applied along the y-direction (i.e., axial direction of the screw mixer). For simplicity, the new x-y plane (x'-y') will be referred to as x-y from this point forward.

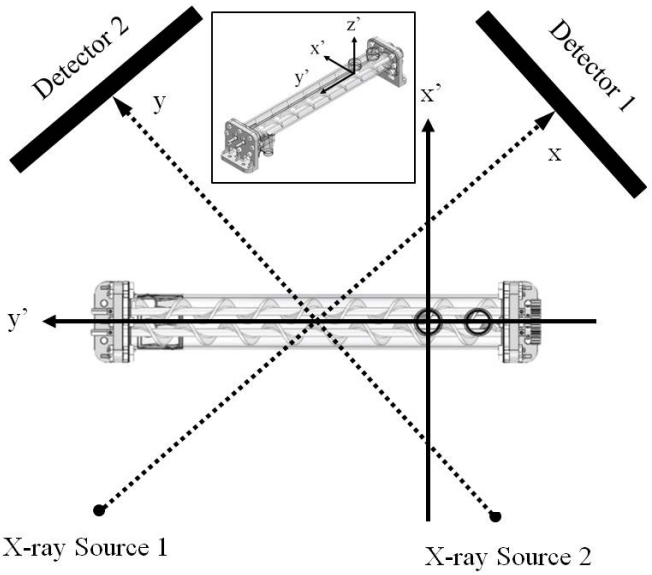

Figure 9.7: Graphical representation of the original x-y plane, and the new x-y plane (x'-y') after the rotational and translational matrix was applied.

9.2.3.4 Calibration Procedure

To ensure accurate particle tracking, a translational and rotational calibration procedure was used to adjust the translational position in the x-, y-, and z-directions and the angle between the mid-line between X-ray source and detector one and the screw mixer's axial direction. The translational calibration procedure began by identifying the finalized origin (i.e., centerline of material injection port two (L/D = 0), mid-plane of the screw shafts, and mid-plane between the screw shafts) from the two X-ray stereography images using the manual tracer particle tracking methods. After the corresponding x, y, and z positions were determined, they were then processed using the cone-beam back-projection algorithm. A constant offset in the x, y, and z directions was then calculated, and these translational offsets were used for subsequent data processing. The x, y, and z translational offsets were determined to be -3.2 mm, 11.2 mm, and 4.1 mm, respectively. These calibration offsets are a result of the translational error between the desired and

actual physical location of the screw mixer's origin. The major source of error resulting from the differences between the desired and actual screw mixer origin is the resolution of the vertical lift system used to hold the screw mixer.

The rotational calibration procedure utilized three 2 mm lead shot particles that were physically attached to the screws of the screw mixer. One lead shot particle was attached to screw number one at approximately L/D = 4.7, and two lead shot particles were attached to screw number two at approximate locations of L/D = 0 and 9. Next, X-ray imaging was performed as the screws were allowed to rotate approximately one revolution. The positions of the three lead shot particles were then processed using manual particle detection and the cone-beam back-projection algorithm. The rotational angle about the z-axis needed to align the pathlines of the two lead shot particles on screw number two was determined to be +0.5°, in addition to the already applied +45° rotation; and this rotational offset was used for subsequent analysis. The rotational error is a result of the angular misalignment between the desired angle of the mid-line between X-ray source and detector one and the axial direction of the screw mixer. Due to the careful leveling processes used to position the leveling plate that holds the screw mixer, and the precision of the image intensifiers placement, it is assumed that a rotational calibration about the x- and y-axes is not needed.

Figure 9.8 illustrates the pathlines of the three lead shot particles before and after the translational and rotational calibration procedures were applied. In both images, the inside surface of the housing is represented by the curved black lines, which illustrates the accuracy of the back-projection algorithm and the usefulness of the calibration procedure. As shown in Figure 9.8a, the particle pathlines fall well outside the inside

surface of the screw mixer's housing, which is not physically possible given this experimental setup. Moreover, it is evident that the two lead shot particles located on screw two are not axially aligned because their pathlines do not overlap one another. However, after the calibration procedures are applied, the three particle pathlines are within the screw mixer's housings. Additionally, the pathlines are approximately symmetrical about the horizontal and vertical lines representing the mid-plane of the screw shafts and the mid-plane between the screw shafts, which demonstrates the accuracy of the leveling plate and validity of the prescribed assumption.

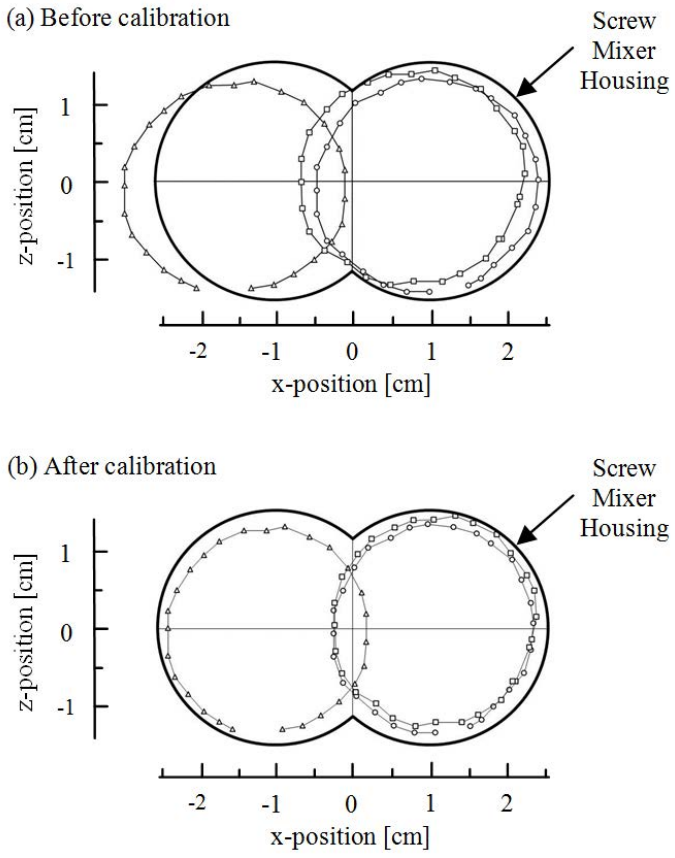

Figure 9.8: Pathlines of three individual lead shot particles (a) before and (b) after calibration procedures were applied.

9.2.3.5 Comparing Cone-beam and Parallel-beam Back-projections

To demonstrate the need for the cone-beam compensation and to show its significance, the same lead shot tracer particles that were used for the calibration procedure were processed using a parallel-beam back-projection algorithm that is commonly used in the literature (Drake et al., 2008; Drake et al., 2009a; Drake et al., 2009b; Lee et al., 2009; Morgan et al., 2013; Morgan and Heindel, 2010; Shimada et al., 2007; Xiao et al., 2005). Note that the calibration procedure that was used in the cone-beam compensated back-projection algorithm was also used in the parallel-beam back-projection algorithm. This removes any variations caused by the calibration procedures and isolates the differences between the two back-projection algorithms.

Shown in Figure 9.9 are the x-z, x-y, and y-z projections of the same three lead shot tracers that were physically attached to the screws and reconstructed using the cone-beam and parallel-beam back-projection algorithms. The open symbols represent the cone-beam back-projection, while the filled symbols represent the parallel-beam back-projection. The inside surface of the screw mixer's housing is represented by the curved black lines in the x-z projection, and the straight horizontal black lines in the x-y and y-z projections. These reference lines aid in illustrating the error associated with the parallel-beam back-projection algorithm. Note that the x-z projection is expanded and is not drawn to scale, as is the case for the x-y and y-z projections, to enhance the visualization of the differences between the parallel-beam and cone-beam back-projections. Moreover, a semi-transparent representation of the screws is shown in the x-y and y-z projections to help orient the observer, and provide reference to the screw mixer's geometry.

As shown, the shape of the pathlines for the lead shot tracer particles is similar in both back-projection algorithms; however, in the case of the parallel-beam back-projection algorithm, the pathline that the particle traces is significantly expanded in all three directions (x, y, and z). This expansion is a direct result of the failure to account for the cone-beam nature of the X-ray source, causing the lead shot particles to appear to be outside the screw mixer's housing. Consequently, the tracer particles' pathlines no longer appear to be intermeshing in the case of the parallel-beam back-projection, as shown in the x-z-projection, which was not the case.

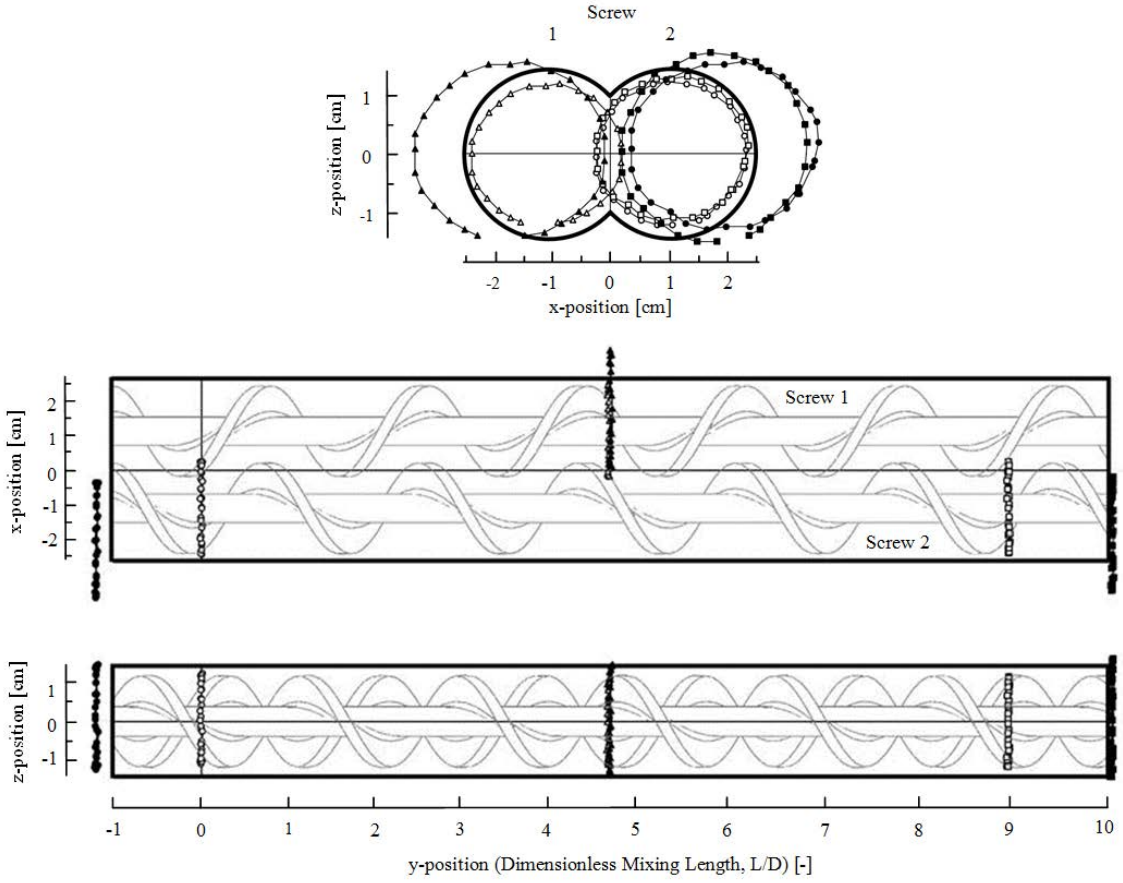

Figure 9.9: Three projections of the screw mixer that illustrate the significant error associated with the parallel-beam back projection (filled symbols) relative to the cone-beam back projection (open symbols).

In addition to this apparent expansion, the parallel-beam back-projection does not take into account the geometric magnification resulting from the 45° angle between the mid-line of X-ray source and detector one, and the screw mixer's axial direction. The geometric magnification is most easily noticed when looking at the tracer particle's pathlines from the parallel-beam back-projection in the y-z- and x-z-projections. As shown in the y-z-projection, the tracer particle pathline that appears to be positioned at L/D = -1.2 is just slightly larger than the screw mixer's housing. However, for the tracer particles that appear to be positioned at L/D = 4.7 and L/D = 10, the particles trace out an increasingly larger pathline, and continue to extend outside the screw mixer's housing further and further with increasing y-position. This geometric magnification is caused by the outlet side of the screw mixer being positioned closer to the X-ray source than the inlet side. This lack of geometric compensation is also noticed in the x-z-projection. Tracer particle three (filled square symbols), which is positioned on screw two, has a particle pathline with a larger diameter than that of particle two (filled triangle symbols), and even larger than particle one (filled circle symbols). This is because the tracer particle three was positioned closer to the X-ray source, due to the 45° rotation angle.

In contrast, in the case of the cone-beam back-projection, no geometric magnification is presented because this is compensated for in the algorithm. Thus, the pathlines of all three tracer particles appear to be the same size, and are independent of the physical location within the screw mixer.

The calibration procedure that was used in the cone-beam compensated back-projection algorithm still accurately corrects the rotational offset for the parallel-beam back-projection algorithm. As shown, the two lead shot tracer particles that are positioned

on screw two are still axially aligned, indicating that the rotational offset is still correct. However, in the case of the parallel-beam back-projection, the translational offset is incorrect. The lead shot tracer particle that is actually positioned at L/D = 0 appears to be positioned at approximately L/D = -1.2. If the translational offset was correct, it would accurately place this tracer particle at L/D = 0.

Overall, there is significant error associated with the assumption that a parallel-beam back-projection is valid when using a cone-beam X-ray source. Thus, a cone-beam compensated back-projection algorithm is needed when using cone-beam X-ray source to accurately track the position of tracer particles using XPTV methods. When not accounted for, the particle's position and velocity will be incorrect.

9.2.3.6 Uncertainty Analysis

An uncertainty analysis was performed to quantify the amount of error associated with the tracer particle's location. The uncertainty associated with the conversion of the tracer particle's projected location on the camera images to its actual 3D location inside the screw mixer was combined with the uncertainty in the 3D location of the X-ray equipment (i.e., X-ray sources, detectors, etc.), the computed distance to pixel ratio, and the manual particle tracking capabilities, using a root sum of squares (RSS) procedure. The uncertainty was calculated for each tracer particle location across the entire pathline, and it was determined that the uncertainty was fairly constant with respect to the location within the screw mixer. The uncertainty in the tracer particle's location ranged from ± 3.1 mm to ± 3.6 mm, which represents only 1.2% to 1.4% of the screw mixer's effective mixing length.

9.2.4 Particle Velocity

9.2.4.1 Central Difference Method

After determining the particle's position as a function of time, the x, y, and z components of the tracer particle's velocity were calculated via numerical differentiation using the central difference method (x-component of the velocity equation is shown here for demonstration purposes):

$$V_x(t) \approx \frac{x(t + \Delta t) - x(t - \Delta t)}{2\Delta t} \tag{9.4}$$

where $x(t + \Delta t)$ is the particle's x-position at time $t + \Delta t$, $x(t - \Delta t)$ is the particle's x-position at time $t - \Delta t$, and Δt is the incremental time between successive frames (55 ms in this study) (Dos Passos, 2011).

9.2.4.2 Rotational and Axial Velocity

In continuous mixing processes, it is convenient to define a rotation and axial velocity to aid in the understanding and visualization of the granular mixing dynamics. The rotational velocity used in this study is defined as the combination of the two velocity components (i.e., x and z) perpendicular to the axis of screw rotation (i.e., y):

$$V_R = \sqrt{V_x^2 + V_z^2} \tag{9.5}$$

where V_x and V_z are the x- and z-components of the velocity. The rotational velocity is always positive per its definition. The axial velocity is simply defined as the y-component of the velocity:

$$V_A = V_y \tag{9.6}$$

The axial velocity's magnitude can either be positive or negative, depending on the particle trajectory inside the screw mixer.

9.2.4.3 LOESS Algorithm

Since the particle velocity was calculated by numerically differentiating the particle position, some noise was introduced into the velocity data set causing the visualization of the velocity data to be slightly more complicated. To aid in removing some of this noise and improve the visualization methods while still maintaining the distinct particle velocity characteristics, the LOESS algorithm that was originally proposed by Cleveland (1979) and further developed by Cleveland and Devlin (1988) was applied to the velocity data. LOESS is a modern method similar to more traditional linear and nonlinear least squares regression, and uses a locally weighted polynomial regression. LOESS allows localized subsets of the data to be used and does not require a global function of any form to be fit to the data. However, this benefit comes at the expense of increased computational time. Note that the LOESS algorithm was only applied to the velocity data (i.e., rotational and axial velocity), but was not applied to the position data.

Shown in Figure 9.10 are plots of the rotational velocity of the particle versus the dimensionless mixing length before and after the LOESS algorithm was applied. As shown, applying the LOESS algorithm minimizes the minor fluctuations in the velocity, but still preserves the major characteristics of the velocity profile.

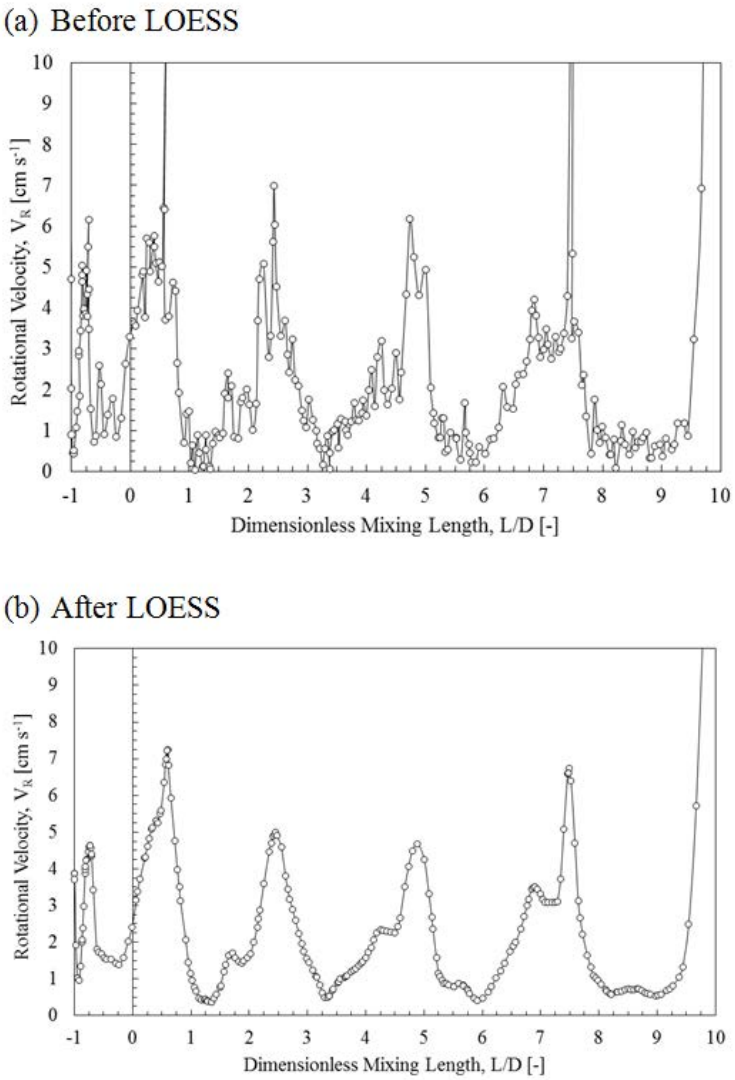

Figure 9.10: Rotational velocity versus dimensionless mixing length (a) before and (b) after the LOESS algorithm was applied.

9.3 Results and Discussion

9.3.1 Particle Position and Velocity Visualization

In order to develop a thorough understanding of the granular mixing dynamics inside the screw mixer, the tracer particle's position and velocity must be visualized simultaneously. Furthermore, the tracer particle's position and velocity must be spatially synced along a similar axis, when possible, thus enabling characteristics in the particle's

position and velocity to be linked together and seen as a whole. To enable this, the axial direction (y-direction) of the screw mixer, represented by the dimensionless mixing length, was intuitively chosen as the common axis and is plotted on the horizontal axis in Figure 9.11. The tracer particle moves in the direction of increasing y-direction, which is shown from left to right in Figure 9.11, with the exception of the x-z projection.

As previously mentioned, the origin of the system is located at the mid-plane between the two screws (x = 0), the beginning of the mixing region [L/D = 0 (also y = 0)], and the mid-plane of the screw shafts (z = 0), and is properly shown as (0, 0, 0) in Figure 9.11. The top three projections of the screw mixer display the particle's position in the x-z, x-y, and y-z projection, respectively. As shown, the only projection which does not share the axial direction of the screw mixer is the x-z projection. The curved profile surrounding the x-z projection represents the inside surface of the screw mixer's housings and is provided for reference.

As previously done, a semi-transparent representation of the screws is shown in the x-y and y-z projections to help orient the observer, and provide reference to the screw mixer's geometry. However, it must be noted that during testing, the screws were rotating and thus the position of the tracer particle shown relative to the position of the screws is irrelevant. The vertical lines on the left and right edge of the x-y and y-z projections represent an axial distance ranging from L/D = -1 to L/D = 10, and the top and bottom lines represent the inside surface of the screw mixer's housing.

The tracer particle's rotational and axial velocity are spatially aligned with the axial direction of the screw mixer and are located directly underneath the position projections. This visualization method allows the relationship between the tracer

particle's position and velocity to be made at each point throughout the screw mixer. As previously mentioned, the LOESS algorithm was applied to the velocity data to improve its visualization.

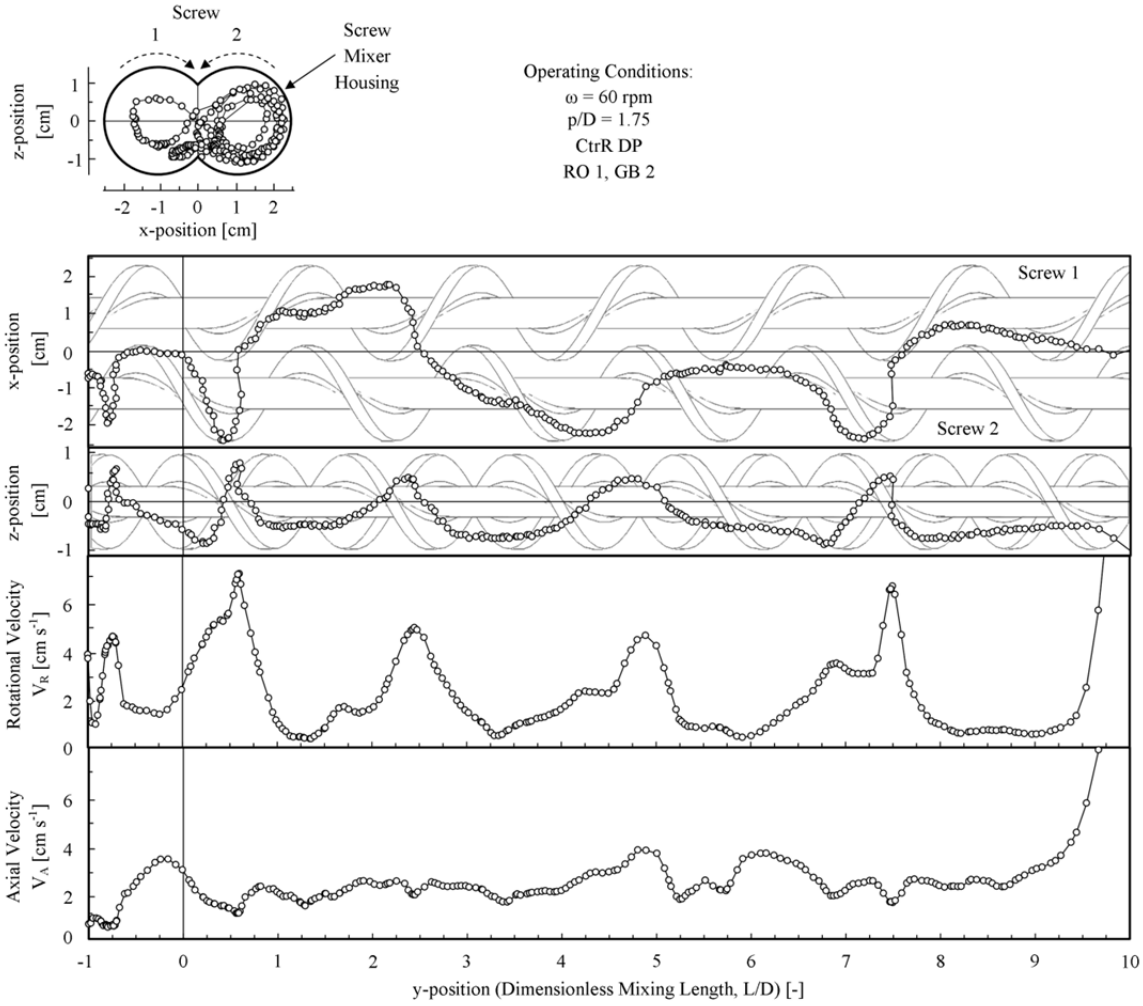

Figure 9.11: The tracer particle's position and velocity that were obtained using the X-ray particle tracking velocimetry (XPTV) methods.

9.3.2 Characterizing the Granular Flow Structures

Several important observations are noticed regarding the tracer particle's position in Figure 9.11. First, the particle initially begins near screw two (i.e., $x < 0$), moves over near screw one (i.e., $x > 0$), back near screw two, and then back near screw one before

finally leaving the screw mixer. This behavior is easily visualized in the x-y projection, but can also be seen in the x-z projection. This movement is believed to be quite beneficial in terms of the mixing effectiveness of the screw mixer because it shows a large amount of convective mixing by utilizing the entire mixing region of the screw mixer.

Second, the tracer particle undergoes periodic changes in height (z-direction) as it moves through the screw mixer, as shown in the y-z projection. Moreover, the peaks in the z-direction, representing areas where the particle is being lifted up towards the top surface of the granular mixture, are aligned with areas in which the particle is experiencing a large shift in the x-direction, either in the positive direction when near screw one, or in the negative direction when near screw two. In both cases, the particle is being translated in the horizontal direction towards the middle of the screw mixer (i.e., the region between the two screws), which is a result of the chosen screw rotation orientation.

Third, at the locations where the particle is being lifted to the top surface of the granular mixture, there is a significantly large increase in the rotational velocity of the particle. These large increases in the rotational velocity are a result of the large translational movement in both the x- and z-directions that were noted in the previous paragraph. In contrast, when the particle is located in the bottom half of the screw mixer (i.e. below the mid-plane of the screw shafts), the rotational velocity is extremely small. This is a result of the increased particle concentration and resulting particle-particle contact, which minimizes the particle’s trajectory.

Fourth, the axial velocity of the particle remains fairly constant, at least in the range from L/D = 0 to L/D = 9. Prior to L/D = 0, the tracer particle undergoes a very chaotic process because of the absence of the glass beads. This behavior is observed in each of the particle's position projections and both of the velocity graphs by its large fluctuations.

Finally, as the tracer particle reaches the end of the screw mixer, the axial and rotational velocity dramatically increases. This behavior is a result of the discharge of the granular materials to the outlet ports which causes a more free-flowing mixture. The behavior of the tracer particle near the beginning and end of the mixing region effectively causes "entrance" and "exit" effects to be present. These effects are analogous to entrance effects found in internal fluid flow applications, where the fluid encounters a developing region upon entering a pipe, and then slowly transitions to a fully developed region.

To ensure that the granular flow structures were repeatable, a repeatability study was conducted. This test consisted of performing five independent trials with a single tracer particle, and then comparing the resulting position and velocity data for the five different trails. The initial starting position of the tracer particle would be slightly different between tests, depending on how the tracer particle was injected into the screw mixer. Despite differences in the initial starting position, the tracer particle's pathline throughout the screw mixer featured similar profiles, and the rotational and axial velocity displayed similar trends.

9.4 Conclusions

XPTV provides the unique ability to track one or more tracer particles in various opaque systems. It is advantageous over other noninvasive measurement techniques because it is capable of providing a balance between temporal and spatial resolution, whereas most other noninvasive measurement techniques can provide one or the other, but not a balance of both. This study has shown that the accuracy of XPTV can be improved through the use of a cone-beam compensated back-projection algorithm, and has been shown to be extremely useful in large systems and systems with large aspect ratios, as was demonstrated by the screw mixer used in this project.

Despite the improvements to XPTV methods, there is still further work to be done to address some of the limitations. For example, in the system shown, the location of the tracer particle had to be marked manually due to geometric constraints associated with the chosen tracer particles; a labor-intensive task. Moreover, obtaining a true velocity field for the system requires very large datasets (several hours) with a single particle or the ability to analyze multiple particles. To provide for time-effective analysis of larger datasets, an automated tracer particle detection method that has the ability to correctly identify multiple tracer particles and accept a wide range of particle geometries should be developed.

The methods developed in this study will be used for a number of future studies. First, the number of trials that use an individual tracer particle will be increased such that an average granular flow structure can be created. Second, the effect that the screw mixer's various operating conditions have on the 3D granular flow structures will be investigated. This will allow for a qualitative comparison between the mixing

effectiveness of the screw mixer found in previous studies (Kingston and Heindel, 2013b, c) and its granular flow structures. Finally, the residence time of individual tracer particles could be determined for the different operating conditions, allowing more precise control of the residence time of individual biomass particles in the thermochemical conversion industry. In general, the developed cone-beam back-projection algorithm can be applied to a wide range of multiphase or opaque flows.

Acknowledgements

Support for portions of this work by Phillips 66 Company is gratefully acknowledged. The X-ray facility used in this research was funded by the National Science Foundation under award number CTS-0216367 and Iowa State University.

CHAPTER 10: CHARACTERIZING 3D GRANULAR FLOW STRUCTURES IN A DOUBLE SCREW MIXER USING X-RAY PARTICLE TRACKING VELOCIMETRY[1]

Todd A. Kingston[2], Taylor A. Geick, Teshia R. Robinson, and Theodore J. Heindel

Department of Mechanical Engineering, Iowa State University, Ames, Iowa, 50011, USA

kingston.todd@gmail.com, tgeick@iastate.edu, teshiar@iastate.edu, and theindel@iastate.edu

Abstract

Granular flows are commonly encountered in many industrial processes, but are difficult to characterize due to the opaque nature of the flow. For instance, screw pyrolyzers are being developed for the thermochemical conversion of biomass into bio-oil, but the granular flow and mixing process inside the reactor lacks fundamental understanding. In this study, X-ray particle tracking velocimetry (XPTV) is used to characterize the three-dimensional (3D) granular flow structures and determine the

[1] Kingston, T.A., Geick, T.A., Robinson, T.R., Heindel, T.J. (2014). Characterizing 3D Granular Flow Structures in a Double Screw Mixer using X-ray Particle Tracking Velocimetry. *Powder Technology* (in preparation for submission).

[2] Corresponding author: Todd A. Kingston (kingston.todd@gmail.com)

residence time of individual tracer particles inside a double screw mixer, which geometrically replicates double screw pyrolyzers, for a wide range of operating conditions. It was determined that high screw rotation speeds, long dimensionless screw pitches, a counter-rotating down-pumping screw rotation orientation, and a material injection configuration with the red oak chips and glass beads injected into port one and two, respectively, resulted in tracer particle pathlines occupying a larger portion of the mixer, which is advantageous in terms of the screw mixer's convective mixing process.

Keywords: Granular flow, mixing, screw mixer, X-ray particle tracking velocimetry.

10.1 Introduction

Granular flows are encountered in many industries including food processing, pharmaceutical production, and energy generation. However, the ability to accurately characterize the three-dimensional (3D) granular flow structures is difficult due to the opaque nature of the flow. A commonly used approach to studying granular flows is through surface visualization via qualitative optical analysis (Kingston and Heindel, 2013b) or quantitative digital image analysis (Aissa et al., 2010a, b; Daumann et al., 2009; Daumann and Nirschl, 2008; Van Puyvelde et al., 1999). While surface visualization has the advantage of being noninvasive, compared to invasive sampling techniques, it does not allow the 3D granular bed to be quantified. Thus, significant effort has gone into developing additional noninvasive visualization and quantification methods which allow 3D characterization of opaque flows (Chaouki et al., 1997; Heindel, 2011).

One noninvasive measurement technique that has shown promise is X-ray particle tracking velocimetry (XPTV), which has been used to characterize multiphase flows

(Drake et al., 2008; Lee and Kim, 2003; Lee et al., 2009; Seeger et al., 2003) and granular flows (Morgan and Heindel, 2010). XPTV provides the ability to characterize opaque flows and offers a good balance between spatial and temporal resolution (Seeger et al., 2003). Moreover, recent developments by Kingston et al. (2013) showed that using an improved cone-beam compensated back-projection algorithm enabled XPTV to be performed, and eliminated significant errors associated with many prior XPTV methods which utilized a parallel-beam back-projection algorithm.

XPTV provides the ability to thoroughly characterize granular flows, which currently lack fundamental understanding. For example, double screw pyrolyzers are being used for the thermochemical conversion of biomass into bio-oil. The screw pyrolyzer's resulting bio-oil yields are significantly influenced by the screw pyrolyzer's ability to mechanically mix low density biomass particles (e.g., red oak chips, ground corncobs, switchgrass, etc.) with high density heat carrier media (e.g., stainless steel shot, refractory sand, etc.). Many research efforts have focused on relating the screw pyrolyzer's operating conditions (e.g., reactor temperature) to the resulting products (Brown and Brown, 2012a; Ingram et al., 2008; Park et al., 2010; Thangalazhy-Gopakumar et al., 2010), but minimal efforts have been directed towards understanding the granular flow inside the screw pyrolyzer due to the challenges associated with visualizing and quantifying the granular flow.

The goal of this study is to characterize the granular flow inside screw pyrolyzers by performing XPTV on a double screw mixer that geometrically resembles the screw pyrolyzer design currently being used in the biomass thermochemical conversion industry (Brown and Brown, 2012a). This goal will be realized through the following objectives:

(i) thoroughly characterize the 3D granular flow structures inside the double screw mixer, (ii) investigate the significance that changing operating conditions have on the resulting granular flow structures, and (iii) determine the residence time of the granular material.

This paper will begin by describing the equipment, granular materials, and the XPTV methods being used in this study. Significant emphasis will be placed on visualizing and interpreting the 3D granular flow structures and residence time inside the screw mixer under different operating conditions. Finally, the conclusions of the study will be presented, and some suggestions for future work will be made.

10.2 Experimental Procedures

10.2.1 Equipment

10.2.1.1 Screw Mixer

Granular studies were performed in the laboratory-scale double screw mixer shown in Figure 10.1. The screw mixer features two intermeshing noncontact screws with a screw diameter of D = 2.54 cm. Screw one and two are positioned on the left-hand and right-hand sides, respectively, when viewing the screw mixer from the inlet ports to the outlet ports. A Lin Engineering Silverpak 23CE stepper motor was used to rotate the screws at the desired screw rotation speed. The screw mixer's housing is transparent in both the optical and X-ray spectrums. The housing features a profile which contours to the screws, and was constructed using an additive manufacturing process (i.e., 3D printing). Two material injection ports are positioned in the top of the housing and allow the different granular material types and the tracer particles to be injected. A series of outlet ports are positioned in the bottom of the housing at the opposite end of the screw

mixer, relative to the inlet ports, and allow the granular material to exit under the force of gravity. The effective mixing length is measured from the centerline of the downstream injection port (port two) to the beginning of the outlet ports, and provides a dimensionless mixing length of L/D = 10. The screw mixer's design geometrically replicates the design of double screw pyrolyzers used in the biomass thermochemical conversion industry (Brown and Brown, 2012a). Additional details regarding the screw mixer's design can be found in Kingston and Heindel (2013d).

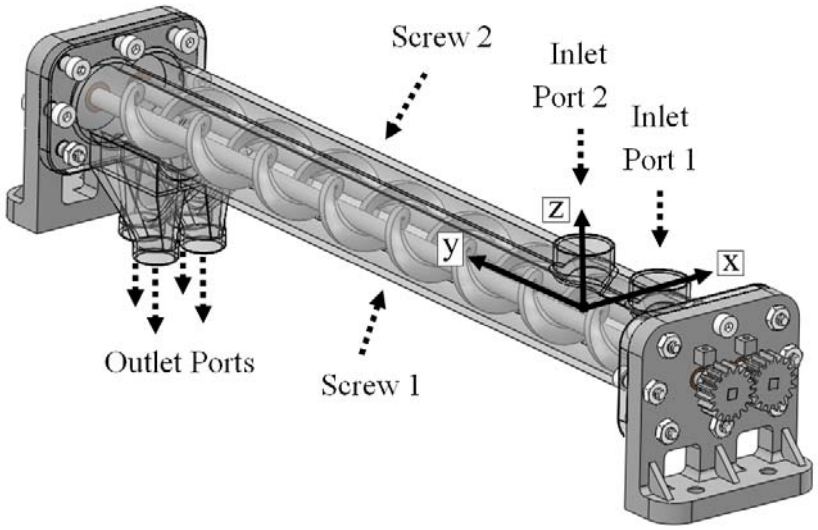

Figure 10.1: The screw mixer that was used to perform X-ray particle tracking velocimetry (XPTV) studies.

In this study, the effect of four parameters are investigated: (i) screw rotation speed at levels of ω = 20, 40, and 60 rpm, (ii) dimensionless screw pitch at levels of p/D = 0.75, 1.25, and 1.75, where p is the screw pitch and D is the screw diameter, (iii) screw rotation orientation at levels of co-rotating (CoR), counter-rotating up-pumping (CtrR UP), and counter-rotating down-pumping (CtrR DP), where up-pumping and down-pumping refer to the direction of the material flow between the two screws, and

(iv) material injection configuration at levels of the red oak chips and glass beads being injected into port one and two, and port two and one, respectively. Of the possible 54 different operating conditions resulting from these various levels of parameters, 12 were tested in this study. The 12 selected operating conditions and their corresponding levels of parameters are shown in Table 10.1. The operating condition naming convention which included all 54 possible operating conditions that was previously developed by Kingston and Heindel (2013c) was maintained for consistency, as shown in column one in Table 1. In these studies, Kingston and Heindel (2013c) determined that operating condition 53 maximized the mixing effectiveness of the screw mixer, and thus was chosen as the "reference condition" in this study, to which all other operating conditions will be compared.

The first eight operating conditions listed in Table 10.1 (operating conditions 5-47) and the reference condition (operating condition 53) correspond to all nine possible combinations of the screw rotation speeds and dimensionless screw pitches. Performing experiments at all nine of these operating conditions enables the effects associated with a single parameter change (i.e., change in either the screw rotation speed or the dimensionless screw pitch while holding the other constant) and a multiple parameter change (i.e., change both parameters simultaneously) to be investigated.

The influence of the screw rotation orientation was investigated by changing the level of this parameter while holding all other parameters constant, as shown in Table 10.1 by operating conditions 49, 51, and 53. Likewise, the influence of the material injection configuration was investigated by changing this parameter and holding all other parameters constant, as shown in Table 10.1 by operating conditions 53 and 54.

Table 10.1: The screw mixer's operating conditions and corresponding levels of parameters that were tested in this study.

Operating Condition	Screw Rotation Speed ω [rpm]	Dimensionless Screw Pitch p/D [-]	Screw Rotation Orientation [-]	Material Injection Configuration RO, GB [-]
5	20	0.75	CtrR DP	1, 2
11		1.25		1, 2
17		1.75		1, 2
23	40	0.75		1, 2
29		1.25		1, 2
35		1.75		1, 2
41	60	0.75		1, 2
47		1.25		1, 2
49		1.75	CoR	1, 2
51		1.75	CtrR UP	1, 2
53*		1.75	CtrR DP	1, 2
54		1.75		2, 1

* Reference condition used for comparison purposes

Additional parameters that were held constant in this study include a 10:1 glass beads to red oak chips mass flow rate ratio, established because of its relevance in the biomass thermochemical conversion industry, and a 65% volumetric fill ratio, which is recommended for screw conveying applications (Colijn, 1985). To satisfy these two parameters, the mass flow rates of the two granular material types were carefully determined for each combination of screw rotation speed and dimensionless screw pitch (Kingston and Heindel, 2013d).

10.2.1.2 X-ray Flow Visualization Facility

X-ray stereography was performed using the X-ray Flow Visualization (XFloViz) Facility at Iowa State University. Two X-ray source and detector pairs were used to simultaneously capture spatially independent X-ray radiographs, which were then coupled together to enable X-ray stereography imaging. Each X-ray source is a liquid-

cooled LORAD LPX200 portable cone-beam source. In this study, X-ray sources one and two featured voltage and current configurations of 150 keV and 3.1 mA, and 140 keV and 3.5 mA, respectively. A single 0.61 mm copper filter was place in front of each X-ray source to absorb the low energy X-rays prior to entering the imaging region. Both detectors were identical Precise Optics PS164X image intensifiers which feature a 40.6 cm diameter input phosphor and 3.5 cm diameter output phosphor. Coupled to the image intensifiers are two identical DVC-1412 12-bit, monochrome, charge-coupled device (CCD) cameras which have a resolution of 1388 × 1024. To improve light sensitivity and increase imaging speed, a 2 × 2 binning configuration, where the signal from adjacent pixels is added together, was used, thus yielding an effective resolution of 640 × 512. Using this binning configuration, the cameras captured images in 55 ms increments resulting in an effective frame rate of 18.2 frames per second (FPS). The image exposure time for both cameras was 5 ms. The X-ray source and detector pairs were mounted at 90° relative to one another about the central vertical axis in the XFloViz Facility to provide two independent projections of the screw mixer. In this study, the position of the X-ray source and detector pair one were held at a constant 45° relative to the screw mixer's axial direction, as shown in Figure 10.2. This enabled the entire effective mixing region to be visualized. Additional details regarding the XFloViz Facility's equipment and capabilities are available in the literature (Heindel et al., 2008).

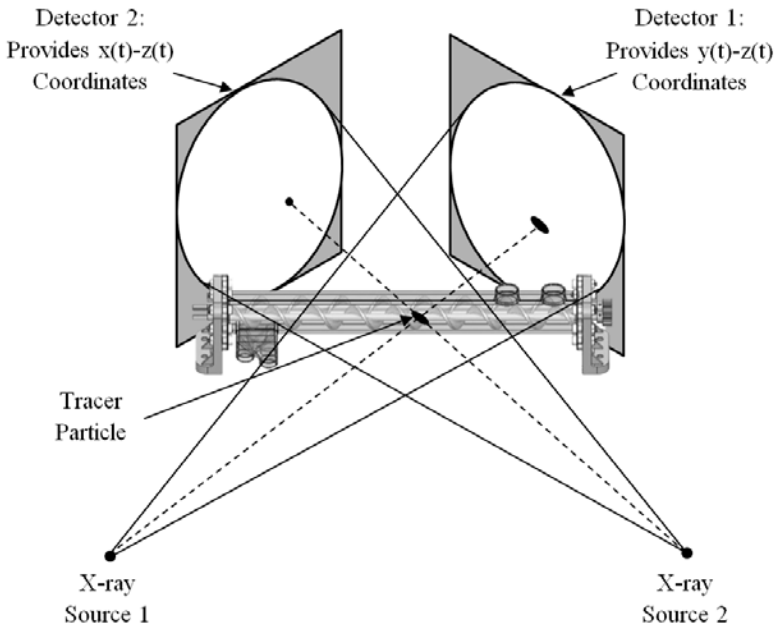

Figure 10.2: X-ray stereography schematic indicating the placement of the X-ray source and detector pairs around the screw mixer.

10.2.2 Granular Materials

A binary mixture of red oak chips and glass beads, shown in Figure 10.3, were mechanically mixed inside the screw mixer. The red oak chips had a particle size ranging from 500 to 6350 μm and an average true density, measured with a pycnometer, of 1350 kg m^{-3}. The glass beads had a particle size ranging from 300 to 500 μm and a true density of 2510 kg m^{-3}. The granular materials were metered into the screw mixer by two independent Tecweigh volumetric auger feeders, and were injected vertically downward into the screw mixer's material injection ports.

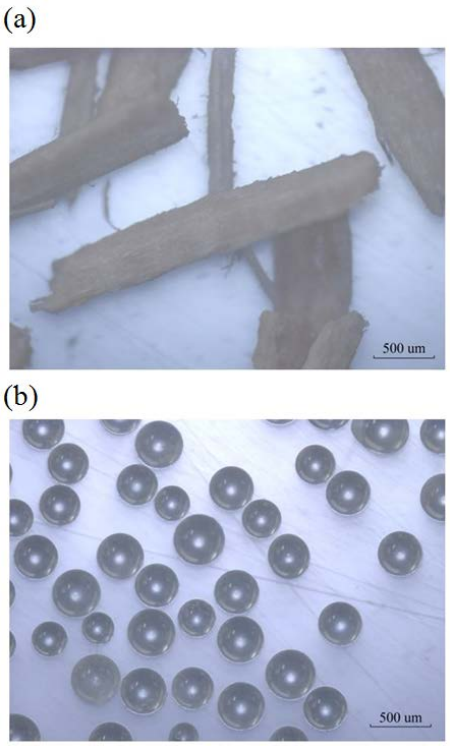

Figure 10.3: Magnified images of (a) 500-6350 μm red oak chips and (b) 300-500 μm glass beads, respectively.

To accurately characterize the dynamic granular mixing processes inside the screw mixer, the tracer particles needed to resemble the granular materials being used in the screw mixer in terms of particle size, shape, and density. Additionally, they needed to provide a large enough X-ray attenuation contrast to be easily identifiable. It was determined from previous studies that the best representation for the actual granular mixing process which leads to successful tracer particles was the use of “modified” red oak chips (Kingston et al., 2013). The modification process consisted of soaking a small number of randomly selected red oak chips in a 58% by weight solution of potassium iodide and water for 24 hours, and then allowing them to dry for 48 hours. Five coats of silver paint (more specifically, pure silver particles in an acrylic lacquer based carrier) were then applied to the outside surface of the red oak chips. Finally, a single coat of

fingernail polish was applied to increase the visual contrast between the tracer particles and the other red oak chips, allowing for extraction and reuse. The combination of potassium iodide and silver paint resulted in a much higher X-ray absorbing tracer particle, while only slightly increasing the average true density of the tracer particles to 1570 kg m^{-3}. The tracer particles were introduced into the red oak chip's material injection inlet stream prior to being injected into the screw mixer.

10.2.3 X-ray Particle Tracking Velocimetry

10.2.3.1 X-ray Stereography

X-ray stereography couples the two independent 2D X-ray radiographs together, and enables the 3D location of the tracer particle to be determined. Figure 10.2 illustrates the X-ray stereography process. One X-ray source and detector pair provides the x-z coordinate of the tracer particle as a function of time, while the other X-ray source and detector pair provides the y-z coordinate as a function of time. In this study, the location of the particle on image one and two for each frame was determined manually for two reasons: (i) the relatively low contrast between the tracer particle and the surrounding objects prevented traditional thresholding particle detection methods from being used (Seeger et al., 2003), and (ii) the tracer particles are not rotation invariant, meaning the tracer particle's geometric projection of its shape onto the two detectors is dependent on its orientation, which prevents the use of normalized cross-correlation methods (Morgan and Heindel, 2010).

10.2.3.2 Particle Position

From the two spatially independent and temporally synced projections, the 3D coordinate of the tracer particle is obtained as a function of time by using a cone-beam

compensated back-projection algorithm that was developed by Kingston et al. (2013). A cone-beam back-projection algorithm is needed because the X-ray sources are cone-beam sources. As demonstrated by Kingston et al. (2013), failure to compensate for the cone-beam X-ray source geometry results in significant error in the tracer particle position.

To improve the visualization and interpretation of the data, a convenient X-ray coordinate system was chosen. The origin was repositioned to the mid-plane between the two screws (x = 0), the beginning of the effective mixing region (y = 0), and the mid-plane of the screw shafts (z = 0), as shown in Figure 10.1. To allow for the ability for scale-up and comparison with other mixers, the y-direction, which represents the axial direction of the screw mixer, will be expressed in terms of the dimensionless mixing length, L/D.

An uncertainty analysis was performed for all the experimental tests conducted in this study. The uncertainty in the 3D location of the X-ray equipment was combined with the uncertainty in the cone-beam back-projection algorithm using a root sum of squares (RSS) procedure. The uncertainty was calculated for each tracer particle at each location within the screw mixer. The maximum uncertainty in the tracer particle's location was ± 3.7 mm, which represents only 1.5% of the screw mixer's effective mixing length.

10.2.3.3 Particle Velocity

Determining the velocity of the granular materials inside the screw mixer is a critical component when characterizing the dynamic mixing process. After determining the tracer particle's position as a function of time, the x, y, and z velocity components were calculated via numerical differentiation using a central difference method outlined

by Dos Passos (2011) (x-component of the velocity equation is shown here for demonstration purposes):

$$V_x(t) \approx \frac{x(t + \Delta t) - x(t - \Delta t)}{2\Delta t} \tag{10.1}$$

where $x(t + \Delta t)$ is the particle's x-position at time $t + \Delta t$, $x(t - \Delta t)$ is the particle's x-position at time $t - \Delta t$, and Δt is the incremental time between successive frames (55 ms in this study).

In granular mixing processes, particularly in continuous mixing processes, it is convenient to define a rotation and axial velocity. This aids in visualizing the granular dynamics, and helps in interpreting the effects that changing operating conditions have on the granular flow structures. The rotational velocity used in this study is defined as the combination of the x and z velocity components, which are perpendicular to the axis of screw rotation (i.e., y-axis):

$$V_R = \sqrt{V_x^2 + V_z^2} \tag{10.2}$$

where V_x and V_z are the x- and z-components of the tracer particle's velocity. The rotational velocity is always positive per its definition. The axial velocity is simply defined as the y-component of the velocity:

$$V_A = V_y \tag{10.3}$$

The axial velocity can either be positive or negative, depending on the particle trajectory inside the screw mixer.

Since the particle velocity was calculated by numerically differentiating the particle position, some noise was introduced into the velocity data set causing the visualization of the velocity data to be slightly more complicated. To aid in removing

some of this noise and improve the visualization methods while still maintaining the distinct particle velocity characteristics, the LOESS algorithm that was originally proposed by Cleveland (1979) and further developed by Cleveland and Devlin (1988) was applied to the velocity data (i.e., rotational and axial velocity), but was not applied to the position data.

10.2.3.4 Residence Time

The residence time of granular material is a critical parameter in many granular mixing applications. For example, in the thermochemical conversion industry, the residence time of individual biomass particles has a significant influence on heat transfer characteristics and resulting products (Mohan et al., 2006). In this study, the residence time of the tracer particle in the mixing region was determined by:

$$t_{res} = t_{L/D = 10} - t_{L/D = 0} \tag{10.4}$$

where $t_{L/D = 10}$ and $t_{L/D = 0}$ are the time stamps when the tracer particle is located at L/D = 10 and L/D = 0, respectively.

10.3 Results and Discussion

10.3.1 Position and Velocity Visualization

10.3.1.1 Reference Condition

The “reference condition” in this study represents the optimized operating condition, in terms of the mixing effectiveness of the screw mixer, that was reported by Kingston and Heindel (2013c). This reference condition will be used to compare the effect of other parameters in terms of their resulting granular flow structures inside the screw mixer, and the resulting differences will be discussed.

To fully characterize the 3D granular flow structures inside the screw mixer, the tracer particle's position and velocity must be visualized simultaneously. To enable this visualization method, a common axis was chosen. The y-axis, which represents the axial direction of the screw mixer, was chosen as this common axis, and is represented in terms of the dimensionless mixing length, L/D, as shown in Figure 10.4. The x-z, x-y, and y-z projections of the screw mixer are shown in Figure 10.4. With the exception of the x-z projection, the tracer particle moves in the direction of increasing y-direction, which is shown from left to right in Figure 10.4. The origin of the screw mixer was conveniently located at the mid-plane between the two screws (x = 0), the beginning of the effective mixing region [L/D = 0 (also y = 0)], and the mid-plane of the screw shafts (z = 0). The curved profile surrounding the x-z projection represents the inside surface of the screw mixer's housings, and is provided for reference. The arrows above the x-z projection indicate the screw rotation orientation for that operating condition. The vertical lines on the left and right edge of the x-y and y-z projection represent an axial distance ranging from L/D = -1 to L/D = 10, and the horizontal lines on the top and bottom edge represent the inside surface of the screw mixer's housing. A semi-transparent representation of the screws are shown in the x-y and y-z projections to help orient the reader, and provide reference to the screw mixer's geometry. However, it must be noted that during testing, the screws were rotating; thus, the position of the tracer particle relative to the screws' position shown in Figure 10.4 is irrelevant.

The two graphs in Figure 10.4 that are spatially aligned with the axial direction of the screw mixer and located directly underneath the position projections are the tracer particle's rotational and axial velocity, respectively. This visualization method allows the

relationship between the tracer particle's position and velocity to be made at each point throughout the screw mixer. As previously mentioned, the LOESS algorithm was applied to the velocity data to improve its visualization.

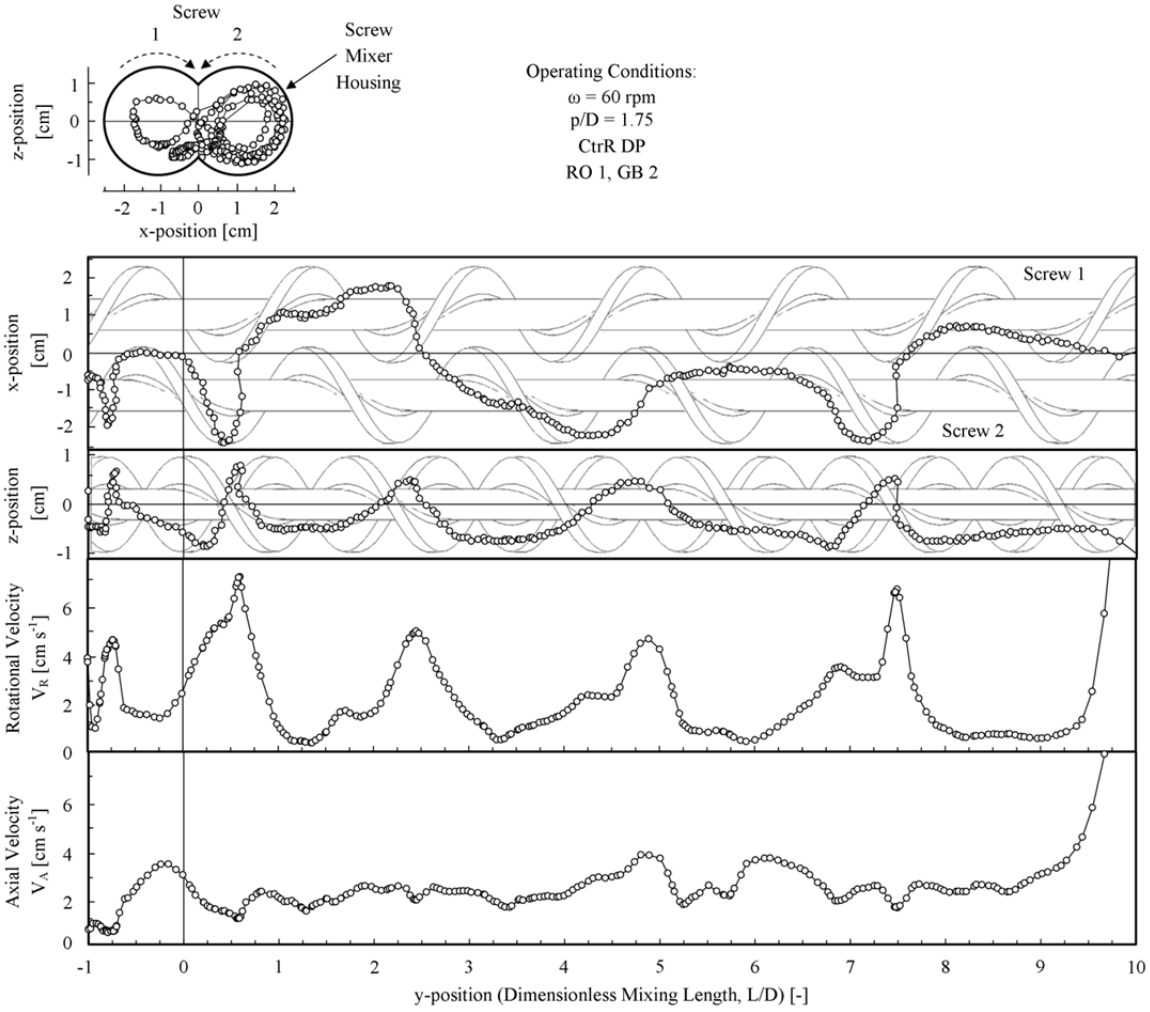

Figure 10.4: The tracer particle's position and velocity for operating condition 53 (reference condition) that were obtained using the X-ray particle tracking velocimetry (XPTV) techniques.

To ensure that the granular flow structures were repeatable, two different repeatability studies were conducted. The first test consisted of performing five independent trials with a single tracer particle, and then comparing the resulting position and velocity data for the five different trails. The initial starting position of the tracer

particle would be slightly different between tests, depending on how the tracer particle encountered the screw mixer's geometrical features (e.g., screws) or the other granular materials. Despite differences in the initial starting position, the tracer particle's pathline throughout the screw mixer featured similar profiles, and the rotational and axial velocity displayed similar trends. The second repeatability test featured the use of five tracer particles that were injected simultaneously into the screw mixer. During the injection into the red oak chips material inlet stream, the tracer particles would disperse and would therefore be injected into the screw mixer at slightly different time instances. As previously mentioned, the initial position of the tracer particle was slightly different. Once again, all five particles featured similar pathlines and velocity profiles. Five trials were performed for the reference condition, and three trails were performed for the remaining operating conditions. However, because of the high degree of repeatability from both of these tests, only one of the trials that were performed for each of the selected operating conditions will be shown in the following sections.

Several important observations are noticed in Figure 10.4 regarding the tracer particle's position. First, the particle enters the screw mixer near screw two (i.e., $x < 0$), moves over near screw one (i.e., $x > 0$), back near screw two, and then back near screw one before finally leaving the screw mixer. This behavior is easily visualized in the x-y projection, but can also be seen in the x-z projection. This behavior is beneficial in terms of the mixing effectiveness of the screw mixer because it illustrates a large amount of convective mixing by utilizing the entire mixing region of the screw mixer and inducing bulk granular flow throughout the screw mixer.

Second, the tracer particle undergoes periodic fluctuations in the z-direction as it moves through the screw mixer, as shown in the y-z projection. The peaks in the z-direction represent locations where the particle is being lifted up towards the top surface of the granular mixture. These locations are also aligned with instances when the particle is experiencing a large shift in the x-position, either in the positive direction when near screw one, or in the negative direction when near screw two. In both cases, the particle is being translated in the horizontal direction towards the middle of the screw mixer (i.e., the region between the two screws), which is a result of the counter-rotating down-pumping screw rotation orientation. This large translation in the x-direction occurs when the particle reaches the top surface of the granular materials because there are fewer particle-particle contacts. This translation results in a significant increase in the rotation velocity of the particle. In contrast, when the particle is located in the bottom half of the screw mixer (i.e. below the mid-plane of the screw shafts), the rotational velocity is extremely small. This is a result of the increased particle concentration and particle-particle contacts, which minimize the particle's trajectory.

Third, the axial velocity of the particle remains fairly constant, at least in the range from L/D = 0 to L/D = 9. Prior to L/D = 0, the tracer particle undergoes a very chaotic process because of the absence of the glass beads. This behavior is observed in the tracer particle's x-y and y-z position projections and both of the velocity graphs by its large fluctuations.

Finally, as the particle reaches the end of the screw mixer, its axial and rotational velocity dramatically increases. This behavior is a result of the discharge of the granular material to the outlet ports which causes a more free-flowing mixture. The behavior of

the particle near the beginning and end of the mixing region essentially causes “entrance” and “exit” effects to be introduced. For this operating condition, the exit effects cause the rotational and axial velocity to increase at approximately L/D = 9.5 and L/D = 9, respectively.

In the following sections, the influence that the screw rotation speed, dimensionless screw pitch, screw rotation orientation, and material injection configuration have on the granular flow structures will be investigated by comparing various operating conditions to the reference condition. The position and velocity data that was obtained for five of the 11 additional operating conditions will be presented. For these five operating conditions, only a single parameter was changed; the other three parameters remained fixed. For example, to demonstrate the effect of the screw rotation speed, operating condition 17 ($\omega = 20$) was compared to the reference condition ($\omega = 60$). Operating condition 41 (p/D = 0.75) was compared to the reference condition (p/D = 1.75) to illustrate the differences resulting from a changing dimensionless screw pitch. Both screw rotation orientations [CoR (operating condition 49) and CtrR UP (operating condition 51)] were then compared to the reference condition (CtrR DP). Finally, operating condition 54 (RO 2, GB 1) was compared to the reference condition (RO 1, GB 2) to demonstrate the influence of the material injection configuration.

The position and velocity data associated with operating condition 35 ($\omega = 40$) and operating condition 47 (p/D = 1.25) are not presented because the influence of those conditions on the granular mixing process were approximately half that of those associated with operating condition 17 ($\omega = 20$) and operating condition 41 (p/D = 0.75). Moreover, the position and velocity data associated with operating condition 5, 11, 23

and 29 are not presented because these conditions represent a multiple factor change (i.e., screw rotation speed and dimensionless screw pitch) relative to the reference condition.

10.3.1.2 Screw Rotation Speed

In previous studies reported by Kingston and Heindel (2013b), it was qualitatively noted that while the screw rotation speed produced a more chaotic mixing process, the granular flow structures appeared to have changed little. However, in those studies, the opaque granular flow only allowed for surface visualization. In this study, the 3D granular flow structures are visualized by using XPTV, allowing for a more accurate characterization of the granular flow.

Shown in Figure 10.5 is the resulting tracer particle position and velocity data that was obtained by maintaining all the same operating conditions as the reference condition shown above, except the screw rotation speed which was changed to ω = 20 rpm (operating condition 17).

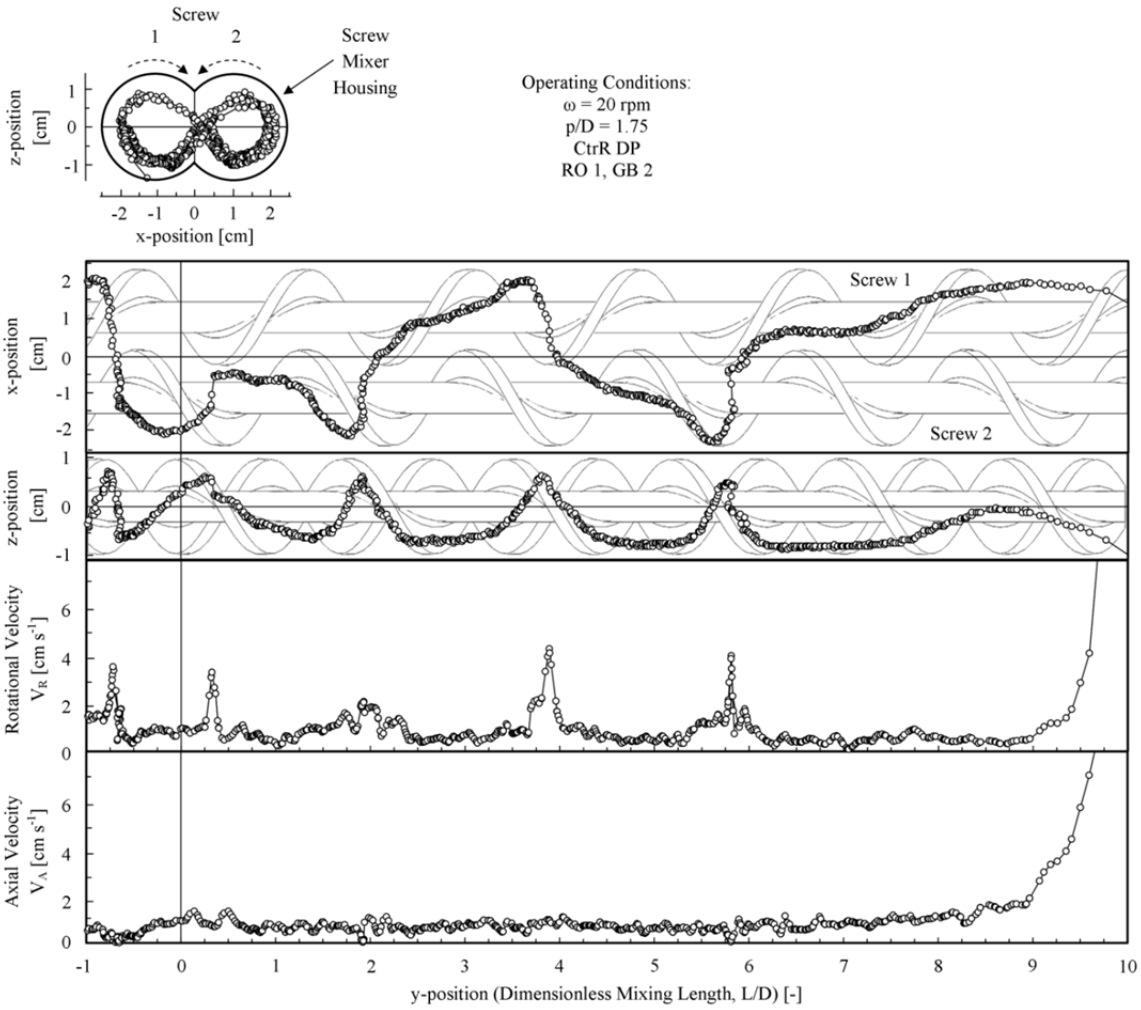

Figure 10.5: The tracer particle's position and velocity for a screw rotation speed of ω = 20 rpm.

Relative to the reference condition, the tracer particle's position looks quite similar. The particle makes frequent changes between the two screw regions, before leaving the screw mixer. Moreover, the particle undergoes similar periodic fluctuations in the z-direction, with about the same frequency as the reference condition. In contrast to the tracer particle's similar position characteristics, the velocity data for the screw rotation speed of ω = 20 is slightly different than for the ω = 60 case, as is expected. In particular, the peaks in the rotational velocity appear to be lower in magnitude and have a much narrower distribution in the y-direction. The axial velocity remains fairly constant,

as was the case for the reference conditions; however, the overall magnitude is lower due to the slower screw rotation speed. A similar finding is noted for the rotational velocity (i.e., smaller magnitude). Finally, the “exit” effects that cause the rotational and axial velocity to increase near the end of the mixer occur at approximately the same axial locations (i.e., L/D = 9.5 and L/D = 9, respectively).

10.3.1.3 Dimensionless Screw Pitch

The influence of the dimensionless screw pitch has been shown to have significant implications in the diffusion coefficient of granular mixing processes (Uchida and Okamoto, 2008). In this study, the granular flow structures were also shown to be significantly influenced. When the screw mixer was operated with a dimensionless screw pitch p/D = 0.75, the tracer particle’s pathline was observed to exhibit similar characteristics to a single screw mixer. More specifically, and in contrast to the reference condition, the tracer particle did not move between the two different screw regions, as shown in Figure 10.6. The tracer particle initially began near screw one, and then circulated around screw one for the duration of the test. This behavior is most easily visualized in the x-z and x-y projections shown in Figure 10.6. The lack of rotational motion around both of the screws is believed to result in a less effective mixing process, as was noted by Kingston and Heindel (2013b, c), and essentially causes the double screw mixer to behave like two single screw mixers. Multiple tests were performed, and this same behavior was noted in each test. Furthermore, periodic fluctuations in the z-direction occurred at approximately half the frequency as the reference condition, which is analogous to the reduced frequency in the sine-like pathline noted by Uchida and

Okamoto (2008) for small dimensionless screw pitches in single screw mixer applications.

The rotational velocity of the tracer particle only experienced two peaks, which corresponded to the two locations where the tracer particle was flipped over the top of the screw shaft. The axial velocity of the tracer particle remained fairly constant throughout the screw mixer. The exit effects did not become apparent until closer to the end of the screw mixer, which occurred at approximately L/D = 9.75 and 9.5 for the rotational and axial velocity, respectively. This is an effect of the changing screw flighting angle and increasing number of screw flights that results from shortening the dimensionless screw pitch, relative to the reference condition. These findings confirm the hypothesis that longer dimensionless screw pitches cause the entrance and exit effects to propagate further into the screw mixer, which was proposed by Kingston and Heindel (2013a) in their investigation of the mixing effectiveness as a function of the screw mixer length.

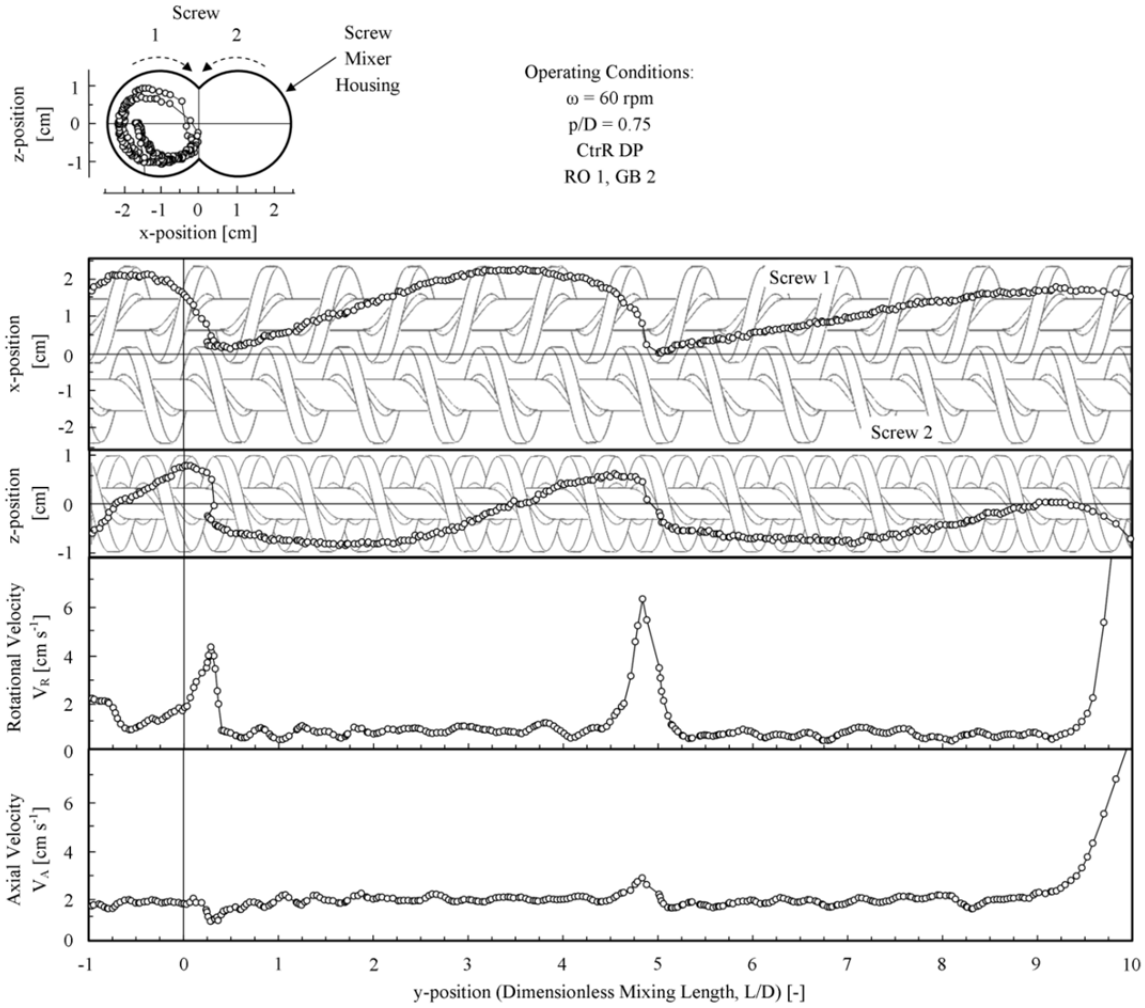

Figure 10.6: The tracer particle's position and velocity for a dimensionless screw pitch of p/D = 0.75.

10.3.1.4 Screw Rotation Orientation

10.3.1.4.1 Co-rotating

Changing the screw rotation orientation to a co-rotating (CoR) configuration resulted in significant changes in the granular flow structure of the tracer particle. First, it caused the tracer particle to reverse its trajectory multiple times instead of moving in a continuous pathline as it did in the reference condition. This effect is most easily visualized in the x-z projection shown in Figure 10.7. The particle first begins near screw one, and is then transmitted toward the right and down between the screws. As the

particle moves to the right and below screw two, the particle reverses its trajectory and begins to move back toward the middle of the screw mixer before it is brought up to the top surface of the granular bed and rotated around screw two. It is proposed that this behavior would have a negative impact on the granular mixing process because it causes the granules to become temporarily stagnant and exhibit minimal mixing. Second, the tracer particle floats on top of the granular bed in between screw two and the housing, from approximately L/D = 5 to L/D = 7, as shown in the x-y projection and the screw two region of the x-z projection. Large red oak agglomerations were noted to frequently occur in this region of the screw mixer in Kingston and Heindel's (2013b, d) previous studies, and ultimately resulted in decreased mixing performance.

In terms of the rotational velocity of the tracer particle, a co-rotating screw rotation orientation displays few changes relative to the reference condition. However, the axial velocity of the tracer particle showed signs of periodic fluctuations, which were not found in the reference case. Moreover, there is a considerable increase in the magnitude of the axial velocity, on average, throughout the screw mixer.

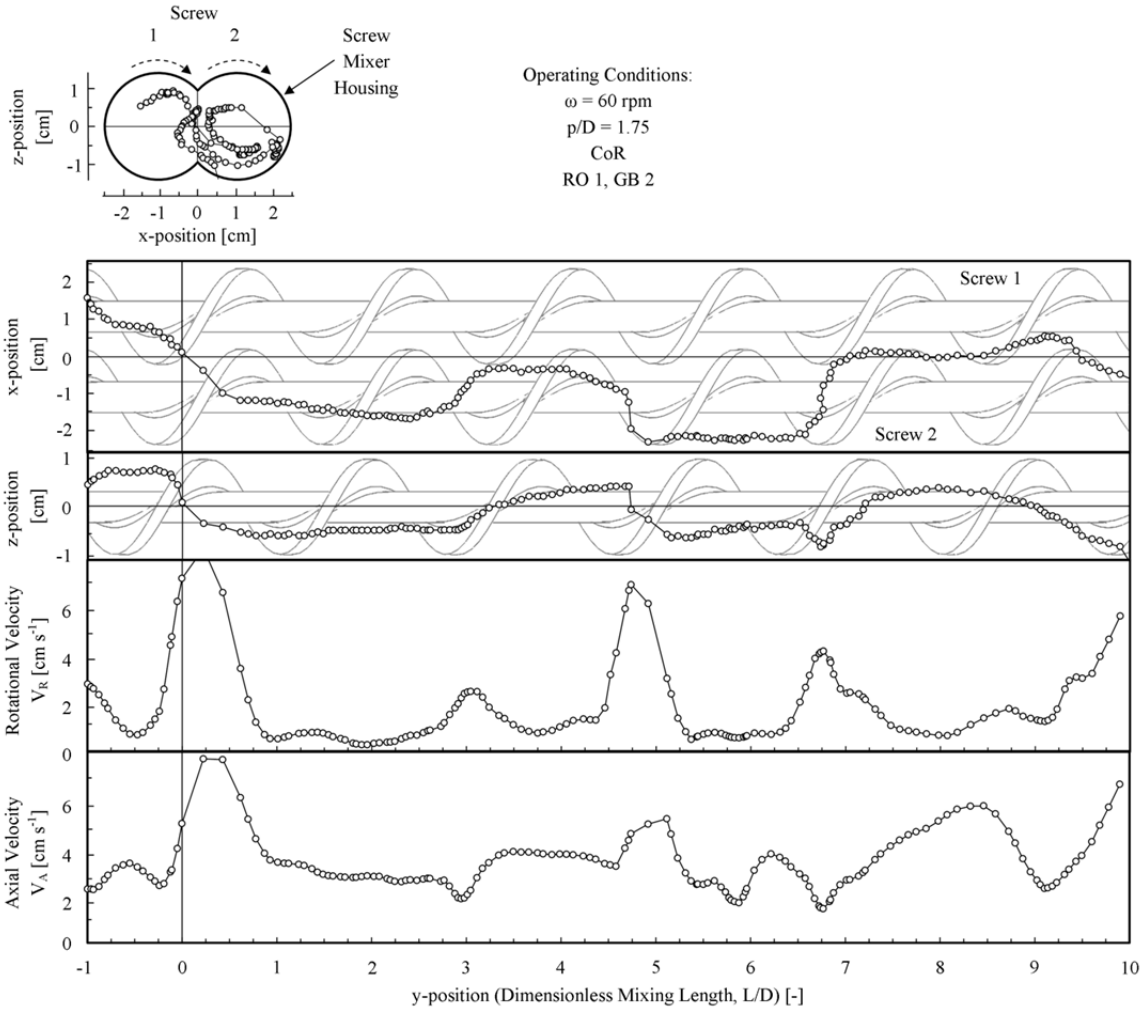

Figure 10.7: The tracer particle's position and velocity for a co-rotating (CoR) screw rotation orientation.

10.3.1.4.2 Counter-rotating Up-pumping

A counter-rotating up-pumping (CtrR UP) screw rotation orientation resulted in similar behavior to that of the dimensionless screw pitch of p/D = 0.75. More specifically, the tracer particle exhibited very little movement between the two screws, as shown in Figure 10.8. In fact, the only time the tracer particle moved from the region near screw one to screw two was before it reached the effective mixing region, after which it stayed near screw two for the duration of the test. The exit effects did begin to influence the tracer particle's rotational velocity at approximately the same location as

the reference condition (i.e., L/D = 9), but the axial velocity of the particle began to experiences changes slightly sooner, at approximately L/D = 8.5.

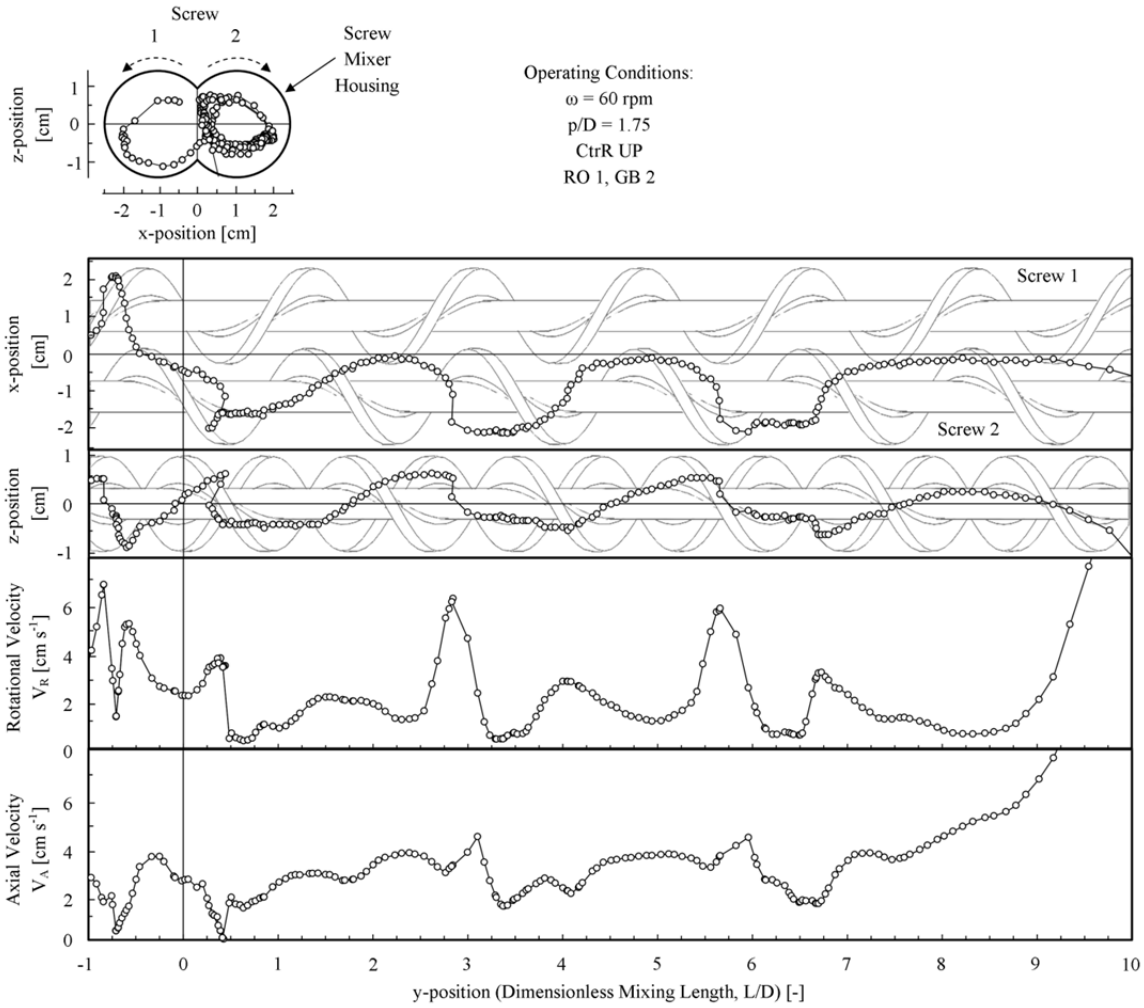

Figure 10.8: The tracer particle's position and velocity for counter-rotating up-pumping (CtrR UP) screw rotation orientation.

10.3.1.5 Material Injection Configuration

The most noticeable effect on the granular flow structures resulting from the change in the material injection configuration came in the form of increased entrance effects associated with the particle's rotational and axial velocity, as shown in Figure 10.9. As the tracer particle was being injected into the screw mixer, at approximately

L/D = 0, it had a large velocity as a result of the free-fall from the volumetric feeders, and propagated about one dimensionless mixing length into the screw mixer. A result of this high initial velocity is a slightly reduced residence time, which will be discussed in the following section. Similar findings to that of the reference condition in terms of the rotational and axial velocity were observed after L/D = 1. Additionally, the particle exhibited the same periodic fluctuations in the z-direction as did the reference condition, but showed very little movement in the x-direction.

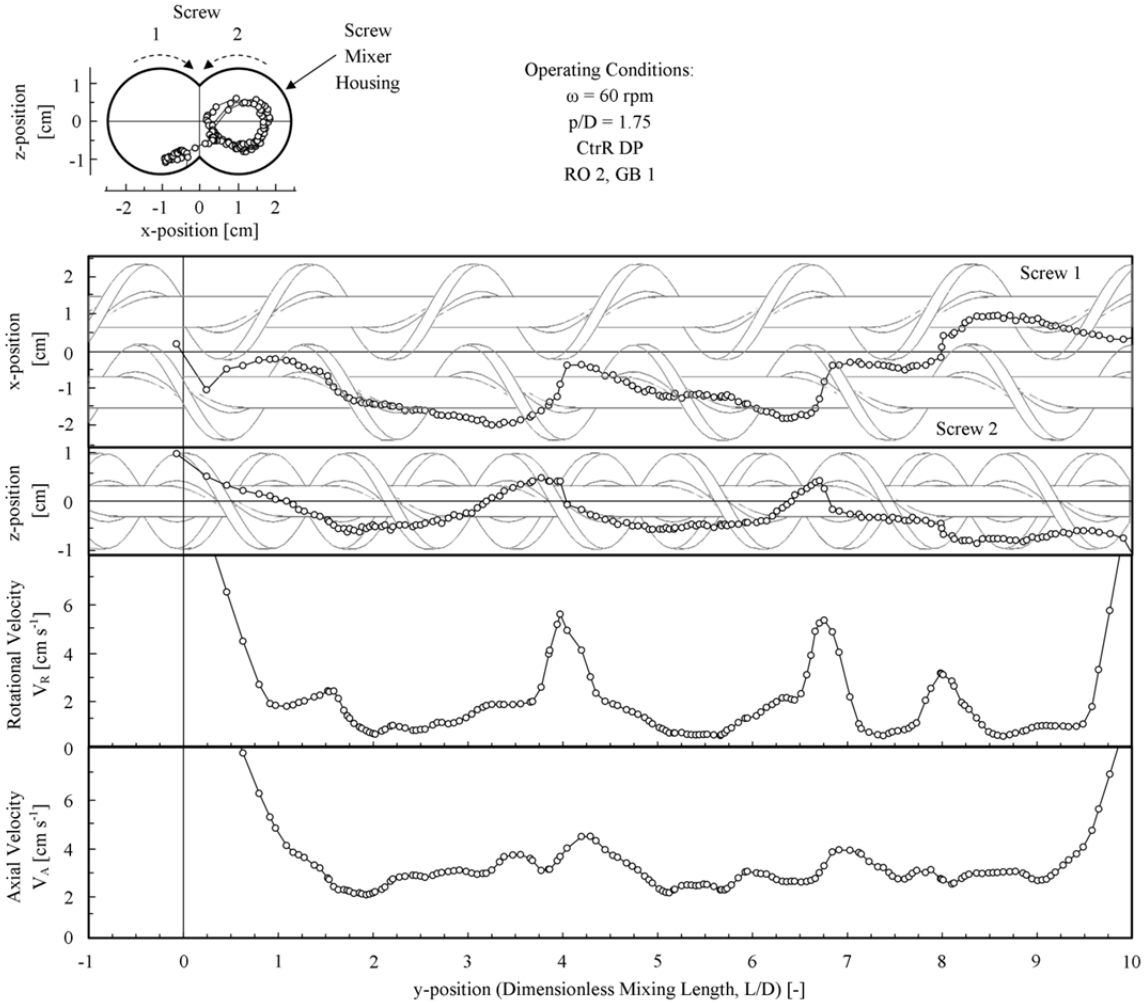

Figure 10.9: The tracer particle's position and velocity for material injection configuration with the red oak chips and glass bead injected into port one and two, respectively.

10.3.2 Residence Time

The residence time of the tracer particle in the effective mixing region ($0 < L/D < 10$) was calculated for each of the trials that were performed for each operating condition. As mentioned, five trials were performed for the reference condition, and three trails were performed for the remaining operating conditions. The average residence time for each operating condition is shown in Figure 10.10 as a function of the screw rotation speed and dimensionless screw pitch. The vertical error bars represent plus and minus one standard deviation that was computed from the multiple trails.

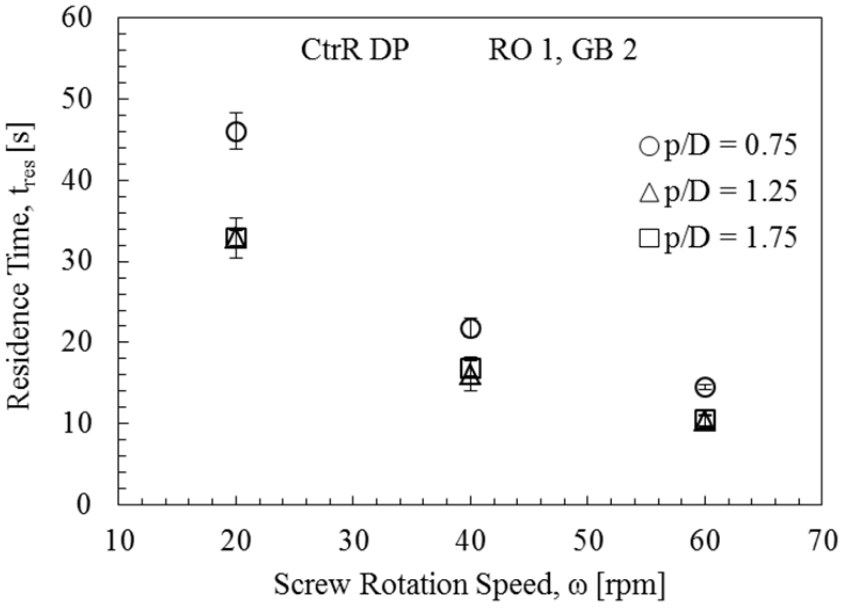

Figure 10.10: The tracer particle's residence time as a function of the screw rotation speed and dimensionless screw pitch.

The residence time of the tracer particle was found to be inversely proportional to the screw rotation speed. When the screw rotation speed was doubled from $\omega = 20$ rpm to $\omega = 40$ rpm, the residence time was reduced by approximately 50% for all three levels of the dimensionless screw pitch. When the screw rotation speed was increased from $\omega = 40$

rpm to ω = 60 rpm (a 50% increase), the residence time was reduced by approximately 35% for all three levels of the dimensionless screw pitch. The changing relationship between the screw rotation speed and the residence time suggests that more “slip” is occurring between the granular materials and the screws at higher screw rotation speeds, resulting in a nonlinear relationship.

A similar nonlinear trend is observed in the case of the dimensionless screw pitch. As the dimensionless screw pitch is changed from p/D = 0.75 to p/D = 1.25, there is approximately a 28% reduction in the material residence time for all three levels of the screw rotation speed. The differences in the residence times for dimensionless screw pitches of p/D = 0.75 and p/D = 1.25 is much greater than the error associated with the measurements, resulting in the ability to distinguish between the two conditions. However, changing the dimensionless screw pitch from p/D = 1.25 to p/D = 1.75 had little effect on the material residence time, as it remained almost constant. Moreover, the differences in the residence times are much less than the error in the measurements, resulting in the inability to distinguish these two conditions. The nonlinear relationship between the dimensionless screw pitch and the residence time agrees with theoretical models that predict a similar nonlinear result (Metcalf, 1964).

The granular flow rate and resulting residence time of individual tracer particles in the screw mixer are significantly influenced by the screw rotation speed, and somewhat influenced by the dimensionless screw pitch. In this study, it was also observed that the screw rotation orientation had an influence on the residence time. As shown in Figure 10.11, a counter-rotating up-pumping (CtrR UP) and co-rotating (CoR) screw rotation orientations resulted in a 16% and 29% reduction in the residence time

relative to the reference condition (CtrR DP), respectively. The differences in the material residence time between these operating conditions is larger than the error associated with the measurements, resulting in the ability to distinguish the different operating conditions.

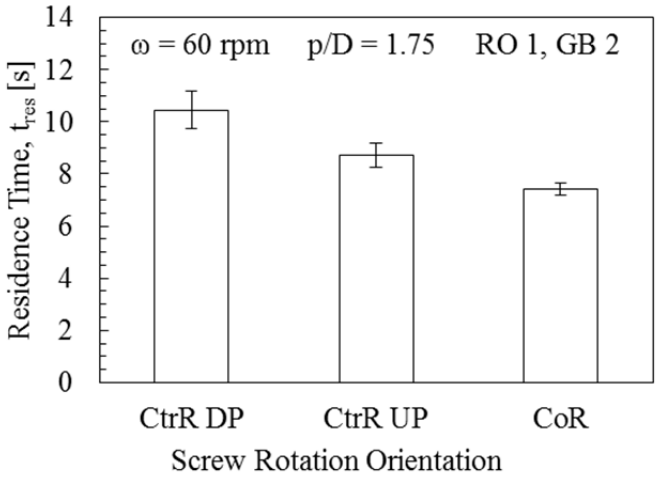

Figure 10.11: Residence time as a function of the screw rotation orientation.

The longer residence time associated with the counter-rotating down-pumping screw rotation orientation was attributed to the increased rotational velocity which caused the particle to be transmitted back and forth between the two screws, and resulted in longer particle pathlines. This outcome also provides significant insight into a critical phenomenon that was noted by Kingston and Heindel (2013c), who discovered that a counter-rotating down-pumping screw rotation orientation offered significant improvements in terms of the mixing effectiveness of the screw mixer. Based on the findings in this study, the increased mixing effectiveness could be partly attributed to the longer residence time, which results in a longer mixing time.

The material injection configuration had a relatively insignificant influence on the residence time. Only a 7% reduction in the material residence time was noted, as shown

in Figure 10.12, when the material injection configuration was changed from the red oak chips and glass beads being injected in port one and two (RO 1, GB 2), respectively, to the red oak chips and glass beads being injected into port two and one (RO 2, GB 1), respectively. The vertical error bars represent plus and minus one standard deviation that was computed from the multiple trials. As shown, the 7% difference is within the limits of the error bars so these two conditions cannot be distinguished.

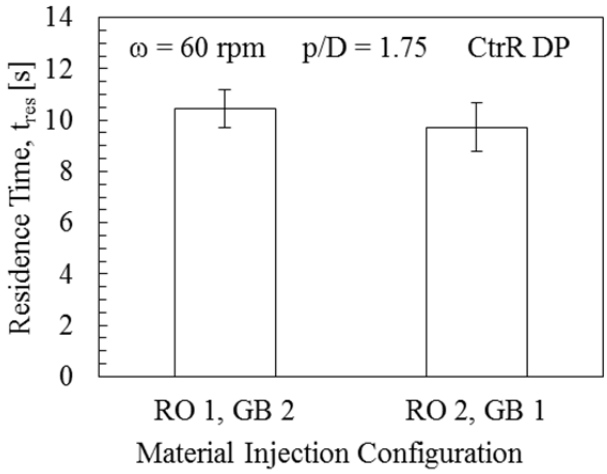

Figure 10.12: Residence time as a function of the material injection configuration.

10.4 Conclusions

Previous studies in the literature have visualized the effect of operating conditions and mixer geometry on the resulting 2D flow structures in single and double screw mixers. However, no study, to the author's knowledge, has characterized the influence of operating conditions on the 3D granular flow structures in a double screw mixer, which could be partly attributed to the opaque nature of the granular flow.

The 3D granular flow structures inside a double screw mixer were shown to be significantly influenced by the selected operating conditions. In general, higher screw rotation speeds, longer dimensionless screw pitches, a counter-rotating down-pumping

screw rotation orientation, and a material injection configuration with the red oak chips and glass beads injected into port one and two, respectively (i.e., the reference condition), resulted in longer tracer particle pathlines and increased movement between and around the two screws. The counter-rotating down-pumping screw rotation orientation also resulted in longer residence times relative to the other two orientations. The increased length of the tracer particle pathline and increased residence time are projected to increase the mixing effectiveness of the screw mixer by providing a more convective mixing process, and allowing the double screw mixer to essentially behave like a double screw mixer (as opposed to two single screw mixers). These findings are consistent with the measured mixing effectiveness by Kingston and Heindel (2013b, c), and further support their conclusions.

Acknowledgements

Support for portions of this work by Phillips 66 Company is gratefully acknowledged. The X-ray facility used in this research was funded by the National Science Foundation under award number CTS-0216367 and Iowa State University.

CHAPTER 11: CONCLUSIONS AND FUTURE WORK

This chapter contains three sections: (i) conclusions from the individual studies that were conducted throughout the course of this project, (ii) some problems that were encountered, and solutions to and/or recommendations to resolve these problems, and (iii) suggestions for future work.

11.1 Conclusions

11.1.1 Double Screw Mixer

Granular mixing processes are important because they have a significant influence on the resulting products in a large number of industries. However, understanding and characterizing granular mixing and segregation is an ambitious task because of the challenges associated with visualizing and quantifying these opaque flows. Throughout this project, a number of different visualization and quantification techniques have been developed and used to evaluate the mixing effectiveness of a screw mixer consisting of red oak chips and glass beads. Four parameters were initially investigated: (i) screw rotation speed, (ii) dimensionless screw pitch, (iii) screw rotation orientation, and (iv) material injection configuration. After identifying the influence that these parameters had on the mixing effectiveness, the effect of the dimensionless mixing length was also investigated.

Optical visualization methods were first used to qualitatively assess the dynamic granular mixing process. The effects of the aforementioned parameters were investigated, and some general recommendations in terms of maximizing the mixing effectiveness of the screw mixer were made.

The spatial heterogeneity of the granular material was then evaluated using an improved granular sampling procedure that satisfies Allen's (1996) two "golden rules of sampling." Quantitative composition and statistical analysis was then performed on granular samples that were collected from the screw mixer's exit stream. Using these methods, the most influential factors were indicated, and the operating conditions of the screw mixer were optimized. The results from the qualitative optical visualization and quantitative composition and statistical analysis were then coupled together to provide a complete assessment of the dynamic mixing process inside the screw mixer and the resulting mixture that exits the screw mixer. Both of these methods indicated that a screw rotation speed of $\omega = 60$ rpm, a dimensionless screw pitch of $p/D = 1.75$, a counter-rotating down-pumping (CtrR DP) screw rotation orientation, and a material injection configuration featuring the red oak chips and glass beads injected into port one and two, respectively, reduced the degree of segregation and produced the most homogeneous granular mixture.

The influence of the dimensionless mixing length was then investigated for a selected number of operating conditions, and the aforementioned optimized operating condition was once again found to offer the best mixing performance, at each dimensionless mixing length that was studied. Other operating conditions showed

significantly higher degrees of segregation, particularly at short dimensionless mixing lengths.

An improved cone-beam compensated back-projection algorithm enabling XPTV of the screw mixer was then developed. The cone-beam compensation was shown to provide a significant reduction in error associated with the tracer particle's position relative to parallel-beam back-projection algorithms. These methods were then used to characterize the 3D granular flow structures inside the screw mixer under various operating conditions. The effects of the aforementioned four factors were investigated, and from the obtained results, similar results to the previous studies in terms of the mixing effectiveness of the screw mixer were noted. A high screw rotation speed, long dimensionless screw pitch, counter-rotating down-pumping screw rotation orientation, and material injection configuration featuring the red oak chips injected into port one and two, respectively, provided advantageous granular flow structures, resulting in improved convective mixing. Moreover, the counter-rotating down-pumping screw rotation orientation, which was found to be the most influential factor using the composition and statistical analysis methods, was also shown to increase the material residence time, resulting in a longer mixing time. This longer mixing time allows the granular material to reach a higher degree of homogeneity.

Overall, a number of different methods were used to characterize the granular mixing process inside the screw mixer. While each of the methods provided a different view on mixing behavior, a common theme was found in terms of the selection of the screw mixer's operating condition for the purpose of maximizing its mixing effectiveness. The screw mixer's improved mixing effectiveness will have far reaching

effects, particularly in the case of screw pyrolyzers because the increased mixing will lead to higher heat transfer rates and resulting bio-oil yields.

11.1.2 Single Screw Mixer

The mixing effectiveness of a single screw mixer was also investigated, and qualitatively compared to the double screw mixer. Optical visualization of the dynamic mixing process in the single screw mixer indicated that increased segregation was present, and the granular material was essentially being conveyed instead of mixed. Composition analysis was also performed, but these results could not be compared to the composition analysis results of the double screw mixer due to geometrical limitations that reduced the number of available samples. Overall, a double screw mixer is highly recommended over a single screw mixer for the aforementioned reasons.

11.2 Encountered Problems

11.2.1 Screw Failure

Throughout the course of this project, numerous screw failures occurred while performing granular mixing studies. The cause of these screw failures were jamming of red oak chip(s) either between the intermeshing screw flights or between the screw flights and the screw mixer housing, as shown in Figure 11.1.

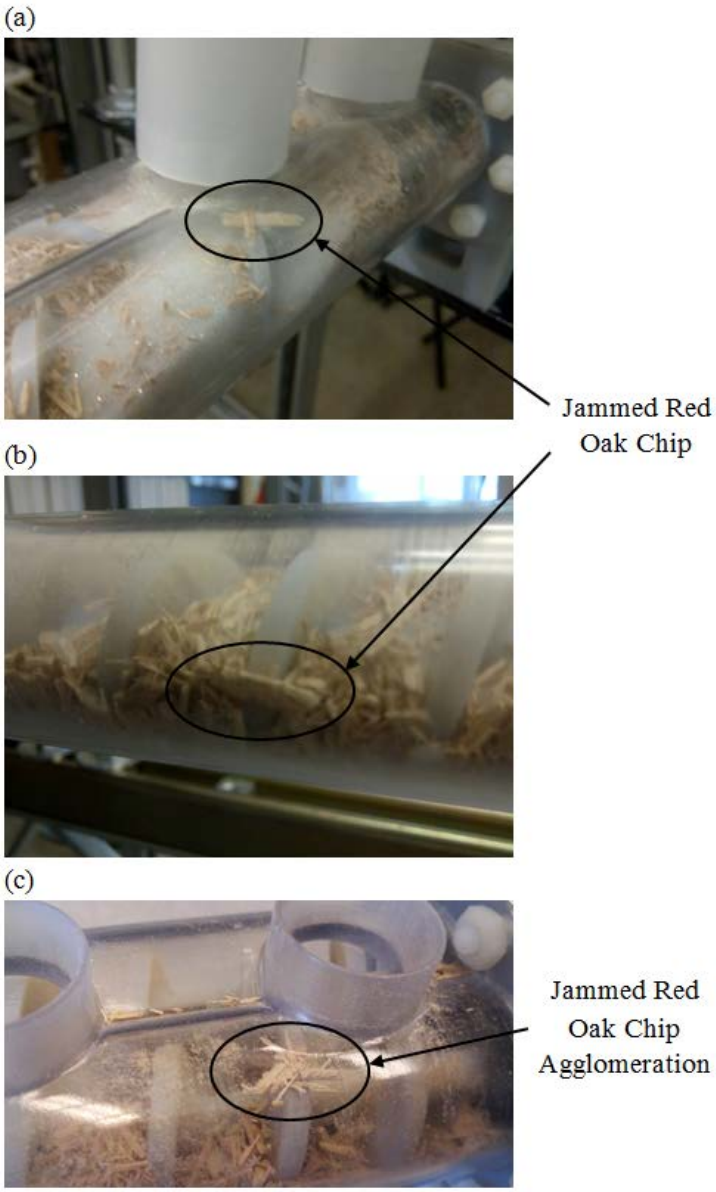

Figure 11.1: Jammed red oak chips ultimately resulting in screw failures.

The jammed red oak chip(s) ultimately resulted in the screw(s) locking up. However, the gearmotor continued to exert a torque on the screws, causing the screw shaft to break in the region where the shaft transitions from a circular cross-section to a square cross-section due to the stress concentration in this area, as shown in Figure 11.2.

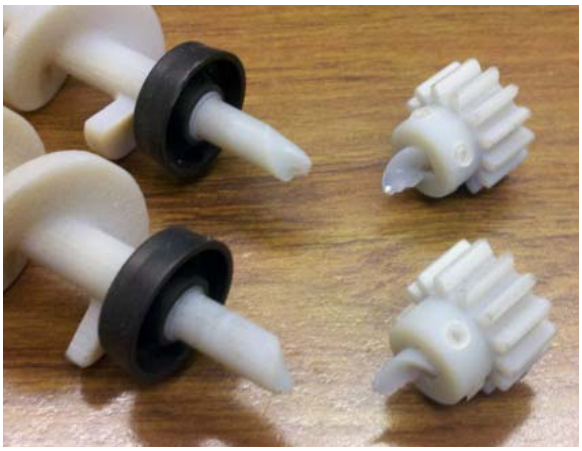

Figure 11.2: Screw shaft failure.

To mitigate some of the screw failures, the manual screening process that was described in Chapter 3 was used to discard the abnormally large and/or hard red oak chips. However, even with many of the large red oak chips removed, the cohesion between the granules still caused red oak chip agglomerations, as shown in Figure 11.1c, which resulted in an occasional screw failure. It is important to note that if the screws and the screw mixer housing were fabricated from stainless steel, as is typical for screw pyrolyzers, it is unlikely that these screw failures would occur.

11.2.2 Humidity

As the properties of the interstitial fluid (e.g., air) between granular particles changes, it influences the granular behavior. As was noted in Chapter 2, when the relative humidity of the atmosphere is relatively high (> 65%), liquid bridge forces are present. In contrast, when the humidity is low, electrostatic forces are more dominant. Throughout the course of this project, the environmental conditions in the laboratory would change depending on the time of year. This change was most noticeable during the winter months when the relative humidity was extremely low (~ 10-15%). This resulted in large electrostatic forces, causing the granules to stick together, or stick to the screw mixer's

housing, due to the cohesive electrostatic force. To minimize this effect, two large Essick EA 14070 evaporative humidifiers were place near the test stand, and allowed to run continuous by installing a Fluidmaster float valve inside the humidifiers and hooking it up to the building's water supply. This float valve regulated the water level inside the humidifier and allowed for continuous operation. The addition of these humidifiers increased the relative humidity near the test stand such that the electrostatic forces were minimal.

11.2.3 Mixing Paddles

As noted in the literature, the use of mixing paddles, which are typically spaced at intervals and set to partially oppose the forward flow of material, in screw mixing applications is thought to increase the mixing effectiveness of the device (Colijn, 1985). Thus, the use of mixing paddles was investigated in the single screw mixer. Mixing paddles were not investigated for the double screw mixer because of the intermeshing design.

Qualitative optical visualization was captured of the dynamic mixing process inside the single screw mixer containing a screw with mixing paddles, which was previously described in Chapter 3. Like the literature suggestions, and was mentioned in Chapter 2, the mixing paddles were set to partially oppose the forward flow of granular material. The single screw mixer's material injection configuration first featured the red oak chips and glass beads being injected into port one and two, respectively, as this configuration was found to be beneficial in terms maximizing the mixing effectiveness. However, with this material injection configuration, it was found that the mixing paddles near the red oak chip inlet port significantly opposed the forward flow of motion, causing

the red oak chips to essentially spin inside the screw mixer housing, and not be conveyed in the axial direction, as shown in Figure 11.3, resulting in a material backup inside the inlet tube.

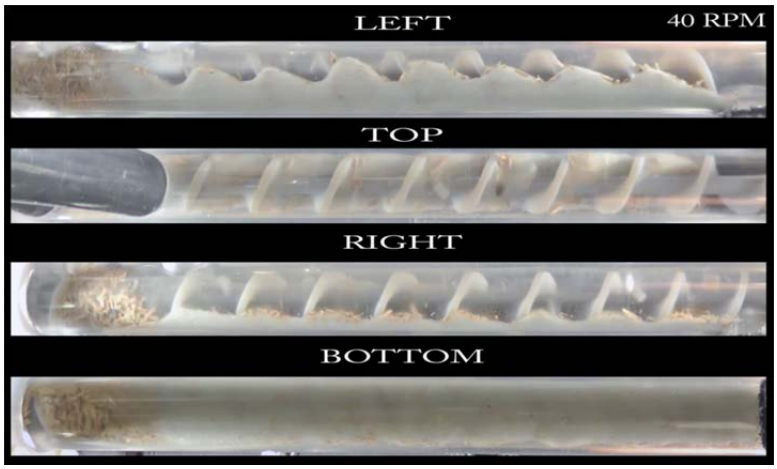

Figure 11.3: Snapshot of the single screw mixer with mixing paddles, and the red oak agglomeration near the inlet port for a material injection configuration of RO 1, GB 2.

The material injection configuration was then changed to the red oak chips and glass beads being injected into port two and one, respectively. In this configuration, the glass beads essentially “fluidized” the red oak chips immediately after the red oak chips were injected, and did allow the granular materials to mix and be conveyed through the single screw mixer. However, the mixing paddles still caused some undesired mixing behavior. Most notably, the mixing paddles produced large red oak chip agglomerations in some screw flight openings, while other openings remained fairly empty. This behavior causes the volumetric fill ratio in portions of the screw mixer to be larger than the recommended 65%, and results in the possibility for jamming; as illustrated in Figure 11.4. These observations coupled with the lower mixing effectiveness associated with the

single screw mixer resulted in recommendations to avoid the use of mixing paddles, at least in the case of a laboratory-scale single screw mixer.

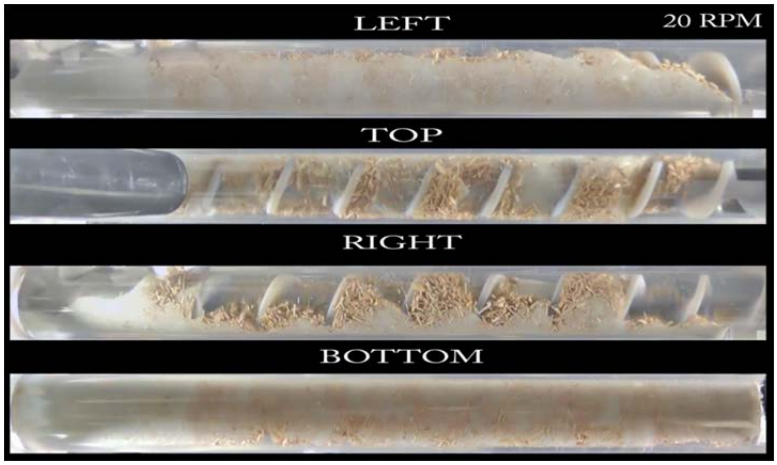

Figure 11.4: Snapshot of the single screw mixer with mixing paddles for a material injection configuration of RO 2, GB 1.

11.2.4 X-ray Computed Tomography

The composition and statistical analysis techniques that were used to measure the mixing effectiveness of the screw mixer provided a gross assessment of the spatial heterogeneity in the granular composition. One goal of this project was to quantitatively characterize the mixing effectiveness of the entire screw mixer on a local scale.

X-ray CT imaging has been used by other researchers to quantify mixing and segregation in cold-flow fluidized beds (Keller et al., 2013). Thus, an attempt to quantify the local mixing effectiveness of the screw mixer used in this project was made. Unlike the simply geometry associated with the fluidized bed that was used by Keller et al. (2013), the geometry of the screw mixer is significantly more complicated. For example, the fluidized bed essentially features of a fixed cylinder with solid particles and a fluidized gas inside, whereas the screw mixer features an intermeshing double cylinder design, with two intermeshing screws that mechanically mix the granular mixing. To

enable successful mixing quantification in the case of the screw mixer, the angular position of the two screws needed to be identical before and after the test. Therefore, the Lin Engineering stepper motor that was described in Chapter 3 was used to vary the screw rotation speed, and ensure accurate angular positioning. A set of three custom stepper motor programs were written using the Lin Engineering syntax to achieve the desired results, as shown in Appendix D. By accurately positioning the screws before and after the test, an empty screw mixer volume file that was obtained from the X-ray CT imaging was subtracted from a screw mixer volume file that was full of granular material. Three individual slices (i.e., end, side, and top views) of the empty screw mixer volume file are shown in Figure 11.5.

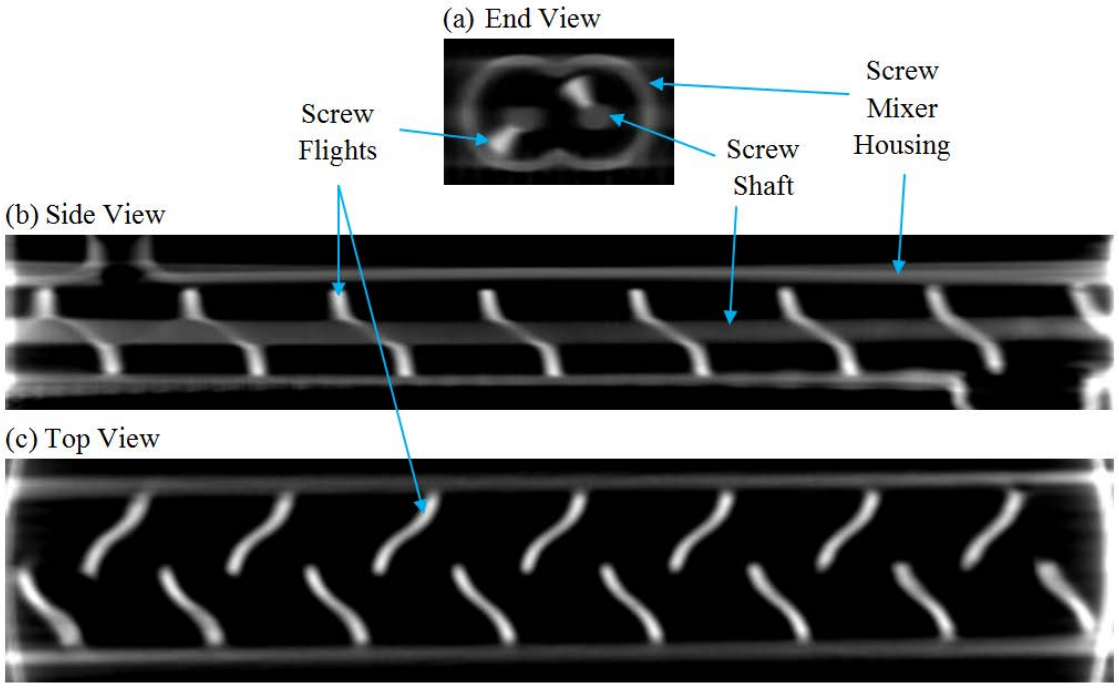

Figure 11.5: Slices obtained from an X-ray CT image of an empty screw mixer.

A noteworthy observation that is shown in Figure 11.5 is that the screw flights and the screw shafts appear to have different X-ray intensities, despite being made of the

same material. However, this difference was also observed in the X-ray CT images of granular mixtures, as will be demonstrated in the following sections; thus, it did not cause any problems.

The subtraction of the empty X-ray CT volume from a volume file consisting of granular material resulted in a new volume file that excluded the screw mixer's geometrical features and included only the granular material. Ideally this would allow the composition of individual voxels (i.e., 3D pixels) to be determined by using a method similar to the one developed in Chapter 4. An X-ray CT image was taken of a screw mixer consisting of 100% red oak chips, as shown in Figure 11.6, and another image was taken of a screw mixer consisting of 100% glass beads, as shown in Figure 11.7. As shown in Figure 11.6, the screw flight and screw shafts appear to have the same change in X-ray intensity as was observed for the empty screw mixer X-ray CT image. Thus, this change is the X-ray intensify is essentially normalized when subtracting the two volume files and yields an acceptable new volume file.

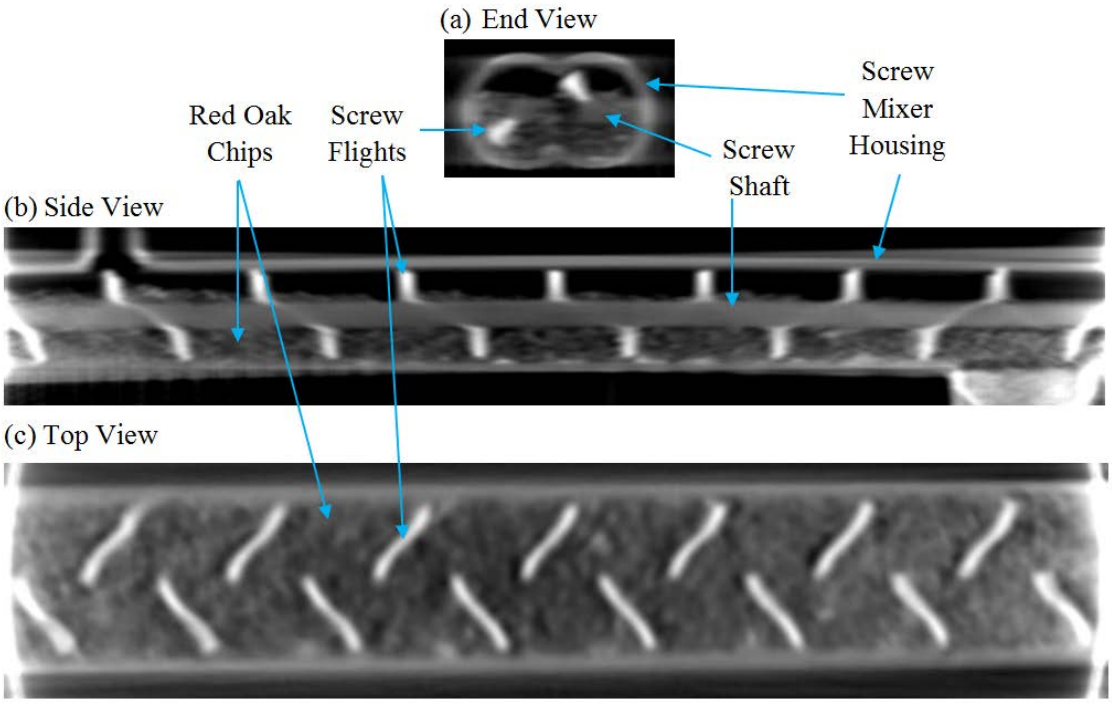

Figure 11.6: Slices obtained from an X-ray CT image of a screw mixer consisting of 100% red oak chips.

While the previous two X-ray CT images showed promising signs of local composition analysis, X-ray CT images of the screw mixer filled with 100% glass beads did not. As shown in Figure 11.7, the X-ray intensity of the portions of the screw flight and screw shaft that are outside the bed of glass beads are vastly different than the portions inside the bed of glass beads. This effect is the most noticeable when viewing the end view in Figure 11.6. The screw flight on the left side of the image is in the glass bead bed, whereas the screw flight on the right side of the image is outside the glass bead bed and is exposed to the air. As shown, the X-ray intensity of these two portions of the screw flighting is vastly different, despite being made of the same material, and is thus an image artifact.

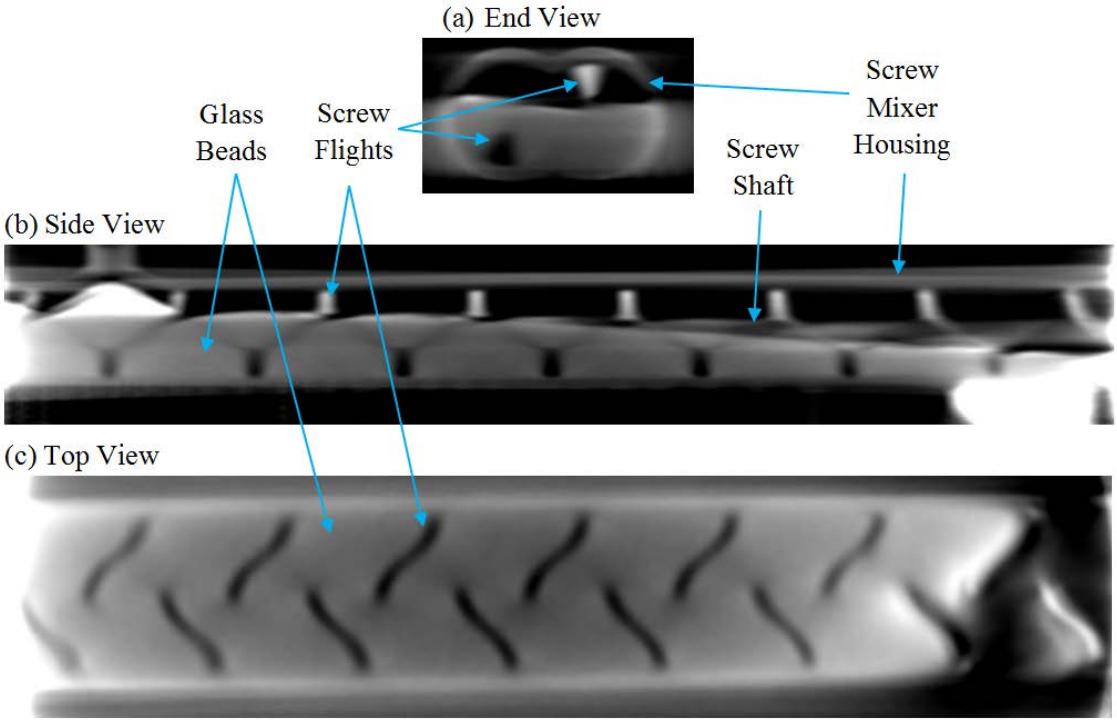

Figure 11.7: Slices obtained from an X-ray CT image of the screw mixer consisting of 100% glass beads.

After encountering this X-ray image artifact, the experts at the Iowa State University Center for Nondestructive Evaluation (ISU CNDE) were consulted. It was determined that this X-ray imaging artifact is a result of “missing data.” Missing data refers to parts of the OOI being imaged in some of the X-ray radiographic images that are used to reconstruct the X-ray CT volume file, and other parts of the OOI not being imaged (i.e., missing data). The reason part of the screw mixer is not being imaged is because the screw mixer has a very long aspect ratio (i.e., ratio of the length to width/height). This causes the ends of the screw mixer to not be imaged when it is positioned perpendicular to the X-ray source and detector mid-line. Moreover, it causes the X-rays to pass through a very long object when it is positioned parallel to the X-ray source and detector mid-line. This X-ray artifact only appears in the case of the glass

beads because the X-ray absorption of the glass beads is much larger than that of air or red oak chips. Thus, it magnifies this phenomenon and results in unusable X-ray imaging.

The influence of beam hardening was investigated as a possible cause of this image artifact phenomenon. Empirical beam hardening corrections were applied to the X-ray images of the screw mixer consisting of 100% glass beads, but little change was found. X-ray CT images of a screw mixer consisting of a mixture of red oak chips and glass beads were also acquired, and the same X-ray artifact was observed. Therefore, attempts to quantify the screw mixer's local mixing effectiveness were abandoned, and additional X-ray stereography studies that were of interest were pursued.

11.3 Future Work

A thorough assessment of the granular mixing process inside the screw mixer was performed for the red oak chips and glass beads. However, there is still many opportunities for future work. First, granular materials that were used in this study could be changed, which is sure to result in vastly different mixing behavior. Now that the optimized operating conditions have been determined, at least for the parameters of this study, different granular materials which resemble other biomass materials (e.g., switchgrass) and heat carrier media (e.g., stainless steel shot) used in the biomass thermochemical conversion industry could be investigated. Moreover, the heat carrier media to biomass mass flow rate ratio could be changed to accommodate various thermodynamic considerations such as the thermal heating capacity of the heat carrier media or the biomass heat transfer requirements.

Accurate granular scaling laws have yet to be developed. Thus, attempting to apply scaling laws in an effort to scale the laboratory-scale screw mixer used for this project to either a pilot-scale or industrial-scale screw mixer without experimental investigation is ill-advised. Another possible project extension would be to characterize the mixing effectiveness of different sized screw mixers, which would be beneficial in terms of bridging the gap between a laboratory-scale and industrial-scale screw mixer.

To verify that the optimized operating conditions in terms of the mixing effectiveness of the screw mixer directly translate to increased bio-oil yields in a screw pyrolyzer, a possible project extension would be to either change the current operating conditions of an existing screw pyrolyzer or build a new screw pyrolyzer with this configuration, and perform fast pyrolysis experiments.

Invasive granular sample collection and analysis methods are quite time consuming, and many times lead to inaccurate results if not performed correctly. A full 3D RGB digital image analysis technique that allows for mixing assessment in continuous mixing processes, and improves upon many of the aforementioned digital image analysis techniques, could be developed. This would allow for a more streamline mixing assessment, and could ultimately be incorporated into the actual granular mixing process, allowing for real-time continuous monitoring.

In the case of larger, industrial size mixers, surface visualization may not be sufficient to accurately determine local 3D mixing. A new X-ray CT imaging device that features a horizontal axis of rotation, in contrast to the vertical axis of rotation found in the XFloViz Facility, could be designed and constructed, enabling local quantitative

mixing assessment of the screw mixer. The horizontal axis of rotation would eliminate many of the aforementioned X-ray CT imaging problems encountered in this project.

Once sufficient experimental data have been collected, computational models could be developed and compared to the experimental results. Doing so would allow for the development of accurate scaling laws, and eliminate much of the cost associated with experimental testing.

REFERENCES

Aissa, A.A., Duchesne, C., Rodrigue, D., 2010a. Polymer powders mixing part I: Mixing characterization in rotating cylinders. Chemical Engineering Science 65, 786-795.

Aissa, A.A., Duchesne, C., Rodrigue, D., 2010b. Polymer powders mixing part II: Multi-component mixing dynamics using RGB color analysis. Chemical Engineering Science 65, 3729-3738.

Allen, T., 1996. Particle size measurement: Volume 1: Powder sampling and particle size measurement. Springer.

Babout, L., Grudzien, K., Maire, E., Withers, P.J., 2013. Influence of wall roughness and packing density on stagnant zone formation during funnel flow discharge from a silo: An X-ray imaging study. Chemical Engineering Science 97, 210-224.

Bahng, M.K., Mukarakate, C., Robichaud, D.J., Nimlos, M.R., 2009. Current technologies for analysis of biomass thermochemical processing: A review. Analytica Chimica Acta 651, 117-138.

Boyer, C., Duquenne, A.M., Wild, G., 2002. Measuring techniques in gas-liquid and gas-liquid-solid reactors. Chemical Engineering Science 57, 3185-3215.

Bridgwater, A.V., 2002. Fast pyrolysis of biomass: A handbook volume 2. CPL Scientific Publishing Services, Limited.

Bridgwater, A.V., 2003. Renewable fuels and chemicals by thermal processing of biomass. Chemical Engineering Journal 91, 87-102.

Bridgwater, A.V., Boocock, D.G.B., 1997. Developments in thermochemical biomass conversion. Blackie Academic & Professional.

Bridgwater, A.V., Meier, D., Radlein, D., 1999. An overview of fast pyrolysis of biomass. Organic Geochemistry 30, 1479-1493.

Bridgwater, A.V., Peacocke, G.V.C., 2000. Fast pyrolysis processes for biomass. Renewable & Sustainable Energy Reviews 4, 1-73.

Bridgwater, J., 2010. Mixing of particles and powders: Where next? Particuology 8, 563-567.

Bridgwater, J., 2012. Mixing of powders and granular materials by mechanical means - A perspective. Particuology 10, 397-427.

Brown, J.N., 2009. Development of a lab-scale auger reactor for biomass fast pyrolysis and process optimization using response surface methodology, MS Thesis, Deparments of Mechanical Engineering and Biorenewable Resources and Technology, Iowa State University, p. 260.

Brown, J.N., Brown, R.C., 2012a. Process optimization of an auger pyrolyzer with heat carrier using response surface methodology. Bioresource Technology 103, 405-414.

Brown, R.C., 2003. Biorenewable resources: Engineering new products from agriculture. Wiley.

Brown, R.C., Brown, T.R., 2012b. Why are we producing biofuels?: Shifting to the ultimate source of energy. Brownia LLC.

Brown, R.C., Stevens, C., 2011. Thermochemical processing of biomass: Conversion into fuels, chemicals, and power. Wiley.

Bruvik, E.M., Hjertaker, B.T., Hallanger, A., 2010. Gamma-ray tomography applied to hydro-carbon multi-phase sampling and slip measurements. Flow Measurement and Instrumentation 21, 240-248.

Busciglio, A., Vella, G., Micale, G., Rizzuti, L., 2009. Analysis of the bubbling behaviour of 2D gas solid fluidized beds part II. Comparison between experiments and numerical simulations via digital image analysis technique. Chemical Engineering Journal 148, 145-163.

Camp, D.W., 1990. Mild coal gasification - Screw pyrolyzer development and design, Tenth Annual Gasification and Gas Stream Cleanup Systems Contractor's Review Meeting, Morgantown, West Virginia.

Campbell, C.S., 2006. Granular material flows - An overview. Powder Technology 162, 208-229.

Carr, J.F., Walker, D.M., 1968. An annular shear cell for granular materials. Powder Technology 1, 369-373.

Chand, R., Khaskheli, M.A., Qadir, A., Ge, B.L., Shi, Q.F., 2012. Discrete particle simulation of radial segregation in horizontally rotating drum: Effects of drum-length and non-rotating end-plates. Physica A - Statistical Mechanics and its Applications 391, 4590-4596.

Chaouki, J., Larachi, F., Dudukovic, M.P., 1997. Noninvasive tomographic and velocimetric monitoring of multiphase flows. Industrial & Engineering Chemistry Research 36, 4476-4503.

Chen, C.-C., Yu, C.-K., 2004. Two-dimensional image characterization of powder mixing and its effects on the solid-state reactions. Materials Chemistry and Physics 85, 227-237.

Cleary, P.W., Sinnott, M.D., 2008. Assessing mixing characteristics of particle-mixing and granulation devices. Particuology 6, 419-444.

Cleveland, W.S., 1979. Robust locally weighted regression and smoothing scatterplots. Journal of the American Statistical Association 74, 829-836.

Cleveland, W.S., Devlin, S.J., 1988. Locally weighted regression: An approach to regression analysis by local fitting. Journal of the American Statistical Association 83, 596-610.

Colijn, H., 1985. Mechanical conveyors for bulk solids. Elsevier Science Publishers B.V., Amsterdam, New York.

Conway, S.L., Lekhal, A., Khinast, J.G., Glasser, B.J., 2005. Granular flow and segregation in a four-bladed mixer. Chemical Engineering Science 60, 7091-7107.

Crowe, C.C.T., Schwarzkopf, J.D., Sommerfeld, M., Tsuji, Y., 2011. Multiphase flows with droplets and particles. Taylor & Francis Group.

Czarnecki, J., Dabros, T., 1980. Attenuation of the van der Waals attraction energy in the particle semi-infinite medium system due to the roughness of the particle surface. Journal of Colloid and Interface Science 78, 25-30.

Dai, J.J., Grace, J.R., 2011. Biomass granular screw feeding: An experimental investigation. Biomass & Bioenergy 35, 942-955.

Daumann, B., Fath, A., Anlauf, H., Nirschl, H., 2009. Determination of the mixing time in a discontinuous powder mixer by using image analysis. Chemical Engineering Science 64, 2320-2331.

Daumann, B., Nirschl, H., 2008. Assessment of the mixing efficiency of solid mixtures by means of image analysis. Powder Technology 182, 415-423.

Davis, S.C., Diegel, S. W., Boundy, R. G., 2012. Transportation energy data book, 31 edition. Oak Ridge National Laboratory, Oak Ridge, Tennessee.

de Jong, J.F., Odu, S.O., van Buijtenen, M.S., Deen, N.G., Annaland, M.V., Kuipers, J.A.M., 2012. Development and validation of a novel digital image analysis method for fluidized bed particle image velocimetry. Powder Technology 230, 193-202.

Defrise, M., Kinahan, P., Michel, C., 2005. Image reconstruction algorithms in PET, Bailey, D., Townsend, D., Valk, P., Maisey, M. (editors), Positron Emission Tomography. Springer London, pp. 63-91.

DeVore, J.L., 2008. Probability and statistics for engineering and the sciences, Seventh edition. Thomson Brooks/Cole, Belmont, California.

Dhenge, R.M., Washino, K., Cartwright, J.J., Hounslow, M.J., Salman, A.D., 2013. Twin screw granulation using conveying screws: Effects of viscosity of granulation liquids and flow of powders. Powder Technology 238, 77-90.

Doering, E.R., 1992. Three-dimensional flaw reconstruction using a real-time X-ray imaging system. PhD Thesis, Department of Electrical Engineering, Iowa State University, Ames, Iowa, pp. 194.

Donahue, W.S., Brandt, J.C., 2009. Pyrolysis: Types, processes, and industrial sources and products. Nova Science Publishers, Incorporated.

Dos Passos, W., 2011. Numerical methods, algorithms, and tools in c#. Taylor & Francis.

Drake, J.B., Franka, N.P., Heindel, T.J., 2008. X-ray particle tracking velocimetry for applications in fluidized beds, ASME International Mechanical Engineering Congress and Exposition, Boston, Massachusetts, USA, Paper No. IMECE2008-66224.

Drake, J.B., Tang, L., Heindel, T.J., 2009b. X-ray particle tracking velocimetry in fluidized beds. ASME Fluids Engineering Division Summer Meeting, Vol 1, Pts A-C, 1733-1742, Paper No. FEDSM2009-78150.

Dudukovic, M.P., 2000. Opaque multiphase reactors: Experimentation, modeling, and troubleshooting. Oil & Gas Science and Technology - Rev. IFP, Energies Nouvelles 55, 135-158.

Dynamotive Energy Systems, 2010, webpage.

Ehrichs, E.E., Jaeger, H.M., Karczmar, G.S., Knight, J.B., Kuperman, V.Y., Nagel, S.R., 1995. Granular convection observed by magnetic resonance imaging. Science 267, 1632-1634.

Energy Information Administration, 2012. Annual energy review 2011. Bernan Association.

Escudero, D., Heindel, T.J., 2011. Bed height and material density effects on fluidized bed hydrodynamics. Chemical Engineering Science 66, 3648-3655.

Fayed, M.E., Otten, L., 1984. Handbook of powder science and technology. Van Nostrand Reinhold Co.

Feldkamp, L.A., Davis, L.C., Kress, J.W., 1984. Practical cone-beam algorithm. Journal of the Optical Society of America A - Optics Image Science and Vision 1, 612-619.

Ford, J.J., Heindel, T.J., Jensen, T.C., Drake, J.B., 2008. X-ray computed tomography of a gas-sparged stirred-tank reactor. Chemical Engineering Science 63, 2075-2085.

Gao, J.S., Lan, X.Y., Fan, Y.P., Chang, J., Wang, G., Lu, C.X., Xu, C.M., 2009. Hydrodynamics of gas-solid fluidized bed of disparately sized binary particles. Chemical Engineering Science 64, 4302-4316.

Gao, Y.J., Vanarase, A., Muzzio, F., Ierapetritou, M., 2011. Characterizing continuous powder mixing using residence time distribution. Chemical Engineering Science 66, 417-425.

Geldart, D., 1973. Types of gas fluidization. Powder Technology 7, 285-292.

Gosselin, R., Duchesne, C., Rodrigue, D., 2008. On the characterization of polymer powders mixing dynamics by texture analysis. Powder Technology 183, 177-188.

Grohse, E.W., 1955. Analysis of gas-fluidized solid systems by X-ray absorption. AIChE Journal 1, 358-365.

Gui, N., Fan, J.R., Cen, K.F., 2010. A macroscopic and microscopic study of particle mixing in a rotating tumbler. Chemical Engineering Science 65, 3034-3041.

Gui, N., Gao, J.S., Ji, Z.L., 2013. Numerical study of mixing and thermal conduction of granular particles in rotating tumblers. AIChE Journal 59, 1906-1918.

Hajra, S.K., Bhattacharya, T., McCarthy, J.J., 2010. Improvement of granular mixing of dissimilar materials in rotating cylinders. Powder Technology 198, 175-182.

Hamaker, H.C., 1937. The london - van der Waals attraction between spherical particles. Physica 4, 1058-1072.

Hardy, E.H., Hoferer, J., Kasper, G., 2007. The mixing state of fine powders measured by magnetic resonance imaging. Powder Technology 177, 12-22.

Heindel, T.J., 2011. A review of X-ray flow visualization with applications to multiphase flows. Journal of Fluids Engineering - Transactions of the ASME 133.

Heindel, T.J., Gray, J.N., Jensen, T.C., 2008. An X-ray system for visualizing fluid flows. Flow Measurement and Instrumentation 19, 67-78.

Hilton, J.E., Cleary, P.W., 2011. The influence of particle shape on flow modes in pneumatic conveying. Chemical Engineering Science 66, 231-240.

Huang, A.N., Kuo, H.P., 2012. A study of the three-dimensional particle size segregation structure in a rotating drum. AIChE Journal 58, 1076-1083.

Ingram, A., Seville, J.P.K., Parker, D.J., Fan, X., Forster, R.G., 2005. Axial and radial dispersion in rolling mode rotating drums. Powder Technology 158, 76-91.

Ingram, L., Mohan, D., Bricka, M., Steele, P., Strobel, D., Crocker, D., Mitchell, B., Mohammad, J., Cantrell, K., Pittman, C.U., 2008. Pyrolysis of wood and bark in an auger reactor: Physical properties and chemical analysis of the produced bio-oils. Energy & Fuels 22, 614-625.

Jain, N., Ottino, J.M., Lueptow, R.M., 2005. Regimes of segregation and mixing in combined size and density granular systems: An experimental study. Granular Matter 7, 69-81.

Jenneson, P.M., Gundogdu, O., 2006. In situ X-ray imaging of nanoparticle agglomeration in fluidized beds. Applied Physics Letters 88.

Kak, A.C., Slaney, M., 2001. Principles of computerized tomographic imaging. Society for Industrial and Applied Mathematics.

Keller, N.K.G., 2012. Mixing and segregation in 3D multi-component, two-phase fluidized beds. PhD Thesis, Department of Mechanical Engineering. Iowa State University, Ames, Iowa.

Keller, N.K.G., Bai, W., Fox, R.O., Heindel, T.J., 2013. Quantifying mixing in 3D binary particulate systems. Chemical Engineering Science 93, 412-422.

Kingston, T.A., Heindel, T.J., 2013a. Characterizing granular mixing homogeneity at various dimensionless mixing lengths in a double screw mixer, ASME Fluids Engineering Division Summer Meeting, Chicago, Illinois, Paper No. FEDSM2014-21048 (abstract accepted, paper in preparation).

Kingston, T.A., Heindel, T.J., 2013b. Granular mixing visualization and quantification in a double screw mixer: Part I - Qualitative optical visualization. Powder Technology (in review).

Kingston, T.A., Heindel, T.J., 2013c. Granular mixing visualization and quantification in a double screw mixer: Part II - Quantitative composition and statistical analysis. Powder Technology (in review).

Kingston, T.A., Heindel, T.J., 2013d. Optical visualization and composition analysis to quantify mixing in a double screw mixer. Powder Technology (in review).

Kingston, T.A., Morgan, T.B., Geick, T.A., Robinson, T.R., Heindel, T.J., 2013. An improved cone-beam compensated back-projection algorithm to enable X-ray particle tracking velocimetry. Flow Measurement and Instrumentation (in preparation).

Koller, D.M., Posch, A., Horl, G., Voura, C., Radl, S., Urbanetz, N., Fraser, S.D., Tritthart, W., Reiter, F., Schlingmann, M., Khinast, J.G., 2011. Continuous quantitative monitoring of powder mixing dynamics by near-infrared spectroscopy. Powder Technology 205, 87-96.

Ku, H.H., 1966. Notes on use of propagation of error formulas. Journal of Research of the National Bureau of Standards Section C - Engineering and Instrumentation C70, 263.

Lacey, P.M.C., 1954. Developments in the theory of particle mixing. Journal of Applied Chemistry 4, 257-268.

Leadbeater, T.W., Parker, D.J., Gargiuli, J., 2012. Positron imaging systems for studying particulate, granular, and multiphase flows. Particuology 10, 146-153.

Lee, S.J., Kim, G.B., 2003. X-ray particle image velocimetry for measuring quantitative flow information inside opaque objects. Journal of Applied Physics 94, 3620-3623.

Lee, S.J., Kim, G.B., Yim, D.H., Jung, S.Y., 2009. Development of a compact X-ray particle image velocimetry for measuring opaque flows. Review of Scientific Instruments 80.

Martelli, F.G., 1983. Twin-screw extruders: A basic understanding. Van Nostrand Reinhold Company Inc.

Masuda, H., Higashitani, K., Yoshida, H., 2010. Powder technology handbook, Third edition. Taylor & Francis.

McCarthy, J.J., Shinbrot, T., Metcalfe, G., Wolf, J.E., Ottino, J.M., 1996. Mixing of granular materials in slowly rotated containers. AIChE Journal 42, 3351-3363.

Meier, D., Faix, O., 1999. State of the art of applied fast pyrolysis of lignocellulosic materials - A review. Bioresource Technology 68, 71-77.

Metcalf, J.R., 1964. The mechanics of the screw feeder, Institution of Mechanical Engineers, pp. 131-146.

Metzger, M.J., Remy, B., Glasser, B.J., 2011. All the brazil nuts are not on top: Vibration induced granular size segregation of binary, ternary, and multi-sized mixtures. Powder Technology 205, 42-51.

Mohan, D., Pittman, C.U., Steele, P.H., 2006. Pyrolysis of wood/biomass for bio-oil: A critical review. Energy & Fuels 20, 848-889.

Morgan, T.B., Halls, B.R., Meyer, T.R., Heindel, T.J., 2013. A high-speed X-ray detector system for noninvasive fluid flow measurements, ASME Fluids Engineering Division Summer Meeting, Incline Village, Nevada, USA, Paper No. FEDSM2013-16427.

Morgan, T.B., Heindel, T.J., 2010. X-ray particle tracking of dense particle motion in a vibration-excited granular bed. ASME International Mechanical Engineering Congress and Exposition - 2010, Vol 7, Pts A and B, 1709-1717, Paper No. IMECE2010-39106.

Muzzio, F.J., Goodridge, C.L., Alexander, A., Arratia, P., Yang, H., Sudah, O., Mergen, G., 2003. Sampling and characterization of pharmaceutical powders and granular blends. International Journal of Pharmaceutics 250, 51-64.

Muzzio, F.J., Robinson, P., Wightman, C., Brone, D., 1997. Sampling practices in powder blending. International Journal of Pharmaceutics 155, 153-178.

Nielsen, A.R., Aniol, R.W., Larsen, M.B., Glarborg, P., Dam-Johansen, K., 2011. Mixing large and small particles in a pilot scale rotary kiln. Powder Technology 210, 273-280.

Niki, N., Kawata, Y., Satoh, H., Kumazaki, T., 1993. 3D imaging of blood-vessels using X-ray rotational angiographic system. Nuclear Science Symposium & Medical Imaging Conference, Vols 1-3, 1873-1877.

Ottino, J.M., Khakhar, D.V., 2000. Mixing and segregation of granular materials. Annual Review of Fluid Mechanics 32, 55-91.

Ottino, J.M., Khakhar, D.V., 2001. Fundamental research in heaping, mixing, and segregation of granular materials: Challenges and perspectives. Powder Technology 121, 117-122.

Park, H.J., Heo, H.S., Park, Y.K., Yim, J.H., Jeon, J.K., Park, J., Ryu, C., Kim, S.S., 2010. Clean bio-oil production from fast pyrolysis of sewage sludge: Effects of reaction conditions and metal oxide catalysts. Bioresource Technology 101, S83-S85.

Paul, E.L., Atiemo-Obeng, V., Kresta, S.M., 2004. Handbook of industrial mixing: Science and practice. Wiley.

Pernenkil, L., Cooney, C.L., 2006. A review on the continuous blending of powders. Chemical Engineering Science 61, 720-742.

Portillo, P.M., Ierapetritou, M.G., Muzzio, F.J., 2009. Effects of rotation rate, mixing angle, and cohesion in two continuous powder mixers - A statistical approach. Powder Technology 194, 217-227.

Portillo, P.M., Vanarase, A.U., Ingram, A., Seville, J.K., Ierapetritou, M.G., Muzzio, F.J., 2010. Investigation of the effect of impeller rotation rate, powder flow rate, and cohesion on powder flow behavior in a continuous blender using PEPT. Chemical Engineering Science 65, 5658-5668.

Rahiman, M.H.F., Rahim, R.A., Rahiman, M.H.F., Tajjudin, M., 2006. Ultrasonic transmission-mode tomography imaging for liquid/gas two-phase flow. IEEE Sensors Journal 6, 1706-1715.

Remy, B., Glasser, B.J., Khinast, J.G., 2010. The effect of mixer properties and fill level on granular flow in a bladed mixer. AIChE Journal 56, 336-353.

Rhodes, J., 1990. Principles of powder technology. Wiley.

Rhodes, M., 2008. Introduction to particle technology. Wiley.

Roels, S., Carmeliet, J., 2006. Analysis of moisture flow in porous materials using microfocus X-ray radiography. International Journal of Heat and Mass Transfer 49, 4762-4772.

Sarkar, A., Wassgren, C., 2009. Simulation of a continuous granular mixer: Effect of operating conditions on flow and mixing. Chemical Engineering Science 64, 2672-2682.

Sarkar, A., Wassgren, C., 2010. Continuous blending of cohesive granular material. Chemical Engineering Science 65, 5687-5698.

Scott, D.S., Majerski, P., Piskorz, J., Radlein, D., 1999. A second look at fast pyrolysis of biomass - The RTI process. Journal of Analytical and Applied Pyrolysis 51, 23-37.

Seeger, A., Kertzscher, U., Affeld, K., Wellnhofer, E., 2003. Measurement of the local velocity of the solid phase and the local solid hold-up in a three-phase flow by X-ray based particle tracking velocimetry (XPTV). Chemical Engineering Science 58, 1721-1729.

Seville, J.P., Tüzün, U., Clift, R., 1997. Processing of particulate solids. Springer.

Shepp, L.A., Kruskal, J.B., 1978. Computerized tomography - New medical X-ray technology. American Mathematical Monthly 85, 420-439.

Shimada, T., Habu, H., Seike, Y., Ooya, S., Miyachi, H., Ishikawa, M., 2007. X-ray visualization measurement of slurry flow in solid propellant casting. Flow Measurement and Instrumentation 18, 235-240.

Siiria, S., Yliruusi, J., 2009. Determining a value for mixing: Mixing degree. Powder Technology 196, 309-317.

Thangalazhy-Gopakumar, S., Adhikari, S., Ravindran, H., Gupta, R.B., Fasina, O., Tu, M., Fernando, S.D., 2010. Physiochemical properties of bio-oil produced at various temperatures from pine wood using an auger reactor. Bioresource Technology 101, 8389-8395.

Tsai, W.R., Lin, C.I., 1994. On the mixing of granular materials in a screw feeder. Powder Technology 80, 119-126.

Uchida, K., Okamoto, K., 2006. Measurement of powder flow in a screw feeder by X-ray penetration image analysis. Measurement Science & Technology 17, 419-426.

Uchida, K., Okamoto, K., 2008. Measurement technique on the diffusion coefficient of powder flow in a screw feeder by X-ray visualization. Powder Technology 187, 138-145.

US vs. Barr Laboratories 812, F. Supp 458, 1993. D. New Jersey.

van Ommen, J.R., Mudde, R.F., 2008. Measuring the gas-solids distribution in fluidized beds - A review. International Journal of Chemical Reactor Engineering 6.

Van Puyvelde, D.R., Young, B.R., Wilson, M.A., Schmidt, S.J., 1999. Experimental determination of transverse mixing kinetics in a rolling drum by image analysis. Powder Technology 106, 183-191.

Vanarase, A.U., Muzzio, F.J., 2011. Effect of operating conditions and design parameters in a continuous powder mixer. Powder Technology 208, 26-36.

Wadell, H., 1933. Sphericity and roundness of rock particles. Journal of Geology 41, 310-331.

Weinekötter, R., Gericke, H., 2006. Mixing of solids. Springer.

White, J.L., Kim, E.K., 2010. Twin screw extrusion: Technology and principles. Hanser Gardner Publications.

Wright, M.M., Daugaard, D.E., Satrio, J.A., Brown, R.C., 2010. Techno-economic analysis of biomass fast pyrolysis to transportation fuels. Fuel 89, S11-S19.

Xiao, Y.M., Amano, R.S., Cai, T.M., Li, J., 2005. New method to determine the velocities of particles on a solid propellant surface in a solid rocket motor. Journal of Heat Transfer - Transactions of the ASME 127, 1057-1061.

Yang, R.Y., Yu, A.B., McElroy, L., Bao, J., 2008. Numerical simulation of particle dynamics in different flow regimes in a rotating drum. Powder Technology 188, 170-177.

Yang, S.C., 2006. Density effect on mixing and segregation processes in a vibrated binary granular mixture. Powder Technology 164, 65-74.

Yoder, J., Galinato, S., Granatstein, D., Garcia-Perez, M., 2011. Economic tradeoff between biochar and bio-oil production via pyrolysis. Biomass & Bioenergy 35, 1851-1862.

Zolfaghari, A.M., Kellogg, E., Wendt, S., Gray, J., 2002. High speed X-ray radiography diagnostic of current interruption in circuit breakers. Review of Scientific Instruments 73, 1945-1948.

APPENDIX A: SCREW MIXER COMPONENT DRAWINGS

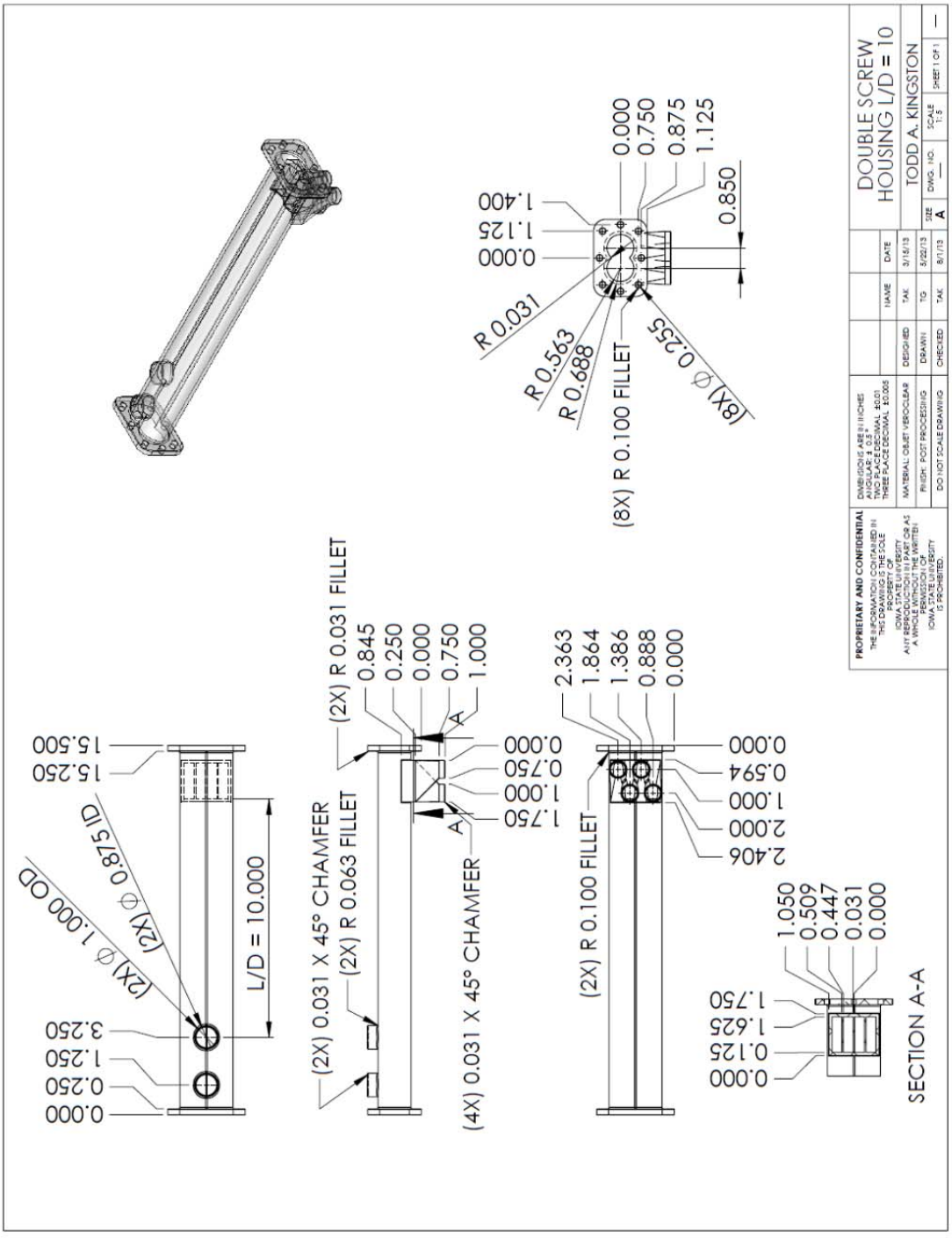

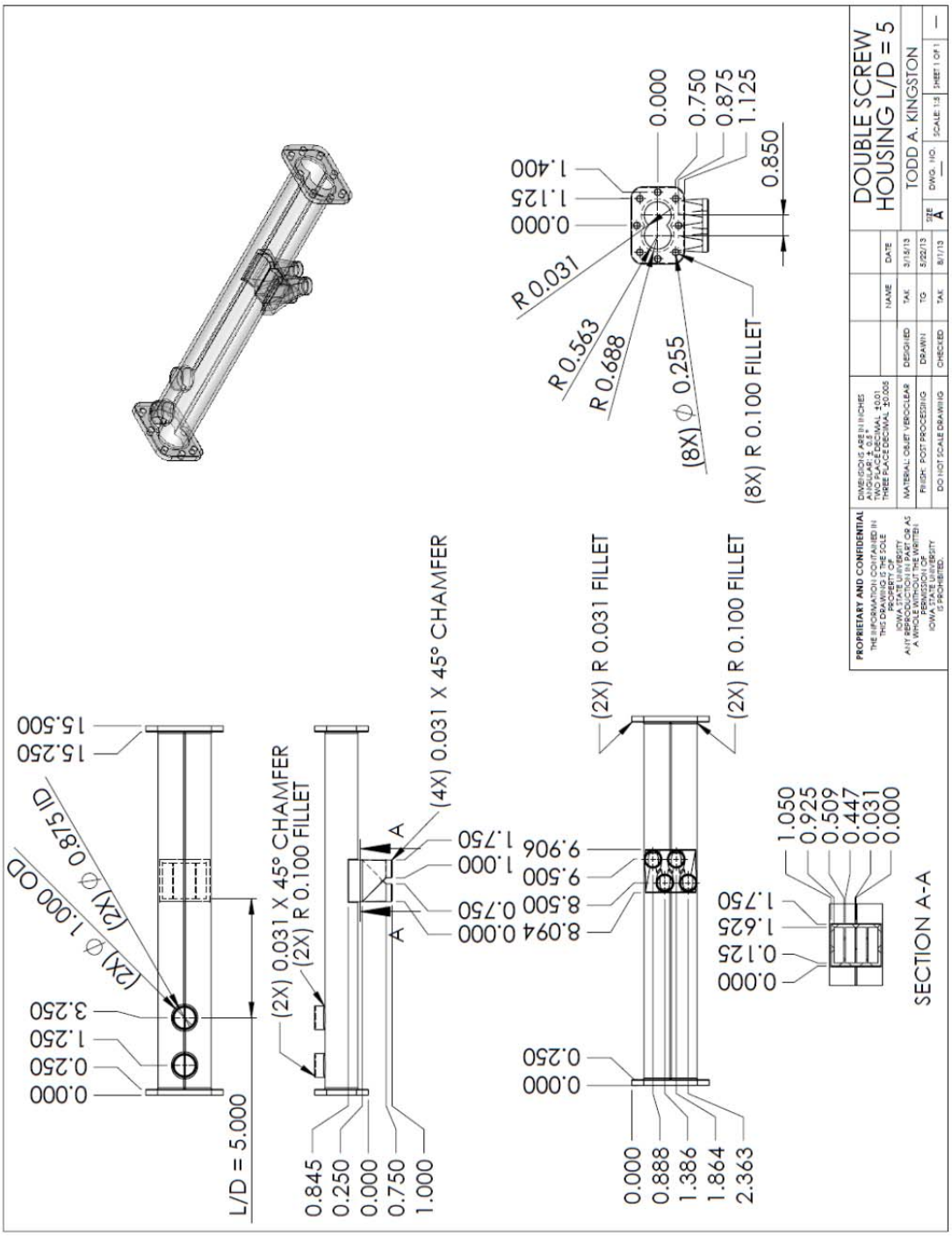
DOUBLE SCREW HOUSING L/D = 5
TODD A. KINGSTON
L/D = 5.000
(2X) 0.031 X 45° CHAMFER
(2X) R 0.100 FILLET
(4X) 0.031 X 45° CHAMFER
(2X) R 0.031 FILLET
(2X) R 0.100 FILLET
(8X) R 0.100 FILLET
(8X) ⌀ 0.255
R 0.031
R 0.563
R 0.688
SECTION A-A
PROPRIETARY AND CONFIDENTIAL

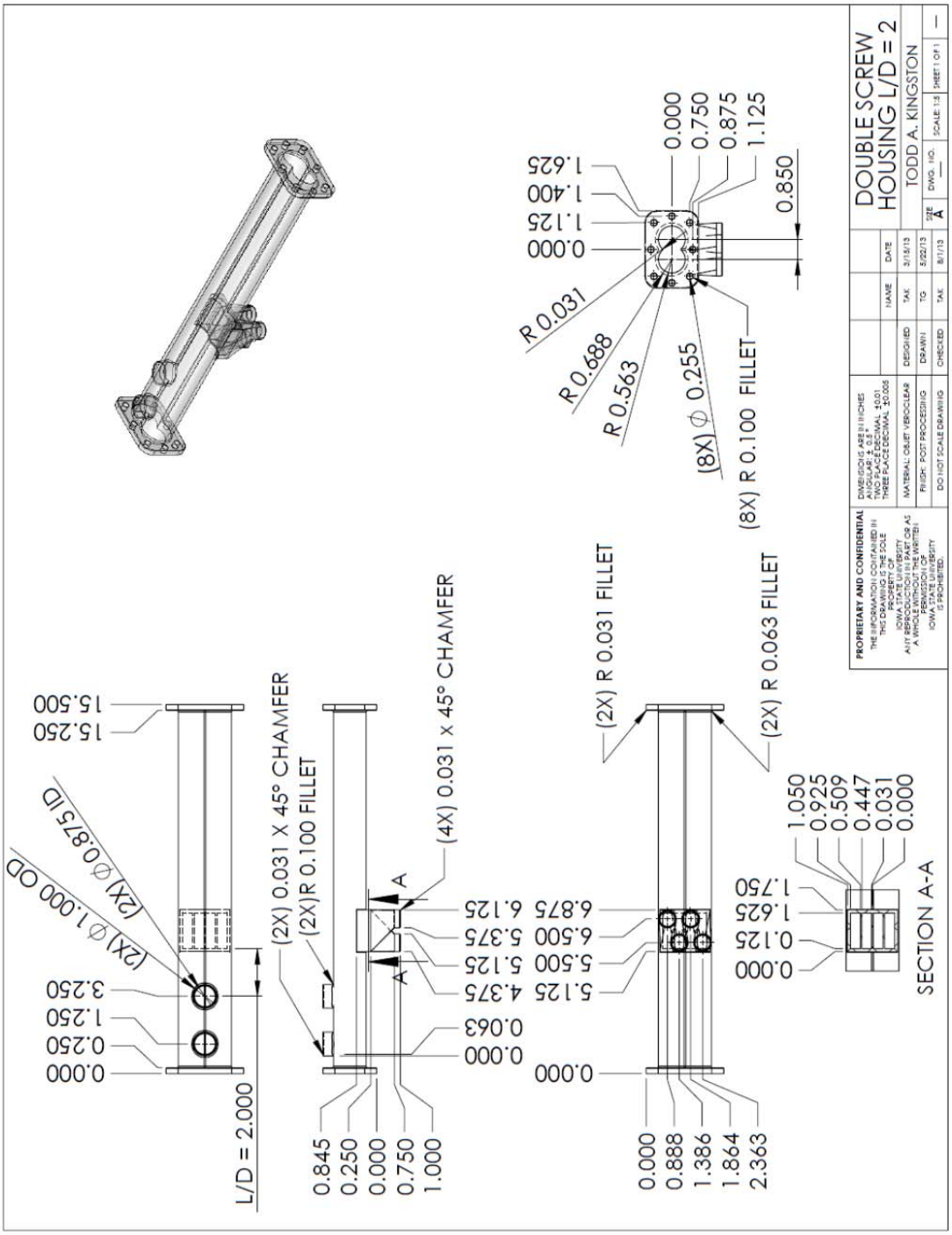
DOUBLE SCREW HOUSING L/D = 2
TODD A. KINGSTON
PROPRIETARY AND CONFIDENTIAL
THE INFORMATION CONTAINED IN THIS DRAWING IS THE SOLE PROPERTY OF IOWA STATE UNIVERSITY
ANY REPRODUCTION IN PART OR AS A WHOLE WITHOUT THE WRITTEN PERMISSION OF IOWA STATE UNIVERSITY IS PROHIBITED.
DIMENSIONS ARE IN INCHES
ANGULAR: ± 0.5°
TWO PLACE DECIMAL: ±0.01
THREE PLACE DECIMAL: ±0.005
DESIGNED TAK 3/15/13
DRAWN TG 5/22/13
CHECKED TAK 8/1/13
SIZE A
DWG. NO. —
SCALE: 1:5
SHEET 1 OF 1
L/D = 2.000
15.500
15.250
0.000
0.250
1.250
3.250
(2X) ⌀1.000 OD
(2X) ⌀0.875 ID
(2X) 0.031 X 45° CHAMFER
(2X) R 0.100 FILLET
(4X) 0.031 x 45° CHAMFER
0.845
0.250
0.000
0.750
1.000
0.063
0.000
6.875 6.125
6.500 5.375
5.500 5.125
5.125 4.375
0.000
(2X) R 0.031 FILLET
(2X) R 0.063 FILLET
0.000
0.888
1.386
1.864
2.363
SECTION A-A
1.050
0.925
0.509
0.447
0.031
0.000
1.750
1.625
0.125
0.000
R 0.031
R 0.688
R 0.563
(8X) ⌀ 0.255
(8X) R 0.100 FILLET
0.850
1.625
1.400
1.125
0.000
0.000
0.750
0.875
1.125

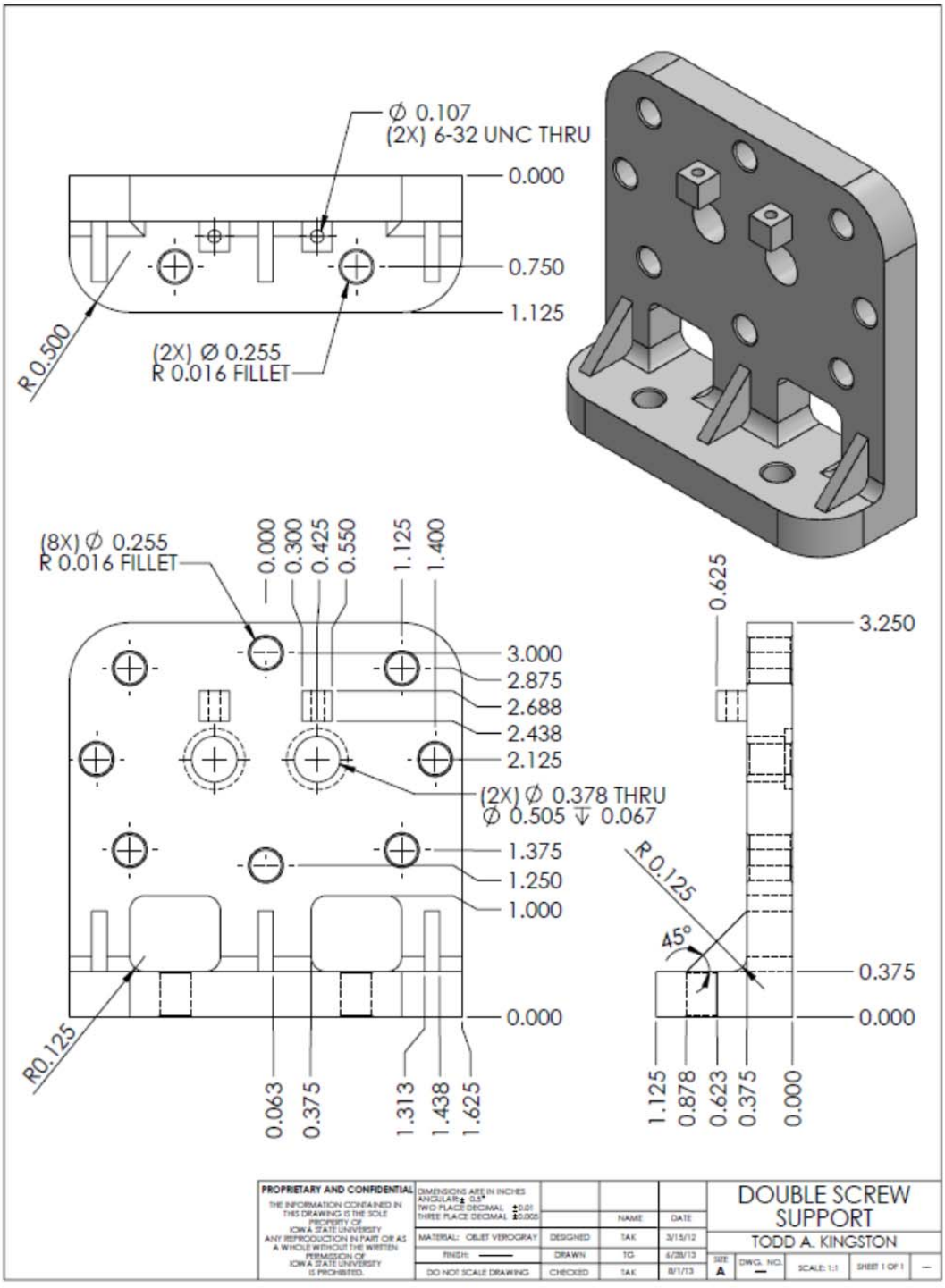
Ø 0.107
(2X) 6-32 UNC THRU
0.000
0.750
1.125
R 0.500
(2X) Ø 0.255
R 0.016 FILLET
(8X) Ø 0.255
R 0.016 FILLET
0.000
0.300
0.425
0.550
1.125
1.400
3.000
2.875
2.688
2.438
2.125
(2X) Ø 0.378 THRU
Ø 0.505 ↧ 0.067
1.375
1.250
1.000
0.000
R0.125
0.063
0.375
1.313
1.438
1.625
0.625
3.250
R 0.125
45°
0.375
0.000
1.125
0.878
0.623
0.375
0.000
PROPRIETARY AND CONFIDENTIAL
THE INFORMATION CONTAINED IN THIS DRAWING IS THE SOLE PROPERTY OF IOWA STATE UNIVERSITY
ANY REPRODUCTION IN PART OR AS A WHOLE WITHOUT THE WRITTEN PERMISSION OF IOWA STATE UNIVERSITY IS PROHIBITED.
DIMENSIONS ARE IN INCHES
ANGULAR: ± 0.5°
TWO PLACE DECIMAL ±0.01
THREE PLACE DECIMAL ±0.005
NAME
DATE
MATERIAL: OBJET VEROGRAY
DESIGNED
TAK
3/15/12
FINISH:
DRAWN
TG
6/28/13
DO NOT SCALE DRAWING
CHECKED
TAK
8/1/13
DOUBLE SCREW SUPPORT
TODD A. KINGSTON
SIZE A
DWG. NO. —
SCALE: 1:1
SHEET 1 OF 1
—

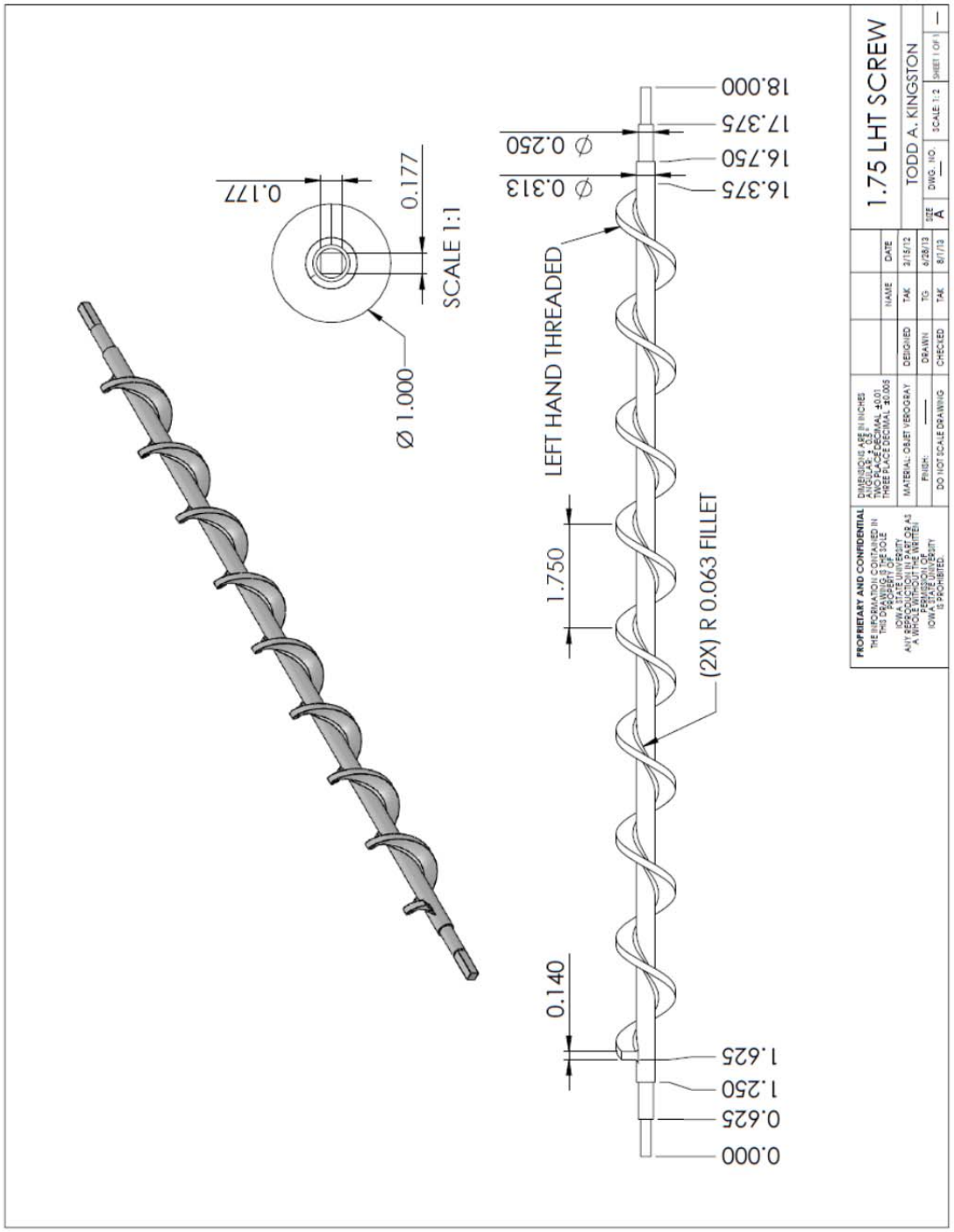
0.177
0.177
SCALE 1:1
Ø 1.000
Ø 0.313
Ø 0.250
LEFT HAND THREADED
1.750
(2X) R 0.063 FILLET
0.140
0.000
0.625
1.250
1.625
16.375
16.750
17.375
18.000
PROPRIETARY AND CONFIDENTIAL
THE INFORMATION CONTAINED IN THIS DRAWING IS THE SOLE PROPERTY OF
IOWA STATE UNIVERSITY
ANY REPRODUCTION IN PART OR AS A WHOLE WITHOUT THE WRITTEN PERMISSION OF
IOWA STATE UNIVERSITY
IS PROHIBITED
DIMENSIONS ARE IN INCHES
ANGULAR: ±1°
TWO PLACE DECIMAL ±0.01
THREE PLACE DECIMAL ±0.005
MATERIAL: OBJET VEROGRAY
FINISH: —
DO NOT SCALE DRAWING
DESIGNED
DRAWN
CHECKED
NAME
TAK
TG
TAK
DATE
3/15/12
6/28/13
8/1/13
1.75 LHT SCREW
TODD A. KINGSTON
SIZE A
DWG. NO. —
SCALE: 1:2
SHEET 1 OF 1

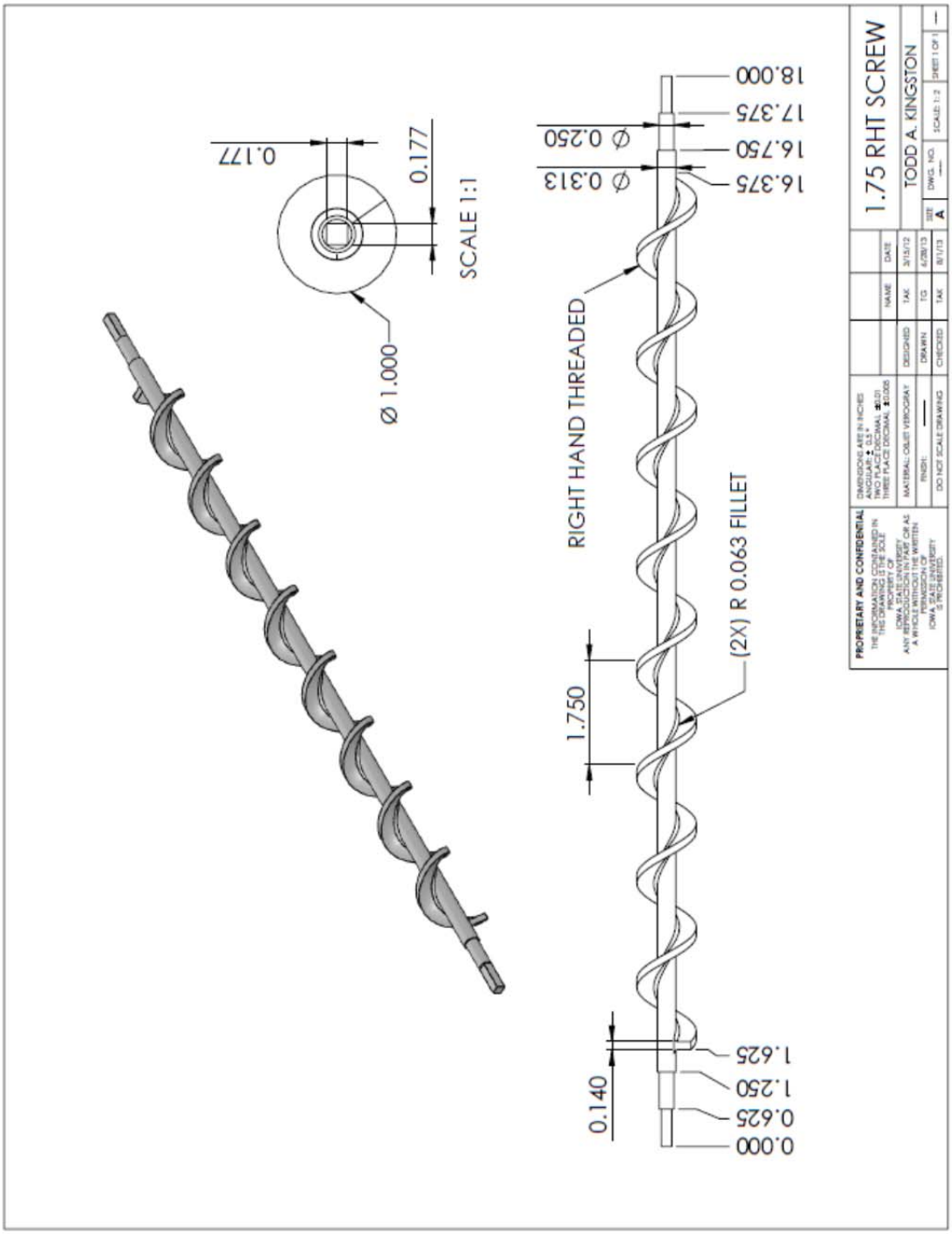
0.177
0.177
SCALE 1:1
Ø 1.000
Ø 0.313
Ø 0.250
18.000
17.375
16.750
16.375
RIGHT HAND THREADED
(2X) R 0.063 FILLET
1.750
0.140
1.625
1.250
0.625
0.000
PROPRIETARY AND CONFIDENTIAL
DIMENSIONS ARE IN INCHES
ANGULAR: ± 0.5°
TWO PLACE DECIMAL: ±0.01
THREE PLACE DECIMAL: ±0.005
NAME
DATE
DESIGNED
TAK
3/15/12
MATERIAL: CAST VERO GRAY
DRAWN
TG
6/28/13
FINISH:
CHECKED
TAK
8/1/13
DO NOT SCALE DRAWING
1.75 RHT SCREW
TODD A. KINGSTON
SIZE
A
DWG. NO.
SCALE: 1:2
SHEET 1 OF 1

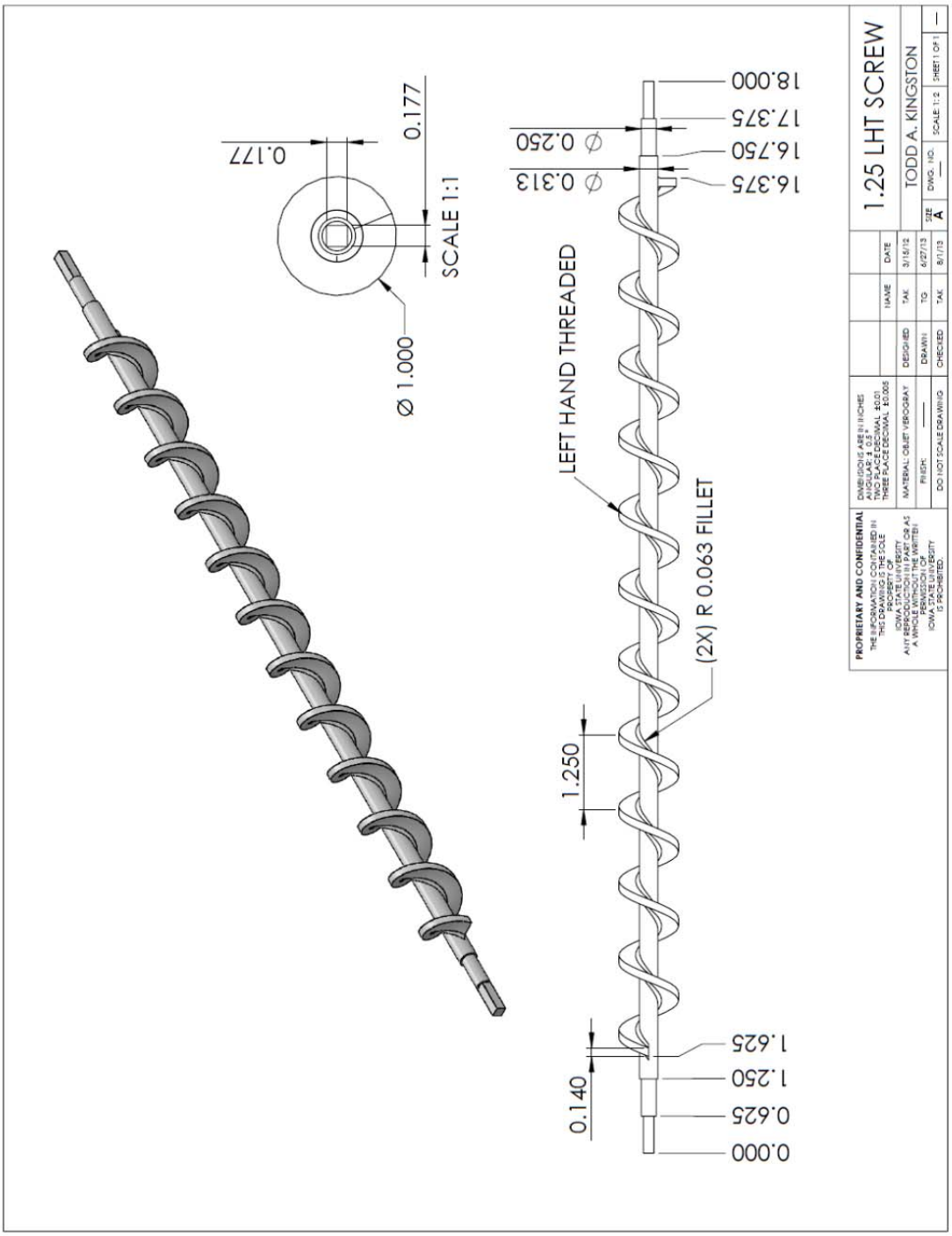
0.177
0.177
Ø 1.000
SCALE 1:1
LEFT HAND THREADED
(2X) R 0.063 FILLET
Ø 0.313
Ø 0.250
18.000
17.375
16.750
16.375
1.250
0.140
1.625
1.250
0.625
0.000
PROPRIETARY AND CONFIDENTIAL
THE INFORMATION CONTAINED IN THIS DRAWING IS THE SOLE PROPERTY OF IOWA STATE UNIVERSITY ANY REPRODUCTION IN PART OR AS A WHOLE WITHOUT THE WRITTEN PERMISSION OF IOWA STATE UNIVERSITY IS PROHIBITED.
UNLESS OTHERWISE SPECIFIED: ANGULAR: ± 0.5° TWO PLACE DECIMAL ±0.01 THREE PLACE DECIMAL ±0.005
MATERIAL: OBJET VEROGRAY
FINISH: ——
DO NOT SCALE DRAWING
NAME
DATE
DESIGNED
TAK
3/15/12
DRAWN
TG
6/27/13
CHECKED
TAK
8/1/13
1.25 LHT SCREW
TODD A. KINGSTON
SIZE A
DWG. NO. ——
SCALE: 1:2
SHEET 1 OF 1

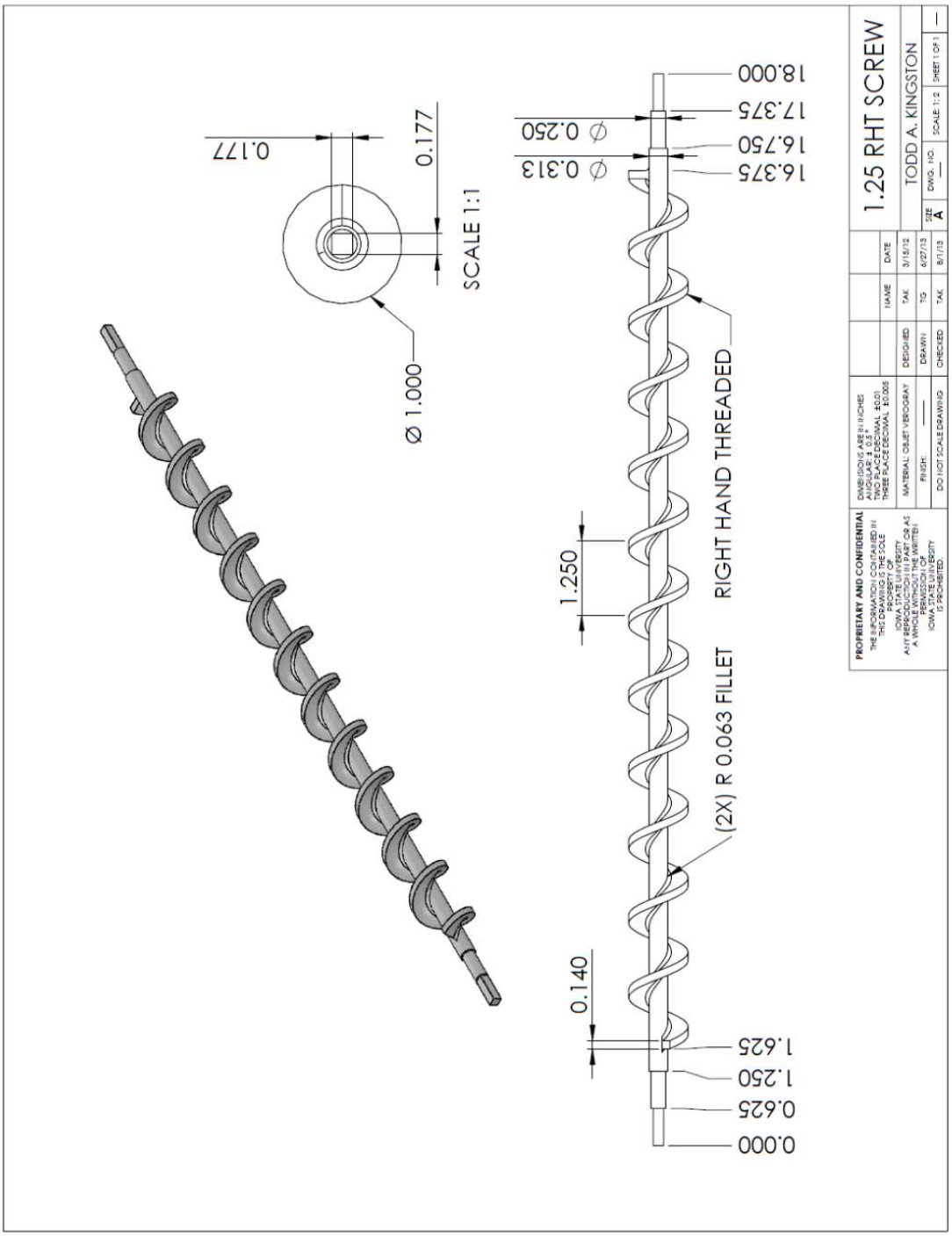
0.177
0.177
Ø 1.000
SCALE 1:1
Ø 0.250
Ø 0.313
18.000
17.375
16.750
16.375
1.250
(2X) R 0.063 FILLET
RIGHT HAND THREADED
0.140
1.625
1.250
0.625
0.000
PROPRIETARY AND CONFIDENTIAL
THE INFORMATION CONTAINED IN THIS DRAWING IS THE SOLE PROPERTY OF IOWA STATE UNIVERSITY ANY REPRODUCTION IN PART OR AS A WHOLE WITHOUT THE WRITTEN PERMISSION OF IOWA STATE UNIVERSITY IS PROHIBITED.
UNLESS OTHERWISE SPECIFIED: ANGULAR: ± 0.5° TWO PLACE DECIMAL ±0.01 THREE PLACE DECIMAL ±0.005
MATERIAL: OBJET VEROGRAY
FINISH: ——
DO NOT SCALE DRAWING
NAME
DATE
DESIGNED
TAK
3/15/12
DRAWN
TG
6/27/13
CHECKED
TAK
8/1/13
1.25 RHT SCREW
TODD A. KINGSTON
SIZE A
DWG. NO. —
SCALE: 1:2
SHEET 1 OF 1
—

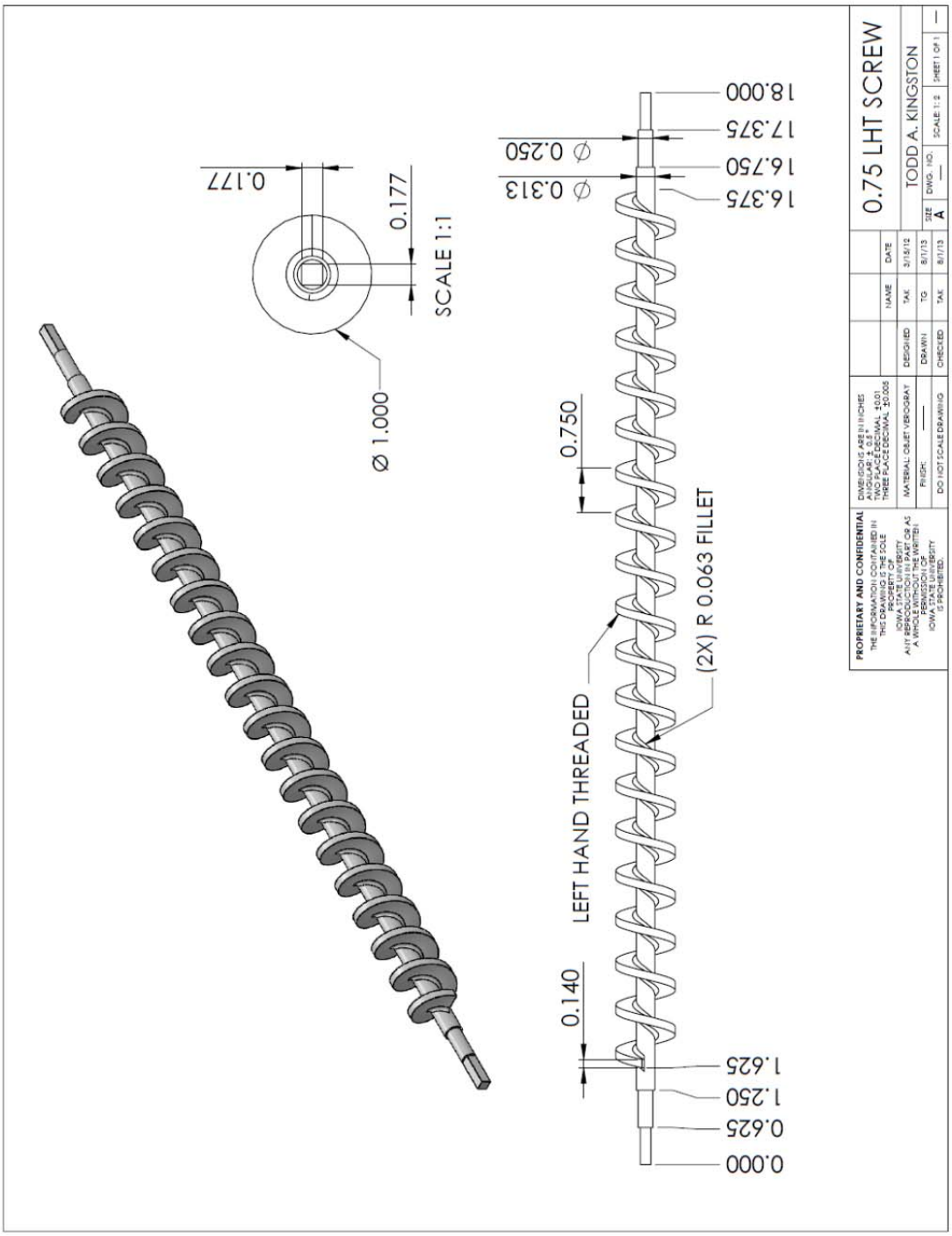
0.177
0.177
SCALE 1:1
Ø 1.000
Ø 0.313
Ø 0.250
18.000
17.375
16.750
16.375
0.750
LEFT HAND THREADED
(2X) R 0.063 FILLET
0.140
1.625
1.250
0.625
0.000
PROPRIETARY AND CONFIDENTIAL
THE INFORMATION CONTAINED IN THIS DRAWING IS THE SOLE PROPERTY OF IOWA STATE UNIVERSITY
ANY REPRODUCTION IN PART OR AS A WHOLE WITHOUT THE WRITTEN PERMISSION OF IOWA STATE UNIVERSITY IS PROHIBITED.
DIMENSIONS ARE IN INCHES
ANGULAR: ± 0.5°
TWO PLACE DECIMAL: ±0.01
THREE PLACE DECIMAL: ±0.005
MATERIAL: OBJET VEROGRAY
FINISH: ——
DO NOT SCALE DRAWING
NAME
DATE
DESIGNED
TAK
3/15/12
DRAWN
TG
8/1/13
CHECKED
TAK
8/1/13
0.75 LHT SCREW
TODD A. KINGSTON
SIZE
A
DWG. NO.
—
SCALE: 1:2
SHEET 1 OF 1

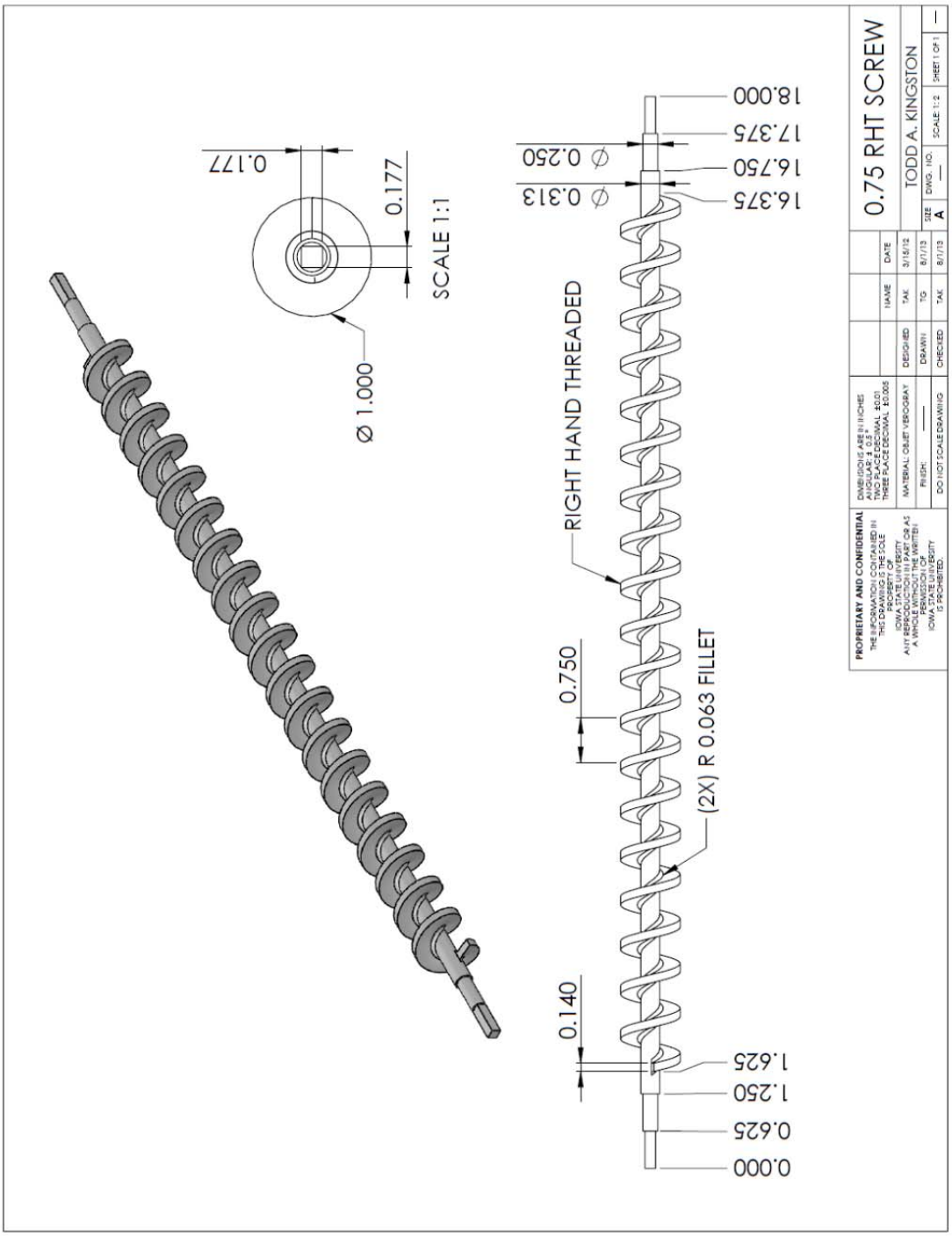
0.75 RHT SCREW
TODD A. KINGSTON
RIGHT HAND THREADED
(2X) R 0.063 FILLET
0.750
0.140
0.000
0.625
1.250
1.625
16.375
16.750
17.375
18.000
Ø 0.313
Ø 0.250
Ø 1.000
0.177
0.177
SCALE 1:1
PROPRIETARY AND CONFIDENTIAL
DO NOT SCALE DRAWING
SCALE: 1:2
SHEET 1 OF 1

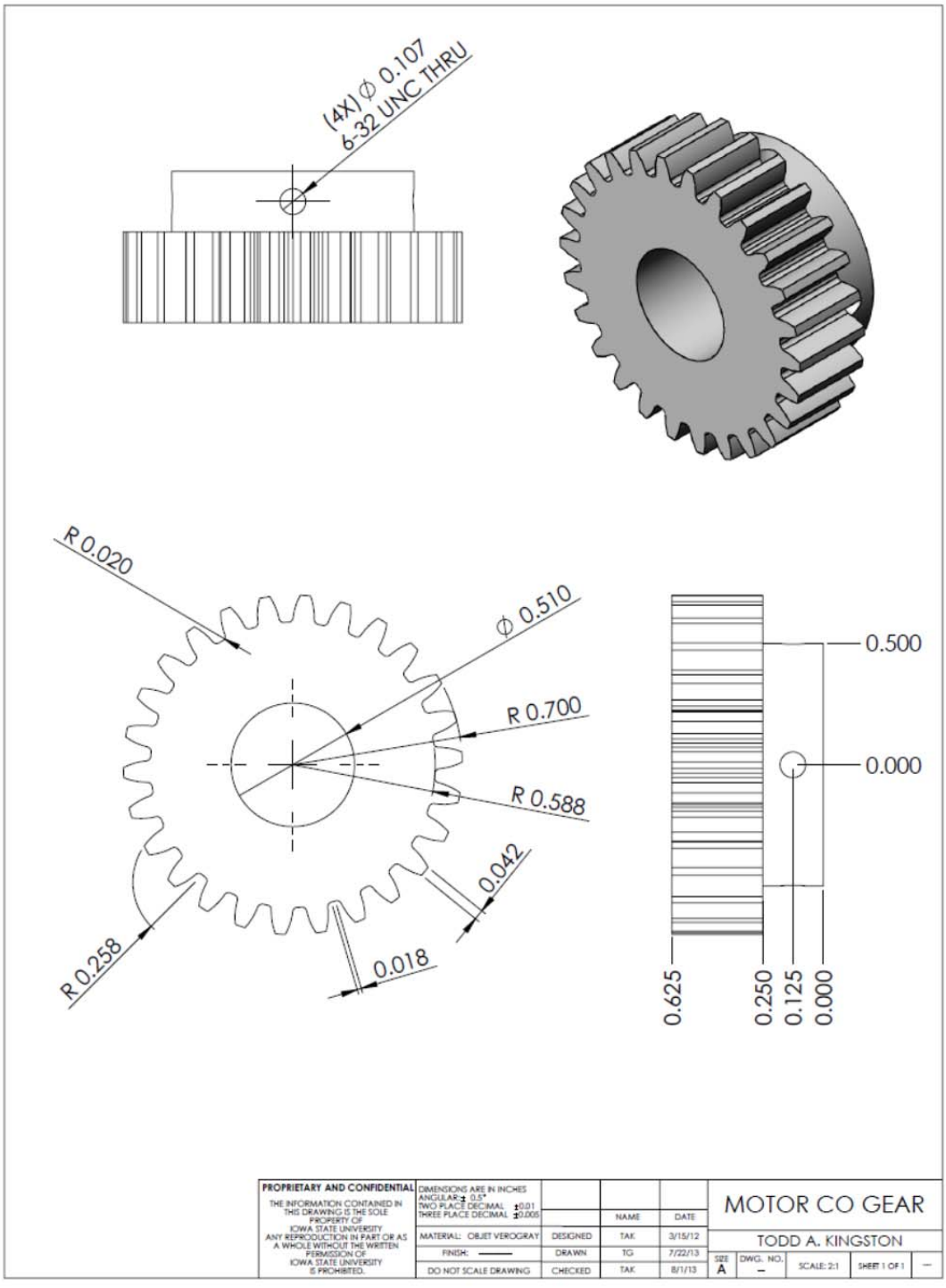

PROPRIETARY AND CONFIDENTIAL THE INFORMATION CONTAINED IN THIS DRAWING IS THE SOLE PROPERTY OF IOWA STATE UNIVERSITY ANY REPRODUCTION IN PART OR AS A WHOLE WITHOUT THE WRITTEN PERMISSION OF IOWA STATE UNIVERSITY IS PROHIBITED.	DIMENSIONS ARE IN INCHES ANGULAR: ± .5° TWO PLACE DECIMAL ±0.01 THREE PLACE DECIMAL ±0.005		NAME	DATE	MOTOR CO GEAR
	MATERIAL: OBJET VEROGRAY	DESIGNED	TAK	3/15/12	TODD A. KINGSTON
	FINISH: ——	DRAWN	TG	7/22/13	SIZE A · DWG. NO. – · SCALE: 2:1 · SHEET 1 OF 1
	DO NOT SCALE DRAWING	CHECKED	TAK	8/1/13	

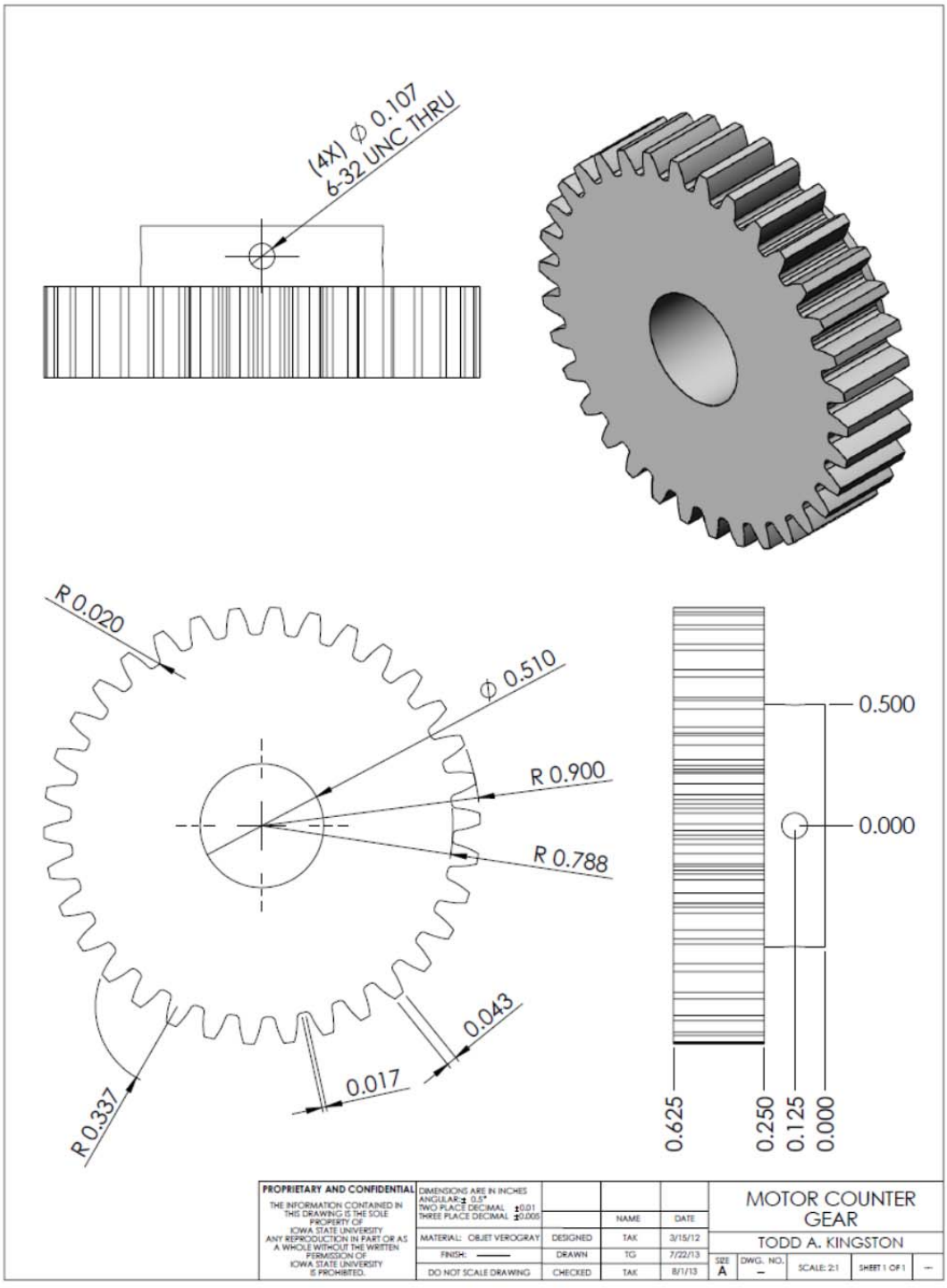

DIMENSIONS ARE IN INCHES
ANGULAR: ± .5°
TWO PLACE DECIMAL ±0.01
THREE PLACE DECIMAL ±0.005

MATERIAL: OBJET VEROGRAY
FINISH: ——
DO NOT SCALE DRAWING

	NAME	DATE
DESIGNED	TAK	3/15/12
DRAWN	TG	7/22/13
CHECKED	TAK	8/1/13

MOTOR COUNTER GEAR

TODD A. KINGSTON

SIZE A | DWG. NO. – | SCALE: 2:1 | SHEET 1 OF 1 | –

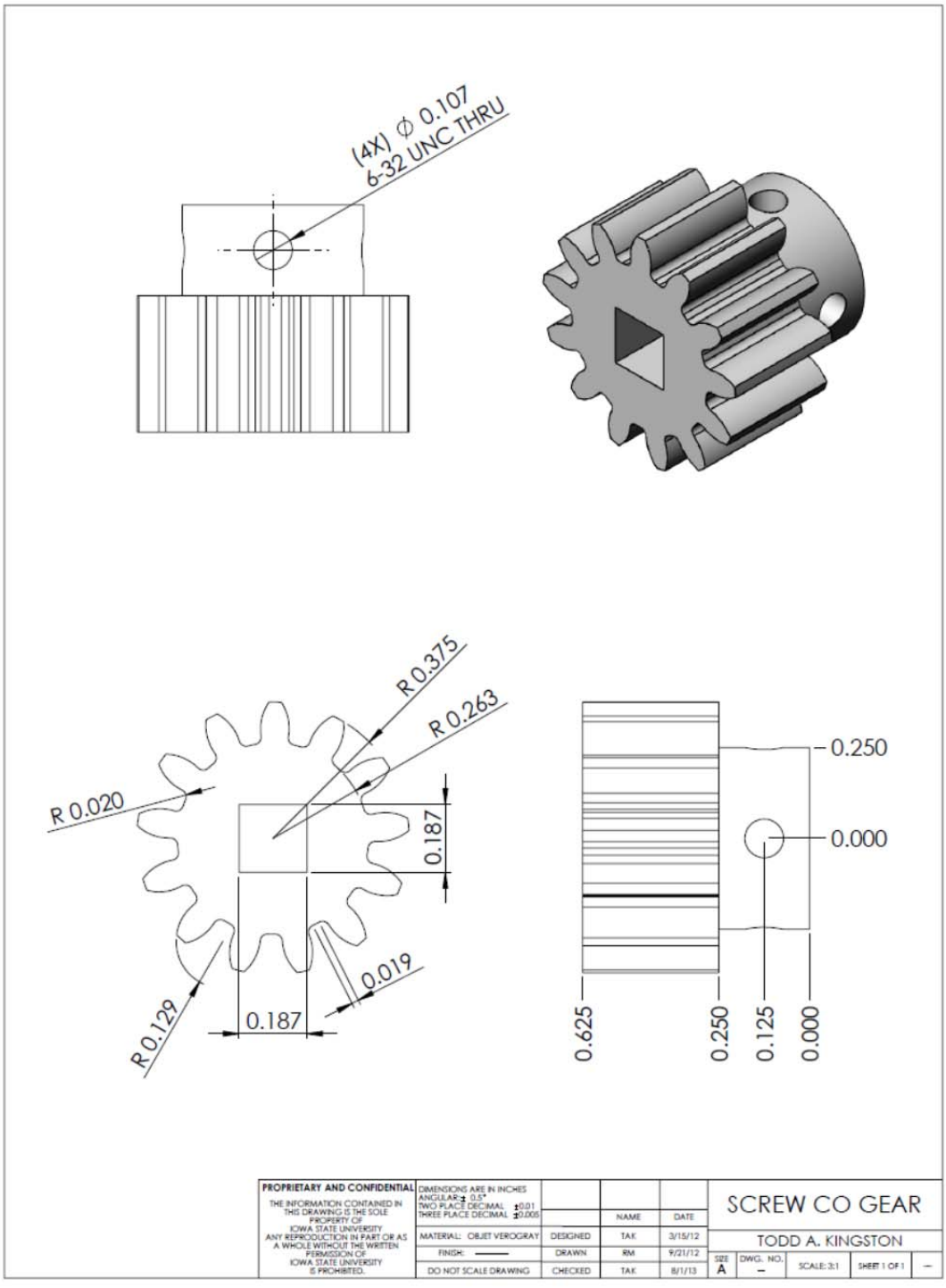

PROPRIETARY AND CONFIDENTIAL THE INFORMATION CONTAINED IN THIS DRAWING IS THE SOLE PROPERTY OF IOWA STATE UNIVERSITY ANY REPRODUCTION IN PART OR AS A WHOLE WITHOUT THE WRITTEN PERMISSION OF IOWA STATE UNIVERSITY IS PROHIBITED.	DIMENSIONS ARE IN INCHES ANGULAR: ± .5° TWO PLACE DECIMAL ±0.01 THREE PLACE DECIMAL ±0.005		NAME	DATE	SCREW CO GEAR
	MATERIAL: OBJET VEROGRAY	DESIGNED	TAK	3/15/12	TODD A. KINGSTON
	FINISH: ——	DRAWN	RM	9/21/12	SIZE A | DWG. NO. – | SCALE: 3:1 | SHEET 1 OF 1 | –
	DO NOT SCALE DRAWING	CHECKED	TAK	8/1/13	

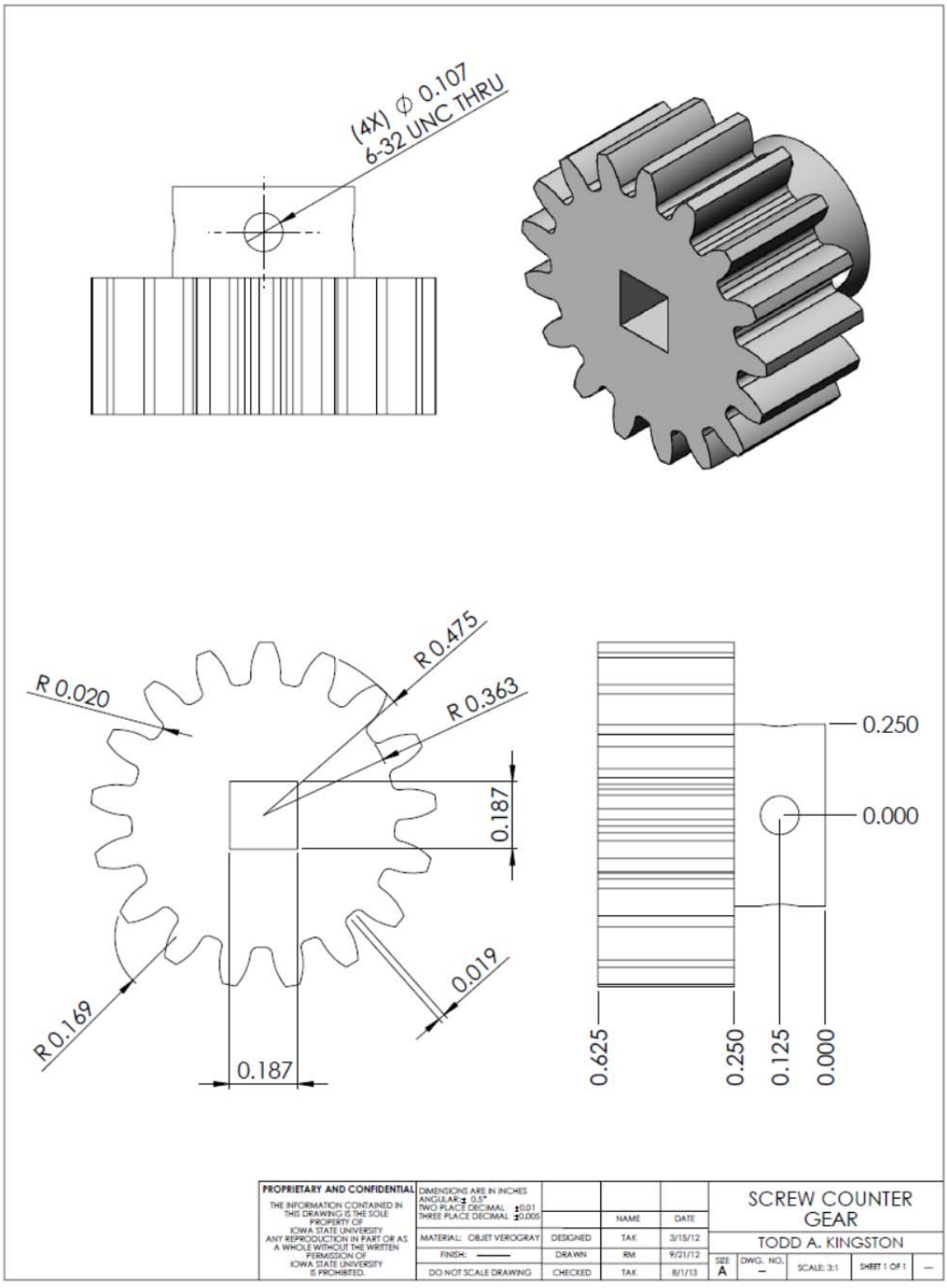

PROPRIETARY AND CONFIDENTIAL THE INFORMATION CONTAINED IN THIS DRAWING IS THE SOLE PROPERTY OF IOWA STATE UNIVERSITY ANY REPRODUCTION IN PART OR AS A WHOLE WITHOUT THE WRITTEN PERMISSION OF IOWA STATE UNIVERSITY IS PROHIBITED.	DIMENSIONS ARE IN INCHES ANGULAR: ± .5° TWO PLACE DECIMAL ±0.01 THREE PLACE DECIMAL ±0.005		NAME	DATE	SCREW COUNTER GEAR
	MATERIAL: OBJET VEROGRAY	DESIGNED	TAK	3/15/12	TODD A. KINGSTON
	FINISH: ——	DRAWN	RM	9/21/12	SIZE A · DWG. NO. – · SCALE: 3:1 · SHEET 1 OF 1 · —
	DO NOT SCALE DRAWING	CHECKED	TAK	8/1/13	

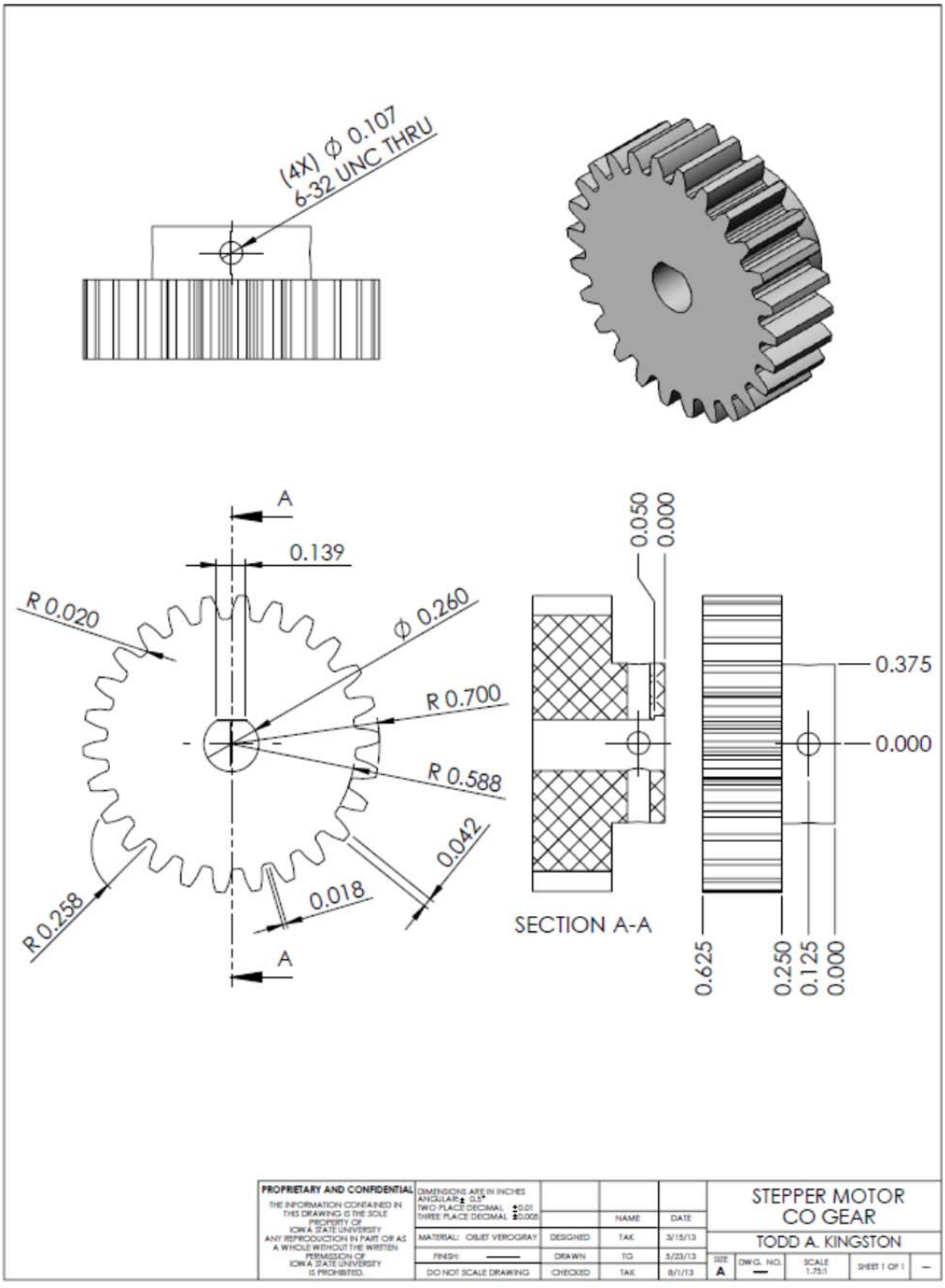

PROPRIETARY AND CONFIDENTIAL THE INFORMATION CONTAINED IN THIS DRAWING IS THE SOLE PROPERTY OF IOWA STATE UNIVERSITY ANY REPRODUCTION IN PART OR AS A WHOLE WITHOUT THE WRITTEN PERMISSION OF IOWA STATE UNIVERSITY IS PROHIBITED.	DIMENSIONS ARE IN INCHES ANGULAR: ± 0.5° TWO PLACE DECIMAL ±0.01 THREE PLACE DECIMAL ±0.005		NAME	DATE	STEPPER MOTOR CO GEAR
	MATERIAL: OBJET VEROGRAY	DESIGNED	TAK	3/15/13	TODD A. KINGSTON
	FINISH: ——	DRAWN	TG	5/23/13	SIZE A | DWG. NO. — | SCALE 1.75:1 | SHEET 1 OF 1 | —
	DO NOT SCALE DRAWING	CHECKED	TAK	8/1/13	

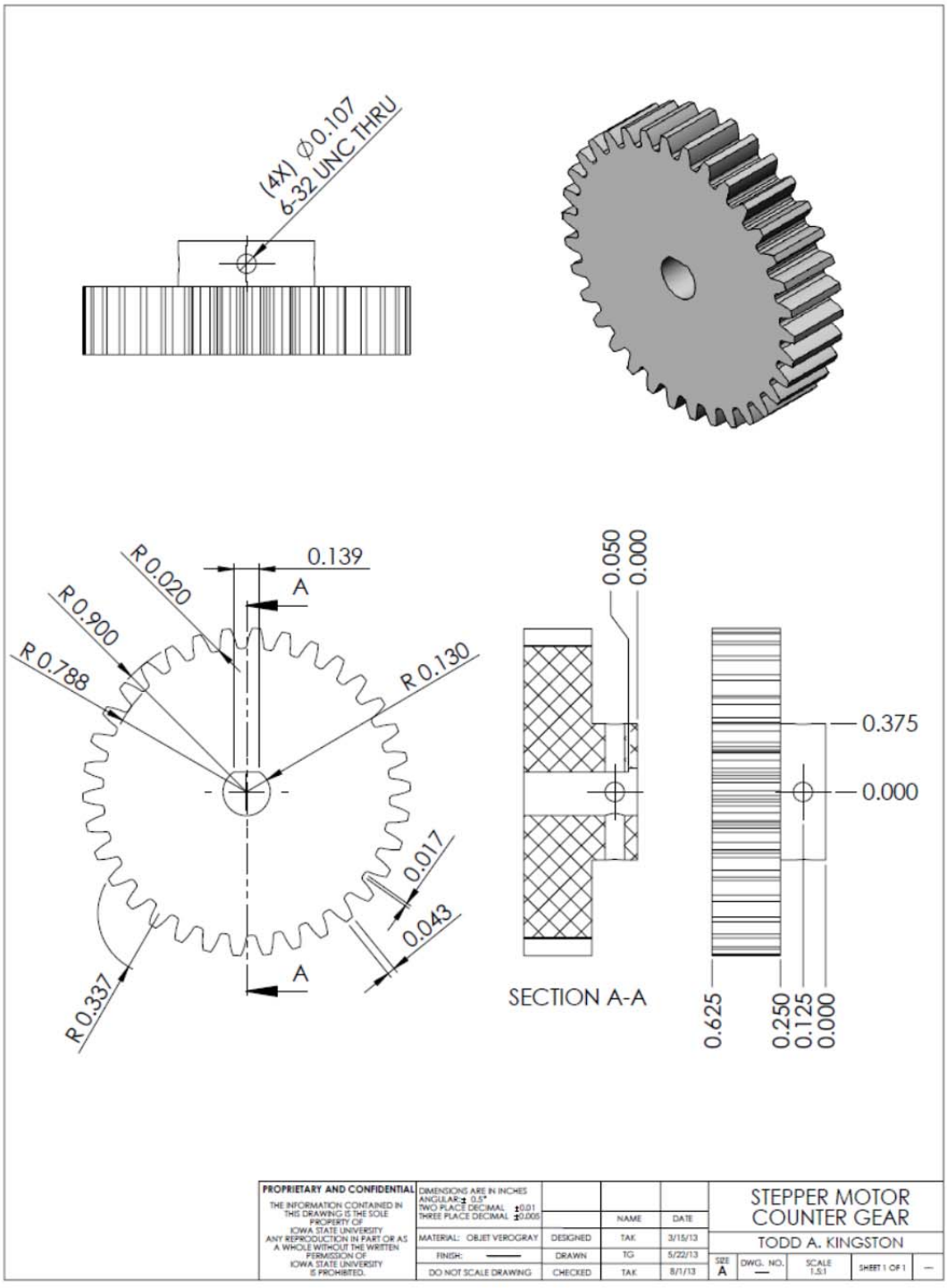

PROPRIETARY AND CONFIDENTIAL THE INFORMATION CONTAINED IN THIS DRAWING IS THE SOLE PROPERTY OF IOWA STATE UNIVERSITY ANY REPRODUCTION IN PART OR AS A WHOLE WITHOUT THE WRITTEN PERMISSION OF IOWA STATE UNIVERSITY IS PROHIBITED.	DIMENSIONS ARE IN INCHES ANGULAR: ± .5° TWO PLACE DECIMAL ±0.01 THREE PLACE DECIMAL ±0.005		NAME	DATE
	MATERIAL: OBJET VEROGRAY	DESIGNED	TAK	3/15/13
	FINISH: ——	DRAWN	TG	5/22/13
	DO NOT SCALE DRAWING	CHECKED	TAK	8/1/13

STEPPER MOTOR COUNTER GEAR

TODD A. KINGSTON

SIZE	DWG. NO.	SCALE	SHEET 1 OF 1	
A	—	1.5:1		—

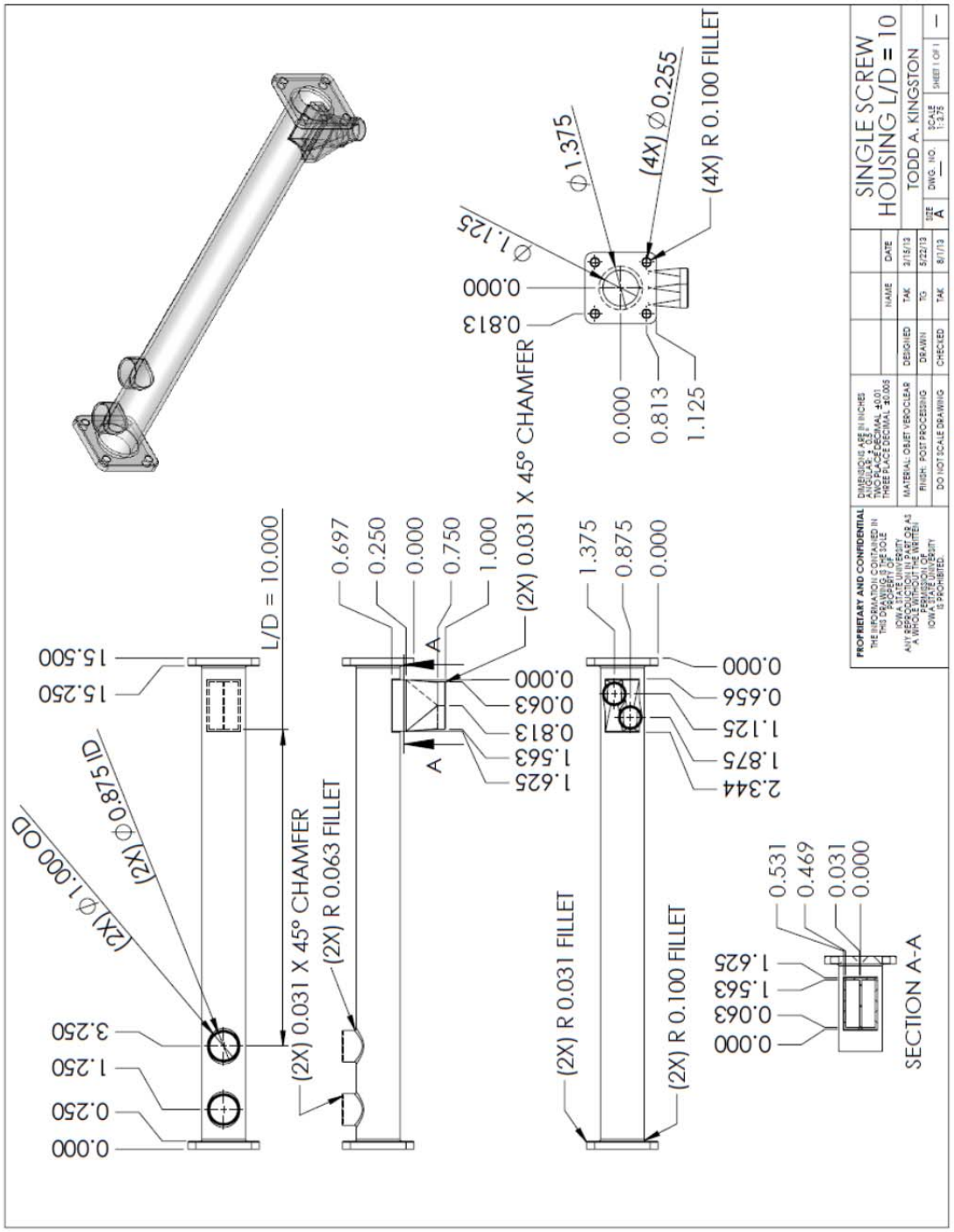
SINGLE SCREW
HOUSING L/D = 10
TODD A. KINGSTON
SECTION A-A
(2X) R 0.031 FILLET
(2X) R 0.100 FILLET
(2X) R 0.063 FILLET
(2X) 0.031 X 45° CHAMFER
(4X) R 0.100 FILLET
(4X) Ø0.255
L/D = 10.000
PROPRIETARY AND CONFIDENTIAL

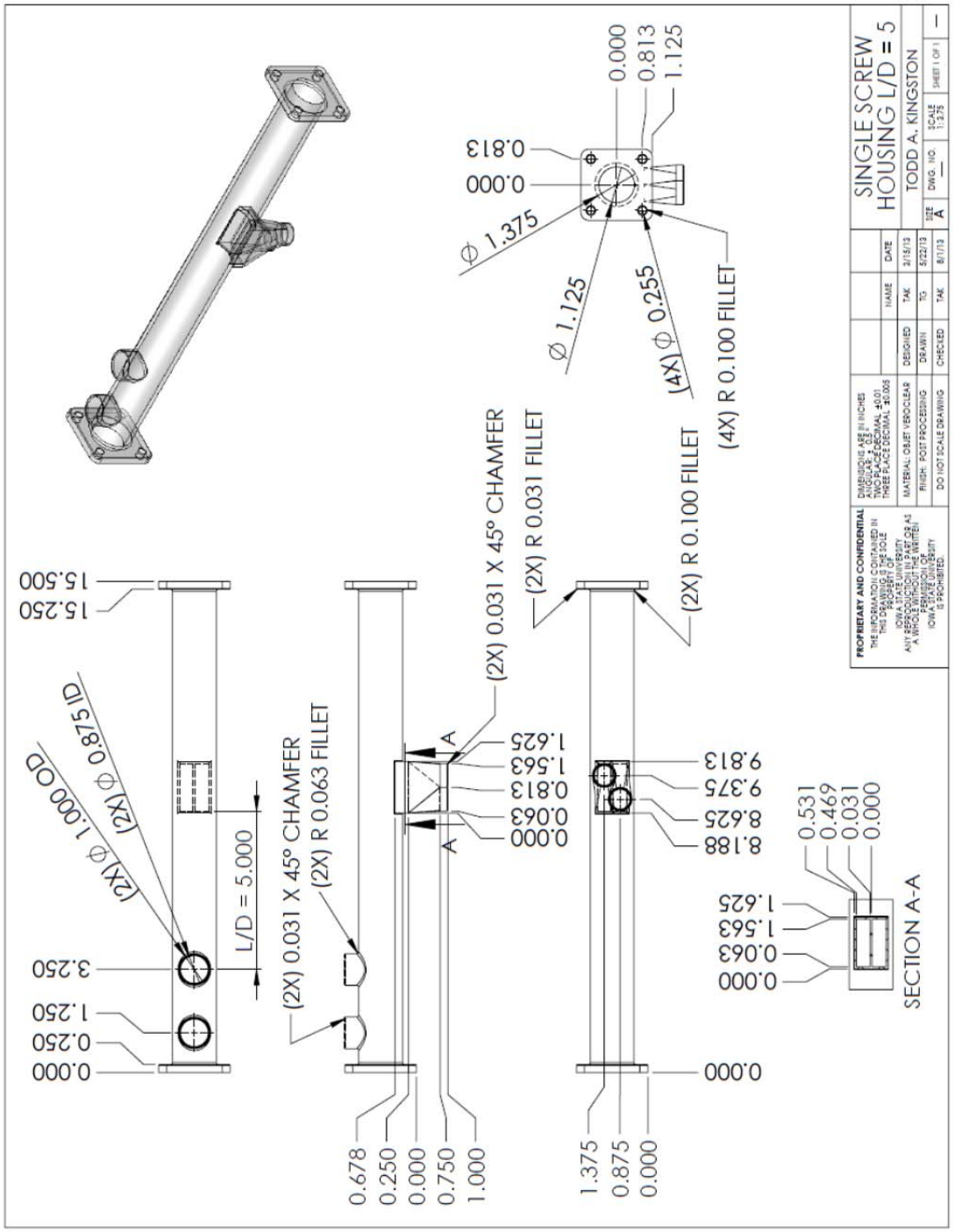
SINGLE SCREW
HOUSING L/D = 5
TODD A. KINGSTON
SCALE 1:3.75
SHEET 1 OF 1
SIZE A
DWG. NO. —
PROPRIETARY AND CONFIDENTIAL
DRAWN
CHECKED
DESIGNED
DATE
NAME
L/D = 5.000
(2X) Φ 0.875 ID
(2X) Φ 1.000 OD
(2X) 0.031 X 45° CHAMFER
(2X) R 0.063 FILLET
(2X) 0.031 X 45° CHAMFER
(2X) R 0.031 FILLET
(2X) R 0.100 FILLET
(4X) R 0.100 FILLET
(4X) Φ 0.255
Φ 1.375
Φ 1.125
SECTION A-A
15.500
15.250
3.250
1.250
0.250
0.000
0.678
0.250
0.000
0.750
1.000
1.625
1.563
0.813
0.063
0.000
9.813
9.375
8.625
8.188
1.375
0.875
0.000
1.625
1.563
0.063
0.000
0.531
0.469
0.031
0.000
0.813
0.000
0.813
0.000
0.813
1.125

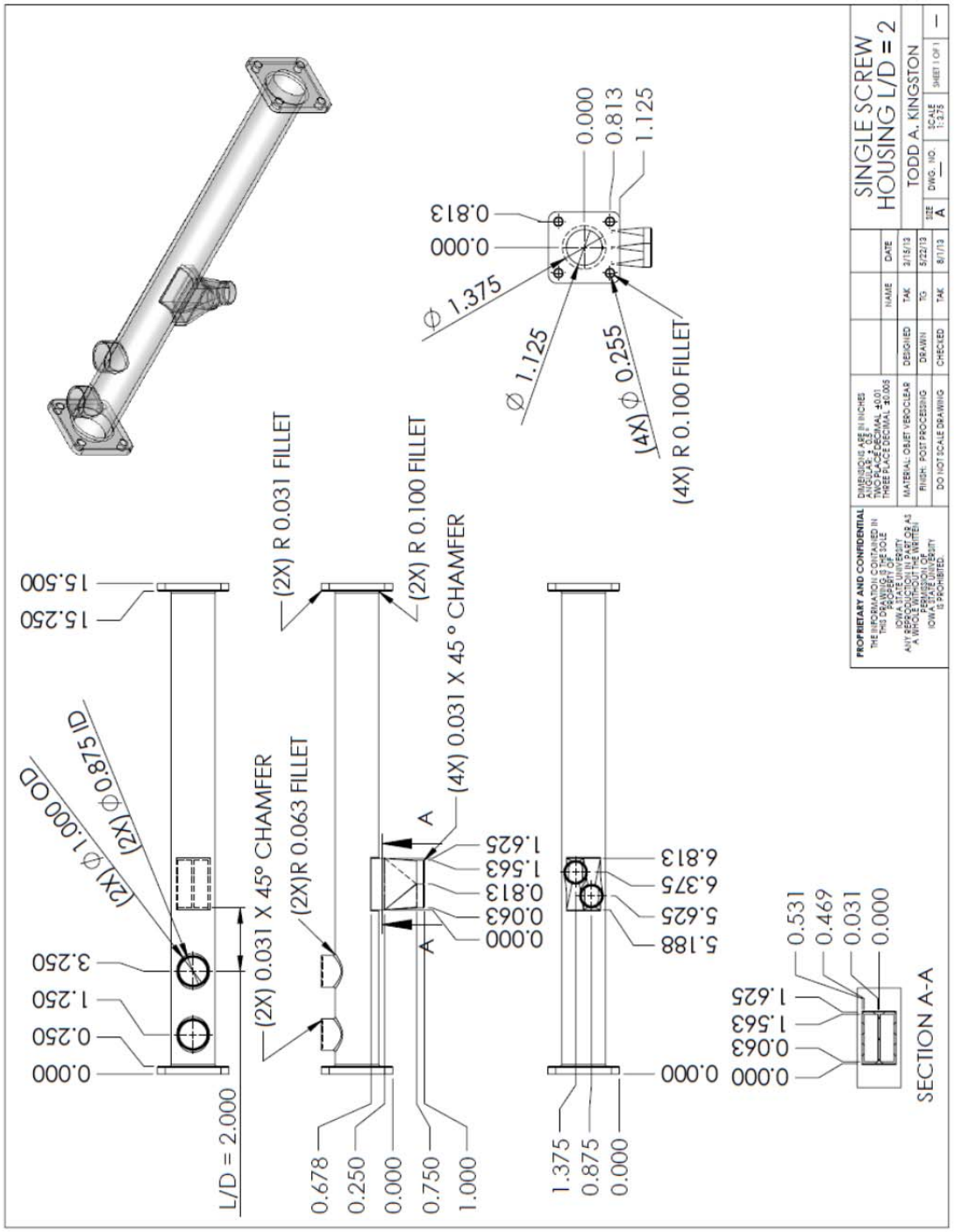
SINGLE SCREW
HOUSING L/D = 2
TODD A. KINGSTON
L/D = 2.000
(2X) 0.031 X 45° CHAMFER
(2X)R 0.063 FILLET
(2X) R 0.031 FILLET
(2X) R 0.100 FILLET
(4X) 0.031 X 45 ° CHAMFER
(4X) R 0.100 FILLET
SECTION A-A

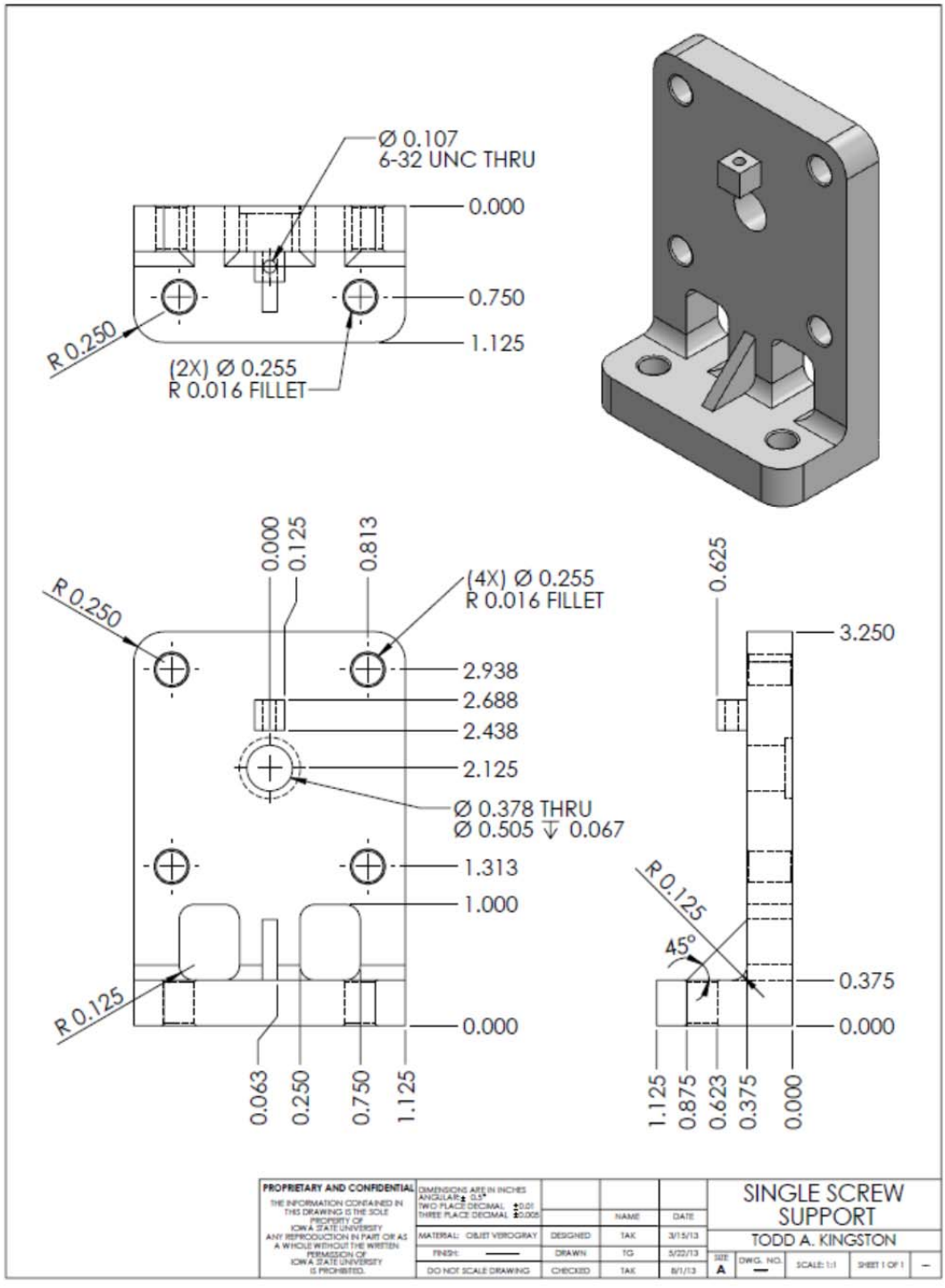
Ø 0.107
6-32 UNC THRU
0.000
0.750
1.125
R 0.250
(2X) Ø 0.255
R 0.016 FILLET
0.000
0.125
0.813
(4X) Ø 0.255
R 0.016 FILLET
R 0.250
2.938
2.688
2.438
2.125
Ø 0.378 THRU
Ø 0.505 ↧ 0.067
1.313
1.000
R 0.125
0.000
0.063
0.250
0.750
1.125
0.625
3.250
R 0.125
45°
0.375
0.000
1.125
0.875
0.623
0.375
0.000
PROPRIETARY AND CONFIDENTIAL
THE INFORMATION CONTAINED IN THIS DRAWING IS THE SOLE PROPERTY OF IOWA STATE UNIVERSITY
ANY REPRODUCTION IN PART OR AS A WHOLE WITHOUT THE WRITTEN PERMISSION OF IOWA STATE UNIVERSITY IS PROHIBITED.
DIMENSIONS ARE IN INCHES
ANGULAR: ± 0.5°
TWO PLACE DECIMAL ±0.01
THREE PLACE DECIMAL ±0.005
NAME
DATE
MATERIAL: OBJET VEROGRAY
DESIGNED
TAK
3/15/13
FINISH: ——
DRAWN
TG
5/22/13
DO NOT SCALE DRAWING
CHECKED
TAK
8/1/13
SINGLE SCREW SUPPORT
TODD A. KINGSTON
SIZE A
DWG. NO. —
SCALE: 1:1
SHEET 1 OF 1
—

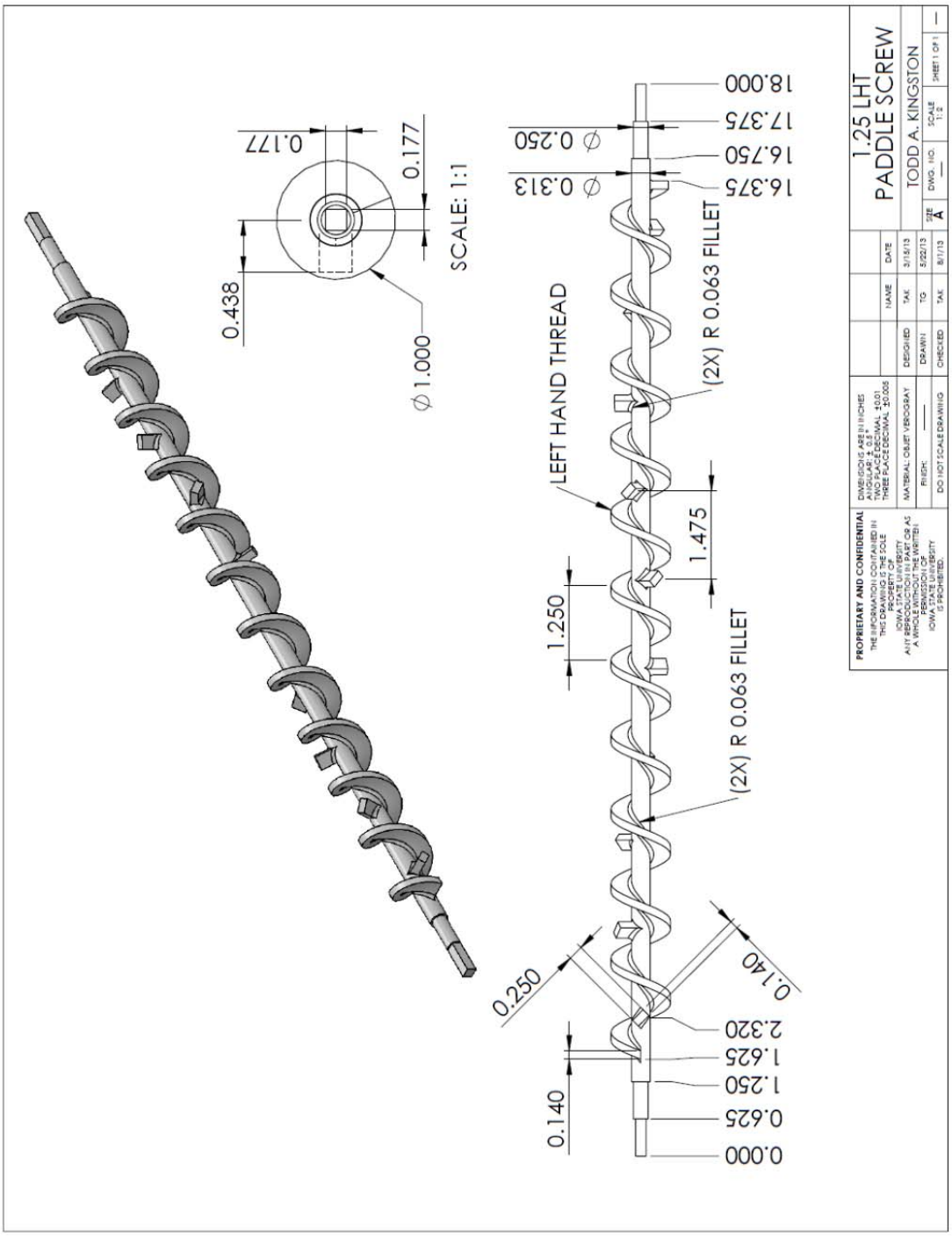
0.177
0.438
0.177
∅ 1.000
SCALE: 1:1
∅ 0.250
∅ 0.313
18.000
17.375
16.750
16.375
LEFT HAND THREAD
(2X) R 0.063 FILLET
1.475
1.250
(2X) R 0.063 FILLET
0.250
0.140
0.140
2.320
1.625
1.250
0.625
0.000
PROPRIETARY AND CONFIDENTIAL
THE INFORMATION CONTAINED IN THIS DRAWING IS THE SOLE PROPERTY OF IOWA STATE UNIVERSITY
ANY REPRODUCTION IN PART OR AS A WHOLE WITHOUT THE WRITTEN PERMISSION OF IOWA STATE UNIVERSITY IS PROHIBITED.
DIMENSIONS ARE IN INCHES
ANGULAR: ±0.5°
TWO PLACE DECIMAL: ±0.01
THREE PLACE DECIMAL: ±0.005
MATERIAL: ONLY VEROGRAY
FINISH: ——
DO NOT SCALE DRAWING
NAME
DATE
DESIGNED
TAK
3/15/13
DRAWN
TG
5/22/13
CHECKED
TAK
8/1/13
1.25 LHT
PADDLE SCREW
TODD A. KINGSTON
SIZE
A
DWG. NO.
——
SCALE
1:2
SHEET 1 OF 1

APPENDIX B: EQUIPMENT CALIBRATION DATA

B.1 Red Oak Chips Volumetric Feeder

Table B.1: Red oak chips volumetric feeder calibration data.

Potentiometer Setting	Time [min]	Trial 1 Weight [g]	Trial 2 Weight [g]	Trial 3 Weight [g]	Trial 4 Weight [g]	Trial 5 Weight [g]	Average Weight [g]	Standard Deviation [g]	Mass Flow Rate Average [kg hr^{-1}]	Mass Flow Rate Standard Deviation [kg hr^{-1}]
100	3	24.37	26.68	26.50	24.98	25.35	0.51	0.99	0.51	0.02
200	3	69.39	69.13	69.51	66.11	67.13	0.98	1.54	1.37	0.03
300	3	108.17	108.71	107.92	111.66	113.17	1.53	2.35	2.20	0.05
400	3	146.73	141.72	146.10	144.56	150.39	2.05	3.17	2.92	0.06
500	3	183.25	186.53	188.46	185.77	189.37	2.06	2.40	3.73	0.05
600	3	218.00	219.93	229.14	228.42	230.46	3.46	5.77	4.50	0.12
700	3	265.77	258.29	263.70	263.48	267.71	2.96	3.52	5.28	0.07
800	3	299.86	295.86	289.26	297.32	295.28	3.30	3.92	5.91	0.08
900	3	331.07	332.63	335.86	338.82	341.95	3.75	4.44	6.72	0.09
999	3	367.36	376.91	385.25	386.98	382.09	5.22	7.90	7.59	0.16

B.2 Glass Beads Volumetric Feeder

Table B.2: Glass beads volumetric feeder calibration data.

Potentiometer Setting	Time [min]	Trial 1 Weight [g]	Trial 2 Weight [g]	Trial 3 Weight [g]	Trial 4 Weight [g]	Trial 5 Weight [g]	Average Weight [g]	Standard Deviation [g]	Mass Flow Rate Average [kg hr^{-1}]	Mass Flow Rate Standard Deviation [kg hr^{-1}]
100	2	121.48	120.09	119.10	120.70	119.75	120.22	0.91	3.61	0.03
200	2	378.44	378.01	373.48	372.19	375.63	375.55	2.74	11.27	0.08
300	2	629.72	627.08	628.89	629.85	634.36	629.98	2.69	18.90	0.08
400	2	887.76	887.16	890.25	888.06	888.87	888.42	1.19	26.65	0.04
500	2	1144.51	1140.30	1142.21	1140.83	1144.40	1142.45	1.96	34.27	0.06
600	2	1403.35	1404.65	1400.09	1410.29	1405.23	1404.72	3.69	42.14	0.11
700	2	1667.87	1663.66	1666.15	1664.61	1668.32	1666.12	2.01	49.98	0.06
800	2	1922.23	1920.90	1930.44	1926.78	1932.35	1926.54	4.99	57.80	0.15
900	2	2182.61	2200.53	2190.15	2186.94	2186.28	2189.30	6.82	65.68	0.20
999	2	2446.73	2458.25	2444.93	2454.34	2443.01	2449.45	6.53	73.48	0.20

B.3 Gearmotor

Table B.3: Gearmotor calibration data.

Gearmotor Supply Voltage [V]	Revolutions	Trial 1 Time [s]	Trial 2 Time [s]	Trial 3 Time [s]	Trial 4 Time [s]	Trial 5 Time [s]	Time Average [min]	Time Standard Deviation [min]	Screw Rotation Speed [rpm]	Screw Rotation Speed Standard Deviation [rpm]
20	25	113.43	113.00	113.10	113.37	113.20	1.89	0.18	13.25	0.02
30	25	71.69	71.87	72.05	72.30	71.94	1.20	0.23	20.84	0.07
40	25	52.71	52.75	52.83	53.01	52.88	0.88	0.12	28.39	0.06
50	25	41.69	41.87	41.70	41.63	41.62	0.07	0.10	35.97	0.09
60	25	34.31	34.44	31.12	34.20	34.25	0.57	0.12	43.78	0.15
70	25	29.19	29.38	29.50	29.06	29.31	0.49	0.17	51.22	0.30
80	25	25.45	24.40	25.38	25.43	25.18	0.42	0.44	59.60	1.07
90	25	22.37	22.50	22.44	22.44	22.37	0.37	0.06	66.89	0.16

APPENDIX C: STEPPER MOTOR POWER ANALYSIS

The power analysis outlined by Colijn (1985) was used to estimate the stepper motor torque required to power the screw mixer, as shown in Table C.1. Only slight modifications have been applied to the procedure to account for the specific screw mixer considerations.

Table C.1: Stepper motor power analysis summary.

Symbol	Description	Value	Units	Notes
ρ_B	Bulk density	1484	kg m^{-3}	Bulk density of RO and GB
m	Mass flow rate	66	kg hr^{-1}	Maximum mass flow rate
Q	Volumetric flow rate	0.044	m^3 hr^{-1}	$Q = m/\rho$
C	Volumetric feed rate	1.57	ft^3 hr^{-1}	$C = Q \times 35.314$
e	Drive efficiency	0.50	-	Estimated mechanical efficiency
F_b	Hanger bearing factor	1.0	-	No hanger bearings present
F_d	Conveyor diameter factor	13.57	-	$F_d = .508x^2 - 2.89x + 15.95$ (x = Screw diameter, inches)
F_f	Flight factor	1.0	-	$F_f = 1.0$ for standard screws
F_m	Material factor	3.0	-	$F_m = 3.0$ for class III materials
F_o	Overload factor	3.0	-	$F_o = 3.0$ max for small motors
F_p	Paddle factor	1.0	-	No mixing paddles
L	Length of conveyor	1.0	ft	Axial length of one screw
H	Lift	0.0	ft	H = 0 for no lift
N	Operating speed	60	rpm	Maximum screw rotation speed
W	Bulk density	92.6	lbs ft^{-3}	$W = r \times 0.06243$
P_f	Conveyor friction power	0.00081	hp	$P_f = (L \times N \times F_d \times F_b) / 1000000$
P_l	Lift power	0.00000	hp	$P_l = (0.5 \times C \times W \times H) / 1000000$
P_m	Transport Power	0.00044	hp	$P_m = C \times L \times W \times F_f \times F_p \times F_m / 1000000$
P	Power required for screws	**0.01501**	hp	$P_T = 2 \times [(P_f + P_l + P_m) \times F_o] / e$
T	Torque required for screws	**1.31363**	ft-lbs	$T = P \times 5252 / N$

APPENDIX D: STEPPER MOTOR COMPUTER PROGRAM

Three custom computer programs were written to enable successful X-ray CT imaging of the screw mixer: (i) a “reset” program that sets the screw mixer’s screws in the reference position, (ii) a “steady state” program that runs the screw mixer for a specific number of revolutions such that it is operating at steady state, and (iii) a “test” program that rotates the screw mixer a desired number of revolutions and then stops the screws at the reference position once again. These three programs allow the screws to be located in the same angular position before and after testing, allowing an empty X-ray CT volume file to be subtracted from a X-ray CT volume file full of granular material. In theory, this would allow for successful composition analysis of individual voxels which contain only granular material. Lin Engineering’s syntax was used such that it was compatible with the stepper motor interface. The syntax for the three programs are:

Reset Program:	/1m100h50j256V25600L1000P358400A0R
Steady State Program:	/1m100h50j256V25600L1000J1P1843200J2R
Test Program:	/1m100h50j256V25600L1000J1P819200J2R

The details of the test program syntax are:

Syntax:	/1m100h50j256V25600L1000J1P819200J2R

Start Loop

/	Start character

1	Motor number

Specify Motor Settings

m100	Set run current to 100% of max 3.0 A
h50	Set hold current to 50% of max 3.0 A
j256	Set step resolution to 256 (i.e., 1.8°/256)
V25600	Set velocity to 25600 steps s^{-1}
L1000	Set acceleration to 1000 steps s^{-2}

Turn on Volumetric Auger Feeders

J1	Turns on I/O driver two

Move Motor

P819200	Moves motor 819200 steps, which equals 1 revolution in positive direction

Turn Off Volumetric Feeders

J2	Turns off I/O driver two

Run Program

R	End-loop command, run loop one time, run-loop command

APPENDIX E: MATERIAL DISTRIBUTION ANALYSIS DATA

Table E.1: Material distribution analysis data.

			Glass Beads	Quikrete Sand
ASTM Sieve Number		Particle Size Range	Mass Fraction Retained $m_i\ m^{-1}$	
(+)	(-)	[µm]	[-]	[-]
	#120	0-125	0.00	0.00
#120	#100	125-150	0.00	0.00
#100	#80	150-180	0.00	0.01
#80	#70	180-212	0.00	0.01
#70	#60	212-250	0.00	0.02
#60	#50	250-300	0.01	0.02
#50	#40	300-425	0.24	0.24
#40	#35	425-500	0.74	0.24
#35	#30	500-600	0.00	0.22
#30	#25	600-710	0.00	0.20
#25	#20	710-850	0.00	0.04
#20		>850	0.00	0.00

APPENDIX F: OPTICAL VISUALIZATION SNAPSHOTS

F.1 Double Screw Mixer

Snapshots of the dynamic mixing process at steady state conditions that were taken using the optical visualization techniques for each of the screw mixer's 54 operating conditions are shown in Figure F.1 through F.54. The details of each operating condition are shown in Table 3.1.

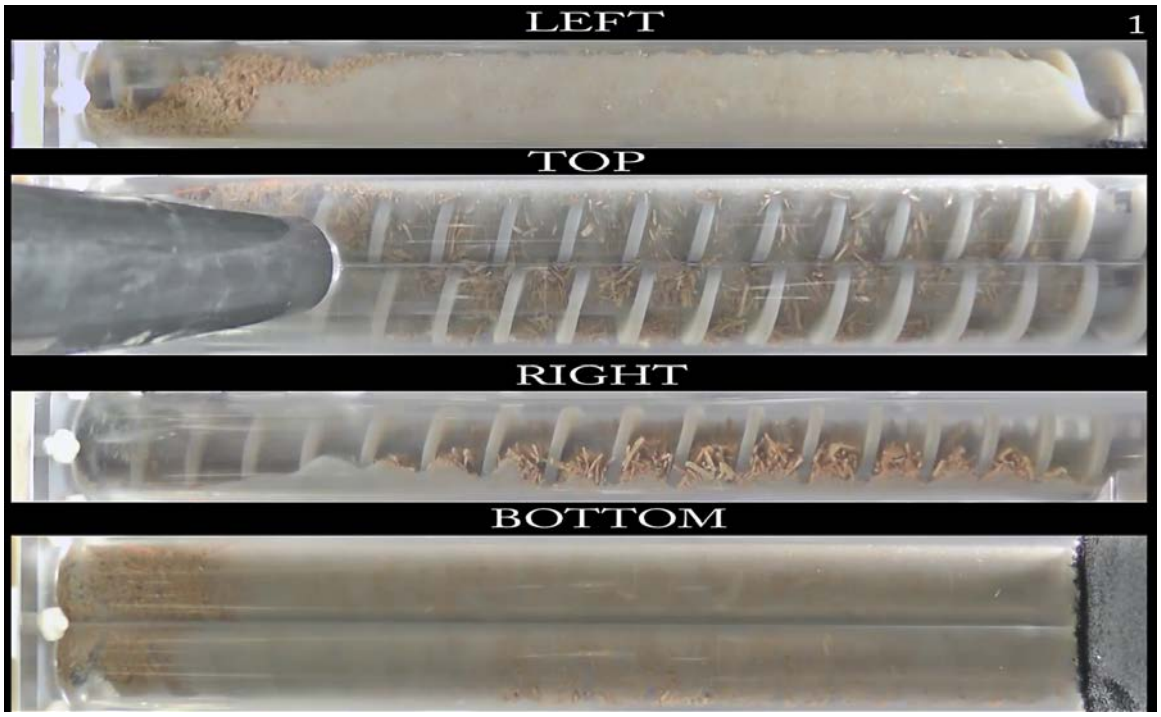

Figure F.1: Operating Condition 1.

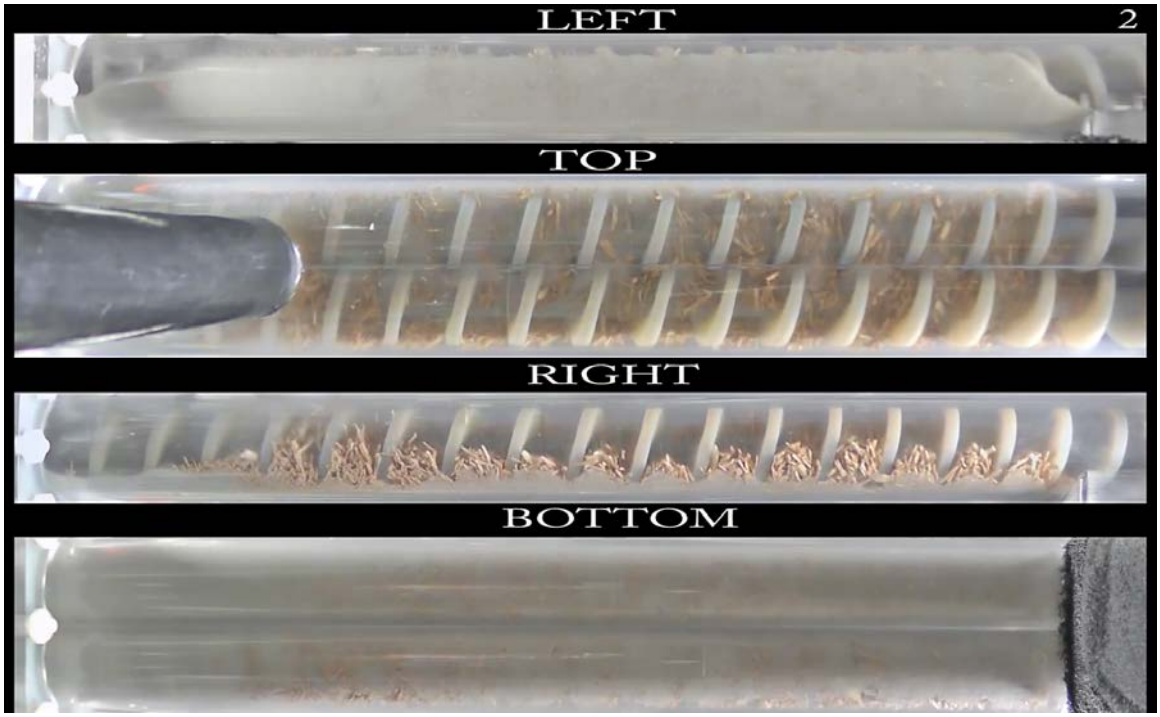

Figure F.2: Operating Condition 2.

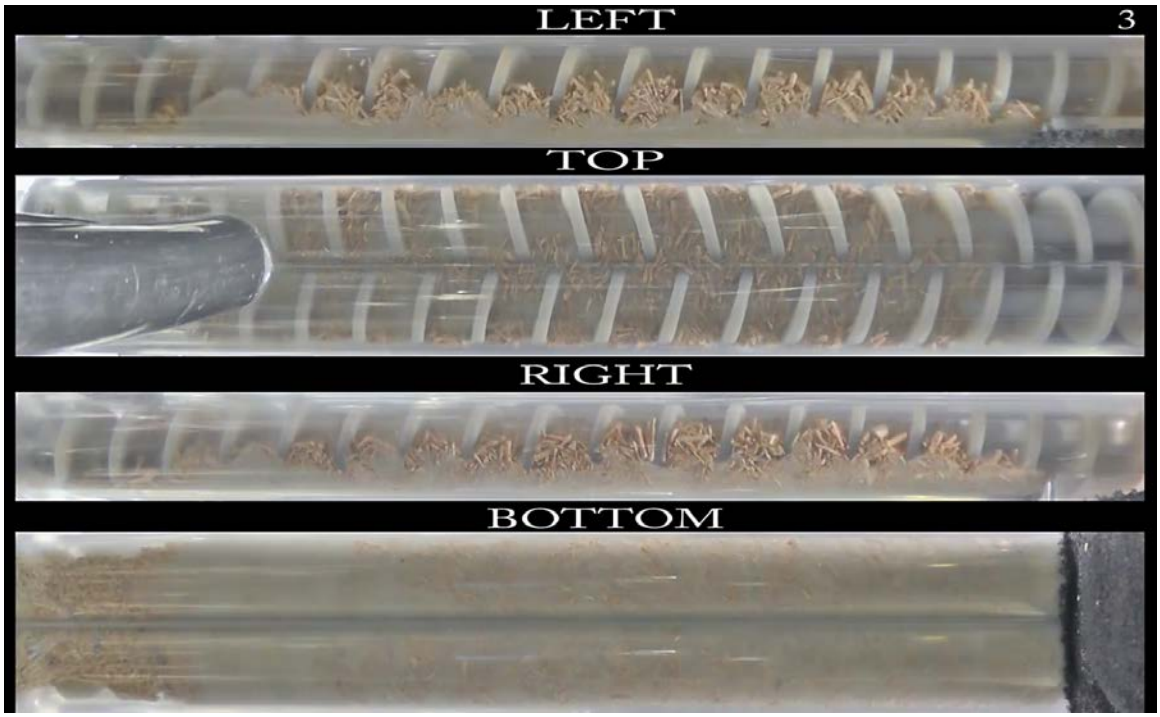

Figure F.3: Operating Condition 3.

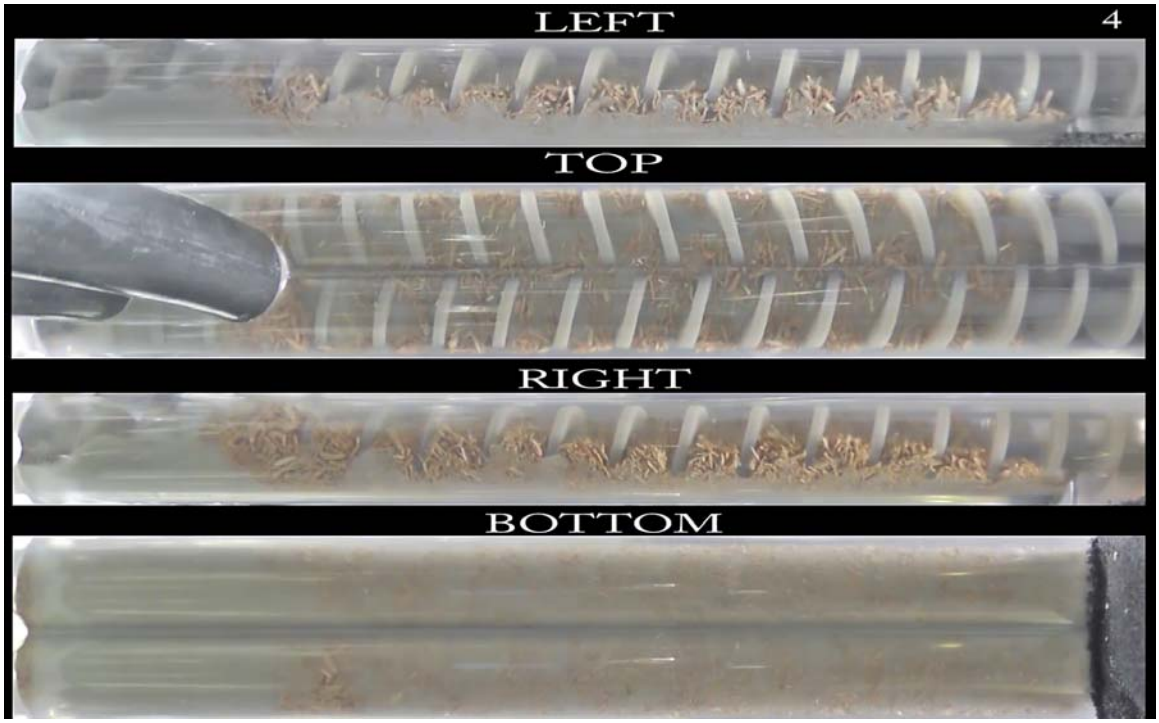

Figure F.4: Operating Condition 4.

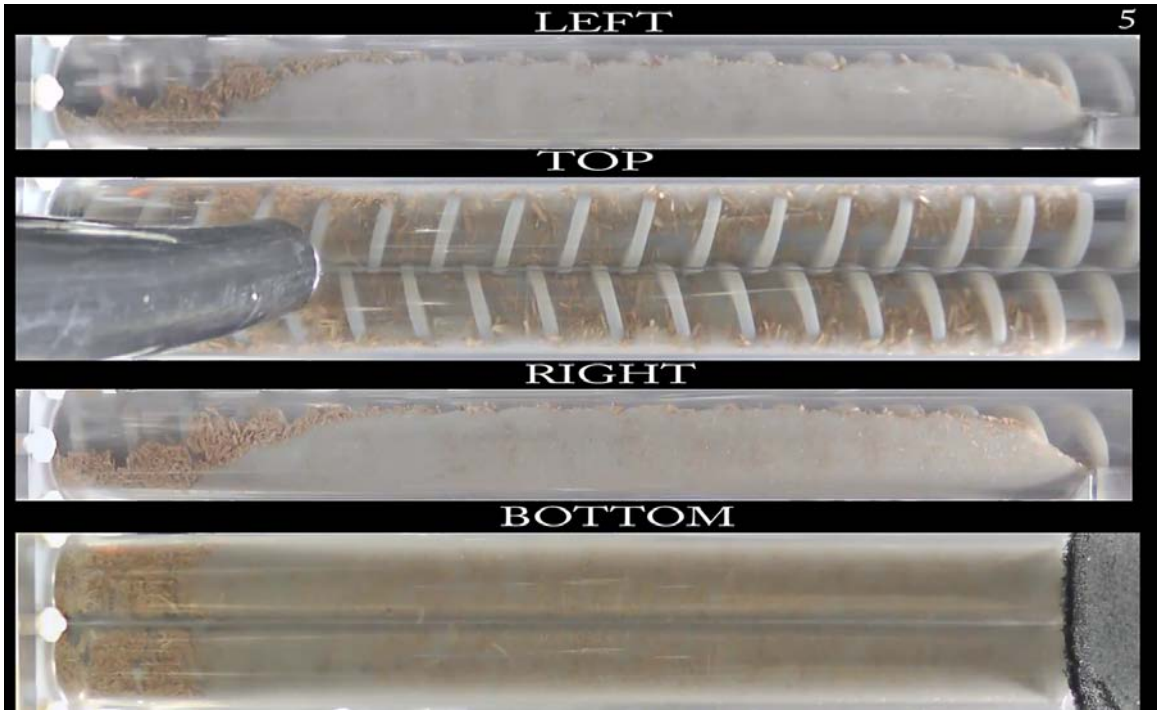

Figure F.5: Operating Condition 5.

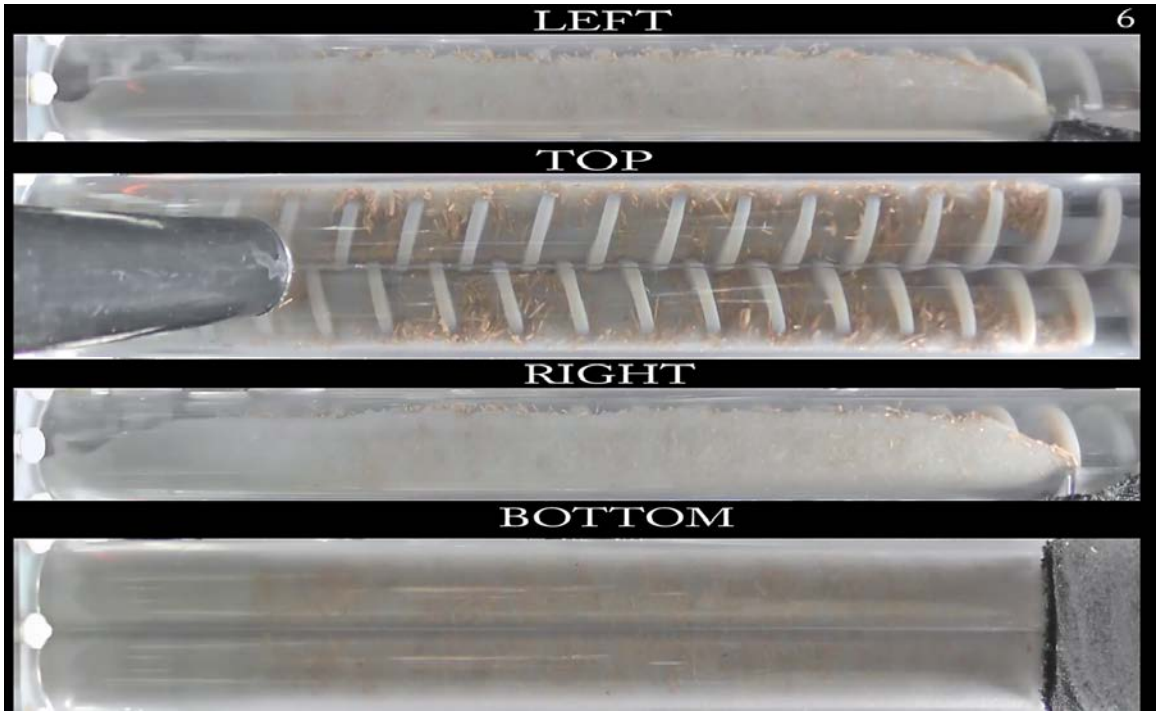

Figure F.6: Operating Condition 6.

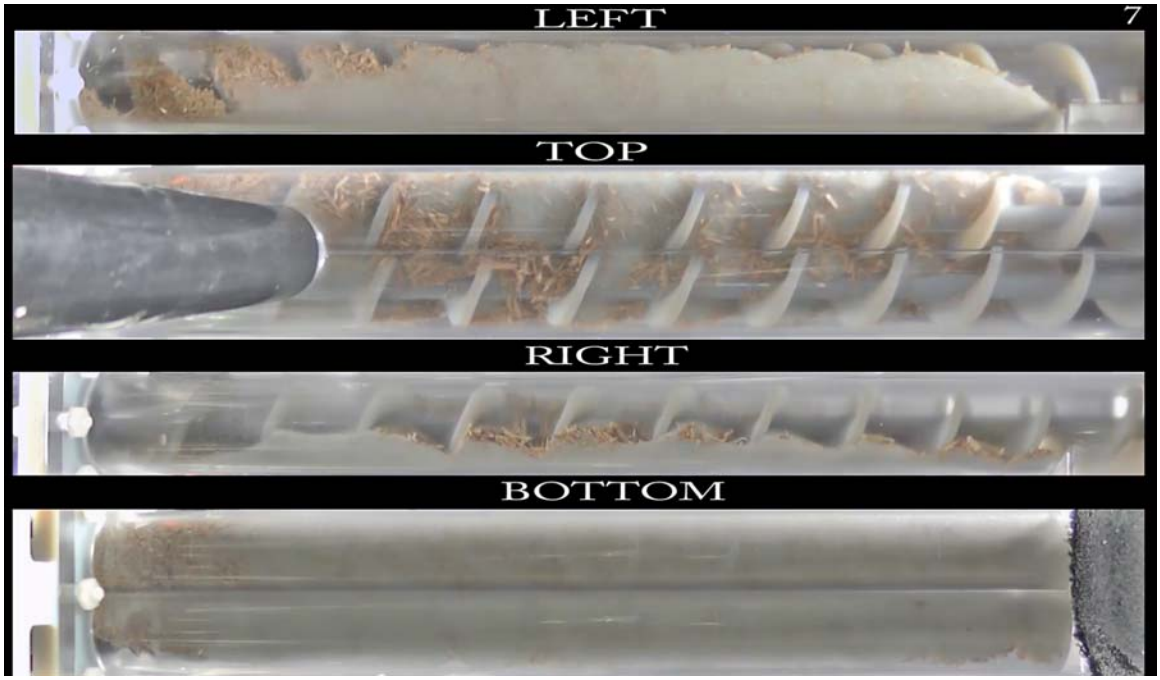

Figure F.7: Operating Condition 7.

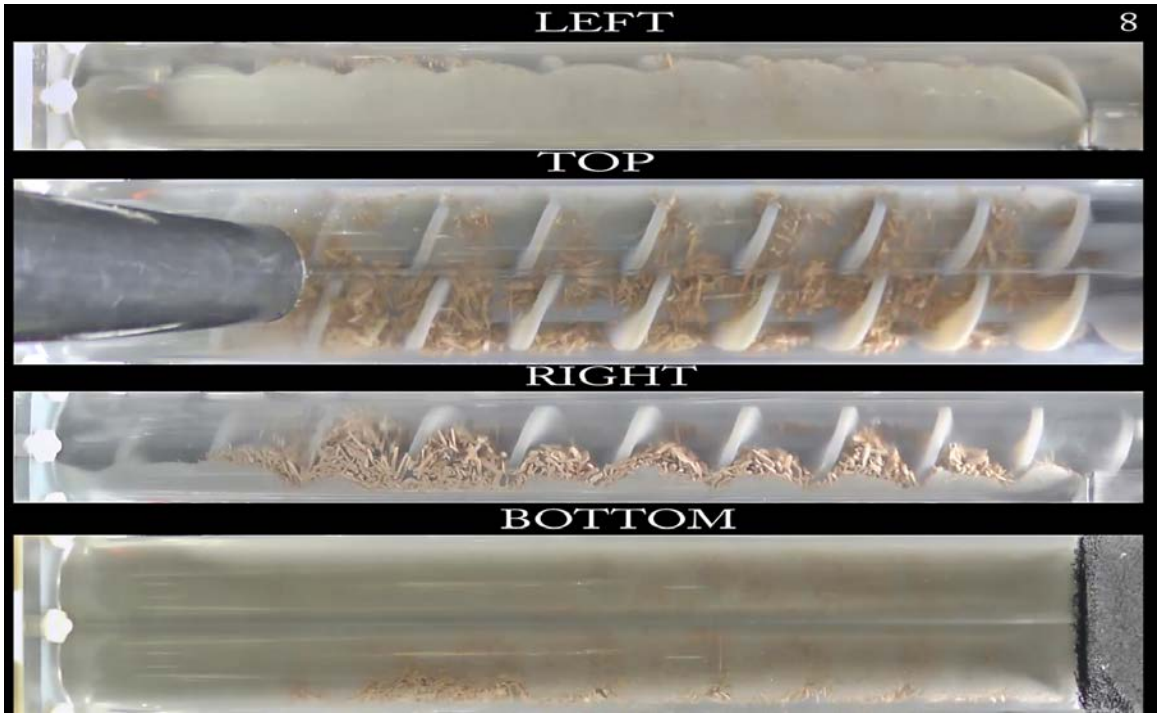

Figure F.8: Operating Condition 8.

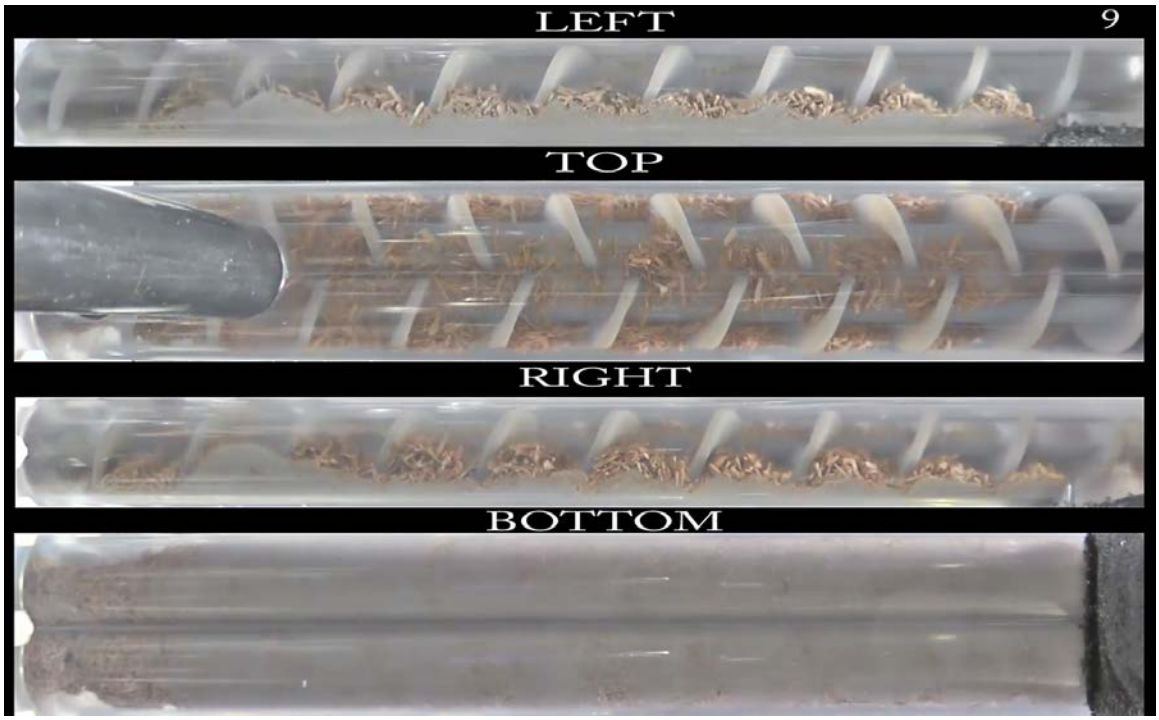

Figure F.9: Operating Condition 9.

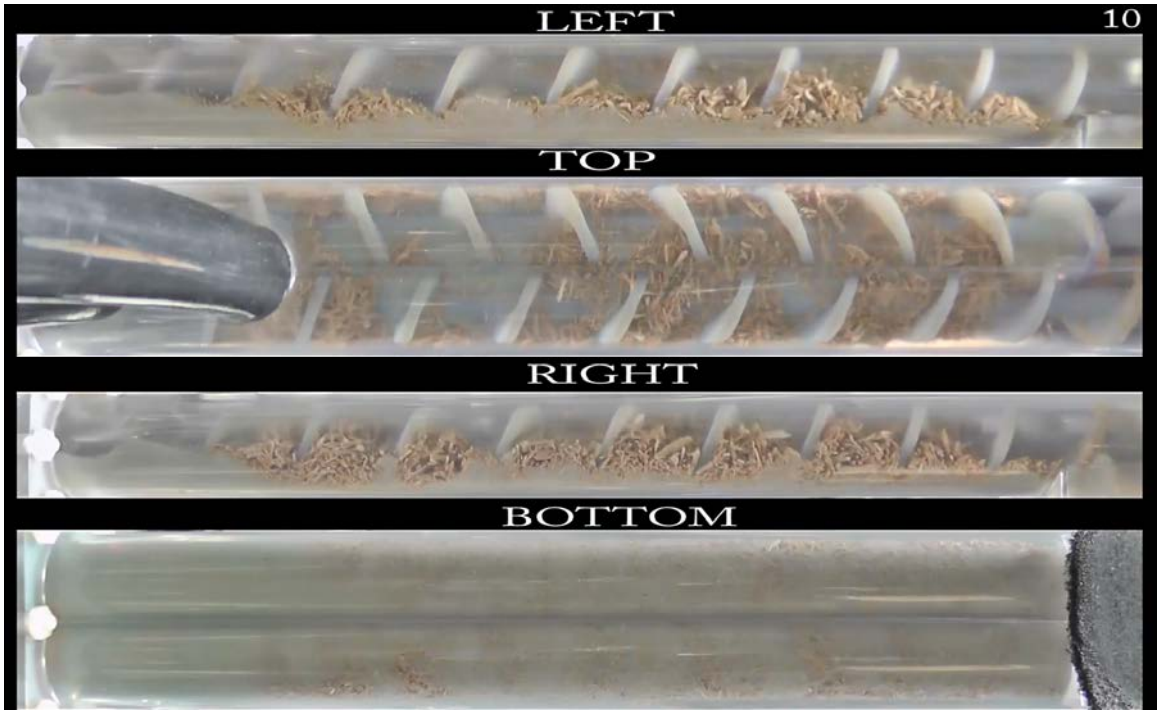

Figure F.10: Operating Condition 10.

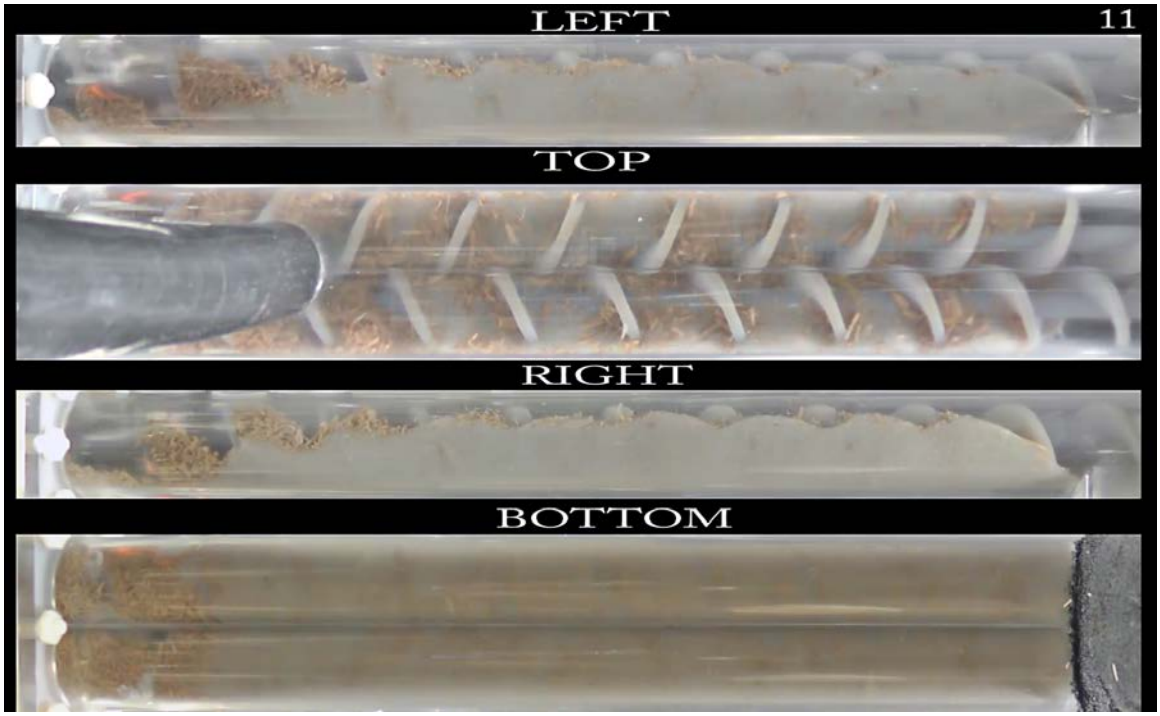

Figure F.11: Operating Condition 11.

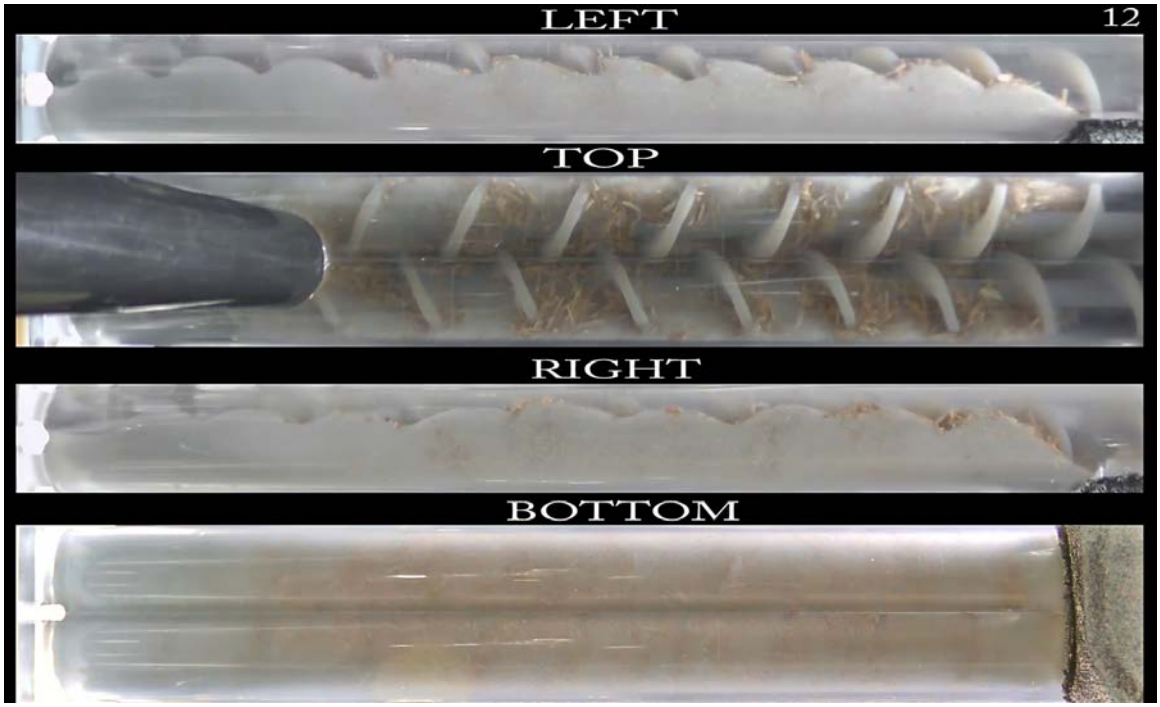

Figure F.12: Operating Condition 12.

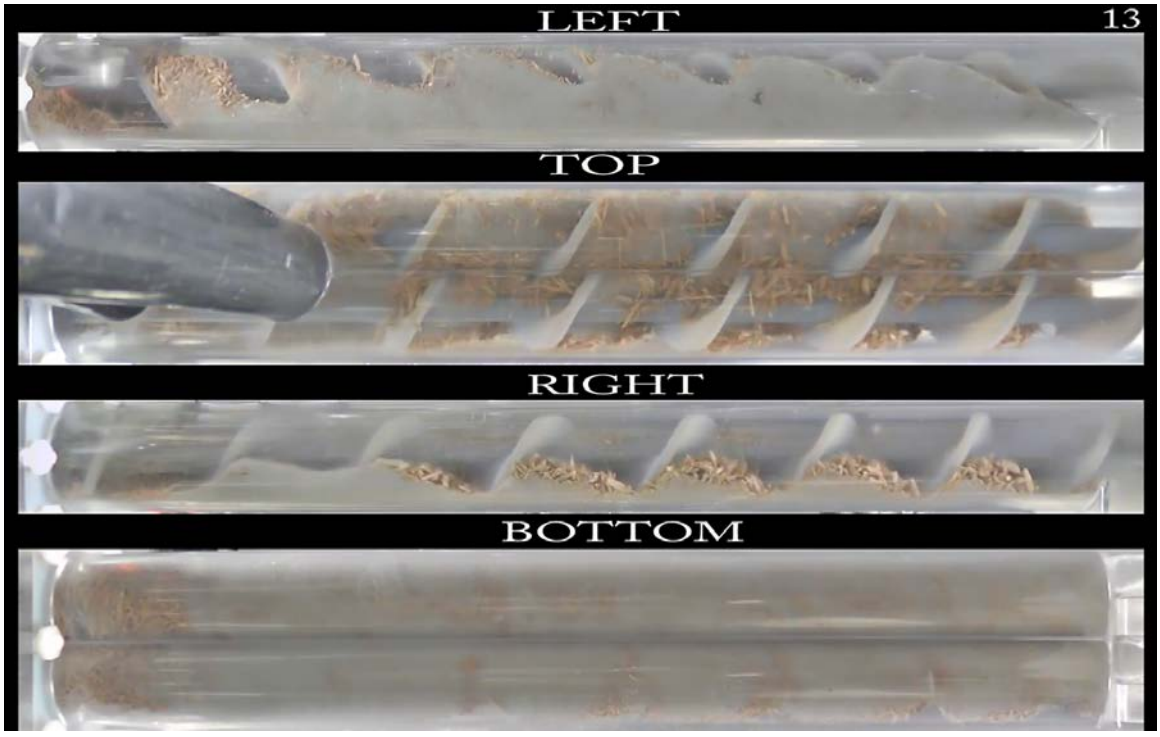

Figure F.13: Operating Condition 13.

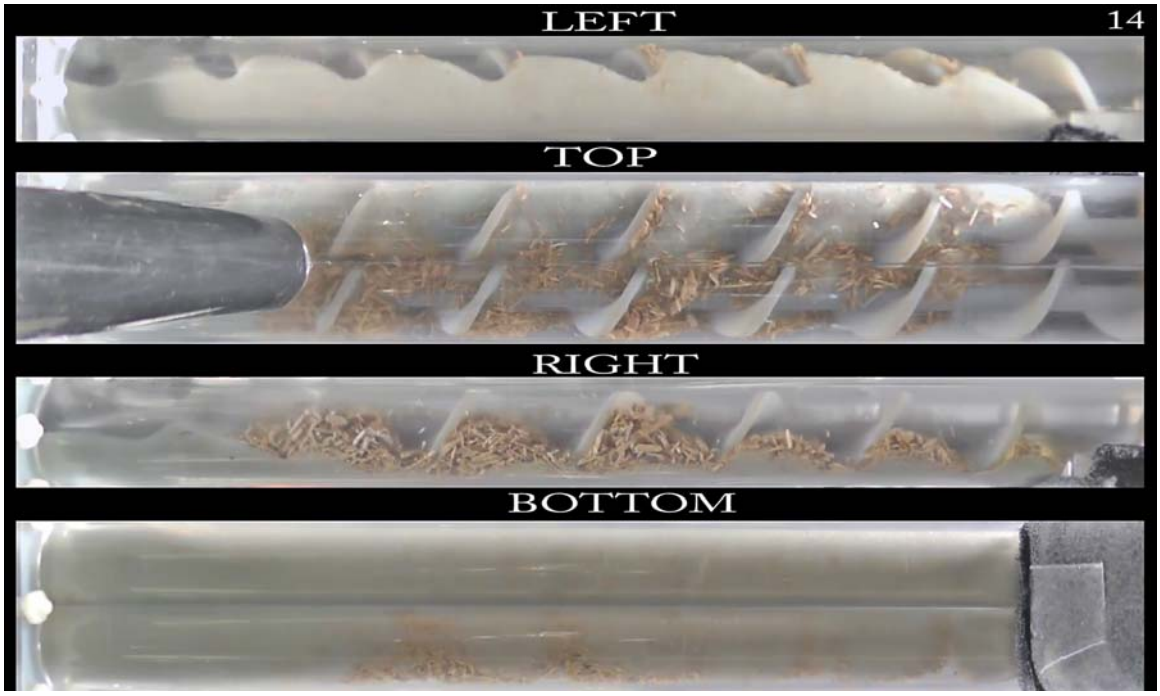

Figure F.14: Operating Condition 14.

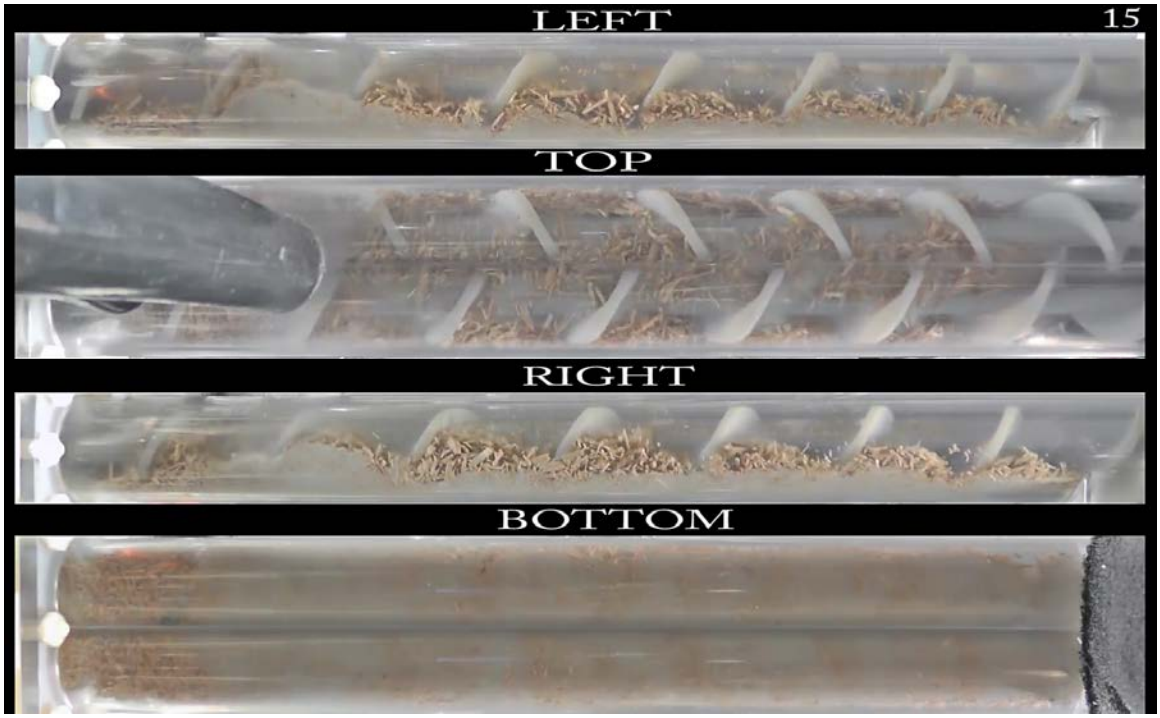

Figure F.15: Operating Condition 15.

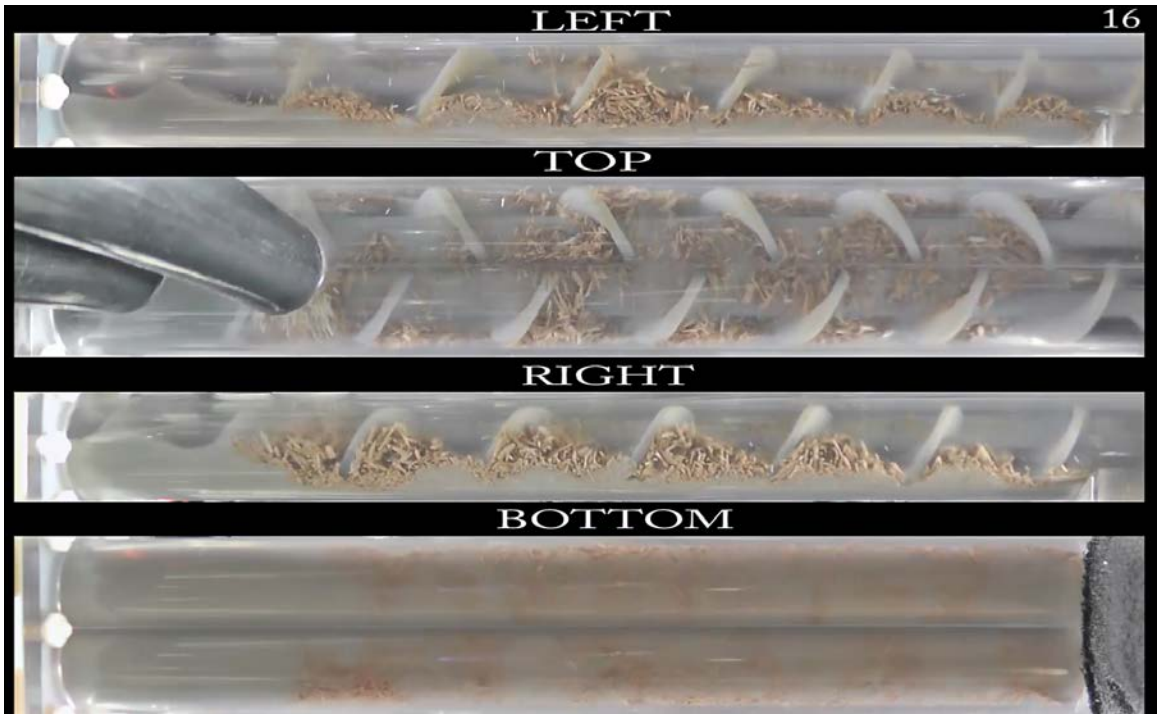

Figure F.16: Operating Condition 16.

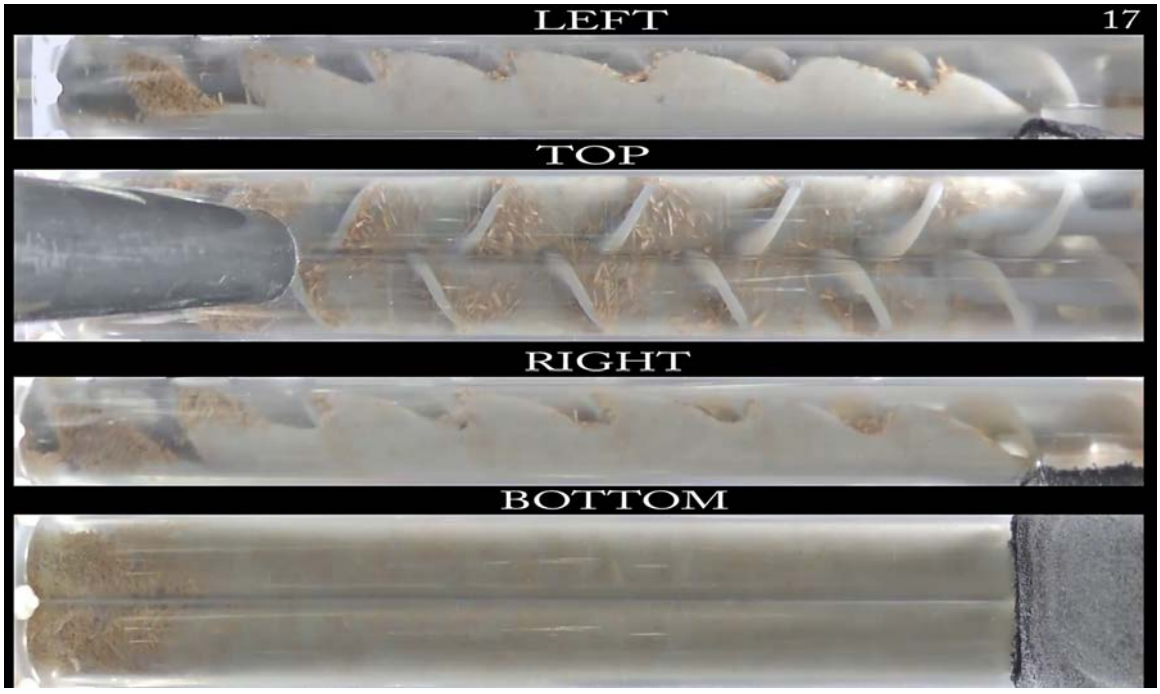

Figure F.17: Operating Condition 17.

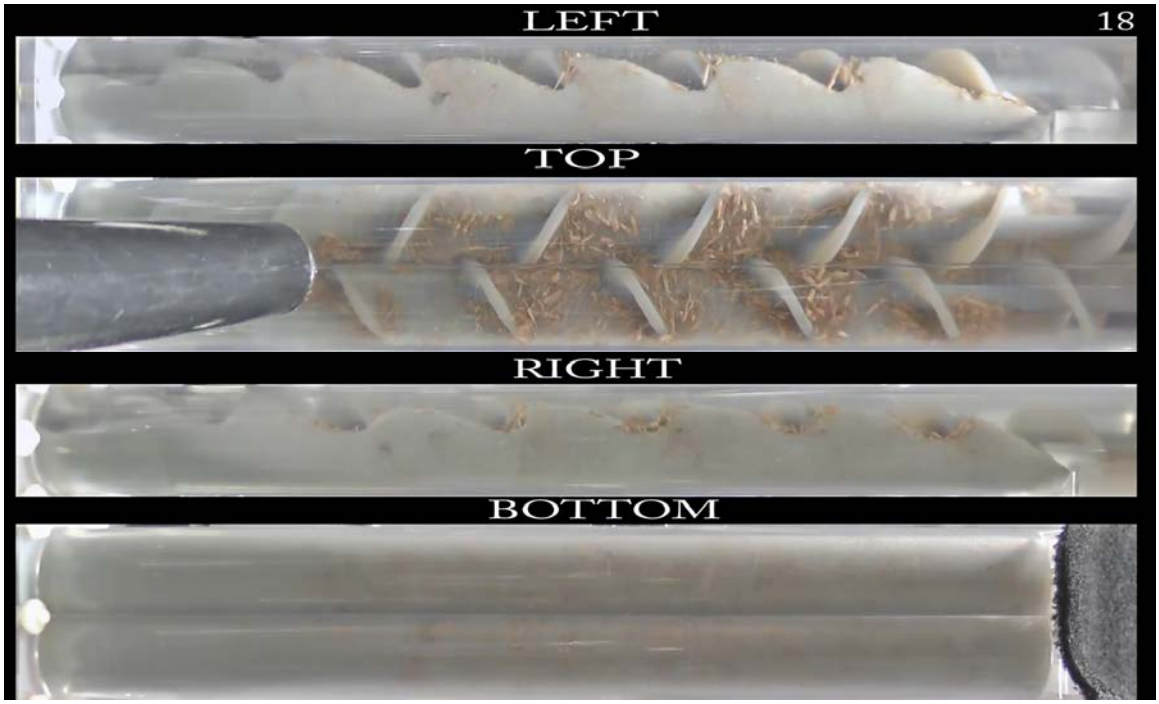

Figure F.18: Operating Condition 18.

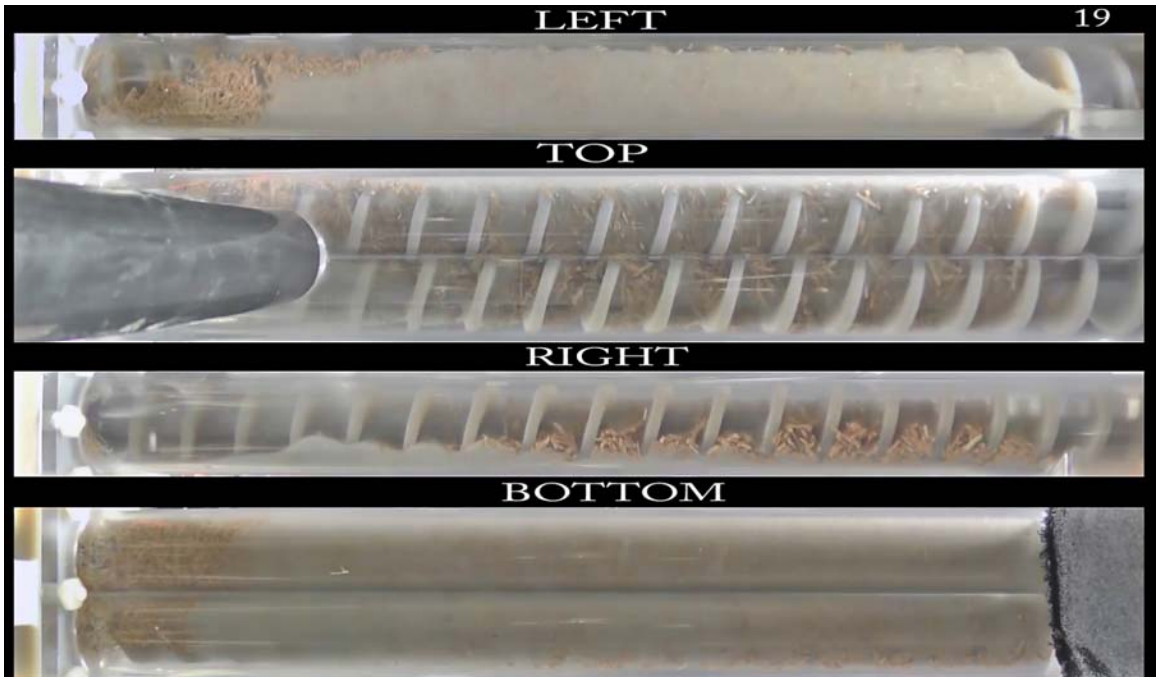

Figure F.19: Operating Condition 19.

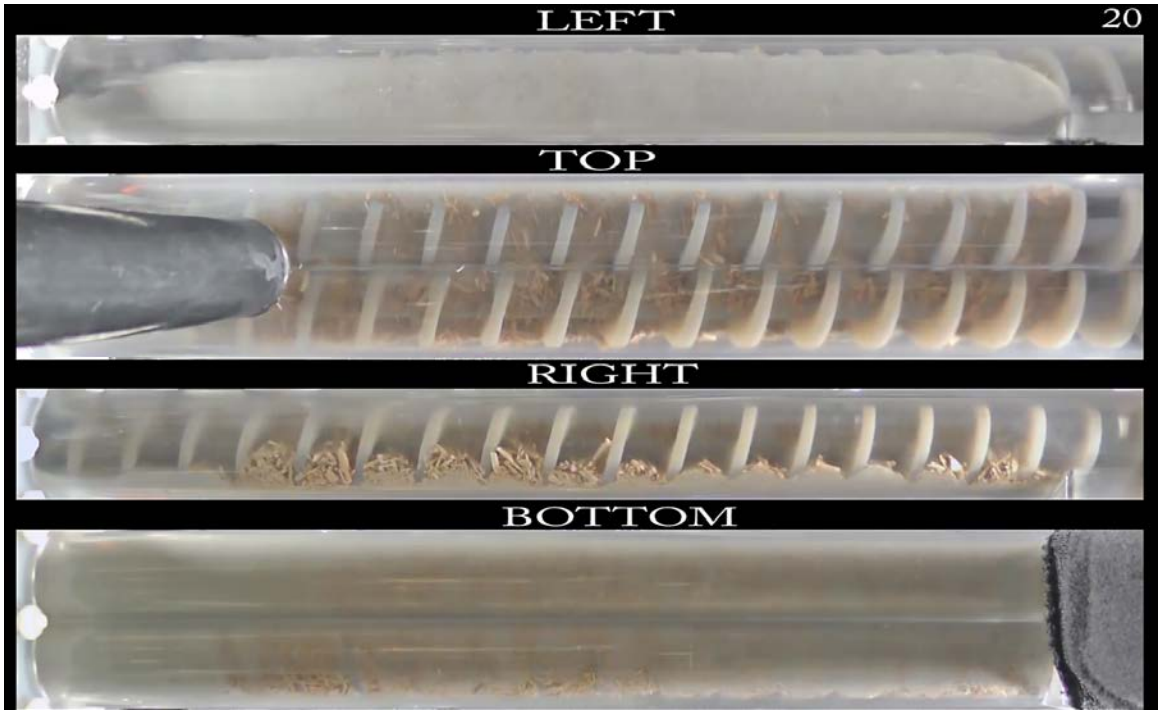

Figure F.20: Operating Condition 20.

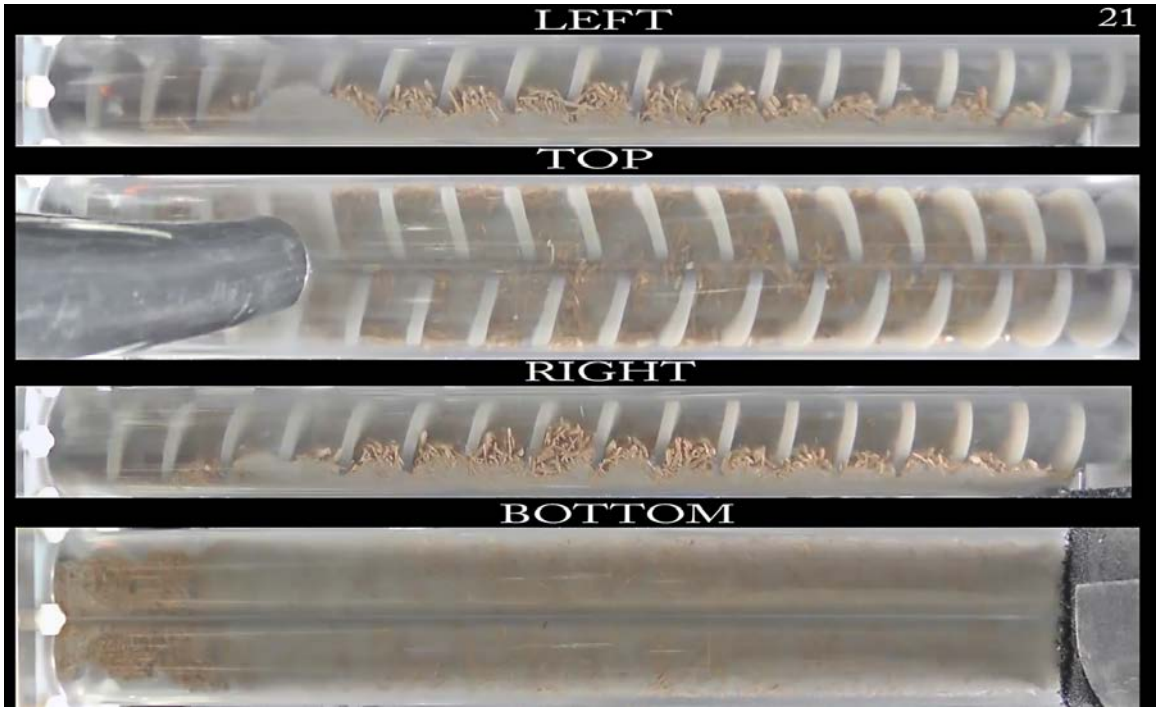

Figure F.21: Operating Condition 21.

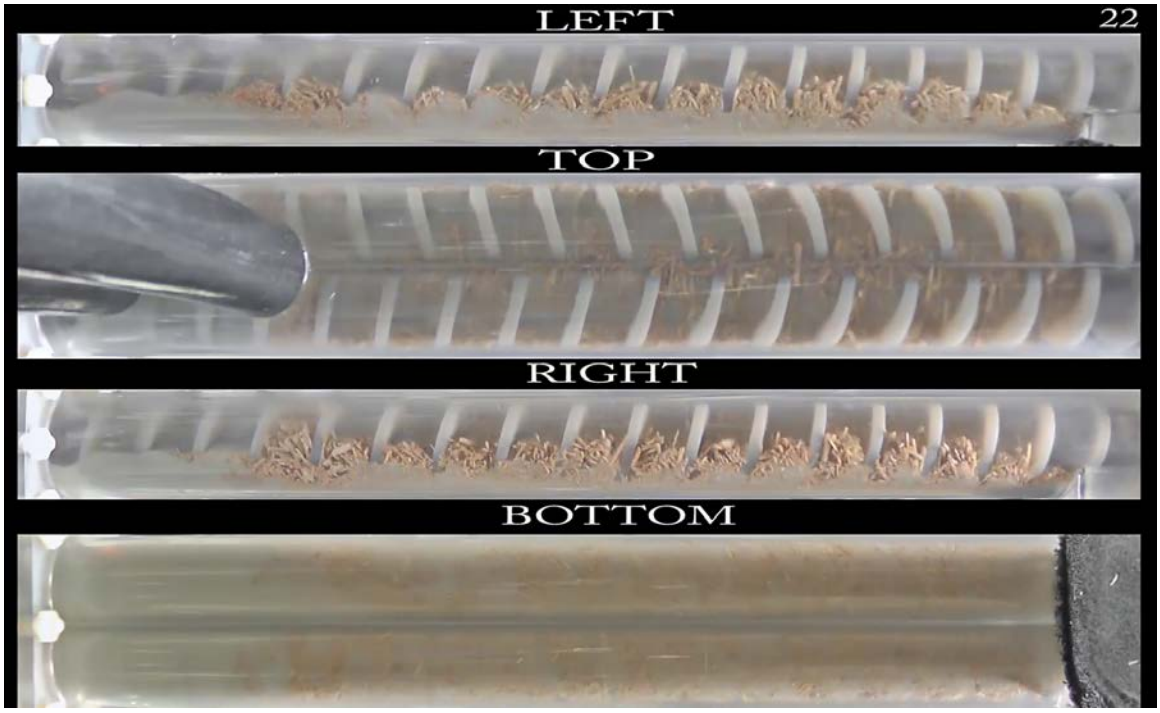

Figure F.22: Operating Condition 22.

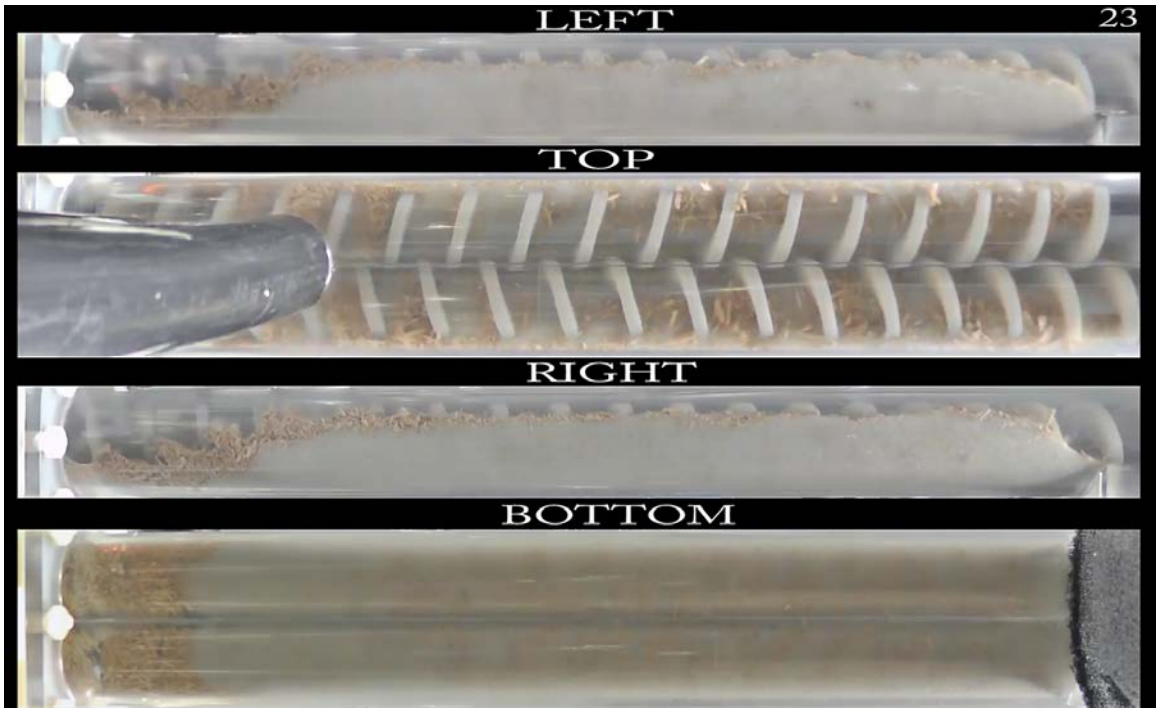

Figure F.23: Operating Condition 23.

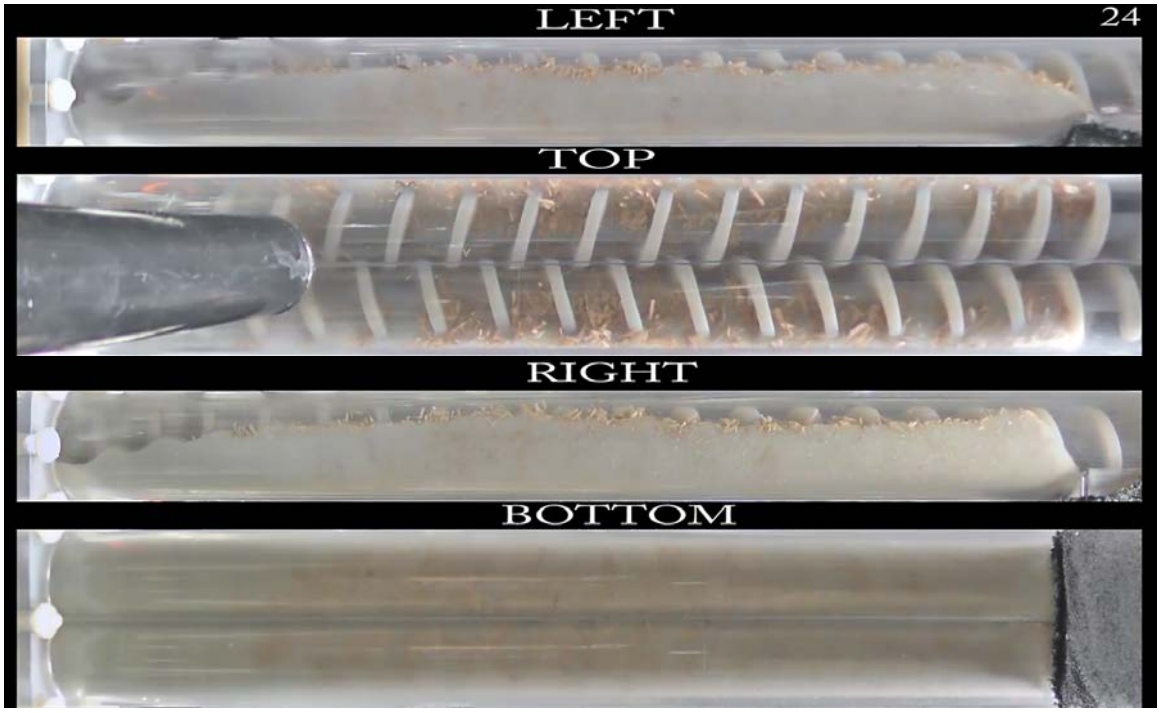

Figure F.24: Operating Condition 24.

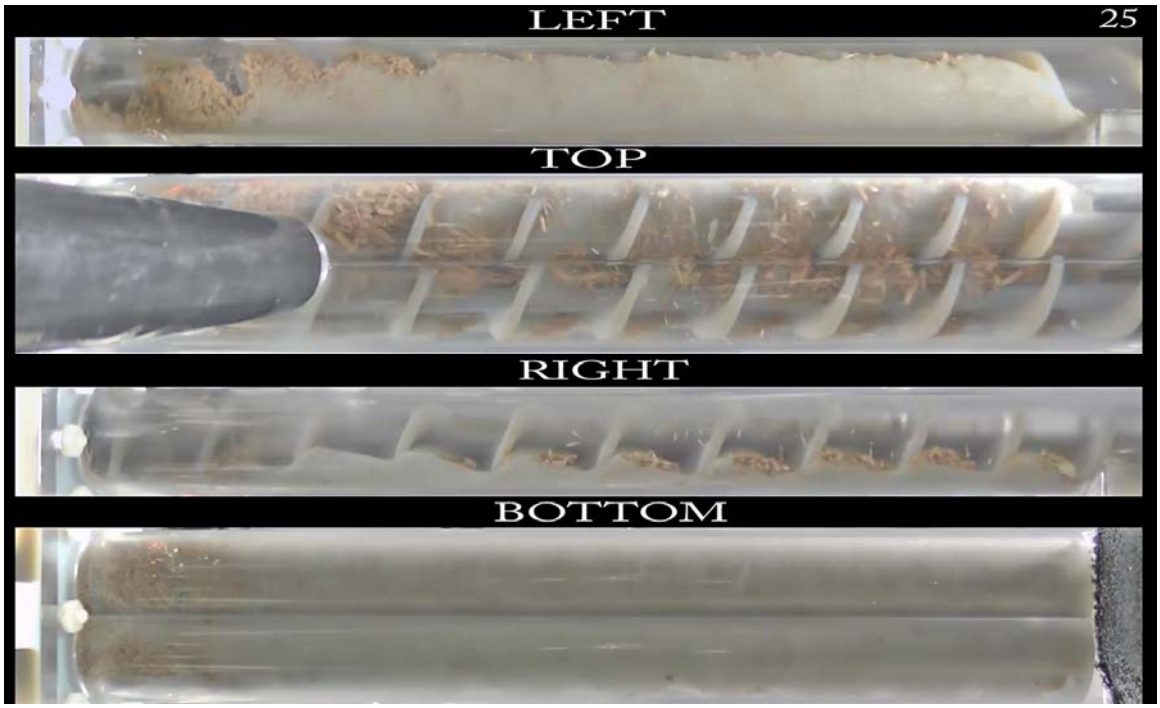

Figure F.25: Operating Condition 25.

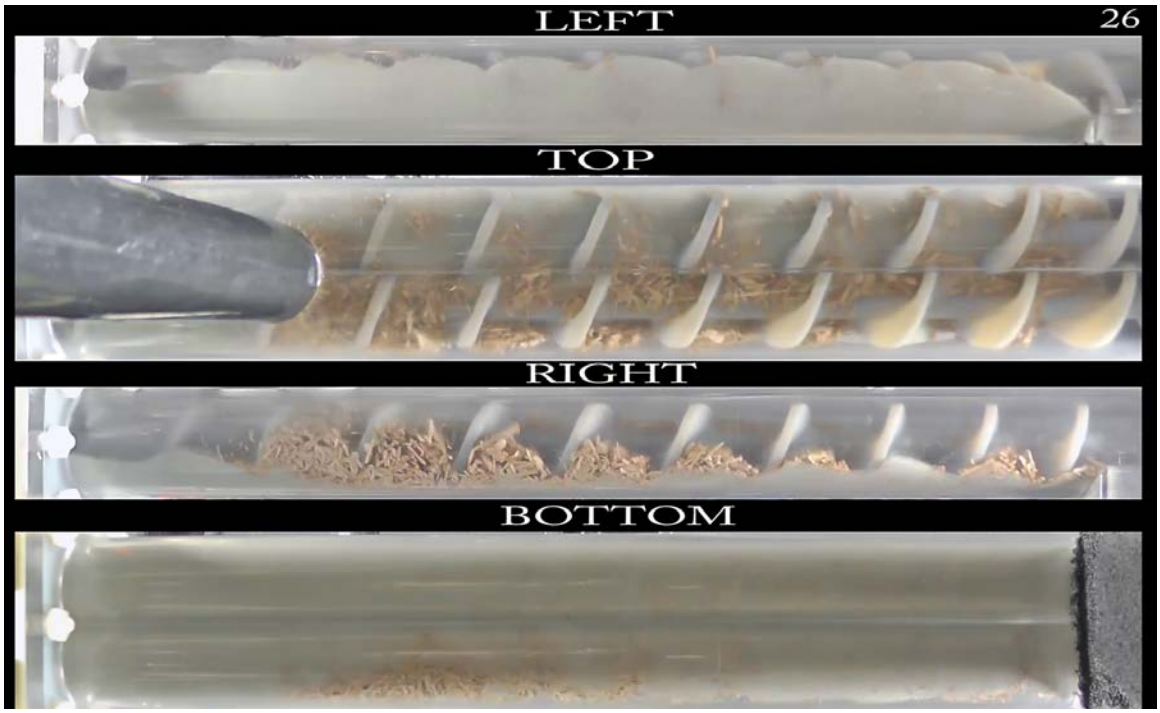

Figure F.26: Operating Condition 26.

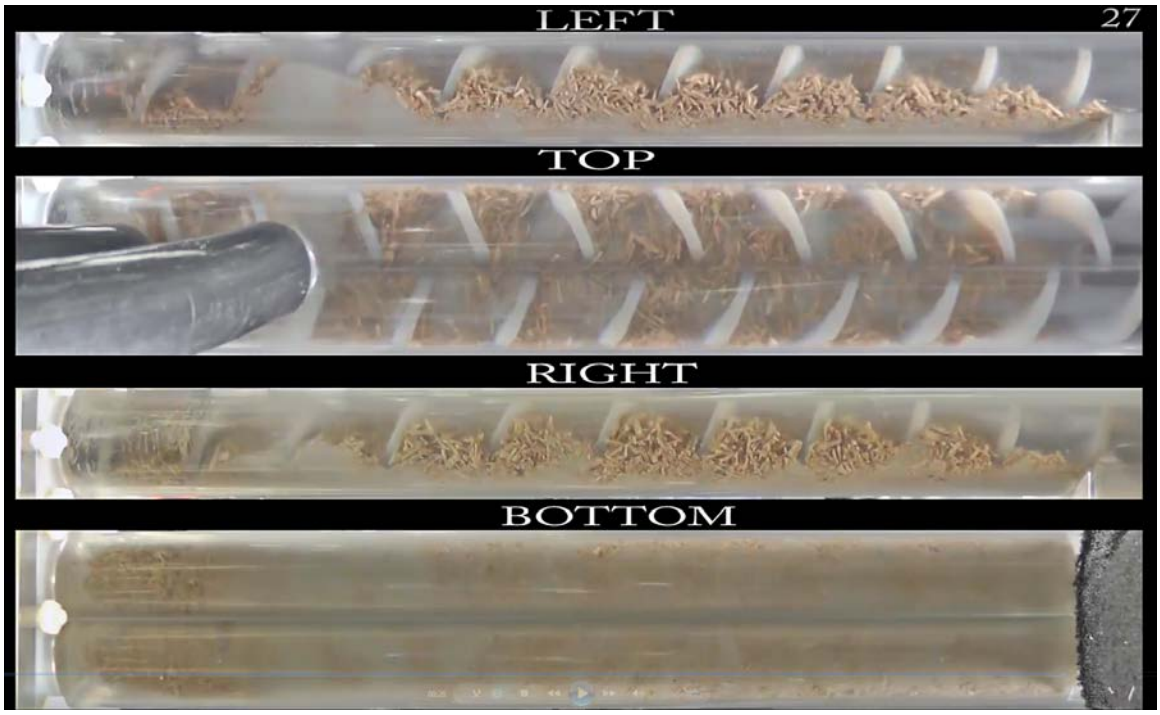

Figure F.27: Operating Condition 27.

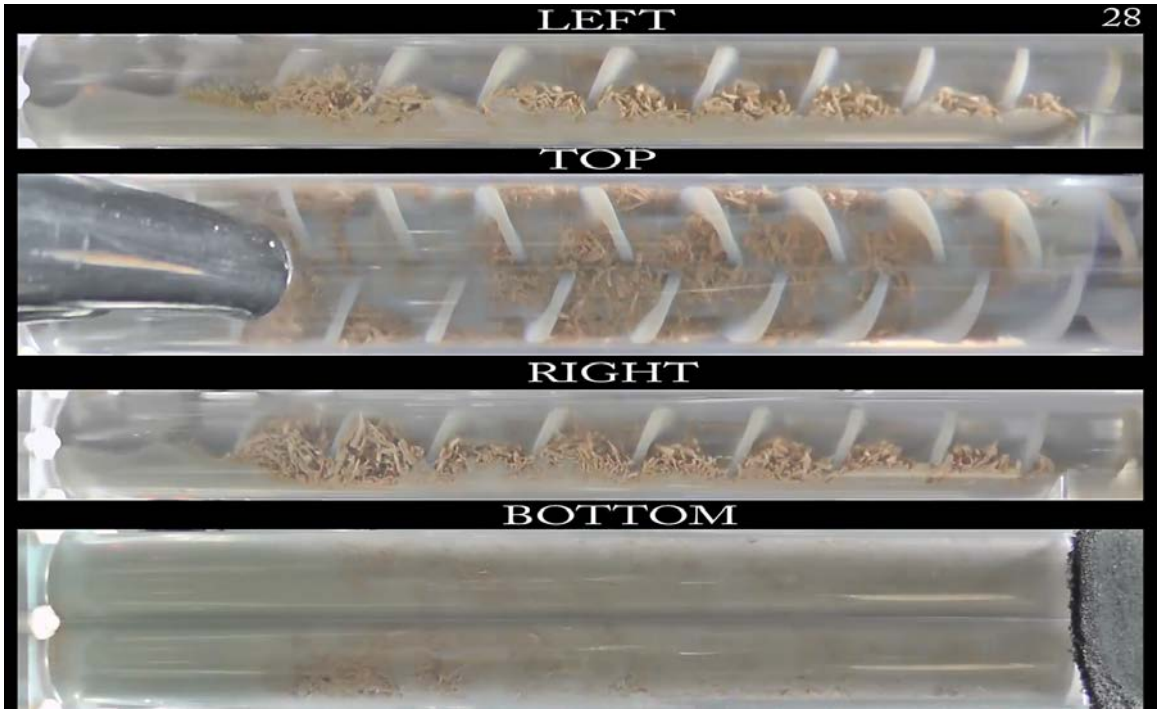

Figure F.28: Operating Condition 28.

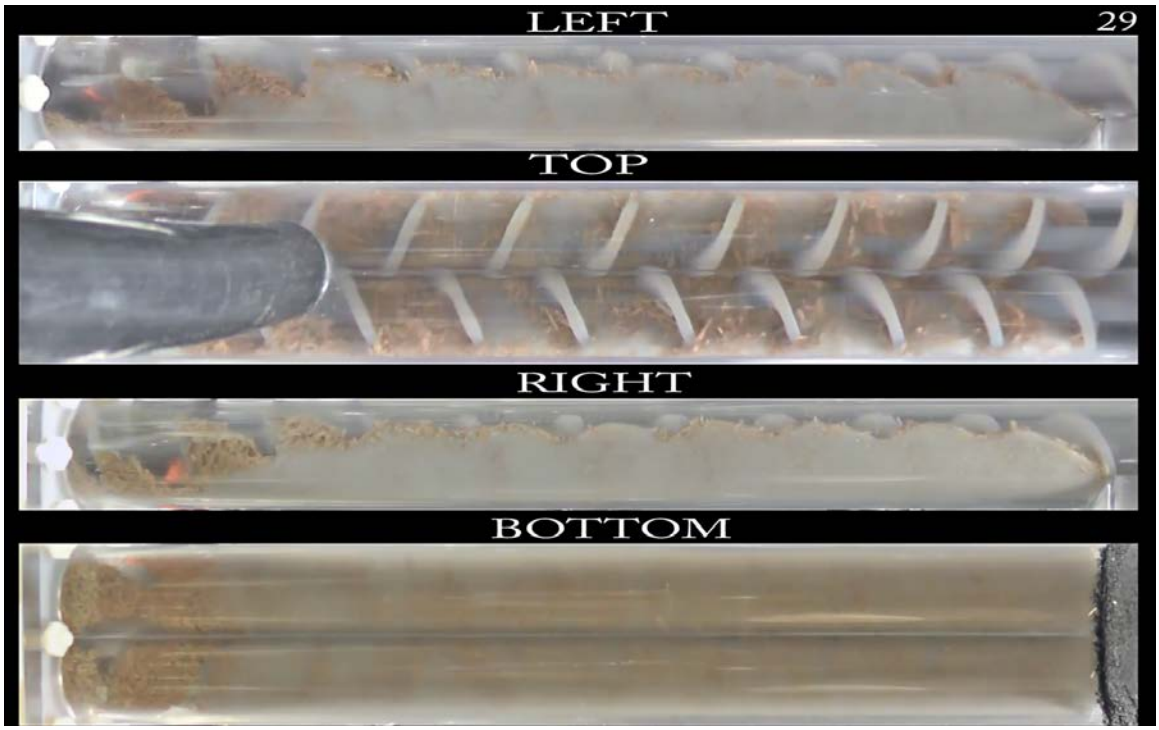

Figure F.29: Operating Condition 29.

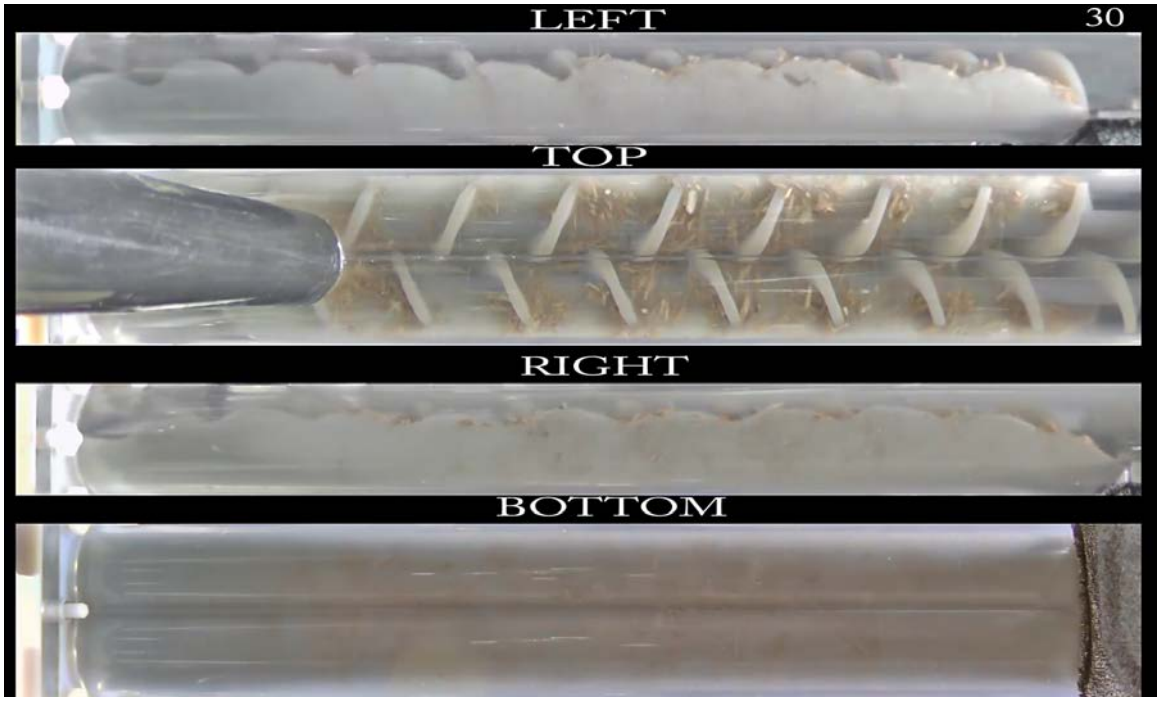

Figure F.30: Operating Condition 30.

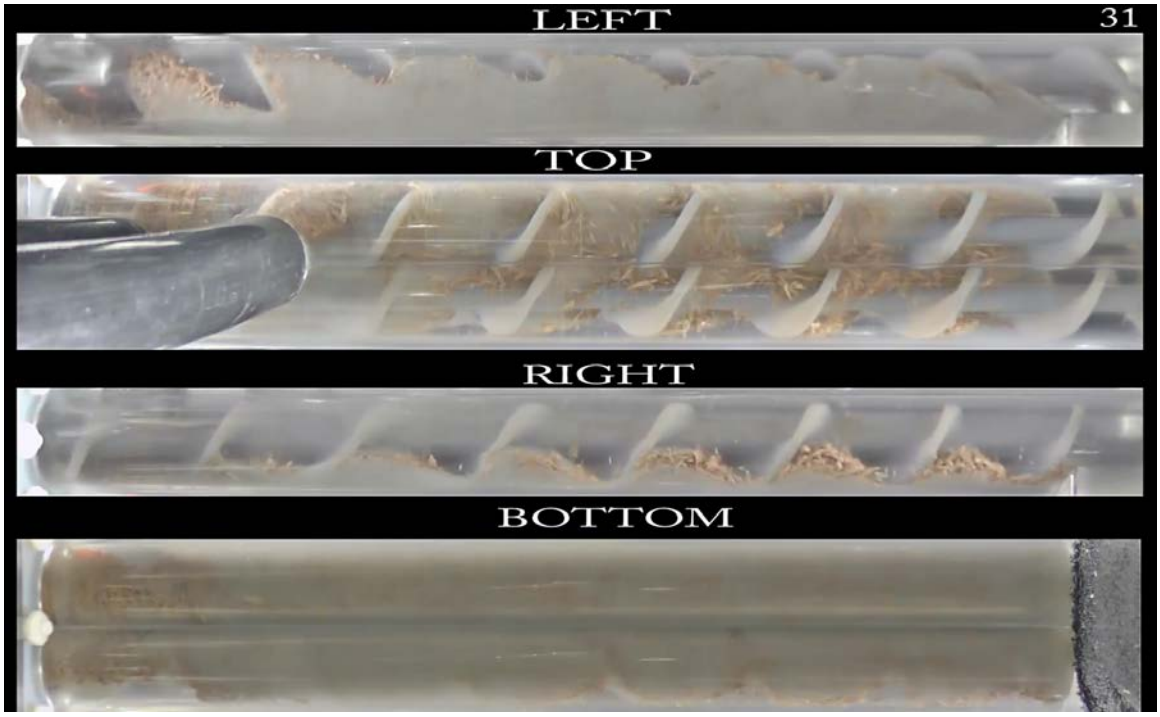

Figure F.31: Operating Condition 31.

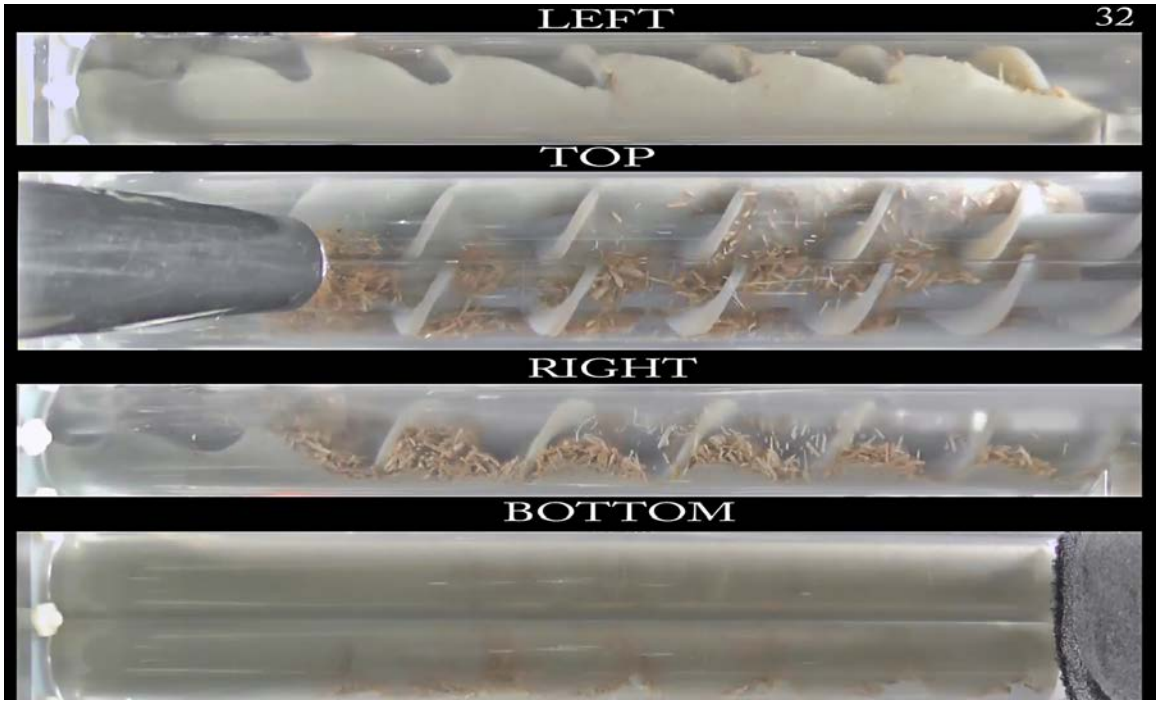

Figure F.32: Operating Condition 32.

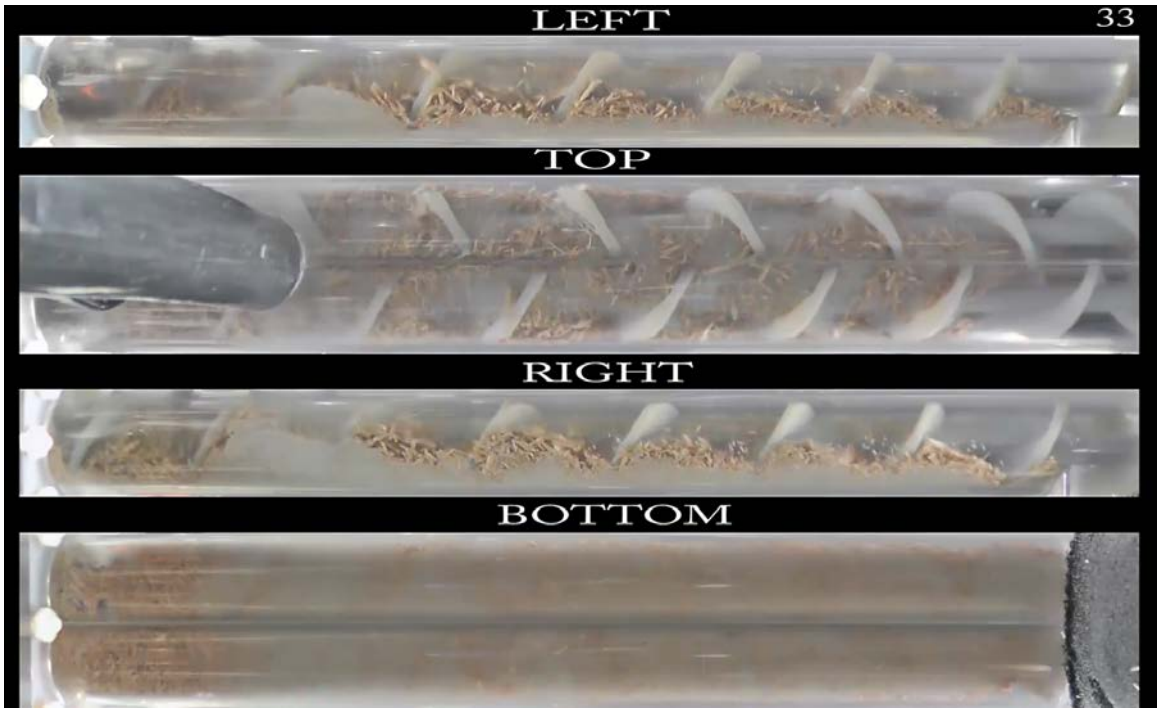

Figure F.33: Operating Condition 33.

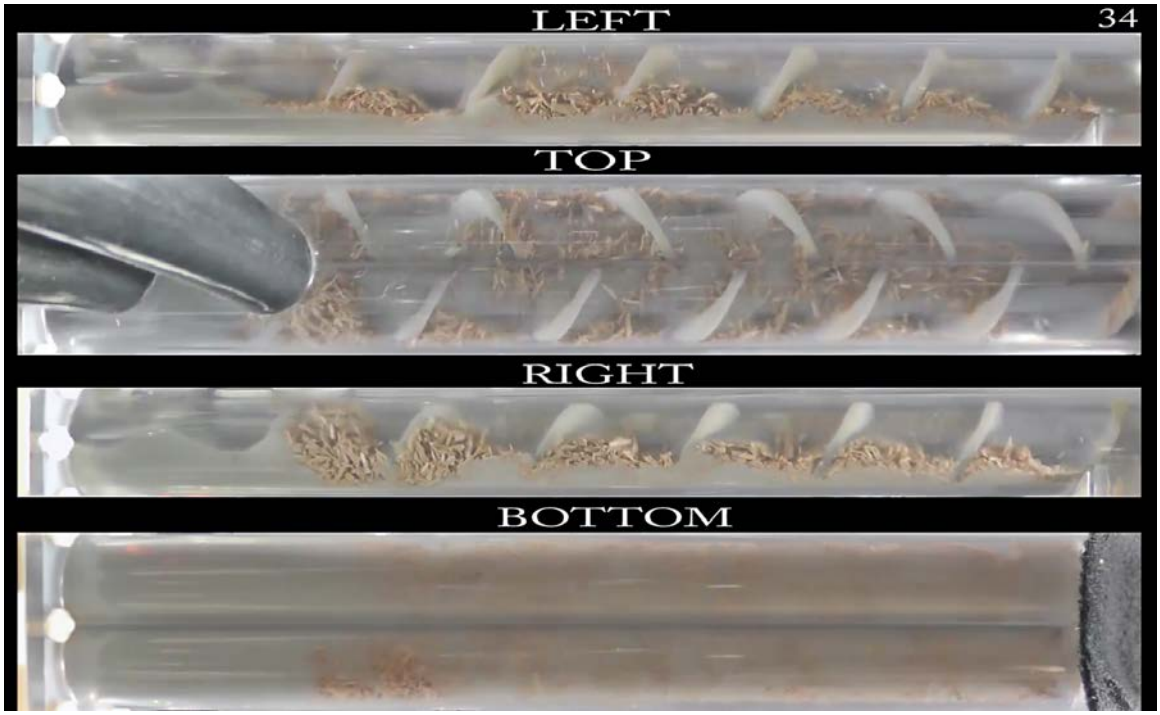

Figure F.34: Operating Condition 34.

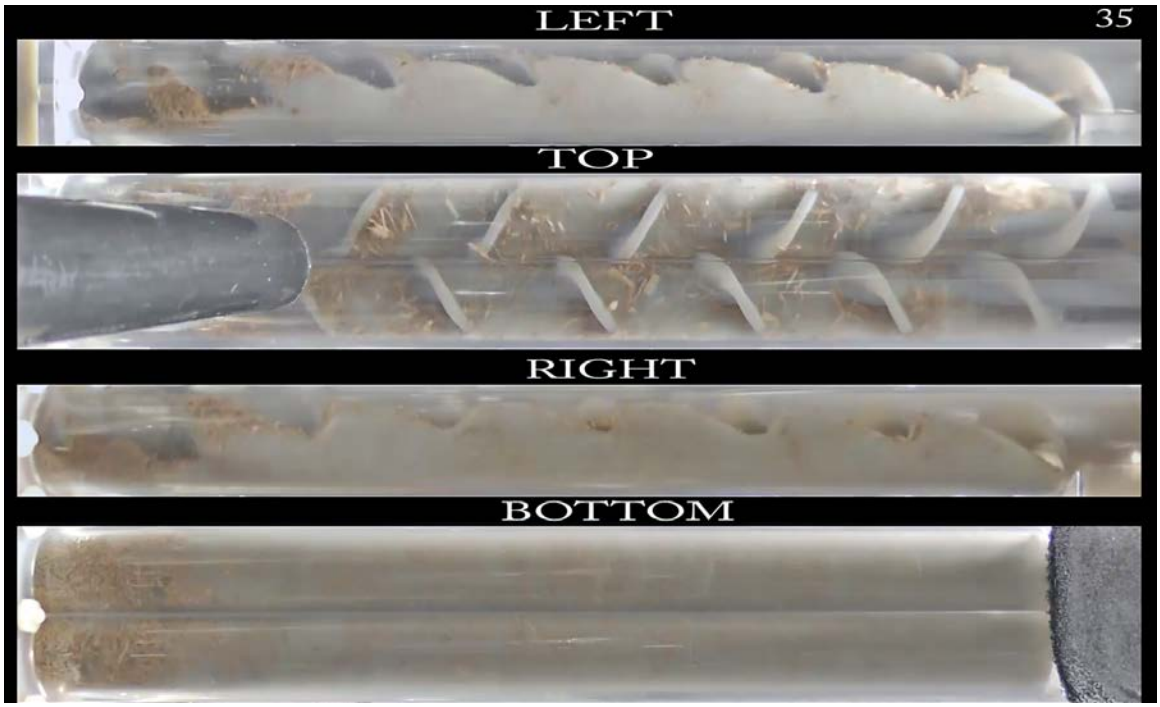

Figure F.35: Operating Condition 35.

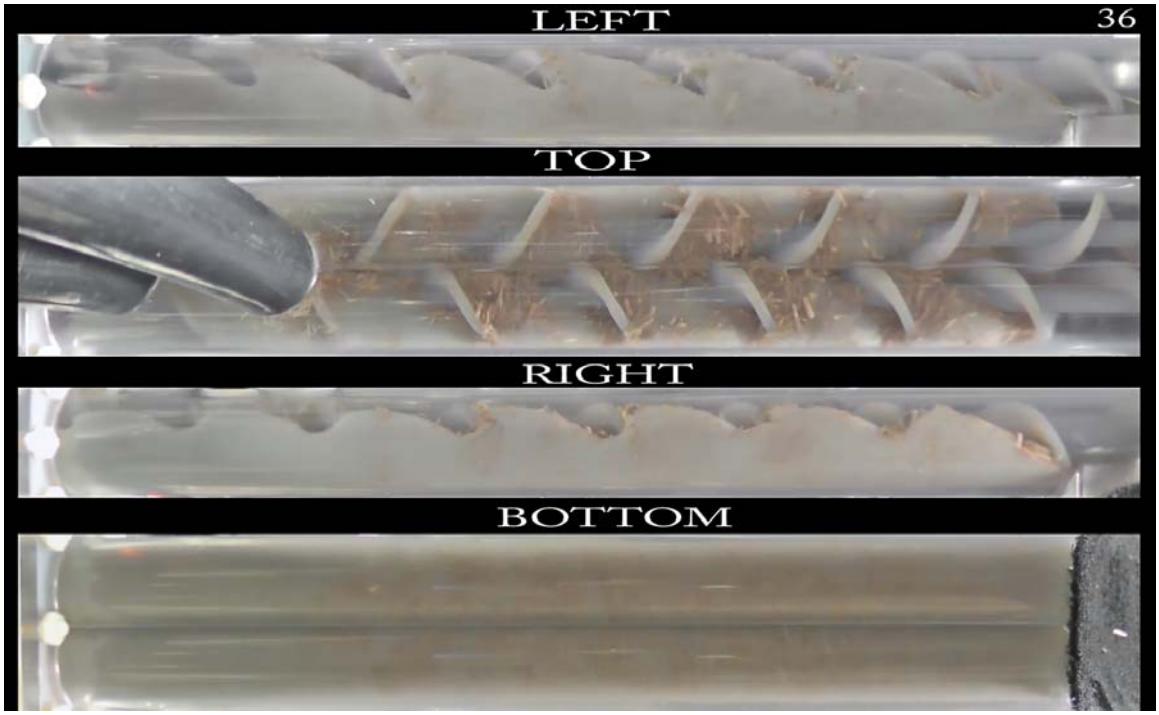

Figure F.36: Operating Condition 36.

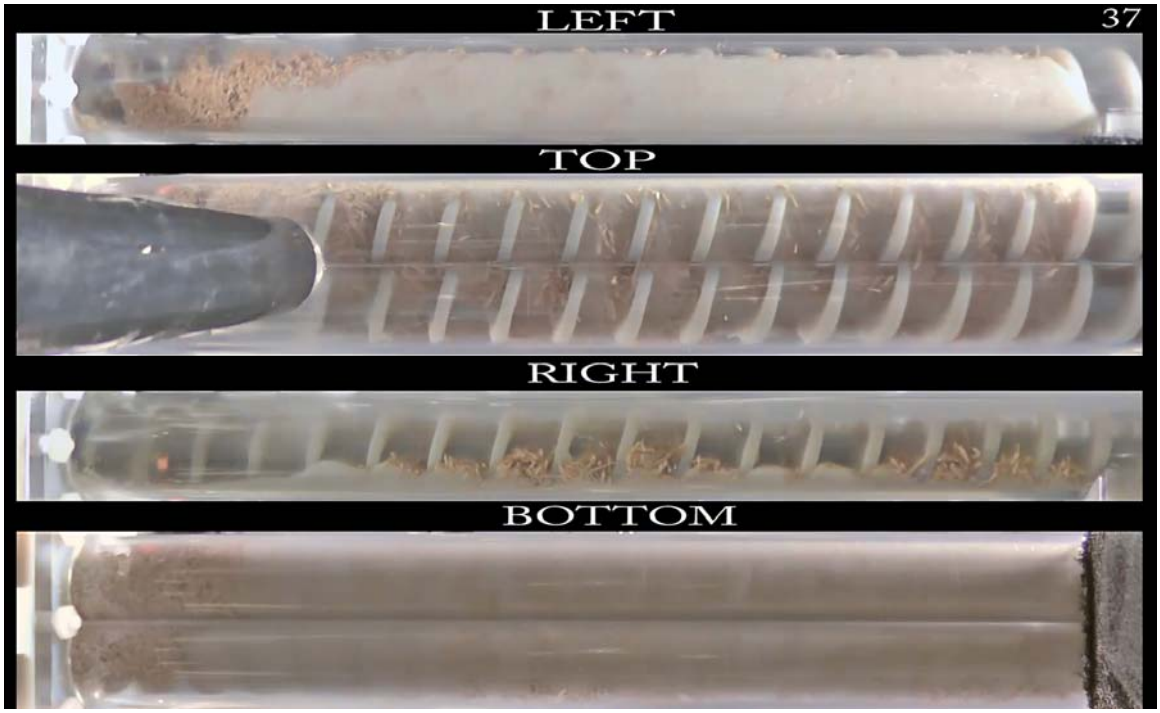

Figure F.37: Operating Condition 37.

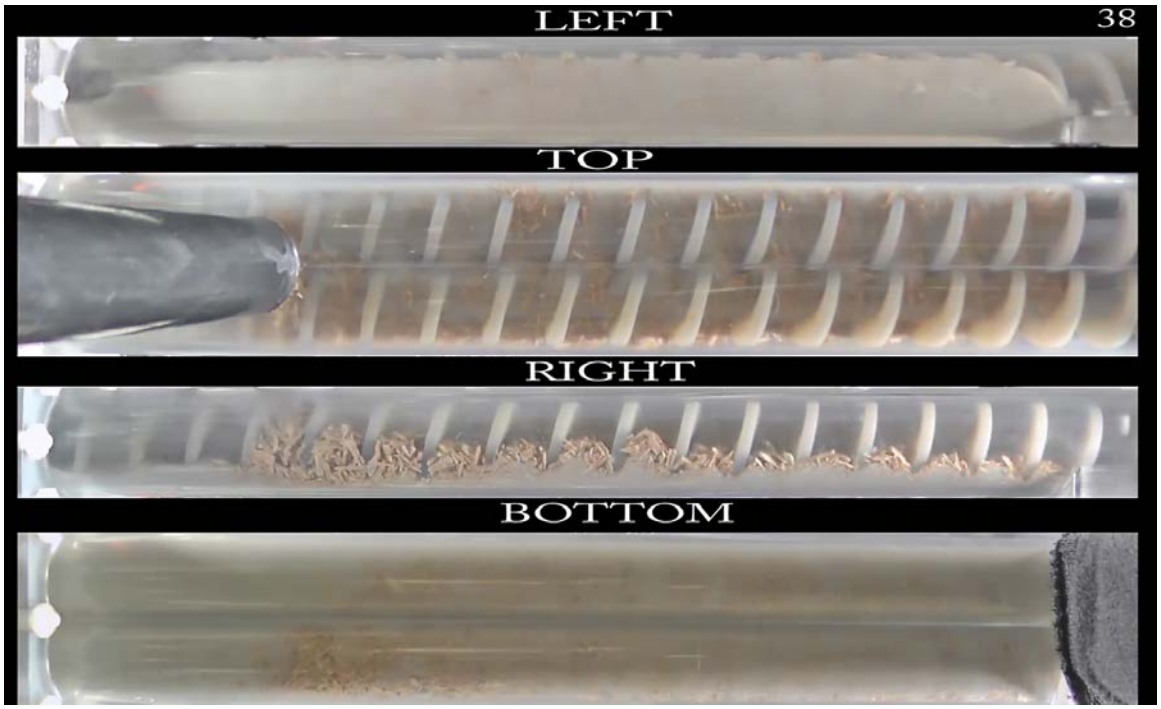

Figure F.38: Operating Condition 38.

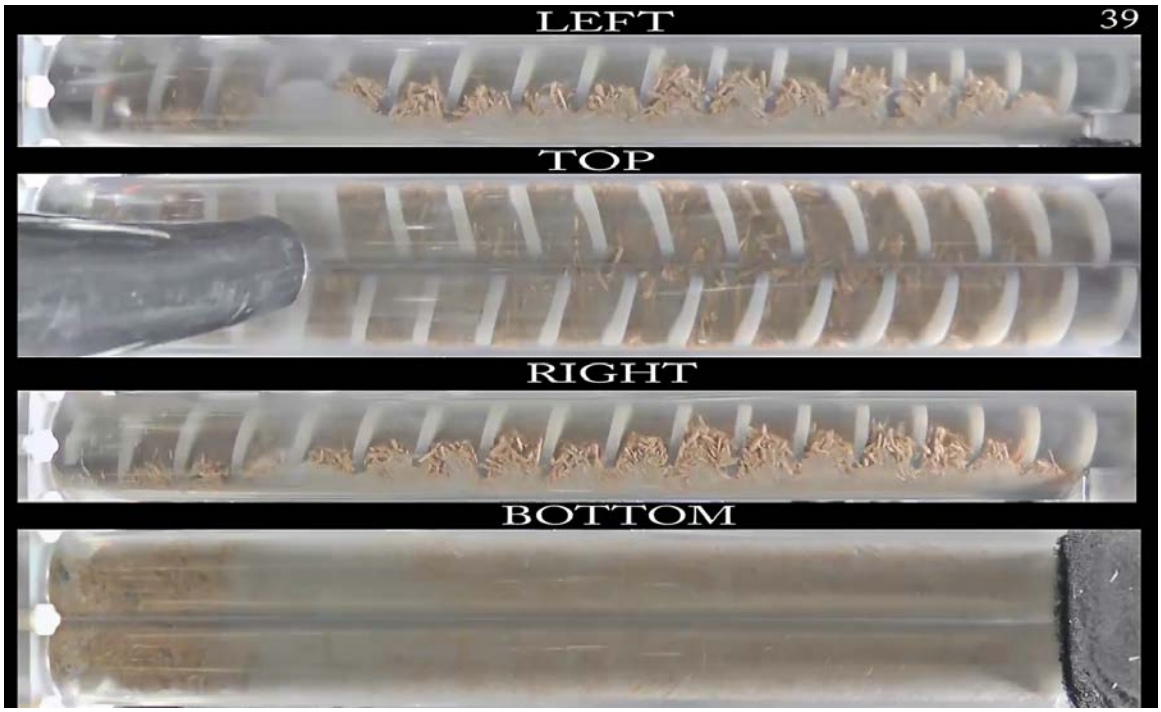

Figure F.39: Operating Condition 39.

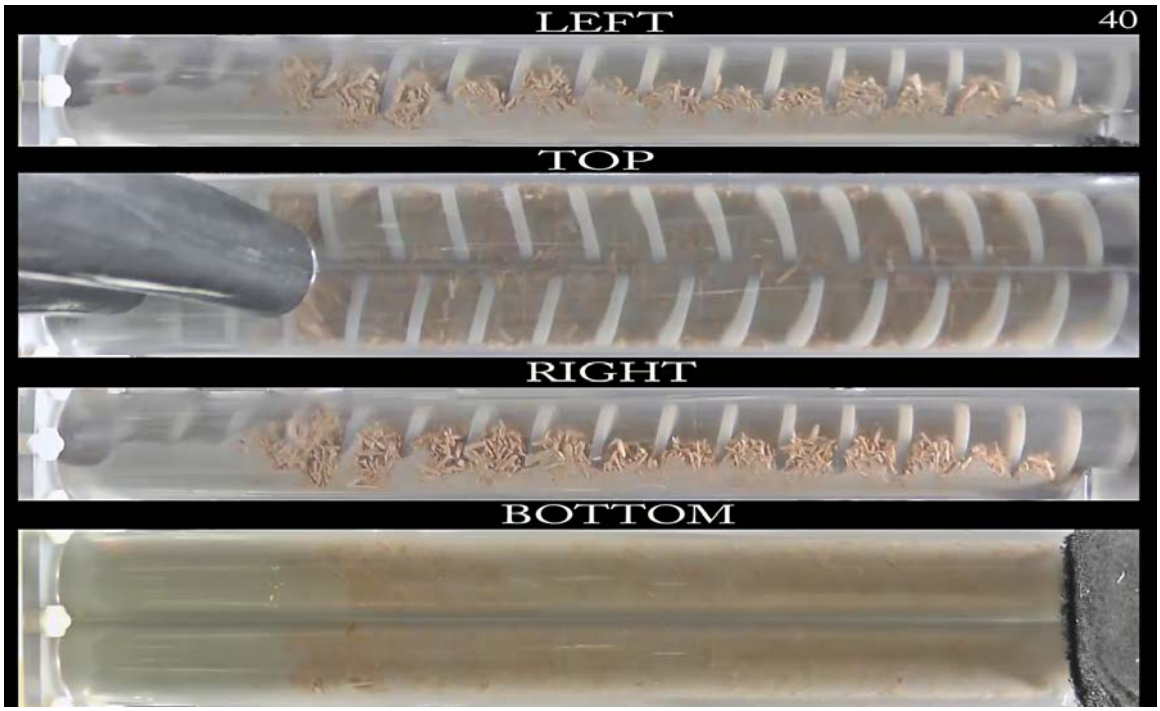

Figure F.40: Operating Condition 40.

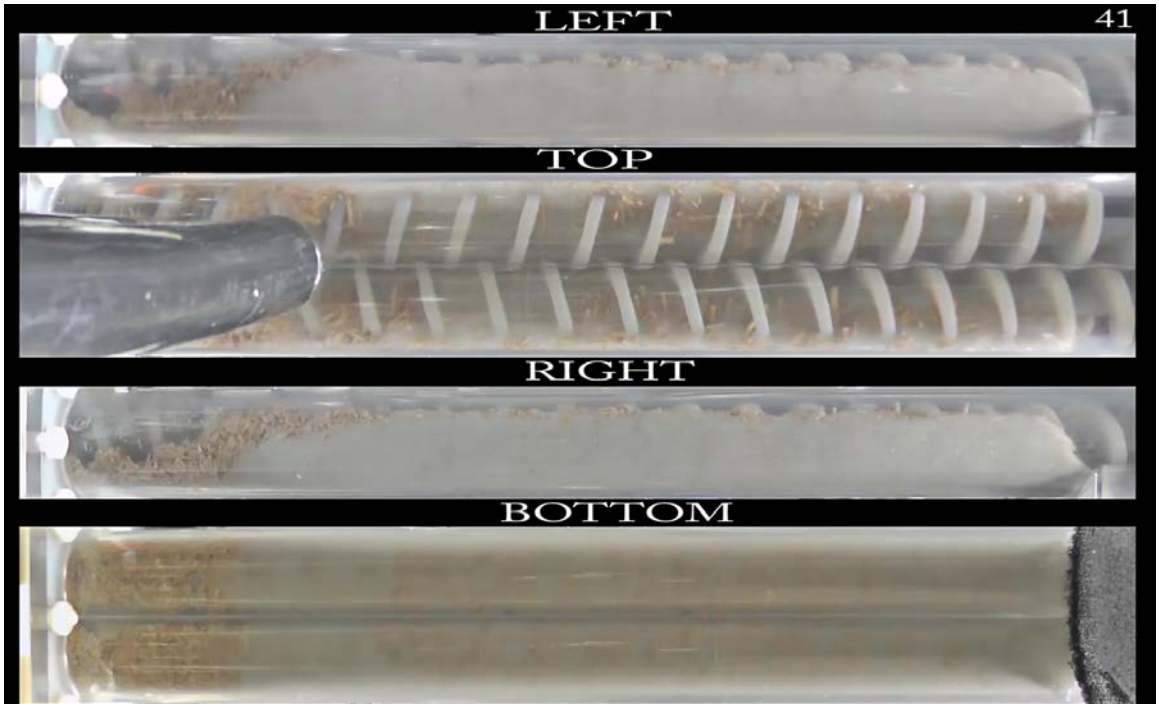

Figure F.41: Operating Condition 41.

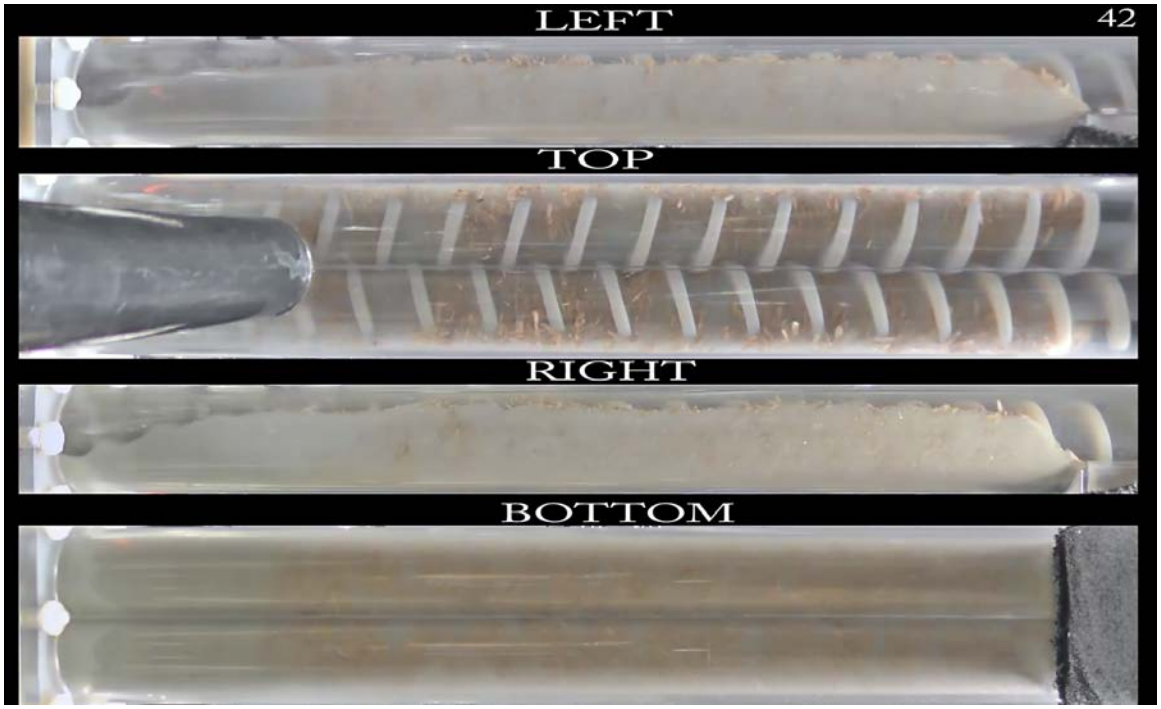

Figure F.42: Operating Condition 42.

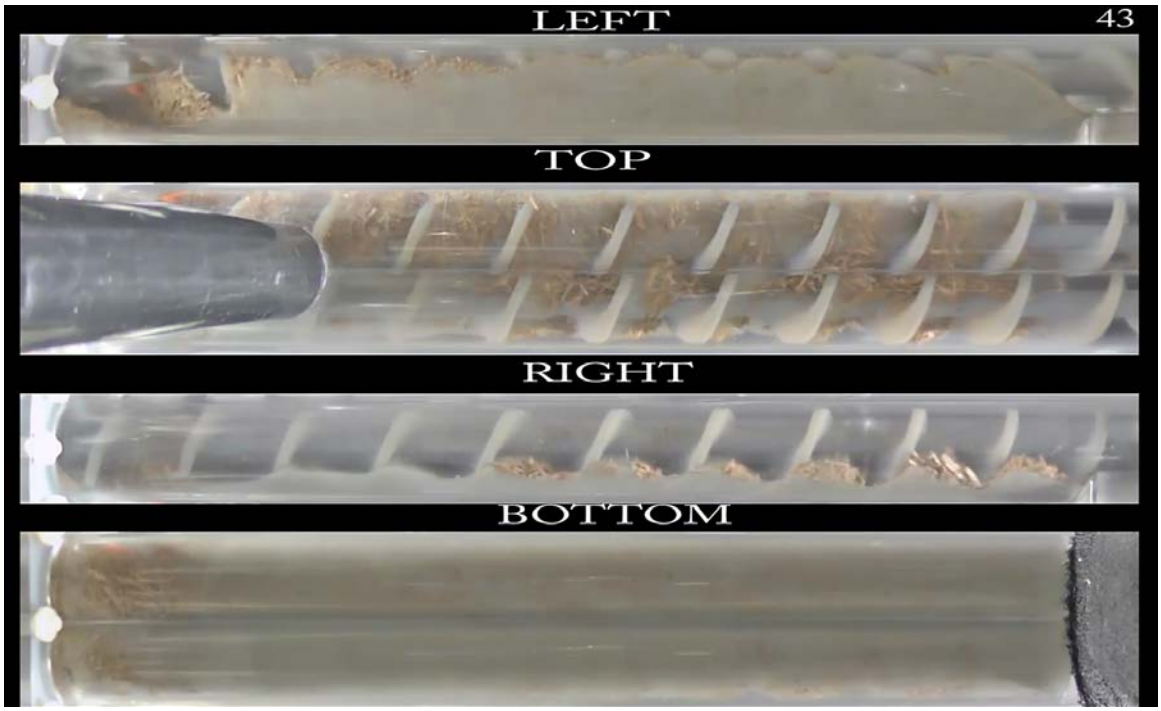

Figure F.43: Operating Condition 43.

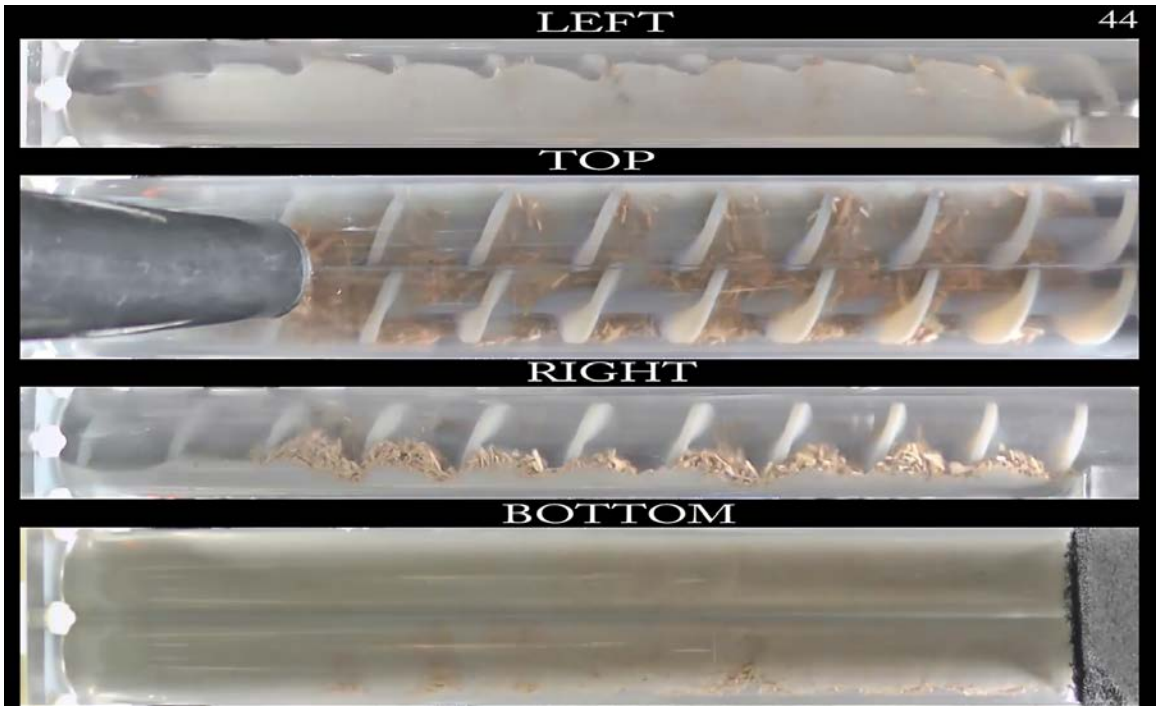

Figure F.44: Operating Condition 44.

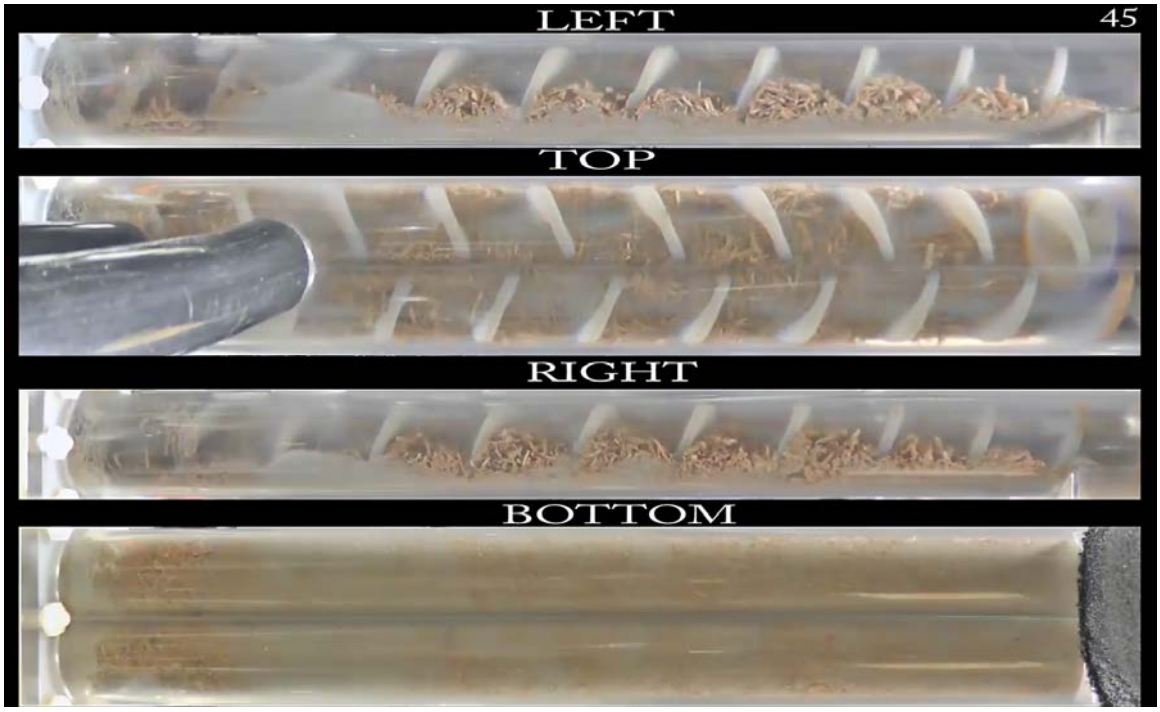

Figure F.45: Operating Condition 45.

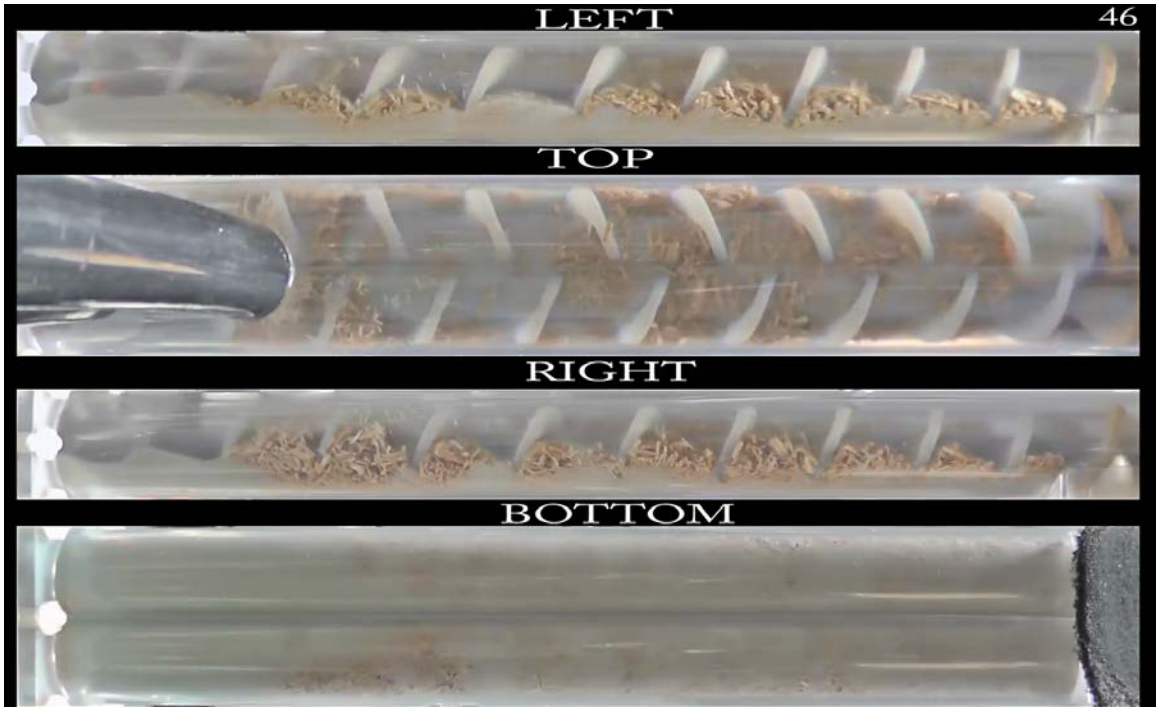

Figure F.46: Operating Condition 46.

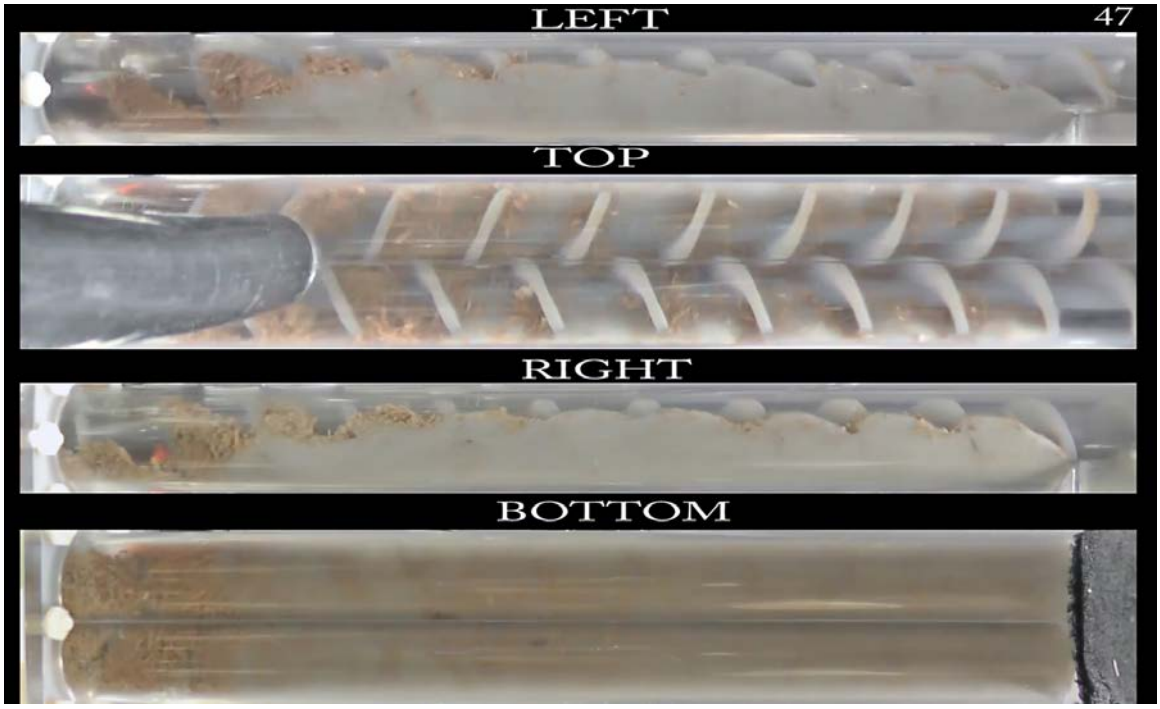

Figure F.47: Operating Condition 47.

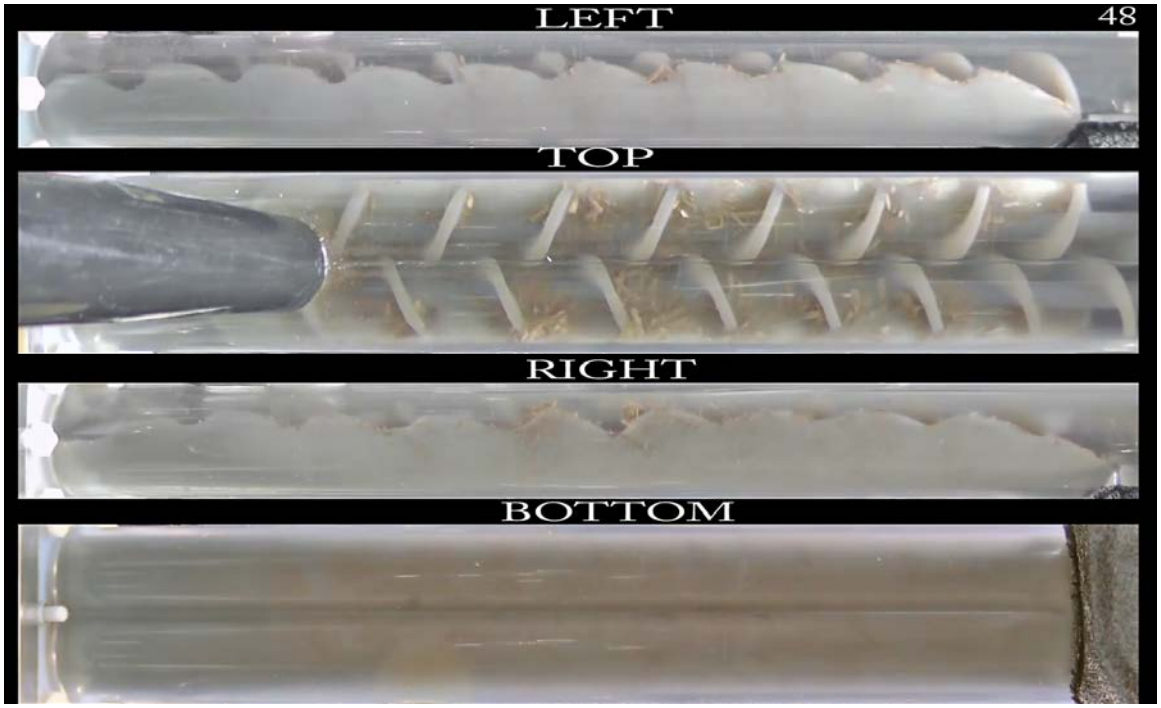

Figure F.48: Operating Condition 48.

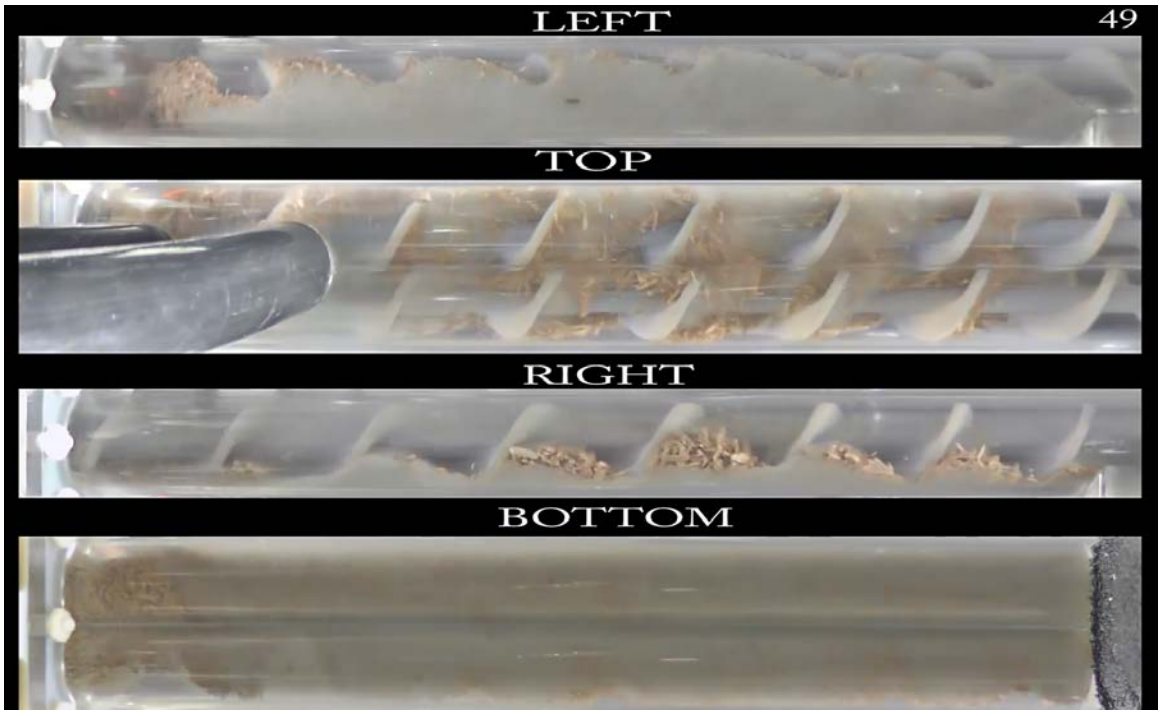

Figure F.49: Operating Condition 49.

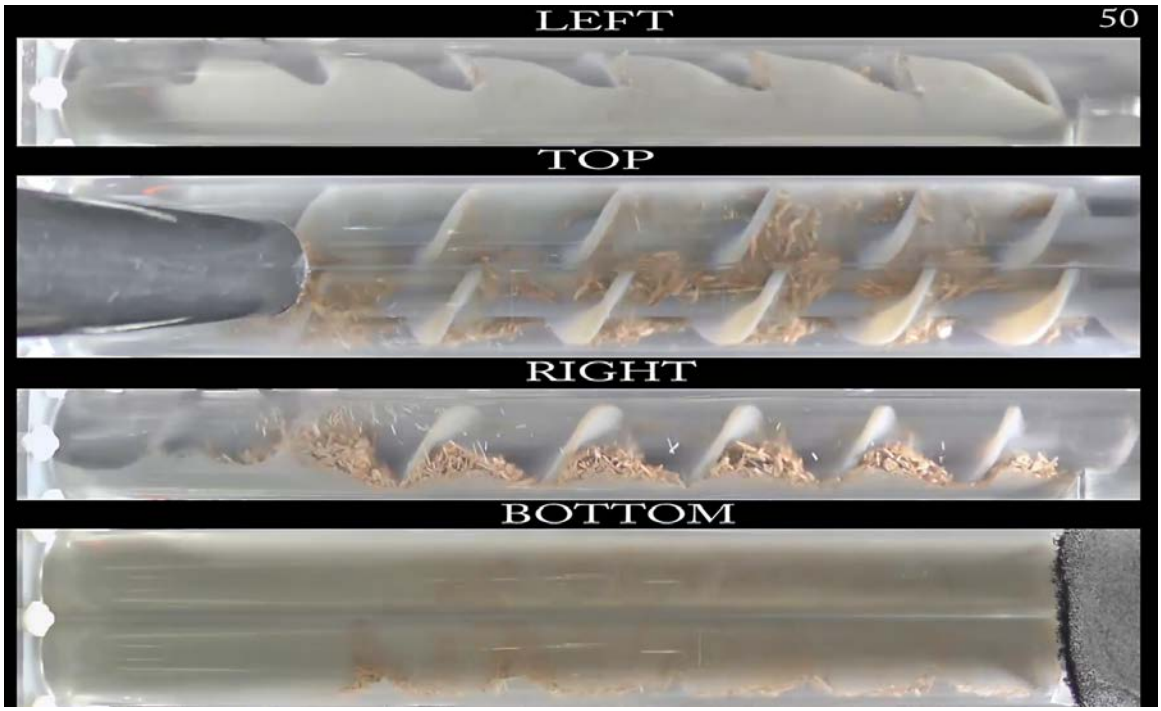

Figure F.50: Operating Condition 50.

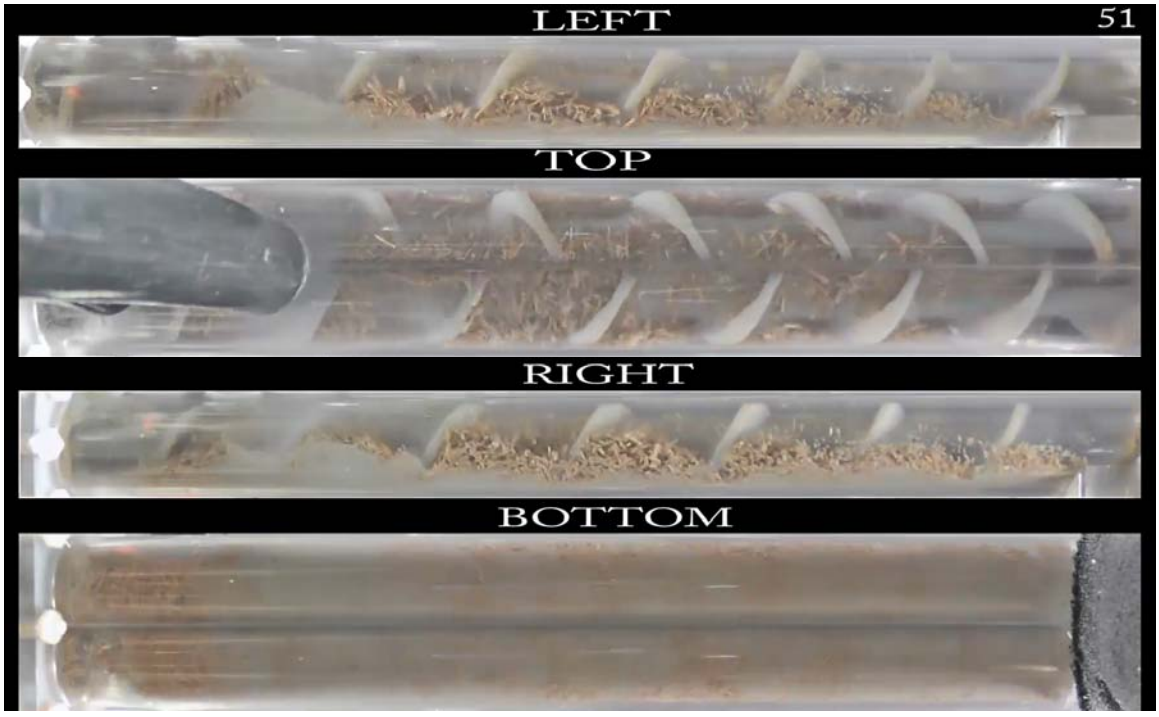

Figure F.51: Operating Condition 51.

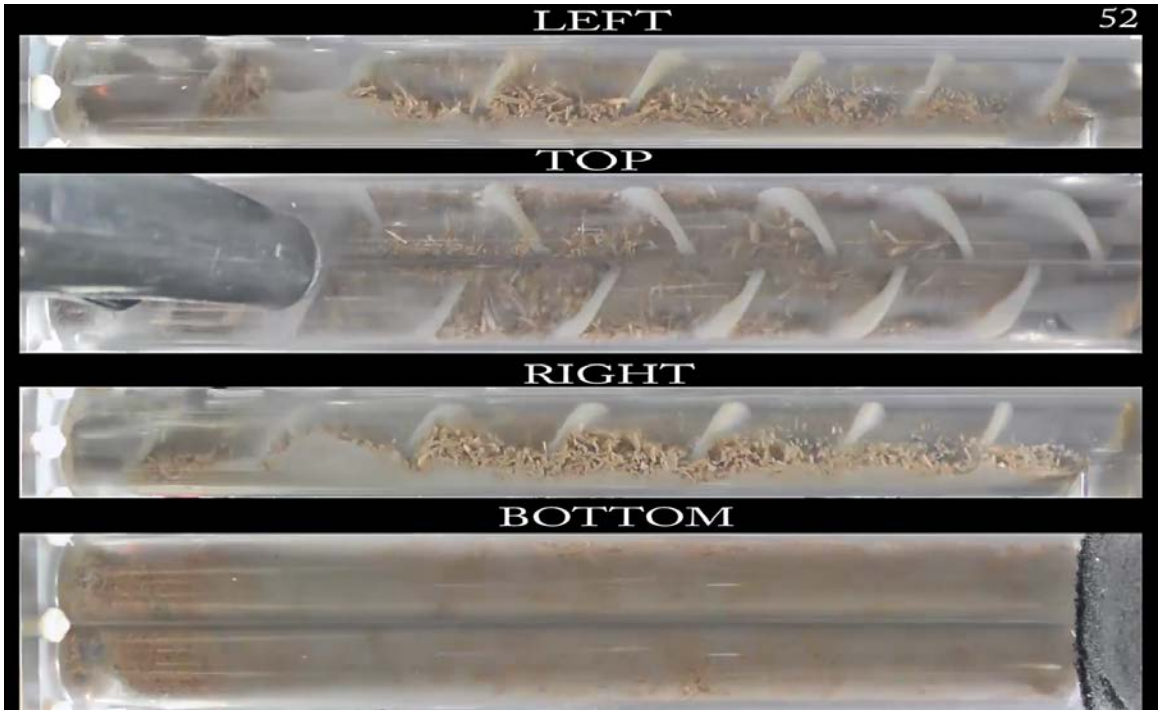

Figure F.52: Operating Condition 52.

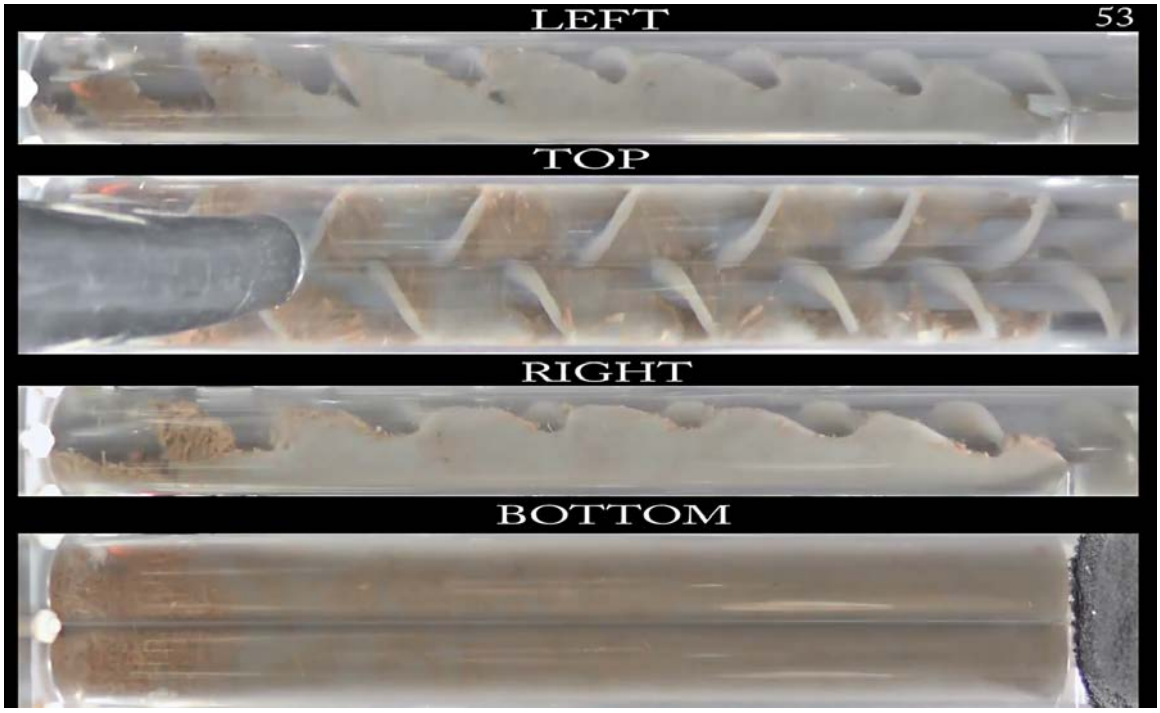

Figure F.53: Operating Condition 53.

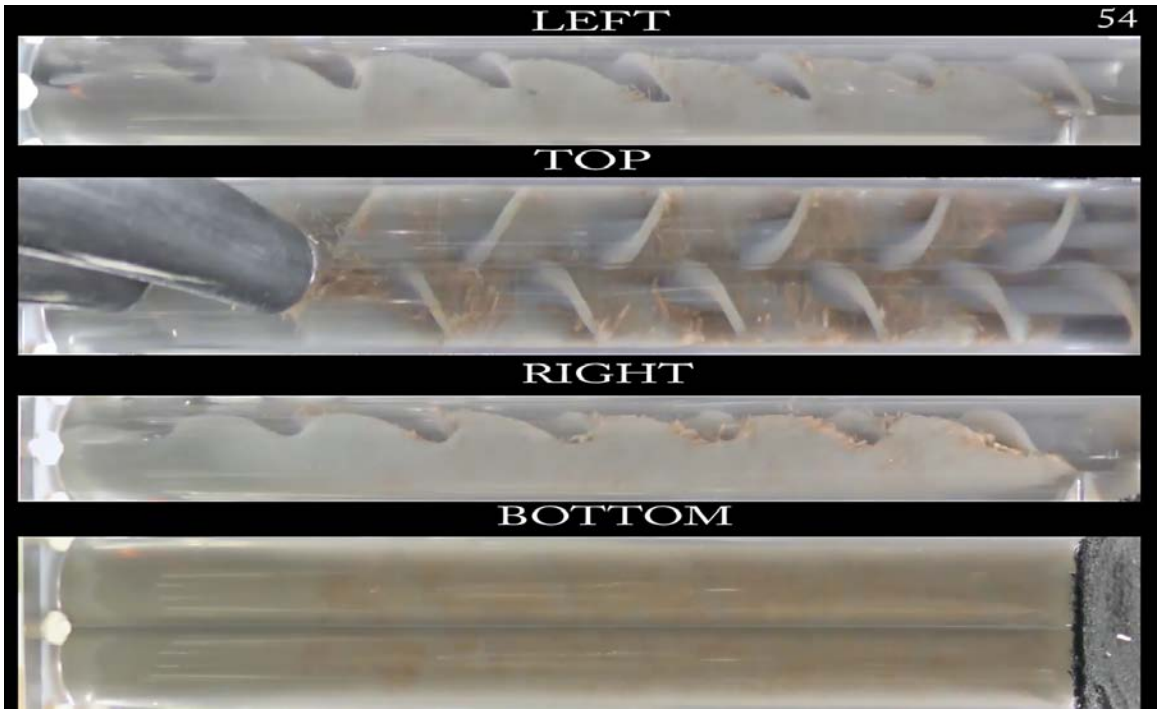

Figure F.54: Operating Condition 54.

F.2 Single Screw Mixer

Snapshots of the dynamic mixing process at steady state conditions that were captured using the optical visualization techniques for each of the single screw mixer's 18 operating conditions are shown in Figure F.1 through F.18. The details of each operating condition are shown in Table 3.3.

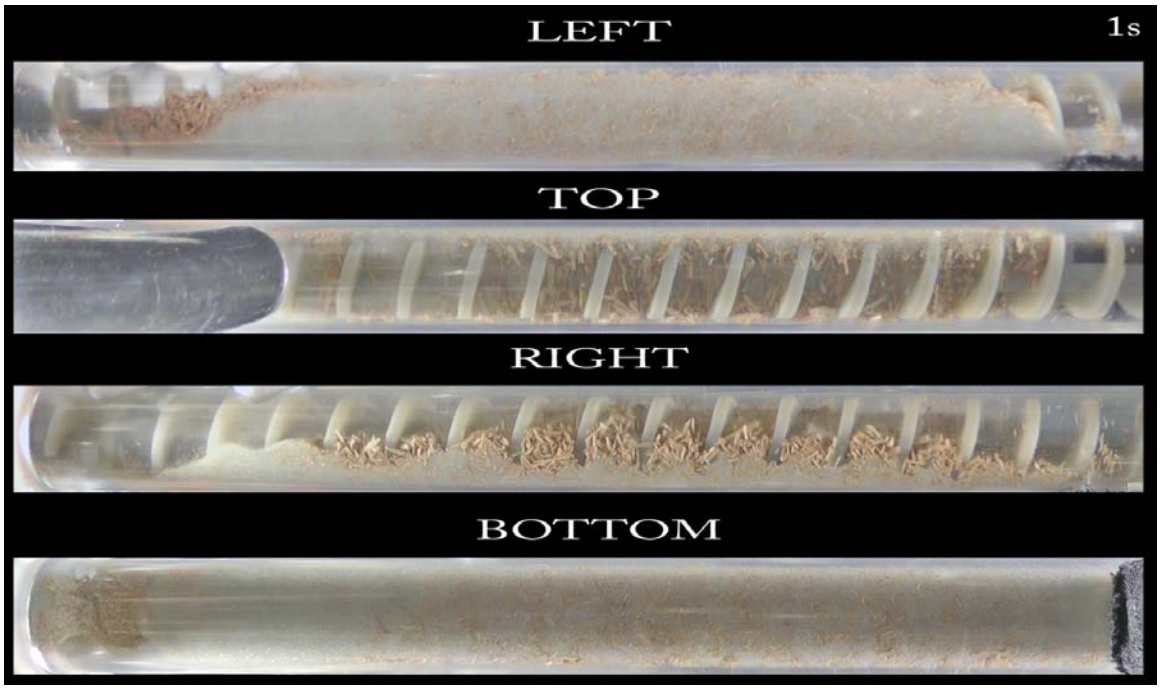

Figure F.55: Operating Condition 1s.

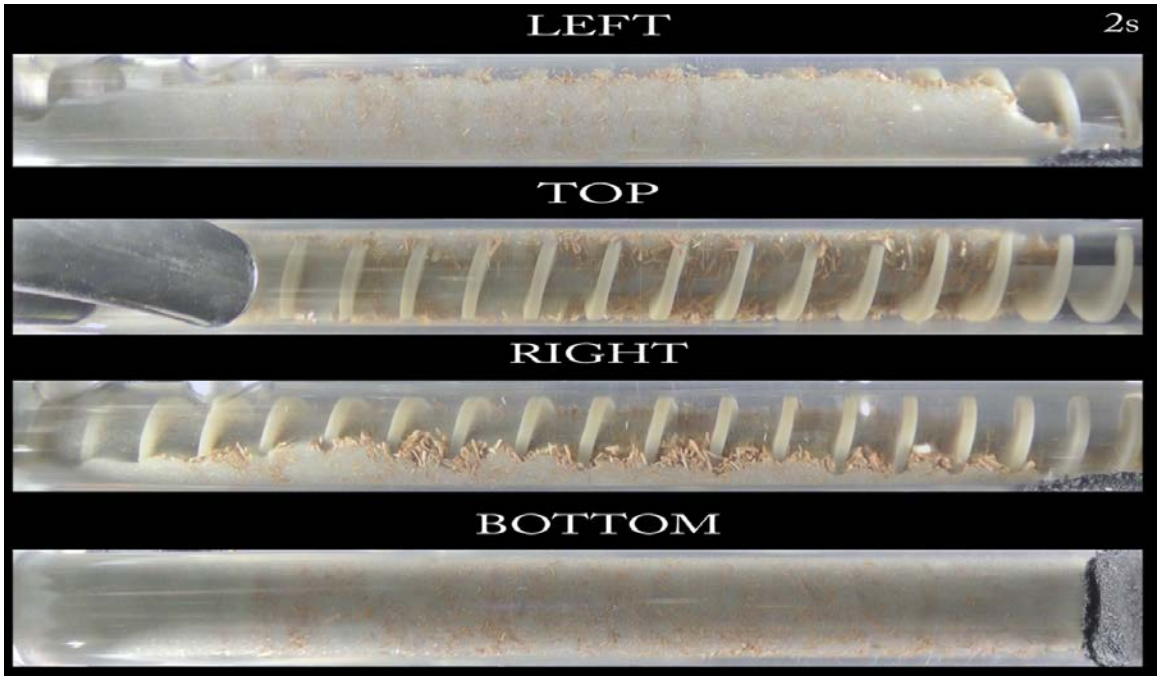

Figure F.56: Operating Condition 2s.

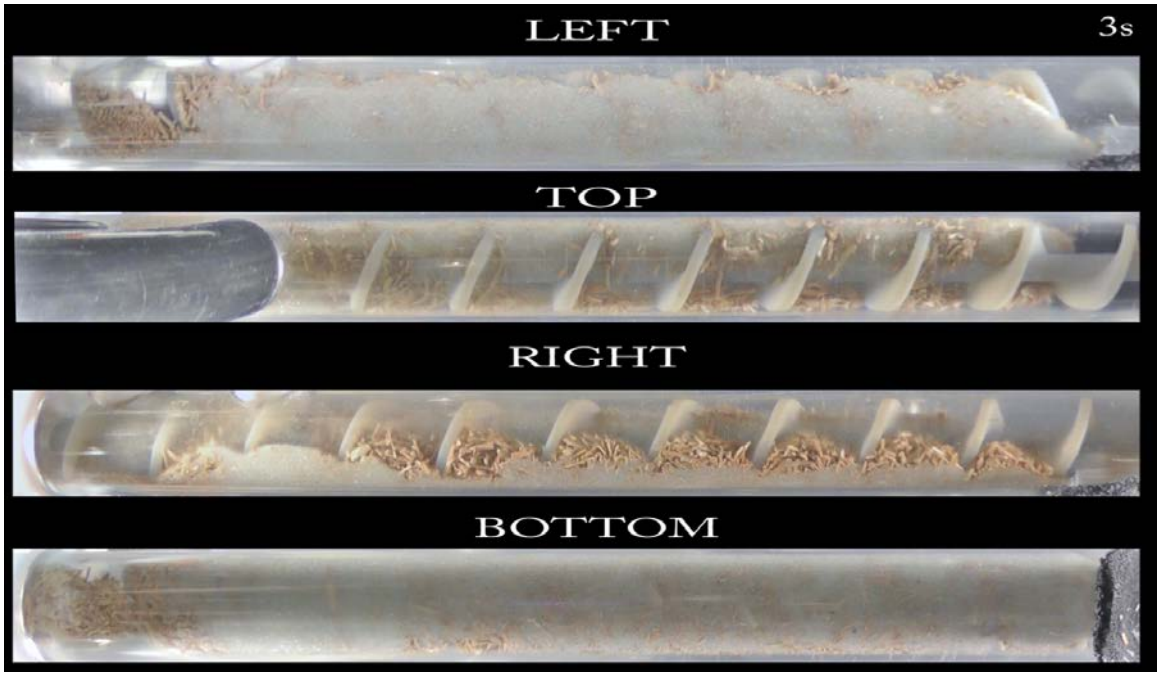

Figure F.57: Operating Condition 3s.

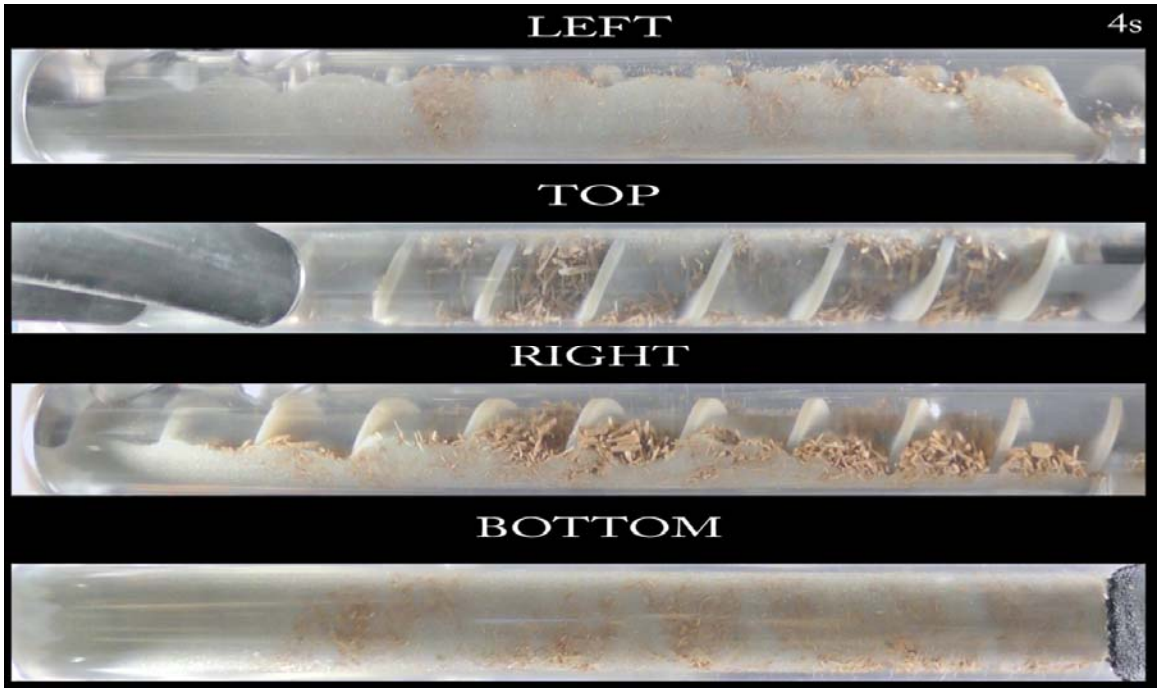

Figure F.58: Operating condition 4s.

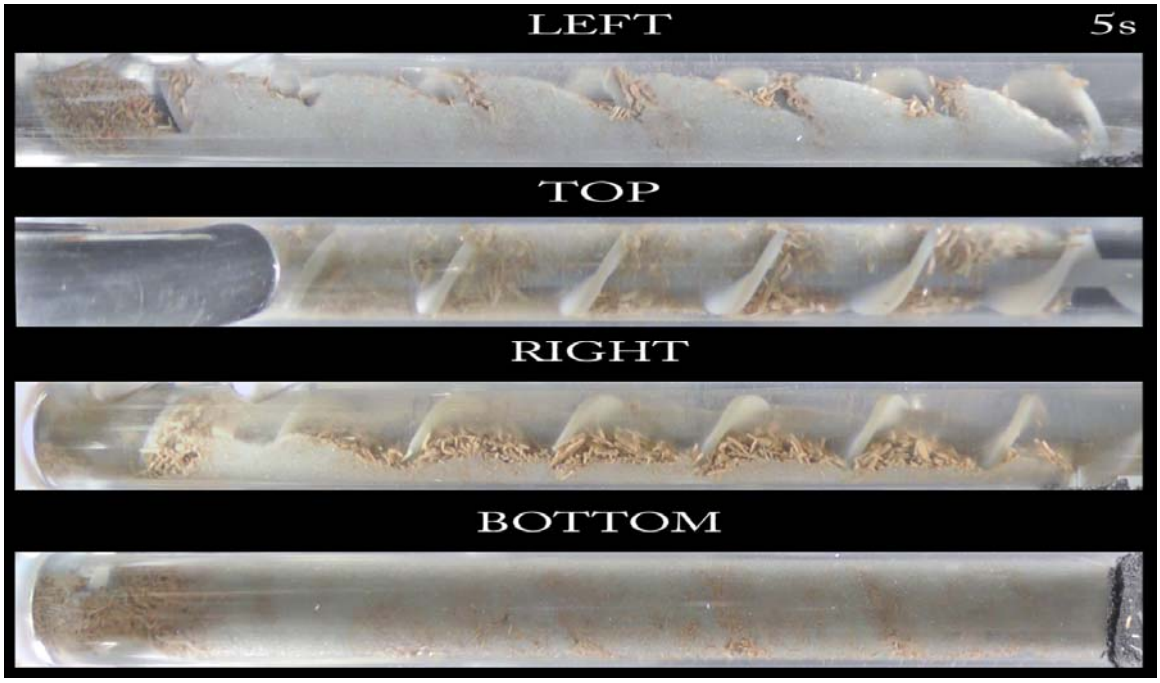

Figure F.59: Operating condition 5s.

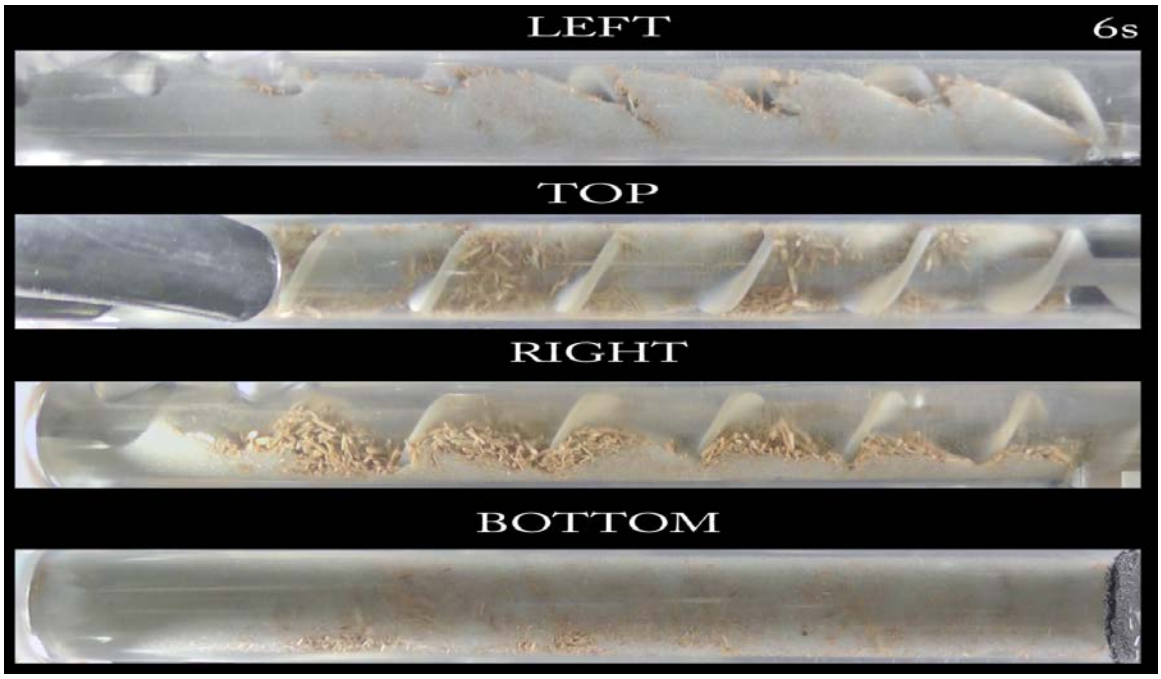

Figure F.60: Operating condition 6s.

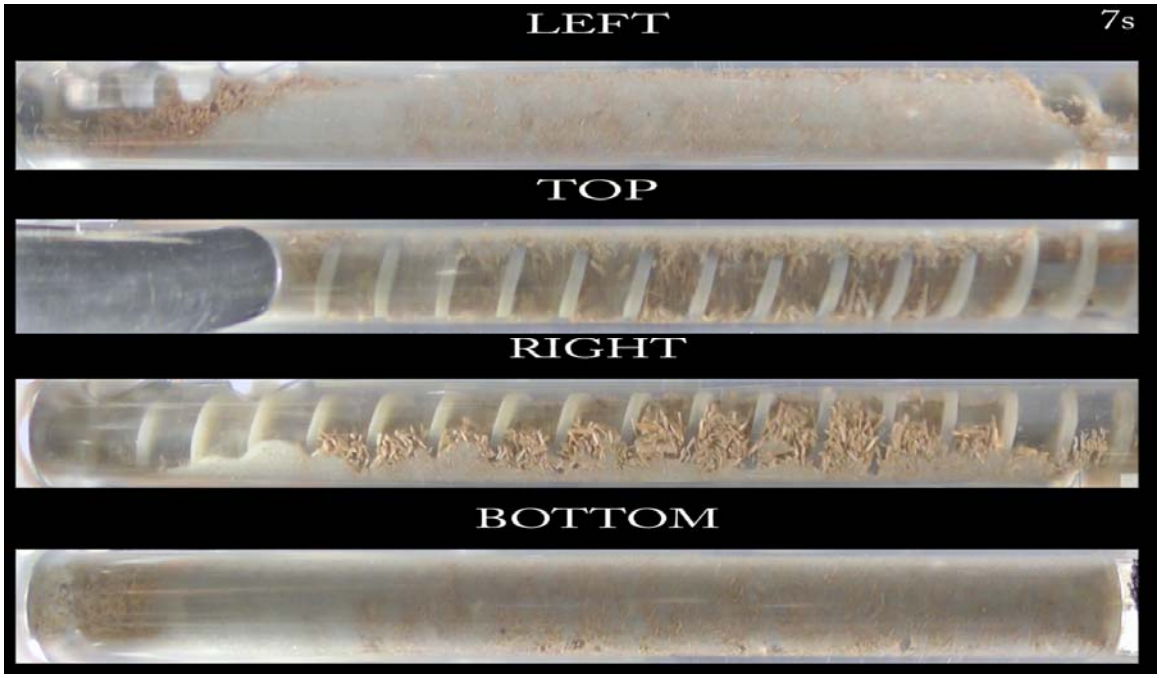

Figure F.61: Operating condition 7s.

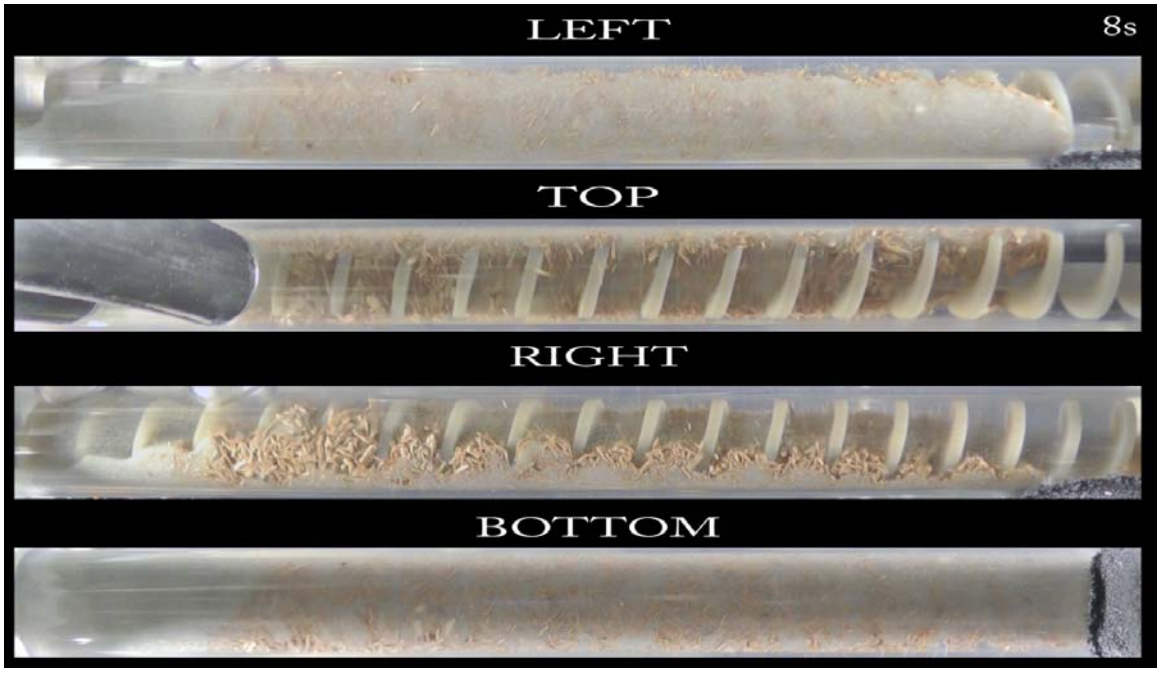

Figure F.62: Operating condition 8s.

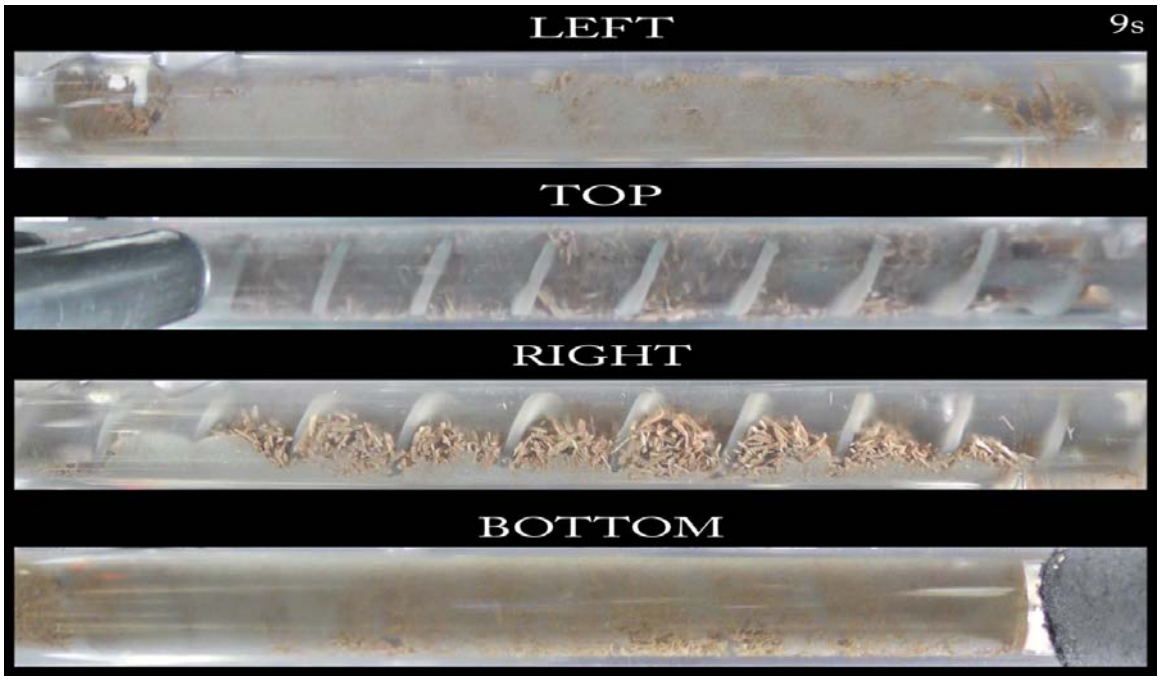

Figure F.63: Operating condition 9s.

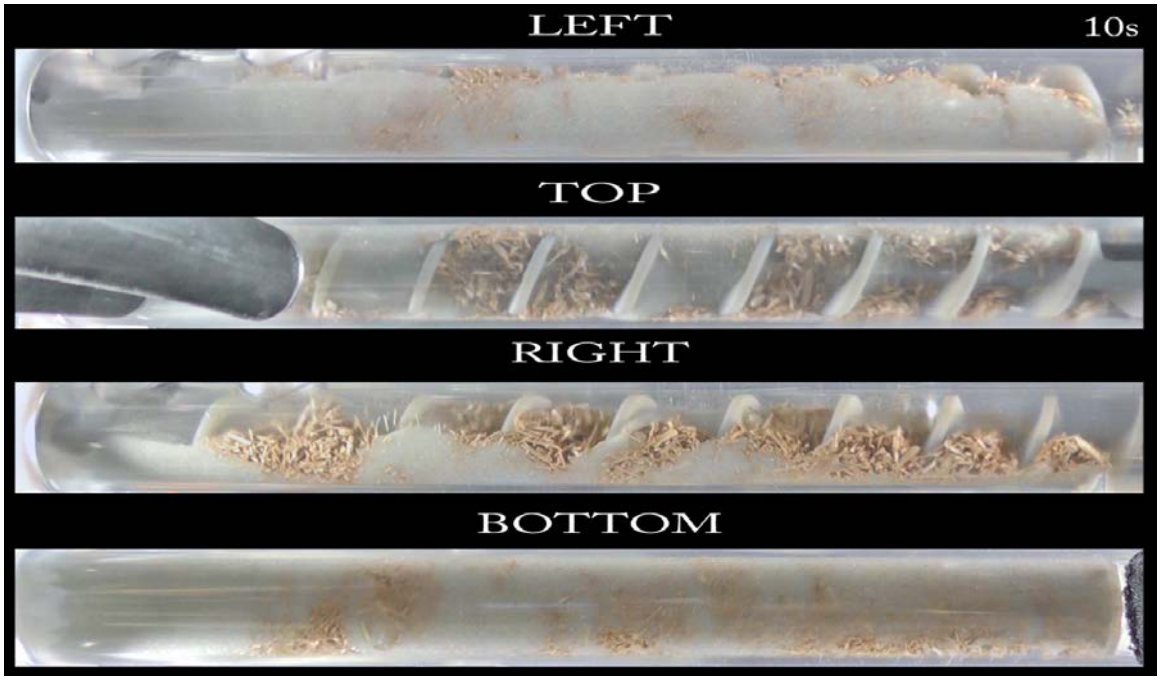

Figure F.64: Operating condition 10s.

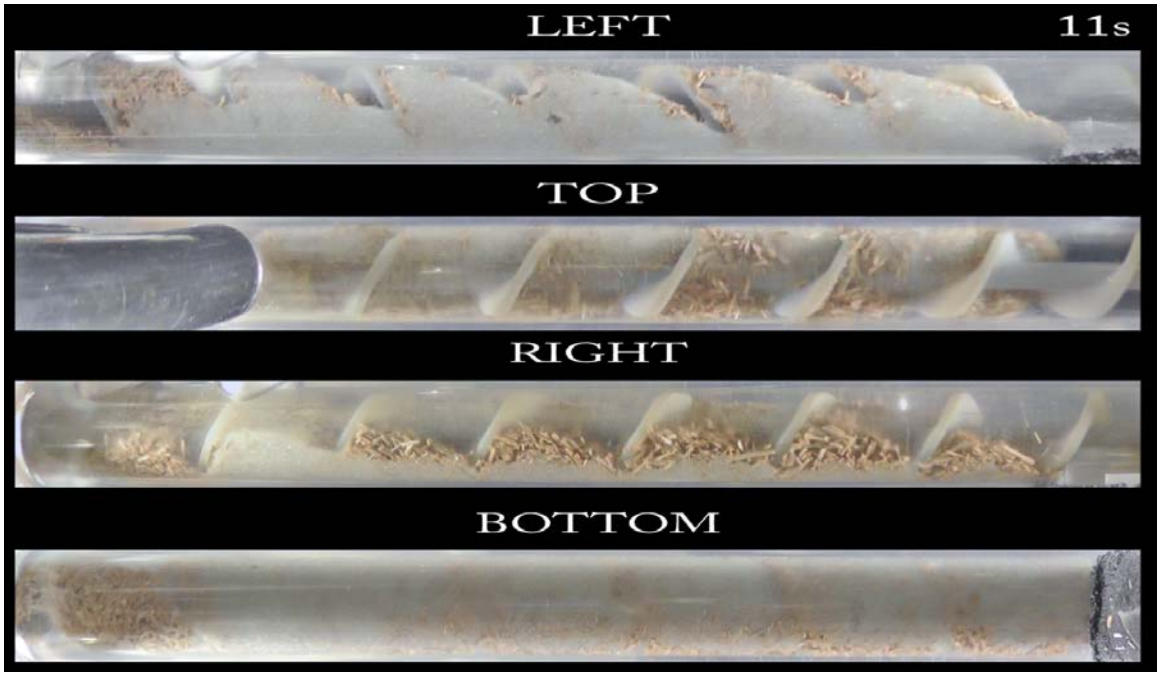

Figure F.65: Operating condition 11s.

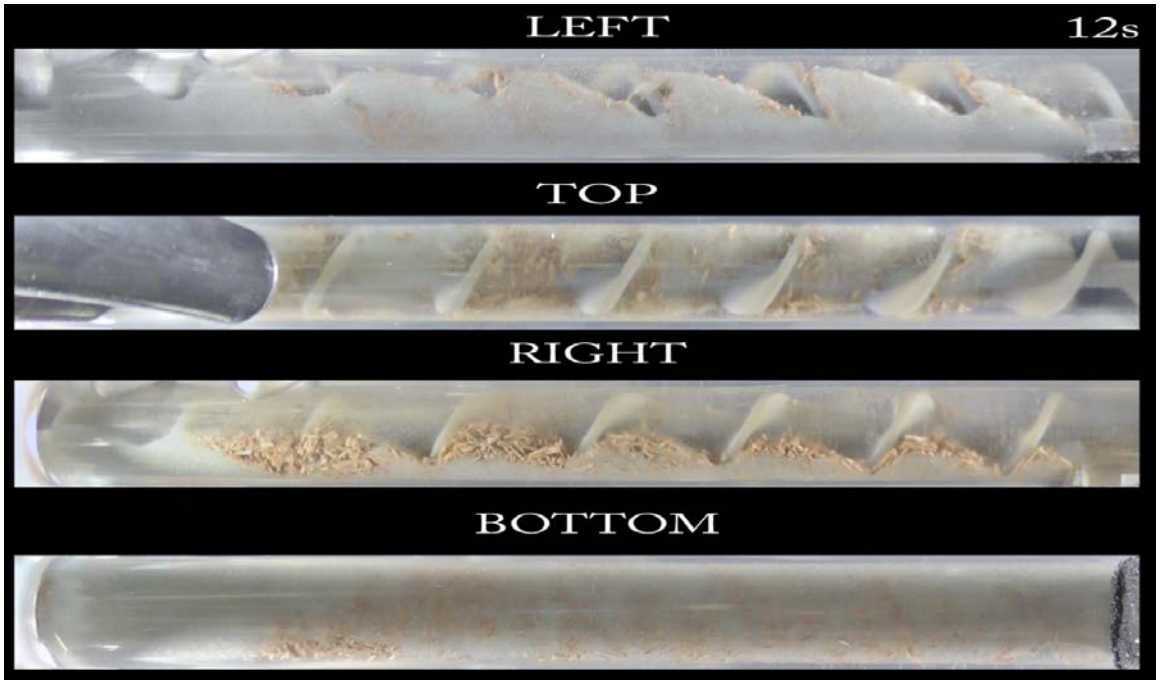

Figure F.66: Operating condition 12s.

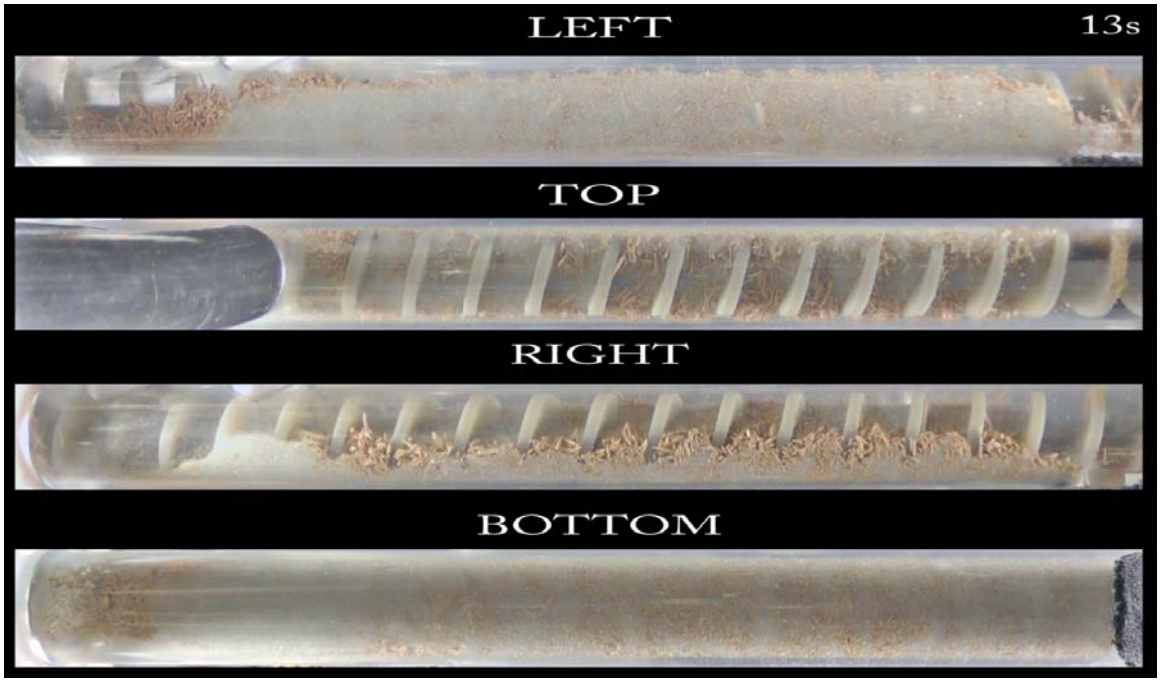

Figure F.67: Operating condition 13s.

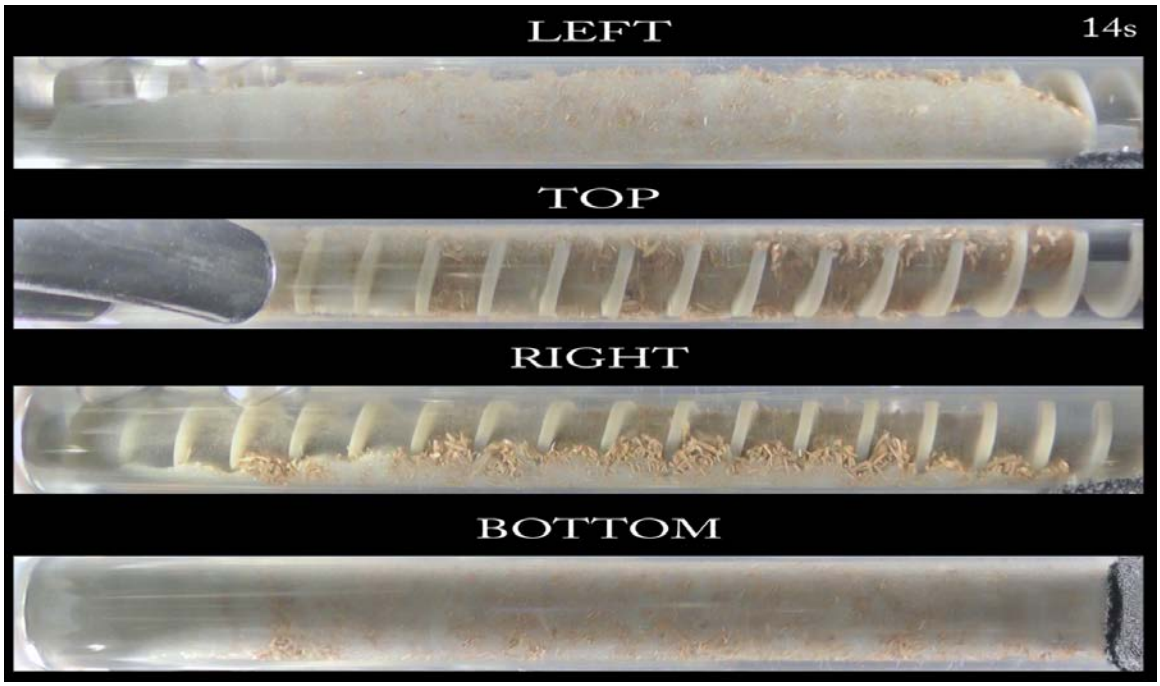

Figure F.68: Operating condition 14s.

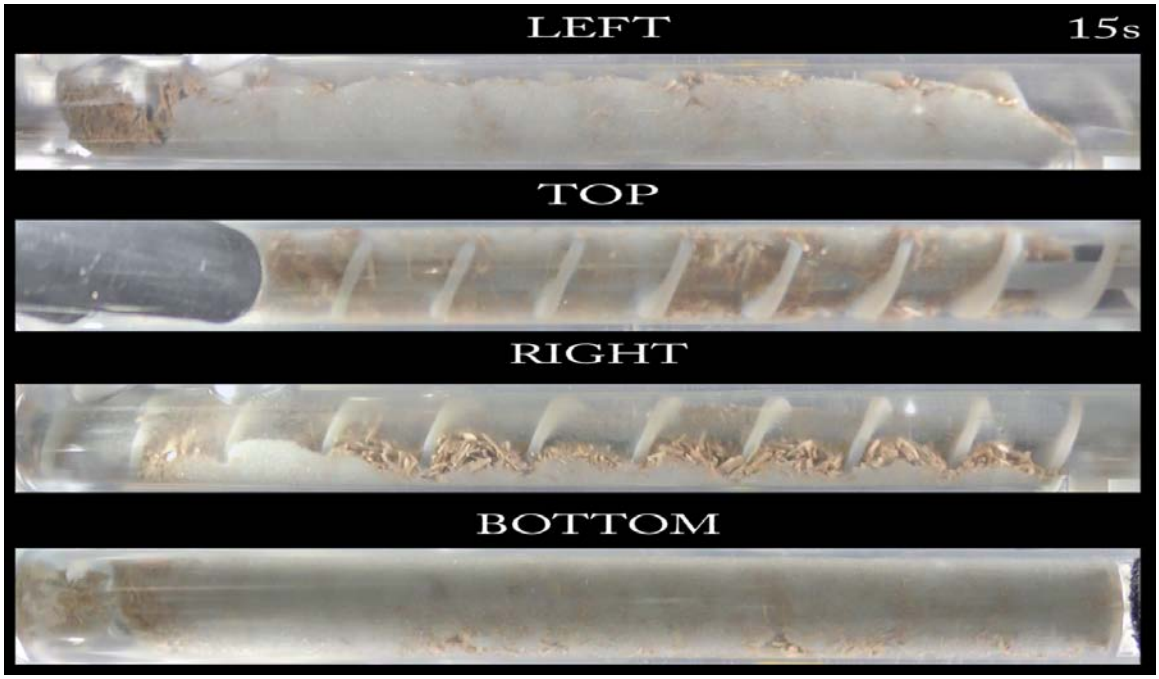

Figure F.69: Operating condition 15s.

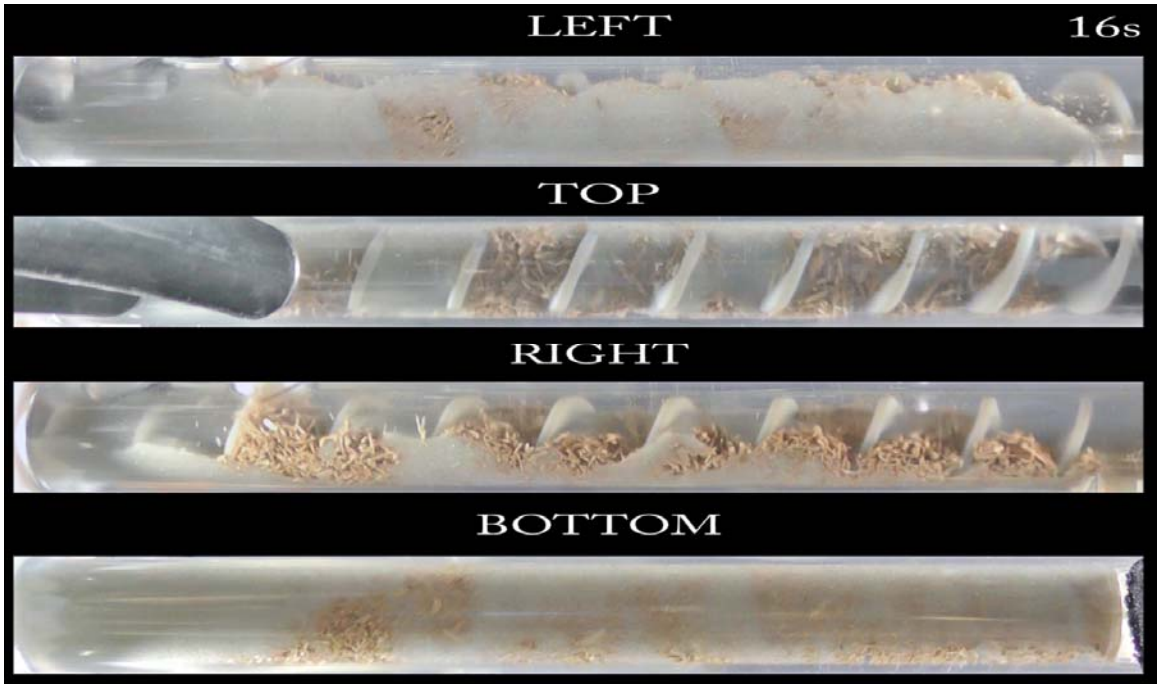

Figure F.70: Operating condition 16s.

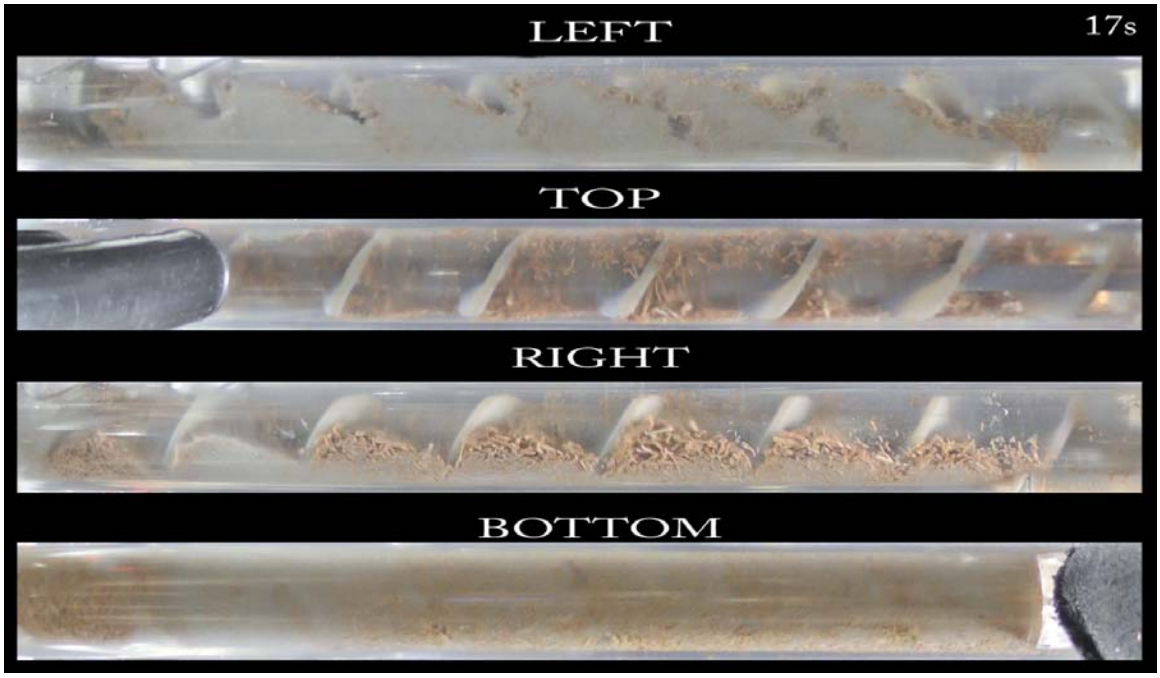

Figure F.71: Operating condition 17s.

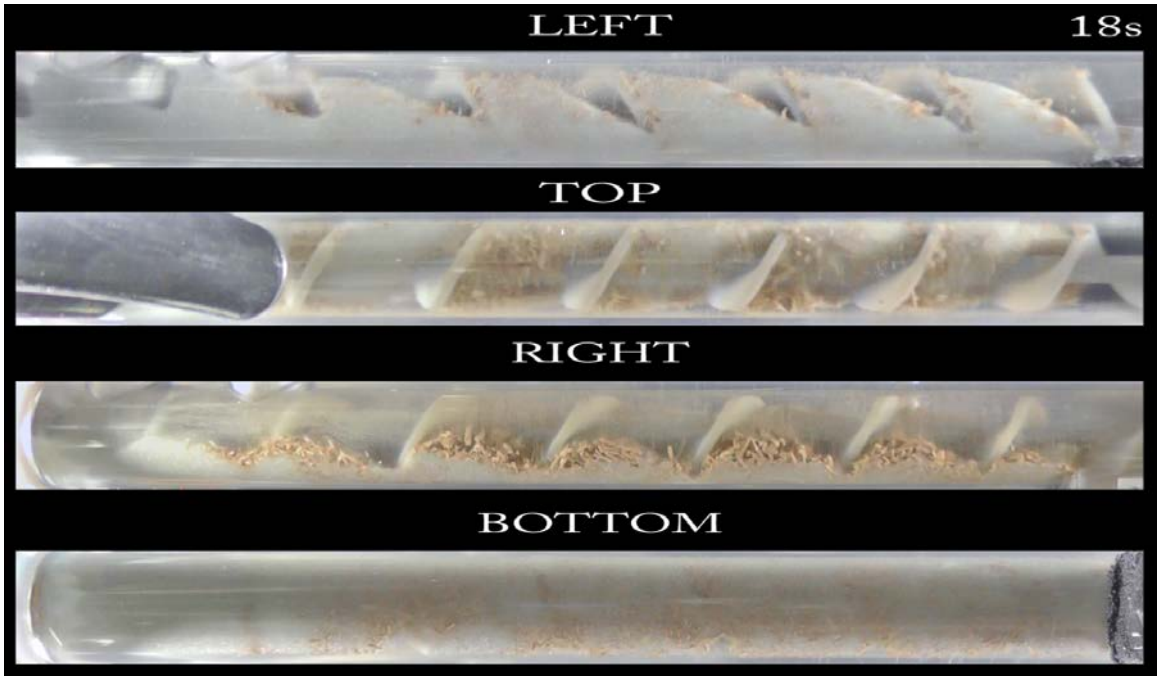

Figure F.72: Operating condition 18s.

APPENDIX G: COMPOSITION ANALYSIS

G.1 Composition Curve Calibration Data

Table G.1: Composition curve calibration data for mixtures of red oak and glass beads.

Sample	Glass Bead Mass [g]	Red Oak Mass [g]	Total Mass [g]	Glass Bead Mass Fraction [-]	Red Oak Mass Fraction [-]	Average True Density [kg m^{-3}]	Average True Density Uncertainty [kg m^{-3}]	Average True Density Uncertainty [%]
1	0.00	23.05	23.05	0.00	1.00	1353	3.8	0.3
2	2.51	22.61	25.12	0.10	0.90	1422	3.9	0.3
3	4.65	18.63	23.29	0.20	0.80	1489	3.5	0.2
4	7.80	18.26	26.06	0.30	0.70	1575	3.7	0.2
5	11.48	17.23	28.70	0.40	0.60	1668	3.9	0.2
6	13.15	13.16	26.31	0.50	0.50	1789	3.3	0.2
7	18.36	12.21	30.58	0.60	0.40	1894	3.6	0.2
8	26.52	11.36	37.89	0.70	0.30	2014	4.2	0.2
9	32.56	8.14	40.70	0.80	0.20	2185	4.2	0.2
10	59.20	6.58	65.79	0.90	0.10	2344	6.3	0.3
11	64.43	0.00	64.43	1.00	0.00	2508	5.7	0.2

G.2 Screw Mixer

G.2.1 Full Study

Table G.2: Screw Mixer Composition Analysis Data.

Operating Condition	Obser.	Outlet Port	Mass m [g]	True Volume V [cm^3]	True Density ρ [$g\ cm^{-3}$]	Comp. x [-]	Weighted Comp. x [-]	Comp. Variance s^2 [-]	Comp. Variance Uncertainty U_s^2 [-]	Comp. Variance Uncertainty Percentage $U_s^2\ s^{-2}$ [%]
1	1	1	73.8433	30.2470	2.4413	0.9616	0.9195	0.001065	0.000018	1.7%
		2	82.0752	35.0818	2.3395	0.9013				
		3	56.7063	24.2962	2.3340	0.8979				
		4	25.9155	11.0540	2.3444	0.9043				
	2	1	60.0396	24.5593	2.4447	0.9635	0.9285	0.001588	0.000021	1.3%
		2	63.9925	26.7936	2.3883	0.9305				
		3	41.5555	18.1632	2.2879	0.8696				
		4	19.5620	8.1377	2.4039	0.9397				
	3	1	36.0087	14.5464	2.4754	0.9812	0.9391	0.002038	0.000024	1.2%
		2	38.0040	15.7359	2.4151	0.9463				
		3	26.2423	11.4180	2.2983	0.8761				
		4	12.0412	5.0521	2.3834	0.9276				
2	1	1	85.7952	35.4299	2.4215	0.9501	0.9146	0.001287	0.000019	1.5%
		2	89.8275	38.0670	2.3597	0.9135				
		3	59.0710	25.8901	2.2816	0.8657				
		4	23.8215	10.1051	2.3574	0.9121				
	2	1	64.1429	26.3028	2.4386	0.9600	0.9230	0.000909	0.000017	1.9%
		2	68.5622	29.1423	2.3527	0.9092				
		3	46.2302	19.8318	2.3311	0.8962				
		4	20.4916	8.6825	2.3601	0.9137				
	3	1	69.6515	28.5684	2.4381	0.9597	0.9241	0.001086	0.000018	1.6%
		2	75.4293	31.7330	2.3770	0.9238				
		3	49.2371	21.2798	2.3138	0.8856				
		4	21.4733	9.1995	2.3342	0.8980				
3	1	1	39.8541	16.3196	2.4421	0.9620	0.9382	0.000196	0.000007	3.4%
		2	87.2007	36.5043	2.3888	0.9308				
		3	88.6269	37.1241	2.3873	0.9299				
		4	40.7648	16.8544	2.4186	0.9484				
	2	1	36.5593	14.9568	2.4443	0.9633	0.9332	0.000416	0.000010	2.4%
		2	73.5907	31.0240	2.3721	0.9209				
		3	78.0578	32.8892	2.3734	0.9216				
		4	34.7785	14.3247	2.4279	0.9538				
	3	1	41.4398	16.9884	2.4393	0.9604	0.9243	0.000499	0.000011	2.1%
		2	84.2912	35.8229	2.3530	0.9094				
		3	88.4561	37.4822	2.3599	0.9136				
		4	39.9836	16.6083	2.4074	0.9418				
4	1	1	45.3082	18.8089	2.4089	0.9427	0.9243	0.000125	0.000005	4.4%
		2	97.1373	40.9053	2.3747	0.9224				
		3	98.9358	41.8879	2.3619	0.9148				
		4	40.8666	17.1038	2.3893	0.9311				
	2	1	39.9425	16.4148	2.4333	0.9569	0.9319	0.000295	0.000008	2.9%
		2	81.8735	34.3465	2.3838	0.9278				
		3	83.7809	35.4091	2.3661	0.9173				
		4	35.3067	14.6027	2.4178	0.9479				
	3	1	44.2512	18.2635	2.4229	0.9509	0.9266	0.000295	0.000008	2.9%
		2	91.8601	38.6873	2.3744	0.9223				
		3	93.0228	39.4640	2.3572	0.9119				
		4	40.2523	16.6974	2.4107	0.9437				

Table G.2: Continued.

Operating Condition	Obser.	Outlet Port	Mass m [g]	True Volume V [cm^3]	True Density ρ [$g\ cm^{-3}$]	Comp. x [-]	Weighted Comp. x [-]	Comp. Variance s^2 [-]	Comp. Variance Uncertainty U_s^2 [-]	Comp. Variance Uncertainty Percentage $U_s^2\ s^{-2}$ [%]
5	1	1	44.1690	18.3451	2.4077	0.9420	0.9250	0.000489	0.000011	2.3%
		2	40.5785	17.3416	2.3400	0.9015				
		3	38.5328	16.3860	2.3516	0.9086				
		4	43.8733	18.1953	2.4112	0.9440				
	2	1	52.6654	21.8811	2.4069	0.9415	0.9255	0.000441	0.000011	2.5%
		2	47.5774	20.3630	2.3365	0.8994				
		3	44.7563	18.9484	2.3620	0.9148				
		4	52.6357	21.8600	2.4079	0.9421				
	3	1	51.6986	21.2691	2.4307	0.9554	0.9281	0.000582	0.000012	2.1%
		2	46.0677	19.5844	2.3523	0.9090				
		3	47.6281	20.3055	2.3456	0.9049				
		4	54.0098	22.4827	2.4023	0.9388				
6	1	1	63.6806	26.5921	2.3947	0.9343	0.9193	0.000396	0.000010	2.6%
		2	58.8041	25.2652	2.3275	0.8940				
		3	58.0303	24.6392	2.3552	0.9108				
		4	64.6726	26.9884	2.3963	0.9353				
	2	1	56.2464	23.4533	2.3982	0.9364	0.9159	0.000401	0.000010	2.6%
		2	50.2270	21.5141	2.3346	0.8983				
		3	50.7023	21.7309	2.3332	0.8974				
		4	57.3083	24.0429	2.3836	0.9277				
	3	1	55.8436	23.2351	2.4034	0.9394	0.9207	0.000280	0.000009	3.1%
		2	49.0706	20.9148	2.3462	0.9053				
		3	49.7540	21.1907	2.3479	0.9064				
		4	57.8031	24.2447	2.3842	0.9281				
7	1	1	55.9506	23.1288	2.4191	0.9486	0.9103	0.001033	0.000019	1.8%
		2	53.2191	22.8949	2.3245	0.8922				
		3	43.8212	18.9663	2.3105	0.8836				
		4	16.2452	6.9018	2.3538	0.9099				
	2	1	59.6619	24.6898	2.4165	0.9471	0.9111	0.001082	0.000018	1.7%
		2	56.5469	24.1999	2.3367	0.8996				
		3	50.7272	22.0711	2.2984	0.8761				
		4	19.0837	8.0189	2.3798	0.9255				
	3	1	68.5012	28.4237	2.4100	0.9433	0.9167	0.000708	0.000015	2.1%
		2	60.7675	26.0109	2.3362	0.8993				
		3	55.1729	23.7109	2.3269	0.8936				
		4	20.8464	8.6622	2.4066	0.9413				
8	1	1	72.0431	29.9638	2.4043	0.9400	0.9107	0.000629	0.000014	2.3%
		2	68.7767	29.4484	2.3355	0.8988				
		3	56.7371	24.4977	2.3160	0.8870				
		4	21.9408	9.3027	2.3585	0.9128				
	2	1	73.6185	30.5929	2.4064	0.9412	0.9092	0.000645	0.000014	2.2%
		2	73.9435	31.6611	2.3355	0.8988				
		3	61.3690	26.4562	2.3196	0.8892				
		4	25.0215	10.7448	2.3287	0.8947				
	3	1	66.6006	27.6731	2.4067	0.9414	0.9198	0.000489	0.000012	2.4%
		2	63.2827	26.9398	2.3490	0.9070				
		3	53.3983	22.8582	2.3361	0.8992				
		4	20.8924	8.6730	2.4089	0.9427				
9	1	1	33.2615	13.6732	2.4326	0.9565	0.9291	0.000466	0.000011	2.3%
		2	63.3096	26.8951	2.3539	0.9100				
		3	68.2187	28.7524	2.3726	0.9212				
		4	38.2311	15.7766	2.4233	0.9511				
	2	1	22.7451	9.3072	2.4438	0.9630	0.9313	0.001299	0.000017	1.3%
		2	54.5914	23.3129	2.3417	0.9026				
		3	56.5342	23.8340	2.3720	0.9208				
		4	25.6182	10.3021	2.4867	0.9876				
	3	1	27.7345	11.2097	2.4742	0.9805	0.9333	0.000945	0.000015	1.6%
		2	61.9353	26.3267	2.3526	0.9092				
		3	66.4618	27.9844	2.3750	0.9226				
		4	30.4188	12.4480	2.4437	0.9629				

Table G.2: Continued.

Operating Condition	Obser.	Outlet Port	Mass m [g]	True Volume V [cm^3]	True Density ρ [$g\ cm^{-3}$]	Comp. x [-]	Weighted Comp. x [-]	Comp. Variance s^2 [-]	Comp. Variance Uncertainty U_s^2 [-]	Comp. Variance Uncertainty Percentage $U_s^2\ s^{-2}$ [%]
10	1	1	36.5017	15.0198	2.4302	0.9551	0.9194	0.000851	0.000014	1.7%
		2	83.4547	35.6135	2.3433	0.9036				
		3	89.6825	38.3456	2.3388	0.9008				
		4	44.4167	18.2487	2.4340	0.9573				
	2	1	29.8367	12.0774	2.4705	0.9784	0.9236	0.001504	0.000019	1.3%
		2	68.5071	28.9217	2.3687	0.9189				
		3	73.1384	31.5629	2.3172	0.8877				
		4	35.8751	14.7074	2.4393	0.9604				
	3	1	24.8262	9.9290	2.5004	0.9954	0.9294	0.001775	0.000021	1.2%
		2	60.7147	25.5858	2.3730	0.9214				
		3	65.2470	28.0392	2.3270	0.8937				
		4	30.5139	12.4400	2.4529	0.9683				
11	1	1	49.0953	20.3109	2.4172	0.9475	0.9252	0.000234	0.000008	3.4%
		2	46.1751	19.5313	2.3642	0.9161				
		3	49.5528	20.9911	2.3607	0.9140				
		4	53.1908	22.3933	2.3753	0.9228				
	2	1	56.0821	23.2619	2.4109	0.9438	0.9228	0.000223	0.000008	3.4%
		2	56.1217	23.7887	2.3592	0.9131				
		3	53.9022	22.8822	2.3556	0.9110				
		4	58.1523	24.4794	2.3756	0.9229				
	3	1	58.9450	24.5625	2.3998	0.9373	0.9243	0.000158	0.000006	4.1%
		2	58.7361	24.7376	2.3744	0.9222				
		3	56.5858	24.0836	2.3496	0.9074				
		4	62.7003	26.2726	2.3865	0.9295				
12	1	1	63.9305	26.9102	2.3757	0.9230	0.9063	0.000207	0.000007	3.6%
		2	59.9799	25.7060	2.3333	0.8975				
		3	58.5805	25.2274	2.3221	0.8907				
		4	68.0109	28.8556	2.3569	0.9118				
	2	1	58.9703	24.5221	2.4048	0.9403	0.9184	0.000265	0.000008	3.2%
		2	56.5733	24.0396	2.3533	0.9096				
		3	58.9744	25.1840	2.3417	0.9026				
		4	64.1105	27.0337	2.3715	0.9205				
	3	1	69.5113	29.2247	2.3785	0.9247	0.9093	0.000142	0.000006	4.3%
		2	65.2704	27.8637	2.3425	0.9031				
		3	65.7728	28.1992	2.3324	0.8970				
		4	73.2421	31.0886	2.3559	0.9112				
13	1	1	68.3767	28.3264	2.4139	0.9456	0.9176	0.000606	0.000014	2.4%
		2	64.5774	27.6734	2.3336	0.8977				
		3	51.9744	22.1894	2.3423	0.9030				
		4	16.4734	6.9189	2.3809	0.9261				
	2	1	91.2460	38.1760	2.3901	0.9316	0.9024	0.000697	0.000016	2.2%
		2	84.1113	36.3538	2.3137	0.8855				
		3	60.7606	26.3658	2.3045	0.8799				
		4	18.4711	7.8562	2.3512	0.9083				
	3	1	80.1384	33.5132	2.3913	0.9323	0.9104	0.000375	0.000011	3.0%
		2	71.6664	30.6052	2.3416	0.9026				
		3	57.0542	24.5570	2.3233	0.8914				
		4	18.3252	7.8160	2.3446	0.9043				
14	1	1	71.4425	29.9843	2.3827	0.9272	0.8999	0.000569	0.000014	2.5%
		2	65.6718	28.3602	2.3156	0.8867				
		3	51.5019	22.3645	2.3028	0.8789				
		4	15.9449	6.8240	2.3366	0.8995				
	2	1	77.7602	32.8163	2.3696	0.9194	0.8977	0.000540	0.000014	2.6%
		2	66.9084	29.1853	2.2925	0.8725				
		3	45.9969	19.7632	2.3274	0.8939				
		4	11.8976	5.0472	2.3573	0.9120				
	3	1	81.7265	34.0420	2.4008	0.9379	0.9184	0.000289	0.000010	3.4%
		2	74.9679	31.9219	2.3485	0.9067				
		3	60.5480	25.8005	2.3468	0.9057				
		4	19.6894	8.2955	2.3735	0.9217				

Table G.2: Continued.

Operating Condition	Obser.	Outlet Port	Mass m [g]	True Volume V [cm^3]	True Density ρ [$g\ cm^{-3}$]	Comp. x [-]	Weighted Comp. x [-]	Comp. Variance s^2 [-]	Comp. Variance Uncertainty U_s^2 [-]	Comp. Variance Uncertainty Percentage $U_s^2\ s^{-2}$ [%]
15	1	1	40.1889	16.6192	2.4182	0.9481	0.9203	0.000984	0.000016	1.6%
		2	107.6872	46.4716	2.3173	0.8877				
		3	116.5727	49.0425	2.3770	0.9238				
		4	47.1941	19.3216	2.4426	0.9623				
	2	1	37.5361	15.4827	2.4244	0.9517	0.9186	0.000730	0.000014	1.9%
		2	104.1357	44.8143	2.3237	0.8917				
		3	111.7670	47.1504	2.3704	0.9199				
		4	43.7489	18.0556	2.4230	0.9509				
	3	1	29.7238	12.1163	2.4532	0.9685	0.9270	0.001244	0.000018	1.4%
		2	83.2367	35.8123	2.3242	0.8920				
		3	91.9052	38.5697	2.3828	0.9273				
		4	37.2686	15.1624	2.4580	0.9712				
16	1	1	31.6597	12.8729	2.4594	0.9720	0.9211	0.001251	0.000018	1.4%
		2	85.8277	37.1174	2.3123	0.8847				
		3	90.9483	38.2052	2.3805	0.9259				
		4	36.5098	15.0702	2.4226	0.9507				
	2	1	25.1198	10.1612	2.4721	0.9793	0.9332	0.001587	0.000020	1.3%
		2	68.5471	29.4580	2.3269	0.8936				
		3	70.6285	29.4734	2.3963	0.9353				
		4	28.6320	11.5588	2.4771	0.9822				
	3	1	22.6688	9.1824	2.4687	0.9774	0.9310	0.001394	0.000019	1.3%
		2	64.2381	27.5753	2.3295	0.8952				
		3	68.1527	28.5396	2.3880	0.9303				
		4	27.6143	11.1838	2.4691	0.9776				
17	1	1	58.5975	24.3222	2.4092	0.9429	0.9177	0.000408	0.000010	2.6%
		2	50.4606	21.5563	2.3409	0.9021				
		3	51.4376	22.0148	2.3365	0.8995				
		4	60.4639	25.4710	2.3738	0.9219				
	2	1	29.6066	12.1097	2.4449	0.9636	0.9396	0.000276	0.000009	3.2%
		2	25.6861	10.7560	2.3881	0.9304				
		3	26.2340	10.9725	2.3909	0.9321				
		4	30.7527	12.8753	2.3885	0.9306				
	3	1	58.4704	24.1308	2.4231	0.9510	0.9338	0.000156	0.000006	4.1%
		2	54.9080	23.0895	2.3780	0.9244				
		3	53.7867	22.6152	2.3783	0.9246				
		4	60.4655	25.2558	2.3941	0.9340				
18	1	1	57.7596	24.4401	2.3633	0.9156	0.8925	0.000323	0.000009	2.9%
		2	42.7183	18.5547	2.3023	0.8785				
		3	41.5812	18.0800	2.2998	0.8770				
		4	61.6217	26.5300	2.3227	0.8911				
	2	1	56.4703	23.5434	2.3986	0.9366	0.9152	0.000260	0.000008	3.2%
		2	46.7452	20.0033	2.3369	0.8997				
		3	48.1505	20.5138	2.3472	0.9059				
		4	59.9299	25.3766	2.3616	0.9146				
	3	1	73.0902	30.4871	2.3974	0.9359	0.9156	0.000262	0.000008	3.2%
		2	63.5089	27.1253	2.3413	0.9024				
		3	61.6739	26.3582	2.3398	0.9015				
		4	78.2441	33.0384	2.3683	0.9186				
19	1	1	79.6160	32.8863	2.4209	0.9497	0.9273	0.001001	0.000015	1.5%
		2	81.1972	34.3235	2.3656	0.9170				
		3	46.7622	20.1948	2.3156	0.8867				
		4	19.5764	7.9422	2.4649	0.9752				
	2	1	85.3690	35.3733	2.4134	0.9453	0.9174	0.000961	0.000016	1.7%
		2	89.4464	37.8416	2.3637	0.9159				
		3	52.8487	23.0678	2.2910	0.8716				
		4	21.2175	8.9105	2.3812	0.9263				
	3	1	80.8324	33.3174	2.4261	0.9528	0.9242	0.001081	0.000017	1.6%
		2	82.2113	34.7911	2.3630	0.9154				
		3	50.7707	22.0262	2.3050	0.8802				
		4	20.6079	8.4805	2.4300	0.9550				

Table G.2: Continued.

Operating Condition	Obser.	Outlet Port	Mass m [g]	True Volume V [cm^3]	True Density ρ [$g\ cm^{-3}$]	Comp. x [-]	Weighted Comp. x [-]	Comp. Variance s^2 [-]	Comp. Variance Uncertainty U_s^2 [-]	Comp. Variance Uncertainty Percentage $U_s^2\ s^{-2}$ [%]
20	1	1	84.5687	34.9902	2.4169	0.9474	0.9140	0.001509	0.000021	1.4%
		2	86.8453	36.6996	2.3664	0.9175				
		3	53.3066	23.5323	2.2652	0.8555				
		4	20.6152	8.7327	2.3607	0.9140				
	2	1	94.6229	39.2345	2.4117	0.9443	0.9186	0.001069	0.000017	1.6%
		2	93.4608	39.5880	2.3608	0.9141				
		3	56.8405	24.8195	2.2902	0.8710				
		4	22.6554	9.3608	2.4202	0.9493				
	3	1	96.2102	39.8028	2.4172	0.9475	0.9128	0.001376	0.000020	1.5%
		2	95.1171	40.4310	2.3526	0.9092				
		3	58.3653	25.6861	2.2723	0.8599				
		4	22.6281	9.5655	2.3656	0.9170				
21	1	1	42.4034	17.6228	2.4062	0.9411	0.9089	0.000491	0.000011	2.1%
		2	95.1079	40.7306	2.3350	0.8986				
		3	99.1266	42.5674	2.3287	0.8947				
		4	38.7484	16.1670	2.3968	0.9355				
	2	1	35.8395	14.6889	2.4399	0.9608	0.9157	0.000916	0.000014	1.6%
		2	77.6665	33.2471	2.3360	0.8992				
		3	80.0197	34.2785	2.3344	0.8982				
		4	31.8046	13.1396	2.4205	0.9495				
	3	1	39.5624	16.1703	2.4466	0.9647	0.9163	0.000825	0.000014	1.7%
		2	84.4695	36.1307	2.3379	0.9003				
		3	87.1508	37.2630	2.3388	0.9009				
		4	35.1184	14.6208	2.4019	0.9386				
22	1	1	42.5849	17.2566	2.4677	0.9768	0.9274	0.001036	0.000016	1.5%
		2	81.0039	34.2938	2.3621	0.9149				
		3	85.0609	36.2975	2.3434	0.9037				
		4	35.4635	14.6048	2.4282	0.9540				
	2	1	43.4191	17.7297	2.4489	0.9660	0.9220	0.000678	0.000013	1.9%
		2	90.3842	38.2755	2.3614	0.9145				
		3	91.0342	38.8823	2.3413	0.9023				
		4	36.2374	15.1005	2.3998	0.9373				
	3	1	43.3257	17.9679	2.4113	0.9441	0.9196	0.000378	0.000009	2.5%
		2	97.6591	41.4021	2.3588	0.9129				
		3	99.7865	42.5397	2.3457	0.9050				
		4	39.4210	16.3241	2.4149	0.9462				
23	1	1	76.6176	32.0943	2.3873	0.9299	0.9150	0.000341	0.000010	2.8%
		2	74.4253	31.9942	2.3262	0.8932				
		3	70.3437	29.9828	2.3461	0.9053				
		4	77.0366	32.2686	2.3874	0.9300				
	2	1	75.3346	31.5829	2.3853	0.9287	0.9157	0.000325	0.000009	2.9%
		2	70.1574	30.0980	2.3310	0.8961				
		3	69.3357	29.5947	2.3428	0.9033				
		4	75.6854	31.6536	2.3910	0.9321				
	3	1	63.9688	26.7046	2.3954	0.9347	0.9251	0.000397	0.000010	2.6%
		2	61.5915	26.1690	2.3536	0.9098				
		3	58.1179	24.7549	2.3477	0.9062				
		4	63.0213	26.0671	2.4177	0.9478				
24	1	1	58.5987	24.5709	2.3849	0.9285	0.9210	0.000344	0.000010	2.8%
		2	52.5535	22.4618	2.3397	0.9014				
		3	50.0750	21.2871	2.3524	0.9090				
		4	55.3431	22.9799	2.4083	0.9423				
	2	1	45.7725	18.9385	2.4169	0.9474	0.9355	0.000227	0.000008	3.4%
		2	41.2254	17.4284	2.3654	0.9169				
		3	42.7674	17.9440	2.3834	0.9276				
		4	47.6456	19.7126	2.4170	0.9474				
	3	1	59.4746	25.1145	2.3681	0.9185	0.9112	0.000442	0.000011	2.5%
		2	55.2815	23.8881	2.3142	0.8858				
		3	51.0006	21.7784	2.3418	0.9027				
		4	60.7014	25.3467	2.3948	0.9344				

Table G.2: Continued.

Operating Condition	Obser.	Outlet Port	Mass m [g]	True Volume V [cm^3]	True Density ρ [$g\ cm^{-3}$]	Comp. x [-]	Weighted Comp. x [-]	Comp. Variance s^2 [-]	Comp. Variance Uncertainty U_s^2 [-]	Comp. Variance Uncertainty Percentage $U_s^2\ s^{-2}$ [%]
25	1	1	72.4625	30.2575	2.3949	0.9344	0.9063	0.000588	0.000014	2.4%
		2	66.6466	28.5921	2.3309	0.8961				
		3	53.6143	23.2162	2.3094	0.8829				
		4	20.5105	8.7669	2.3395	0.9013				
	2	1	77.4880	32.3272	2.3970	0.9357	0.9126	0.000390	0.000012	3.0%
		2	71.5125	30.6770	2.3311	0.8962				
		3	56.0176	23.9312	2.3408	0.9020				
		4	22.7378	9.6479	2.3568	0.9117				
	3	1	79.8865	33.4152	2.3907	0.9320	0.9061	0.000507	0.000013	2.5%
		2	71.7198	30.8221	2.3269	0.8936				
		3	63.4290	27.4127	2.3139	0.8856				
		4	26.1168	11.0900	2.3550	0.9106				
26	1	1	77.4676	32.5888	2.3771	0.9239	0.8960	0.000728	0.000015	2.1%
		2	67.7914	29.2959	2.3140	0.8857				
		3	52.7348	23.1200	2.2809	0.8653				
		4	18.7241	7.9872	2.3443	0.9042				
	2	1	79.2271	33.0749	2.3954	0.9347	0.9065	0.000661	0.000015	2.2%
		2	68.8214	29.6275	2.3229	0.8912				
		3	60.5035	26.2017	2.3091	0.8828				
		4	25.2596	10.6799	2.3652	0.9167				
	3	1	81.0116	33.8230	2.3952	0.9346	0.9089	0.000534	0.000013	2.5%
		2	71.6110	30.7286	2.3304	0.8958				
		3	61.2768	26.4443	2.3172	0.8877				
		4	22.1450	9.3666	2.3643	0.9162				
27	1	1	28.1935	11.3091	2.4930	0.9912	0.9271	0.001018	0.000014	1.4%
		2	66.4442	28.0481	2.3689	0.9190				
		3	67.5456	28.7472	2.3496	0.9074				
		4	29.8765	12.5231	2.3857	0.9290				
	2	1	29.0177	11.6892	2.4824	0.9852	0.9333	0.000861	0.000014	1.6%
		2	68.4162	28.7253	2.3817	0.9266				
		3	66.7497	28.3475	2.3547	0.9104				
		4	27.9101	11.5247	2.4218	0.9502				
	3	1	42.8198	17.5245	2.4434	0.9628	0.9172	0.000596	0.000011	1.9%
		2	101.6162	43.0684	2.3594	0.9133				
		3	101.9449	43.6608	2.3349	0.8985				
		4	42.5561	17.8822	2.3798	0.9255				
28	1	1	42.4932	17.7409	2.3952	0.9346	0.9183	0.000131	0.000006	4.3%
		2	92.5679	39.3617	2.3517	0.9087				
		3	95.9884	40.6363	2.3621	0.9149				
		4	45.2470	18.9525	2.3874	0.9300				
	2	1	48.6578	20.2141	2.4071	0.9416	0.9106	0.000310	0.000008	2.7%
		2	108.1615	46.2566	2.3383	0.9005				
		3	110.7905	47.3480	2.3399	0.9015				
		4	49.2216	20.7307	2.3743	0.9222				
	3	1	42.0954	17.4532	2.4119	0.9444	0.9136	0.000353	0.000009	2.5%
		2	94.2342	40.3070	2.3379	0.9003				
		3	98.4376	41.9408	2.3471	0.9058				
		4	44.1232	18.4864	2.3868	0.9296				
29	1	1	73.1504	30.4377	2.4033	0.9394	0.9241	0.000131	0.000006	4.5%
		2	66.5824	28.1397	2.3661	0.9173				
		3	66.6478	28.2458	2.3596	0.9134				
		4	77.1353	32.4324	2.3783	0.9246				
	2	1	62.4399	25.9133	2.4096	0.9431	0.9186	0.000340	0.000010	2.8%
		2	56.2754	23.9787	2.3469	0.9057				
		3	56.5078	24.1334	2.3415	0.9025				
		4	66.0610	27.8618	2.3710	0.9202				
	3	1	78.2874	32.7284	2.3920	0.9327	0.9130	0.000239	0.000008	3.3%
		2	70.4854	29.9790	2.3512	0.9083				
		3	70.7698	30.3783	2.3296	0.8953				
		4	83.7138	35.4779	2.3596	0.9134				

Table G.2: Continued.

Operating Condition	Obser.	Outlet Port	Mass m [g]	True Volume V [cm^3]	True Density ρ [$g\ cm^{-3}$]	Comp. x [-]	Weighted Comp. x [-]	Comp. Variance s^2 [-]	Comp. Variance Uncertainty U_s^2 [-]	Comp. Variance Uncertainty Percentage $U_s^2\ s^{-2}$ [%]
30	1	1	67.3296	28.4038	2.3704	0.9199	0.8972	0.000449	0.000011	2.4%
		2	53.5516	23.2209	2.3062	0.8809				
		3	50.9625	22.2088	2.2947	0.8738				
		4	67.7666	28.8916	2.3455	0.9049				
	2	1	76.6232	32.1004	2.3870	0.9297	0.9135	0.000156	0.000006	4.2%
		2	66.0149	28.1775	2.3428	0.9033				
		3	67.2681	28.7061	2.3433	0.9036				
		4	78.8770	33.3977	2.3617	0.9147				
	3	1	75.9446	32.1610	2.3614	0.9145	0.9017	0.000139	0.000006	4.4%
		2	64.3538	27.7067	2.3227	0.8910				
		3	67.8220	29.2030	2.3224	0.8909				
		4	80.9701	34.4609	2.3496	0.9074				
31	1	1	98.3585	41.1891	2.3880	0.9303	0.9095	0.000314	0.000010	3.2%
		2	88.1741	37.7370	2.3365	0.8995				
		3	71.2021	30.4793	2.3361	0.8992				
		4	24.5211	10.5485	2.3246	0.8922				
	2	1	83.3434	34.7955	2.3952	0.9346	0.9089	0.000474	0.000013	2.7%
		2	90.9228	39.0340	2.3293	0.8951				
		3	58.6592	25.2391	2.3241	0.8919				
		4	20.0730	8.4993	2.3617	0.9147				
	3	1	101.2076	42.4700	2.3830	0.9274	0.9049	0.000446	0.000012	2.7%
		2	74.0262	31.6859	2.3363	0.8993				
		3	71.8805	31.0380	2.3159	0.8869				
		4	23.3354	10.1203	2.3058	0.8807				
32	1	1	87.0285	36.9062	2.3581	0.9125	0.8961	0.000243	0.000008	3.3%
		2	75.2906	32.3861	2.3248	0.8923				
		3	61.8059	26.6883	2.3158	0.8869				
		4	21.2616	9.2937	2.2878	0.8695				
	2	1	97.8498	41.2178	2.3740	0.9220	0.9091	0.000128	0.000007	5.2%
		2	88.9499	38.0131	2.3400	0.9016				
		3	71.0694	30.4033	2.3376	0.9001				
		4	24.6252	10.4516	2.3561	0.9113				
	3	1	95.8386	40.4535	2.3691	0.9191	0.8978	0.000377	0.000011	2.9%
		2	84.7650	36.4324	2.3266	0.8935				
		3	69.8909	30.3931	2.2996	0.8769				
		4	23.1499	9.9807	2.3195	0.8891				
33	1	1	24.6560	10.0824	2.4454	0.9640	0.9295	0.001022	0.000016	1.5%
		2	64.0040	27.4019	2.3358	0.8990				
		3	68.8136	28.8638	2.3841	0.9280				
		4	27.2869	11.0839	2.4619	0.9734				
	2	1	27.1397	11.2223	2.4184	0.9482	0.9183	0.000784	0.000014	1.8%
		2	74.3999	32.0218	2.3234	0.8915				
		3	78.2630	33.0755	2.3662	0.9173				
		4	33.5967	13.8169	2.4316	0.9559				
	3	1	36.5492	14.9640	2.4425	0.9623	0.9173	0.001239	0.000017	1.4%
		2	95.0927	41.1014	2.3136	0.8855				
		3	99.3903	42.1241	2.3595	0.9133				
		4	39.9066	16.3402	2.4422	0.9621				
34	1	1	36.4852	14.9657	2.4379	0.9596	0.9128	0.000751	0.000013	1.7%
		2	97.1445	41.5511	2.3380	0.9003				
		3	100.0419	42.9133	2.3313	0.8963				
		4	40.6878	16.9115	2.4059	0.9409				
	2	1	35.5460	14.6323	2.4293	0.9546	0.9110	0.000821	0.000013	1.6%
		2	93.8877	40.3016	2.3296	0.8953				
		3	99.0537	42.5065	2.3303	0.8957				
		4	40.6791	16.8389	2.4158	0.9467				
	3	1	34.0825	13.8648	2.4582	0.9713	0.9187	0.001181	0.000016	1.4%
		2	90.2087	38.5898	2.3376	0.9001				
		3	94.1320	40.2710	2.3375	0.9000				
		4	38.5309	15.7883	2.4405	0.9611				

Table G.2: Continued.

Operating Condition	Obser.	Outlet Port	Mass m [g]	True Volume V [cm^3]	True Density ρ [$g\ cm^{-3}$]	Comp. x [-]	Weighted Comp. x [-]	Comp. Variance s^2 [-]	Comp. Variance Uncertainty U_s^2 [-]	Comp. Variance Uncertainty Percentage $U_s^2\ s^{-2}$ [%]
35	1	1	56.8603	23.6557	2.4037	0.9396	0.9188	0.000272	0.000009	3.1%
		2	46.1230	19.5948	2.3538	0.9099				
		3	44.7494	19.1290	2.3393	0.9012				
		4	58.7697	24.8081	2.3690	0.9190				
	2	1	61.2279	25.5414	2.3972	0.9358	0.9223	0.000144	0.000006	4.3%
		2	48.8568	20.7825	2.3509	0.9081				
		3	49.4019	20.9043	2.3632	0.9156				
		4	61.4065	25.8018	2.3799	0.9255				
	3	1	65.8586	27.3229	2.4104	0.9435	0.9250	0.000197	0.000007	3.7%
		2	56.0982	23.7801	2.3590	0.9131				
		3	59.2610	25.0928	2.3617	0.9146				
		4	69.9989	29.4025	2.3807	0.9260				
36	1	1	64.4955	27.1209	2.3781	0.9244	0.9027	0.000525	0.000012	2.2%
		2	46.3631	20.0984	2.3068	0.8813				
		3	42.0507	18.2782	2.3006	0.8775				
		4	62.9421	26.6846	2.3587	0.9129				
	2	1	68.3942	28.6079	2.3907	0.9320	0.9135	0.000270	0.000009	3.2%
		2	54.3538	23.2962	2.3332	0.8974				
		3	51.9530	22.2348	2.3366	0.8995				
		4	68.5133	28.9317	2.3681	0.9185				
	3	1	62.8314	26.4025	2.3798	0.9254	0.9066	0.000367	0.000010	2.7%
		2	49.5797	21.4030	2.3165	0.8873				
		3	49.1957	21.2091	2.3196	0.8891				
		4	64.1392	27.1239	2.3647	0.9164				
37	1	1	91.9587	38.1989	2.4074	0.9418	0.9148	0.002045	0.000023	1.1%
		2	87.5272	36.6110	2.3907	0.9320				
		3	55.2584	24.6399	2.2426	0.8412				
		4	20.8745	8.8134	2.3685	0.9187				
	2	1	91.8017	38.1633	2.4055	0.9407	0.9116	0.001738	0.000022	1.3%
		2	87.7200	36.8924	2.3777	0.9242				
		3	55.4974	24.6685	2.2497	0.8457				
		4	20.6770	8.8123	2.3464	0.9054				
	3	1	95.4659	39.6708	2.4065	0.9412	0.9154	0.002332	0.000025	1.1%
		2	92.6287	38.5355	2.4037	0.9396				
		3	57.7652	25.8195	2.2373	0.8378				
		4	21.7528	9.2710	2.3463	0.9054				
38	1	1	102.8834	42.7454	2.4069	0.9415	0.9181	0.001674	0.000022	1.3%
		2	63.5281	26.5259	2.3949	0.9344				
		3	55.1957	24.4030	2.2618	0.8534				
		4	21.7969	9.1655	2.3782	0.9245				
	2	1	91.1455	37.6871	2.4185	0.9483	0.9186	0.001658	0.000021	1.3%
		2	86.3789	36.1719	2.3880	0.9303				
		3	55.1759	24.3612	2.2649	0.8553				
		4	21.4087	9.1089	2.3503	0.9078				
	3	1	102.2835	42.5619	2.4032	0.9393	0.9059	0.002441	0.000026	1.1%
		2	98.6244	41.5165	2.3755	0.9229				
		3	61.5839	27.7232	2.2214	0.8277				
		4	23.3922	10.0544	2.3266	0.8934				
39	1	1	44.1409	18.1142	2.4368	0.9590	0.9206	0.000787	0.000014	1.8%
		2	81.3373	34.7602	2.3400	0.9015				
		3	84.7248	36.1222	2.3455	0.9049				
		4	42.3629	17.5104	2.4193	0.9488				
	2	1	41.6729	17.1917	2.4240	0.9515	0.9240	0.000637	0.000012	1.9%
		2	80.0178	34.1584	2.3425	0.9031				
		3	87.1980	36.9361	2.3608	0.9141				
		4	42.3801	17.4209	2.4327	0.9566				
	3	1	49.7043	20.5976	2.4131	0.9451	0.9186	0.000415	0.000010	2.4%
		2	101.5276	43.3951	2.3396	0.9013				
		3	109.6534	46.5232	2.3570	0.9118				
		4	51.1286	21.2428	2.4069	0.9415				

Table G.2: Continued.

Operating Condition	Obser.	Outlet Port	Mass m [g]	True Volume V [cm^3]	True Density ρ [$g\ cm^{-3}$]	Comp. x [-]	Weighted Comp. x [-]	Comp. Variance s^2 [-]	Comp. Variance Uncertainty U_s^2 [-]	Comp. Variance Uncertainty Percentage $U_s^2\ s^{-2}$ [%]
40	1	1	49.8491	20.5102	2.4305	0.9553	0.9218	0.000590	0.000012	2.1%
		2	91.3802	38.5750	2.3689	0.9190				
		3	91.5444	39.2166	2.3343	0.8981				
		4	41.5325	17.2757	2.4041	0.9398				
	2	1	49.8716	20.4862	2.4344	0.9576	0.9210	0.000523	0.000011	2.2%
		2	92.9942	39.2594	2.3687	0.9189				
		3	92.5172	39.5732	2.3379	0.9003				
		4	42.2329	17.7144	2.3841	0.9280				
	3	1	55.6960	22.9572	2.4261	0.9527	0.9142	0.000614	0.000013	2.0%
		2	104.5112	44.3105	2.3586	0.9128				
		3	104.6689	45.0706	2.3223	0.8908				
		4	48.6206	20.4588	2.3765	0.9235				
41	1	1	59.7010	25.0039	2.3877	0.9301	0.9149	0.000372	0.000010	2.7%
		2	51.0721	21.9923	2.3223	0.8908				
		3	51.7766	22.0878	2.3441	0.9041				
		4	61.0825	25.5966	2.3864	0.9294				
	2	1	72.1229	30.4099	2.3717	0.9206	0.9080	0.000339	0.000009	2.8%
		2	59.7247	25.7526	2.3192	0.8889				
		3	59.9938	25.8055	2.3248	0.8924				
		4	72.0158	30.2858	2.3779	0.9243				
	3	1	71.1409	29.8639	2.3822	0.9269	0.9133	0.000329	0.000009	2.8%
		2	63.0906	27.0711	2.3306	0.8958				
		3	61.8437	26.5199	2.3320	0.8967				
		4	75.3206	31.5797	2.3851	0.9286				
42	1	1	83.2418	34.9217	2.3837	0.9278	0.9146	0.000447	0.000011	2.4%
		2	71.1331	30.6849	2.3182	0.8883				
		3	69.8721	29.8354	2.3419	0.9027				
		4	84.5212	35.3173	2.3932	0.9334				
	2	1	77.4869	32.8197	2.3610	0.9142	0.9075	0.000169	0.000007	4.0%
		2	67.1107	28.8664	2.3249	0.8924				
		3	66.2278	28.3468	2.3363	0.8994				
		4	79.4386	33.4964	2.3716	0.9206				
	3	1	82.9004	34.7044	2.3888	0.9308	0.9188	0.000407	0.000010	2.6%
		2	75.5578	32.4989	2.3249	0.8924				
		3	72.2957	30.6739	2.3569	0.9118				
		4	82.5579	34.4088	2.3993	0.9370				
43	1	1	64.0693	27.0005	2.3729	0.9214	0.8977	0.000489	0.000013	2.6%
		2	56.2647	24.4205	2.3040	0.8796				
		3	45.4169	19.6766	2.3082	0.8822				
		4	18.6525	7.9299	2.3522	0.9089				
	2	1	81.5356	34.2632	2.3797	0.9254	0.9030	0.000460	0.000012	2.7%
		2	71.2794	30.6651	2.3244	0.8921				
		3	56.2442	24.3945	2.3056	0.8806				
		4	21.8104	9.2489	2.3582	0.9125				
	3	1	72.9207	30.5428	2.3875	0.9300	0.9098	0.000424	0.000012	2.7%
		2	62.1247	26.7479	2.3226	0.8910				
		3	52.5452	22.5279	2.3324	0.8970				
		4	21.3764	8.9749	2.3818	0.9267				
44	1	1	55.1951	22.9566	2.4043	0.9400	0.9208	0.000549	0.000013	2.4%
		2	50.1052	21.5190	2.3284	0.8945				
		3	37.7143	15.9235	2.3685	0.9187				
		4	12.7226	5.2633	2.4172	0.9475				
	2	1	79.9805	33.5055	2.3871	0.9298	0.9003	0.001117	0.000018	1.6%
		2	70.2357	30.5831	2.2966	0.8750				
		3	53.2507	23.2050	2.2948	0.8739				
		4	19.3231	8.0207	2.4092	0.9428				
	3	1	75.2174	31.3395	2.4001	0.9375	0.9113	0.000540	0.000014	2.5%
		2	65.8100	28.2016	2.3336	0.8977				
		3	52.1028	22.4378	2.3221	0.8907				
		4	19.0612	8.0877	2.3568	0.9117				

Table G.2: Continued.

Operating Condition	Obser.	Outlet Port	Mass m [g]	True Volume V [cm^3]	True Density ρ [$g\ cm^{-3}$]	Comp. x [-]	Weighted Comp. x [-]	Comp. Variance s^2 [-]	Comp. Variance Uncertainty U_s^2 [-]	Comp. Variance Uncertainty Percentage $U_s^2\ s^{-2}$ [%]
45	1	1	57.0947	23.6948	2.4096	0.9431	0.9109	0.000314	0.000009	2.7%
		2	130.5123	55.3667	2.3572	0.9120				
		3	134.7074	57.7997	2.3306	0.8959				
		4	58.4999	24.8226	2.3567	0.9117				
	2	1	36.9516	14.9317	2.4747	0.9808	0.9168	0.001026	0.000015	1.4%
		2	87.2778	37.0809	2.3537	0.9099				
		3	91.3724	39.2048	2.3306	0.8959				
		4	39.2973	16.5663	2.3721	0.9209				
	3	1	37.4615	15.2839	2.4510	0.9672	0.9170	0.000915	0.000015	1.6%
		2	85.0807	36.0540	2.3598	0.9135				
		3	86.1151	37.0919	2.3217	0.8904				
		4	37.8833	15.8074	2.3965	0.9354				
46	1	1	33.4405	13.5799	2.4625	0.9738	0.9361	0.000394	0.000009	2.3%
		2	74.4485	31.2600	2.3816	0.9265				
		3	75.8428	31.8704	2.3797	0.9254				
		4	36.3519	15.0817	2.4103	0.9435				
	2	1	38.3160	15.7005	2.4404	0.9611	0.9182	0.000579	0.000011	2.0%
		2	82.9070	35.3726	2.3438	0.9039				
		3	85.7690	36.5234	2.3483	0.9066				
		4	38.3740	16.0465	2.3914	0.9324				
	3	1	36.8203	15.1063	2.4374	0.9593	0.9191	0.000562	0.000011	2.0%
		2	84.5393	36.0362	2.3460	0.9052				
		3	84.9535	36.1694	2.3488	0.9069				
		4	37.4810	15.6051	2.4018	0.9385				
47	1	1	77.3158	32.4210	2.3847	0.9284	0.9116	0.000234	0.000008	3.4%
		2	62.2181	26.6536	2.3343	0.8981				
		3	60.9392	26.1275	2.3324	0.8970				
		4	76.3912	32.2864	2.3660	0.9173				
	2	1	73.6527	30.8056	2.3909	0.9320	0.9141	0.000266	0.000008	3.2%
		2	59.8001	25.5434	2.3411	0.9023				
		3	58.1525	24.9458	2.3312	0.8962				
		4	74.6943	31.5151	2.3701	0.9197				
	3	1	62.6645	26.1560	2.3958	0.9350	0.9173	0.000184	0.000007	3.8%
		2	50.7404	21.6261	2.3463	0.9054				
		3	50.6142	21.5379	2.3500	0.9076				
		4	64.5246	27.2742	2.3658	0.9171				
48	1	1	74.9724	31.7484	2.3615	0.9145	0.8992	0.000303	0.000009	2.9%
		2	55.2402	24.0394	2.2979	0.8758				
		3	56.9645	24.5585	2.3195	0.8891				
		4	77.7878	33.0817	2.3514	0.9085				
	2	1	78.0785	32.8517	2.3767	0.9236	0.9041	0.000316	0.000009	2.9%
		2	60.1156	25.9522	2.3164	0.8872				
		3	60.0860	25.9273	2.3175	0.8879				
		4	78.6740	33.4195	2.3541	0.9101				
	3	1	88.3229	37.2459	2.3713	0.9204	0.9057	0.000187	0.000007	3.8%
		2	70.7663	30.3287	2.3333	0.8975				
		3	71.1931	30.6895	2.3198	0.8893				
		4	91.9439	39.0463	2.3547	0.9105				
49	1	1	82.8855	34.9918	2.3687	0.9189	0.9039	0.000377	0.000010	2.7%
		2	70.5899	30.4469	2.3185	0.8885				
		3	49.0291	21.1169	2.3218	0.8905				
		4	15.1115	6.2947	2.4007	0.9378				
	2	1	90.0793	38.0823	2.3654	0.9169	0.8914	0.000564	0.000013	2.3%
		2	78.8106	34.1144	2.3102	0.8834				
		3	59.0761	25.7317	2.2958	0.8746				
		4	18.8121	8.3041	2.2654	0.8556				
	3	1	92.7401	38.9869	2.3788	0.9248	0.9032	0.000378	0.000011	3.0%
		2	80.1682	34.4526	2.3269	0.8936				
		3	59.2188	25.6009	2.3132	0.8852				
		4	19.4314	8.3449	2.3285	0.8946				

Table G.2: Continued.

Operating Condition	Obser.	Outlet Port	Mass m [g]	True Volume V [cm^3]	True Density ρ [$g\ cm^{-3}$]	Comp. x [-]	Weighted Comp. x [-]	Comp. Variance s^2 [-]	Comp. Variance Uncertainty U_s^2 [-]	Comp. Variance Uncertainty Percentage $U_s^2\ s^{-2}$ [%]
50	1	1	59.1339	24.8943	2.3754	0.9228	0.9037	0.000606	0.000013	2.1%
		2	52.1386	22.4991	2.3174	0.8878				
		3	37.5136	16.2497	2.3086	0.8824				
		4	11.4784	4.7524	2.4153	0.9464				
	2	1	83.5972	35.5367	2.3524	0.9091	0.8912	0.000381	0.000011	2.8%
		2	72.1748	31.3094	2.3052	0.8803				
		3	59.0516	25.7716	2.2913	0.8718				
		4	20.5110	8.6951	2.3589	0.9130				
	3	1	81.6342	34.6395	2.3567	0.9116	0.8953	0.000213	0.000008	3.9%
		2	70.5103	30.3685	2.3218	0.8905				
		3	56.6897	24.5735	2.3069	0.8814				
		4	19.3450	8.3638	2.3130	0.8851				
51	1	1	38.1326	15.6217	2.4410	0.9614	0.9197	0.000927	0.000015	1.6%
		2	93.7414	40.2675	2.3280	0.8943				
		3	97.8779	41.4976	2.3586	0.9128				
		4	38.7267	15.9102	2.4341	0.9574				
	2	1	38.6403	15.6687	2.4661	0.9759	0.9214	0.001094	0.000015	1.4%
		2	97.0606	41.5818	2.3342	0.8981				
		3	100.7353	42.8014	2.3535	0.9098				
		4	38.9992	16.0459	2.4305	0.9553				
	3	1	40.9171	16.6372	2.4594	0.9720	0.9195	0.001128	0.000016	1.4%
		2	99.4695	42.6051	2.3347	0.8984				
		3	102.3710	43.6668	2.3444	0.9042				
		4	39.8722	16.3781	2.4345	0.9576				
52	1	1	41.9779	17.2636	2.4316	0.9559	0.9123	0.000984	0.000015	1.5%
		2	109.3214	47.2188	2.3152	0.8865				
		3	115.3221	49.1498	2.3463	0.9054				
		4	44.4551	18.3289	2.4254	0.9523				
	2	1	37.2097	15.0635	2.4702	0.9782	0.9216	0.001357	0.000018	1.3%
		2	94.1871	40.5620	2.3221	0.8907				
		3	98.7519	41.8234	2.3612	0.9143				
		4	38.7630	15.8890	2.4396	0.9606				
	3	1	40.3593	16.3657	2.4661	0.9759	0.9168	0.001299	0.000017	1.3%
		2	102.1422	44.0249	2.3201	0.8895				
		3	107.5084	45.7964	2.3475	0.9061				
		4	43.0145	17.7277	2.4264	0.9529				
53	1	1	57.2988	23.8533	2.4021	0.9387	0.9236	0.000149	0.000006	4.3%
		2	46.3584	19.6285	2.3618	0.9147				
		3	45.1475	19.1533	2.3572	0.9119				
		4	57.1135	24.0111	2.3786	0.9248				
	2	1	67.6961	28.2797	2.3938	0.9338	0.9177	0.000182	0.000007	3.9%
		2	51.6896	21.9917	2.3504	0.9079				
		3	50.3314	21.4739	2.3438	0.9039				
		4	67.2413	28.3729	2.3699	0.9196				
	3	1	72.8675	30.4961	2.3894	0.9312	0.9188	0.000173	0.000007	3.9%
		2	54.4428	23.0998	2.3569	0.9117				
		3	51.5035	22.0192	2.3390	0.9010				
		4	70.9436	29.8347	2.3779	0.9243				
54	1	1	70.0731	29.6744	2.3614	0.9145	0.8954	0.000498	0.000011	2.3%
		2	43.9242	19.1279	2.2963	0.8749				
		3	43.0326	18.8314	2.2852	0.8679				
		4	69.8075	29.7336	2.3478	0.9063				
	2	1	73.6591	31.0663	2.3710	0.9202	0.9092	0.000167	0.000007	3.9%
		2	53.4469	22.7824	2.3460	0.9052				
		3	53.4699	23.0365	2.3211	0.8901				
		4	74.7341	31.6360	2.3623	0.9150				
	3	1	64.6600	27.0423	2.3911	0.9322	0.9220	0.000143	0.000006	4.2%
		2	48.4010	20.4001	2.3726	0.9212				
		3	47.9124	20.4480	2.3431	0.9035				
		4	66.1099	27.7659	2.3810	0.9262				

G.2.2 Shorter Mixing Length Study

Table G.3 Shorter Mixing Length Screw Mixer Composition Analysis Data

Operating Condition	Obser.	Outlet Port	Mass m [g]	True Volume V [cm^3]	True Density ρ [$g\ cm^{-3}$]	Comp. x [-]	Weighted Comp. x [-]	Comp. Variance s^2 [-]	Comp. Variance Uncertainty U_s^2 [-]	Comp. Variance Uncertainty Percentage $U_s^2 s^{-2}$ [%]
5(2)	1	1	74.6924	31.2563	2.3897	0.9313	0.8912	0.001927	0.000022	1.2%
		2	58.4183	25.6187	2.2803	0.8649				
		3	52.1635	23.3987	2.2293	0.8328				
		4	72.7785	30.8553	2.3587	0.9129				
	2	1	78.7757	33.0439	2.3840	0.9279	0.8874	0.001730	0.000021	1.2%
		2	62.7374	27.5364	2.2783	0.8637				
		3	58.1201	26.0676	2.2296	0.8329				
		4	80.6634	34.3770	2.3464	0.9055				
	3	1	79.8382	33.3598	2.3932	0.9334	0.8906	0.001819	0.000022	1.2%
		2	65.0016	28.4943	2.2812	0.8655				
		3	58.9286	26.3872	2.2332	0.8352				
		4	84.6920	36.0328	2.3504	0.9079				
5(5)	1	1	61.5094	25.7051	2.3929	0.9332	0.9016	0.000652	0.000013	2.0%
		2	57.1466	24.8806	2.2968	0.8752				
		3	51.1661	22.1018	2.3150	0.8864				
		4	65.8513	28.0376	2.3487	0.9068				
	2	1	61.0498	25.6401	2.3810	0.9262	0.9102	0.001332	0.000019	1.4%
		2	55.9854	24.2472	2.3089	0.8826				
		3	52.6800	22.9982	2.2906	0.8713				
		4	68.1251	28.1650	2.4188	0.9485				
	3	1	59.5965	24.9980	2.3841	0.9280	0.8968	0.000623	0.000013	2.1%
		2	50.6902	21.9726	2.3070	0.8814				
		3	48.9501	21.3822	2.2893	0.8705				
		4	64.5147	27.6015	2.3374	0.9000				
5(10)	1	1	44.1690	18.3451	2.4077	0.9420	0.9250	0.000489	0.000011	2.3%
		2	40.5785	17.3416	2.3400	0.9015				
		3	38.5328	16.3860	2.3516	0.9086				
		4	43.8733	18.1953	2.4112	0.9440				
	2	1	52.6654	21.8811	2.4069	0.9415	0.9255	0.000441	0.000011	2.5%
		2	47.5774	20.3630	2.3365	0.8994				
		3	44.7563	18.9484	2.3620	0.9148				
		4	52.6357	21.8600	2.4079	0.9421				
	3	1	51.6986	21.2691	2.4307	0.9554	0.9281	0.000582	0.000012	2.1%
		2	46.0677	19.5844	2.3523	0.9090				
		3	47.6281	20.3055	2.3456	0.9049				
		4	54.0098	22.4827	2.4023	0.9388				
11(2)	1	1	57.2655	24.9913	2.2914	0.8718	0.8847	0.000188	0.000007	3.8%
		2	66.4568	28.5545	2.3274	0.8939				
		3	59.5594	25.5253	2.3333	0.8975				
		4	51.1842	22.3325	2.2919	0.8721				
	2	1	61.5742	27.0126	2.2795	0.8644	0.8785	0.000109	0.000005	5.0%
		2	68.0229	29.3554	2.3172	0.8877				
		3	63.7844	27.5964	2.3113	0.8841				
		4	54.7280	23.8075	2.2988	0.8764				
	3	1	53.1210	23.0347	2.3061	0.8809	0.8893	0.000135	0.000006	4.4%
		2	62.0817	26.6530	2.3293	0.8951				
		3	54.9346	23.4736	2.3403	0.9017				
		4	46.6470	20.2906	2.2989	0.8765				

Table G.3 Continued.

Operating Condition	Obser.	Outlet Port	Mass m [g]	True Volume V [cm^3]	True Density ρ [$g\ cm^{-3}$]	Comp. x [-]	Weighted Comp. x [-]	Comp. Variance s^2 [-]	Comp. Variance Uncertainty U_s^2 [-]	Comp. Variance Uncertainty Percentage $U_s^2 s^{-2}$ [%]
11(5)	1	1	74.9395	31.7213	2.3624	0.9151	0.8771	0.001622	0.000021	1.3%
		2	60.7417	27.1388	2.2382	0.8384				
		3	62.5607	27.9460	2.2386	0.8387				
		4	79.0658	33.7981	2.3394	0.9012				
	2	1	69.9648	29.5202	2.3701	0.9197	0.8796	0.001613	0.000021	1.3%
		2	60.1752	26.6638	2.2568	0.8502				
		3	56.2543	25.2130	2.2312	0.8339				
		4	73.2008	31.3035	2.3384	0.9006				
	3	1	69.6686	29.2804	2.3794	0.9252	0.8856	0.001707	0.000021	1.2%
		2	61.3083	27.0242	2.2686	0.8576				
		3	54.7494	24.5069	2.2340	0.8358				
		4	73.4734	31.2455	2.3515	0.9085				
11(10)	1	1	49.0953	20.3109	2.4172	0.9475	0.9252	0.000234	0.000008	3.4%
		2	46.1751	19.5313	2.3642	0.9161				
		3	49.5528	20.9911	2.3607	0.9140				
		4	53.1908	22.3933	2.3753	0.9228				
	2	1	56.0821	23.2619	2.4109	0.9438	0.9228	0.000223	0.000008	3.4%
		2	56.1217	23.7887	2.3592	0.9131				
		3	53.9022	22.8822	2.3556	0.9110				
		4	58.1523	24.4794	2.3756	0.9229				
	3	1	58.9450	24.5625	2.3998	0.9373	0.9243	0.000158	0.000006	4.1%
		2	58.7361	24.7376	2.3744	0.9222				
		3	56.5858	24.0836	2.3496	0.9074				
		4	62.7003	26.2726	2.3865	0.9295				
17(2)	1	1	62.0817	26.9737	2.3016	0.8781	0.8831	0.000415	0.000010	2.5%
		2	52.6630	23.2752	2.2626	0.8538				
		3	62.7814	26.9170	2.3324	0.8970				
		4	61.3227	26.2519	2.3359	0.8991				
	2	1	63.9013	27.7944	2.2991	0.8765	0.8832	0.000188	0.000007	3.7%
		2	57.1301	25.0337	2.2821	0.8660				
		3	68.3275	29.3016	2.3319	0.8966				
		4	65.2123	28.0800	2.3224	0.8909				
	3	1	68.4272	29.7789	2.2978	0.8758	0.8811	0.000432	0.000011	2.4%
		2	58.7207	25.9855	2.2597	0.8520				
		3	70.8028	30.2586	2.3399	0.9015				
		4	69.1135	29.7791	2.3209	0.8899				
17(5)	1	1	70.3031	29.9219	2.3496	0.9073	0.8851	0.000446	0.000011	2.4%
		2	60.2649	26.2319	2.2974	0.8755				
		3	58.5096	25.7776	2.2698	0.8583				
		4	70.2384	30.1945	2.3262	0.8932				
	2	1	60.2137	25.5262	2.3589	0.9130	0.8903	0.000444	0.000011	2.5%
		2	52.3582	22.8546	2.2909	0.8715				
		3	49.6227	21.6713	2.2898	0.8708				
		4	59.8736	25.6158	2.3374	0.9000				
	3	1	68.1406	29.1213	2.3399	0.9015	0.8867	0.000498	0.000012	2.3%
		2	60.0707	26.2220	2.2909	0.8715				
		3	57.3353	25.2186	2.2735	0.8607				
		4	70.0564	29.8318	2.3484	0.9066				
17(10)	1	1	58.5975	24.3222	2.4092	0.9429	0.9177	0.000408	0.000010	2.6%
		2	50.4606	21.5563	2.3409	0.9021				
		3	51.4376	22.0148	2.3365	0.8995				
		4	60.4639	25.4710	2.3738	0.9219				
	2	1	29.6066	12.1097	2.4449	0.9636	0.9396	0.000276	0.000009	3.2%
		2	25.6861	10.7560	2.3881	0.9304				
		3	26.2340	10.9725	2.3909	0.9321				
		4	30.7527	12.8753	2.3885	0.9306				
	3	1	58.4704	24.1308	2.4231	0.9510	0.9338	0.000156	0.000006	4.1%
		2	54.9080	23.0895	2.3780	0.9244				
		3	53.7867	22.6152	2.3783	0.9246				
		4	60.4655	25.2558	2.3941	0.9340				

Table G.3 Continued.

Operating Condition	Obser.	Outlet Port	Mass m [g]	True Volume V [cm^3]	True Density ρ [g cm^{-3}]	Comp. x [-]	Weighted Comp. x [-]	Comp. Variance s^2 [-]	Comp. Variance Uncertainty U_s^2 [-]	Comp. Variance Uncertainty Percentage $U_s^2 s^{-2}$ [%]
23(2)	1	1	56.9712	24.0048	2.3733	0.9216	0.8880	0.000992	0.000017	1.7%
		2	44.0350	19.1964	2.2939	0.8734				
		3	44.9192	19.9166	2.2554	0.8493				
		4	49.6079	21.2638	2.3330	0.8973				
	2	1	76.2115	32.2683	2.3618	0.9147	0.8834	0.000788	0.000015	1.9%
		2	60.4383	26.5033	2.2804	0.8650				
		3	55.0557	24.3664	2.2595	0.8519				
		4	67.2860	28.9862	2.3213	0.8902				
	3	1	46.4804	19.1482	2.4274	0.9535	0.9094	0.001213	0.000019	1.5%
		2	38.5509	16.6464	2.3159	0.8869				
		3	33.5572	14.5769	2.3021	0.8784				
		4	38.2695	16.3059	2.3470	0.9058				
23(5)	1	1	68.7822	28.8835	2.3814	0.9264	0.8914	0.000941	0.000016	1.7%
		2	58.4111	25.5774	2.2837	0.8670				
		3	53.2203	23.4246	2.2720	0.8597				
		4	73.5437	31.4400	2.3392	0.9011				
	2	1	64.8274	27.2720	2.3771	0.9238	0.8941	0.000760	0.000014	1.9%
		2	52.5500	23.0022	2.2846	0.8676				
		3	46.7431	20.4418	2.2866	0.8689				
		4	65.0327	27.7430	2.3441	0.9041				
	3	1	60.6539	25.6807	2.3619	0.9147	0.8865	0.000629	0.000013	2.1%
		2	50.3368	22.0526	2.2826	0.8663				
		3	44.9551	19.7755	2.2733	0.8605				
		4	62.2524	26.7432	2.3278	0.8942				
23(10)	1	1	76.6176	32.0943	2.3873	0.9299	0.9150	0.000341	0.000010	2.8%
		2	74.4253	31.9942	2.3262	0.8932				
		3	70.3437	29.9828	2.3461	0.9053				
		4	77.0366	32.2686	2.3874	0.9300				
	2	1	75.3346	31.5829	2.3853	0.9287	0.9157	0.000325	0.000009	2.9%
		2	70.1574	30.0980	2.3310	0.8961				
		3	69.3357	29.5947	2.3428	0.9033				
		4	75.6854	31.6536	2.3910	0.9321				
	3	1	63.9688	26.7046	2.3954	0.9347	0.9251	0.000397	0.000010	2.6%
		2	61.5915	26.1690	2.3536	0.9098				
		3	58.1179	24.7549	2.3477	0.9062				
		4	63.0213	26.0671	2.4177	0.9478				
29(2)	1	1	66.6513	28.9285	2.3040	0.8796	0.8824	0.000118	0.000006	4.8%
		2	64.5283	27.6704	2.3320	0.8967				
		3	56.0566	24.3111	2.3058	0.8807				
		4	56.6523	24.7406	2.2899	0.8708				
	2	1	63.3571	27.7095	2.2865	0.8687	0.8698	0.000246	0.000008	3.3%
		2	60.4169	26.0158	2.3223	0.8908				
		3	52.5674	23.2375	2.2622	0.8536				
		4	55.8282	24.5054	2.2782	0.8636				
	3	1	88.5701	38.6439	2.2920	0.8721	0.8722	0.000109	0.000005	4.9%
		2	85.7432	37.0996	2.3112	0.8840				
		3	75.0909	32.7532	2.2926	0.8726				
		4	75.3031	33.1777	2.2697	0.8583				
29(5)	1	1	86.3496	36.3235	2.3772	0.9239	0.8813	0.001828	0.000022	1.2%
		2	64.9799	28.8577	2.2517	0.8470				
		3	62.9008	28.2066	2.2300	0.8332				
		4	83.5877	35.7612	2.3374	0.9000				
	2	1	89.9025	37.6651	2.3869	0.9297	0.8758	0.002469	0.000026	1.0%
		2	65.7494	29.2513	2.2477	0.8445				
		3	59.8832	27.2185	2.2001	0.8139				
		4	89.3549	38.6021	2.3148	0.8862				
	3	1	92.6952	39.0213	2.3755	0.9229	0.8790	0.002203	0.000024	1.1%
		2	64.2761	28.6558	2.2430	0.8415				
		3	59.8136	27.0528	2.2110	0.8210				
		4	90.1113	38.5756	2.3360	0.8991				

Table G.3 Continued.

Operating Condition	Obser.	Outlet Port	Mass m [g]	True Volume V [cm^3]	True Density ρ [g cm^{-3}]	Comp. x [-]	Weighted Comp. x [-]	Comp. Variance s^2 [-]	Comp. Variance Uncertainty U_s^2 [-]	Comp. Variance Uncertainty Percentage $U_s^2 s^{-2}$ [%]
29(10)	1	1	73.1504	30.4377	2.4033	0.9394	0.9241	0.000131	0.000006	4.5%
		2	66.5824	28.1397	2.3661	0.9173				
		3	66.6478	28.2458	2.3596	0.9134				
		4	77.1353	32.4324	2.3783	0.9246				
	2	1	62.4399	25.9133	2.4096	0.9431	0.9186	0.000340	0.000010	2.8%
		2	56.2754	23.9787	2.3469	0.9057				
		3	56.5078	24.1334	2.3415	0.9025				
		4	66.0610	27.8618	2.3710	0.9202				
	3	1	78.2874	32.7284	2.3920	0.9327	0.9130	0.000239	0.000008	3.3%
		2	70.4854	29.9790	2.3512	0.9083				
		3	70.7698	30.3783	2.3296	0.8953				
		4	83.7138	35.4779	2.3596	0.9134				
35(2)	1	1	89.7101	38.7235	2.3167	0.8874	0.8745	0.000461	0.000011	2.3%
		2	70.3421	31.3929	2.2407	0.8400				
		3	78.4707	34.0940	2.3016	0.8781				
		4	82.7586	35.7498	2.3149	0.8863				
	2	1	78.3315	33.7398	2.3216	0.8904	0.8691	0.000374	0.000010	2.6%
		2	60.0237	26.7478	2.2441	0.8421				
		3	70.4655	30.7929	2.2884	0.8699				
		4	74.0418	32.4069	2.2848	0.8677				
	3	1	75.3459	31.9804	2.3560	0.9112	0.8797	0.000828	0.000015	1.8%
		2	58.5908	26.1319	2.2421	0.8409				
		3	66.6448	29.0667	2.2928	0.8727				
		4	70.4055	30.4442	2.3126	0.8849				
35(5)	1	1	79.1576	33.9559	2.3312	0.8962	0.8845	0.000259	0.000008	3.1%
		2	65.9952	28.6701	2.3019	0.8783				
		3	60.3675	26.5381	2.2747	0.8614				
		4	78.7719	33.8070	2.3300	0.8955				
	2	1	78.3356	33.0623	2.3693	0.9192	0.8861	0.000897	0.000015	1.7%
		2	64.0494	28.1315	2.2768	0.8627				
		3	60.3763	26.6695	2.2639	0.8546				
		4	78.4999	33.6692	2.3315	0.8964				
	3	1	80.8301	34.5733	2.3379	0.9003	0.8752	0.000689	0.000013	1.9%
		2	68.9727	30.2064	2.2834	0.8668				
		3	61.9911	27.7100	2.2371	0.8377				
		4	82.9320	35.8365	2.3142	0.8858				
35(10)	1	1	56.8603	23.6557	2.4037	0.9396	0.9188	0.000272	0.000009	3.1%
		2	46.1230	19.5948	2.3538	0.9099				
		3	44.7494	19.1290	2.3393	0.9012				
		4	58.7697	24.8081	2.3690	0.9190				
	2	1	61.2279	25.5414	2.3972	0.9358	0.9223	0.000144	0.000006	4.3%
		2	48.8568	20.7825	2.3509	0.9081				
		3	49.4019	20.9043	2.3632	0.9156				
		4	61.4065	25.8018	2.3799	0.9255				
	3	1	65.8586	27.3229	2.4104	0.9435	0.9250	0.000197	0.000007	3.7%
		2	56.0982	23.7801	2.3590	0.9131				
		3	59.2610	25.0928	2.3617	0.9146				
		4	69.9989	29.4025	2.3807	0.9260				
41(2)	1	1	77.5075	32.3486	2.3960	0.9351	0.8911	0.001977	0.000023	1.1%
		2	56.9923	24.9609	2.2833	0.8668				
		3	47.3520	21.2862	2.2245	0.8297				
		4	70.1599	29.9340	2.3438	0.9039				
	2	1	66.9588	28.0126	2.3903	0.9317	0.8861	0.002307	0.000025	1.1%
		2	47.9823	21.2460	2.2584	0.8512				
		3	40.6420	18.3460	2.2153	0.8238				
		4	62.4338	26.6226	2.3451	0.9047				
	3	1	65.4025	27.2947	2.3962	0.9352	0.8870	0.002405	0.000025	1.0%
		2	48.8912	21.4000	2.2846	0.8676				
		3	41.4171	18.8129	2.2015	0.8149				
		4	63.4057	27.1407	2.3362	0.8993				

Table G.3 Continued.

Operating Condition	Obser.	Outlet Port	Mass m [g]	True Volume V [cm^3]	True Density ρ [$g\ cm^{-3}$]	Comp. x [-]	Weighted Comp. x [-]	Comp. Variance s^2 [-]	Comp. Variance Uncertainty U_s^2 [-]	Comp. Variance Uncertainty Percentage $U_s^2 s^{-2}$ [%]
41(5)	1	1	69.8959	29.4882	2.3703	0.9198	0.8882	0.000969	0.000016	1.6%
		2	53.9330	23.3863	2.3062	0.8809				
		3	49.1326	21.8929	2.2442	0.8422				
		4	73.7365	31.6730	2.3281	0.8943				
	2	1	65.6409	27.4712	2.3894	0.9312	0.8951	0.000926	0.000016	1.7%
		2	53.7246	23.3557	2.3003	0.8773				
		3	48.6091	21.3879	2.2727	0.8602				
		4	66.8025	28.5911	2.3365	0.8994				
	3	1	73.7413	31.3234	2.3542	0.9101	0.8878	0.000546	0.000012	2.1%
		2	59.6397	25.7339	2.3176	0.8879				
		3	79.7182	34.2999	2.3242	0.8919				
		4	54.7560	24.2377	2.2591	0.8516				
41(10)	1	1	59.7010	25.0039	2.3877	0.9301	0.9149	0.000372	0.000010	2.7%
		2	51.0721	21.9923	2.3223	0.8908				
		3	51.7766	22.0878	2.3441	0.9041				
		4	61.0825	25.5966	2.3864	0.9294				
	2	1	72.1229	30.4099	2.3717	0.9206	0.9080	0.000339	0.000009	2.8%
		2	59.7247	25.7526	2.3192	0.8889				
		3	59.9938	25.8055	2.3248	0.8924				
		4	72.0158	30.2858	2.3779	0.9243				
	3	1	71.1409	29.8639	2.3822	0.9269	0.9133	0.000329	0.000009	2.8%
		2	63.0906	27.0711	2.3306	0.8958				
		3	61.8437	26.5199	2.3320	0.8967				
		4	75.3206	31.5797	2.3851	0.9286				
47(2)	1	1	56.5178	24.3925	2.3170	0.8876	0.8865	0.000704	0.000014	2.0%
		2	54.2313	22.8545	2.3729	0.9214				
		3	47.3282	20.6502	2.2919	0.8721				
		4	48.6946	21.4238	2.2729	0.8603				
	2	1	71.3081	30.8136	2.3142	0.8858	0.8776	0.000421	0.000011	2.5%
		2	67.9717	29.0976	2.3360	0.8991				
		3	54.6523	23.9309	2.2838	0.8671				
		4	58.9427	26.0763	2.2604	0.8524				
	3	1	67.1405	29.0292	2.3129	0.8850	0.8868	0.000689	0.000014	2.0%
		2	65.4613	27.6417	2.3682	0.9186				
		3	57.0217	24.6368	2.3145	0.8860				
		4	58.5471	25.8687	2.2632	0.8542				
47(5)	1	1	90.1622	37.7873	2.3860	0.9292	0.8776	0.002142	0.000024	1.1%
		2	64.2970	28.7053	2.2399	0.8395				
		3	59.5514	26.7843	2.2234	0.8289				
		4	84.8133	36.6492	2.3142	0.8858				
	2	1	96.5225	40.4330	2.3872	0.9299	0.8749	0.002085	0.000024	1.2%
		2	68.0878	30.3203	2.2456	0.8431				
		3	66.7576	30.0553	2.2212	0.8275				
		4	95.0972	41.4015	2.2969	0.8752				
	3	1	96.4818	40.5083	2.3818	0.9266	0.8777	0.002354	0.000025	1.1%
		2	67.4095	30.1577	2.2352	0.8365				
		3	64.8970	29.3133	2.2139	0.8229				
		4	92.9965	39.9305	2.3290	0.8949				
47(10)	1	1	77.3158	32.4210	2.3847	0.9284	0.9116	0.000234	0.000008	3.4%
		2	62.2181	26.6536	2.3343	0.8981				
		3	60.9392	26.1275	2.3324	0.8970				
		4	76.3912	32.2864	2.3660	0.9173				
	2	1	73.6527	30.8056	2.3909	0.9320	0.9141	0.000266	0.000008	3.2%
		2	59.8001	25.5434	2.3411	0.9023				
		3	58.1525	24.9458	2.3312	0.8962				
		4	74.6943	31.5151	2.3701	0.9197				
	3	1	62.6645	26.1560	2.3958	0.9350	0.9173	0.000184	0.000007	3.8%
		2	50.7404	21.6261	2.3463	0.9054				
		3	50.6142	21.5379	2.3500	0.9076				
		4	64.5246	27.2742	2.3658	0.9171				

Table G.3 Continued.

Operating Condition	Obser.	Outlet Port	Mass m [g]	True Volume V [cm^3]	True Density ρ [g cm^{-3}]	Comp. x [-]	Weighted Comp. x [-]	Comp. Variance s^2 [-]	Comp. Variance Uncertainty U_s^2 [-]	Comp. Variance Uncertainty Percentage $U_s^2 s^{-2}$ [%]
53(2)	1	1	64.5544	27.5554	2.3427	0.9032	0.8816	0.000410	0.000010	2.5%
		2	51.1221	22.5784	2.2642	0.8548				
		3	54.2902	23.6426	2.2963	0.8748				
		4	61.4742	26.5382	2.3164	0.8872				
	2	1	68.3023	29.0368	2.3523	0.9090	0.8860	0.000425	0.000011	2.5%
		2	53.9959	23.6976	2.2785	0.8638				
		3	57.6620	25.1684	2.2910	0.8716				
		4	63.9534	27.4954	2.3260	0.8930				
	3	1	72.6479	31.0343	2.3409	0.9021	0.8759	0.000429	0.000011	2.6%
		2	55.7519	24.4735	2.2781	0.8635				
		3	58.5244	25.8298	2.2658	0.8558				
		4	68.3473	29.7520	2.2972	0.8754				
53(5)	1	1	93.2341	40.0655	2.3270	0.8937	0.8822	0.000265	0.000008	3.1%
		2	71.3336	31.1435	2.2905	0.8712				
		3	69.0281	30.3418	2.2750	0.8616				
		4	90.8309	39.0048	2.3287	0.8947				
	2	1	72.9585	30.9656	2.3561	0.9113	0.8972	0.000173	0.000007	3.9%
		2	57.7697	24.8863	2.3213	0.8902				
		3	53.8857	23.3717	2.3056	0.8806				
		4	70.8220	30.2806	2.3389	0.9009				
	3	1	81.4490	34.7085	2.3467	0.9056	0.8908	0.000229	0.000008	3.4%
		2	64.1001	27.7574	2.3093	0.8828				
		3	61.2481	26.7463	2.2900	0.8709				
		4	80.6144	34.5575	2.3328	0.8972				
53(10)	1	1	57.2988	23.8533	2.4021	0.9387	0.9236	0.000149	0.000006	4.3%
		2	46.3584	19.6285	2.3618	0.9147				
		3	45.1475	19.1533	2.3572	0.9119				
		4	57.1135	24.0111	2.3786	0.9248				
	2	1	67.6961	28.2797	2.3938	0.9338	0.9177	0.000182	0.000007	3.9%
		2	51.6896	21.9917	2.3504	0.9079				
		3	50.3314	21.4739	2.3438	0.9039				
		4	67.2413	28.3729	2.3699	0.9196				
	3	1	72.8675	30.4961	2.3894	0.9312	0.9188	0.000173	0.000007	3.9%
		2	54.4428	23.0998	2.3569	0.9117				
		3	51.5035	22.0192	2.3390	0.9010				
		4	70.9436	29.8347	2.3779	0.9243				

G.3 Single Screw Mixer

Table G.4 Single Screw Mixer Composition Analysis Data.

Operating Condition	Obser.	Outlet Port	Mass m [g]	True Volume V [cm^3]	True Density ρ [$g\ cm^{-3}$]	Comp. x [-]	Weighted Comp. x [-]	Comp. Variance s^2 [-]
1s	1	1	68.3830	29.2787	2.3356	0.8989	0.8997	0.000002
		2	49.6744	21.2391	2.3388	0.9009		
	2	1	62.2059	26.2828	2.3668	0.9177	0.9203	0.000019
		2	44.7464	18.8219	2.3774	0.9240		
	3	1	59.8109	25.3095	2.3632	0.9155	0.9196	0.000043
		2	45.7450	19.2295	2.3789	0.9249		
2s	1	1	80.3605	33.2864	2.4142	0.9458	0.9339	0.000466
		2	48.8023	20.6693	2.3611	0.9143		
	2	1	72.0215	30.7220	2.3443	0.9042	0.9025	0.000008
		2	47.5184	20.3293	2.3374	0.9000		
	3	1	70.7526	29.1806	2.4246	0.9519	0.9487	0.000028
		2	51.3349	21.2867	2.4116	0.9443		
3s	1	1	66.3103	28.3988	2.3350	0.8985	0.9022	0.000039
		2	44.8276	19.0762	2.3499	0.9076		
	2	1	62.6618	27.0194	2.3191	0.8889	0.8895	0.000001
		2	39.5225	17.0239	2.3216	0.8904		
	3	1	70.3394	30.3366	2.3186	0.8886	0.8976	0.000221
		2	51.8854	22.0443	2.3537	0.9098		
4s	1	1	65.4802	27.7091	2.3631	0.9155	0.9196	0.000049
		2	44.7534	18.8038	2.3800	0.9256		
	2	1	77.0517	33.7788	2.2811	0.8654	0.8685	0.000031
		2	48.7626	21.2565	2.2940	0.8734		
	3	1	90.0616	38.1260	2.3622	0.9150	0.9102	0.000070
		2	59.1016	25.2340	2.3421	0.9029		
5s	1	1	72.0919	31.1926	2.3112	0.8840	0.8884	0.000061
		2	45.5006	19.5306	2.3297	0.8953		
	2	1	65.8953	27.7986	2.3705	0.9199	0.9151	0.000075
		2	40.9366	17.4241	2.3494	0.9073		
	3	1	86.5049	37.3848	2.3139	0.8857	0.8936	0.000189
		2	57.7006	24.5901	2.3465	0.9055		
6s	1	1	86.7193	37.2727	2.3266	0.8934	0.8915	0.000012
		2	55.3498	23.8736	2.3184	0.8885		
	2	1	77.5832	33.5386	2.3132	0.8853	0.8829	0.000019
		2	44.7226	19.4201	2.3029	0.8789		
	3	1	63.2178	27.5516	2.2945	0.8737	0.8770	0.000040
		2	33.9981	14.7195	2.3097	0.8831		
7s	1	1	70.6303	30.5359	2.3130	0.8851	0.8971	0.000419
		2	48.2031	20.4109	2.3616	0.9146		
	2	1	70.2056	30.5495	2.2981	0.8759	0.8963	0.001104
		2	52.7294	22.1892	2.3764	0.9234		
	3	1	73.7572	32.1999	2.2906	0.8713	0.8879	0.000799
		2	51.0027	21.6369	2.3572	0.9120		
8s	1	1	100.2664	43.2396	2.3189	0.8887	0.8849	0.000047
		2	62.5561	27.1667	2.3027	0.8788		
	2	1	88.6943	36.8382	2.4077	0.9420	0.8941	0.009181
		2	44.3207	20.3678	2.1760	0.7982		
	3	1	107.6839	44.7030	2.4089	0.9427	0.8974	0.007823
		2	56.4144	25.6948	2.1956	0.8110		
9s	1	1	67.5930	29.4638	2.2941	0.8735	0.8871	0.000532
		2	47.1712	20.0872	2.3483	0.9066		
	2	1	78.1726	33.8812	2.3073	0.8816	0.8920	0.000344
		2	48.9266	20.8060	2.3516	0.9086		
	3	1	91.4056	39.4727	2.3157	0.8868	0.8887	0.000013
		2	51.3355	22.0850	2.3245	0.8921		

Table G.4 Continued.

Operating Condition	Obser.	Outlet Port	Mass m [g]	True Volume V [cm^3]	True Density ρ [$g\ cm^{-3}$]	Comp. x [-]	Weighted Comp. x [-]	Comp. Variance s^2 [-]
10s	1	1	98.3661	41.2752	2.3832	0.9275	0.8877	0.005770
		2	53.8133	24.4391	2.2019	0.8151		
	2	1	79.0258	33.2248	2.3785	0.9247	0.8928	0.004082
		2	39.4319	17.7364	2.2232	0.8288		
	3	1	86.1319	36.5187	2.3586	0.9128	0.9006	0.000525
		2	48.7819	21.1807	2.3031	0.8791		
11s	1	1	81.1978	35.5147	2.2863	0.8686	0.8764	0.000200
		2	48.9184	21.0872	2.3198	0.8893		
	2	1	90.6895	39.3103	2.3070	0.8814	0.8870	0.000100
		2	55.2365	23.6984	2.3308	0.8960		
	3	1	78.5761	34.4443	2.2812	0.8655	0.8744	0.000271
		2	46.3554	19.9783	2.3203	0.8896		
12s	1	1	105.0127	44.6394	2.3525	0.9091	0.8824	0.002613
		2	57.1315	25.6147	2.2304	0.8334		
	2	1	92.7644	39.5819	2.3436	0.9038	0.8848	0.001396
		2	47.5968	21.1236	2.2533	0.8479		
	3	1	95.1268	40.0424	2.3757	0.9230	0.8865	0.005584
		2	45.3806	20.6835	2.1940	0.8100		
13s	1	1	81.5863	34.9272	2.3359	0.8991	0.8996	0.000001
		2	45.9332	19.6436	2.3383	0.9006		
	2	1	62.9682	26.8821	2.3424	0.9030	0.9063	0.000042
		2	32.4963	13.7791	2.3584	0.9127		
	3	1	74.9031	32.0898	2.3342	0.8980	0.8974	0.000002
		2	37.4216	16.0551	2.3308	0.8960		
14s	1	1	69.3672	30.1378	2.3017	0.8781	0.8848	0.000171
		2	35.4121	15.1747	2.3336	0.8977		
	2	1	69.1565	29.6382	2.3334	0.8975	0.9033	0.000129
		2	34.8700	14.7656	2.3616	0.9146		
	3	1	81.4505	35.0895	2.3212	0.8902	0.8907	0.000001
		2	40.9902	17.6394	2.3238	0.8917		
15s	1	1	78.8652	33.9232	2.3248	0.8923	0.8912	0.000006
		2	38.2582	16.4990	2.3188	0.8887		
	2	1	79.8219	33.9954	2.3480	0.9064	0.9057	0.000002
		2	36.8282	15.7105	2.3442	0.9041		
	3	1	110.2312	47.6602	2.3129	0.8850	0.8814	0.000057
		2	50.4413	21.9864	2.2942	0.8735		
16s	1	1	92.5495	40.3201	2.2954	0.8743	0.8709	0.000049
		2	43.0272	18.8867	2.2782	0.8636		
	2	1	88.8665	38.3733	2.3158	0.8869	0.8845	0.000023
		2	42.4661	18.4306	2.3041	0.8797		
	3	1	92.9886	40.0447	2.3221	0.8907	0.8937	0.000038
		2	43.8696	18.7675	2.3375	0.9001		
17s	1	1	96.1039	40.7700	2.3572	0.9120	0.9050	0.000195
		2	47.5377	20.4675	2.3226	0.8910		
	2	1	86.3197	37.5614	2.2981	0.8759	0.8760	0.000000
		2	36.5737	15.9145	2.2981	0.8760		
	3	1	106.5271	45.6987	2.3311	0.8962	0.8997	0.000053
		2	49.1763	20.9317	2.3494	0.9072		
18s	1	1	92.4596	40.0531	2.3084	0.8823	0.8775	0.000114
		2	36.6895	16.0825	2.2813	0.8655		
	2	1	106.1732	45.7819	2.3191	0.8889	0.8848	0.000077
		2	46.6063	20.2879	2.2972	0.8754		
	3	1	95.2753	40.8374	2.3330	0.8974	0.8974	0.000000
		2	43.5893	18.6810	2.3334	0.8975		

G.4 Uncertainty Analysis

An uncertainty analysis was performed to quantify the amount of error associated with computing the composition variance, s^2, from the four granular samples that were collected for each operating condition's observation. A Taylor series expansion propagation of error procedure (Ku, 1966), which combines the uncertainty in the mass and volume measurements with the uncertainty in the empirical correlation using the root sum of squares (RSS) procedure. Overall, the uncertainty in the double screw mixer's composition variance, U_{s^2}, ranged from 1.1 to 5.2% of the composition variance, s^2. The details of the uncertainty analysis are described below.

The error in the composition variance has two sources: (i) the uncertainty in the measured mass and volume of the samples, which are used to determine the uncertainty in the mixture density, U_ρ, and (ii) the uncertainty in the empirical correlation used to convert the measured mixture density to its composition, $U_{\rho_{corr}}$. These two uncertainties were combined using the root sum of squares:

$$U_{\rho_{total}} = \sqrt{U_\rho{}^2 + U_{\rho_{corr}}{}^2} \tag{G.1}$$

First, the uncertainty in the mixture density was determined:

$$U_\rho = \sqrt{\left(\frac{\partial \rho}{\partial m} U_m\right)^2 + \left(\frac{\partial \rho}{\partial V} U_V\right)^2} \tag{G.2}$$

where

$$\frac{\partial \rho}{\partial m} = \frac{1}{V} \tag{G.3}$$

and

$$\frac{\partial \rho}{\partial V} = \frac{-m}{V^2} \tag{G.4}$$

and U_m and U_V are the uncertainties in the mass and volume measurements, respectively. Next the uncertainty in the empirical correlation was determined:

$$U_{\rho_{corr}} = \sqrt{\left(\frac{\partial \rho_{corr}}{\partial m} U_m\right)^2 + \left(\frac{\partial \rho_{corr}}{\partial V} U_V\right)^2} \tag{G.5}$$

where

$$\frac{\partial \rho_{corr}}{\partial m} = \frac{1}{V} \tag{G.6}$$

and

$$\frac{\partial \rho_{corr}}{\partial V} = \frac{-m}{V^2} \tag{G.7}$$

For simplicity, $U_{\rho_{total}}$ will simply be referred to as U_ρ. The uncertainty in the mixture density is then propagated though to the uncertainty in the mixture composition (i.e., glass beads mass fraction) using the empirical correlation that was developed in this study and is described in Chapter 4:

$$\rho = 623.4\, x^2 + 526.8\, x + 1358 \tag{G.8}$$

where ρ is the mixture density and x is the mixture composition. Rearranging the empirical correlation to solve for the mixture composition yields:

$$x = 0.040\sqrt{(\rho - 1245.7)} - 0.423 \tag{G.9}$$

Note that two possible solutions are obtained when solving for the mixture composition; however, one of these solutions yields an unrealistic solution (i.e., negative composition) and is therefore omitted. The uncertainty in the mixture composition is then computed:

$$U_x = \sqrt{\left(\frac{\partial x}{\partial \rho} U_\rho\right)^2} \tag{G.10}$$

where

$$\frac{\partial x}{\partial \rho} = \frac{0.020}{\sqrt{\rho - 1246.7}} \tag{G.11}$$

yielding:

$$U_x = \sqrt{\left(\frac{0.633}{\sqrt{\rho - 1.25}} U_\rho\right)^2} \tag{G.12}$$

The uncertainty in the composition variance, U_{s^2}, can then be determined by determining the uncertainty in each of the contributing terms. First, the definition of the composition variance:

$$s^2 = \frac{\sum_{i=1}^{i=n} m_i \left(x_i - \overline{x_w}\right)^2}{\left(\frac{N-1}{N}\right) \sum_{i=1}^{i=n} m_i} \tag{G.13}$$

where n is the number of the i^{th} sample, m_i is the mass of the i^{th} sample, x_i is the composition of the i^{th} sample, $\overline{x_w}$ is the mass weighted mean composition of the samples, and N is the total number of samples, is expanded out to yield:

$$s^2 = \frac{m_1\left(x_1 - \overline{x_w}\right)^2 + m_2\left(x_2 - \overline{x_w}\right)^2 + m_3\left(x_3 - \overline{x_w}\right)^2 + m_4\left(x_4 - \overline{x_w}\right)^2}{\frac{N-1}{N}\left(m_1 + m_2 + m_3 + m_4\right)} \tag{G.14}$$

where m_i and x_i correspond to the mass and composition of the sample from outlet ports one through four, and:

$$\overline{x_w} = \frac{m_1 x_1 + m_2 x_2 + m_3 x_3 + m_4 x_4}{m_1 + m_2 + m_3 + m_4} \tag{G.15}$$

For simplicity, the sum of the four outlet ports' mass can be rewritten as:

$$m_{total}=m_1+m_2+m_3+m_4 \tag{G.16}$$

and a dummy variable, N' can be assigned:

$$N'=\frac{N-1}{N} \tag{G.17}$$

resulting in Eqn. (G.14) to be rewritten as:

$$s^2=\frac{m_1\left(x_1-\overline{x_w}\right)^2+m_2\left(x_2-\overline{x_w}\right)^2+m_3\left(x_3-\overline{x_w}\right)^2+m_4\left(x_4-\overline{x_w}\right)^2}{N'\,m_{total}} \tag{G.18}$$

The uncertainty in the weighted composition is then determined:

$$U_{\overline{x_w}}=\left(\left(\left(\frac{\partial\overline{x_w}}{\partial m_1}U_m\right)^2+\left(\frac{\partial\overline{x_w}}{\partial x_1}U_x\right)^2+\left(\frac{\partial\overline{x_w}}{\partial m_2}U_m\right)^2+\left(\frac{\partial\overline{x_w}}{\partial x_2}U_x\right)^2+\left(\frac{\partial\overline{x_w}}{\partial m_3}U_m\right)^2+\left(\frac{\partial\overline{x_w}}{\partial x_3}U_x\right)^2+\left(\frac{\partial\overline{x_w}}{\partial m_4}U_m\right)^2+\left(\frac{\partial\overline{x_w}}{\partial x_4}U_x\right)^2\right)\right)^{\frac{1}{2}} \tag{G.19}$$

where

$$\frac{\partial\overline{x_w}}{\partial m_1}=\frac{x_1\left(m_{total}-m_1\right)}{\left(m_{total}\right)^2}-\frac{m_2x_2}{m_{total}^2}-\frac{m_3x_3}{m_{total}^2}-\frac{m_4x_4}{m_{total}^2} \tag{G.20}$$

$$\frac{\partial\overline{x_w}}{\partial x_1}=\frac{m_1}{m_{total}} \tag{G.21}$$

$$\frac{\partial\overline{x_w}}{\partial m_2}=\frac{x_2\left(m_{total}-m_2\right)}{\left(m_{total}\right)^2}-\frac{m_1x_1}{m_{total}^2}-\frac{m_3x_3}{m_{total}^2}-\frac{m_4x_4}{m_{total}^2} \tag{G.22}$$

$$\frac{\partial\overline{x_w}}{\partial x_2}=\frac{m_2}{m_{total}} \tag{G.23}$$

$$\frac{\partial\overline{x_w}}{\partial m_3}=\frac{x_3\left(m_{total}-m_3\right)}{\left(m_{total}\right)^2}-\frac{m_1x_1}{m_{total}^2}-\frac{m_2x_2}{m_{total}^2}-\frac{m_4x_4}{m_{total}^2} \tag{G.24}$$

$$\frac{\partial \overline{x_w}}{\partial x_3} = \frac{m_3}{m_{total}} \tag{G.25}$$

$$\frac{\partial \overline{x_w}}{\partial m_4} = \frac{x_4\left(m_{total}-m_4\right)}{\left(m_{total}\right)^2} - \frac{m_1 x_1}{m_{total}^{\ 2}} - \frac{m_2 x_2}{m_{total}^{\ 2}} - \frac{m_3 x_3}{m_{total}^{\ 2}} \tag{G.26}$$

$$\frac{\partial \overline{x_w}}{\partial x_4} = \frac{m_4}{m_{total}} \tag{G.27}$$

The uncertainty in the weighted composition is then computed:

$$U_{\overline{x_w}} = \left(\begin{array}{l} \left(\left(\left(\frac{x_1\left(m_{total}-m_1\right)}{\left(m_{total}\right)^2} - \frac{m_2 x_2}{m_{total}^{\ 2}} - \frac{m_3 x_3}{m_{total}^{\ 2}} - \frac{m_4 x_4}{m_{total}^{\ 2}} \right) U_m \right)^2 + \left(\frac{m_1}{m_{total}} U_x \right)^2 \right) \\ + \left(\left(\frac{x_2\left(m_{total}-m_2\right)}{\left(m_{total}\right)^2} - \frac{m_1 x_1}{m_{total}^{\ 2}} - \frac{m_3 x_3}{m_{total}^{\ 2}} - \frac{m_4 x_4}{m_{total}^{\ 2}} \right) U_m \right)^2 + \left(\frac{m_2}{m_{total}} U_x \right)^2 \\ + \left(\left(\frac{x_3\left(m_{total}-m_3\right)}{\left(m_{total}\right)^2} - \frac{m_1 x_1}{m_{total}^{\ 2}} - \frac{m_2 x_2}{m_{total}^{\ 2}} - \frac{m_4 x_4}{m_{total}^{\ 2}} \right) U_m \right)^2 + \left(\frac{m_3}{m_{total}} U_x \right)^2 \\ + \left(\left(\frac{x_4\left(m_{total}-m_4\right)}{\left(m_{total}\right)^2} - \frac{m_1 x_1}{m_{total}^{\ 2}} - \frac{m_2 x_2}{m_{total}^{\ 2}} - \frac{m_3 x_3}{m_{total}^{\ 2}} \right) U_m \right)^2 + \left(\frac{m_4}{m_{total}} U_x \right)^2 \end{array} \right)^{\frac{1}{2}} \tag{G.28}$$

allowing the uncertainty in the composition variance to be determined:

$$U_{s^2} = \left(\begin{array}{l} \left(\frac{\partial s^2}{\partial m_1} U_m \right)^2 + \left(\frac{\partial s^2}{\partial x_1} U_x \right)^2 + \left(\frac{\partial s^2}{\partial m_2} U_m \right)^2 + \left(\frac{\partial s^2}{\partial x_2} U_x \right)^2 + \left(\frac{\partial s^2}{\partial m_3} U_m \right)^2 \\ + \left(\frac{\partial s^2}{\partial x_3} U_x \right)^2 + \left(\frac{\partial s^2}{\partial m_4} U_m \right)^2 + \left(\frac{\partial s^2}{\partial x_4} U_x \right)^2 + \left(\frac{\partial s^2}{\partial \overline{x_w}} U_{\overline{x_w}} \right)^2 \end{array} \right)^{\frac{1}{2}} \tag{G.29}$$

where

$$\frac{\partial s^2}{\partial m_1} = \frac{\left(m_{total}-m_1\right)\left(\overline{x_w}-x_1\right)^2 + m_2\left(x_2-\overline{x_w}\right)^2 + m_3\left(x_3-\overline{x_w}\right)^2 + m_4\left(x_4-\overline{x_w}\right)^2}{m_{total}^{\ 2} N'} \tag{G.30}$$

$$\frac{\partial s^2}{\partial x_1} = \frac{2m_1\left(x_1 - \overline{x_w}\right)}{m_{total}N'} \tag{G.31}$$

$$\frac{\partial s^2}{\partial m_2} = \frac{\left(m_{total} - m_2\right)\left(\overline{x_w} - x_2\right)^2 + m_1\left(x_1 - \overline{x_w}\right)^2 + m_3\left(x_3 - \overline{x_w}\right)^2 + m_4\left(x_4 - \overline{x_w}\right)^2}{m_{total}^{\ 2}N'} \tag{G.32}$$

$$\frac{\partial s^2}{\partial x_2} = \frac{2m_2\left(x_2 - \overline{x_w}\right)}{m_{total}N'} \tag{G.33}$$

$$\frac{\partial s^2}{\partial m_3} = \frac{\left(m_{total} - m_3\right)\left(\overline{x_w} - x_3\right)^2 + m_1\left(x_1 - \overline{x_w}\right)^2 + m_2\left(x_2 - \overline{x_w}\right)^2 + m_4\left(x_4 - \overline{x_w}\right)^2}{m_{total}^{\ 2}N'} \tag{G.34}$$

$$\frac{\partial s^2}{\partial x_3} = \frac{2m_3\left(x_3 - \overline{x_w}\right)}{m_{total}N'} \tag{G.35}$$

$$\frac{\partial s^2}{\partial m_4} = \frac{\left(m_{total} - m_4\right)\left(\overline{x_w} - x_4\right)^2 + m_1\left(x_1 - \overline{x_w}\right)^2 + m_2\left(x_2 - \overline{x_w}\right)^2 + m_3\left(x_3 - \overline{x_w}\right)^2}{m_{total}^{\ 2}N'} \tag{G.36}$$

$$\frac{\partial s^2}{\partial x_4} = \frac{2m_4\left(x_4 - \overline{x_w}\right)}{m_{total}N'} \tag{G.37}$$

$$\frac{\partial s^2}{\partial \overline{x_w}} = \frac{2\left(m_{total}\overline{x_w} - m_1x_1 - m_2x_2 - m_3x_3 - m_4x_4\right)}{m_{total}N'} \tag{G.38}$$

The total uncertainty in the composition variance is then determined:

$$U_{s^2} = \left(\left(\left(\left(\frac{(m_{total}-m_1)(\overline{x_w}-x_1)^2 + m_2(x_2-\overline{x_w})^2 + m_3(x_3-\overline{x_w})^2 + m_4(x_4-\overline{x_w})^2}{m_{total}^2 N'} \right) U_m \right)^2 + \left(\left(\frac{2m_1(x_1-\overline{x_w})}{m_{total}N'} \right) U_x \right)^2 + \left(\left(\frac{(m_{total}-m_2)(\overline{x_w}-x_2)^2 + m_1(x_1-\overline{x_w})^2 + m_3(x_3-\overline{x_w})^2 + m_4(x_4-\overline{x_w})^2}{m_{total}^2 N'} \right) U_m \right)^2 + \left(\left(\frac{2m_2(x_2-\overline{x_w})}{m_{total}N'} \right) U_x \right)^2 + \left(\left(\frac{(m_{total}-m_3)(\overline{x_w}-x_3)^2 + m_1(x_1-\overline{x_w})^2 + m_2(x_2-\overline{x_w})^2 + m_4(x_4-\overline{x_w})^2}{m_{total}^2 N'} \right) U_m \right)^2 + \left(\left(\frac{2m_3(x_3-\overline{x_w})}{m_{total}N'} \right) U_x \right)^2 + \left(\left(\frac{(m_{total}-m_4)(\overline{x_w}-x_4)^2 + m_1(x_1-\overline{x_w})^2 + m_2(x_2-\overline{x_w})^2 + m_3(x_3-\overline{x_w})^2}{m_{total}^2 N'} \right) U_m \right)^2 + \left(\left(\frac{2m_4(x_4-\overline{x_w})}{m_{total}N'} \right) U_x \right)^2 + \left(\left(\frac{2(m_{total}\overline{x_w}-m_1x_1-m_2x_2-m_3x_3-m_4x_4)}{m_{total}N'} \right) U_{\overline{x_w}} \right)^2 \right)^{\frac{1}{2}} \quad \text{(G.39)}$$